Structure and Properties of Atomic Nanoclusters

Julio A. Alonso

Imperial College Press

Structure and Properties of Atomic Nanoclusters

This page intentionally left blank

Structure and Properties of Atomic Nanoclusters

Julio A. Alonso
Universidad de Valladolid, Spain

Imperial College Press

ICP

Printed in Singapore.

Dedicated to Yolanda, Cristina, Victor, Alejandra and Helena.

This page intentionally left blank

Foreword

Towards the end of my stay as a postdoctoral fellow at the University of Pennsylvania, I asked my supervisor, Professor L. A. Girifalco, which are the topics, in his opinion, that would be good for research in the future. He suggested as one of the topics "small particles", a term used in the early 1980s for an emerging field devoted to the study of small groups of atoms, or atomic clusters – nanoscience was not yet a fashionable term. This insightful advice was given a few years before the two key experimental discoveries in the field. One of those was the observation and explanation of electronic shell effects in metallic clusters in 1984. The second was the detection, only a few months later, of the fullerene cluster C_{60} and the proposal for its peculiar cage structure. The First International Symposium on Small Particles and Inorganic Clusters (ISSPIC-1) had taken place in Lyon in 1976. With the passing of time this symposium established itself as the main joint activity in this field, and ISSPIC-12 took place in Nanjing in 2004. The advice I received from Professor Girifalco gave me the motivation to initially dedicate a modest fraction of my research effort to the study of atomic clusters, and this involvement later increased until it became my main research activity. Due to this interest I have been able to follow the development of the now mature cluster field.

In this monograph I present some of the main developments in atomic clusters and the actual status of the field. The range of topics covered is broad, but evidently not comprehensive, and this is due to several reasons. One is my own interest, which is reflected in the selection of topics and illustrative examples. The second reason has to do with the limitations of my knowledge of the field. Third, I consider an in-depth presentation of a limited number of topics more adequate than a lighter presentation of an enlarged list of topics or systems. Finally, I have tried to achieve a proper balance between those considerations and the size of the monograph.

The book is intended to be useful to graduate students in the fields of Nanoscience, Molecular Sciences and Condensed Matter, and also to scientists interested in entering the field of Atomic Clusters.

Contents

Acknowledgments

This page intentionally left blank

1. Introduction to Clusters

1.1 The Field of Clusters

Atomic clusters are aggregates of atoms containing from few to a few thousand atoms. Due to their small size, the properties of the clusters are, in general, different from those of the corresponding material in the macroscopic bulk phase. The differences result from the fact that the number of atoms forming the surface is a substantial fraction of the number of atoms forming the cluster, while this fraction is negligible in the case of a macroscopic solid (of course the surface of a solid is relevant in itself, giving rise to the technologically important field of surface science). Many of the differences between clusters and bulk can also be viewed as arising from the small volume of the potential well confining the electrons in the clusters. In this case the electrons fill discrete levels, instead of having the continuous distribution (bands) characteristic of the solid. Of course the two views are inter-related. By studying the properties of clusters, scientists expect to obtain information on the early stages of growth of matter, and on the evolution of the properties towards the bulk. An interesting question which still lacks a convincing answer in many cases is the following: how many atoms are required for a cluster to show the properties of the bulk material? To make affairs more complicated, sometimes different properties of a given type of clusters appear to converge at a different rate. But, even more important, is knowing the precise behavior of a given property, like the cluster geometry, or the values of the ionisation potential, as the number of atoms increases one by one. These questions have motivated the development of experimental techniques for producing small clusters, as well as a series of experimental and theoretical studies of their structure and properties. The existence of especially stable clusters is sometimes advocated to construct models of amorphous materials.

Two discoveries, nearly simultaneous in time, stand at the top of the field of clusters, and have added strong impetus for its development. The first one, reported by Knight and coworkers in 1984, is the discovery of magic numbers in the abundance of clusters of the alkali metals [1]. These magic numbers are interpreted as reflecting an electronic structure characterized by the formation of discrete electronic shells separated by energy gaps, like electrons in atoms or nucleons in nuclei. In short, clusters with filled electronic shells are more stable and less reactive than clusters with open shells. This parallels the behavior of atoms across the Periodic Table: the inert gas atoms He, Ne, Ar, Kr, Xe and Rn have filled electronic shells, and consequently they are chemically unreactive. Also, some particular nuclei are specially stable because the nucleons (protons and neutrons) have a structure of closed shells in those nuclei. In summary, this is a general property of fermions moving in a common potential well of finite size. In fact, the shape of the potential well confining the electrons in the alkali metal clusters (smooth and nearly constant inside the cluster and rising abruptly at the surface) is qualitatively more similar to the potential well binding the nucleons in the nuclei as opposed to the potential that the electrons feel in the atom, where the strong Coulombic attraction of the highly charged point nucleus, screened of course by the core electrons, dominates. The electronic shell effects become reflected in many properties of clusters of the simple metals (with *sp* electrons) and many examples are discussed throughout this monograph. The second key work was the discovery by Kroto *et al.* [2] of the C_{60} fullerene in 1985 and the proposal of its peculiar cage structure. Those two discoveries were made possible by the efforts in many laboratories in developing experimental methods to produce clusters in the gas phase as molecular beams. Those experimental methods are described in Chapter 2. It is also worth noting that the experimental confirmation of the structure proposed for the fullerene was achieved five years after the discovery of C_{60}, when a method was developed [3] to purify and separate C_{60} in quantities large enough to allow spectroscopic studies to be performed.

Close in importance to these two key discoveries are other findings that will be discussed at length in this volume: like the formation of shells of atoms in the clusters of the inert gases [4], the excitation of collective modes similar to the giant dipole excitation of nuclei, *etc.* The spatial arrangement of the atoms, that is, the geometrical structure, is the

source of the differences between the properties of clusters of similar sizes; sizes that can differ by just one atom. In contrast to bulk solids, the structure of clusters is difficult to assign. Even more, several (or many) low lying isomers (for a given cluster size) often exist with binding energies differing very little from that of the ground state. This means that different isomers may be populated under typical experimental conditions. On the other hand, the existence of many isomers makes the theoretical identification of the ground state difficult, even if one uses sophisticated computational methods based on first principles theory.

1.2 Types of Clusters

The clusters can be classified according to the type of chemical bonding between the atoms forming the aggregate. The types of clusters that are considered in this monograph are now briefly introduced. The list is broad but it may not be comprehensive, since it reflects the personal selection of the author, motivated by reasons like his own interest and experience. For the same reasons, a selection of examples, taken from the abundant literature, has been made for the different types of clusters, but it is hoped that the selection reflects faithfully the relevant characteristics and properties of each type.

1.2.1 Van der Waals clusters

The interactions between inert gas atoms are weak and can be described accurately by central pair forces. The origin of the short-range repulsive part of the interaction is the quantum mechanical repulsion between cores with closed shell electronic configurations, and the attractive part is due mainly to the induced-dipole dispersion force. The strength of the binding is about 0.3 eV per atom or less. Due to the simple central force the most stable clusters are those with high atomic density, that is, with a close-packing of atoms. The weak binding leads to low melting and boiling points, and have made these clusters attractive to experimentalists. The simplicity of the interatomic forces makes them equally popular between theorists, who have used molecular dynamics techniques to simulate and enlighten the difficult problem of the solid to

liquid phase transition in systems with a small number of atoms. Van der Waals clusters are treated in Chapter 3. Molecular clusters, formed as aggregates of closed shell molecules, like $(I_2)_N$, $(N_2)_N$, $(CO_2)_N$, $(SF_6)_N$ also belong to this class. Aggregates of inert gas atoms also form in cavities in metals during ion beam mixing experiments [5]. In those experiments, inert gas ions with high kinetic energies are used to induce the mixing of metallic multilayers to produce amorphous alloys.

1.2.2 Metal clusters

The interatomic forces in metals are not simple. Many metals have non close-packed structures because the interatomic forces are partially directional. One can distinguish between simple metals, like Na or Al, with valence electrons of *sp* character, and transition metals, like Fe or Co, where the localized *d* electrons play an important role. Some polyvalent nontransition elements like Pb form a group inbetween. The clusters reflect these characteristics. The strength of the binding in metallic clusters ranges from moderate to strong, say from 0.5 to 3 eV per atom.

The main property of the clusters of the simple *sp* elements is the existence of electronic shell effects [1], discussed in detail in Chapter 4. There is a close connection between geometrical and electronic structure at the beginning of the growth staircase, when the addition of each new atom changes the properties of the system substantially. The simplicity of the *sp* clusters captured the attention of theorists and experimentalists, and a lot of progress has been made in the understanding of their electronic properties, which is reported in Chapter 5. In particular, the delocalized character of the electronic states allows for the occurrence of collective electronic excitations at relatively low energies. The induced fragmentation of these clusters, reviewed in Chapter 6, is also influenced by electronic shell effects. The solid to liquid phase transition, also considered in Chapter 6, is still an open problem. The observed trends are complex and the theoretical studies encounter two main difficulties. First, the interatomic potential is complex; strictly speaking it is a many-atom interaction as opposed to the simple two-body force of the Van der Waals clusters, and this makes designing potentials that could be used with confidence in molecular dynamics simulations a very difficult task. Of course, accurate first principles techniques are now available, but these become computationally very demanding as the cluster size

increases. Since the surface atoms represent a substantial fraction of the cluster, it is not surprising that the simulations seem to indicate the occurrence of steps in the melting transition.

The variety of bulk metallic alloys is enormous because many different elements can be combined, and for a given A–B pair, there is an additional variable, the relative concentration of the two components. Similarly, many A_nB_m mixed bimetallic clusters have been produced and their variety is also enormous: the nature of the elements and their relative compositions are again the relevant variables. The properties of alloy clusters are studied in Chapter 7. Mixing two elements in the adequate proportion may be a way to produce highly stable clusters that could form the building blocks of future cluster assembled new materials.

The *d* electrons present in the transition metals make the corresponding clusters substantially more complex than the clusters of the *sp* elements. Their structure and electronic properties are considered in Chapter 8. Part of the interest in these clusters comes from their potential use in catalysis, and in fact, their reactivity with different molecular species has been studied. Another topic of great interest deals with the magnetic properties, especially the nature of the magnetic ordering and its evolution with the size of the cluster. Chapter 9 presents a discussion of the trends in this evolution.

1.2.3 Clusters of ionic materials

Ionic materials are composed of closed shell ions, for instance Na^+ cations and Cl^- anions in the NaCl salt. In general these materials are formed from electropositive metals on the left side of the Periodic Table and electronegative elements on the right side. The cohesion in $(NaCl)_N$ and similar clusters can be described by potentials composed of an attractive part due to electrostatic monopole forces and a repulsive part from the quantum mechanical overlap of the electronic clouds of ions with filled electronic shells. The bonding is strong: 2–4 eV/atom. The structures of many of these clusters, described in Chapter 10, can be interpreted as having the shape of rectangular nanocrystals cut from the solid. This is in accordance with the brittle character of the bulk crystals. Some computer simulations of the assembling of clusters to form new materials suggest that it may be possible to assemble solids formed by

large anionic clusters separated by cations, with a structure similar to that of the typical ionic crystals. In fact, this is also the structure of some natural alloys.

1.2.4 Network clusters

Covalent bonding leads to the formation of atomic networks in clusters of materials like Si, Ge and C. Networks also form in the corresponding solid crystals and in the amorphous forms of those elements. Since many atoms in small clusters are on the cluster surface, these surface atoms have dangling bonds and important structural reconstruction is expected, as in the case of the solid surfaces. The binding energy in network clusters is strong, typically between 1 and 4 eV per atom or more. Network clusters are studied in Chapter 11, taking as representative examples first carbon clusters, since the popular C_{60} fullerene belongs to this class, and then the so called metcars, formed by carbon and transition metal atoms.

1.2.5 Cluster assembled solids

The possibility of building highly stable and symmetrical nanostructures makes the class of network clusters the most promising one for the purposes of cluster assembling. In fact the self-assembling of C_{60} clusters to form the fullerite solid provides the best example [3], as discussed in Chapter 12. This chapter discusses the idea and the possibilities of building new materials by assembling very stable clusters.

References

1. Knight, W. D., Clemenger, K., de Heer, W. A., Saunders, W. A., Chou, M. Y., and Cohen, M. L., *Phys. Rev. Lett.*, **52**, 2141 (1984).
2. Kroto, H. W., Heat, J. R., O'Brian, S. C., Curl, R. F., and Smalley, R. E., *Nature*, **318**, 162, (1985).
3. Krätschmer, W., Lamb, L. D., Fostiropoulos, K., Huffman, D. R., *Nature* **347**, 354, (1990).
4. Echt, O., Sattler, K., and Rechnagel, E., *Phys. Rev. Lett.*, **47**, 1121 (1981).
5. Mitchell, D. R. G., Donnelly, S. E., and Evans, J, H., *Phil. Mag. A* , **61**, 53 (1990).

2.   Experimental Production of Clusters

2.1 Formation of Clusters in Matrices

2.1.1 Chemical reaction in a liquid medium

Several procedures have been used to obtain particles with sizes in the 1–50 nanometer scale through chemical reactions. Those procedures vary from simple precipitations to chemical reductions, including hydrolisis processes, thermal decompositions, *etc.* For example a procedure for obtaining amorphous NdFeB magnetic nanoparticles [1] consists of the reduction of Fe^{2+} and Nd^{3+} salts using borohydride ions in aqueous solution. The concentration and speed of addition of the reactants, the control of the pH, the temperature and the atmosphere under which the reaction is carried out are parameters affecting the characteristics of the particles obtained. In order to control the growth of the particles and fix their size so as to obtain a quasi-monodisperse distribution of particles, procedures have been developed based on carrying out the reaction in a microstructured medium. The use of microemulsions is particularly convenient because the system is thermodynamically stable and easy to reproduce, and the size of the microreactor (microdroplets) can be easily controlled. Semiconductor and metallic nanoparticles can be produced by injecting molecular precursors into a hot surfactant solution [2]. For instance, monodisperse cobalt nanoparticles are formed by the thermal decomposition of carbonyl dicobalt, $Co_2(CO)_8$. This decomposes according to the reaction $Co_2(CO)_8 \rightarrow 2Co + 8\ CO$, and an appropriate combination of surfactants and stabilizing ligands controls the growth and stabilizes the particles, also preventing their oxidation [3].

Gold clusters have been grown by a condensation process [4] starting from unstable AuSR stoichiometric molecules (SR indicates an alkyl

thiolate, where R = C_nH_{2n+1} and S is a sulfur atom binding to the gold atom), in the presence of excess RSSR

$$N(AuSR) \rightarrow Au_N(SR)_M, \quad N \gg M. \tag{2.1}$$
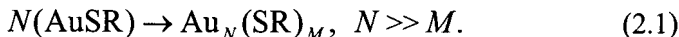
This process can be stimulated at room temperature by the action of a reducing agent, like dispersed Na

$$Na + AuSR \rightarrow NaSR + Au. \tag{2.2}$$
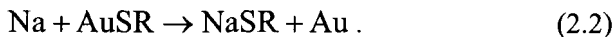
The liberated gold atoms combine to form the growing clusters, and coalescence of clusters is prevented by the presence of RSSR groups weakly bound to the cluster surface.

X-ray irradiation has been used to induce the chemical reactions that lead to the formation of copper clusters in aqueous solutions of $CuCl_2$ [5]. The secondary radiation produced through scattering of the incident X-rays causes the formation of hydrated electrons (e^-_{aq}), which in turn react with the Cu^{2+} ions in the solution and cause their reduction by a two step process

$$e^-{}_{aq} + Cu^{2+} \rightarrow Cu^+, \tag{2.3}$$

$$e^-{}_{aq} + Cu^+ \rightarrow Cu^0. \tag{2.4}$$

A distribution of Cu clusters with diameters ranging from 5 to 10 Å is observed, although the exact kinetics of agglomeration to form the clusters is not known. Radiolytic reduction of aqueous solutions of copper compounds and organic molecules leading to formation of Cu clusters has also been observed [6].

2.1.2 Irradiation of a solid

Irradiation of an ionic crystal like LiF with neutrons produces interstitial Li atoms as well as other types of defects in the crystal. When the irradiation dose is large enough (higher than 3×10^{21} neutrons/m²), the Li atoms tend to agglomerate forming Li clusters. Irradiation of lithium

oxide (Li_2O) with electrons leads to the formation of Li nanoclusters with a few thousand atoms [7, 8].

Another irradiation technique is ion implantation in glass matrices. Sequential implantation of two different elements, for instance Cu^+ and Au^+, produces alloy clusters of nanometer size [9]. The energy and dose can be tailored so as to control the relative concentration.

2.1.3 Immersion of a porous glass in a liquid metal

Some inorganic glasses related to SiO_2 contain near spherical cavities with diameters up to 30 nm. When the porous glass is immersed in a molten metal and pressures up to 7000 torr are applied, the metal atoms enter the small pores forming droplets. Zeolites are minerals that contain natural microscopic cavities which can easily accommodate metallic clusters. Fe aggregates trapped into the pores of zeolites and silica minerals form the active ingredient of some commercial catalysts used in the production of hydrocarbons starting with CO and H_2. Other clusters in zeolites catalyze the polymerization of ethylene to give polyethylene.

2.1.4 Condensation on a substrate

A metallic vapor obtained by heating a metal in an oven can be condensed on an inert solid substrate (NaCl or a metallic oxide). In this way clusters of nanometric dimensions are formed by diffusion-controlled aggregation [10]. Thin films formed by clusters have also been prepared. On the other hand atomic manipulation with the STM (Scanning Tunneling Microscope) constitutes a well controlled route for nanofabrication, and arrays of clusters have been produced by moving the STM tip. The production of arrays and films of atomic clusters would be of great interest for the microelectronics industry [11]. The possibility of building parts of circuits with nanosize clusters would allow the fabrication of electronic devices at a molecular scale. Applications are also envisaged in optical memories and image processing. Molecular Beam Epitaxy is employed nowadays to produce crystalline semiconductor superlattices of high quality. Use of a beam of clusters, instead of atoms, would allow the production of more complex superstructures.

2.2 Liquid Metal Ion Source

This method has been used to produce clusters of metals with low melting points, like rubidium [12]. The metal is first placed in an oven. By differential heating, Rb is distilled into a tungsten capillary needle, which is itself heated to keep Rb in the liquid state. By establishing a high electric field between the tip of the capillary needle and an extraction electrode, copious field emission of cluster ions of different sizes results when the potential difference between the tungsten needle and the extractor electrode exceeds 2 kV. An assembly of electrostatic lenses is used to collimate the ion beam. Single charged and multiply charged clusters are produced in this way.

2.3 Ion Bombardment

A beam of inert gas ions with a high kinetic energy, for instance Xe^+ of 10 kV energy, directed towards the sample (spot size about 1 mm in diameter) removes cluster ions. In this way positively and negatively charged clusters of the noble metal and Zn groups have been obtained [13]. Sputtering by ion bombardment of solid surfaces is a relatively cheap method for the production of clusters even from materials with a high boiling temperature. The method has been used in particular to produce clusters of ionic materials, like alkali halides.

Ion induced erosion of a solid is explained by the collision cascades originating from the impacts of single primary ions. There is the consensus that a cluster stems from atoms of a collision cascade excited by a single projectile. Disagreement exists, however, whether the atoms forming an emerging cluster originate from neighboring lattice sites in the solid or whether cluster formation is a statistical recombination process of independently sputtered atoms from one collision cascade.

2.4 Supersonic Nozzle Sources

Figure 2.1 shows the main chamber of a supersonic nozzle source used in obtaining alkali metal clusters. The nozzle is composed of a channel, typically 0.15 mm long, terminated in a hole aperture with a diameter

smaller than 0.8 mm. The nozzle is mounted at the end of a nozzle tube and the other end of that tube is connected to the reservoir [14]. Metal of high purity is introduced into the reservoir through a heated inlet pipe. The source and nozzle are further heated so that the desired metal vapor pressure (50–300 Torr) is obtained, and the nozzle is kept about 100 K hotter that the reservoir to prevent plugging. The vapor exiting the nozzle then adiabatically expands into the vacuum, and the density and temperature of the jet decrease rapidly (typically, the density and temperature in an argon beam are reduced by about 25% and 13%, respectively, within one nozzle diameter from the nozzle exit [15]). Clusters form both in the nozzle channel and in the region just outside the nozzle.
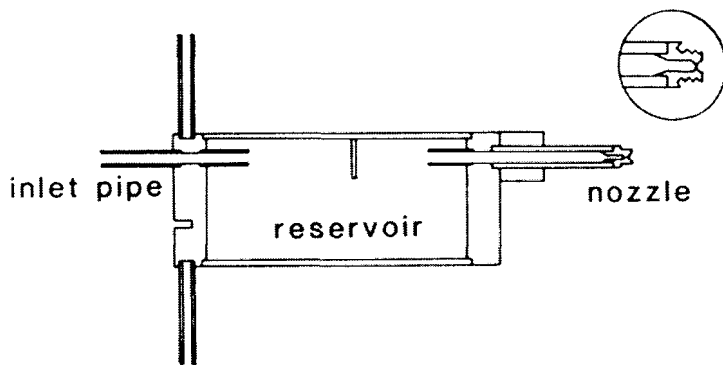
Figure 2.1. Supersonic nozzle source chamber. Reproduced from W. A. de Heer *et al.*, *Solid State Physics* **40**, 93 (1987) with permission of Academic Press.

The product P_0D, where P_0 is the gas pressure just before it enters the nozzle channel and D is the nozzle diameter, is an important parameter controlling cluster formation. For small values of P_0D (larger, however, than a threshold value) most aggregates are produced in the throat. For larger values of P_0D, progressively more clusters are produced outside the nozzle.

This pure vapor source is efficient to produce Van der Waals clusters. In the case of metallic clusters it produces mainly small clusters, and some medium size clusters but with very low abundances. This source is not well suited for the formation of large metallic clusters

because the process of atom aggregation leaves the cluster in an excited state and the metal vapor must act also as a heat bath to cool the clusters.

2.4.1 Kinetics of coagulation

When atoms begin to condense, the cluster growth first proceeds by successive addition of monomers, and when the supply of these decreases, fusion of larger clusters increasingly contributes. These two processes are characterized by typical size distributions. Nucleation theory predicts exponentially decreasing size distributions in the first case. On the other hand, growth of particles by coalescence leads to a Gaussian distribution for the logarithm of the size. Although both behaviors had been seen earlier, the transition from monomer addition to coagulation was only clearly demonstrated after the experimental work of Soler *et al.* [16] for the formation of CO_2 clusters. Working at a temperature $T = 225$ K, an exponential intensity decrease was observed up to pressures of 700 mbar. The abundance distributions then became gradually peaked with increasing pressure, and for P_0 higher than 2000 mbar, small clusters were absent. These experimental results were explained by a model that allows the size distribution to be fitted as a function of a single parameter which measures the degree of condensation. If evaporation processes are neglected, the kinetic equations for the concentration (per unit volume) of clusters of size k can be written [16]

$$\frac{dn_k}{dt} = \sum_{i+j=k} C_{ij} n_i n_j - \sum_i C_{ik} n_i n_k . \tag{2.5}$$

The first term on the right hand side is the rate at which clusters of size k are formed by coagulation and the second is the rate at which these are lost by growth to larger sizes. Assuming thermal velocities for all the k-mers, the rate coefficients are

$$C_{ij} = 2\sigma_{ij} \left(\frac{2k_B T}{m\pi} \right)^{\frac{1}{2}} \left(\frac{i+j}{ij} \right)^{\frac{1}{2}} \tag{2.6}$$

where T is the temperature, k_B is the Boltzmann constant and m is the mass (equal) of all monomers. A crucial feature is that $C_{1j} \gg C_{ij}$ for $i \gg 1$. This means that monomer addition dominates the kinetics of the early stages of growth because of the fast thermal monomer motion. The cross section $\sigma_{ij} = f_{ij}\sigma_{ij}^0$ is the product of a geometrical cross section σ_{ij}^0 proportional to $(i^{1/3} + j^{1/3})^2$ and a sticking coefficient f_{ij}. If the classical limit $f_{ij} = 1$ is assumed, then the kinetic equations can be integrated numerically. The solutions are specified by a parameter τ related to a kinetically weighted average of $T^{1/2}\rho$, where ρ is the density of the gas. The result is that τ determines the average cluster size, and $\langle n_k \rangle$ increases for increasing τ, a prediction in agreement with experiment.

2.4.2 Seeded nozzle sources

In a seeded nozzle source [14], an inert carrier gas is mixed with a low concentration of the seed, for instance the alkali metal vapor (typical mixing ratios are 1–10 %), and the mixture is ejected through the nozzle. When the seed condenses, clusters are formed in the expansion. This process differs from the pure vapor expansion in that the carrier gas serves as a heat bath for the seed. The fact that the carrier is an inert gas guarantees that it does not react with the seed. When the vapor pressure is high enough, collisions between seed and seed facilitate establishing equilibrium among the cluster species in the nozzle channel. The carrier gas mediates the equilibration and absorbs most of the heat of condensation, which is transformed into translational kinetic energy of the beam. Although the seeded source is a simple and reliable method of producing small and medium size clusters, its operation requires rather high vapor pressures, and hence it is not suitable for metals with high boiling points.

2.4.3 Gas aggregation sources

In a nozzle source the metal vapor exists in a supersaturated state for only a short time, and large clusters do not form abundantly. The corresponding times in gas aggregation sources are longer and large clusters form easily. In a gas aggregation source the metal vapor from

the oven enters a condensation chamber, where it mixes with a stream of inert gas at pressures about 1 Torr and temperatures below 100 K. Cluster growth continues in the condensation chamber until the mixture of gas and clusters is discharged through an orifice into a sourrounding vacuum chamber. The distribution of cluster sizes is controlled by the temperatures of the oven and condensation chamber and by the gas flow rate. The parameters can be adjusted to produce clusters up to sizes of 10^5 atoms.

2.4.4 Laser vaporization

This method was developed in the groups of Smalley [17] and Bondybey [18]. This technique can produce aggregates with up to 100 atoms or more of any substance which exists in the solid state, even the most refractory metals. A pulsed laser beam hits a metallic rod or disk placed in a tube. The laser pulse evaporates atoms producing an extremely hot plasma. This vapor is cooled by a stream of inert gas flowing through the tube and condensation of the vapor produces clusters of different sizes. The flowing current carries the clusters to a vacuum chamber where the pressure difference induces a supersonic expansion of the beam. Collisions ocurring during the expansion cool the aggregates down to a low temperature. Both neutral and ionized clusters are obtained.

2.4.5 Clusters in helium droplets

In these experiments [19] a beam of helium clusters is first produced in a supersonic expansion and then reacted with a secondary beam of atoms (Ar, Kr, Xe) or molecules (H_2O, SF_6). Large liquid ^4He droplets ($N > 1000$ atoms) capture up to 30 foreing particles (atoms or molecules) successively, and the foreing particles appear to coagulate to form clusters on the He droplets or inside.

2.5 Mass Analysis

When clusters are produced by any of the methods presented above, a distribution of sizes is obtained, that is, clusters with different numbers of atoms are generated in the same experiment. The first task of the

experimentalist is then to analyze the size distributions. This is done with the help of a mass spectrometer. But before entering the mass spectrometer, a laser or an electron beam are used to ionize the clusters. Some of the production techniques described above already produce ionized clusters.

In a Time-of-Flight (TOF) spectrometer, a voltage V accelerates all singly charged cluster ions ($q = +1$) into the same kinetic energy $qV = mv^2/2$. Clusters then acquire a mass dependent velocity $v = (2qV/m)^{1/2}$, and clusters of different sizes, that is of different masses m, can be distinguished by the different flight times t_f required to reach a detector placed at a distance L

$$t_f = \frac{L}{v} = L\left(\frac{m}{2qV}\right)^{1/2}. \qquad (2.7)$$

Since the fight time is proportional to $m^{1/2}$, the heavier clusters reach the detector later than the lighter ones.

Cluster growth in the supersaturated vapor occurs by sequential aggregation of atoms that collide with the clusters. Most colliding atoms are just scattered, and only a small part of those atoms stick to the cluster. This part of the process gives rise to a smooth population distribution. That is, the function $\rho(N)$ giving the abundance of clusters with N atoms, varies smoothly with N. But the process of atom attachment to the clusters (condensation) is an exothermic process, and the clusters become vibrationally hot as they grow. One of the roles of the inert gas carrier mixed with the seed is, in fact, to help in the cooling of the growing clusters, but this cooling is only partially efficient. Then, after becoming sufficiently hot, the clusters cool down by evaporating atoms. This is a very efficient mechanism. For example, in Na_N clusters initially at a temperature of 600 K, the evaporation of a single atom from a cluster with N about 50 cools the cluster by nearly 80 K; for a larger cluster, with N about 200, the corresponding temperature drop is smaller, only about 20 K. The difference is due to the lower heat capacity of the smaller clusters. The activation energy required to evaporate a single atom from a cluster X_N (X indicates a generic chemical element) through the process

$$X_N \rightarrow X_{N-1} + X \tag{2.8}$$

that is,

$$E_{vap}(X_N) = E(X_{N-1}) + E(X) - E(X_N) \tag{2.9}$$

is usually a very sensitive function of N. In this equation $E(X_{N-1})$ and $E(X_N)$ indicate the energies of the clusters with N-1 and N atoms, respectively, and $E(X)$ is the energy of the free atom. Consequently, very stable clusters with large E_{vap} evaporate atoms at a slower rate than less stable clusters, and this effect becomes reflected in the abundance mass spectrum, that gets a lot of non trivial structure. Mild differences in evaporation energies can lead to large differences in cluster abundance. Roughly speaking, very stable clusters will be characterized by large populations in the beam. A simple method has been devised to calculate the cluster population distributions in the beam under conditions of thermodynamic equilibrium [14]. The equilibrium distributions are calculated by examining all the possible reactions of the form

$$X_I + X_J + \cdots + X_k \leftrightarrow X_L + X_M + X_N. \tag{2.10}$$
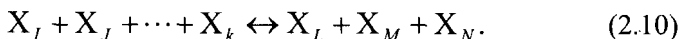
The method uses the mass-action law and a simple model for the partition functions f_N of the N-atom clusters. Although the model is specifically aimed to describe metallic clusters, the assumptions have more general validity. The result for the relation between the densities $\rho(N)$ of clusters of neighboring sizes is

$$\ln \frac{\rho(N)^2}{\rho(N-1)\rho(N+1)} = \frac{\Delta_2(N)}{k_B T} \tag{2.11}$$

where the quantity

$$\Delta_2 = E(X_{N+1}) + E(X_{N-1}) - 2E(X_N) \tag{2.12}$$

measures the relative energy of a cluster of N atoms compared to clusters with $N+1$ and $N-1$ atoms. If the variations in the detection efficiency with cluster size are small, densities $\rho(N)$ can be replaced by intensities $I(N)$. Relating $\Delta_2(N)$ to the evaporation energies, Eq. (2.11) can be written in an alternative way

$$\ln \frac{I(N)^2}{I(N-1)I(N+1)} = \frac{E_{vap}(X_N) - E_{vap}(X_{N+1})}{k_B T}. \qquad (2.13)$$

This relation indicates that an enhancement of the population of clusters of size N is expected if there is a substantial drop in stability between X_N and X_{N+1}. This concept is important to explain the abundance variations for types of clusters displaying atomic or electronic shell structure, a topic that will be treated in full detail in other chapters.

The relation between abundances and binding energies has been studied by Hansen and Näher [20, 21] for the case of a purely evaporative ensemble using an statistical decay theory. Specifically, the following problem was analyzed: given a collection of free, hot clusters with a smooth and broad initial abundance distribution, what is the resulting abundance distribution at a later time if the evaporation energies vary with cluster size? The first result is that the rate constants for monomer evaporation can be expressed as

$$k_N = \omega N^{2/3} e^{-D_N/T} \qquad (2.14)$$

where ω is a vibrational frequency, $N^{2/3}$ accounts for the fact that the atoms evaporate from the surface, and D_N is the activation energy, that can be identified with the evaporation energy. Then one obtains for the abundances

$$I_N \propto D_{N+1} - \frac{C_V}{\ln B} \Delta D_N. \qquad (2.15)$$

Here $\Delta D_N = D_{N+1} - D_N$ is essentially the difference of evaporation energies, C_V is the heat capacity and $B = N^{2/3} t \omega$, with t representing a typical inverse cooling time (the inverse of the rate constant). This result

is valid for small clusters, and also for large clusters under certain circumstances. The prefactor of the difference term is quite large, and for clusters displaying shell structure the second term often dominates the variations of the first one by a large factor. Under appropriate experimental conditions abundances reflect evaporation rates in an unambiguous way. Hence, variations in abundance will reflect variations in activation energy with cluster size.

Consequently the study of the structure of the mass spectrum can be a useful tool to get information on the local variations of cluster stability as a function of N. The study of these effects will be the subject of other sections in this book. Also, a cluster beam can be intentionally warmed up by crossing the cluster beam with laser radiation, in order to enhance the population differences arising from the dependence of cluster stability with N. In experiments for clusters of fullerene molecules $(C_{60})_N$ Hansen *et al.* [22] have found that the small difference of about 20% in the activation energies for evaporation of C_{60} molecules from $(C_{60})_{13}$ and clusters of nearby sizes $((C_{60})_{14} ...)$ is enough to induce a much higher abundance of $(C_{60})_{13}$ as compared to the others in a laser heated cluster beam. These workers have suggested that the laser heating of cluster beams could provide a method to routinely produce macroscopic amounts of large, stable mass-selected clusters for nanoscale applications.

References

1. López-Quintela, M. A. and Rivas, J., *Current Opinion in Colloid and Interface Science*, **1**, 806 (1996).
2. Puntes, V. F., Krishan, K. M., and Alivisatos, A. P., *Science*, **291**, 2115 (2001).
3. Yang, H. Y., Shen, C. M., Su, Y. K., Yang, T. Z., Gao, H. J., and Wang, Y. G., *Appl. Phys. Lett.*, **82**, 4729 (2003).
4. Alvarez, M. M., Koury, J. T., Schaaff, T. S., Shafigullin, M., Vezmar, I., and Whetten, R. L., *Chem. Phys. Lett.* , **266**, 91 (1997).
5. Jayanetti, S., Mayanovic, R. A., Anderson, A. J., Basset, W. A., and Chou, I. M., *J. Chem. Phys.*, **115**, 954 (2001).
6. Henglein, A., *J. Phys. Chem. B*, **104**, 1206 (2000).
7. Vajda, P., and Beunen, F., *Phys. Rev. B*, **53**, 5335 (1996).
8. Krexner, G., Premm, M., Beunen, F., and Vajda, P., *Phys. Rev. Lett.*, **91**, 135502 (2003).

9. Mattei, G., De Marchi, G., Maurizio, C., Mazzoldi, P., Sada, C., Bello, V., and Battaglin, *Phys. Rev. Lett.*, **90**, 85502 (2003).
10. Röder, H., Hahn, E., Brune, H., Bucher J. P., and Kern, K., *Nature,* **366**, 141 (1993).
11. Cuberes, M. T., Schlittler, R. R., and Gimzewski, J. K., *Appl. Phys. Lett.*, **69**, 3016 (1996).
12. Bhaskar, N. D., Frueholz, R. P., Klimcak, C. M., and Cook, R. A., *Phys. Rev. B*, **36**, 4418 (1987).
13. Katakuse, I., Ichihara, T., Fujita, Y., Matsuo, T., Sakurai, T., and Matsuda, H., *Int. J. Mass Spectrom. Ion Proc.,* **74**, 33 (1986).
14. de Heer, W. A., Knight, W. D., Chou, M. Y., and Cohen, M. L., *Solid State Physics,* **40**, 93 (1987).
15. Stein, G., *Surf. Sci.*, **156**, 44 (1985).
16. Soler, J. M., García, N., Echt, O., Sattler, K., and E. Recknagel, E., *Phys. Rev. Lett.*, **49**, 1857 (1982).
17. Dietz, T. Y. G., Duncan, M. A., Powers, D. O., and Smalley, R. E., *J. Chem. Phys.*, **74**, 6511 (1981).
18. Bondybey, V. E., and English, J. H., *J. Chem. Phys.*, **76**, 2165 (1982).
19. Lewerenz, M., Schilling, B., and Toennies, J. P., *J. Chem. Phys.,* **102**, 8191 (1995).
20. Näher U., and Hansen, K., *J. Chem. Phys.*, **101**, 5367 (1994).
21. Hansen, K., and Näher, U., *Phys. Rev. A,* **60**, 1240 (1999).
22. Hansen, K., Hohman, H., Müller, R. and Campbell, E. E. B., *J. Chem. Phys.,* **105**, 6088 (1996).

This page intentionally left blank

3. Van der Waals Clusters

3.1 Structure of Van der Waals Clusters

The mass spectrum of xenon clusters (Xe_N) obtained by Echt, Sattler and Recknagel [1] is given in Fig. 3.1. It is apparent that the abundance varies in a rather peculiar way as a function of size N, and this behavior is the same each time the experiment is repeated. The abundance is not at all a monotonic function of size. Certain particular sizes are formed with high abundance, while the sizes following those abundant ones are, instead, especially rare. Main breaks at sizes $N = 13$, 55 and 147 are particularly noticeable. These, so called *magic numbers*, are elements of a series

$$N = 1 + \sum_{p=1}^{n} 10p^2 + 2 \tag{3.1}$$

with $n = 1$, 2 and 3, respectively. Further elements in the series are $N = 309$, 561 and 923, corresponding to $n = 4$, 5 and 6. This series describes the packing of spheres in a family of closed icosahedral arrangements, named after Mackay [2], and n gives the number of concentric atomic layers in the icosahedron. An icosahedron has 12 five-fold symmetry axes. It also has 20 triangular faces and each of these can be constructed with close-packed spheres. Atoms in the interior of the icosahedon are 12-fold coordinated, just as in a close-packed lattice. Figure 3.2 shows the first five perfect Mackay icosahedra ($n = 1$–5 layers). In subsequent experiments [3] the same group was able to show that main abundance breaks also occurred in the mass spectra of rare gas clusters at the magic numbers 309, 561 and 923. That coincidence between the experimental magic numbers and those from the series (3.1) is not accidental. Indeed,

diffraction experiments show that the diffraction patterns from argon clusters coming from a nozzle source agreed with an icosahedral packing for a broad size range [4]. Experiments for clusers of small molecules interacting by Van der Waals forces (CO, CH$_4$) show the same set of magic numbers [3]. CO and CH$_4$ are molecules with closed electronic shells, which leads to a low anisotropy of their intermolecular interaction potentials.
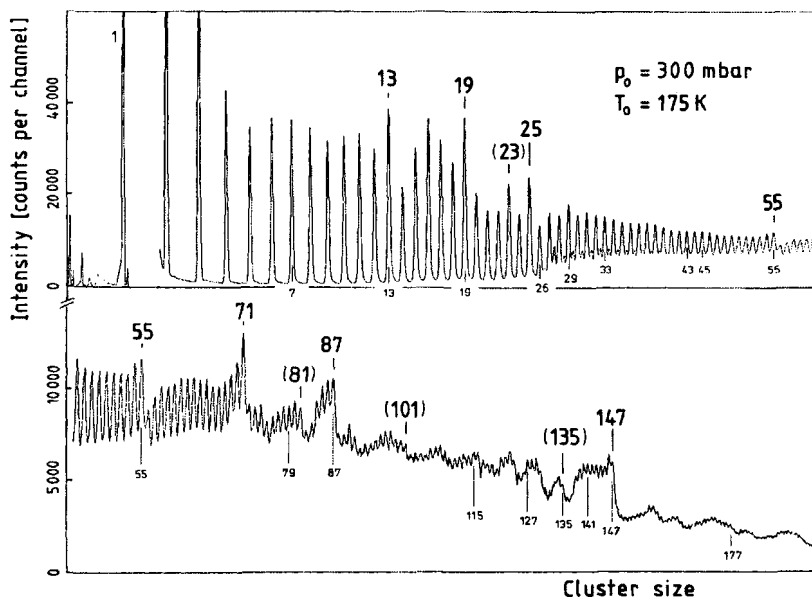
Figure 3.1. Concentration profile of xenon clusters produced by adiabatic expansion and ionized by an electron beam. Reproduced from O. Echt, K. Sattler and E. Rechnagel, *Phys. Rev. Lett.* **47**, 1121 (1981) with permission of the American Physical Society.

According to the arguments in Section 2.5, the observed main breaks are due to the special stability of the clusters with 13, 55, 147... atoms. The enhanced stability of Van der Waals clusters with the structure of complete icosahedra is substantiated by theoretical calculations [5, 6]. The interatomic interactions between inert gas atoms can be extremely well described by a simple central pair potential having a steep repulsive short-range wall, arising from the strong overlap repulsion between the

closed electronic shells when the atoms approach each other too closely, and a weakly attractive long-range term due to the attractive dispersion forces. This type of interatomic interaction leads to compact, high density structures. A Lennard–Jones (LJ) potential

$$U(r) = 4\varepsilon \left[\left(\frac{\sigma}{r} \right)^{12} - \left(\frac{\sigma}{r} \right)^{6} \right] \qquad (3.2)$$

with parameters ε and σ fitted to gas phase data (see Table 3.1) describes well the interaction between inert gas atoms as a function of their distance r. The average binding energy per atom, E_b, of icosahedral clusters calculated with the Lennard–Jones potential shows local maxima (defining $E_b > 0$) for sizes N corresponding to icosahedra with filled shells [6]. Those maxima are appreciated most clearly in the calculated evaporation energies. Molecular dynamics simulations of the evaporation of atoms from argon clusters confirm these ideas [7]: at a given temperature, the magic cluster Ar_{13} evaporates less than clusters of neighboring sizes.

Table 3.1. Lennard–Jones parameters for rare gas interactions.

	σ (Å)	ε / k_B (K)
Ne–Ne	2.75	35.60
Ar–Ar	3.40	120.0
Kr–Kr	3.83	164.0
Xe–Xe	4.10	222.3

The mass spectra of Ar, Kr, Xe, CO and CH_4 clusters exhibit additional intensity anomalies between icosahedral shell closures [3]. Those anomalies, maxima or breaks in the abundance, are not defined as precisely as the main magic numbers, but are nevertheless common to all the Van der Waals materials listed above. Two of those anolamies, the abundance maxima at $N = 19$ and $N = 23$, can be seen in the mass spectrum of Xe clusters in Fig. 3.1, and a complete list is given in Table

3.2. Those effects have been interpreted as steps towards the completion of a full shell, that is, as subshell closures of a partially decorated icosahedral shell [3]. The intensity maximum at $N = 19$, for instance, results from capping the $N = 13$ cluster with a pentagonal pyramid formed by six atoms. The resulting structure is often called a double icosahedron.
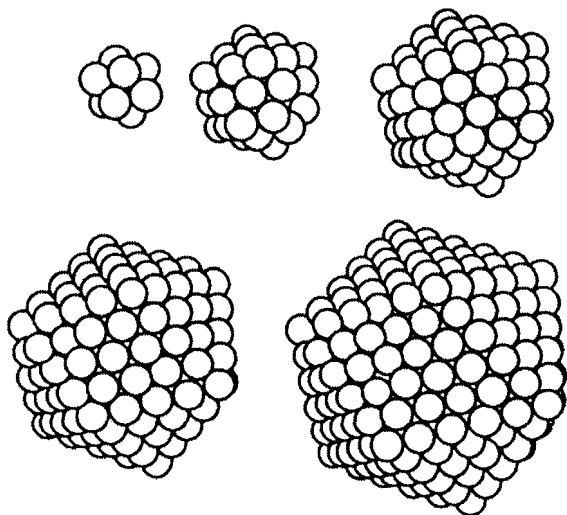
Figure 3.2. Mackay icosahedra with increasing number of layers. The number of spheres in each cluster is 13, 55, 147, 309 and 561, respectively.

The full set of secondary magic numbers can be interpreted by assuming a particular model for the decoration of the underlying icosahedral core. A perfect icosahedron is formed by 20 triangular faces joined by 30 edges and 12 vertices. The smallest perfect icosahedral cluster ($n = 1$) can be labelled Ico13. In this cluster, one atom occupies the central position and the other 12 atoms occupy the 12 vertices. Atoms can be added on top of this icosahedral core in two different ways, illustrated on the upper panel of Fig. 3.3. In a first type of decoration, atoms cover sites at the center of the triangular faces (F sites) and vertex sites (V sites, mono-coordinated to Ico13). Those F and V sites provide a total of 32 sites (20 + 12) to cover Ico13, and this

coverage produces a cluster with 45 atoms. This type of decoration will be denoted FC (face centered), as it emphasizes the coverage of the faces of the icosahedron. Alternatively, atoms can be added decorating edges (E sites, having coordination two with the atoms of the underlying Ico13) and vertices (V). Those provide a total of 42 sites (30 + 12) to cover Ico13, and completion of this layer leads to the next Mackay icosahedron, Ico55. These are called multilayer icosahedral (or MIC) structures.

Covering of Ico_{13}

MIC   FC

Covering of Ico_{55}

MIC   FC
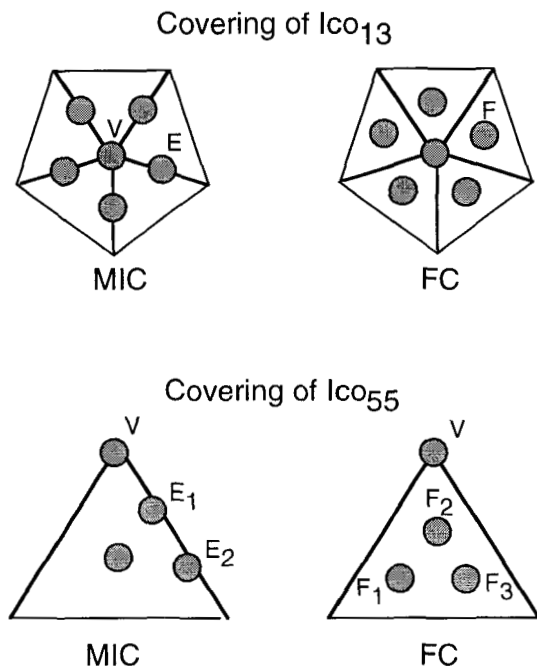
Figure 3.3. MIC and FC coverings of Ico13 and Ico55 icosahedral clusters. V, E and F sites indicate Vertex, Edge and Face sites, respectively. The upper panel shows the formation of FC and MIC caps.

Starting now with Ico55, the FC covering can be generalized, by decorating the 12 vertex sites and covering the three pockets on each face with three atoms (sites F1, F2 and F3 in Fig. 3.3). This leads to a shell formed by 72 atoms (12 + 60), and then to a cluster with 127 atoms

(55 + 72). Instead, MIC decoration leads the next multilayered Mackay icosahedron, Ico147. This is obtained by covering the 12 vertex sites, placing two atoms on top of each edge (sites E1 and E2 in Fig. 3.3, giving a total of 60 E-type atoms), and one atom above the center of each of the 20 faces. The MIC covering corresponds to the series of Eq. (3.1).

Table 3.2. Predicted and experimentally observed subshell closures of inert gas clusters with p complete icosahedral shells, plus an incomplete outermost layer. Observed magic numbers are given with respect to the predicted values, *i.e.*, 0 means full agreement. Weak anomalies are bracketed. Data collected from [3].

$p=1$	$p=1$	$p=2$	$p=2$
Predicted	Exp.	Predicted	Exp.
13	0	55	0
19	0	71	0
23	0	81	0
26	0	88	-1
39	(0)	92	-1
43	0	101	0
46	0	110	-1
49	0	116	0
55	0	125	-1
		131	0
		137	-1
		147	0

In the ideal MIC covering, there are two first neighbor distances of 1.0 and 1.05 (short bonds), in units of the radius of the Ico13, and a second neighbor distance of 1.45. The distance 1.0 corresponds to first neighbors on different shells, and the distance 1.05 to first neighbors on the same shell. For ideal FC covering, there are more bond lengths of value 1.0 than in MIC, but some of the bond lengths of magnitude 1.05 are replaced by larger ones with values 1.13 and 1.21 (the density of surface atoms for FC covering is lower). Consequently, FC growth becomes favorable at the begining of a shell up to a point when the MIC growth becomes preferred. This occurs because the atoms added give rise to more short bonds in the FC mode, as compared to the MIC mode, in the initial stages of covering, but the opposite occurs beyond a certain

size. The crossing point depends on the fine details of the interatomic interactions, so different materials have different crossing points [8, 9].

Assuming that decoration of Ico13 begins with FC covering, the first six atoms added form a cap (or umbrella) as in the upper right panel of Fig. 3.3, giving rise to the double icosahedron structure for $N = 19$, with two inner atoms and 17 surface atoms. By decorating the surface with four additional atoms in appropriate positions, an adjacent FC umbrella is completed for $N = 23$. Those two umbrellas share two common faces, and this structure can be viewed as three interpenetrating double icosahedra. A third adjacent umbrella is completed for $N = 26$. If we consider the two pairs formed by those three umbrellas, each pair of umbrellas shares two faces. The structure for $N = 23$ can be viewed as composed of five interpenetrated double icosahedra. In this way, completion of FC umbrellas gives special stability for clusters with $N = 19, 23, 26, 29, 32, ...$ However, the strain accumulated by completing more and more umbrellas makes the FC structures eventually less stable compared to MIC covering, and a transition from FC to MIC structure is likely to occur around $N = 27$–28. For this, a complete reordering of atoms in the incomplete outer layer has to occur, since the FC and MIC lattices are mutually exclusive. Then, $N = 28$ contains three complete adjacent MIC umbrellas, and new MIC umbrellas are completed for $N = 32, 36, 39, 43, 46$ and 49, until the shell is closed at Ico55. Again clusters become very stable with the filling of each new MIC umbrella. All the studies indicate that the FC and MIC decorations are competitive in a transition region, say $N = 27$–33, until the MIC decoration dominates with a further increase of N. The gain in stability by filling umbrellas (both of FC or MIC types) is explained by a particular enhancement in the number of bonds at the umbrella closing [10]. The model presented here for the growth of clusters on inert gases finds full support from calculations using interatomic Lennard–Jones potentials [11, 12]. The experimental features listed in Table 3.2 are in agreement with this model. The subshell closings at $N = 13, 19, 23, 26$, and then at $N = 39, 43, 46, 49$, have been seen in the experiments. The former subset is explained by FC decoration, and the later one by MIC covering. Also, the lack of magic numbers in the intermediate region is explained by the competition between the two decorations.

Starting with the Ico55, the first FC umbrella of the third layer is completed by adding 16 atoms, that is at $N = 71$, and two additional

adjacent umbrellas at $N = 81$ and $N = 88$. Again those umbrellas share triangular faces. On the other hand MIC umbrellas form at $N = 71$, 83, 92, 101, 110, 116, 125, 131 and 137, and the Mackay icosahedron is completed for $N = 147$. The FC fillings at $N = 71$, 81 and 88, as well as the MIC fillings at $N = 92$, 101, 110, 116, 125, 131, 137 and 147 have been observed (see Table 3.2). Calculations [13] indicate that the two decorations are competitive in the region $N = 77$–85, that agrees with the observed transition region. Other small features are observed at $N = 95$, 104 and 119, and the stability of these three clusters can be explained by analyzing in detail the increase in the number of bonds as the cluster grows in the MIC mode [14]. The success of this interpretation extends to other shells, but the experimental subshell closing numbers are less sharply defined [3].

Magic Van der Waals clusters are characterized by a particularly stable structure. But there is also a less obvious property that makes those clusters special. A detailed investigation of the enormous amount of isomeric structures above the ground state for Lennard–Jones clusters with N between 25 and 60, shows that the magic clusters $N = 26$, 29, 32, 36, 39, 43, 46, 49 and 55 have large energy gaps between their absolute energy minimum and their next low lying energy configuration, compared to their neighbor clusters [11]. This property is relevant to explain the thermal properties (see Section 3.3).

In summary, growth of Van der Waals clusters by the packing of spheres occurs in stages; each stage terminates with the completion of a Mackay icosahedron. The five-fold symmetric icosahedra with layers arranged like onion skins around a central atom are not found in crystals. Regular macroscopic crystals do not have a shell structure around a central atom. The atoms in a crystal are, instead, packed as bricks in a three-dimensional periodic lattice (although the so called metallic quasicrystals have quasi-periodicity consistent with a local icosahedral structure [15]).

3.2 Transition to the Bulk

The embrionic growth of rare gas clusters appears to continue beyond 100 atoms with no sign of transforming to their regular, translationally invariant, macroscopic crystal structure. But, evidently, at some point

this transition should occur. Experiments suggest that the transition to the *fcc* (face centered cubic) crystal structure of the bulk rare gas solids occurs for cluster sizes of a few thousand atoms [4]. The reason is that hard spheres cannot really be packed into the icosahedral structure such that adjacent spheres are touching each other. The spheres have to be soft. Then the packing becomes possible, but the spheres in the inner part of the cluster will be closer to each other than the spheres in the outer layers. As a result, internal strain is stored in the cluster as it grows, and at some stage it becomes favorable to release the strain by a rearrangement of the atoms leading to the structure of the macroscopic crystal. In fact, with a small concerted displacement of the atoms it is possible to transform an icosahedron into a cuboctahedron, which is a polyhedron with triangular and square faces that can be cut from the *fcc* lattice. Molecular dynamics simulations have been performed for clusters composed of particles interacting via Lennard–Jones potentials [6]. The static energies of clusters with an underlying *fcc* structure and varying surface structures were compared with those having icosahedral structures, and the icosahedral family was found to have the lowest static energies for sizes up to a few thousand atoms. That work also demonstrated that the critical cluster size where the energy of the *fcc* clusters becomes lower than that of icosahedral clusters is not easily determined, because the energy of the *fcc* clusters is sensitive to the surface structure and this is difficult to determine for such large clusters. Smirnov *et al.* [16] have considered the same problem using Morse pair potentials

$$U(r) = D\left(e^{-2\alpha(r-r_e)} - 2e^{-\alpha(r-r_e)}\right), \tag{3.3}$$

where r_e is the equilibrium distance between atoms in the diatomic molecule and D is the dissociation energy. The value of α was used as an adjustable range parameter to change the relation between the short-range and long-range parts of the interaction potential. It was found that α determines the critical cluster size N_{cr} at which the transition from icosahedral to *fcc* structure occurs: N_{cr} decreases as α increases, that is, as the repulsive part of the potential becomes harder. A value $\alpha r_e = 6$ makes the Morse potential similar to the Lennard–Jones potential, and for this case it predicts that N_{cr} is larger that one thousand atoms, in agreement with works using the Lennard–Jones potential [6, 13].

Decahedral clusters form a family that can be competitive with the icosahedral one in the transition to the bulk. To understand the structure of decahedral clusters one may first notice that an icosahedron can be viewed as formed by 20 distorted tetrahedral units all meeting at the cluster center. Each tetrahedron shares three of its faces with neighbor units, and the last face is one of the external surface facets of the icosahedron. The crystallographic arrangement of atoms in each (111)-like face of the tetrahedron is *fcc*, and the plane of atoms that two neighboring tetrahedra share is a twinning plane; that is, the stacking sequence in the direction normal to this plane is mirrored in it. However, 20 perfect tetrahedra cannot be assembled together to make an icosahedron, because if the surface vertices of neighboring units are aligned the units will overlap at the center of the icosahedron. To solve this problem, the tetrahedral units must be strained to make the three sides meeting at the central vertex about 5% shorter than the other three sides laying on the surface. Turning now to a classic decahedron, with the form of a pentagonal bipyramid, this is formed by five slightly distorted tetrahedral units joined at a common edge. Each unit shares two of its (111) faces as twinning planes with neighboring units and contributes the other two (111) faces to the surface of the decahedron. The ten faces of the classical decahedron are equilateral triangles. The strain energy in the decahedron is lower compared to the icosahedron. However, the decahedron is less spherical, so it results in a larger surface area and higher surface energy. Truncation of the five vertices in the mid-plane of the bipyramid exposes five rectangular (100)-like facets, making the structure more spherical [17]. Additional truncations which create (111)-like reentrant facets stabilise further the decahedral structure [18]. Calculations [19] for Lennard–Jones clusters predict a transition from icosahedral to decahedral structures at about $N = 1700$. Decahedral clusters with 35000 atoms are still more stable than crystalline *fcc* clusters. Fitting the binding energies of decahedral and *fcc* clusters to functions of $N^{1/3}$ and extrapolation to very large sizes predicts that the decahedral $\rightarrow$ *fcc* transition occurs at about $N = 200000$.

As indicated at the begining of Section 2.5, to discriminate the sizes of the different clusters present in the molecular beam it is necessary to ionize the clusters when they enter the time-of-flight section of the mass spectrometer. But in clusters bound by weak Van der Waals forces the ionization process may induce evaporation of atoms. The arguments

discussed in that section indicate that such evaporative cooling would further enhance the population of magic clusters over neighboring sizes. The same effect may explain some curious anolamies sometimes observed in the measured intensities. It has been suggested [20] that about 1 ps after ionization the charge localizes in these clusters, leading to the formation of a dimer ion like Ar_2^+ on the cluster surface, with a contracted interatomic separation with respect to that in neutral Ar_2. The contraction, expressed by the ratio between the bond length d^+ of the ionized dimer and that of the neutral, is estimated as $d^+/d = 0.66$ for Ar_2 and 0.75 for Xe_2 [21]. Then the Ar_2^+ dimer occupies a volume not much larger than that of a neutral atom, and the structure of the cluster Ar_{14}^+ may become similar to that of a neutral 13-atom icosahedral cluster, with perhaps a slight distortion. This may explain the observation in some experiments [3] of intensity peaks at Ne_{14} and Ne_{56} (instead of the usual Ne_{13} and Ne_{55}), at Ar_{14} and Ar_{148} (instead of Ar_{13} and Ar_{147}), and at $(CH_4)_{14}$ (instead of $(CH_4)_{13}$); that is, peaks shifted by one unit with respect to the usual magic numbers.

3.3 Thermal Properties

3.3.1 Solid to solid transitions

A few small LJ clusters break the rule by having nonicosahedral lowest energy structures at $T = 0$ K. For $N < 150$ there are only eight such cases [22]: the global minimum is *fcc* for $N = 38$, decahedral for $N = 75\text{--}77$, 102–104, and it has an unusual tetrahedral structure for $N = 98$. At those sizes the nonicosahedral morphologies have optimum shapes, whereas the icosahedral structures have an incomplete outer layer. But above 0 K the most stable structure is the one with the lowest free energy, and entropic effects make a contribution. Doye and Calvo [19] have predicted that entropic effects give rise to a solid to solid transition from the nonicosahedral to the icosahedral structure for all those clusters. The solid to solid transition temperature T_{ss} occurs when the partition functions of the two competing structural types are equal, that is, $Z_A = Z_B$. In the harmonic approximation this gives

$$\sum_{i \in A} \frac{n_i \exp(-\beta E_i)}{\overline{V_i}^{3N-6}} = \sum_{j \in B} \frac{n_j \exp(-\beta E_j)}{\overline{V_j}^{3N-6}} \qquad (3.4)$$

where $\beta = 1/k_B T$. The sums are restricted to the subsets of minima of types A or B in the potential energy surface, E_i is the potential energy of minimum i, $\overline{V_i}$ is the geometric mean vibrational frequency, and n_i is the number of permutational isomers of structure i. One contribution to the entropy arises from the number of energy minima of that type. This favors the icosahedra for the eight clusters considered, because there are many low energy icosahedral minima, corresponding to different arrangements of the atoms in the incomplete outer layer. Another contribution comes from the symmetry of the cluster. For the cases $N = 38$, 75, 98, this again favors the icosahedral structures because the nonicosahedral global minimum has high symmetry. Finally, the vibrational entropy always favors the icosahedra for any size because these have a lower mean vibrational frequency. The predicted transition temperatures are given in Table 3.3, in units of εk_B^{-1} (ε is the parameter of the Lennard–Jones potential (3.2)). The transition temperature decreases rapidly with cluster size, which reflects the increasing dominance of the vibrational entropy. T_{ss} is equal to $0.121\varepsilon k_B^{-1}$ for $N = 38$ and equal to $0.007\varepsilon k_B^{-1}$ for $N = 104$. For comparison we notice that melting temperatures have values around $0.3\varepsilon k_B^{-1}$ for those clusters (melting will be discussed in the next section). The use of Eq. (3.4) is not practical for very large clusters. By assuming that all the minima associated to a given morphology have the same energy $E_A(E_B)$ and the same vibrational frequency $\overline{V}_A (\overline{V}_B)$, and that the number on minima is approximately the same for both subsets, the simple formula

$$T_{ss} = \frac{\Delta E}{k_B(3N-6)\log(\overline{V}_A / \overline{V}_B)}, \qquad (3.5)$$

was derived [19], where $\Delta E = E_A - E_B$. Predictions with this simpler formula are also given in Table 3.3 and the results improve as N increases.

Table 3.3. Estimates of the transition temperature T_{ss} (in units of $\varepsilon\, k_B^{-1}$) to the icosahedral structure for Lennard–Jones clusters with nonicosahedral ground state. Data collected from [19].

N	T_{ss} Eq. (3.4)	T_{ss} Eq. (3.5)
38	0.121	0.316
75	0.082	0.119
76	0.046	0.053
77	0.048	0.057
98	0.004	0.006
102	0.013	0.014
103	0.016	0.018
104	0.007	0.008

Temperature also affects the predictions made in Section 3.2 for the icosahedral $\rightarrow$ decahedral $\rightarrow$ *fcc* transitions. The entropic effect favors the stability of LJ icosahedral clusters against decahedral ones, moving the phase boundary to larger N with increasing temperature. In an analogous way, temperature shifts the decahedral $\rightarrow$*fcc* transition even higher.

3.3.2 Melting transition

When a macroscopic solid material is heated slowly, the atoms first begin to vibrate around their equilibrium positions. In this regime, the internal energy of the system is a nearly linear function $E(T)$ of the temperature. At some point the solid undergoes a first order phase transition and melts. This occurs at the melting temperature T_m. At this temperature the internal energy experiences an abrupt jump. Its magnitude is the latent heat of fusion, which is the energy required to destroy the lattice of the crystal. The bulk heat capacity, which is defined as the partial derivative $C(T) = \partial E / \partial T$, is therefore only weakly temperature dependent, save for a delta function at T_m. The case of small clusters is different. These do not have a sharp phase transition. Instead, melting occurs over a finite interval of temperatures, although the width of the interval becomes smaller as the cluster increases in size. A feature

that adds interest is that neither the width of the interval, nor its location are smooth functions of *N*.

Understanding the melting transition of inert gas clusters has been possible mainly through the work of theorists, employing computer simulation techniques: molecular dynamics (MD) and Monte Carlo (MC) simulations. Cluster behavior in the phase-change region is complex: solid-like and liquid-like isomers dynamically coexist for some clusters [23], whose structure fluctuates back and forth between relatively long lived solid-like and liquid-like states, while other clusters show a smooth progression of isomerizations occurring through that region [24].

Several indicators can be used to elucidate cluster melting from the analysis of the results of computer simulations. Although a single indicator is sometimes enough, a proper characterization of melting is in general only possible by the combined use of several indicators. The first one is the equation of state of the cluster, also called caloric curve, which gives the thermal response to an increase in energy, *i.e.*, the cluster temperature *T* as a function of the total energy. The total energy in a MD simulation is given as a sum of kinetic and potential energies

$$E = \langle E_{kin} \rangle + \langle U \rangle, \qquad (3.6)$$

where the symbol $< >$ indicates the time average of the instantaneous values of the bracketed quantity over an entire simulation trajectory. For a given total energy, the cluster temperature is defined in MD simulations by the expression

$$T = \frac{2}{(3N-6)k_B} \langle E_{kin} \rangle. \qquad (3.7)$$

That is, the time average $\langle E_{kin} \rangle$ of the instantaneous kinetic energy of the cluster per degree of freedom equals half of the thermal energy, given by $k_B T$.

The simulations show that the clusters behave as a solid at low temperatures, with the atoms performing oscillations around their equilibrium positions without changing the overal shape of the cluster. The low temperature behavior is quasi-harmonic, and the temperature

increases linearly with increasing total energy at the rate given by the equipartition theorem. As the temperature is increased further, the caloric curve starts deviating from the harmonic limit. This indicates that the contribution from the anharmonic part of the potential is already significant. The cluster then reaches a transition region where the slope of the curve flattens; that is, a significant increase of the energy results in only a small (although higher that zero) increase in the temperature. This region corresponds to the melting transition. At the end of the transition region the slope of the caloric curve increases again in the liquid-like region.
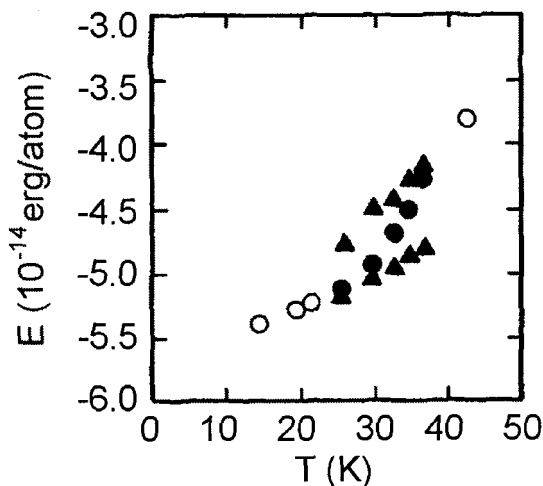
Figure 3.4. Caloric curve of Ar_{13} obtained by Monte Carlo simulations. Open circles are used outside the coexistence region, and dark symbols in the coexistence region. Triangles represent points calculated separately over each phase inside the two phase region and dark circles represent an average over coexisting forms. Adapted from H. L. Davis, J. Jellinek, and R. S. Berry, *J. Chem. Phys.* **86**, 6456 (1987) with permission of the American Institute of Physics.

Figure 3.4 shows the region of the caloric curve of Ar_{13} corresponding to the phase change [25]. The interactions were represented by LJ potentials, and the potential energies, for temperature

T, were obtained from MC simulations. In this case $\langle U \rangle$ is the ensemble average of the potential energy over an entire MC simulation. To those energies a kinetic energy was added in the spirit of Eq. (3.6). The cluster exhibits sharp but unequal freezing and melting temperatures, T_f and T_m respectively. T_f is the lower bound of the stability of the liquid phase and T_m is the upper bound of the stability of the solid form. In the transition region the potential energy and the total energy are two-valued functions of T. The temperatures T_f and T_m define a finite coexistence region (26–37 K) where two stable forms of the cluster, one solid-like and one liquid-like, exist in stable equilibrium. The calculated points in this region are characterized in Fig. 3.4 by the dark symbols: the triangles correspond to points calculated separately over each phase, and the circles represent a combined average over coexisting forms. The dynamical coexistence is easily demonstrated using constant energy or constant temperature MD simulations. For constant-T simulations, averages of the potential energy over short time periods (times corresponding to a few breathing periods) can be obtained. When those short time averages $\langle U \rangle_{sa}$ are plotted as a function of time, they separate into two bands corresponding to the solid-like and liquid-like forms. The simulation shows that the system frequently exchanges from one band to the other, although stays in a given form for times large compared with typical vibrational frequencies [25]. A similar way of separation is obtained by calculating a distribution for those short time averages of the potential energy. Outside the coexistence region the distribution presents a single peak, but for temperatures in the coexistence region the distribution is bimodal. Although the dynamical coexistence behavior is not a general feature, the MD simulations have shown that it occurs also for many other small inert gas clusters, especially for the magic number sizes [23, 25]. An energy gap between a lowest energy structure, or more generally a band of low energy states, and another band of high energy states, as it occurs for the magic clusters, is considered to be necessary for dynamical solid–liquid coexistence [26, 27].

The changes in slope of the caloric curve become reflected on the specific heat

$$C_V = \frac{1}{N}\frac{\partial E}{\partial T}. \tag{3.8}$$

In MD simulations this can be calculated as

$$C_V = \left[N - N\left(1 - \frac{2}{3N-6}\right)\langle E_{kin}\rangle\langle E_{kin}^{-1}\rangle \right]^{-1}. \tag{3.9}$$

This magnitude is related to the fluctuations in the kinetic energy; it has peaks associated to the slope changes in the caloric curve. At low temperatures and for all cluster sizes, C_V goes to the classical (harmonic) limit $C_V = k_B$. Plotted as a function of temperature, C_V for Ar_{13} begins to increase steeply near 26 K and has a broad peak centered at 35 K [25]. At this temperature C_V reaches a value five times its value at low temperature. The features of the peak (width and position of the maximum) are consistent with the position and shape of the coexistence region in the caloric curve.
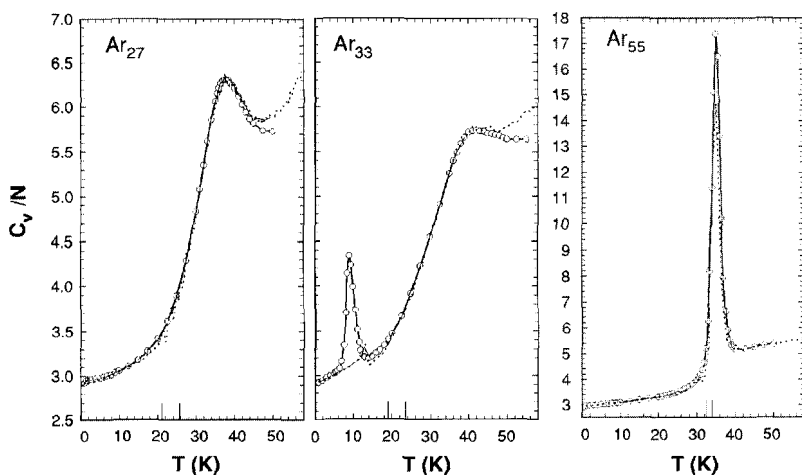
Figure 3.5. Heat capacity per particle as a function of temperature for Ar_{27}, Ar_{33} and Ar_{55}, obtained from Monte Carlo simulations. Solid and dotted lines are results from simulations with different sampling. The large ticks on the temperature axis indicate the temperatures where the r.m.s. bond length fluctuations rise sharply in MC simulations with walks of 107 and 108 passes per temperature. Adapted from D. D. Frantz, *J. Chem. Phys.* **115**, 6136 (2001) with permission of the American Institute of Physics.

Franz [11, 12] has performed a systematic study for argon clusters with sizes up to $N = 60$ using Monte Carlo methods. The interactions were simulated by LJ potentials. In this case, instead of using Eq. (3.9), C_V is calculated from the alternative expression

$$C_V = \frac{3(N-6)k_B}{2} + \frac{\langle U^2 \rangle - \langle U \rangle^2}{T^2}. \tag{3.10}$$

The C_V curves change nonmonotonically with cluster size. For $N = 4$, 5 and 8, C_V rises slowly with T until the clusters reach the dissociation region where C_V increases sharply. For $N = 7$ and $N = 15$–17, there is a shoulder in the solid–liquid transition region. All the other clusters have at least one peak in the heat capacity curves. There is agreement, concerning the position and width of the peak, for those clusters for which MD simulations have also been performed, although some discrepancies between the MC and MD simulations have been noticed. Although the MC simulations cannot display the dynamical coexistence, many of the results obtained by MC simulations are consistent with this view, specially for the magic number clusters.

Selected examples are shown in Fig. 3.5. Ar_{27} shows a broad peak centered at $T = 27$ K. In addition to a similar broad peak, Ar_{33} has a smaller, but sharp peak, at $T = 10$ K. Finally, a single sharp peak appears for Ar_{55}. Systematic trends on the number and magnitude of the peaks are evident in Fig. 3.6, showing that cluster sizes $N = 13, 19, 23, 36, 39, 43, 49$ and 55 have peaks significantly higher than those of their neighbors, so the special stability of those magic clusters reappears in the behavior of C_V. Clusters with $N < 30$ have a single broad peak (shown for Ar_{27} in Fig. 3.5). A second, sharp peak, emerges for Ar_{30}, and its magnitude increases as the first peak gradually disappears. The two peaks coexist up to Ar_{36} (see the case of Ar_{33} in Fig. 3.5), and for Ar_{37} and larger clusters only the sharp peak remains. The emergence of the sharp peak nearly coincides with the transition from FC to MIC covering, and the cluster sizes with two peaks correspond to those sizes having the greater density of low lying isomers [11]. Doye *et al.* [28] found that the high density of states in this size range is due to small energy differences between various structural types, FC, MIC, decahedral, *etc.* The presence of two heat capacity peaks makes the

determination of the melting temperatures ambiguous in that size range, and the use of other indicators is convenient.
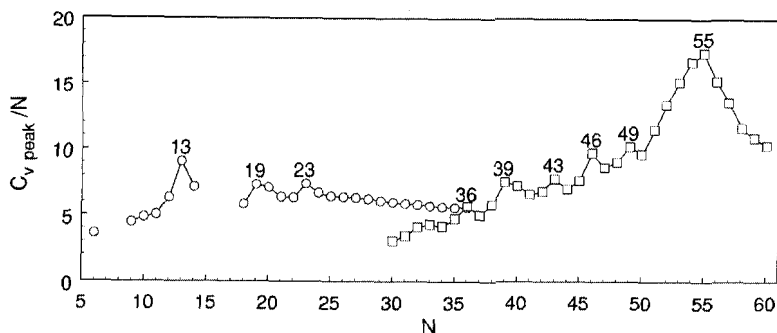
Figure 3.6. Reduced heat capacity peak values of Ar$_N$ clusters. Results from Monte Carlo simulations. Adapted from D. D. Frantz, *J. Chem. Phys.* **115**, 6136 (2001) with permission of the American Institute of Physics.

A measure and characterization of the movements of the atoms is given by the relative root mean square (r.m.s.) bond length fluctuation

$$\delta = \frac{2}{N(N-1)} \sum_{i<j} \frac{\left(\left\langle r_{ij}^2 \right\rangle - \left\langle r_{ij} \right\rangle^2\right)^{1/2}}{\left\langle r_{ij} \right\rangle} \tag{3.11}$$

where r_{ij} is the instantaneous distance between atoms i and j, and the sum runs over all the atom pairs. The interpretation of δ is based on the Lindemann criterion. According to it, melting occurs in a bulk solid when δ is about 0.1. However, care must be taken when interpreting r.m.s. bond length fluctuations obtained from computer simulations, since the choice $\delta = 0.1$ does not necessarily extend to finite clusters [29]. Also, δ may depend on the length of the simulation runs. But in spite of these reservations r.m.s. bond fluctuation curves have a qualitative validity and provide insight.

Figure 3.7 shows δ as a function of temperature for $N = 19, 20, 21$. The temperature is given in reduced units $T^* = k_B T/\varepsilon$. A nearly linear

increase of the fluctuations occurs as the temperature is increased in the solid-like region. Then δ rises sharply in the transition region as the clusters have enough energy to overcome potential barriers to rearrangement, and finally the fluctuations level off in the liquid region. $N = 19$ displays its special character by the higher temperature for the occurrence of the transition, and in the steepest rise of δ. The size dependence of the temperatures corresponding to a Lindemann-like threshold of $\delta = 0.2$ is shown in Fig. 3.8. That threshold was chosen because it was near the inflection point of the δ curves in the transition region [11]. For the size range plotted, there is first a general decrease of the melting temperature with increasing size, reaching a minimum near $N = 37$, then it increases reaching a maximum for $N = 55$, and decreases thereafter. Superposed to this behavior, local maxima are obtained for the magic clusters.
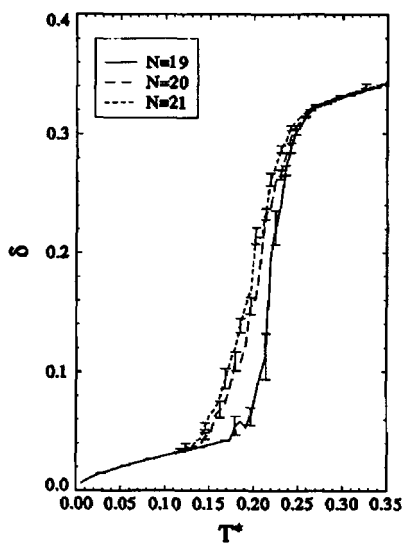
Figure 3.7. R.m.s. bond length fluctuation as a function of temperature, obtained by Monte Carlo simulations for Lennard–Jones clusters with N = 19–21. Temperature is given in reduced units. Adapted from D. D. Frantz, *J. Chem. Phys.* **102**, 3747 (1995) with permission of the American Institute of Physics.
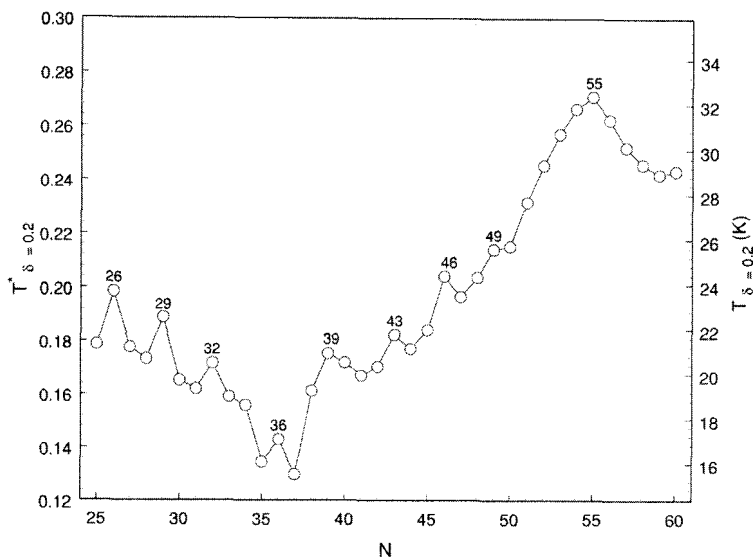
Figure 3.8. Reduced melting temperatures (left axis) associated with a Lindemann-type threshold $\delta = 0.2$ of the r.m.s. bond length fluctuations. Magic number behavior is observed as a function of cluster size. The results have been obtained by MC simulations. The right hand axis is representative of argon. Adapted from D. D. Frantz, *J. Chem. Phys.* **115**, 6136 (2001) with permission of the American Institute of Physics.

A comparison with Fig. 3.5 shows that the melting temperatures of Ar_{27} and Ar_{55} predicted by $\delta = 0.2$, namely $T_m = 21$ K and $T_m = 32$ K, respectively, lie on the rising side of the C_V curves and not at their maxima. In fact, the peaks of C_V occur at temperatures such that $\delta = 0.3$ or higher [11], that is, well in the liquid phase. This is a general feature for the clusters with a single peak in the C_V curve. However, there is a clear distinction between the two families: the C_V curve rises and reaches its peak over an interval of 10–20 K in clusters like Ar_{27}, while the interval is very narrow in the sharp-peak clusters like Ar_{55}. In the cases of a double peak, like Ar_{33}, the melting temperature defined by $\delta = 0.2$ lies in between the two peaks. Although the heat capacity curves of $N = 5$ and 8 lack features suggesting a melting transition, the r.m.s. bond length fluctuation curves are similar to those for $N = 6$ and $N = 7$ respectively, and show the sharp rise of δ (T) characteristic of a

transition. The shape of the $\delta(T)$ curve for $N = 4$ is consistent with the absence of a solid to liquid transition. This stresses the convenience of employing several indicators to study the melting transition.

3.3.3 Mixed inert gas clusters

Different inert gas atoms have different sizes and dimer binding energies. Consequently, mixing those atoms leads to clusters with structural and thermodynamic features different from those of the homogeneous clusters. Heterogeneous clusters with 13 atoms have been studied in detail. The homogeneous 13-atom clusters show a large C_V peak in the solid to liquid transition region that is a consequence of the large energy gap between the ground state icosahedral structure and the higher lying nonicosahedral isomers. The interatomic potentials for the Ar–Ar and Kr–Kr interactions are relatively similar, $\varepsilon_{Ar-Ar} / \varepsilon_{Kr-Kr} = 0.728$, and $\sigma_{Ar-Ar} / \sigma_{Kr-Kr} = 0.942$, so only mild differences with respect to the homogeneous clusters are expected. Calculations for mixed Ar_pKr_{13-p} clusters using pair interactions determined by the usual mixing rules, *i.e.*, $\varepsilon_{Ar-Kr} = (\varepsilon_{Ar-Ar} \, \varepsilon_{Kr-Kr})^{1/2}$ and $\sigma_{Ar-Kr} = (\sigma_{Ar-Ar} + \sigma_{Kr-Kr}) / 2$, predict that all those clusters have icosahedral ground states, with the smaller Ar atom at the center, and that the structure of most low lying isomers is also icosahedral [30]. The shape of the heat capacity curves is similar to that for homogeneous clusters. There is a linear increase in the peak temperature from Ar_{13} to Ar_7Kr_6 followed by a steeper linear rise from Ar_6Kr_7 to Kr_{13}. Peak heights are relatively similar, with the differences between the maximum and minimum values being only about 12% of the peak height of Ar_{13}. An interesting difference with respect to the homogeneous clusters occurs: an additional very small peak at very low temperatures, arising from the low lying permutational isomers.

In contrast to the Ar–Kr case, Ne–Ne and Ar–Ar potentials are rather different: $\varepsilon_{Ne-Ne} / \varepsilon_{Ar-Ar} = 0.298$, $\sigma_{Ne-Ne} / \sigma_{Ar-Ar} = 0.807$. The structure of the ground state varies across the Ne_pAr_{13-p} series. It is an icosahedron on the two composition extremes, Ne-centered for $Ne_{12}Ar$ and $Ne_{11}Ar_2$, and Ar-centered for Ne_4Ar_9 to $NeAr_{12}$. But the difference of atomic sizes affects negatively the stability of the icosahedral structure and the ground state is nonicosahedral for middle compositions $Ne_{10}Ar_3$ to Ne_5Ar_8. The low lying isomers are mostly nonicosahedral. By looking at the shape of the C_V curves, the clusters can be associated into three groups: Ne_{13} to

$Ne_{10}Ar_3$ have melting temperatures (identified with the temperature of the maximum of the C_V peak) in the range 5–10 K, much lower than the others, Ne_9Ar_4 to Ne_4Ar_9 , which have melting temperatures in the range 22–26 K, and finally Ne_3Ar_{10} to Ar_{13}, whose peak temperatures rise linearly. The peaks are high for Ne_{13} , $NeAr_{12}$ and Ar_{13}, that is, on the two extremes, because the energy gaps between the ground state and the band of low lying isomers are high for those three clusters, but not for the others. Then, peaks are much lower for compositions in between. The peaks in the group Ne_9Ar_4 to Ne_4Ar_9 are broad.

For Ar–Xe, $\varepsilon_{Ar-Ar} / \varepsilon_{Xe-Xe} = 0.540$ and $\sigma_{Ar-Ar} / \sigma_{Xe-Xe} = 0.829$. All the Ar_pXe_{13-p} clusters have an icosahedral ground state. The stronger binding favors the Xe-centered structure, but this is disfavored by the loss of packing efficiency arising from having the larger atom at the cluster center, so the ground state is an icosahedron centered on an Ar atom. The lowest Xe-centered isomer is also icosahedral. The difference in energy between the lowest Ar-centered and Xe-centered states increases from $Ar_{12}Xe$ to Ar_6Xe_7 and then decreases, nearly vanishing for $ArXe_{12}$ [31]. In $ArXe_{12}$ the two nearly degenerate icosahedral ground states form separate basins in the potential energy surface, separated by substantial energy barriers. Each basin has a set of low and high energy states. MD heating cycles starting from those two icosahedral states indicate that the two basins separately undergo substantial melting (in different regions of the configuration space, and to a larger extent within the Ar-centered basin) before merging. This melting whithin a particular basin can be interpreted as surface melting, since there are no exchanges between the central atom and the surface atoms. The complete melting occurs when the energy allows for frequent interbasin motion. Those liquid phases which access only a resticted region of configuration space have been called isomerization fluids [32]. Also for other compositions the configuration space is divided into two basins. The temperature for barrier crossing decreases when the number of Xe atoms decreases, so surface melting is only well separated from complete melting for the Xe-rich clusters. This particular basin structure does not seem to exist for Ne_pAr_{13-p} and $Ar_p Kr_{13-p}$.

3.3.4 Liquid to gas phase transition in hydrogen clusters

Gross and coworkers [33] have concluded that the best signature of a first or second order phase transition in a finite system is provided by the

specific shape of the caloric curve, that is, the thermodynamic temperature as a function of the total energy of the system. The caloric curve of size-selected hydrogen clusters has been determined in high energy collision experiments [34, 35] and has been interpreted as indicating the transition from a bound cluster to the gas phase.

In these experiments, the mass selected hydrogen cluster ions are prepared by first forming the clusters in a cryogenic cluster jet expansion source and then using a high performance electron ionizer and an ion accelerator [36]. The neutral clusters are molecular clusters formed by H_2 molecules weakly bound to each other by Van der Waals forces. Ionization of a molecule in the cluster or in a H_2 crystal is followed by the exothermic ion–neutral reaction

$$H_2^+ + H_2 \rightarrow H_3^+ + H \tag{3.12}$$

and the exothermicity (1.7 eV) usually ejects the H atom from the cluster. The H_3^+ cation is stabilized by the other H_2 molecules, that form a solvating shell around it [37, 38]. The cluster cations then have the composition $H_3^+(H_2)_m$. The same effect occurs in *hcp* hydrogen crystals [39] where the stabilization of the cation trimer produces a microcrystal, evidently with a structure different from that of the gaseous cluster cations. In the experiments of Gobet *et al.* [34, 35], the collisions between size-selected ionized clusters $H_3^+(H_2)_m$ with $m \leq 14$, accelerated to kinetic energies of 60 keV/amu, and a helium gas target were analysed. A sophisticated multidetector device records for each collision event simultaneously the number (multiplicity) of each mass-identified fragment ion resulting from the reaction. The fragmentation reactions have the general form

$$H_3^+(H_2)_m + He \rightarrow H_3^+(H_2)_k + bH_3^+ + cH_2^+ + dH^+ + eH_2 + fH \tag{3.13}$$
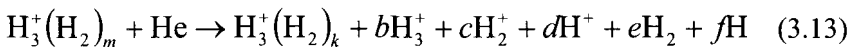
with $a–f = 0,1,\ldots$ (neutral species larger than the dimer are absent). Construction of the caloric curve requires the simultaneous determination of the energy and the temperature of the system. The cluster energy, that is the energy deposited into the cluster by the collision with a He atom, is determined by the nature and multiplicity of the products in the reaction (3.13). On the other hand, the temperature of

the cluster prior to decay is obtained using a relationship [40], tested successfully in nuclear physics, between the characteristic shape of a fragment mass distribution and the temperature of decaying nuclei [41].
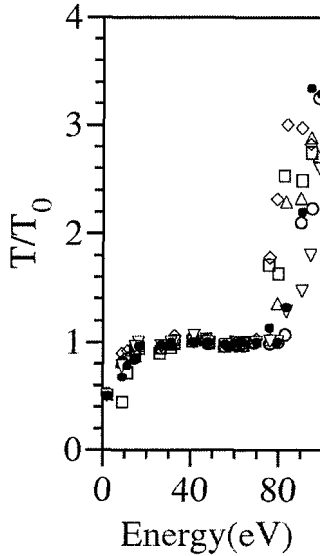
Figure 3.9. Caloric curves for cluster fragmentation. Reduced temperature (with T_0 the temperature in the plateau of the curve) is given *vs* the energy deposited on the clusters $H_3^+(H_2)_m$, with $m = 6$ (open squares), $m = 8$ (open circles), $m = 9$ (triangles), $m = 11$ (diamonds), $m = 12$ (inverted triangles) and $m = 14$ (filled circles). Reproduced from F. Gobet *et al.*, *Phys. Rev. Lett.* **89**, 183403 (2002) with permission of the American Physical Society.

The results [34, 35] for $H_3^+(H_2)_m$ with $m = 6, 8, 9, 11, 12$ and 14 are collected in Fig. 3.9. The caloric curves show three parts: after an initial rise, a plateau is present before the curve rises again. The curves show the typical prerequisites of a first order phase transition. According to Gobet *et al.* [35] the curves show backbending (this is more clear by plotting a curve with the geometric means for all the clusters), that is, a negative heat capacity, that has been predicted to be possible for small systems [33].

3.4 Electronic Effects

3.4.1 Delocalized electronic states of excess electrons

Inert gas atoms have their last electronic shell filled and do not bind additional electrons due to the efficient screening of the positive core by the closed shells. On the other hand, the collective polarizability of rare gas atoms produces an effect that binds excess electrons in solid xenon, with the bottom of its conduction band lying about 0.6 eV below the vacuum level [42]. Experimental evidence for the existence of stable negatively charged $(Xe_N)^-$ clusters was provided by Haberland [43]. From this work and theoretical calculations [44, 45] it is known that the minimal size for the stability of the negatively charged cluster is around 6–7 atoms. The tiny small binding of the solvated electron in the inert gas clusters makes spectroscopic studies difficult, but those studies become easier for Xe clusters doped with a highly electronegative impurity like iodine [46, 47]. $(IXe_N)^-$ clusters have been produced by a supersonic expansion of a mixture of 5% Xe and 95% Ar passed through a cooled (-60 °C) reservoir of methyl-iodide. The clusters became negatively charged by crossing the expansion by an electron beam. In its ground state the extra electron of the cluster is localized on the iodine atom, which is solvated by the Xe cluster. That is, the cluster can be labeled as I^-Xe_N. Photons of 4.66, 5.01 and 5.27 eV were used to measure the photoelectron spectra (PES) of mass selected clusters. All the spectra are characterized by two peaks about 0.95 eV apart (see Fig. 3.10). Those peaks are assigned to the vertical detachment transitions from the ground state of the solvated anion I^- to the $J = 3/2$ (ground state) and $J = 1/2$ spin states, respectively, of the neutral I with the neutral IXe_N cluster in the same geometrical structure of the negative one. The evolution of the lowest energy peak ($J = 3/2$) giving the vertical binding energies *VBE*, is reported in Table 3.4. The difference

$$E_{stab} = VBE_{3/2}(N) - VBE_{3/2}(0),\qquad(3.14)$$

given also in that Table, represents the stabilization of the ground state by the polarization interaction of the iodine with the xenon solvent. The dependence of E_{stab} with cluster size reflects the grouping of Xe atoms

around the iodine ion. E_{stab} increases fast until $N = 12$, and then increases more slowly for clusters containing more than 12 xenon atoms. This indicates that 12 atoms form the first solvation shell around the ion.
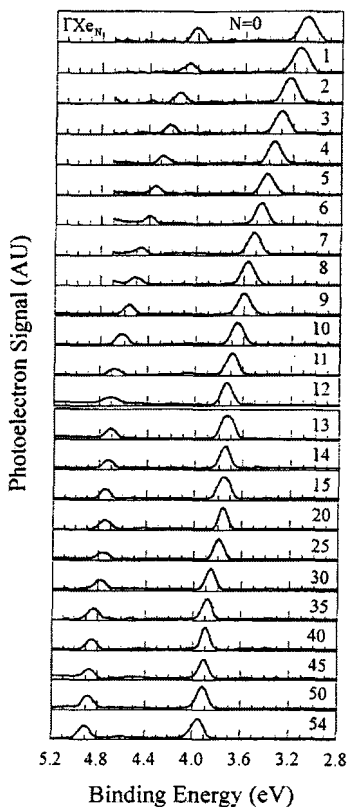
Figure 3.10. Photoelectron spectra of I^-Xe_N clusters with $N = 0$–54, obtained using photons of 5.01 and 5.27 eV. Reproduced from I. Becker. and O. Cheshnovsky, *J. Chem. Phys.* **110**, 6288 (1999) with permission of the American Institute of Physics.

A tunable laser was then used to study the excitation spectrum of the I^- impurity in mass selected clusters over an spectral range $3.0 - 4.95$ eV. For this excitation, electron emission was the only observed decay

channel. The excitation spectra has an interesting evolution. Fig. 3.11 shows that peaks appear at energies below the $VBE_{3/2}(N)$ and $VBE_{1/2}(N)$. Those peaks (bands) narrow with increasing N and the distance between these bands and $VBE_{3/2}(N)$ or $VBE_{1/2}(N)$, respectively, increases with N. It is clear that electron detachment below $VBE_{3/2}$ is connected with cluster geometric rearrangements. These bands, above the adiabatic detachment energy, correspond to transitions from the localized electron of the iodine ion to delocalized states on the Xe cluster.

Table 3.4. Experimental vertical binding energies (VBE), stabilization energy $E_{stab}=VBE(N)-VBE(0)$, vertical delocalization energy (VDE), and binding energy of the delocalized electron (VBE-VDE) of iodine in I^-Xe_N clusters. Data collected from [46, 47].

N	VBE (eV) (± 20 meV)	VDE (eV) (± 3 meV)	Binding energy of delocalized electron (meV) (± 20 meV)	E_{stab} (eV)
0	3.06			
1	3.13			0.07
2	3.22	3.255	-35	0.16
3	3.29	3.295	-5	0.23
4	3.35	3.339	11	0.29
5	3.41	3.391	19	0.35
6	3.46	3.440	20	0.40
7	3.41	3.486	24	0.45
8	3.56	3.532	28	0.50
9	3.60	3.569	31	0.54
10	3.65	3.608	42	0.59
11	3.69	3.461	49	0.63
12	3.73	3.675	55	0.67
13	3.746	3.678	68	0.686
15	3.763	3.690	73	0.703
20	3.793	3.712	81	0.750
30	3.848	3.757	91	0.788
40	3.894	3.787	107	0.834
50	3.935			0.875
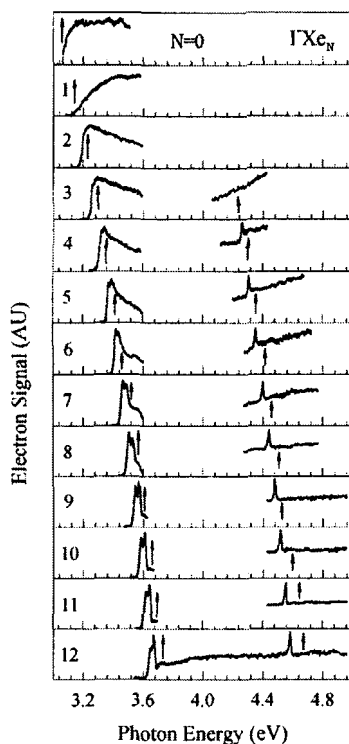
Figure 3.11. Spectra of I^-Xe_N clusters with $N = 0–12$. Arrows indicate vertical binding energies (*VBE*) of iodine with final $J = 3/2$ and $J = 1/2$ spin state. Reproduced from I. Becker and O. Cheshnovsky, *J. Chem. Phys.* **110**, 6288 (1999) with permission of the American Institute of Physics.

The transitions to delocalized states are precursors of the impurity to conduction band transitions in the bulk. One of the bands was identified as giving the vertical delocalization energy (*VDE*) of the impurity electron, whose values are also given in Table 3.4. The difference *VBE-VDE* gives the binding energy of the delocalized electron; its value changes from negative to positive and the critical size for the binding of such states is $N = 4$. As N grows, the binding energy increases due to the confinement. The detachment of the delocalized electron takes place by a process similar to thermionic emission.

3.4.2 Core level spectroscopy

The wave functions of core levels have atomic character and are highly localized, even in solids. But the small changes induced by the local atomic environment become reflected in the core level spectra. Of particular interest is the evolution of the electronic core levels with cluster size and their relation to the geometrical structure. The study of resonant X-ray absorption (XA) in neon clusters has provided useful information [48]. The electronic structure of the neon atom is $1s^2\, 2s^2\, 2p^6$ and its K shell excitation spectrum is characterised by a Rydberg series ($1s \rightarrow$ np). In the atom, the $1s \rightarrow 3p$ and $1s \rightarrow 4p$ transitions to unoccupied bound states are well resolved at 867.1 eV and 868.7 eV, respectively. The simple character is preserved for Ne clusters, but the lines are shifted and split into surface and bulk components. For small clusters ($N < 100$) the two observed resonances correspond closely to the atomic lines. The energy of the $1s \rightarrow 3p$ line first increases a little with the cluster size due to the caging effect of the surrounding atoms. Then, for N around 100, that line becomes split in two. First, a low energy component continues the smooth evolution of the original line and can be identified as being associated to $1s \rightarrow 3p$ transitions for atoms at the surface of the cluster. Second, a new feature emerges at 868.4 eV. This new feature, that becomes more prominent for increasing cluster size, is attributed to the $1s \rightarrow 3p$ excitation of atoms having a bulk-like environment in the cluster. The $1s \rightarrow 4p$ line also shows an interesting evolution. It first shifts downwards in energy. This cannot be explained by caging effects. Instead it indicates that the $4p$ is a Rydberg orbital located largely outside the cluster, so the energy required for that excitation will be reduced due to screening of the core hole by the other atoms. For clusters of about 300 atoms this line vanishes and a new line appears around 869.6 eV. The interpretation is that the Rydberg state no longer exists for large clusters, and that the new line at 869.6 eV is just the bulk-like $1s \rightarrow 4p$ line.

Combined X-ray absorption and X-ray photoelectron (XP) spectroscopies applied to the $2p$ core levels of argon clusters have also allowed to identify bulk and surface features [49]. In the free Ar atom the XA spectrum is due to transitions from the $2p$ core level to unoccupied Rydberg orbitals, and the lowest energy transition $2p_{3/2} \rightarrow 4s$ is located at an energy of 244.39 eV. In the cluster this excitation is shifted to higher energy and splits into two components. The component line with

lower energy is dominant for small clusters and shifts upward in energy with growing cluster size with respect to the atomic line. It reaches a value of 244.70 eV for clusters with a few hundred atoms (a shift of +0.31 eV with respect to the atom). On the other hand the higher energy line, absent for very small clusters, has a nearly constant energy 245.24 eV over the whole range of sizes studied (up to a few thousand atoms). The high energy line becomes dominant as the cluster sizes increases, evolving towards the core exciton observed for the solid, while the other line vanishes. The final $2\ p_{3/2}^{-1}\ 4s$ Rydberg state has a substantially larger spacial extent than the ground state, but in a cluster it is a little bit compressed by the surrounding atoms, leading to a slight loss of binding of the Rydberg state with respect to the free atom. The excitation energy $2p_{3/2} \rightarrow 4s$ then increases with increasing atomic coordination. Consequently, the size-independent high energy line was interpreted as corresponding to bulk-like atoms and the size-dependent low energy line as arising from surface atoms, since the coordination number of surface atoms (or effective confinement) increases with cluster size.

More quantitative information about surface coordination is obtained from the XP spectrum, which measures the binding energy of the core electrons. In the spectrum of the Ar atom, the two $2p_{1/2}$ and $2p_{3/2}$ spin-orbit lines are observed at 248.4 and 250.6 eV binding energies, respectively. For clusters, those lines are gradually shifted to lower energies. In the size range of thousand atoms the shifts are 0.62 and 0.95 eV respectively. Furthermore, each line is split in two components. In the clusters, the ionized core polarizes the surrounding atoms, and this polarization screening lowers the binding energy of the $2p$ level with respect to the free atom. The nearest neighbors are the most efficient for screening and the two split components can be attributed to atoms in the bulk (low binding component) and surface (high binding component) of the cluster, respectively. The bulk-like component becomes the prominent one for large clusters due to the decreasing fraction of surface atoms. Extrapolation of the results to large N can be used to derive values for the binding energies of the $2p$ electrons in bulk and surface atoms in a macroscopic solid. Furthermore, a linear model for the shift as a function of the number of nearest neighbors (12 in the bulk solid) predicted effective coordination numbers at the surface of the cluster varying from five, for clusters of about 10 atoms, to eight for the largest clusters studied, $N = 4000$.

The decay of a core hole vacancy by electron emission is known as Auger decay. It is traditionally assumed that in molecules, atomic aggregates and bulk matter, only electrons at the excited site take active part in the decay, but a novel decay mechanism has been predicted to be possible in weakly bound Van der Waals clusters [50]. In this novel mechanism, electron emission from neighboring sites of the vacancy takes place. Experimental evidence for this new process has been found in small Ne clusters, with average sizes of 30 and 70 atoms [51]. Using sincrotron radiation to irradiate a beam of clusters, a hole was first created in the $2p$ inner valence subshell of one of the Ne atoms in the cluster. This atom then adopts the electron configuration Ne^+: $2s^1\ 2p^6$. For a free Ne atom, the 2s vacancy cannot decay by an Auger process because the transition from Ne^+: $2s^1\ 2p^6$ to the final state Ne^{2+}: $2s^2\ 2p^4$ by electron emission is not energetically possible. But in the cluster, the $2s$ vacancy can relax from the state Ne^+: $2s^1\ 2p^6$ to $(Ne^+$: $2s^2\ 2p^5)_2$, that is, the two vacancies are distributed among neighboring atoms in the final state. The Coulomb repulsion between them is reduced, and then also the total energy. The process has been termed *interatomic Coulomb decay* [50].

3.5 Clusters of SF_6 and CO_2 Molecules

The transition to the bulk structure for molecules interacting by Van der Waals forces involving some angular anisotropy occurs much earlier than for the simpler atomic Van der Waals clusters. This is the case for $(SF_6)_N$ and $(CO_2)_N$. The experiments that have revealed this transition use Electron Attachment Time-of-Flight (EA-TOF) mass spectrometry [52] and electron diffraction [53, 54]. Negative cluster ions are formed in the molecular beam by directing a continuous electron beam along the TOF axis of the mass spectrometer. Electrons are readily captured by the SF_6 molecule, since this molecule has a positive electron affinity. In contrast, the energy of the local minimum of $(CO_2)^-$ is ≈ 0.6 eV above the energy of the autodetachment products [55], that is, the electron affinity is negative, so $(CO_2)^-$ is not simple to detect; however, negatively charged dimers and larger clusters are bound.

The low mass spectrum of $(SF_6)_N$ reveals, as its most prominent feature, the enhanced abundance of $(SF_6)_{13}$. Although $N = 19$ is not prominent, drops in the population occur after $N = 23$, 27 and 34 [52]. This gives evidence for icosahedral structures, since the above numbers correspond to the perfect icosahedron (13) and to clusters formed by interpenetrating icosahedra (23, 27, 34). The small differences with respect to the numbers for completing FC umbrellas given in Section 3.1 are simply due to the way of constructing those capping umbrellas. For instance, $N = 27$ (instead of 26) is obtained when the third umbrella is adjacent to the first one but not the second. There is no evidence for icosahedral packing beyond $N = 34$, but the mass spectra for sizes up to about $N = 600$ showed characteristic intensity oscillations, indicating atomic shells. The analysis of those oscillations using a geometrical theory developed by Martin and coworkers [56] revealed a single packing motif in that size range. Molecular beam diffraction experiments had earlier provided diffraction patterns for clusters with 100–1000 SF_6 molecules [53, 54], and the comparison of the measured diffraction patterns to calculated ones for different structural models led to the conclusion that SF_6 clusters are packed in the low-temperature monoclinic crystal structure (a distorted body centered cubic structure) observed in the bulk [57]. Since the size ranges covered by the electron diffraction and the EA-TOF experiments overlap strongly, this immediately suggests that the geometrical shell closing pattern detected by the EA-TOF experiments corresponds to the monoclinic crystal structure, and that this structure persists to very small clusters. The overall geometrical characteristics of the clusters, derived from the analysis of the oscillations in mass spectra are consistent with the monoclinic structure [52]. Two pronounced intensity maxima close to the transition region, namely $(SF_6)_{59}$ and $(SF_6)_{52}$ apparently correspond to nearly spherical clusters cut from the crystal, and this suggests that the transition for these clusters may be related to the size where nearly spherical clusters may be built out of the bulk crystal.

CO_2 clusters are more weakly bound than SF_6 clusters. The comparison of electron diffraction patterns to molecular dynamics simulations indicated that the CO_2 molecules in large $(CO_2)_N$ clusters are packed in the face centered cubic (*fcc*) structure of the bulk, and that this packing persists to clusters as small as $N = 100$ [58–60]. The EA-TOF mass spectra show oscillations indicating shells [52], and the analysis

was performed in a similar fashion as for SF_6 clusters. The data for clusters larger than $(CO_2)_{75}$ is consistent with a distorted *fcc* packing. It is intriguing why clusters formed by SF_6 and CO_2 molecules achieve the bulk packing so early.

3.6 Interaction with Ultrafast Laser Pulses

Experiments have been conducted to examine the interactions of intense ultrafast laser pulses with Van der Waals clusters. Laser pulses focused to intensities between 10^{16} and 10^{18} W/cm^2 have shown very bright X-ray emission in the 100 to 5000 eV range from the plasmas produced [61]. This indicates an efficient coupling of the laser light to the cluster. The coupling is very efficient compared to the irradiation of monatomic gases and is a consequence of the near solid density within the individual clusters. The dynamics of femtosecond laser interactions has also been examined. A remarkable observation is that clusters irradiated at intensities above 10^{15} W/cm^2 eject ions with high kinetic energies [62].

The irradiation of a dense beam of deuterium clusters has driven nuclear fusion [63]. The deuterium clusters are molecular clusters formed by D_2 molecules. The dissociation energy of a D_2 molecule in two deuterium atoms is 4.8 eV. On the other hand, the molecules are bound to each other in the cluster by weak Van der Waals forces. Irradiation leads to the multiple ionization of the clusters, which then explode under the action of the repulsive Coulomb forces between the ionized atoms. Using an intense and fast enough laser pulse (35 fs pulses were used in the experiments), the clusters can be stripped of almost all their electrons before exploding. This maximizes the Coulomb energy that is converted into kinetic energy of the exploding ions. The initial radius R of the cluster determines the maximum energy E_{max} produced in the explosion. A simple estimation gives

$$E_{\max} = \frac{q n_D e^2 R^2}{3\varepsilon_0} \tag{3.15}$$

where n_D is the initial ion density in the cluster ($\approx 3 \times 10^{22}$ cm^{-3} for D_2), and q is the average charge state. From this formula one finds that fully

stripped deuterium clusters of radii greater than 25 Å are enough to produce the multi-keV ions necessary for fusion when fast deuterium ions ejected from the exploding clusters collide with ions ejected from other clusters in the plasma. In the experiments of Zweiback *et al.* [63] an inverse correlation has been found between the neutron yield and the temperature of the clusters before irradiation, that is, the neutron yield decreases when the temperature increases. The cluster beam is prepared at a specified temperature by passing the beam though a cooling jacket, and as a consequence the average cluster size in the beam decreases by increasing the temperature (in all cases the beams are prepared with temperatures between 80 K and room temperature). Then, the observed behavior of the neutron yield is a consequence of the variation of the average cluster size with beam temperature. Larger cluster sizes allow for larger electrostatic energies to be converted to ion kinetic energies. Measurable neutron yields start at cluster radii of about 25 Å (molecular jet temperatures about 125 K) and rapidly increase, by more than an order of magnitude, until the radius reaches 50 Å (temperatures of 100 K). For larger radii, the neutron yield becomes a constant or even decreases because clusters are too large.

Ions with kinetic energies of several 100 keV are ejected from the explosion of large Ar_N and Xe_N clusters with average sizes in the range 1.8×10^5 atoms for argon and 2.0×10^6 for xenon, irradiated by 130 fs laser pulses and intensities of 5×10^7 W cm^{-2} [62]. The kinetic energies in the case of the Ar clusters fit well into a Coulomb explosion mechanism, in which the kinetic energies $E_k(q)$ of the ions depend on their charge q as

$$E_k(q) = \alpha q^2 \tag{3.16}$$

where α is a constant ($\alpha = 160$ for E_k in eV for Ar). For Xe, the cluster size is an order of magnitude larger. Also, the electron temperature is expected to be larger, since the electron heating rises proportional to the square of the atomic number Z^2. Ions as highly charged as Xe^{30+} have been detected in these explosions. The Xe explosions exhibit a behavior that is a mixture of Coulomb explosion and hydrodynamic expansion mechanisms. In the hydrodynamic expansion model the energy

$$E(q) = qkT_e \qquad (3.17)$$

is determined by the electron temperature T_e. However, the most energetic ions in the Xe cluster explosions arise from the Coulomb repulsion.

References

1. Echt, O., Sattler, K., and Rechnagel, E., *Phys. Rev. Lett.*, **47**, 1121 (1981).
2. Mackay, A. L., *Acta Crystall.*, **15**, 916 (1962).
3. Echt, O., Kandler, O., Leisner, T., Miehle, W., and Recknagel, E., *J. Chem. Soc. Faraday Trans.*, **86**, 2411 (1990).
4. Farges, J., De Feraudy, M. G., Raoult, B., and Torchet, G., *J. Chem. Phys.*, **84**, 3491 (1986).
5. Alpress. J. G., and Sanders, J., *Aust. J. Phys.*, **23**, 23 (1970).
6. Boyer, L. L., Broughton, J. Q., *Phys. Rev. B*, **42**, 11461 (1990).
7. Rey, C., Gallego, L. J., Iñiguez. M. P., and Alonso, J. A., *Physica B*, **179**, 273 (1992).
8. Harris, I. A., Kidwell, R. S., and Northby, J. A., *Phys. Rev. Lett.*, **53**, 2390 (1984).
9. Sung, M. W., Kawai, R., and Weare, J. H., *Phys. Rev. Lett.*, **73**, 3552 (1994).
10. Alonso, J. A., *Chem. Rev.*, **100**, 637 (2000).
11. Frantz, D. D., *J. Chem. Phys.*, **115**, 6136 (2001).
12. Frantz, D. D., *J. Chem. Phys.*, **102**, 3747 (1995).
13. Northby, J. A., *J. Chem. Phys.*, **87**, 6166 (1987).
14. Montejano, J. N., Iñiguez, M. P., Alonso, J. A., and López, M. J., *Phys. Rev. B*, **54**, 5961 (1996).
15. Myers, H. P., *Introductory Solid State Physics*, second edition. Taylor and Francis, London (1997).
16. Smirnov, B. M., Strizhev, A. Y., and Berry, R. S., *J. Chem. Phys.*, **110**, 7412, (1999).
17. Ino, S., *J. Phys. Soc. Japan*, **21**, 346 (1966).
18. Marks, L. D., *Philos. Mag. A*, **49**, 81 (1984).
19. Doye, J. P. K., and Calvo, F., *Phys. Rev. Lett.*, **86**, 3570 (2001).
20. Haberland, H., *Surf. Sci.*, **156**, 305 (1985).
21. Soler, J. M., Sáez, J. J., García, N., and Echt, O., *Chem. Phys, Lett.*, **109**, 71 (1984).
22. Leary, R. H., and Doye, J. P. K., *Phys. Rev. E*, **60**, R6320 (1999).
23. Berry, R. S., Beck, T. L., Davis, H. L., and Jellinek, J., *Advances in Chemical Physics*, ed. I. Prigogine and S. A. Rice. Wiley, New York, **70B**, 75 (1988).

24. Adams, J. E., and Stratt, R. M., *J. Chem. Phys.*, **93**, 1332 (1990).
25. Davis, H. L., Jellinek, J., and Berry, R. S., *J. Chem. Phys.*, **86**, 6456 (1987).
26. Bixon, M., and Jortner, J., *J. Chem. Phys.*, **91**, 1631 (1989).
27. Matsuoka, H., Hirokawa, T., Matsui, M., and Doyama, M., *Phys. Rev. Lett.*, **69**, 297 (1992).
28. Doye, J. P. K., Miller, M. A., and Wales, D. J., *J. Chem. Phys.*, **111**, 8417 (1999).
29. Calvo, F., and Spiegelman, F., *J. Chem. Phys.*, **112**, 2888 (2000).
30. Frantz, D. D., *J. Chem. Phys.*, **105**, 10030 (1996).
31. Mehra, V., Prasad, A., and Ramaswamy, R., *J. Chem. Phys.*, **110**, 501 (1999).
32. Calvo, F., and Labastie, P., *J. Phys. Chem. B*, **102**, 2051 (1998).
33. Gross, D. H. E., *Phys. Reports*, **279**, 119 (1997).
34. Gobet, F., Farizon, B., Farizon, M., Gaillard, M. J., Buchet, J. P., Carré, M., and Märk, T. D., *Phys. Rev. Lett.*, **87**, 203401 (2001).
35. Gobet, F., Farizon, B., Farizon, M., Gaillard, M. J., Buchet, J. P., Carré, M., Scheier, P., and Märk, T. D., *Phys. Rev. Lett.*, **89**, 183403 (2002).
36. Farizon, B., Farizon, M., Gaillard, Gobet, F., Carré, M., Buchet, J. P., Scheier, P., and Märk, T. D., *Phys. Rev. Lett.*, **81**, 4108 (1998).
37. Howard, I. A., Leys, F. E., March, N. H., Van Alsenoy, C., Alonso, J. A., and Rubio, A. , *Proc. of SPIE*, Vol. 5118, *Nanotechnology*, Eds. R. Vajtai, X. Aimerich, L. B. Kish and A. Rubio, SPIE, Bellingham, p. 331 (2003).
38. Prosmiti, R., Villareal, P., and Delgado-Barrio, G., *J. Phys. Chem. A*, **107**, 4768 (2003).
39. Momose, T., Lindsay, C. M., Zhang, Y., and Oka, T., *Phys. Rev. Lett.*, **86**, 4795 (2001).
40. Fisher, M. E., *Rep. Prog. Phys.*, **30**, 615 (1967).
41. Belkacem, M., Latora, V., Bonasera, A., *Phys. Rev. C*, **52**, 271 (1995).
42. von Zdrjewski, W., Rabe, J. G., and Schmidt, W. F., *Z. Naturforsch. A*, **35**, 672 (1980).
43. Haberland, H., Kolar, T., and Reiners, T., *Phys. Rev. Lett.*, **63**, 1219 (1989).
44. Martyna. G. J., and Berne, B. J., *J. Chem. Phys.*, **88**, 4516 (1988); *J. Chem. Phys.*, **90**, 3744 (1989).
45. Stampfli, P., and Benneman, K. H., *Phys. Rev. A*, **38**, 4431 (1988); *Z. Phys. D*, **20**, 53 (1991).
46. Becker, I., Markovich, G., Cheshnovsky, O., *Phys. Rev. Lett.*, **79**, 3391 (1997).
47. Becker. I., and Cheshnovsky, O., *J. Chem. Phys.*, **110**, 6288 (1999).
48. Federmann, F., Björneholm, O., Beutler, A., and Möller, T., *Phys. Rev. Lett.*, **73**, 1549 (1994)
49. Björneholm, O., Federmann, F., Fössing, F., and Möller, T., *Phys. Rev. Lett.*, **74**, 3017 (1995).
50. Santra, R., and Cederbaum, L. S., *Phys. Reports*, **368**, 1 (2002).

51. Marburger, S., Kugeler, O., Hergenhahn, U., and Möller, T., *Phys. Rev. Lett.*, **90**, 203401 (2003).
52. Ingolfsson, O., and Wodtke, A. M., *J. Chem. Phys.*, **117**, 3721 (2002).
53. Bartell, L. S., Valente, E. J., and Caillat, J. C., *J. Phys. Chem.*, **91**, 2498 (1987).
54. Torchet, G., *Z. Phys. D*, **20**, 251 (1991).
55. Compton, R. N., Reinhardt, P. W., and Cooper, C. D., *J. Chem Phys.*, **63**, 3921 (1973).
56. Naher, U., Zimmermann, U., and Martin, T. P., *J. Chem. Phys.* **99**, 2256 (1993).
57. Dove, M. T., Powell, B. M., Pawley, G. S., and Bartell, L. S., *Mol. Phys.*, **65**, 353 (1988).
58. Torchet, G., de Feraudy, M. F., Boutin, A., and Fuchs, A. H., *J. Chem. Phys.*, **105**, 3671 (1996).
59. Maillet, J. B., Boutin, A., Fuchs, A. H., *J. Chem. Phys.*, **111**, 2095 (1999).
60. Ikeshoji, T., Torchet, G., de Feraudy, M. F., and Koga, K., *Phys. Rev. E*, **63**, 031101 (2001).
61. Ditmire, T., Donelly, T., Falcone, R., and Perry, M., *Phys. Rev. Lett.*, **75**, 3122 (1995).
62. Lezius, M., Dobosz, S., Normand, D., and Schmidt, M., *Phys. Rev. Lett.*, **80**, 261 (1998).
63. Zweiback, J., Smith, R. A., Cowan, T. E., Hays, G., Wharton, K. B., Yanovsky, V. P., and Ditmire, T., *Phys. Rev. Lett.*, **84**, 2634 (2000).

4. Electronic and Atomic Shells in Metal Clusters

4.1 Experimental Observation of Electronic Shells

Sodium vapor, or other alkaline vapors, can be expanded supersonically from a hot stainless steel oven with a fine exit nozzle, resulting in well focused cluster beams. Clusters form as a result of collisions between the atoms in the tiny expansion zone, terminating some tenths of a millimiter beyond the nozzle. The clusters warm up because the condensation is an exothermic reaction, so there is also a tendency for evaporation. As the expansion proceeds, collisions between Na atoms end, and the tendency to evaporate atoms from the hot clusters dominates. Each cluster loses mass and cools down. In the evaporation chains, clusters with low evaporation rates, *i.e.*, with strong binding energies, tend to become abundant. In 1984, Knight and his coworkers made a remarkable discovery [1, 2]. They found that the abundance distribution shows a nonmonotonic variation as a function of cluster size, with prominent maxima and/or steps at cluster sizes $N = 8, 20, 40, 58$ and 92. Their original results are shown on Fig. 4.1, which has become one of the best known and most influential results in cluster physics. The arguments given above indicate that clusters of those sizes are especially stable. Similar experiments confirmed the same magic numbers in the mass spectra of other alkaline elements (Li, K, Rb, Cs). Furthermore, measurements of the ionization potential, *IP*, as a function of cluster size shown in Fig. 4.2, indicate that the value of *IP* drops abruptly between N and $N+1$ precisely at the values $N = 8, 20, 40, 58$ and 92, that is, at the magic numbers, as well as at $N = 2$ and 18 [2]. The ionization potential is the energy required to remove one electron from the cluster. That coincidence indicates a common underlying reason, related to the

behavior of the valence electrons. Since sodium is a monovalent element, the number of valence electrons in these clusters is 8, 20, 40, 58 and 92, respectively, and those experiments show that the electrons are bound more tightly in the magic clusters. Evidently, these magic numbers are different from those observed in the Van der Waals clusters.
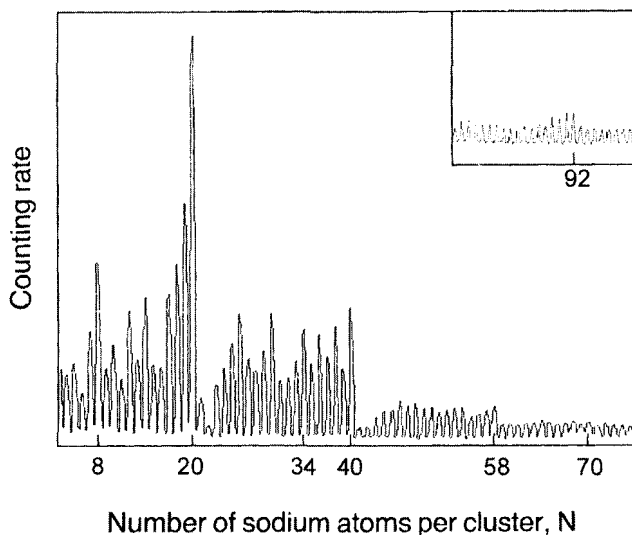
Figure 4.1. Mass spectrum of sodium clusters. Adapted from W. D. Knight *et al.*, *Phys. Rev. Lett.* **52**, 2141 (1984) with permission of the American Physical Society.

Cluster stabilities have also been deduced from dissociation energies in fragmentation experiments [3]. In a typical photodissociation experiment, cluster ions like Na_N^+ are excited by a laser to a highly excited state $(Na_N^+)^*$. The excited cluster can evaporate a neutral atom

$$\left(Na_N^+\right)^* \rightarrow Na_{N-1}^+ + Na \qquad (4.1)$$
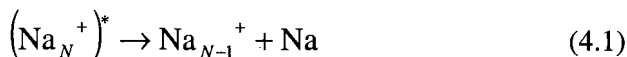
if enough excitation energy to overcome the binding energy D of the Na atom

$$D = E\left(\mathrm{Na}_{N-1}{}^{+}\right) + E(\mathrm{Na}) - E\left(\mathrm{Na}_{N}{}^{+}\right) \tag{4.2}$$

is localized into a single vibrational mode.
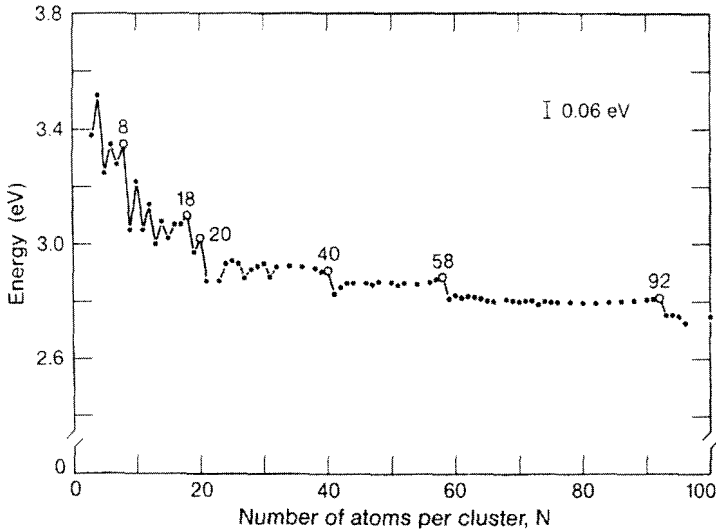
Figure 4.2. Measured ionization potentials of potassium clusters. Reproduced from W. A. de Heer *et al.*, W. A., *Solid State Phys.* **40**, 93 (1987) with permission of Academic Press.

Statistical methods, together with experimental information on the fraction of dissociated clusters have been used [3] to obtain the binding energy in the case of the photodissociation of $\mathrm{Na}_{N}{}^{+}$ and $\mathrm{K}_{N}{}^{+}$. The most relevant conclusion is the occurrence of abrupt drops of the evaporation energy between $\mathrm{Na}_{3}{}^{+}$ and $\mathrm{Na}_{4}{}^{+}$, between $\mathrm{Na}_{9}{}^{+}$ and $\mathrm{Na}_{10}{}^{+}$ and between $\mathrm{Na}_{21}{}^{+}$ and $\mathrm{Na}_{22}{}^{+}$. Similar behavior was observed for potassium clusters.The photodissociation experiments are performed for charged clusters in which the number of valence electrons is $N_e = N$-1. Thus, high binding energies occur for clusters with 2, 8 and 20 electrons. The experiments indicate unambiguously that the magic character is associated with the number of valence electrons in the cluster, and corroborate the magic numbers observed in the abundance spectra. The

same conclusion can be deduced from the analysis of the mass spectra of clusters generated by the liquid metal ion source (LMIS) technique [4], in which nascent cluster ions are produced directly.

4.2 Spherical Well Model of Metallic Clusters

The free and nearly free electron models of simple metals are well known in solid state physics [5]. The foundation of those models is the fact that the effective potential seen by the conduction electrons in metals like Na or K is nearly constant through the volume of the metal. This is so because (a) the ion cores occupy only a small fraction of the volume of the metal, and (b) the effective ionic potential (or, more properly, pseudopotential) is weak. Under these circumstances, a constant potential in the interior of the metal is a good approximation, even better if the metal is liquid. However, electrons cannot escape from the metal spontaneously; in fact, the energy required to extract one electron through the surface is called the work function. This means that the confining potential rises abruptly at the surface of the metal. If the metallic piece has microscopic dimensions and for simplicity we asssume its form to be spherical, like a classical liquid drop, then the effective potential confining the valence electrons will be spherically symmetric, with a form intermediate between an isotropic harmonic oscillator and a square well [1, 6]. These simple model potentials can already give a faithful idea of the reason for the magic numbers in Na or K clusters: the formation of electronic shells.

Energy levels for electrons bound in such a spherically symmetric potential can be characterized by a radial quantum number k (k-1 is equal to the number of nodes in the radial wave function), and an angular momentum quantum number l. For fixed k and l, the magnetic quantum number m_l can take the values $m_l = l, l$-1, ... -l, and the spin quantum number takes the two values $m_s = +1/2, -1/2$. This gives a total degeneracy 2(2l+1) for a (k, l) subshell. It is well known from atomic and molecular physics that closed shell electronic configurations are very stable because of the existence of energy gaps between the electronic shells. The detailed form of the confining potential controls the precise ordering of the subshells, and also dictates which gaps are large and which are small. Only large gaps lead to enhanced stability. So, for a

precise explanation of the magic numbers of the alkali metal clusters, a realistic representation of the effective confining potential is needed.

An accurate selfconsistent potential can be constructed by applying the Density Functional Formalism (DFT) [7, 8] within the context of the spherical jellium model (SJM) [2, 9, 10]. In the jellium model the background of positive ions is smeared out over the volume of the cluster, to form a distribution of positive charge with density

$$n_+(\mathbf{r}) = n_+^0 \, \Theta(R - r),$$ (4.3)

where $\Theta(R - r)$ is the step function, with values 1 for $r < R$ and 0 for $r > R$. The radius R of the positive background is related to the number of atoms in the cluster by the equation

$$\frac{4}{3}\pi R^3 = N \, \Omega$$ (4.4)

where Ω is the experimental volume per atom in the bulk metal. The constant n_+^0 is related to Ω and to the valence Z ($Z = 1$ for alkali elements) by

$$Z = n_+^0 \, \Omega.$$ (4.5)

The positive charge background generates an attractive external potential (using Hartree atomic units in this section)

$$V_{ext}(\mathbf{r}) = -\int \frac{n_+(\mathbf{r}')}{|\mathbf{r} - \mathbf{r}'|} d^3 r'$$ (4.6)

which is a parabolic potential indide the sphere of radius R and purely Coulombic outside. DFT is then used to calculate the ground state electronic distribution for interacting electrons subject to this external potential. This is achieved by solving the Kohn–Sham single-particle equations [8, 11]

$$\left(-\frac{1}{2}\nabla^2 + V_{eff}(\mathbf{r})\right)\phi_i(\mathbf{r}) = \varepsilon_i \, \phi_i(\mathbf{r}). \qquad (4.7)$$

From these equations one obtains the single-particle energy eigenvalues ε_i and orbitals ϕ_i. The electron density is then constructed from the occupied orbitals

$$n(\mathbf{r}) = \sum_{i=1}^{occ} |\phi_i(\mathbf{r})|^2. \qquad (4.8)$$

The effective potential $V_{eff}(\mathbf{r})$ in Eq. (4.7) represents the combined effect of the attraction from the positive background and the repulsion from the other electrons. It is given by

$$V_{eff}(\mathbf{r}) = V_{ext}(\mathbf{r}) + V_H(\mathbf{r}) + V_{xc}(\mathbf{r}). \qquad (4.9)$$

$V_H(\mathbf{r})$ is the classical repulsive electrostatic potential of the electronic cloud

$$V_H(\mathbf{r}) = -\int \frac{n(\mathbf{r}')}{|\mathbf{r}-\mathbf{r}'|} d^3 r' \qquad (4.10)$$

and $V_{xc}(\mathbf{r})$ is the potential due to exchange and correlation between the electrons [8]. Exchange effects between the electrons come from the requirement that the many-electron wave function of a system of identical fermionic particles has to be antisymmetric. Two electrons cannot be simultaneously in the same single-particle state (characterized by orbital and spin quantum numbers) and this has the consequence of building a hole (Fermi hole) around an electron that excludes the presence of other electrons of the same spin orientation (up or down, in the usual notation for the z component). In addition, there are Coulombic correlations between the instantaneous positions of the electrons due to the fact that these are charged particles that repel each other. Because of this fact, two electrons cannot approach each other too closely, independently of their spin orientation. The sum of Fermi and Coulomb correlations can be described as an exchange–correlation hole around the

electron. In practice $V_{xc}(\mathbf{r})$ is calculated using its definition in DFT, as the functional derivative of an exchange–correlation energy functional $E_{xc}[n]$, that is,

$$V_{xc}(\mathbf{r}) = \frac{\delta E_{xc}[n]}{\delta n(\mathbf{r})}.$$ (4.11)

The local density approximation (LDA) [8] is often used to calculate $E_{xc}[n]$ and $V_{xc}(\mathbf{r})$. The LDA uses as input the exchange–correlation energy of a homogeneous electron gas. In that system the exchange energy per unit volume has the expression

$$e_x(n^0) = -\frac{3}{4}\left(\frac{3}{\pi}\right)^{1/3}(n^0)^{4/3}$$ (4.12)

where n^0 is the constant density of the homogeneous gas. The exchange energy of an inhomogeneous system with density $n(\mathbf{r})$ is then approximated by assuming that expression (4.12) is valid locally, that is,

$$E_x[n] = -\frac{3}{4}\left(\frac{3}{\pi}\right)^{1/3}\int n(\mathbf{r})^{4/3} d^3r.$$ (4.13)

Application of Eq. (4.11) then leads to

$$V_x^{LDA}(\mathbf{r}) = -\left(\frac{3}{\pi}\right)^{1/3} n(\mathbf{r})^{1/3}.$$ (4.14)

Well known expressions also exist for the correlation energy (per unit volume) $e_c(n^0)$ of a homogeneous electron gas [8], from which the corresponding LDA correlation potential

$$V_c^{LDA}(\mathbf{r}) = \left[\frac{de_c(n)}{dn}\right]_{n=n(\mathbf{r})}$$ (4.15)

is obtained. In other words, in the LDA, $V_{xc}^{LDA}(\mathbf{r})$ at point $\mathbf{r}$ in space is assumed to be equal to the exchange–correlation potential in a homogeneous electron gas with "constant" density, precisely equal to the local density $n(\mathbf{r})$ at that point.
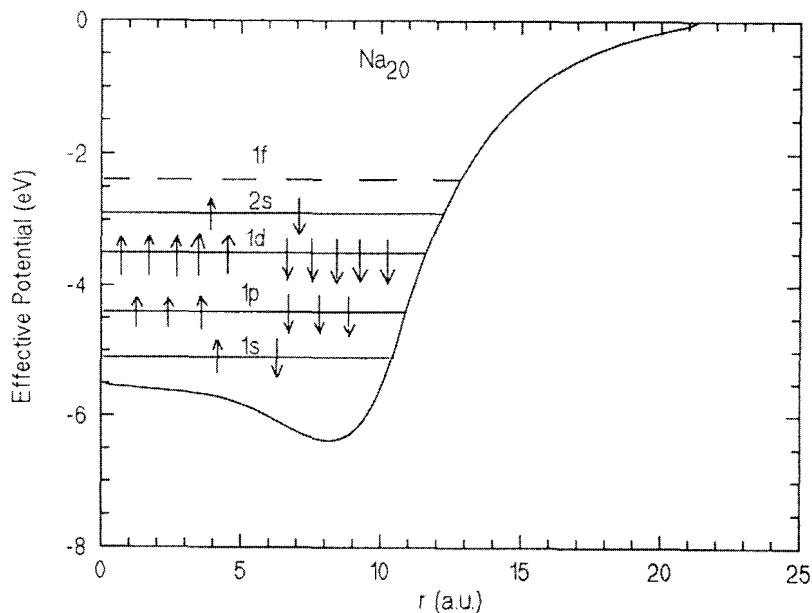
Figure 4.3. Selfconsistent effective potential of a Na_{20} cluster in the spherical jellium model. The occupied 1s, 1p, 1d, and 2s electronic subshells are represented by the continuous lines. The 1f is the lowest unoccupied subshell.

The spherical jellium model has been applied to alkali metal clusters. Figure 4.3 shows the selfconsistent effective potential confining the electrons in a neutral sodium cluster with $N = 20$, that is, with 20 valence electrons. The 1s, 1p, 1d and 2s subshells are filled. In a cluster with $N = 21$, the last electron will be placed in the 1f subshell (the dashed line in the figure). That electron is less tightly bound than the electrons of the 2s subshell by at least 0.5 eV, and should be easier to remove by photoionization. This explains why the value of the ionization potential drops with the opening of a new shell.

The total energy $E(N)$ of a cluster with N atoms is given by the usual DFT expression

$$E(N) = \sum_{i=1}^{occ} -\frac{\langle \phi_i | \nabla^2 | \phi_i \rangle}{2} + \frac{1}{2} \iint \frac{n(\mathbf{r})n(\mathbf{r}')}{|\mathbf{r} - \mathbf{r}'|} d^3r d^3r'$$

$$+ \int V_{ext}(\mathbf{r}) n(\mathbf{r}) d^3r + E_{xc}[n] + E_{self}. \qquad (4.16)$$

The first term on the r.h.s. is the single-particle kinetic energy of the electrons [8], the second gives the classical electrostatic energy of the electronic cloud, and the third one gives the interaction between the electrons and the ionic background. $E_{xc}[n]$ is the exchange–correlation energy of the electrons and finally E_{self} is the electrostatic self-interaction of the ionic background. The cohesive energy per atom can be written in terms of the energies of the free atom and the cluster

$$E_{coh}(N) = E(atom) - \frac{E(N)}{N}. \qquad (4.17)$$

When plotted as a function of cluster size, $E_{coh}(N)$ shows a local maximum for the magic sizes $N = 8, 18, 20, 34, 40, 58, 92, \ldots$ [2]. However, the quantity

$$\Delta_2(N) = E(N+1) + E(N-1) - 2E(N) \qquad (4.18)$$

displays better the abrupt changes in the total energy. This quantity represents the relative stability of a cluster of N atoms in comparison with clusters of $(N+1)$ and $(N-1)$ atoms. If the highest occupied electronic subshell is filled in a cluster of N atoms, and the next available subshell is separated by a sizable energy gap, the cluster energy will jump from $E(N)$ to $E(N+1)$. This gives rise to a peak in $\Delta_2(N)$, indicating that the cluster of size N is very stable. As a consequence of the higher stability, this cluster will be more abundant in the mass spectrum than clusters of sizes $N+1$ or $N-1$ (see Chapter 2). $\Delta_2(N)$ is shown in Fig. 4.4. Peaks appear at $N = 2$ (not shown), 8, 18, 20, 34, 40,

58 and 92. This is consistent with the measured mass spectra. The calculations confirm that the magic numbers are due to the closing of electronic shells: the subshells are filled in the order $1s$, $1p$, $1d$, $2s$, $1f$, $2p$,$1g$, $2d$, $1h$, $3s$,... Filling those subshells leads to the magic numbers 2, 8, 18, 20, 34, 40, 58, 68, 90, 92,... The size $N = 34$, which appears after filling the $1f$ subshell, is a magic number of secondary importance also observed in the experiments. The numbers 68 and 90, which correspond to the filling of the $2d$ and $1h$ subshells, are more difficult to observe because the gaps between the $2d$ and $1h$ subshells, and between the $1h$ and $3s$ subshells, are small. Only large gaps lead to observable consequences.
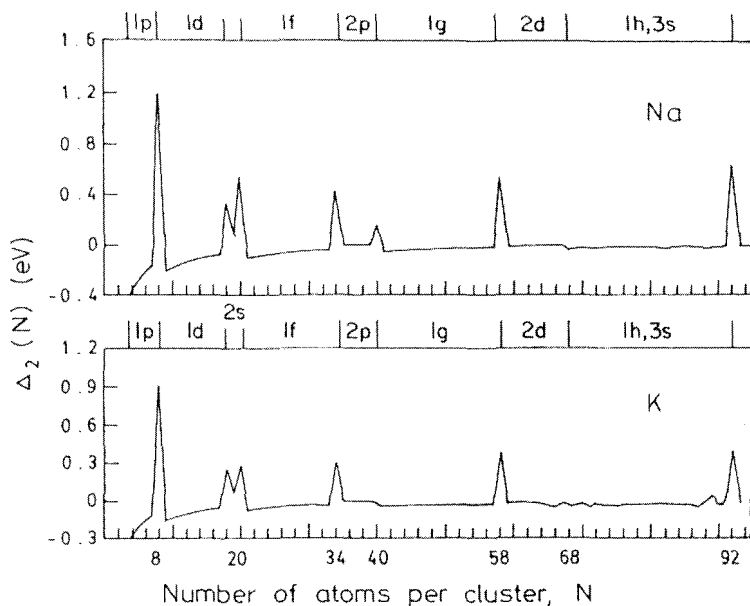
Figure 4.4. Relative stability $\Delta_2(N) = E(N+1) + E(N-1) - 2E(N)$, of sodium and potassium clusters as a function of cluster size N.

The ionization potentials of Li, Na and K clusters calculated by the spherical jellium model reproduce the drops associated with the closing of electronic shells [2], although exaggerating their magnitude. This is due to the spherical symmetry assumed by the model for both closed

shell and open shell clusters. For the same reason the spherical jellium model yields saw toothed curves which lack the fine structure between shell closings.

Experiments for noble metal clusters (Cu_N, Ag_N, Au_N) indicate the existence of shell effects, similar to those observed in the alkali clusters. These are reflected in the mass spectrum [6] and in the variations of the ionization potential with N. The magic numbers are the same ones seen for the alkaline elements. Cu, Ag and Au atoms have an electronic configuration of the type $nd^{10}(n+1)s^1$, so the spherical jellium model explains these magic numbers if one assumes that the s electrons (one per atom) move in the spherically symmetric, effective jellium potential.

4.3 Electronic Shell Effects in Large Clusters

When the size of an alkali cluster increases, the number of valence electrons in the cluster also increases, as well as the number of occupied shells. Since the depth of the confining potential remains approximately constant, the gaps between electronic subshells become narrower [9]. Eventually, for N sufficiently large, the discrete energy levels evolve into the quasi-continuous energy bands of the solid. When does this occur? Or, in other words, when are electronic shell effects no longer discernible? Experiments indicate that shell effects remain important for clusters with a few thousand valence electrons [12–15]. As an example, Table 4.1 lists the shell closing numbers observed by Martin and coworkers [13] for sodium clusters with sizes up to about 850. The observed magic numbers appear at approximately equal intervals when the cluster abundances are plotted in a $N^{1/3}$ scale ($N^{1/3}$ gives the linear dimension of the clusters). More precisely, $\Delta N^{1/3}$ is approximalely 0.6 between consecutive magic numbers. Before undertaking the explanation of this periodicity, an interesting feature of the experiments detecting the magic numbers in Table 4.1 is worth discussing. In those experiments, photons with energies $h\nu$ very close to the ionization threshold were used to ionize the clusters in the beam before detection in the mass spectrometer. Since the magnitude of the ionization potential drops between clusters of sizes N and $N+1$ when a shell is completed at size N, the measured cluster intensities show local minima at the magic numbers due to the lower ionization efficiency of those magic clusters, arising

from their larger *IP*s. This result is different from the picture in Fig. 4.1, where the spectrum reveals the intrinsic abundances in the beam, and then the intensities of the magic clusters are higher. Evidently, the two results are consistent: the closed shell clusters are the most abundant in the beam, because these are the most stable ones, and at the same time they have the largest ionization potentials. Consequently, in a mass spectrum obtained with photon energies near the ionization threshold, those clusters will be characterized by local intensity minima, as in the experiments of Martin [13, 16]. But for photon energies well above the ionization threshold, the intensities reflect the intrinsic abundances in the beam, so the closed shell clusters are characterized by intensity maxima, as in the experiments made by Knight [1].

Table 4.1. Total number of valence electrons in closed shell sodium clusters. Experimental results are compared to calculations for an inhomogeneous jellium model. Data collected from [13].

Shell	Experiment	Inhomogen. Jellium
A	2	2
B	8	8
C	18	18
D	20	20
E	34	34
F	40	40
G	58	58
H	68	68
I	92	92
J	138	138
K	198 ± 2	196
L	263 ± 5	268
M	341 ± 5	338
N	443 ± 5	440
O	557 ± 5	562
P	700 ± 15	704
Q	840 ± 15	854

Returning to the $\Delta N^{1/3} = 0.6$ periodicity, one can understand why the shell closings should occur at approximately equal intervals on an $N^{1/3}$

scale [13]. An expansion of N in terms of the shell index k has a leading term proportional to k^3. One power of k arises because we have to sum over all shells up to k in order to obtain the total number of particles. A second power of k arises because the number of subshells in a shell increases approximately linearly with the shell index. Finally, the third power of k arises because the number of particles in the largest subshell also increases with the shell index. Then

$$N_k \approx k^3. \tag{4.19}$$

This qualitative argument is supported by theoretical calculations. When the number of electrons in the cluster increases, the number of electronic shells also increases. Nevertheless, for large clusters groups of energy levels bunch together, leaving sizable energy gaps separating those bunches. Although handling such a large number of electrons becomes more difficult, DFT calculations lead to the bunching effect, that is to the $N^{1/3}$ periodicity, and give magic numbers in close agreement with experiment [17–19]. The results of calculations within the spherical jellium model are displayed in Fig. 4.5. After calculating the cluster energy as a function of N, this energy can be conveniently separated into smooth, $E_{av}(N)$, and oscillating, $E_{shell}(N)$, parts

$$E(N) = E_{av}(N) + E_{shell}(N), \tag{4.20}$$

which is in accord with the idea of the Strutinski Shell Correction Theorem [20]. The Liquid Drop Model allows to write $E_{av}(N)$ as the sum of volume, surface and curvature terms [21]

$$E_{av}(N) = e_b N + a_s N^{2/3} + a_c N^{1/3}. \tag{4.21}$$

The bulk energy per atom, e_b, is obtained from the theory of the homogeneous electron gas [5]

$$e_b = \frac{3}{10}\left(3\pi^2\right)^{2/3} n_0^{2/3} - \frac{3}{4}\left(\frac{3}{\pi}\right)^{1/3} n_0^{1/3} + e_c(n_0). \tag{4.22}$$

As the electrostatic contributions cancel out in the model, e_b, which is a function of the average valence electron density n^0, just contains kinetic (first term), exchange (second term) and correlation (third term) contributions. The jellium model for a planar surface [22] can be used to calculate a_s. However, Genzken [18] obtained a_s from a plot of the slope of $(E(N)/N)\text{-}e_b$ versus $N^{1/3}$, to suppress the shell oscillations for large values of N. Finally, the curvature energy a_c was fixed in a similar way by the slope of a plot of $E(N) - e_b N - a_s N^{2/3}$ as a function of $N^{-1/3}$.
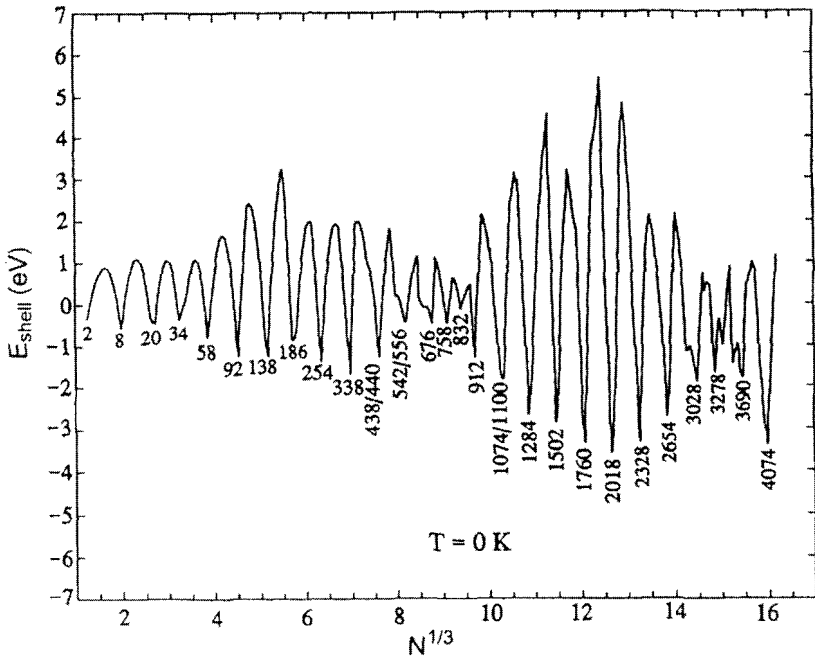
Figure 4.5. The periodically varying contribution of valence electrons to the binding energy of spherical sodium clusters (E_{shell} in Eq. (4.20)). Magic numbers are indicated. Adapted from O. Genzken, *Mod. Phys. Lett. B* **7**, 197 (1991) with permission of World Scientific.

Subtracting the average part $E_{av}(N)$ from $E(N)$ defines the shell correction term $E_{shell}(N)$ in Eq. (4.20). This term is the energy plotted versus $N^{1/3}$ in Fig. 4.5. The pronounced oscillations of $E_{shell}(N)$ exhibit sharp minima at the shell closing numbers. The differences between

these and the experimental magic numbers [14, 15] are small. One can notice that the amplitude of the shell oscillations varies with size. The shell oscillations are enveloped by a slowly varying amplitude, the supershell. That is, the shell effects vanish periodically, but with a much larger size scale, $\Delta N^{1/3} = 6$ between consecutive supershell nodes. The first supershell node occurs in Fig. 4.5 near $N = 850$. Calculations by Nishioka *et al.* [17] give $N \approx 1000$. This node has been observed, although the experiments also show some discrepancies: the first node is located at $N \approx 1000$ in ref. [14], while it is found at $N \approx 800$ in [15]. The discovery of supershells confirms the predictions of nuclear physicists. However, supershells have not been observed in nuclei due to an insufficient number of particles. The existence of supershells is a rather general property of a system formed by a large number of fermions in a confining potential. The supershell structure of lithium clusters has also been studied [18, 19], and the agreement with experiment [23] is even better than for sodium. The experimental and the theoretical first supershell node are found at $N \approx 820$.

The effect of temperature on the shells and supershells has been analyzed for sodium clusters. For this purpose calculations of the cluster free energy were performed by treating the valence electrons as a canonical ensemble in the heat bath of the ions [24]. The spherical jellium model for the ionic background is even better at finite temperatures. The amplitudes of shell and supershell oscillations decrease with increasing T. This is particularly important in the region of the first supershell node at $N \approx 850$, which becomes smeared out at a moderate temperature of 600 K. However, temperature does not shift the positions of the magic numbers.

Similar shells and supershells have been observed for the clusters of the trivalent metals Al, Ga and In [25–27], but in order to explain the details it is necessary to go beyond the spherical jellium model. Another early example of the necessity to go beyond the jellium model is provided by the work of Lange *et al.* [16]. These authors performed DFT calculations of the ionization potential of large sodium clusters with the purpose of understanding the drops in the measured ionization potentials. However, to reproduce the precise details, the homogeneous background model had to be relaxed by making the inner part of the clusters more dense. The results obtained with this inhomogeous spherical jellium model are given in Table 4.1.

4.4 Spheroidal Deformations of the Cluster Shape

The spherical assumption for the ionic background explains the most prominent features of the mass spectrum and the ionization potential of simple metal clusters. However there is evidence of other features that the spherical jellium model is unable to explain. When a top shell is not completely filled (that is, for $N \neq 2, 8, 20, ...$), the electronic density becomes nonspherical, which in turn leads to a distortion of the ionic background. This Jahn–Teller type of distortion, similar to those observed for molecules and nuclei [28], leads to a splitting of the spherical shells into subshells. Deformed clusters are prevalent for open shell configurations. Deformations of the alkali clusters were first studied by Clemenger [29] by allowing the spherical shape to change to a spheroid with axial symmetry. For this purpose Clemenger used a model Hamiltonian based on a modified three-dimensional harmonic oscillator potential. The model allows for different oscillation frequencies ω_z and ω_p along the z axis (chosen as the symmetry axis) and perpendicular to the z axis. The Hamiltonian also contains an anharmonic term that serves to flatten the bottom of the potential well to make it more realistic; in the case of a spherical oscillator that term breaks the l-degeneracy of the single-particle energy levels in a (k, l) shell. If the system is cylindrically symmetric, the energy levels are either two-fold ($l = 0$) or four-fold ($l > 0$) degenerate. The model reminds the spheroidal model of nuclei developed by Nilsson [28, 30]. Due to the deformation, the highly degenerate spherical shells split into spheroidal subshells. Denoting the semiaxes of the spheroid by a and b, a distortion parameter η can de defined

$$\eta = \frac{2(a-b)}{a+b} = \frac{2(\omega_p - \omega_z)}{\omega_p + \omega_z}, \qquad (4.23)$$

that describes the deformation, oblate or prolate, of the positive background. For each cluster, η is determined minimizing the total energy. The essential feature of the spheroidal model is to produce splittings in the shells which for small distortions are linear in η. Alkali clusters with $N = 3, 4$ become prolate, and those with $N = 5–7$ oblate.

After the spherical cluster with $N = 8$, again clusters are prolate for $N =$ 9–13, and oblate for $N = 14$–19, and so on.

In a more fundamental treatment of the same problem, Ekardt and Penzar [31, 32] have extended the jellium model to account for spheroidal deformations: the ionic background is represented by a distribution of positive charge with constant density and a distorted, spheroidal shape. The advantage over the Clemenger model is that the spheroidal jellium model is parameter-free and the calculation of the electronic wave functions is performed selfconsistently. Due to the cylindrical symmetry of the problem, the azimutal quantum number m is still a good quantum number for the electronic states, as is the parity with respect to reflection at the midplane. However the angular momentum l is no longer a good quantum number and, as a consequence, the problem is intrinsically two-dimensional. In addition to the usual peaks of the spherical jellium model, the stability function $\Delta_2(N)$ has smaller subshell filling peaks at $N = 10$, 14, 18, 26, 30, 34, 36, 38, 44, 50, 54, *etc.* All these fine-structure peaks have been observed in the experimental mass spectra [2]. In particular, one can notice that the four-fold patterns in the $1f$ and $1g$ shells appear correctly, as well as the two-fold pattern in the $2p$ shell, corresponding to the filling of a prolate subshell at $N = 36$ and an oblate shell at $N = 38$.

Proceeding further along these lines, Manninen and coworkers [33, 34] have introduced the Ultimate Jellium Model, in which the positive background charge is allowed to be completely deformable, both in shape and in density profile, in order to minimize the energy. The result is that the background adapts itself perfectly to the electronic charge, and the positive density $n_+(\mathbf{r})$ becomes everywhere the same as the electron density $n(\mathbf{r})$. Consequently the Coulomb energy of the system cancels out and the electrons move in their own exchange–correlation potential $V_{xc}(\mathbf{r})$, a model earlier used by Brown and March for the metallic surface [35]. Qualitatively the cluster shapes follow the pattern seen above for the spheroidal model, but the additional freedom adds richness to the variety of shapes. Clusters with $N = 3$, 4, 6, 7, 9, 14, 21 and 22 have axial and inversion symmetries. $N = 10$ has only axial symmetry, and $N = 5$, 11, 13, 15 have only inversion symmetry. $N = 12$, 16, 17, 18 are more complex: these have neither inversion nor axial symmetry. Shapes up to $N = 8$ can be simply understood in terms of the symmetries of the s, p_x, p_y and p_z single-particle wave functions of a spherical system. An

explanation in terms of the filling of d and s levels is still possible between $N = 8$ and $N = 20$, at least near the magic numbers, although it is more difficult in the middle of the shell, due to the strong deformation.

$$2 + 2 = 4 \qquad\qquad 2 + 8 = 10$$

$$2 + 2 + 8 = 12 \qquad\qquad 2 + 14 = 16$$
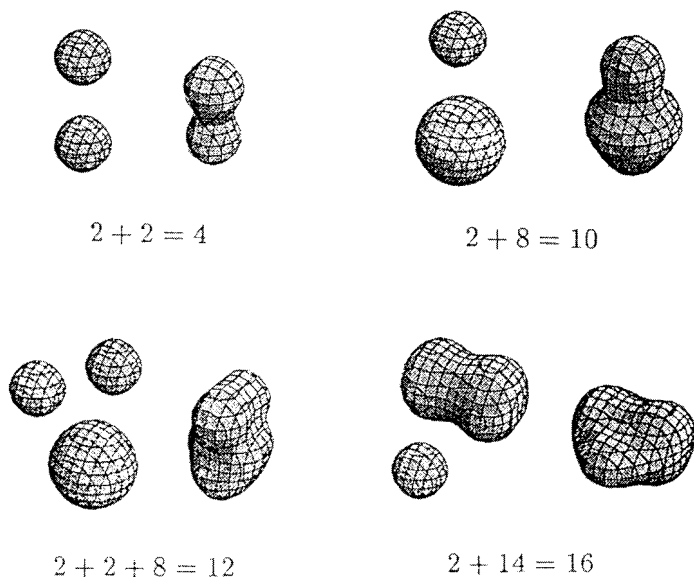
Figure 4.6. Molecular interpretation of some ground state cluster geometries in the ultimade jellium model. Reproduced from M. Koskinen, P. O. Lipas and M. Manninen, *Z. Phys. D* **35**, 285 (1995) with permission of Springer–Verlag.

A striking new feature of the ultimate jellium model is the prediction of some cluster shapes that can be interpreted as *molecules* built from magic clusters. As shown in Fig. 4.6, the 4-electron cluster is formed by two dimers, with a separation energy of only 0.10 eV. The 10-electron cluster can be viewed as a dimer attached to an 8-electron sphere, with a separation energy of 0.15 eV. $N = 12$ can be interpreted as two dimers attached to an 8-electron cluster, and $N = 16$ as a composite of the strongly deformed, yet very stable 14-electron cluster, and a dimer. The clusters without inversion symmetry have symmetric isomers and are extremely soft against deformation. For instance, $N = 10$ has a pear-shaped ground state and a prolate isomer with axial and inversion symmetries, only 0.5 eV above the ground state in a region of the energy

surface that is extremely flat. Related softness of the pear shape has been observed in nuclear physics [36, 37]. These molecular-like features are due to the high stability of the dimer.

4.5 A Full Description of the Cluster Structure

Experiments provide only indirect information on the geometric structure of metallic clusters. In contrast, *ab initio* calculations predict the structures directly. Those calculations require a substantial computational effort, in part because the number of isomers grows rapidly with N and the task of identifying the lowest energy configuration between those of isomers with similar binding energies is hard. For this reason the calculations are usually restricted to small clusters. For the prototypical case of sodium clusters, *ab initio* calculations [38–43] have been performed for sizes up to $N = 20$. Figures 4.7–4.9 show the results of calculations by Solovyov and coworkers [43]. For N up to 8, both DFT and Möller–Plesset (MP) perturbation theory [44], and a basis of Gaussian functions, were used to optimize the geometries. The particular implementation of DFT employed by them was the so called B3LYP [45]. This hybrid method, introduced by Becke [45], expresses the exchange and correlation energies as a parameterized functional which includes a mixture of Hartree–Fock and DFT exchange along with DFT correlation. For larger clusters only the B3LYP method was used in the optimizations.

The point symmetry group is indicated for each cluster in the figures, and several low lying isomers are given for $N = 3, 4, 6, 10, 11$, and 20. Small Na_N clusters with $N \leq 5$ have a planar structure. MP predicts the isosceles triangle, C_{2v} symmetry, as the lowest energy structure of Na_3, although the other C_{2v} structure, with a broken bond, lies only 0.008 eV higher in energy. Na_4 illustrates how the geometry can be influenced by the spin multiplicity of an electronic state. The rhombic geometry, corresponding to D_{2h} symmetry, occurs for spin multiplicity one, while a multiplicity of three leads to the square, D_{4h} symmetry; the first one is, in fact, more stable. Three-dimensional structures begin to appear for Na_6. The flat pentagonal pyramid is more stable than the planar isomer, but only by 0.02 eV. Na_3 and Na_4 have prolate shapes, and Na_5 to Na_7 oblate shapes, in agreement with the deformed jellium models.
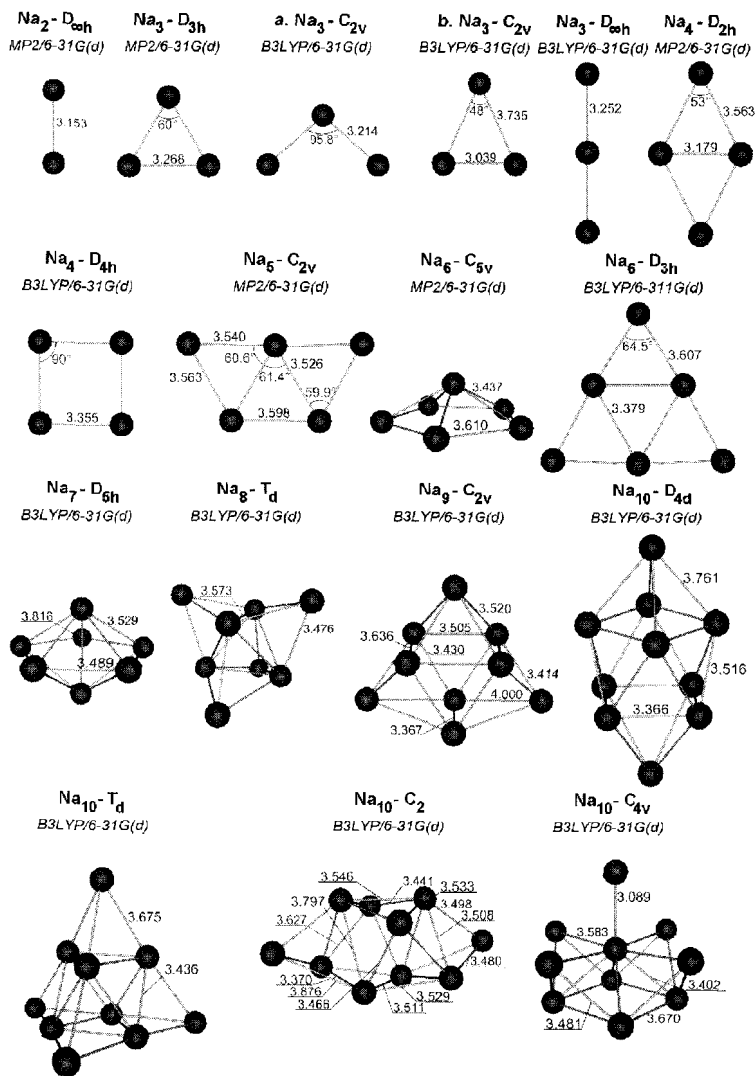
Figure 4.7. Optimized geometries of sodium clusters with $N = 2$–10. Several isomers are given for $N = 3, 4, 6, 10$. Interatomic distances are given in angstroms. Reproduced from I. A. Solovyov *et al.*, *Phys. Rev. A* **65**, 53203 (2002) with permission of the American Physical Society.
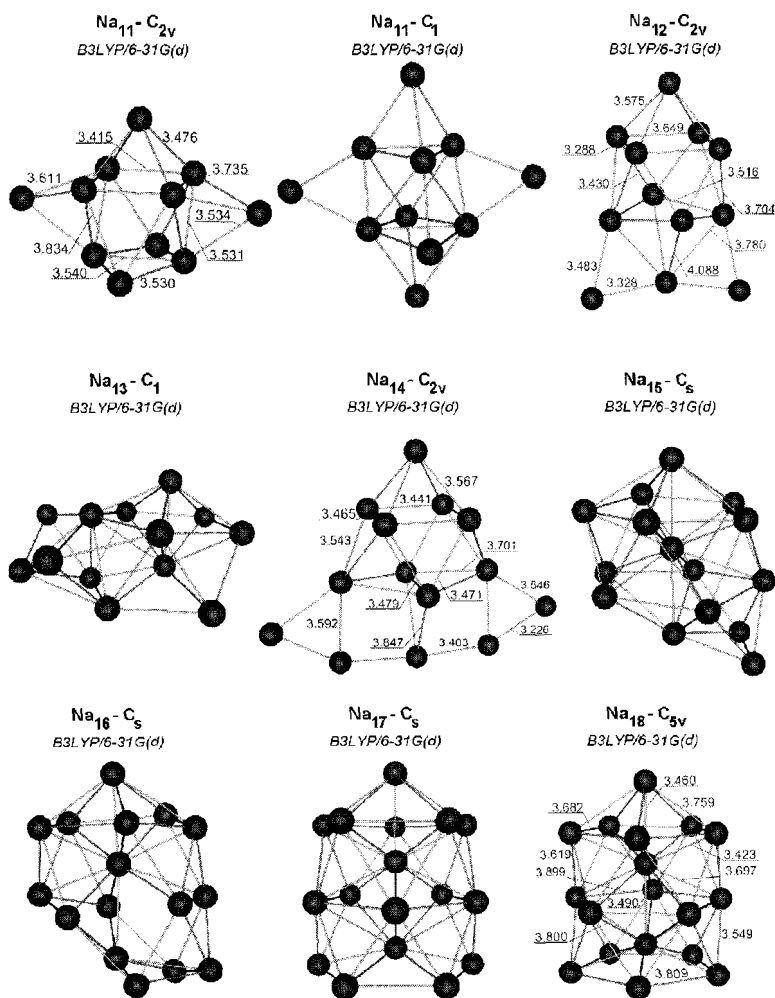
Figure 4.8. Optimized geometries of sodium clusters with $N = 11-18$. Interatomic distances are given in angstroms. Reproduced from I. A. Solovyov *et al.*, *Phys. Rev. A* **65**, 53203 (2002) with permission of the American Physical Society.

B3LYP leads to some differences with respect to MP. The ground state of Na_3 is the linear isomer, and the broken triangle lies 0.008 eV above. The planar isomer is the ground state of Na_6. This shows the difficulties in predicting structures by total energy calculations.
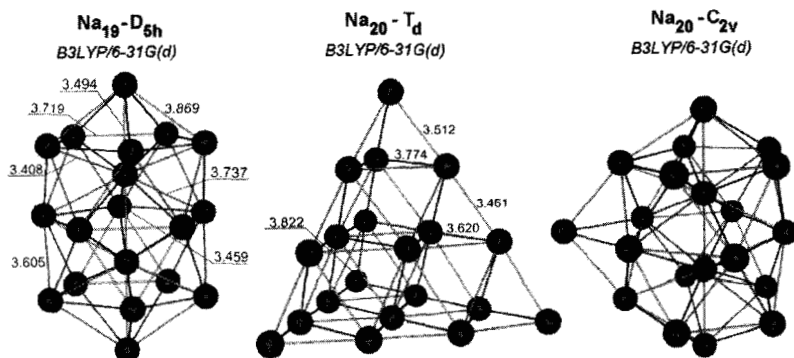
Figure 4.9. Optimized geometries of Sodium clusters with N =19-20. Interatomic distances are given in angstroms. Reproduced from I. A. Solovyov *et al., Phys. Rev. A* **65**, 53203 (2002) with permission of the American Physical Society.

A noticeable feature of the clusters with $N \geq 8$, studied by B3LYP, is that Na_8 and Na_{20} have higher symmetry (T_d) than others. This is consistent with the formation of closed shells in the jellium model. The ground state of Na_{10} has the C_2 symmetry, and the D_{4d} isomer lies 0.07 eV above. The binding energies of the two isomers of Na_{11} only differ by 0.03 eV. Na_{10}, Na_{11} and Na_{12} are approximately prolate, and Na_{14} is approximately oblate, again in agreement with the deformed jellium models. For other clusters the triaxiality is substantial. Nevertheless, Na_{17}, Na_{18} and Na_{19} appear close to prolate. This is at variance with the jellium models and originates in the underlying double icosahedron structure of these three clusters, complete for Na_{19} and incomplete for Na_{17} and Na_{18}. That structure, well known for inert gas clusters (see Chapter 3, Section 3.1) arises from atomic packing effects, which are not

captured by the deformed jellium models. These packing effects are specially important for very large clusters (see Section 4.6).

Ionization affects the geometries of the smallest clusters [43]. The structure of Na_3^+ is an equilateral triangle. MP calculations predict that Na_4^+ is a near equilateral triangle with the fourth atom attached to the apex, and that the rhombus is close in energy (by 0.01 eV); the order is reversed by B3LYP. Na_5^+ can be viewed as formed by two oppositely oriented isosceles triangles sharing an atom along a common axis. The structure is planar, but one triangle can easily rotate in such a way that the planes of the two triangles become perpendicular to each other. The structures of Na_6^+ and Na_8^+ are also different from those of Na_6 and Na_8. The structural changes become less drastic for $N \geq 10$.
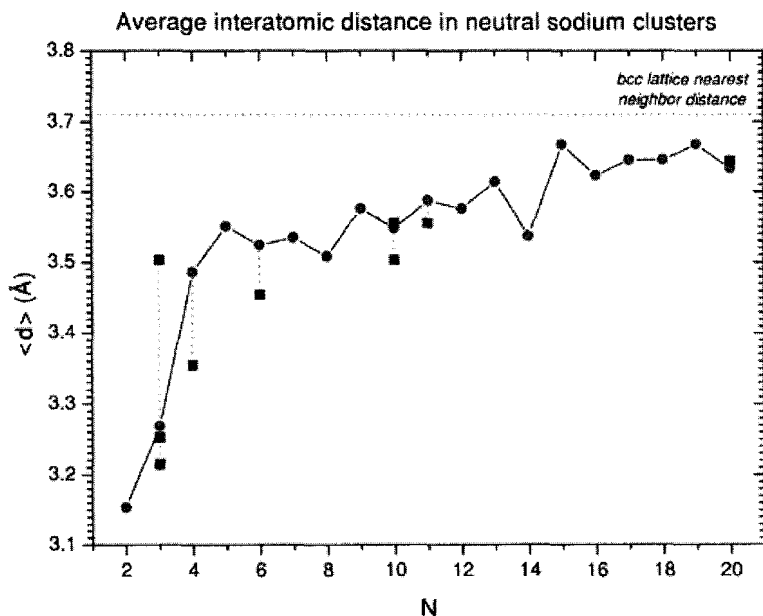
Figure 4.10. Calculated average bond distance of sodium clusters as a function of cluster size. Several isomers have been considered for some clusters. Those isomers are given in Figs. 4.7–4.9. Adapted from I. A. Solovyov *et al.*, *Phys. Rev. A* **65**, 53203 (2002) with permission of the American Physical Society.

An effect generally observed in most calculations is a characteristic evolution of the interatomic distances, illustrated in Fig. 4.10 [43]. The averaged interatomic distance $< d >$ first grows fast from $N = 2$ to $N = 5$–6, that is, in the region characterized by planar structures. Then, after the transition to three-dimensional structures, $< d >$ evolves slowly towards the value for the bulk material, approaching this value from below. The evolution is, however, full of small bumps. The structures in Figs. 4.7–4.9 show that the clusters have many atoms on the surface, so $< d >$ can be expected to converge to the bulk value only when the fraction of atoms with a bulk-like environment begins to dominate. For the range of sizes plotted in Fig. 4.10, an even–odd oscillation of $< d >$ is apparent, with even-N clusters having values of $< d >$ smaller than their odd-N neighbors. Those oscillations, also appearing in the evolution of other properties with cluster size, have a quantum mechanical origin, and will be discussed in Chapter 5.

Some of the clusters in Figs. 4.7–4.9 have electric dipole moments, because the electronic and ionic charge distributions do not always match; that is, the center of gravity of those two charge distributions do not coincide. The calculations indicate that only clusters with C point symmetry groups have dipole moments with a magnitude up to 1 Debye or a little more [43]. For instance, the dipole moments of the $D_{\infty h}$ isomer and the two C_{2v} isomers of Na_3 (labelled **a** and **b** in Fig. 4.7) are equal to 0.0, 0.28 and 1.30 Debye, respectively. The sizable differences between the dipole moments of different isomers have led Solovyov and coworkers to propose a method for the separation of isomers, by passing a mass selected cluster beam through an inhomogeneous electric field. For a cluster with intrinsic dipole moment **D**, the force acting on the cluster in an inhomogeneous electric field $\mathbf{E(r)}$ is equal to [44]

$$\mathbf{F(r)} = \nabla\big(\mathbf{DE(r)}\big). \qquad (4.24)$$

If the cluster spends a time τ passing through the inhomogeneous electric field, an estimation of the distance Δ by which the clusters are deviated during this period of time from its original direction of motion is given as $\Delta \approx F\tau^2/2m$, where m is the mass of the cluster. For typical values of the time period, $\tau \approx 10^{-3}$ seconds, and of the inhomogeneity of the

electric field, $\nabla E \approx 5000$ V/cm^2, the isomers with $N = 3$ and dipole moment difference $\delta D \approx 1$ Debye become separated by $\Delta \approx 0.7$ mm, which illustrates the capabilities of the proposed method. A similar analysis for clusters having quadrupole moments shows analogous promise.

Other strategies have been proposed to indirectly infer the geometrical structure, based on comparing experiment and calculations of a given property for different isomeric forms with similar energies. The isomeric structure leading to the best agreement with experiment is then assumed to correspond to the experimental structure. Examples of this strategy will be reported in other chapters. The transition from planar to three-dimensional structures at $N = 6, 7$ is a robust property in clusters characterized by *sp*-bonding mainly. The structures of the Cu$_N$ clusters [46] with $N = 2$–7 are similar to those in Fig. 4.7, although Cu$_6$ is still planar and the first three-dimensional cluster is Cu$_7$.

4.6 Shells of Atoms

It was pointed out in Section 4.3 that if the abundance spectrum of large sodium clusters (sizes up to ≈ 1500 atoms) is plotted as a function of $N^{1/3}$, the magic numbers appear at approximately equal intervals $\Delta N^{1/3} = 0.6$. However, the period of appearance of these features changes abruptly at $N \approx 1500$ [13, 47]. The new periodicity, $\Delta N^{1/3} = 1.5$, which persists up to the largest clusters studied, $N \approx 22000$, is interpreted as reflecting the formation and the filling of shells of atoms. For small or medium size clusters the cluster shape changes every time an atom is added. However, when the cluster is large enough, changes in its global shape become more and more difficult and a new growth pattern emerges: large clusters grow by adding shells of atoms to a rigid cluster core. The magic numbers observed in the experiments suggest that as alkali metal clusters grow sufficiently large they form close-packed or nearly close-packed polyhedra with icosahedral or cuboctahedral (*fcc*) shapes (both structures are consistent with the sequence of magic numbers). The total number of atoms in icosahedral or cuboctahedral clusters containing K shells of atoms is [47, 48]

$$N_K = \frac{10}{3}K^3 - 5K^2 + \frac{11}{3}K - 1. \qquad (4.25)$$

The numbers obtained from this equation are in very good agreement with the magic numbers observed in the mass spectrum. Keeping only the leading term (K^3), Eq. (4.25) can be rewritten

$$K \approx 1.5\, N_K^{1/3}. \qquad (4.26)$$

The coefficient 1.5 is precisely the observed interval between magic numbers in a plot of the abundance versus $N^{1/3}$. An equivalent statement is that a plot of $N_K^{1/3}$ against the shell index K gives a straight line.

Similar features have been observed for the clusters of the alkaline earth elements Sr, Ca and Ba [47, 49–52]. In this group, the analysis of the weaker subshell structure ocurring between shell closings is possible. This analysis gives information about the progressive formation of each shell, and indicates a faceting process. The shell develops by the formation of umbrellas. Although not identical, this process is quite similar to the formation of umbrellas in the inert gas clusters discussed in Chapter 3. The experimental subshell structure unambiguously indicates the formation of icosahedral (and not *fcc* cuboctahedral) structures for the alkaline earths. A similar analysis for alkali clusters has not yet been performed. The structure in the mass spectra revealing the atomic shell structure [13, 49, 50] reflects size dependent variations of the ionization potential, a topic that will be discussed in the next chapter.

This method of analysis of the mass spectra is powerful because not only the icosahedral or cuboctahedral arrangements, but also other close-packed arrangements like the tetrahedral, decahedral, octahedral structures, *etc.*, can be constructed and the number of atoms for perfect structures with K shells can be written in a form similar to Eq. (4.25), but with different coefficients. For instance, the number of atoms for an octahedron with K shells is

$$N_K = \frac{2}{3}K^3 + \frac{1}{3}K. \qquad (4.27)$$

The octahedron can be cut out from an *fcc* crystal. This analysis has also been applied to induce the structure of Al_N clusters [47, 53]. These clusters form octahedral structures. The octahedral structure requires coverage of only half of the surface to complete a new shell, and the oscillations in the mass spectrum indicate that formation of a new shell proceeds by first covering one of the triangular faces of the underlying octahedron, then a second, adjacent triangular facet, and so on.

How can the transition from shells of electrons to shells of atoms be interpreted? Small sodium clusters are soft, and there is no difficulty for the atoms to arrange themselves into a spherical configuration if this is demanded by the closing of an electronic shell, or for the cluster to adopt a deformed shape in the case of open electronic shells. Small clusters then behave as soft droplets, but not necessarily liquid. When the size reaches about 1500 atoms, the electronic shell effects have become less intense and changes in the global cluster shape are more difficult. In this case, formation of close-packed symmetrical structures is more effective, and further growth takes place by condensation of atoms onto the surface of a rigid core to form new shells of atoms.

The experiments for sodium clusters in the size range $N = 1500$–20000 are consistent with icosahedral (or *fcc* cuboctahedral) structures. But the structure of bulk Na and other alkali metals is *bcc*. Consequently, the transition to the bulk structure has not yet occurred for $N \approx 20000$. In the same way, inert gases crystallize in the *fcc* structure. So, the icosahedral structure of inert gas clusters and some metallic clusters can be considered as precrystalline. Precrystalline structures have also been observed for some metallic alloys in condensed units large enough to yield sharp electron diffraction patterns [54, 55]. These are called quasicrystals. It has been proposed [56] that the reason why the *bcc* phase is not yet formed in the Sodium clusters at those large sizes is that the screening cloud $n_{scr}(\mathbf{r})$ around a Na^+ ion in a finite Na cluster depends so strongly on cluster size, due to the presence of the surface, that $n_{scr}(\mathbf{r})$ has not converged to its bulk limit for clusters with ten thousand atoms. Since $n_{scr}(\mathbf{r})$ determines the effective interionic potential, which, in turn, determines the crystal structure of a metal [5], it is not surprising that much larger sizes appear to be required for the *bcc* structure of the bulk to develop.

4.7 Approximate Treatment of the Geometrical Structure

4.7.1 Spherically Averaged Pseudopotential Model

Approximate descriptions of the cluster structure, intermediate between the simple uniform background model and the fully unconstrained treatment of the geometry of the ionic skeleton, have been used to study some properties of the clusters. One of those is the Spherically Averaged Pseudopotential Model (SAPS) [57, 58]. Consider a cluster with the ions at positions $\{\mathbf{R}_j\}$, $j = 1,... \ N$. If each ion is replaced by a local pseudopotential $v_{ps}(|\mathbf{r}\text{-}\mathbf{R}_j|)$, then the total external potential seen by the valence electron cloud is given by

$$V_{ps}(\mathbf{r}) = \sum_{j=1}^{N} v_{ps}\left(\left|\mathbf{r} - \mathbf{R}_j\right|\right). \tag{4.28}$$

Experience with the spherical jellium model (SJM) suggests that for clusters with a nearly spherical shape this external potential can be replaced by its spherical average about the cluster center

$$V_{ps}(\mathbf{r}) \rightarrow V^{SAPS}(r). \tag{4.29}$$

The simplification greatly reduces the computational effort of calculating the electronic levels since the electrons now move in a spherically symmetric potential well. However the SAPS model goes beyond the SJM, since: (a) the radial structure of the cluster becomes reflected in the SAPS potential, and (b) the ion–ion interaction is calculated for the true three-dimensional arrangement of the ions [58]. One can set limits of validity to the SPAS model. The cluster cannot be too small, because small clusters substantially deform away from the spherical shape. On the other hand, very large clusters have a tendency to form planar surface facets. The range of intermediate sizes is then the most appropriate one. Calculations using this model have predicted a contraction of the cluster volume with respect to that of an equivalent piece of bulk metal [59]. This contraction, which is well documented experimentally [60], appears to be a general feature for small metallic clusters, and seems to explain

some trends in the measured polarizabilities of Al clusters (see Section 5.6). It was mentioned at the end of Section 4.3 that Martin and coworkers [16] had to modify the SJM in order to obtain the required sequence of magic numbers, reflected in the sudden drops of the ionization potential, for large clusters of alkali metals. Success was achieved by making the inner part of the cluster denser. SAPS calculations [61] have provided a microscopic interpretation for this change. An analysis of the calculated interatomic distances in Cs_N with sizes up to $N = 80$ shows that the distribution of interatomic distances is not homogeneous, those in the inner region of the cluster being shorter than in the outer region. Calculations for Mg clusters indicate the same effect [62].

In an extension of the SAPS model, Schöne *et al.* [63] expand the external potential of Eq. (4.28) about the center of the cluster

$$V_{ps}(\mathbf{r}) = V^{SAPS}(r) + \sum_{l=1}^{\infty} \sum_{m=-l}^{l} V_{l,m}(r) Y_l^m(\theta, \varphi) \qquad (4.30)$$

where the first term in the expansion is the SAPS potential. The other part was included perturbatively up to second order on top of a SAPS calculation. Selecting several isomeric geometries taken from *ab initio* DFT molecular dynamics calculations they obtained the same ground state geometry of Na_8 as in the *ab initio* DFT calculations. Similar ideas, based on a perturbative introduction of geometrical efects beyond SAPS, were also applied by Rubio *et al.* to the C_{60} molecule [64]. In contrast, a simplified version of SAPS has been used by Spina and Brack [65]. Their assumption was that the atoms in a given shell are at exactly the same distance from the cluster centre. As an additional simplification, the discrete point-like distribution of the ionic charges in a shell was replaced by a uniform continuous distribution. The number of atoms in each shell and their radii are variational parameters in this model.

Lermé *et al.* [66] have used SAPS to study shells and supershells in large clusters. Their first aim was to investigate to what extent the granularity of the ionic background modifies the electronic structure given by the SJM. Calculations for clusters having up to a few thousand electrons show that, in spite of the periodic radial distortions which modulate the effective potentials, the same strong level bunching observed in the SJM again occurs. However, there are some differences

in the electronic subshell structure. The details of the subshell structure are also sensitive to the use of the Spina–Brack simplification. Lermé and coworkers then turned to study the supershells. The introduction of pseudopotentials shifts the supershell nodes to lower electron numbers compared to the SJM; the particular parameterization of the ionic pseudopotential is also of importance. The electronic shell structure is mainly controlled by the structure of the layers near the surface, and the non Coulombic short-range behavior of the pseudopotential results in an increase of the softness of the effective potential at the cluster surface.

4.7.2 Cylindrically Averaged Pseudopotential (CAPS) Model

The SAPS model has limitations for small clusters because many of these have deformed shapes. But calculations using a deformed jellium background indicate that most metallic clusters still maintain axial symmetry and that truly triaxial deformations are rare. This provides a good reason to assume that the valence electron cloud is nearly axially symmetric. Taking up this idea Montag and Reinhard have developed the cylindrically averaged pseudopotential (CAPS) model [67], which is an extension of SAPS. Using cylindrical coordinates, the external ionic potential is substituted by its cylindrical average

$$V^{CAPS}(z,\rho) = \sum_{j=1}^{N} \overline{v}_{ps}(z,\rho;z_j,\rho_j), \qquad (4.31)$$

$$\overline{v}_{ps}(z,\rho;z_j,\rho_j) = \frac{1}{2\pi}\int_{0}^{2\pi} v_{ps}\left(\left|\mathbf{r}-\mathbf{R}_j\right|\right)d\varphi. \qquad (4.32)$$

A proper choice of the z axis is critical for the success of the method. Montag and Reinhard considered the inertia tensor $\hat{I}$ of the ionic distribution and identified the z axis with the principal axis of $\hat{I}$ whose momentum I_i deviates most from the average momentum $\overline{I} = (I_1 + I_2 + I_3)/3$. Since the electrons see an axially symmetric potential, their wave functions separate accordingly as

$$\phi_{n\mu}(\rho,\varphi,z) = R_{n\mu}(\rho,z)e^{-i\mu\varphi}. \qquad (4.33)$$

The calculation of the ground state geometry and electronic structure then proceeds by an interlaced iteration of the Kohn–Sham equations and the ionic stationary conditions.

The results obtained show that the geometry of the small clusters can be characterized in *slices* of ions with the same cylindrical coordinates (ρ_j, z_j). The cluster can be classified by the sequence $\{n_1, n_2, \ldots n_k\}_{o/p}$ of n_s, the number of ions in a slice s, and the global shape, oblate (o) or prolate (p), of the configuration. The ions of a slice are arranged on a ring, with or without a central ion. The structures predicted for several neutral and charged Na clusters are: $Na_2 - \{11\}_p$, $Na_3^+ - \{3\}_o$, $Na_4 - \{121\}_p$, $Na_6 - \{15\}_o$, $Na_7^+ - \{151\}_p$, $Na_8 - \{2222\}_p$, $Na_{10} - \{1441\}_p$. In all these cases there is agreement with the geometries predicted by *ab initio* DFT [68, 69] and Configuration Interaction (CI) methods [40, 41, 70]. For Na_5^+ the CAPS ground state geometry is $\{122\}_p$, and a low lying isomer $\{212\}_p$ was also found. *Ab initio* DFT and CI methods also predict that these are the two lowest isomers, although in the opposite order. To summarize, CAPS provides an efficient method to calculate the structure of metal clusters. CAPS can be useful for studying the fission of doubly charged clusters, where the repulsion between the excess positive charges often leads to axial symmetry along the fission path (see Chapter 6). Also CAPS can be useful in the study of metallic nanowires.

4.8 Clusters of the Aluminum Group

4.8.1 Aluminum clusters

After the alkali clusters, aluminum clusters are among the best studied ones. Aluminum is a nearly free electron metal, so the electronic structure of these clusters is expected to be relatively simple. The electronic configuration of the valence electrons in the free atom is $3s^2$ $3p^1$ and the s and p levels are separated by an energy gap of 4.99 eV. Al behaves as a monovalent atom in very small clusters, but experiments [71–73] and calculations [74] indicate that the gap is reduced as the cluster grows, and s–p hybridization begins to develop at Al_8. Already for Al_{13} the s–p hybridization is complete and photoelectron spectroscopy

[71–73] confirms the validity of the jellium model for the electronic structure of Al_N clusters for $N \geq 13$.

The calculated structures [75] are planar up to Al_5 and coincide with those of the alkali clusters, a result consistent with the monovalent character of the Al atoms in those small clusters. The geometries become three-dimensional starting with Al_6 (see Fig. 4.11). The first cluster that develops a pentagonal arrangement of atoms is Al_9. Clusters with 11 atoms or more contain at least one internal atom with a bulk-like coordination. In the small size range, the calculated evaporation energy (Eq. (2.9)) reveals that Al_7^+ is very stable. This is because the cluster has 20 external electrons. The high stability is also a property of neutral Al_7, and in fact, this has been identified as a magic cluster in the experiments of Jarrold [76]. In general, the geometries of small charged clusters are similar to those of the neutrals, with few exceptions.
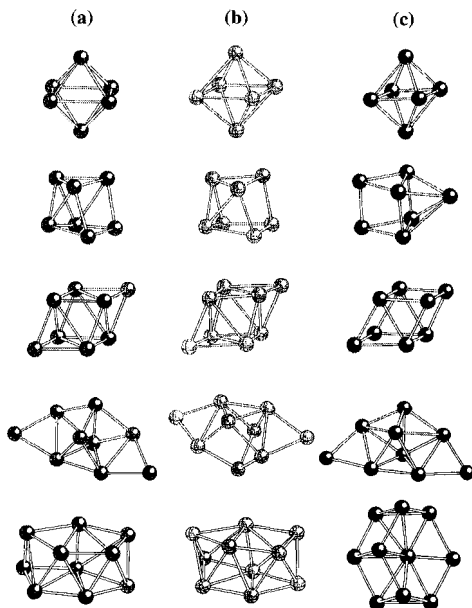
Figure 4.11. Calculated ground state geometries of neutral (a), cationic (b) and anionic (c) aluminum clusters with 6–10 atoms. Reproduced from B. K. Rao and P. Jena, *J. Chem. Phys.* **111**, 1890 (1999) with permission of the American Institute of Physics.

Interest in Al_{13} arises from the fact that this cluster has 39 electrons, excluding evidently the ionic cores, short of just one electron to form a 40 electron closed shell cluster. For this reason, the doping of Al_{13} has been proposed as a way to force the shell closure, and to obtain a highly stable cluster, possible candidate for cluster assembled solids. The lowest energy structure of Al_{13} is a distorted icosahedron. A distorted decahedron, in which two pentagonal caps join to form square faces [75, 77, 78], lies 0.2 eV above in energy. The distortions are a Jahn–Teller effect due to the open shell electronic configuration. This gives the icosahedral cluster a slighly oblate shape. The anionic Al_{13}^- has closed electronic shells [79]. Consequently this cluster has a more regular icosahedral structure. In contrast, a larger distortion compared to the neutral and a small volume expansion are obtained for the cation Al_{13}^+.

4.8.2 Boron clusters

Boron is a trivalent element with an external s^2p^1 electronic configuration, similar to Al. However, this element is characterized by a short covalent radius and a tendency to form strong directional bonds that produce a semiconducting solid. Boron cluster cations, B_N^+, with N in the range 3–20 atoms, produced by laser ablation of the solid, show magic numbers at $N = 5$, 11 and 13 in the mass spectrum [80, 81]. Theoretical investigations of boron clusters with two and three-dimensional structures have shown that these can be classified into four topological groups: quasi-planar, tubular, convex and spherical [82, 83]. One of the factors that determine the preferred structure is the curvature strain, that favors planar-like structures. But those structures have dangling bonds, and the elimination of those bonds is a second important factor that opposes the first one and favors tubular and cage-like structures. For small boron clusters, the curvature strain is very large and the clusters are quasi-planar [82–84]. This is confirmed by photoelectron spectroscopy [84]. These clusters exhibit aromaticity and anti-aromaticity according to the Hückel rules, like planar hydrocarbons ($4n+2$ π electrons lead to aromaticity and $4n$ to anti-aromaticity). B_{10}, B_{11}^- and B_{12} possess six π electrons each, and are aromatic. B_{13}^- and B_{14} both have eight π electrons and are anti-aromatic. With ten π electrons,

B_{15}^- is again aromatic. The aromatic clusters have more circular shapes whereas the anti-aromatic ones are elongated. For medium size clusters, like B_{32}, tubular structures become competitive [85]. Although similar effects (curvature strain and elimination of dangling bonds) operate in carbon clusters, a key difference is that carbon clusters and nanotubes prefer atomic coordination 3 (allowing for sp^2 hybrids) while the boron atoms prefer a higher coordination.

References

1. Knight, W. D., Clemenger, K., de Heer, W. A., Saunders, W. A., Chou, M. Y., and Cohen, M. L., *Phys. Rev. Lett.,* **52**, 2141 (1984).
2. de Heer, W. A., Knight, W. D., Chou, M. Y., and M. L., Cohen, *Solid State Phys.,* **40**, 93 (1987).
3. Bréchignac, C., Cahuzac, P., Carlier, F., de Frutos, M., and Leygnier, J., *J. Chem. Soc. Faraday Trans.*, **86**, 2525 (1990).
4. Baskar, N. D., Frueholz, R. P., Klimcak, C. M., and Cook, R. A., *Phys. Rev. B,* **36**, 4418 (1987).
5. Alonso, J. A., and March, N. H., *Electrons in Metals and Alloys*, Academic Press, London (1989).
6. Katakuse, I., Ichihara, Y., Fujita, Y., Matsuo, T., Sakurai, T., and Matsuda, H., *Int. J. Mass Spectrom. Ion Proc.*, **74**, 33 (1986).
7. Hohenberg, P., and Kohn, W., *Phys. Rev.,* **166**, B 864 (1964).
8. Lundqvist, S., and March, N. H., editors, *Theory of the Inhomogeneous Electron Gas*, Plenum Press, New York (1986).
9. Ekardt, W., *Phys. Rev. B,* **29**, 1558 (1984).
10. Beck, D., *Solid State Commun.*, **49**, 381 (1984).
11. Kohn, W., and Sham, L. J., *Phys. Rev.,* **140**, A1133 (1965).
12. Bjornholm, S., Borgreen, J., Echt, O., Hansen, K., Pedersen, J. and Rasmussen, H. D., *Phys. Rev. Lett.* **65**, 1629 (1990).
13. Martin, T. P., Bergmann, T., Göhlich, H. and Lange, T., *Z. Phys. D,* **19**, 25 (1991).
14. Pedersen, J., Bjornholm, S., Borgreen, J., Hansen, K., Martin, T. P., and Rasmussen, H. D., *Nature,* **353**, 733 (1991).
15. Martin, T. P., Bjornholm, S., Borgreen, J., Brechignac, C., Cahuzac, Ph., Hansen, K. and Pedersen, J., *Chem. Phys. Lett.,* **186**, 53 (1991).
16. Lange, T., Göhlich, H., Bergmann, T., and Martin, T. P., *Z. Phys. D,* **19**, 113 (1991).
17. Nishioka, H., Hansen, K. and Mottelson, B. R., *Phys. Rev. B,* **42**, 9377 (1990).

18. Genzken, O., *Mod. Phys. Lett. B,* **7**, 197 (1991).
19. Genzken, O., and Brack, M., *Phys. Rev. Lett.,* **67**, 3286 (1993).
20. Strutinsky V. M., *Nucl. Phys. A,* **122**, 1 (1968).
21. Mañanes, A., Membrado, M., Pacheco, A. F., Sañudo, J. and Balbás, L. C., *Int. J. Quantum Chem.,* **52**, 767 (1994); Seidl, M., and Brack, M., *Ann. Phys. (N. Y.),* **245**, 275 (1996).
22. Lang, N, D., *Solid State Phys.,* **28**, 225 (1973).
23. Bréchignac, C., Cahuzac, P., de Frutos, M., Roux, P., and Bowen, K., in *Physics and Chemistry of Finite Systems: from Clusters to Crystals,* Eds. Jena, P., Khanna, S., and Rao, B. K., Kluwer, Boston,p. 369, (1992).
24. Brack, M., Genzken, O., and Hansen, K., *Z. Phys. D,* **19**, 51 (1991).
25. Pellarin, M., Baguenard, B., Bordas, C., Broyer, M., Lermé, J., and Vialle, J. L., *Phys. Rev. B,* **48**, 17645 (1993).
26. Pellarin, M., Baguenard, B., Broyer, M., Vialle, J. L., and Pérez, A., *J. Chem. Phys.,* **98**, 944 (1993).
27. Baguenard, B., Pellarin, M., Bordas, C., M., Lermé, J., and Vialle, J. L., and Broyer, M., *Chem. Phys. Lett.,* **205**, 13 (1993).
28. Ring, P., and Schuck, P., *The Nuclear Many Body Problem,* Springer–Verlag, Berlin (1980).
29. Clemenger, K., *Phys. Rev. B,* **32**, 1359 (1985).
30. Nilsson, S. G., *Mat. Fis. Medd. K. Dan. Videsk. Selsk.,* **29**, N 16 (1955).
31. Ekardt, W., and Penzar, Z., *Phys. Rev. B,* **38**, 4273 (1988).
32. Penzar, Z., and Ekardt, W., *Z. Phys. D,* **17**, 69 (1990).
33. Koskinen, M., Lipas, P. O., and Manninen, M., *Europhys. Lett.,* **30**, 519 (1995).
34. Koskinen, M., Lipas, P. O., and Manninen, M., *Z. Phys. D,* **35**, 285 (1995).
35. Brown, R. C., and March, N. H., *J. Phys. C,* **6**, L 363 (1973).
36. Bohr A., and Mottelson B, *Nuclear Structure, Vol. 2.* Benjamin, New York (1975).
37. Ahmad, I., and Butler, P. A., *Annu. Rev. Nucl. Part. Sci.,* **43**, 71 (1993).
38. Boustani, I., Pewestorf, W., Fantucci P., Bonacic-Koutecky, V., and Koutecky, J., *Phys. Rev. B,* **35**, 9437 (1987).
39. Bonacic-Koutecky, V., Fantucci P., and Koutecky, J., *Phys. Rev. B,* **37**, 4369 (1988).
40. Boustani, I., and Koutecky, J., *J. Chem. Phys.* **88**, 5657 (1988).
41. Bonacic-Koutecky, V., Boustani, I., Guest, M. F., and Koutecky, J., *J. Chem. Phys.* **89**, 4861(1988).
42. Rayane, D., Allouche, A. R., Bennichou, E., Antoine, R., Aubert-Frecon, M., Dugourd, Ph., Broyer, M., Ristori, C., Chandezon. F., Huber, B. A., and Guet, C., *Eur. Phys. J. D,* **9**, 243 (1999).
43. Solovyov, I. A., Solovyov, A. V., and Greiner, W., *Phys. Rev. A,* **65**, 53203 (2002).
44. Landau, L. D., and Lishitz, E. M., *Quantum Mechanics* (Pergamon, London, 1965).

45. Becke, A. D., *Phys. Rev. A*, **38**, 3098 (1988).
46. Jaque, P., and Toro-Labbé, A., *J. Chem. Phys.* **117**, 3208 (2002).
47. Martin, T. P., *Phys. Reports*, **273**, 199 (1996).
48. Mackay, A. L., *Acta Crystall.*, **15**, 916 (1962).
49. Martin, T. P., Bergmann, T., Göhlich , H., and Lange, T., *Chem. Phys. Lett.,* **183**, 343 (1991).
50. Martin, T. P., Näher, U., Bergmann, T., Göhlich , H., and Lange, T., *Chem. Phys. Lett.,* **183**, 119 (1991).
51. Martin, T. P., and Bergmann, *J. Chem. Phys.* **90**, 6664 (1990).
52. Rayane, D., Melinon, P., Cabaud, B., Horeau, A., Tribollet, B., and Broyer, M., *Phys. Rev. A,* **39**, 6056 (1989).
53. Martin, T. P., Näher, U., and Schaber, H., *Chem. Phys. Lett.,* **199**, 470 (1991).
54. Schechtman, D., Blech, I., Gratias, D., and Chan, J. W., *Phys. Rev. Lett.*, **53**, 1951 (1984).
55. Janot, C., and Dubois, J. M., *J. Non-Cryst. Solids*, **106**, 193 (1988).
56. Alonso, J. A., González, L. E., and Iñiguez, M. P., *Phys. Chem. Liq.,* **29**, 23 (1995).
57. Iñiguez, M. P., Alonso, J. A., and Balbás, L. C., *Solid State Commun.*, **57**, 85 (1986)
58. Iñiguez, M. P., López, M. J., Alonso, J. A., and Soler, J. M., *Z. Phys. D*, **11**, 163 (1989).
59. Lammers, U., Borstel, G., Mañanes, A., and Alonso, J. A., *Z. Phys. D*, **17**, 203 (1990).
60. Solliard C., and Flueli, M., *Surf. Sci.*, **156**, 487 (1985).
61. Mañanes, A., Alonso, J. A., Lammers, U., and Borstel, G., *Phys. Rev. B*, **44**, 7273 (1991).
62. Glossman, M. D., Iñiguez, M. P., and Alonso, J. A., *Z. Phys. D*, **22**, 541 (1992).
63. Schöne, W. D., Ekardt, W., and Pacheco, J. M., *Phys. Rev. B*, **50**, 11079 (1994).
64. Rubio, A. Alonso, J. A., López, J. M., and Stott, M. J., *Physica B*, **183**, 247 (1993).
65. Spina, M. E., and Brack, M., *Z. Phys. D*, **17**, 225 (1990).
66. Lermé, J., Pellarin, M., Baguenard, B., Bordas, C., Vialle, J. L., and Broyer, M., *Phys. Rev. B*, **50**, 5558 (1994).
67. Montag, B., and Reinhard, P. G., *Phys. Lett. A*, **193**, 380 (1994).
68. Martins, J. L., Buttet, J., and Car, R., *Phys. Rev. B*, **31**, 1804 (1985).
69. Röthlisberger, U., and Andreoni, W., *J. Chem. Phys.*, **94**, 8129 (1991).
70. Bonacic-Koutecky, V., Fantucci, P., and Koutecky, J., *Chem. Rev.*, **91**, 1035 (1991).
71. Ganteför, G., and Eberhardt, W., *Chem. Phys. Lett.*, **217**, 600 (1994).
72. Akola, J., Manninen, M., Häkkinen, H., Landman, U., Li, X., and Wang, L. S., *Phys. Rev. B*, **60**, 11297 (1999).

73. Li, X., Wu, H., Wang, X. B. and Wang, L. S., *Phys. Rev. Lett.* , **81**, 1909 (1998).
74. Duque, F., and Mañanes, A., *Eur. Phys. J. D*, **9**, 223 (1999).
75. Rao, B. K., and Jena, P., *J. Chem. Phys.*, **111**, 1890 (1999).
76. Jarrold, M. F., Bower, J. E., and Kraus, J. S., *J. Chem. Phys.*, **86**, 3876 (1987).
77. Cheng, H. P., Berry, R. S., and Whetten, R. L., *Phys. Rev. B*, **43**, 10647 (1991).
78. Fowler, J. E., and Ugalde, J. M., *Phys. Rev. A*, **58**, 383 (1998).
79. Duque, F., Mañanes, A., Molina, L. M. , López, M. J., and Alonso, J. A., *Int. J. Quantum Chem.*, **86**, 226 (2002).
80. Ruatta, S. A., Hintz, P. A., and Anderson, S. L., *J. Chem. Phys.*, **94**, 2833 (1991).
81. Hintz, P. A., Sowa, M. B., Ruatta, S. A., and Anderson, S. L., *J. Chem. Phys.*, **94**, 6446 (1991).
82. Boustani, I. *Surf. Sci.* **370**, 355 (1997).
83. Boustani, I., *Phys. Rev. B*, **55**, 16426 (1997).
84. Zhai, H. J., Kiran. B., Li, J., and Wang, L. S., *Nature Materials*, **2**, 827 (2003).
85. Boustani, I., Rubio, A., and Alonso, J. A., *Chem. Phys. Lett.*, **311**, 21 (1999).

This page intentionally left blank

5. Electronic and Optical Properties of Simple Metal Clusters

5.1 Ionization Potential and Electron Affinity

The first ionization potential IP is the lowest energy necessary to remove one electron from a neutral cluster X_N. In terms of the total energies of the neutral and ionized species, IP is given as

$$IP(X_N) = E(X_N^+) - E(X_N).$$ (5.1)

This energy can be determined from a photoionization efficiency spectrum. In this, the ion signal in the mass spectrometer is plotted against the photon energy of the ionizing light. The curves obtained have a smoothed step form and the ionization energy can be extracted from the analysis of that curve; for instance, by fitting the data with an error function. The maximum of the first derivative of that function is then identified with the average ionization potential of an ensemble of clusters with that mass [1].

For a macroscopic solid the ionization potential is called the work function. In the uniform background model of a metal, the work function W can be expressed as the sum of three terms [2]

$$W = \mu_{xc} + D_{es} - E_F$$ (5.2)

where all contributions are taken to be positive. In this model, the electrostatic potential that the ionic background exerts on a electron and the classical potential due to the electronic cloud cancel exactly one another deep in the interior of the metal, so the only potential remaining

is $\mu_{xc}(n^0)$, the sum of the exchange (x) and correlation (c) contributions to the chemical potential of a uniform electron gas with a density n^0 equal to the average conduction electron density of the metal. $\mu_{xc}(n^0)$ is just the sum of the two potentials V_x^{LDA} and V_c^{LDA} of Eqs. (4.14) and (4.15) respectively, evaluated for the density n^0. But the metal has a surface and D_{es} is an electrostatic contribution representing the surface dipole barrier resulting from the spilling of the electronic cloud beyond the ionic background. These two terms determine the depth of the potential well. The kinetic energy term E_F is the Fermi energy of the metal, measured with respect to the bottom of the effective potential, so the difference in Eq. (5.2) gives the difference in energy between the Fermi level and the vacuum level outside the metal. Work functions obtained from this equation reproduce the qualitative trend for the alkali metals [2]. A perturbative inclusion of the ionic pseudopotentials lowers the calculated values by $\approx 10\%$ and leads to work functions in reasonable accord with experiment. Similar agreement is also obtained for other *sp* metals.

When the size of the metallic piece is microscopic, a correction term is required. If this correction is calculated from simple electrostatic considerations as the energy required to remove an electron from a metallic sphere of radius R, the following result is obtained for the ionization potential [3]

$$IP = W + \frac{1}{2}\frac{e^2}{R}. \tag{5.3}$$

The electron affinity AE, which is the binding energy of one excess electron in the cluster,

$$EA(X_N) = E(X_N) - E(X_N^-) \tag{5.4}$$

has a corresponding expression

$$EA = W - \frac{1}{2}\frac{e^2}{R}. \tag{5.5}$$

Considerations based on DFT, which trascend the simple electrostatic arguments, indicate a more correct form of these equations [4]

$$IP = W + \left(\frac{1}{2} - c \right) \frac{e^2}{R}, \tag{5.6}$$

$$EA = W - \left(\frac{1}{2} + c \right) \frac{e^2}{R}, \tag{5.7}$$

where the leading terms neglected are $O(R^{-2})$. The constant $1/2$ comes from the classical electrostatic energy (see Eqs. (5.3) and (5.5)) and c is a material-dependent constant with a quantum mechanical origin, arising from the kinetic and exchange-correlation energies of the electrons. These equations are valid for R large compared to the atomic radius, that is, when electronic shell effects become negligible. The exact values of c are not known, but experiments and theoretical calculations indicate that c ranges between 0 and 0.14. DFT calculations within the Spherical Jellium model give $c \approx 0.08$ [5, 6]. The Stabilized Jellium model [7] also gives $c = 0.08$ for alkali metal clusters [8]. This model starts from an expression for the total energy of a system of electrons and close-packed ions with the electron-ion interaction described by pseudopotentials. Only the first order term in the electron–ion interaction is retained and the second and higher order terms are neglected. That first order term, which amounts to a constant potential in the interior of the metal, is adjusted such that the total energy as a function of the bulk density is minimized at the experimental bulk density of that particular metal. A jellium calculation with an approximate treatment of the electronic kinetic energy (an extended Thomas–Fermi functional [9]) gives $c \approx 0.14$ [10]. The experimental ionization energies of sodium clusters [11, 12] are fitted well with $c = 0.08$ [8]. Various experimental studies for medium size clusters, $N \leq 100$, of different metallic elements obtained good fits to the data using $c = 0.125$ [13–15]. This is shown in Fig. 5.1 for Fe, Hg, K, Na and Pb clusters. An empirical value $c \approx 0.12 \pm 0.06$ was obtained from a photoemisssion study of very large Ag clusters containing 5000–40000 atoms [16]. However, another experimental study of Ag clusters gave c very close to zero [17].
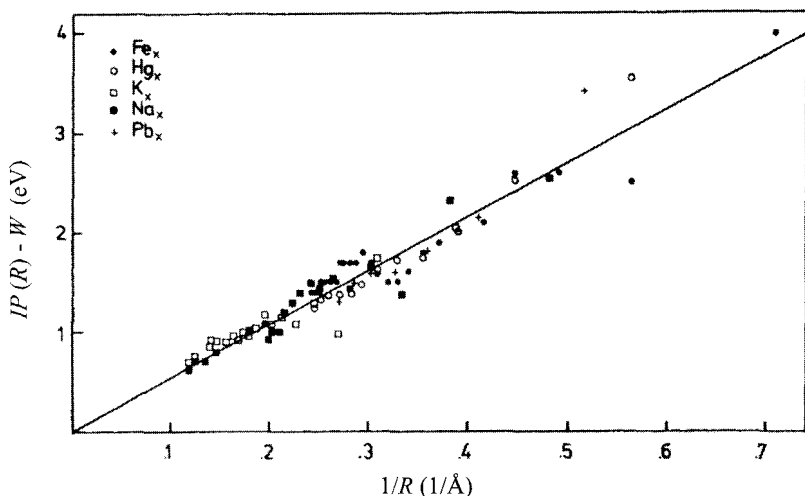
Figure 5.1. Ionization potentials for Fe, Hg, K, Na and Pb clusters as a function of the inverse cluster radius $1/R$. The magnitude plotted is the difference between the measured ionization potential and the extrapolated bulk work function based on the spherical drop model of Eq. (5.6). Reproduced from M. M. Kappes *et al.*, *J. Chem. Phys.* **84**, 1863 (1986) with permission of the American Institute of Physics.

The usual method to measure the electron affinity is the photoelectron spectroscopy of negatively charged clusters. In a photodetachment experiment a negatively charged cluster X_N^- is irradiated with a laser of fixed photon energy $h\nu$. Imagine, for simplicity, that the corresponding neutral cluster X_N has closed electronic shells, so the extra electron occupies the lowest unoccupied molecular orbital(LUMO) level. The photon then removes an electron from this level (this process corresponds to transition 3 in Fig. 5.2) or from deeper orbitals (transitions 1 and 2). The difference $h\nu - E_{kin}$, where E_{kin} is the outgoing kinetic energy of the detached electron, gives a direct measure of the binding energy of the corresponding orbital. The photoelectron spectrum is composed of a series of peaks. The threshold in the spectrum gives an estimate of the adiabatic electron affinity. This threshold energy corresponds to a transition from X_N^- into the ground state of the neutral

X_N. Often the ground state geometries of X_N^- and X_N are not the same. The consequence is that the maximum of the first photoelectron peak does not coincide with the threshold value. The maximum gives the vertical detachment energy, corresponding to a transition in which the cluster geometry does not change during the detachment process.
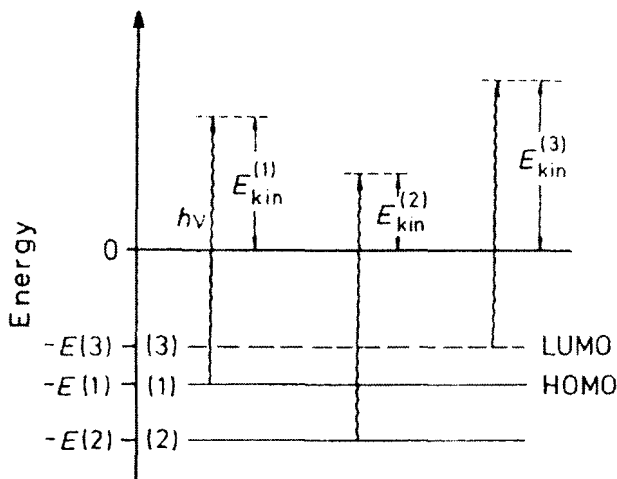
Figure 5.2. Schematic view of electron photodetachment from a negatively charged cluster within a frozen orbital picture. A laser of photon energy $h\nu$ ionizes an electron from the LUMO level (this is the level occupied by the extra electron in the anionic cluster) or from a deeper level. The difference $h\nu - E_{kin}$ between the photon energy and the kinetic energy of the ejected electron is a measure of the binding energy of the electron.

The electron affinities of clusters of nontransition metals like Al_N, In_N and Tl_N [18] have been measured by this technique and the data is consistent with Eq. (5.7). The general agreement of the spherical droplet predictions with the measured values of the ionization potential and the electron affinity has several implications: (1) The assumption of spherical symmetry is viable, except for very small clusters. (2) The size dependence of *IP* and *EA* is mainly determined by changes in curvature. (3) Valence electrons in metallic clusters are delocalized, even for small clusters.

Superimposed to the smooth behavior described by Eqs. (5.6) and (5.7), the experimental data on ionization potentials and electron affinities show two additional features. One, which has been discussed in Chapter 4, is the shell closing effect. Measurements [19] of the electron affinity of Ag_N clusters indicate agreement with the shell closing numbers of the spherical jellium model if one applies this model to the $5s$ electrons of the Ag atoms. Another interesting case is aluminum. The valence shell configuration of the isolated Al atom is $3s^2\ 3p^1$ and the energy separation between the atomic $3s$ and $3p$ levels is 3.6 eV. The solid is a nearly free electron metal [20] and this occurs because the original $3s$–$3p$ gap disappears in the solid. Photoelectron spectroscopy of Al_N^- anionic clusters [21–23] has shown that the gap between the p and s bands is rapidly reduced as N grows and the two bands are completely mixed starting at Al_9. The jellium model should then be applicable for $N \geq 9$. The photoelectron measurements reveal, indeed, that the clusters Al_{11}^-, Al_{13}^-, Al_{19}^-, Al_{23}^-, Al_{35}^-, Al_{37}^-, Al_{55}^- and Al_{73}^- have closed shell configurations [21, 24]: the binding energies of the first photodetachment peak are high in all those clusters, and exhibit large degeneracies, whereas clusters with one additional atom (Al_{N+1}^-) show low energy features and an energy gap between the first peak and the next one (the HOMO–LUMO gap of the neutral). The number of valence electrons in those closed shell anionic clusters is $3N+1 = 34, 40, 58, 70, 106, 112, 166$ and 220, respectively. Also, the energy gaps detected in the spectra of Al_{46}^-, Al_{52}^-, and Al_{56}^- indicate that the corresponding neutrals Al_{46}, Al_{52}, and Al_{56} have closed shells, with $3N = 138, 156$ and 168 electrons, respectively. All the shell closing numbers given above are consistent with the shell filling of the spherical jellium model for Al clusters: $1s$ (2), $1p$ (8), $1d$ (18), $2s$ (20), $1f$ (34), $2p$ (40), $1g$ (58), $2d$ (68), $3s$ (70), $1h$ (92), $2f$ (106), $3p$ (112), $1i$ (138), $2g$ (156), $3d$ (166), $4s$ (168), $1j$ (198), $2h$ (220), where the numbers acompanying the shell symbols give the accumulated number of electrons [25].

Equations (5.6) and (5.7) have been generalized to clusters in a charge state $+q$ (this means that the cluster has already lost q electrons). In this case, the energy to remove an additional electron is [26]

$$IP(+q) = W + \left(q + \frac{1}{2} - c\right)\frac{e^2}{R}. \tag{5.8}$$

Using photons of energy 6.42 eV in the ultraviolet range, Hoffman *et al.* [26] have employed photoelectron spectroscopy to determine several succesive ionization potentials of large aluminum clusters, Al_{2000}^{-} and Al_{32000}^{-}. The measured photoelectron intensity of each cluster first presents an onset which gives the electron affinity (3.9 eV and 4.1 eV for Al_{2000} and Al_{32000}, respectively). At higher binding energies a series of steps appear, with the step width roughly of equal size (0.7 eV and 0.3 eV for the two clusters, respectively). Those "Coulomb staircases" can be explained by the following argument: at the laser fluence used in the experiment the clusters absorb several photons. Emission of an electron results (almost) after the absorption of each photon, until a maximum charge state is achieved for which $IP(+q)$ is higher than the photon energy. The photoelectron spectra of all those ionizations add up and the recorded spectrum is a superposition of the spectra of several clusters (for instance, Al_{2000}^{-}, Al_{2000}, Al_{2000}^{+} and Al_{2000}^{2+} in the first case, and of seven charge states in the second). For a given cluster the positions of those steps give the succesive ionization potentials $IP(+q)$. The measured values of $IP(+q)$ plotted versus q display a perfect linear relationship, and the slope of that line gives e^2/R, or in other words, the radius of the cluster, from which the atomic density can be deduced. On the other hand the crossing point of the two lines allows to calculate c and the work function W of the bulk metal. A value of 4.28 (± 0.03) eV was obtained for W, which equals the literature value for polycrystalline Al, a fact indicating that this technique may be an efficient alternative for measuring the work function of reactive metals.

Although an isolated atom cannot stabilize more than one extra electron because of the increasingly strong Coulomb repulsion, this number can be larger in a cluster. Using similar arguments to those leading to Eqs. (5.6) and (5.7), an equation has been derived [6, 8] for the energy of a charged spherical cluster having q excess electrons (that is, with net charge $-q$)

$$E(-q) = E(0) - q\left(W - \frac{c}{R}\right) + \frac{q^2}{2(R+\delta)}, \qquad (5.9)$$

where atomic units, $e = 1$, are assumed. The parameter δ is a measure of the spillout of the electronic charge beyond the positive ionic background; this means that the effective cluster radius $R+\delta$ is a little larger than R. The charged particle will be stable as long as $E(-q) < E(0)$. For Al, with $\delta \approx 1.0$ a.u., the predicted minimum sizes to stabilize one, two or three extra electrons are $N_m(-q) = 2$, 86 and 434, for $q = 1, 2$ and 3 electrons, respectively [8]. The corresponding numbers for Na ($\delta \approx 1.3$ a.u.) are $N_m(-q) = 1$, 38, 185, and for Cs, $N_m(-q) = 1$, 30, 145. These predictions have to be taken with caution, since the treatment of negatively charged particles is notoriously difficult for a theoretical treatment within the DFT framework. Nevertheless the trend of decreasing $N_m(-q)$, at fixed q, with decreasing conduction electron density n^0 of the metal is clear (see also the analysis in ref. [6]). A decreasing n^0 is equivalent to a larger volume per atom, so the trend can be explained by the larger cluster volume, which implies a smaller Coulomb repulsion between the excess electrons.

5.2 Odd–Even Effects

A second effect, which has been observed in clusters of monovalent s-electron metals (alkaline and noble metals), is an odd–even effect, also apparent in the mass spectrum. Some examples are now given:
(i) The measured ionization potentials of N-even clusters of the alkali metals Na$_N$ and K$_N$ with $N < 20$ have values systematically larger than their N-odd neighbors [27, 28].
(ii) The inverse effect is found for the electron affinities of the noble metal clusters, with N-odd clusters having larger electron affinities. Or, in terms of the quantities experimentally measured, anionic M_N^- clusters (M indicates a noble metal element) with N odd have higher photodetachment thresholds [29]. Notice that a noble metal cluster M_N^- has $N+1$ valence electrons (originating from the atomic s-electrons).

(iii) The mass spectra of positively and negatively charged noble metal clusters obtained by ion bombardment show an odd–even alternation in the abundances, with N-even clusters being less abundant than their N-odd neighbors [30, 31]. This effect is observed up to $N \approx 40$. In the ion bombardment technique the nascent clusters are already charged.

(iv) The odd–even alternation is observed in the dissociation energies of small alkali clusters [32, 33]. This is the smallest energy to fragment the cluster in two pieces, which is usually the energy to evaporate one atom.

(v) The dissociation energies of singly and doubly charged Cu clusters (Cu_N^+ and Cu_N^{2+} respectively) also display odd–even effects [34]. In the first case, for instance, the dissociation energies of N odd clusters are larger than the averaged values of their even size neighbors.

DFT calculations using the local spin density approximation (LSDA) for exchange and correlation reproduce the odd–even effects in the ionization potentials and binding energies [35]. In those calculations the ionic cores are replaced by accurate pseudopotentials and the geometry of the cluster was optimized for each size.

The odd–even effect results from the interplay between cluster deformation and spin effects. Figure 5.3 shows the evolution of the molecular orbitals for the calculated most stable conformations of alkali clusters [36] with sizes $N \leq 14$. A notation which reflects the nodal character of the molecular orbitals, and that allows to relate those orbitals to the orbitals of the jellium model, is employed here. There is a smooth increase of the binding energy of the $1s$ orbital (that is, more negative orbital energies in the Figure) with increasing N. The binding energies of the manifold of $1p$ levels also show an overall increase with N. However, contrary to the predictions of the spherical jellium model the $1p_x$, $1p_y$ and $1p_z$ orbitals are, in general, nondegenerate. The splitting occurs because the cluster (and thus the potential acting on the electrons) is nonspherical. The characteristic shapes of the clusters, prolate (PE), oblate (OE) or spherical (S), are indicated at the bottom of the figure. The splitting of the p levels is a selfconsistent effect. When the p shell is not fully occupied, the electron density is not spherically symmetric. This induces a distortion of the cluster geometry away from the spherical shape that leads to a Jahn–Teller-like splitting of the p levels. The magnitude of the energy difference between ($1p_x$, $1p_y$) and $1p_z$ levels reflects the degree of distortion. The $1p_z$ level has a lower binding energy than ($1p_x$, $1p_y$) in oblate clusters, and the order is reversed for prolate

shapes. This splitting, combined with the fact that double occupancy of a *p* orbital increases its binding energy over that for single occupation (spin pairing effect), explains the odd–even effect observed in the ionization potentials, the electron affinities and in the cluster abundances. Similar arguments applied to the splitting of the *d* shell explain the odd–even effect in larger clusters.
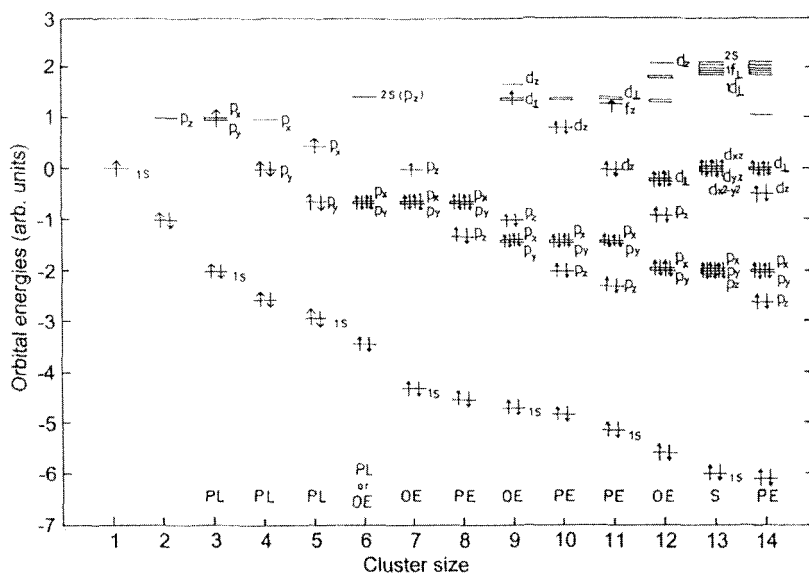
Figure 5.3. Evolution of the binding energies of the molecular orbitals of alkali clusters with cluster size. Orbital energies are given in arbitrary units. PL and S denote planar and spherical structures, and OE and PE indicate oblate and prolate ellipsoids, respectively. Redrawn from data in D. M. Lindsay *et al.*, *J. Chem. Phys.* **86**, 3500 (1987).

The strong fluctuation of *IP* is thus an electronic structure effect reflecting the global shape of the cluster. This is shown in Fig. 5.4, where the ionization potentials of sodium clusters obtained with the spheroidal jellium model [37] are compared to the experimental values [12]. The odd–even oscillations for low *N* are reproduced well by the calculations. The amplitude of these oscillations is exaggerated, but this is corrected [38] by using the local spin density approximation, instead of the simple LDA. The same occurs for the staggering of the mass

abundance and dissociation energies [39]. The LSDA [40, 41] uses as an input the exchange–correlation energy $E_{xc}[n_\uparrow; n_\downarrow]$ of a spin polarized homogeneous electron gas where the densities $n_\uparrow$ and $n_\downarrow$ for $\uparrow$ and $\downarrow$ spins are different. Consequently, by applying the local density idea as in Section 4.2, one arrives at exchange–correlation potentials $V_{xc}^{\uparrow}(\mathbf{r})$ and $V_{xc}^{\downarrow}(\mathbf{r})$ for the real system, that are different for electrons with $\uparrow$ and $\downarrow$ spins.
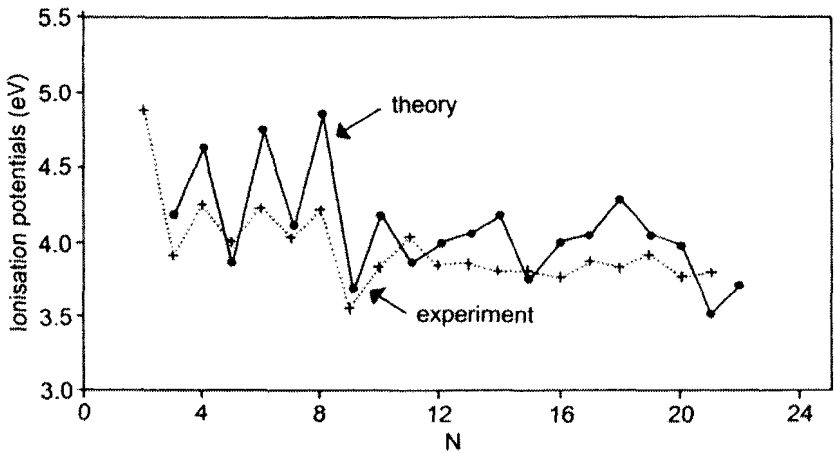
Figure 5.4. Comparison of the experimental ionization potentials [12] of sodium clusters, Na$_N$, and those obtained with the spheroidal jellium model. Redrawn from data in Z. Penzar and W. Ekardt, *Z. Phys. D* **17**, 69 (1990).

It is noticeable that the noble metals behave like the alkali metals. This is not surprising for the ionization potential, but it is striking that the dissociation energies also display odd–even effects since the *d*-electrons contribute to the cohesion of the cluster. The explanation is that the localized *d*-electrons give a contribution that varies smoothly with cluster size and the odd–even effects arise from the contribution to the cohesion from the delocalized valence electrons.

5.3 Temperature Dependence of the Ionization Potential

The experiments measuring *IP* are performed with the clusters at finite temperatures. Temperature leads to vibrations of the atoms, that is, to fluctuations of the cluster shape, and also to electronic entropy effects. The influence of the temperature on *IP* has been studied theoretically by Yannouleas and Landman [42] using a shell-correction method (see Section 4.3) corrected for finite temperature effects. The method incorporates several key ingredients: (1) static deformations of the cluster with respect to the spherical shape, (2) dynamic shape fluctuations due to temperature, and (3) electronic entropy. In this case the ionization potential is calculated as

$$IP = \langle F(T, N, q = +1) \rangle - \langle F(T, N, q = 0) \rangle \qquad (5.10)$$

where $F(T, N, q = +1)$ and $F(T, N, q = 0)$ represent the free energies of the ionized and neutral cluster at temperature T and the symbol $\langle \ \rangle$ indicates that the free energies are averaged over the shape fluctuations

$$\langle F(T, N, q) \rangle = \int d\tau \, F(T, N, q; \beta, \gamma) P(\beta, \gamma). \qquad (5.11)$$

The parameters β and γ specify the triaxial shape of the droplet. These are also used in nuclear physics, where they are called Hill–Wheeler parameters [43]. Equation (5.11) indicates that the cluster explores the free energy surface $F(T, N, q; \beta, \gamma)$ obtained by the finite temperature shell correction method with a probability

$$P(\beta, \gamma) = \frac{\exp\left[-F(T, N, q; \beta, \gamma) \middle/ k_B T\right]}{\int d\tau \exp\left[-F(T, N, q; \beta, \gamma) \middle/ k_B T\right]} \qquad (5.12)$$

where the denominator is the partition function.

Yannouleas and Landman have compared the experimental ionization potentials of potassium clusters [27, 44] to calculations performed at $T = 10$, 300 and 500 K. The calculated *IP*s at $T = 10$ K

show steps at the major shell closings larger than the experimental ones, and also a detailed fine structure in between major shell closures that is not present in the experiments. The agreement is substantially improved for the calculations at $T = 300$ K. The fine structure features are smeared out above K_{21} and the calculated curve follows closely the smooth modulations of the experimental data, with rounded humps ending at the subshell closures at $N = 26$, 30 and 34. Also, the drops of *IP* at the main shell closures are reduced. The odd–even alternation for $N \leq 20$ remains well defined. Finally, for calculations at $T = 500$ K the smearing out of the shell structure is too drastic and the agreement seen at $T = 300$ K is now lost. Further analysis of the calculations for $T = 300$ K indicates that the shape fluctuations play a secondary role compared to the other two factors, static deformations and electronic entropy. Application of the same methods to silver clusters again shows that finite temperature corrections improve the agreement between measured and calculated *IP*s.

The temperature dependence of the ionization potentials of large alkali clusters of nanometer size has been measured by Kresin and coworkers [45]. For this purpose a beam of clusters was generated in a metal vapor condensation source and the particles were ionized by near-UV light of variable frequency. The yield of positive ions was then measured. In the free flight towards the ionization zone, the collimated beam passes through a cylindrical thermalization tube and thermal equilibrium is established between the tube and the clusters. The tube, whose temperature is controlled by electrical heating, can be maintained at any temperature between 300 K and 500 K, with a difference of less than 2 K between the two ends of the tube. The experiment allows then to measure the ion yield as a function of the frequency v of the laser photons for different temperatures. The particles are not size-selected, having instead a broad size distribution. The time-of-flight spectra indicate a distribution with an average radius of ≈ 3–5 nm (≈ 2000–30000 atoms) and a full with at half maximum of ≈ 2 nm.

The yield of ionized particles can be analyzed by considering as a starting point the Fowler formula for the photoion yield from cold bulk surfaces [46]

$$Y \propto \left(h v - W \right)^2 . \tag{5.13}$$

Here $h\nu$ is the photon energy and W is the work function. In addition, this relation was successful in describing the photoion yield in a study of silver nanoparticle aerosols in gas suspension [47], and also for cold alkali nanoclusters [48]. A thermal smearing of the Fermi–Dirac distribution allows for an extension of the Fowler formula to finite temperatures

$$\ln\left(\frac{Y}{T^2}\right) = B + \ln f\left(\frac{h\nu - W}{k_B T}\right) \qquad (5.14)$$

where f is a known function [45]. A plot of $\ln(Y/T^2)$ as a function of $(h\nu - W)/k_B T$ is called a Fowler plot. Fits of the measured yield as a function of the frequency for different temperatures were used to extract a temperature dependent work function $W(T)$, or more properly $IP(T)$, in the case of Li, Na and K nanoclusters [45]. This function is linear in the temperature range studied, 0–475 K for lithium, 0–450 K for sodium, and 0–370 K for potassium, and the slopes $\Delta IP/\Delta T$ obtained from those fits are -1.9, -1.9 and -2.7$\times$ 10^{-4} eV/K. The extrapolation of the $IP(T)$ to $T = 0$ K reproduces accurately the low temperature work functions of the bulk metals. From Eq. (5.6) one could expect a small difference of ≈ 0.1 eV between $IP(T=0)$ of clusters with a radius of 5 nm and the work function of the bulk metal. The observed difference is actually smaller than this value because the cluster beam contains a broad distribution of particle sizes and the ion yield is dominated in the experiment by the largest clusters in the distribution. This is due to the scaling of the photoabsorption cross section with the surface area (or with the volume) of the particle, which supresses the contribution from smaller particles due to their smaller cross sections. Evidently this gas phase method provides an alternative for measuring the work function of highly reactive metals, since perfect, uncontaminated surfaces are difficult to prepare for these metals.

5.4 Hardness and Reactivity

Understanding the reactivity of metallic clusters is a complex subject. With regard to the reaction kinetics, there is a wide variability in

reactivity in terms of the nature of the metal and the size of the cluster. Insight into the effects of the geometry and electronic structure on the reactivity can have tremendous impact on such diverse areas as thin film coating and catalysis

A concept used in discussing the reactivity of molecules is the Chemical Hardness κ, a quantity that can be measured as [49, 50]

$$\kappa = \frac{IP - EA}{2}. \tag{5.15}$$

Its meaning can be understood by writing the change ΔE in the energy of the molecule, or cluster, due to a small change ΔN_e in the number of electrons, maintaining the nuclei at fixed positions,

$$\Delta E = \frac{\partial E}{\partial N_e} \Delta N_e + \frac{1}{2} \frac{\partial^2 E}{\partial N_e^2} (\Delta N_e)^2 + \dots \tag{5.16}$$

The coefficient $\partial E / \partial N_e$ of the first term can be identified with the electronegativity, or chemical potential of the system (atom, molecule or cluster), and the coefficient $\dfrac{1}{2} \dfrac{\partial^2 E}{\partial N_e^2}$ of the second term with its chemical hardness κ [50, 51]. Using a finite difference approximation to evaluate the derivatives in Eq. (5.16)

$$E(N_e) \approx E(N_e^0) - \frac{1}{2}(IP + AE)(N_e - N_e^0) - \frac{1}{2}(IP - AE)(N_e - N_e^0)^2 \tag{5.17}$$

where N_e^0 is the number of electrons in the neutral species. The electronegativity is then given by $\mu = (IP+EA)/2$ and the hardness κ by Eq. (5.15). κ, which measures the curvature of the function $E(N)$, gives the resistance of the molecule or cluster to a change in the number of electrons. From Eqs. (5.5) and (5.6), $\kappa = e^2/R$ is obtained. This reflects the fact that IP and EA become closer and closer as the cluster size

increases, and that these two quantities approach a common value, the work function W of the metal, at the rate $1/R$, or $N^{-1/3}$. This asymptotic behavior has been confirmed by calculations of *IP* and *EA* for large clusters [52]. The predicted linearity of *IP-EA* versus $N^{-1/3}$ is also confirmed by a plot using experimental results for aluminum [52], although deviations are observed for small N. Shell effects are relevant in the small size range and impart structure to the function $\kappa(N)$. The value of *IP(N)* drops between N_c and N_c+1, where N_c indicates a shell closing cluster size. On the other hand *EA* drops between N_c-1 and N_c. Consequently, a cluster of size N_c has a large *IP* and a small *EA*, and thus a large value of the hardness is expected. Calculations for Na clusters [52] predict local maxima of the hardness for the closed shell clusters. These are the less reactive clusters. The same argument leads us to expect even–odd oscillations in the cluster reactivity.

In an exact DFT treatment *IP* is equal to the binding energy of the highest occupied molecular orbital (HOMO) of the neutral [53], that is, the energy eigenvalue with the opposite sign. For the same reason *EA* is the binding energy of the HOMO of the anionic cluster, that is, the lowest unoccupied molecular orbital, or LUMO, of the neutral (if the change of the energy eigenvalue due to charging is neglected). Then,

$$\kappa = \varepsilon_{LUMO} - \varepsilon_{HOMO}. \qquad (5.18)$$

In the practical, but approximate, implementations of DFT the relations $IP = -\varepsilon_{HOMO}$ and $EA = -\varepsilon_{LUMO}$ are not exactly fulfilled but Eq. (5.18) preserves its semiquantitative utility. In this way, clusters having a large HOMO–LUMO gap are chemically hard. These are the clusters having closed electronic shells; the resistance to either donating or accepting an electron makes these clusters relatively inert.

Examples of the experimental verification of this idea exist. Leuchtner *et al.* [54] have reacted anionic and cationic Al clusters with oxigen in a flow tube reactor. An etching reaction was observed and rate constants were reported. The most striking feature was the negligible reactivity of Al_7^+, Al_{13}^- and Al_{23}^-. These clusters are not only unreactive; they are produced by reactions of larger clusters. According to the jellium model those three species are closed shell clusters with 20, 40 and 70 electrons respectively. Another feature observed is the even–odd

alternation in the rate constants. For the cations this occurs for Al_{18}^+ and above, the even atom clusters showing higher reactivity. A cluster Al_N^+ has $3N$-1 valence electrons. This number is odd for N even, and even for N odd. By applying the pairing arguments discussed in Section 5.2, we find that one electron is unpaired for clusters with N even, whereas all the electrons are paired for N odd. Cationic Al clusters with even N can then be expected to be more reactive, as experimentally observed. For Al_N^- anions the odd–even effect is also observed: anions with N even are more reactive. The explanation is the same by noticing that Al_N^- has $3N$+1 valence electrons.

The theoretical and experimental results discussed above are consistent with the principle of Maximum Hardness, proposed by Pearson [55]. This principle states that molecular systems at equilibrium present the highest values of hardness. So, it is reasonable that the clusters with the highest hardness are those with closed electronic shells. Also consistent with this principle are the odd–even oscillations in the reactivity of Al_N^+. An odd–even alternation of the hardness of Na_N and Cu_N clusters has been predicted from DFT calculations [56, 57], clusters having an even number of electrons being harder than neighbor clusters with an odd number of electrons.

5.5 Mass Spectrum Obtained at Near-Threshold Ionization Energies

When the photon energies employed to ionize the clusters in the beam are sufficiently high above the ionization threshold, the measured mass spectrum reveals the intrinsic cluster population in the beam as a function of cluster size. This is the usual situation. However, photons with energies near the ionization threshold have also been used, and the corresponding mass spectra have provided crucial information on the geometrical structure of sodium clusters with sizes between 1500 and 20000 atoms. The same technique has been used to estimate the melting temperature of those large clusters (see Chapter 6).

Imagine that the value of *IP* drops between two clusters of sizes *N* and *N*+1. If the laser photons have energies $h\nu$ only slightly above *IP(N)*, both clusters of sizes *N* and *N*+1 can be ionized, but the cross section is smaller for size *N*. In the limiting case when $h\nu$ is in between the two ionization potentials, that is, $IP(N) > h\nu > IP(N+1)$, only the cluster of size *N*+1 will be ionized. This is the physical basis underlying the experiments of Martin and coworkers which led to the discovery of shells of atoms in large sodium clusters (see Section 4.6). Two mass spectra [58, 59], taken at wavelengths $\lambda = 415$ nm and $\lambda = 423$ nm, are shown in Fig. 5.5. The cluster abundance oscillates with size, and minima are observed for sizes $N = 1980, 2820, 3800, 5070, 6550, 8170, 10200, 12500, 15100, 18000$ and 21300. The experiments do not allow for a higher precision, but this sequence of sizes reproduces the series *N* = 2869, 3871, 5083, 6525, 8217, 10179, 12431, 14993, 17885 and 21127 well. This is just the series that can be obtained from Eq. (3.1), that is, the series of icosahedral clusters with a number of shells ranging from *p* = 10 (*N* = 2869) to *p* = 19 (*N* = 21127). The conclusion is that the clusters formed in those experiments have icosahedral structure (or a cuboctahedral structure, since the same shell closing numbers occur also for cuboctahedral clusters). The abundance minima occur in the size region of the closed shells and the maxima occur for sizes midway between two closed shells. This can be explained by the argument given above: the ionization potentials have maximum values for closed icosahedral shells and local minima in between [59]. Consequently, for mass spectra taken at photon energies near the ionization threshold, the lowest ionization cross sections occur for the clusters with closed icosahedral shells.

Although it is clear why the ionization potential has a maximum value for a closed electronic shell followed by a drop to a substantially lower value, it is less evident why a similar drop occurs after the closing of a shell of atoms. Studies for solid surfaces offer a plausible explanation. The work function of a metal is lowered by the presence of steps on its surface, and the amount of lowering is proportional to the step density [60]. It is argued that the steps create a dipole moment that lowers the ionization energy. Icosahedral (or cuboctahedral) clusters with incomplete shells have atomic vacancies on the surface facets, which give rise to many surface steps, accounting for the observed lowering of *IP*.
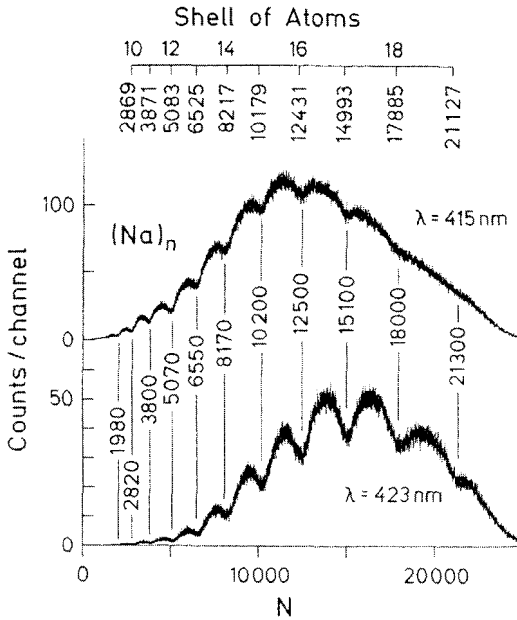
Figure 5.5. Mass spectra of sodium clusters ionized with photons of 2.99 and 2.93 eV. Minima occur at values of N corresponding to icosahedral (cuboctahedral) shell closings given at the top. Reproduced from T. P. Martin, *Phys. Reports* **273**, 199 (1996) with permission of Elsevier.

Density Functional calculations have been performed for model clusters with *bcc* structure and nearly spherical shape [61]. The clusters were modeled by starting with a central atom and adding a first coordination shell of 8 atoms around that central atom, then a second coordination shell of 6 atoms, *etc.* In this way the cluster can be viewed as built by concentric spherical atomic shells. In the calculation of the electronic wave functions a simplifying approximation was used: the total pseudopotential of the ionic background was spherically averaged about the cluster center. This is the so called SAPS approximation [62], described in Chapter 4. The fact that the model clusters are nearly spherical makes the SAPS approximation reasonable. The ionization potential $IP(N)$ was calculated as a function of cluster size in the

neighborhood of several atomic shell closing numbers, $N = 169, 331,$ $531, 941, 1243, 1807$ and 2085. The calculations predict that *IP* experiences a drastic change after the completion of a shell of atoms: a change of slope was found in all cases, and often also a maximum. The clusters formed in the experiments have icosahedral or cuboctahedral shapes, that is, these have faceted surfaces and are less spherical than the model *bcc* clusters of the calculation. However, the idea of an appreciable change of *IP* after the completion of atomic shells can be expected to be a property valid for different types of atomic shells.

5.6 Response to a Static Electric Field

The net force acting on a cluster in the presence of a static (that is, time independent) inhomogeneous electric field $\mathbf{E}(\mathbf{r})$ can be expanded as

$$\mathbf{F} = \mathbf{E}(\mathbf{r}_0)\int\Delta n(\mathbf{r})d^3r + [\nabla\cdot\mathbf{E}](\mathbf{r}_0)\int\Delta n(\mathbf{r})(\mathbf{r}-\mathbf{r}_0)d^3r + ... \quad (5.19)$$

where $\Delta n(\mathbf{r}) = n(\mathbf{r}) - n_+(\mathbf{r})$, and $n(\mathbf{r})$ and $n_+(\mathbf{r})$ are the electronic and ionic densities, respectively. The point $\mathbf{r}_0$ can be identified with the cluster center. The first term in (5.19) does not contribute for a neutral system, and the second is the product of $[\nabla\cdot\mathbf{E}](\mathbf{r}_0)$ times the induced dipole moment $\mathbf{D}$. If the deformation of the ionic density due to the applied field is small, then the force on a neutral cluster is, in first order,

$$\mathbf{F} = [\nabla\cdot\mathbf{E}](\mathbf{r}_0)\mathbf{D} \quad (5.20)$$

where the induced dipole moment can be written as $\mathbf{D} = \alpha\mathbf{E}(\mathbf{r}_0)$, that is, the product of the static polarizability α and the applied field. The static polarizability measures the charge redistribution in the cluster when a static electric field is applied. The electric dipole polarizabilities of clusters of alkali metals [63, 64], aluminum [65] and semiconducting materials [66] have been determined by measuring the deviation from the original trajectory of a mass selected cluster beam that travels along the axis of a pair of electrodes which produce an inhomogeneous transverse electric field. Since the deflection Δz is proportional to the product of

$\nabla \cdot \mathbf{E}$ and $\mathbf{D}$, both of which are proportional to the applied field, Δz is proportional to E^2 (here E is the root mean square electric field over the path length L of the electrodes).

The measurements for Na_N and K_N showed that the polarizabilities per atom, α/N, follow a downward trend toward the bulk value with some abrupt drops related to electronic shell closing (minima of α/N for $N = 2, 8, 18$). Results for selected Na clusters are given in Table 5.1. The classical static polarizability of a metallic sphere of radius R is $\alpha = R^3$ [67], and the experimental results, given in the Table in units of R^3, are higher than the classical values. The enhancement over the classical prediction is due to the spilling of the electronic charge beyond the classical cluster radius R in the field-free system.

Table 5.1. Static electric dipole polarizability of neutral Na_N clusters in the spherical jellium model, in units of the classical value R^3, using different descriptions of exchange and correlation (LDA, WDA, SIC; see text). Results obtained for a jellium with a smoothed surface (DJM) are also given. R is the radius of the spherical positive background.

N	LDA-SJM [71]	LDA-DJM [71]	WDA-SJM [74]	SIC-SJM [72]	Exp. [63, 64]
8	1.45	1.71	1.81	1.66	1.77
18	1.33	1.53	1.59	1.55	1.71
20	1.37	1.61	1.63	1.59	1.68
34	1.27	1.46	1.47	1.47	1.61
40	1.32	1.56	1.53	1.56	1.59

The polarizability can be calculated using linear response theory in the framework of DFT [68]. If the small electric field is characterized by a multipole potential $\delta V_l = E_0\, r^{\,l}\, Y_{l0}(\Omega)$, where E_0 is a small number and $Y_{l0}(\Omega)$ is a spherical harmonic, the cluster develops an induced moment $\mathbf{P}_l$ of magnitude $P_l = \alpha_l E_0$ in response to the field. To first order, the response of the system is characterized by a small change in the electronic orbitals: $\phi_i(\mathbf{r}) = \phi_i(\mathbf{r}) + \delta\phi_i(\mathbf{r})$. Using first order perturbation theory a set of equations is obtained for the changes $\delta\phi_i(\mathbf{r})$

$$\left[-\frac{1}{2}\nabla^2 + V_{eff}(\mathbf{r}) - \varepsilon_i\right]\delta\phi_i(\mathbf{r}) = -\delta V_{eff}(\mathbf{r})\phi_i(\mathbf{r}). \qquad (5.21)$$

Here ε_i are the one-electron energy eigenvalues associated to the unperturbed (field-free) wavefunctions ϕ_i and

$$\delta V_{eff}(\mathbf{r}) = E_0 r^l Y_{l0}(\Omega) + \int d^3 r' \frac{\delta n(\mathbf{r}')}{|\mathbf{r} - \mathbf{r}'|} + \int d^3 r' \frac{\delta V_{xc}(\mathbf{r})}{\delta n(\mathbf{r}')}\delta n(\mathbf{r}') \qquad (5.22)$$

is the change in the selfconsistent potential. The second term on the r.h.s. represents the change in the electrostatic potential of the electronic cloud and the last one is the change of the exchange–correlation potential. The calculation of the polarizability proceeds by first solving the Kohn–Sham equations for the field-free cluster, and obtaining ϕ_i and ε_i. Solving then Eqs. (5.21) and (5.22) to get the functions $\delta\phi_i(\mathbf{r})$, the density change $\delta n(\mathbf{r})$ can be evaluated, and from this the static polarizability

$$\alpha_l = \frac{1}{E_0}\int d^3 r\, r^l Y_{l0}(\Omega)\delta n(\mathbf{r}). \qquad (5.23)$$

In particular, for a dipole field ($l = 1$), $\delta V = E_0 z$, and

$$\alpha_{l=1} = \frac{1}{E_0}\int d^3 r\, z\, \delta n(\mathbf{r}), \qquad (5.24)$$

that is, the electric dipole polarizability is the ratio between the induced dipole moment and the external field strength.

   Polarizabilities have also been calculated using a finite field approach [69]. In that method, a small electric field is applied and the Kohn–Sham equations are solved with and without field applied. The polarizability is then calculated in a finite difference approximation

$$\alpha_{ij} = \frac{\Delta D_i(\mathbf{E})}{\Delta E_j} = \frac{D_i(E_j) - D_i(E = 0)}{E_j}. \qquad (5.25)$$

In this equation, E_j is the magnitude of the electric field applied along the j-axis. The average probability is then obtained as the average of the polarizability tensor α_{ij}, that is, $\langle\alpha\rangle = \left(\alpha_{xx} + \alpha_{yy} + \alpha_{zz}\right)/3$.

The dipole polarizabilities of alkali clusters have been calculated using the LDA and the spherical jellium model [70–72]. Results reported in the column LDA-SJM of Table 5.1 show the expected enhancement of α over the classical value. However, compared to experiment, the theory still underestimates the polarizability by about 20%. Different corrections have been applied. The first one consists of replacing the LDA with a better description of exchange and correlation. In a neutral cluster, the exchange–correlation potential $V_{xc}^{LDA}(\mathbf{r})$ goes to zero exponentially outside the cluster. However the exact asymptotic decay should be $\propto -1/r$. An improved asymptotic behavior is achieved, for instance, a nonlocal description of exchange and correlation effects known as the Weighted Density Approximation (WDA) [73]. The slower decay of $V_{xc}(\mathbf{r})$ produces a more extended electron density tail, and a higher number of bound unoccupied states in the single-particle spectrum. Those effects lead to higher polarizabilities [74], improving the agreement with experiment. Self-interaction corrections (SIC) also include nonlocal effects beyond the LDA. In this approach, the spurious self-interaction of one electron with itself which is present in the Hartree potential (see Eq. (4.10)) is exactly removed. The polarizabilities also improve [72]. A different route for improvement consists in smoothing the sharp discontinuity of the jellium background at the cluster surface. For this purpose the abrupt step density (see Eq. (4.3)) has been replaced by a continuous function modeling a surface with a finite thickness. As a consequence, the electronic density is more extended in this diffuse jellium model (DJM) and the polarizability increases (column labeled LDA-DJM in Table 5.1). All this indicates that a better description of the polarizability per atom is obtained with the formula

$$\alpha = \frac{(R + \delta)^3}{N} \tag{5.26}$$

where δ measures the spatial extent of the electronic spillout, and is nearly independent of R.

The static polarizabilities of Al_N clusters with N up to 61 have been measured by de Heer *et al.* [65]. A comparison with the predictions of the SJM leads to the conclusion that the jellium predictions are successful for N larger than 40, but fail for smaller clusters. The discrepancies are, in this case, opposite to those found for alkali clusters. Namely, the calculated polarizabilities are higher than the measured ones. This over-estimation can be ascribed to an over-estimation of the radius R, which in the SJM is equal to the radius of a spherical piece of bulk matter. In contrast, a contraction of the interatomic distances seems to be a general feature in small metallic clusters [75]. Methods using pseudopotentials predict smaller polarizabilities [76].

The high stability associated to closed electronic shells is a robust feature also imprinted in the electric dipole polarizabilities of alkali clusters [63, 64, 69]: similarly to the inert gas atoms, closed shell clusters have a weakly polarizable electronic cloud. Na_2, Na_8 and Na_{18} have low polarizabilities compared to neighbor clusters [63, 64]. Not only those main features, but also the detailed variation of the polarizabilities with size N are reasonably reproduced by calculations including the cluster geometry [69, 77–79]. In fact, the polarizabilities provide information on the cluster structure. A comparison between measured polarizabilities and calculations for several isomeric structures of the cluster skeleton have been used to identify the most stable geometry [69, 78, 80, 81]. For the typical temperatures at which polarizabilities are measured, there is a delicate interplay between geometry and electronic shell effects [69, 82].

5.7 Dynamical Response

5.7.1 Relation between theory and experiment

The linear response theory can also be applied, within the DFT framework, to the case of the interaction between the cluster and a time dependent electric field characterized by a potential

$$V_{ext}(\mathbf{r};t) = \int d\omega \, e^{-i\omega t} V_{ext}(\mathbf{r};\omega). \qquad (5.27)$$

This leads to the time dependent Density Functional Theory [83–85]. The external field induces a time dependent perturbation of the electron density

$$\delta n(\mathbf{r};t) = \int d\omega \, e^{-i\omega t} \, \delta n(\mathbf{r};\omega) \qquad (5.28)$$

with Fourier components $\delta n(\mathbf{r};\omega)$. The key quantity to calculate the response of the system in the linear regime is the dynamical susceptibility $\chi(\mathbf{r},\mathbf{r}';\omega)$, which relates the individual components of the induced density to those of the external potential

$$\delta n(\mathbf{r};\omega) = \int d^3 r' \, \chi(\mathbf{r},\mathbf{r}';\omega) V_{ext}(\mathbf{r}';\omega). \qquad (5.29)$$

Again the main interest arises in the case of a dipole field. The dynamical polarizability $\alpha(\omega)$, which is the ratio between the induced dipole moment and the intensity of the applied field, becomes

$$\alpha(\omega) = \frac{1}{E_0} \int d^3 r \, z \delta n(\mathbf{r};\omega). \qquad (5.30)$$

The dynamical polarizability reduces to the static one of Eq. (5.24) for $\omega = 0$. Dissipation results in $\delta n(\mathbf{r};\omega)$ being a complex function, and its imaginary part represents the power absorption of the cluster, that is due to electronic excitations. Using the Golden Rule, one obtains the photoabsorption cross section

$$\sigma(\omega) = \frac{4\pi\omega}{c} \operatorname{Im}\alpha(\omega), \qquad (5.31)$$

where c is the velocity of light and $\operatorname{Im}\alpha(\omega)$ is the imaginary part of the dynamical polarizability.

Experiments have been performed to measure the photoabsorption spectrum. The experimental configuration [64, 86] is shown in Fig. 5.6. The cluster beam is first collimated by a rectangular aperture. Further downstream the clusters are photoionized by the light of a ultraviolet

lamp and the resulting cluster cations enter a quadrupole mass analyzer (QMA). Then the cluster beam is illuminated by a collinear and counter-propagating laser beam. Upon absorption of light, the clusters warm up and fragment. The transverse recoil removes the daughter clusters away from the initial direction of motion of the collimated beam, and the ratio between the number of clusters of a given size arriving at the detector with and without light excitation present is proportional to the absorption cross section.
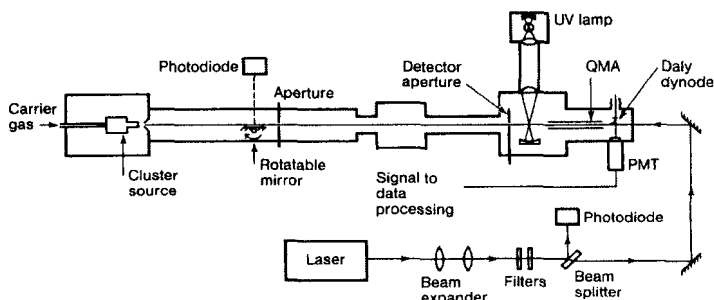

Figure 5.6. Measurement of the photoabsorption cross section. The collimated beam is ionized with ultraviolet light and the ionized clusters enter a quadrupole mass analyzer (QMA). A colinear, counterpropagating laser beam heats up the clusters. Some clusters evaporate atoms and are removed from the beam. The ratio between the number of clusters of a given size arriving at the detector with and without laser excitation gives the absorption cross section. Reproduced from K. Selby *et al.*, *Phys. Rev. B* **40**, 5417 (1989) with permission of the American Physical Society.

The process responsible for the fragmentation of the clusters is the excitation of a collective plasmon, which is analogous to the surface plasmon excitation in solids. The valence electrons from all the atoms of the cluster participate together in this collective resonance, in which the electrons move back and forth uniformly against the positive ionic background [87]. For sodium clusters, for example, the excitation energy of the plasmon is about 3 eV. This energy is higher than the binding energy of an atom in the aggregate, which is below 1 eV, and the excited cluster decays by evaporating single atoms. Using statistical models, the

time required to evaporate an atom, if one assumes that the energy of the collective excitation is converted into atomic vibrations, turns out to be, for small clusters (say, smaller than $N = 40$), orders of magnitude smaller than the time-of-flight of the molecular beam in the spectrometer. Consequently, it can be confidently assumed that the photoabsorption and photofragmentation cross sections are equal. When the cluster size increases, the time required to evaporate atoms also increases and multiphoton absorption techniques have been used [28]. The surface plasmons in metallic clusters are similar to the giant dipole resonances in nuclei [88].

The integral of $\sigma(\omega)$ leads to the so called dipole sum rule

$$\int_0^\infty \sigma(\omega)d\omega = 2\pi^2 \frac{e^2\hbar^2}{m_e c} Z , \qquad (5.32)$$

where e and m_e are the electron charge and mass respectively, $\hbar$ is the Planck constant divided by 2π, and Z is the total number of electrons taking part in the collective motion. Consequently, the experimental determination of $\sigma(\omega)$ helps identifying the collective nature of a resonance. The observed resonances of alkali clusters typically account for $\approx 60\%$ of the total dipole strength.

For spherical metal particles of a diameter $2R$ much smaller than the photon wavelength, the classical theory of the dynamical polarizability developed by Mie [67] predicts the following expression for the photoabsorption cross section

$$\sigma(\omega) = \frac{4\pi Z e^2}{m_e c} \frac{\omega^2 \Gamma}{\left(\omega^2 - \omega_{Mie}^2\right)^2 + \left(\omega \Gamma\right)^2} , \qquad (5.33)$$

where ω_{Mie} and Γ represent the frequency and the width of the resonance, respectively. This relation assumes that all the dipole oscillator strength is exhausted by the surface plasma resonance at ω_{Mie}. The frequency of the single dipole resonance, representing the collective oscillation of the valence electrons with respect to the positive ions, is related to the cluster radius by

$$\omega_{Mie} = \sqrt{\frac{Z\hbar^3 c}{m_e R^3}}. \qquad (5.34)$$

This gives for ω_{Mie} a value equal to one third of the bulk plasma frequency ω_{pl}.

5.7.2 Sum rules

The photoabsorption cross section is determined, through Eq. (5.31), by the imaginary part of the polarizability tensor $\alpha(\omega)$. Alternatively [89], one can use the strength function $S(E)$, which is related to the polarizability $\alpha(\omega)$ by

$$S(E) = \sum_n \delta(E - E_n) \left| \langle n|Q|0\rangle \right|^2 = -\frac{1}{\pi} \mathrm{Im}\,\alpha(\omega), \qquad (5.35)$$

where $|0\rangle$ represents the electronic ground state of the cluster and the sum $\sum_n$ is extended over the excited "many-body" states of the system.

E_n are the excitation energies and $E = \hbar\,\omega$. The operator Q represents the external field, the electric dipole operator in most cases of interest. For some applications the full response is not required and a knowledge of some moments of the strength function,

$$m_k = \int dE\, E^k S(E), \qquad (5.36)$$

also called sum rules, is enough to have a correct picture of the physical processes (in this equation k is an integer number, positive or negative). For instance, the centroid (that is, the average energy $\overline{E}$) and the variance σ^2 of the photoabsorption spectrum can be obtained from the knowledge of m_0, m_1 and m_2, as $\overline{E} = m_1/m_0$ and $\sigma^2 = m_2/m_0 - (m_1/m_0)^2$. A direct evaluation of the moments is difficult because the whole spectrum of excitations is needed, but the odd moments can be obtained without much effort with RPA precission [89, 90]. The RPA, or Random

Phase Approximation [91], can be derived as the small amplitude limit of the time dependent Hartree–Fock theory by linearizing the equations of motion. The characteristic feature of RPA is to construct excited states as a superposition of one particle–hole excitations. The linear moment m_1 for the electric dipole operator is model independent, and its RPA value

$$m_1 = \frac{\hbar^2 e^2 Z}{2m_e} \qquad (5.37)$$

is exact, so one obtains the sum rule of Eq. (5.32).

By defining mean energies as $e_k = (m_k/m_{k-2})^{1/2}$, the bounds $e_1 \le \overline{E} \le e_3$ and $\sigma^2 \le (e_3^2 - e_1^2)/4$ can be demonstrated. Another result is that the inverse energy-weighted sum rule m_{-1} is related to the static polarizability [92]

$$m_{-1} = \alpha / 2 \, . \qquad (5.38)$$

Consequently, one may estimate the centroid and the variance of $S(E)$ by evaluating the three RPA moments m_{-1}, m_1 and m_3. The physical significance of the upper limit e_3 of $\overline{E}$ is that of a rapid oscillation (diabatic) of the valence electrons against the ions, whereas the lower limit e_1 is connected with a slow adiabatic motion of the electrons adjusting their density at any moment to the external field. This lower limit turns out to be a good estimation of the experimental energy of the collective excitation for metallic clusters [28, 89]. The moment m_3 represents the restoring force parameter for the collective translational oscillations of the electrons against the ionic background [89]. For a model of spherically symmetric densities m_3 is given by an overlap integral of the electronic and ionic densities [93]

$$m_3 = \frac{e^4}{2}\left(\frac{\hbar^2}{m}\right)\frac{4\pi}{3} \int n_+ (r) n(r) d^3 r \, . \qquad (5.39)$$

This integral is easily evaluated for a cluster of radius $R = r_s Z^{1/3}$ in the spherical jellium model (r_s is related to the average electron density n_0 of the bulk metal by $r_s = (3/4\pi n_0)^{1/3}$), giving

$$m_3 = \frac{\hbar^4 e^4 Z}{2m_e^2 r_s^3}\left(1 - \frac{\delta Z}{Z}\right) \qquad (5.40)$$

where δZ measures the net spillout of the electronic charge beyond the radius of the positive ionic background, that is

$$\delta Z = 4\pi \int_R^\infty r^2 n(r) dr . \qquad (5.41)$$

By neglecting the electronic spillout ($\delta Z = 0$), then $2m_{-1} = R^3$, and $e_3 = \sqrt{\hbar^2 e^2 Z / m_e \alpha} = e_1$ gives the resonance frequency of the classical Mie surface plasmon. In general, if most of the absorption strength is concentrated in a narrow region, $\overline{E}$ is a good estimation for the resonance energy. This is the starting point of the plasmon-pole models. In those models $e_1 = e$ and the knowledge of the static polarizability determines the value of the dipolar plasma resonance energy as

$$e_3 = \hbar\omega_{pl}\sqrt{\left(\frac{1}{3} - \frac{\delta Z}{3Z}\right)} \qquad (5.42)$$

where $\omega_{pl} = \sqrt{4\pi e^2 n_0 / m_e}$ is the bulk plasma frequency. For $\delta Z = 0$, e_3 becomes equal to the classical Mie frequency.

Table 5.2 gives the calculated bounds e_1 and e_3 of the dipole surface collective mode for some neutral and charged Na and K clusters [74]. LDA labels the results obtained using the local density approximation to exchange and correlation in the calculation of the density and the single-particle orbitals needed in the RPA formulas for m_k and e_k. On the other hand, NL corresponds to results using a nonlocal approximation [73]. The experimental energies of the surface plasma resonance are in reasonable agreement with e_1, in particular when the NL approximation

is used, and those experimental values are given in parenthesis under the calculated value of e_1(NL). The effect of the charge is to increase the resonance energy. The analysis of e_1 and e_3 for larger clusters shows that the resonance energy increases with size [74], a prediction in agreement with experiment [94]. The theory also allows to obtain an upper bound of the variance of the photoabsorption cross section, but the predicted widths of the resonances are, of course, larger than the experimental widths. The variance is found to decrease by charging the cluster.

Table 5.2. Calculated RPA mean energies e_1 and e_3 (in eV) of the dipole surface collective mode of neutral and charged sodium and potassium clusters. LDA and NL refer to the local density and nonlocal approximations to exchange and correlation effects. The experimental surface plasma resonance energies are given in parenthesis. Data collected from [74].

	e_1	e_3		e_1	e_3
LDA Na$_8$	2.83	3.14	LDA Na$_9^+$	3.05	3.16
NL Na$_8$	2.53 (2.53)	2.81	NL Na$_9^+$	2.79	2.93
LDA Na$_{20}$	2.91	3.14	LDANa$_{21}^+$	3.04	3.19
NL Na$_{20}$	2.67 (2.46)	2.97	NL Na$_{21}^+$	2.77	3.03
LDA K$_8$	2.21	2.32	LDA K$_9^+$	2.33	2.39
NL K$_8$	1.96	2.12	NL K$_9^+$	2.13 (1.93)	2.22
LDA K$_{20}$	2.25	2.37	LDA K$_{21}^+$	2.32	2.40
NL K$_{20}$	2.06	2.24	NL K$_{21}^+$	2.16 (1.98)	2.28

The general expressions for the odd moments corresponding to q- and l- dependent external fields $j_l(qr)Y_{l0}(\Omega)$ are given in [89]. This field

represents the angular decomposition of an incident photon, described as a plane wave $e^{i(\mathbf{q}\mathbf{r}-\omega t)}$. With those operators one can analyze the multipolar response and also the inelastic scattering of electrons. In small metallic clustes, and for fields of high multipolarity, there is a competition between the Coulombic contribution to the response (diffusivity and collective excitations) and the kinetic energy contribution (single-particle excitations). The later dominates for large l or large momentum transfer $\mathbf{q}$, indicating the vanishing of collective effects. The response of a metallic sphere to a photon of intermediate energy is dominated by dipolar excitations, and at large energies by electron–hole excitations [89, 95, 96].

5.7.3 Calculation of the dynamical susceptibility

Let us return to the calculation of the susceptibility $\chi(\mathbf{r},\mathbf{r}';\omega)$, which is required to obtain $\delta n(\mathbf{r};\omega)$ and then $\alpha(\omega)$. In its Kohn–Sham formulation, DFT is a theory of independent particles moving in an effective selfconsistent potential. Thus Eq. (5.29) can be written in the alternative way

$$\delta n(\mathbf{r};\omega) = \int d^3 r' \, \chi_0(\mathbf{r},\mathbf{r}';\omega) \delta V_{\!e\!f\!f}(\mathbf{r}';\omega), \qquad (5.43)$$

where $\chi_0(\mathbf{r},\mathbf{r}';\omega)$ is the noninteracting (or independent-particle) dynamical susceptibility and $\delta V_{\!e\!f\!f}(\mathbf{r};\omega)$ is the selfconsistent perturbing potential

$$\delta V_{\!e\!f\!f}(\mathbf{r};\omega) = V_{ext}(\mathbf{r};\omega) + \int d^3 r' K(\mathbf{r},\mathbf{r}';\omega) \delta n(\mathbf{r}';\omega), \qquad (5.44)$$

sum of the external potential $V_{ext}(\mathbf{r};\omega)$ and the induced potential (the second term). The nonlocal kernel $K(\mathbf{r},\mathbf{r}';\omega)$ is the sum of the electron–electron Coulomb interaction and an exchange–correlation local field correction

$$K(\mathbf{r},\mathbf{r}';\omega) = \frac{1}{|\mathbf{r}-\mathbf{r}'|} + \frac{\delta^2 E_{xc}[n]}{\delta n(\mathbf{r};\omega)\,\delta n(\mathbf{r}';\omega)}. \qquad (5.45)$$

An adiabatic (frequency independent) approximation is usually taken for the local field correction

$$K_{xc}(\mathbf{r},\mathbf{r}') = \frac{\delta^2 E_{xc}[n]}{\delta n(\mathbf{r})\delta n(\mathbf{r}')}, \tag{5.46}$$

and, if the LDA is used for $E_{xc}[n]$, then K_{xc} becomes a local function of $\mathbf{r}$. Since the results for $\delta n(\mathbf{r};\omega)$ from Eqs. (5.29) and (5.43) are the same, the following relation between the noninteracting and interacting dynamical susceptibilities is obtained [83–85]

$$\chi(\mathbf{r},\mathbf{r}';\omega) = \chi_0(\mathbf{r},\mathbf{r}';\omega) + \iint d^3r_1 d^3r_2 \,\chi_0(\mathbf{r},\mathbf{r}_1;\omega) K(\mathbf{r}_1,\mathbf{r}_2). \tag{5.47}$$

This Dyson-type equation, which has to be solved iteratively, closes the calculation of $\chi(\mathbf{r},\mathbf{r}';\omega)$, once $\chi_0(\mathbf{r},\mathbf{r}';\omega)$ is known. The last quantity has the expression [83, 84]

$$\chi_0(\mathbf{r},\mathbf{r}';\omega) =$$
$$\sum_i^{occ} \left[\phi_i^*(\mathbf{r})\phi_i(\mathbf{r}')G(\mathbf{r},\mathbf{r}';\varepsilon_i + \hbar\omega) + \phi_i(\mathbf{r})\phi_i^*(\mathbf{r}')G^*(\mathbf{r},\mathbf{r}';\varepsilon_i - \hbar\omega) \right] \tag{5.48}$$

where ϕ_i are the occupied single-particle orbitals of the Kohn–Sham Hamiltonian for the field free cluster, ε_i are the corresponding one-electron energy eigenvalues and $G(\mathbf{r},\mathbf{r}';\varepsilon_i \pm \hbar\omega)$ are the retarded Green functions associated to the effective Kohn–Sham ground state potential

$$\left[E + \frac{1}{2}\nabla^2 - V_{eff}(\mathbf{r}) \right] G(\mathbf{r},\mathbf{r}';E) = \delta(\mathbf{r} - \mathbf{r}'). \tag{5.49}$$

When the LDA is used all along for exchange and correlation, this formalism is known as TDLDA [83–85].

5.7.4 Spherical clusters

Linear response theory can be applied to study the interaction between a cluster and a time dependent electric field. The TDLDA, in conjunction with the jellium model, follows the Mie result of Eq. (5.33) in a qualitative way, shown schematically in Fig. 5.7. The dipole absorption cross section of spherical sodium clusters usually exhibits a dominant peak, which exhausts 75–90 % of the dipole sum rule, and is shifted by 10–20 % with respect to the Mie result. The centroid of the strength distribution tends towards the Mie resonance in the limit of a macroscopic metal sphere. Its red shift in finite clusters is a quantum mechanical finite size effect closely related to the spillout of the electrons beyond the jellium edge. About 10–25 % of the dipole strength is typically found at higher energies, and can be interpreted as a reminescence of a strongly fragmented volume plasmon. Often, the dominant peak is fragmented into two or more lines. For spherical clusters this can be attributed to the interference of specific particle–hole (or more complicated) excitations with the predominant collective mode. This fragmentation may be compared to the Landau damping in a solid.

The results of a TDLDA calculation [97, 98] of the photoabsorption spectrum for Na_{20} within the spherical jellium model are shown in Fig. 5.8. The dotted curve is the spectrum obtained using the independent particle susceptibility χ_0 in Eq. (5.29), and the continuous line is the result for the interacting susceptibility χ. The ground state electronic configuration of Na_{20} in the spherical jellium model is $1s^2\ 1p^6\ 1d^{10}\ 2s^2$. Above these occupied subshells there are other, unoccupied ones, $1f$, $2p$, $1g$, $2d$, $3s$, $3p$, and the peaks in the noninteracting spectrum represent allowed particle–hole excitations in which one electron is promoted from an occupied state to an unoccupied one. When electron–electron interactions are switched on (using the fully interacting χ) some particle–hole transitions are shifted in energy, and others lose their individual identities, merging into a collective resonance.

Compared to experiments, the LDA calculations for the spherical jellium [89, 98] yield an insufficient red shift of the collective Mie resonance. This is connected to the predicted low polarizability. It is evident for Na_{20} in Fig. 5.9, where the calculated resonance lines [98] have been broadened to simulate finite temperature effects [89, 99]. The form of the LDA spectrum is similar to the experimental one [100], but the main LDA peak is shifted 0.3 eV to higher energy.
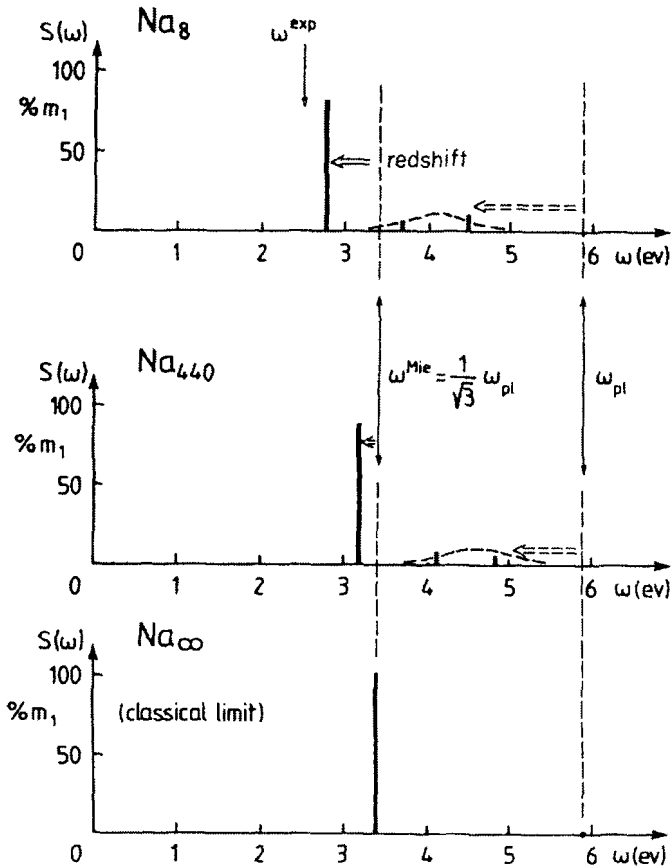
Figure 5.7. Collective dipole spectrum of sodium clusters. $S(\omega)$ is plotted as the percentage of the total dipole strength m_1, normalized to 100% (see Eqs. (5.32) and (5.37)). The lowest panel represents the classical limit, where all the strength is concentrated in the surface plasmon, of frequency ω_{Mie}, and the volume plasmon (of frequency ω_{pl}) has zero strength. For finite clusters the surface plasmon is red shifted and its missing strength is distributed over the remainder of the strongly fragmented volume plasmon. Reproduced from M. Brack., *Rev. Mod. Phys.* **65**, 677 (1993) with permission of the American Physical Society.

The physical process underlying the fragmentation of the spectrum of Na_{20} is, however, not well described by the LDA. In this calculation, fragmentation occurs because of the proximity to the plasmon resonance line of a particle–hole excitation ($2s \rightarrow 3p$) with energy $\hbar\omega = 2.8$ eV. In addition, the $3p$ subshell is practically degenerate with the vacuum level, and the fragmented line is broadened by the proximity of one-electron transitions from the $2s$ states to scattering states in the energy continuum. In contrast, the experimental ionization threshold lies at an energy of 3.76 eV, more than 1 eV higher than the main plasmon peak. A calculation using a jellium with a smooth surface (the deformed jellium model of Table 5.1) improves the position of the dipole resonance [71].
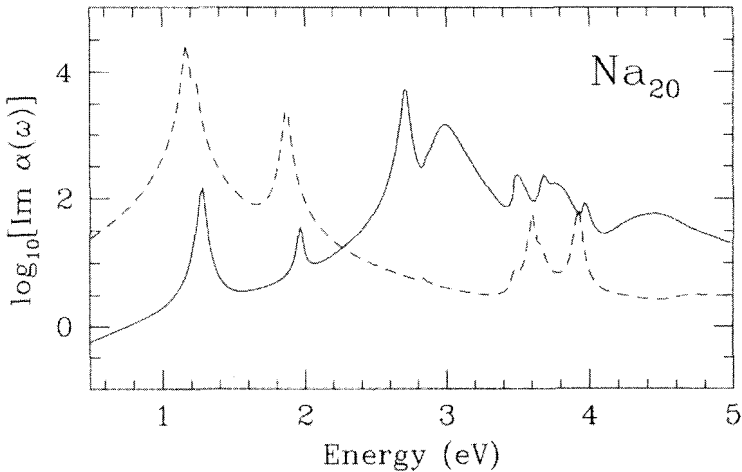

Figure 5.8. Imaginary part of the dynamical polarizability (per electron) of Na_{20}. The calculations employed the spherical jellium model and the LDA. Dotted and continuous curves are obtained using the noninteracting (χ_0) and fully interacting (χ) dynamical susceptibilities. Reproduced from A. Rubio *et al.*, *Int. J. Mod. Phys. B* **11**, 2727 (1997) with permission of World Scientific.

Replacing the LDA by a nonlocal description of exchange and correlation provides a step in the correct direction. A calculation [97]

using the Weighted Density Approximation [73] (the continuous line in Fig. 5.9) shifts the plasmon resonance to lower energies, with the main peak now at 2.56 eV, substantially improving the agreement with the experiment. This effect arises from a better description of the asymptotic (large r) region of the exchange–correlation potential V_{xc} and from the improvement of the local field correction in Eq. (5.46). The more accurate V_{xc} also leads to an accurate ionization threshold, 3.27 eV, which does not interact with the plasmon because of the large separation between those two features. Instead, a shoulder develops at ≈ 2.7–2.8 eV, and a pronounced secondary peak appears on the low energy side of the resonance, at ≈ 2.2 eV, both features being due to the interaction of the plasmon with particle–hole excitations. Three resonances observed [101] at ≈ 2.19, 2.41 and 2.76 eV, support the predicted spectrum in the region below 2.9 eV. Calculations including self-interaction corrections (SIC) also improve the results with respect to the LDA [102, 103].
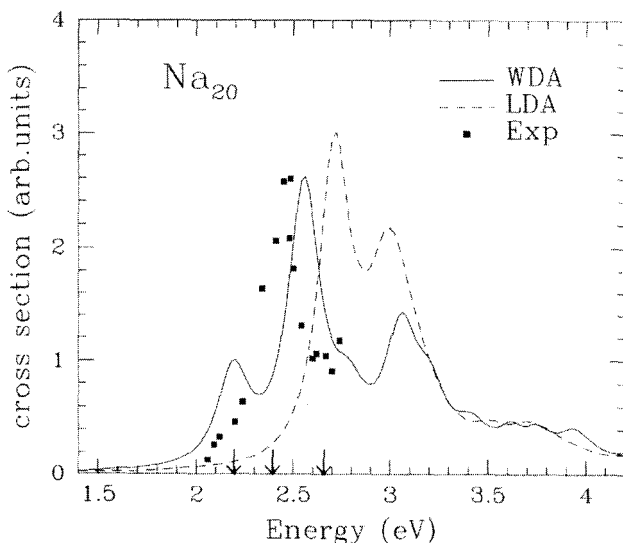

Figure 5.9. Calculated (LDA, WDA) [97, 98] and experimental [100] photoabsorption cross sections (per electron) of Na_{20}. Arrows mark positions of observed peaks [101]. Reproduced from A. Rubio *et al.*, *Int. J. Mod. Phys. B* **11**, 2727 (1997) with permission of World Scientific.
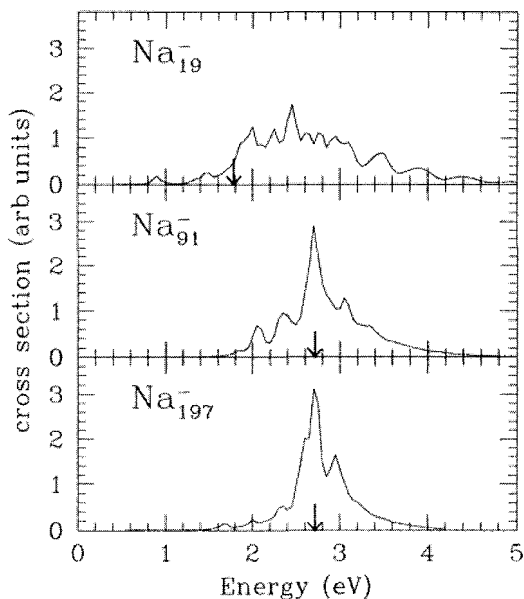
Figure 5.10. Calculated photoabsorption crosss sections, per electron, of sodium cluster anions. The clusters are described by the spherical jellium model and the nonlocal WDA approximation was used for exchange and correlation. Arrows mark the binding energy of the least bound level. Reproduced from A. Rubio *et al.*, *Int. J. Mod. Phys. B* **11**, 2727 (1997) with permission of World Scientific.

Interesting effects can be expected when the plasmon excitation energy is close to the ionization threshold. This is the case for large cluster anions [97, 104]. For small negatively charged clusters, the electron detachment threshold is low, and the energy of the collective resonance lies in the region of electronic excitations to the continuum of states, where Landau damping produces a broadening of the resonance. This is noticed by comparing the calculated spectrum of Na_{19}^- given in Fig. 5.10 with that for neutral Na_{20} in Fig. 5.9 (both clusters have 20 electrons). The electron detachment threshold of Na_{19}^- is indicated by the arrow in the figure. As the cluster size increases, the plasmon

approaches the region of discrete states. Then, when the detachment threshold of the negative cluster lies in the region of the plasmon resonance, electron emission becomes a decay mechanism which competes with the usual one of atom evaporation. The calculated photoabsorption cross sections of Na_{91}^{-} and Na_{197}^{-} are also given in Fig. 5.9. In those two clusters, the detachment threshold overlaps with the collective resonance.

Reiners and Haberland [105] have measured the photoabsorption cross section of Na_{91}^{-} and have found a broad collective resonance centered at 2.65 eV (its width is 0.92 eV), whose decay can lead to two final channels: atom and electron emission. They also state that the electron emission contributes an extra escape width. The calculated position of the collective resonance in Fig. 5.10 is 2.69 eV, in good agreement with experiment. Changing the net cluster charge, from anionic to neutral and then to cationic clusters, for a fixed total number of valence electrons, has the effect of shifting slightly the plasmon to higher energies. For instance, the maximum of the resonance occurs at 2.65 and 2.77 eV for Na_{91}^{-} and Na_{93}^{+} respectively; the corresponding width decreases from 0.92 eV to 0.51 eV.

5.7.5 Effect of shape deformations

In clusters with open electronic shells, a splitting of the dipole resonance is observed which is a consequence of the static deformation of the cluster shape. A double peak in the photoabsorption cross section has been observed for K and Na clusters [64, 106, 107], and for Ag clusters in the region $10 \leq N \leq 16$ [108]. The two modes correspond to excitations along and perpendicular to the main axis of the spheroid.

The results for cationic Sodium clusters [107], shown in Fig. 5.11, reveal the systematics of cluster shapes when adding electrons to the $N = 8$ and $N = 20$ spherical clusters. The observed trend goes: spherical → prolate → oblate → spherical. This systematics is reproduced by total energy calculations within the spheroidal jellium model [37], and the splitting of the collective resonance is obtained by the TDLDA applied to the deformed clusters [109]. For larger clusters, it is difficult to disentangle the effects originating from static shape deformations from those due to the fragmentation mechanism discussed above.

A splitting of the dipole resonance into three peaks has been observed in some Na clusters [64, 107]. This is interpreted as corresponding to collective vibrations of the valence electrons in the directions of the principal axis of a triaxially deformed cluster and has motivated the extension of the jellium model to fully triaxial shapes [110–113]. Let us illustrate these ideas with two examples, Na_{12} and Na_{14}, taken from the work of Lauritsch *et al.* [110].
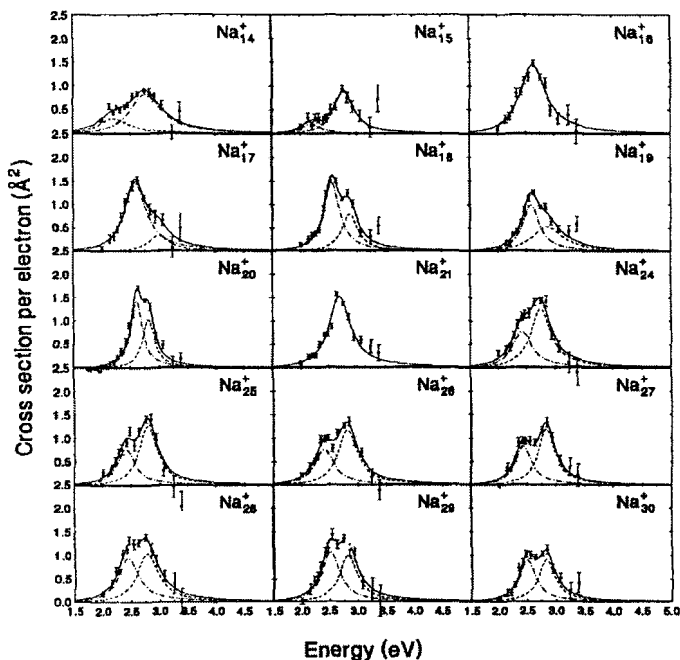

Figure 5.11. Experimental photoabsorption spectra of Na_N cations. Lorentz functions are fitted to the data. Reproduced from J. Borggreen *et al.*, *Phys. Rev. B* **48**, 17507 (1993) with permission of the American Physical Society.

The potential energy surfaces of those two clusters were calculated with the intention to study the splitting of the dipole resonance as well as the competition between possible isomers with different shapes. The triaxial deformation of the uniform background can be classified in terms of the Hill–Wheeler coordinates β and γ [43]. β describes the overall

quadrupole deformation. $\gamma = 0°$, $120°$, $240°$ describe prolate deformations, and $\gamma = 60°$, $180°$, $300°$ oblate ones; all other values of γ give truly triaxial shapes. In addition to the shape deformation of the positive background, the jellium background was also allowed to have a diffuse density profile [71]. The ground state of Na_{12} is triaxial, with deformation parameters $\beta = 0.54$, $\gamma = 15°$, and is energetically well separated from competing prolate and oblate configurations. Na_{14} is characterized by axially symmetric minimum energy structures: the two lowest configurations, prolate and oblate respectively, are almost degenerate in energy. The oblate minimum is rather soft in the γ direction whereas the prolate minimum predicts stiffer γ vibrations. The pronounced shape isomerism found for both clusters bears some resemblance to that found by fully microscopic quantum chemical [114] and *ab initio* DFT calculations [115]. The resonance energies of the collective dipole excitations were obtained from the approximate expression

$$\omega_i^2 = \frac{1}{Nm_e} \int n(\mathbf{r}) \frac{\partial^2}{\partial r_i^2} V_{ext}(\mathbf{r}) d^3r \qquad (5.50)$$

obtained from the RPA sum rules [89]. In this equation, V_{ext} is the electrostatic jellium potential, and i runs over the spatial directions, *i.e.*, $\mathbf{r}_i = \{x, y, z\}$ for the triaxial clusters and $\mathbf{r}_i = \{r, z\}$ for axial ones.

Table 5.3. Surface dipole plasmon energies (in eV) for the triaxial ground state of Na_{12} and for the oblate (OE) and prolate (PE) isomers of Na_{14}, obtained from the RPA sum rule, Eq. (5.50). Data collected from [110].

Na_{12}			Na_{14}		Na_{14}	
Triax.			OE		PE	
$\hbar\omega_x$	$\hbar\omega_y$	$\hbar\omega_z$	$\hbar\omega_r$	$\hbar\omega_z$	$\hbar\omega_r$	$\hbar\omega_z$
2.857	3.238	2.313	2.531	3.401	3.102	2.313

The resonance energies, calculated for the ground state of Na_{12} and for the two degenerate minima of Na_{14} are given in Table 5.3. Three different resonances are obtained for Na_{12}, reflecting its triaxial shape. The three energies are in qualitative agreement with the experimental peaks [107, 64], although the calculated energies are 10–15% too high due to the simple sum rule approximation used. Each of the two competing axial isomers of Na_{14} is characterized by a double peak structure where $\hbar\omega_r$ has double weight compared to $\hbar\omega_z$. The actual strength distribution will be an incoherent superposition of the two isomeric minima.

Kohl *et al.* [116] extended the calculations to a larger set of sodium clusters ($N = 2$–20). They confirm the results of the spheroidal jellium model: prolate clusters after the magic numbers $N = 2$ and $N = 8$, and oblate ones before $N = 8$ and $N = 20$. However, a transition region formed by triaxial shapes was found separating the prolate and oblate ends. The width of the transition regime is very small between $N = 2$ and $N = 8$, containing only the cluster $N = 5$, but comparatively large between $N = 8$ and $N = 20$. The triaxial minimum is well developed in Na_5 but the others are extremely soft, such that thermal fluctuations will easily wash out the triaxial signatures in the dipole resonance energies. For cationic Na_N^+ clusters, Kasperl *et al.* [111] have concluded that the signal of triaxiality on the resonance energies is faint for clusters larger than Na_6^+. The mechanisms responsible for the width of the plasmon resonance have been investigated [117] for the spherical clusters Na_9^+, Na_{21}^+ and Na_{41}^+ in the framework of the *structurally averaged* jellium model [118]. In this model the effects of the ionic structure are added in an averaged manner: first, as an additional potential on the electrons, second as an average Madelung energy in the volume, and third as an ionic surface energy. The two leading mechanisms for the line broadening are fragmentation of the resonance into nearby particle–hole transitions, and splitting through thermal quadrupole fluctuations [99].

5.7.6 Effect of the ion granularity

The experimental photoabsorption cross section of the closed shell cluster Na_{21}^+ indicates a plasmon resonance in the region 2.65–2.74 eV;

more precisely, at 2.65 eV in [106], at 2.68 eV in [107], and at 2.74 eV in [119], with an averaged value of 2.69 eV. Although this cluster is isoelectronic with Na_{20}, the plasmon resonance occurs at a slightly higher energy in Na_{21}^+, due to the stronger confining potential. A TDLDA calculation within the jellium model, shown in the upper panel of Fig. 5.12, gives 2.95 eV, overestimating the energy of the plasmon [120]. The introduction of nonlocal corrections to exchange and correlation improves the position of the resonance (2.63 eV), but a well separated fragmentation peak appears. This fragmentation has not been observed, although a shoulder has been detected by Borgreen *et al.* [107] and by Reiners *et al.* [119] on the blue side of the peak.

The cross sections obtained with the SAPS model are plotted in the bottom panel of the same figure. The structure of this cluster is rather spherical (O_h symmetry in a recent calculation [78]), so the use of the SAPS model is justified. The LDA again overestimates the experimental plasmon energy, but the nonlocal (WDA) calculation places the plasmon at 2.70 eV; this time the strong fragmentation has disappeared, and only small features remain at 3.0 eV and 3.5 eV, which correlate with the observed shoulders [107, 119]. The photoabsorption spectrum of Na_{41}^+ has also been calculated [121] using SAPS and the WDA, and the position and shape of the plasmon resonance are again in good agreement with experiment. The TDLDA formulation has been applied [122] to calculate the optical spectrum of the closed shell clusters Na_9^+ and Na_{18} using the perturbative extension of the SAPS model discussed in connection with Eq. (4.30). Quantitative agreement with experiment was obtained, but the method becomes difficult to apply to clusters with low symmetry.

TDLDA calculations of the optical spectrum with a full account of the geometry of the cluster have also been performed. Apart from being more realistic compared to other calculations retaining only the overall shape characteristics, this can provide a method to determine the cluster geometries. Sometimes the differences in binding energy between the ground state and some low lying isomers obtained by *ab initio* calculations are so small as to cast doubts about the calculated lowest energy structure, and a comparison of the experimental optical spectrum and those calculated for different isomers with similar energies can help in the identification of the ground state.
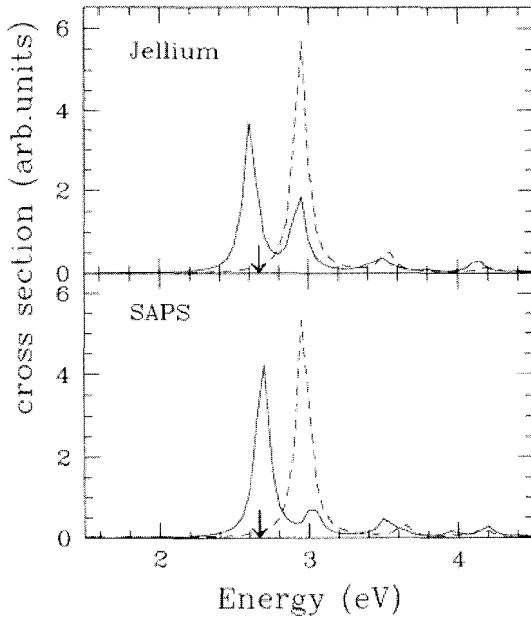
Figure 5.12. Calculated photoabsorption spectrum of Na_{21}^{+} in the jellium and SAPS models. Dashed and continuous curves correspond to LDA and nonlocal WDA treatments of exchange and correlation. Arrows indicate the position of the plasmon, averaged over three experimental results. Reproduced from A. Rubio *et al.*, *Z. Phys. D* **26**, 284 (1993) with permission of Springer–Verlag.

A method based on a space and time representation of the response functions of large systems has been developed that takes advantage of the rather sparse Hamiltonian matrix in a coordinate representation [123, 124]. The advantage is related to the localization range of the independent particle susceptibility $\chi_0(\mathbf{r},\mathbf{r}';\omega)$ and other response functions, since localized objects are easily described in real space. In practice, the response functions of nonmetallic systems decay rapidly as $|\mathbf{r}-\mathbf{r}'| \to \infty$, so that for each $\mathbf{r}$, $\chi_0(\mathbf{r},\mathbf{r}';\omega)$ needs to be calculated only for $\mathbf{r}'$ inside a region of radius R_{max} around $\mathbf{r}$. However, for metals and small gap semiconductors the decay rate may be slow and R_{max} may span many unit cells. This problem can be solved by a mixed space

representation $\chi_q(\mathbf{r}, \mathbf{r}'; \omega)$ of the response functions, where $\mathbf{r}$ and $\mathbf{r}'$ are restricted to a single cell and $\mathbf{q}$ spans the irreducible part of the Brillouin zone [124]. The method, described in references [98] and [124], has been adapted to clusters by using a supercell formalism, in which the unit cell is periodically repeated in space [125]. The unit cell volume has to be sufficiently large to avoid interaction between clusters in neighbor cells.
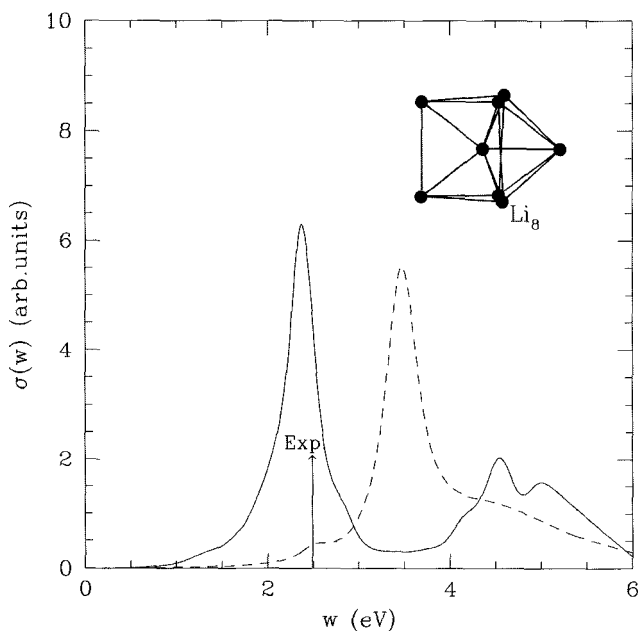

Figure 5.13. Photoabsorption cross section of Li_8. Jellium model (dashed line); full account of the geometrical structure (continuous line). The centroid of the experimental resonance is indicated by the arrow. The inset shows the cluster structure.

The calculated lowest energy structure of Li_8, given in Fig. 5.13, is a centered trigonal prism with an atom capping one of the lateral faces. The averaged value of the electric dipole polarizability $(\alpha_{xx} + \alpha_{yy} + \alpha_{zz})/3$ is 97 $\mathring{A}^3$ [125, 126], which is larger than the SJM value of 63 $\mathring{A}^3$. From classical arguments, a larger polarizability should correspond to a lower resonance frequency, so a red shift of the resonance with respect to the

jellium value of 3.5 eV should be expected (the jellium spectrum is given by the dashed curve in Fig. 5.13). Indeed, the effect of explicitly accounting for the cluster structure (the continuous curve spectrum) produces a redshift of 1 eV which leads to agreement between the calculated resonance at 2.45 eV and the experimental value of 2.5 eV [127]. The red shift can be tracked down to an increase of the electron effective mass, an effect of the Li pseudopotential. The nearly isotropic polarizability tensor explains the presence of a single resonance.

Other authors have accounted for the cluster structure in TDLDA calculations using different methods. Vasiliev *et al.* [128] have calculated the optical spectrum of Na_2, Na_4 and Na_8. The TDLDA remarkably reproduces the experimental spectral shape [129], and the peak positions agree with experiment within 0.1–0.2 eV. The calculated spectrum of Na_2 exhibits three peaks in the 2–5 eV range. Na_4 has a rhombic shape and its spectrum consists of three peaks in the 1.5–3.0 eV range, and a broader feature at higher energy. The results are almost as accurate as the spectra calculated by the Configuration Interaction method [130]. For increasing cluster size the spacing between the discrete lines decreases, evolving towards the collective plasmon. For Na_8 a single peak is already obtained. Vasiliev *et al.* have stressed the importance of electronic screening, discussed above in connection with Fig. 5.8. Pacheco and Martins [131] have calculated the photoabsorption cross section of Li_8, Li_{20}, Na_8 and Na_{20}.

Another efficient method has been developed to calculate the optical spectrum in finite systems. This is achieved by directly solving the time dependent Kohn–Sham equations of DFT after introducing a small (linear) perturbation to the ground state electronic wave functions. This method, originally used to study nuclear reactions [132] has been later applied to clusters [133–135]. The linear dipole response is obtained from the time dependent induced dipole moment of the electron cloud

$$\mathbf{D}(t) = \sum_{i=1}^{occ} \left\langle \phi_i(t) | \mathbf{r} | \phi_i(t) \right\rangle. \qquad (5.51)$$

More generally, as an output one obtains the induced density $\delta n(\mathbf{r},t)$ from which, by Fourier transformation to frequencies ω, one can infer the optical spectrum. For instance, the dynamical polarizability $\alpha(\omega)$ is, essentially, the Fourier transform of the dipole moment $\mathbf{D}(t)$. One

interesting aspect of the method is that it also allows to calculate the response of the system to a strong external field beyond the linear regime; for example, the reponse to intense ultrashort laser pulses. Marques *et al.* [134] have applied the method to Na_2 and Na_4, investigating the performance of several exchange–correlation functionals: the LDA, the generalized gradient approximation (GGA), and others. The agreement with experiment is quite good, but the calculated peaks are slightly shifted towards higher energies for all the functionals tested. This was explained by the competition between the Coulomb repulsion contribution to the response and the electron–hole attraction from the exchange–correlation part (see Eqs. (5.45) and (5.47)); that is, the electronic transition energies can be expressed [134]

$$\Delta\varepsilon = \varepsilon_c - \varepsilon_v + \left\langle \phi_v\phi_c \left| \frac{1}{|\mathbf{r} - \mathbf{r}'|} \right| \phi_v\phi_c \right\rangle + \Delta_{xc} \qquad (5.52)$$

for a given valence–conduction $(v \rightarrow c)$ transition. For the usual adiabatic approximation of Eq. (5.46), Δ_{xc} introduces only an effective static attractive electron–hole interaction. Dynamical effects may be needed in the kernel to recover this minor effect.

Quantum chemical Configuration Interaction (CI) methods have been applied by Bonacic-Koutecky and coworkers [136], with an effective core potential. CI provides an accurate account of electronic correlations. A comprehensive study of cluster cations, Na_N^+, $N = 2–9$, 11, 21, was performed, and the depletion spectrum was constructed from the oscillator strengths for the optically allowed transitions. The comparison between the experimental spectrum and those calculated for several isomers with competitive energies allowed to discriminate clearly between those competitive isomers. This capacity to determine the cluster structure of small clusters is one of the virtues of a detailed analysis of the optical spectrum.

5.7.7 Vibrational structure of the optical response

The calculated ground state structure of Li_4^+ is a rhombus [137] and the electronic wave function has $^2B_{1u}$ symmetry. The optical spectrum is given in Fig. 5.14. The spectrum calculated whithin linear response using

quantum chemical methods, shown by the vertical lines and the dotted
curve in the lower panel of the figure, is in excellent agreement with the
experimental spectrum at 105 K, given by the data points and the solid
curve in the same panel [137]. The shape of the spectrum, with three
large peaks, is remarkably similar to that of Na_4^+ [137]. The line near 2
eV is due to a transition to the first electronic excited state of ^2A_g
symmetry. This peak looks noisy. Using a laser frequency scan with
higher resolution Ellert *et al.* [137] were able to resolve the noisy peak
into two sharp peaks, with energies of 1.950 and 1.988 eV, respectively,
and two (or possibly three) broad peaks. This fine structure has been
interpreted as due to vibrational structure of the excited state. In a similar
way, the peak at 2.8 eV is resolved into two sharp peaks and a broad one.
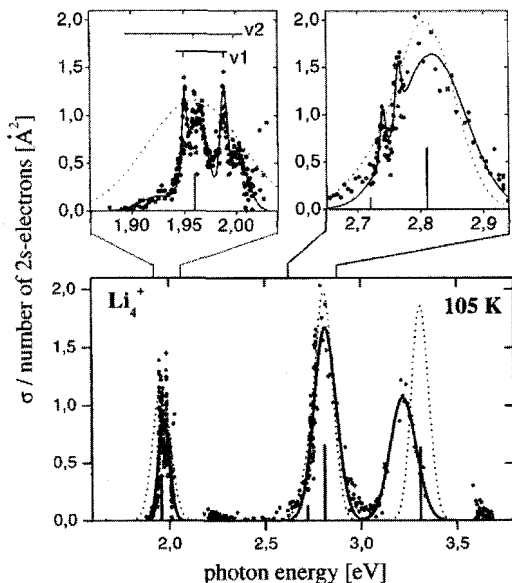
Figure 5.14. Optical spectrum of Li_4^+. The calculated absorption spectrum is
shown by vertical lines and Lorentzian broadening is indicated by dashed lines.
Data points give the measured cross section. These have been fitted to
Gaussians (solid lines). Peaks are resolved in the top panels. Two sharp peaks
are labeled v_1 and three broad peaks as v_2. Reproduced from C. Ellert *et al., J.
Chem. Phys.* **117**, 3731 (2002) with permission of the American Institute of
Physics.

The distance between the two sharp peaks in the upper left panel is 38 ± 2 meV, a value in very good agreement with the calculated vibrational spacing (39.6 meV) of the totally symmetric vibration of the excited ^2A_g electronic state. The two broad peaks on the right side of the sharp ones are at a distance of 5–20 meV from these. Since there are several excited state vibrations in that energy range, the broad structure could be due to unresolved transitions into those vibrational states.

5.7.8 Thermal line broadening

When comparing the calculated optical spectrum to experiment, the spectral lines, calculated for a static geometrical configuration of the cluster, are broadened through convolution with Gaussian or Lorentzian functions [109, 124]. A precise description of absolute magnitudes, peak positions and line broadening can be achieved by calculating the photoabsorption cross sections along finite temperature molecular dynamics simulation trajectories. Moseler *et al.* [138] have calculated the TDLDA optical spectra of Na_3^+, Na_5^+ and Na_9^+ at finite temperatures by averaging the calculated cross sections for a propagation time of 10 ps. The results are shown in Fig. 5.15. Na_3^+ has the form of an equilateral triangle, and its optical spectrum at 100 K, given in panel (a), shows two peaks. The low energy peak originates from two transitions, $\hbar\omega_1 = \hbar\omega_2 = 2.65 eV$, from the occupied *s*-like state to two empty *p*-like states with orbitals in the plane of the cluster. The three relevant orbitals are shown in the inset on the left of panel (a). The second peak, centered at an energy of 3.41 eV, is due to the excitation to the other *p*-like orbital, perpendicular to the cluster plane (see inset on the right side of the same panel). The positions of the two calculated peaks agree well with experiment, given by the continuous line [139]. The intensity and width of the low energy peak are correctly predicted, but the measured high energy peak is less intense than the calculated one. The reason is that the experimental cross section is determined by measuring the photodepletion of the Na_3^+ intensity due to dissociation. The two *p*-like states in the cluster plane are antibonding, so excitation into these states promotes dissociation, but excitation into the *p*-like state perpendicular to the cluster plane does not have a direct destabilizing effect. Thermal motion distorts the symmetry and lifts the degeneracy of the ω_1 and ω_2 transitions. The mean bond distance is anticorrelated with the average of

ω_1 and ω_2, and also with ω_3. The experimental linewidth can then be explained by the combined effect of (1) the line splitting caused by symmetry breaking (called *degeneracy lifting* by Moseler *et al.*, and (2) breathing vibrations (or *spectral sweeping* mechanism).
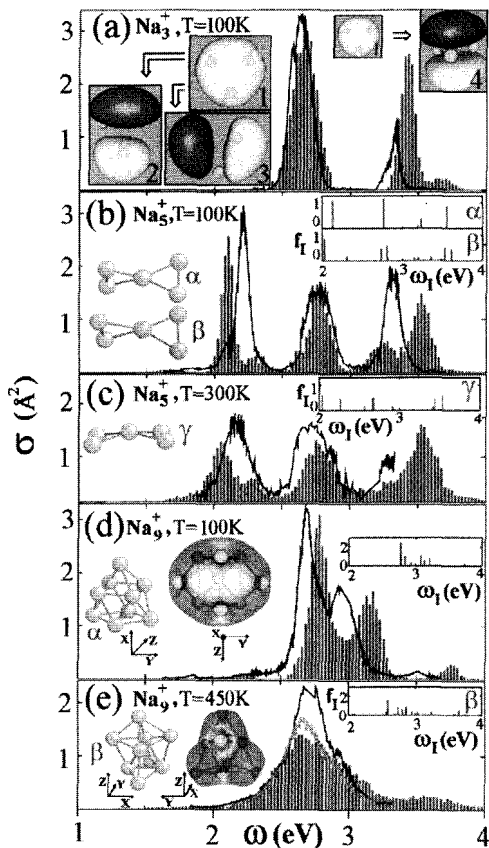

Figure 5.15. Theoretical (histograms) and experimental (solid curves) photoabsorption cross sections of Na_3^+, Na_5^+ and Na_9^+. Insets in panel (a) show density contour plots for relevant electronic orbitals. Contour plots in panels (d) and (e) correspond to the total electron density. Insets on the right sides of panels (b), (c), (d) and (e) give the oscillator strength for cluster structures shown on the left. Reproduced from M. Moseler *et al.*, *Phys. Rev. Lett.* **87**, 053401 (2001) with permission of the American Physical Society.

At a temperatute of 100 K the dynamics distorts the ground state D_{2d} symmetry of Na_5^+ (compare structures α and β in the inset in panel (b), where the left triangle of structure β is more elongated) and fragments the absorption line at $\hbar\omega = 2.8\,eV$ into two spectral lines (compare the oscillator strengths given in the upper right inset in panel (b)). Increasing T to 300 K results in bent geometries (structure γ in panel (c)). In this case the low energy line at 2 eV is fragmented. All the lines are further broadened by the effect of the breathing modes. For larger clusters, *thermal isomerization* leads to another line broadening mechanism, which adds to the other two discussed above. The ground state of Na_9^+ is oblate (the contours of constant electron density have the shape of an ideal oblate spheroid). Consequently the absorption lines at $T = 100$ K have a bimodal distribution, with further broadening arising from the line fragmentation and breathing mechanisms. By increasing the temperature to 450 K, the spectrum transforms to one with a single broad maximum. The main reason for the change in shape is the transformation between the low temperature ground state structure α (a tricapped trigonal prism) and the isomer labeled β. The static spectrum of this isomer is shifted to lower energies compared to that of the ground state, and the broad spectrum at 450 K is due to contributions from both isomers.

References

1. Göhlich, H., Lange, T., Bergmann, T., Näher, U., and Martin, T. P., *Chem. Phys. Lett.*, **187**, 67 (1991).
2. Lang, N. D., and Kohn, W., *Phys. Rev. B*, **3**, 1215 (1971).
3. Seidl, M., and Perdew, J. P., *Phys. Rev. B*, **50**, 5744 (1994).
4. Perdew, J. P., *Phys. Rev. B*, **37**, 6175 (1988).
5. Engel, E., and Perdew, J. P., *Phys. Rev. B.*, **43**, 1331 (1991).
6. Mañanes, A., Membrado, M., Pacheco, A. F., Sañudo, J., and Balbás, L. C., *Int. J. Quantum. Chem.* , **52**, 767 (1994).
7. Perdew, J. P., Tran, H. Q., and Smith, D., *Phys. Rev. B*, **42**, 11627 (1990).
8. Seidl, M., Perdew, J. P., Brajcewska, M., and Fiolhais, C., *J. Chem. Phys.*, **108**, 8182 (1998).
9. Parr, R. G., and Yang, W., *Density Functional Theory of Atoms and Molecules*, Oxford University Press, New York, (1989).
10. Rubio, A., Balbás, L. C., and Alonso, J. A., *Physica B*, **167**, 19 (1990).
11. Honea, E. C., Homer, M. L., Persson, J. L., and Whetten, R. L., *Chem. Phys. Lett.*, **171**, 147 (1990).

12. Kappes, M. M., Schar M., Rothlisberger, U., Yeretzian Ch., and Schumacher, E., *Chem.Phys. Lett.*, **143**, 251 (1988).
13. Kappes, M. M., Schar M., Radi, P., and Schumacher, E., *J. Chem. Phys.*, **84**, 1863 (1986).
14. Bréchignac, C., Cahuzac, Ph., Carlier, P., and Leygnier, J., *Phys. Rev. Lett.*, **63**, 1368 (1989).
15. Seidl, M., Meiwes-Broer K. H., and Brack, M., *J. Chem. Phys.*, **95**, 1295 (1991).
16. Müller, U., Schmidt-Ott, A., and Burstcher, H., *Z. Phys. B*, **73**, 103 (1988).
17. Jackschath, C., Rabin, I., and Schulze, W., *Z. Phys. D.*, **22**, 517 (1992).
18. Gausa, M., Ganteför, G., Lutz, H. O., and Meiwes-Broer, K. H., *Int. J. Mass Spectrom. Ion Proc.*, **102**, 227 (1990); Meiwes-Broer, K. H., *Advances in Metal and Semiconductor Clusters*, Ed. M. A. Duncan, JAI Press, London, Vol. 1, p. 37 (1993).
19. Ganteför, G., Gausa, M., Meiwes-Broer, K. H., and Lutz, H. O., *J. Chem. Soc. Faraday Trans.*, **86**, 2483 (1990).
20. Alonso, J. A., and March, N. H., *Electrons in Metals and Alloys*, Academic Press, London (1989).
21. Li, X., Wu, H., Wang, X. B., and Wang, L. S., *Phys. Rev. Lett.*, **81**, 1909 (1998).
22. Ganteför, G., and Eberhardt, W., *Chem. Phys. Lett.*, **217**, 600 (1994).
23. Cha, C. Y., Ganteför, G., and Eberhardt, W., *J. Chem. Phys.*, **100**, 995 (1994).
24. Taylor, K. J., Pettiete, C. L., Craycraft, M. J., Chesnovsky, O., and Smalley, R. E., *Chem. Phys. Lett.*, **152**, 347 (1988).
25. Balbás, L. C., Rubio, A., and Alonso, J. A., *Physica B*, **168**, 32 (1991).
26. Hoffmann, M. A., Wrigge, G., and Issendorf, B. V., *Phys. Rev. B*, **66**, 41404 (2002).
27. Saunders, W. A., Clemenger, K., de Heer, W. A., and Knight, W. D., *Phys. Rev. B*, **32**, 1366 (1985)
28. de Heer, W. A., *Rev. Mod. Phys.*, **65**, 611 (1993).
29. Ho, J., Ervin, K. M., and Lineberger, W. C., *J. Chem. Phys.*, **93**, 6987 (1990).
30. Katakuse, I., Ichihara, T., Fujita, Y., Matsuo, T., Sakurai, T., and Matsuda, H., *Int. J. Mass Spectrom. Ion Proc.*, **67**, 229 (1985).
31. Katakuse, I., Ichihara, T., Fujita, Y., Matsuo, T., Sakurai, T., and Matsuda, H., *Int. J. Mass Spectrom. Ion Proc.*, **74**, 33 (1986).
32. Bréchignac, C., Cahuzac, P., Carlier, F., de Frutos, M., and Leygnier, J., *J. Chem. Soc. Faraday Trans.*, **86**, 2525 (1990).
33. Bréchignac, C., Cahuzac, P., Carlier, F., de Frutos, M., and Leygnier, J., *J. Chem. Phys.*, **93**, 7449 (1990).
34. Krückeberg, S., Schweikhard. L., Ziegler, J., Dietrich, G., Lützenkirchen, K., and Whalther, C., *J. Chem Phys.*, **114**, 2955 (2001).
35. Martins, J. L., Buttet, J., and Car, R., *Phys. Rev. B*, **31**, 1804 (1985).

36. Lindsay, D. M., Wang, Y., and George, T. F., *J. Chem. Phys.*, **86**, 3500 (1987).
37. Penzar, Z., and Ekardt, W., *Z. Phys. D*, **17**, 69 (1990).
38. Kohl, C., Montag, B., and Reinhard, P. G., *Z. Phys. D*, **35**, 57 (1995).
39. Manninen, M., Mansikka-aho, J., Nishioka, H., and Takahasi, Y., *Z. Phys. D*, **31**, 259 (1994).
40. Von Barth, U., and Hedin, L., *J. Phys. C*, **5**, 1629 (1972).
41. Callaway, J., and March, N. H., *Solid State Phys.*, **38**, 135 (1984).
42. Yannouleas, C., and Landman, U., *Phys. Rev. Lett.*, **78**, 1424 (1997).
43. Hill, D. L., and Wheeler, J. A., *Phys. Rev.*, **89**, 1102 (1953).
44. Saunders, W. A., Ph D dissertation, University of California, Berkeley (1986).
45. Wong, K., Tikhonov, G., and Kresin, V. V., *Phys. Rev. B,* **66**, 125491 (2002).
46. Fowler, R. H., *Phys. Rev.*, **38**, 45 (1931).
47. Schmidt-Ott, A., Schurtenberger, P., and Siehmann, H. C., *Phys. Rev. Lett.*, **45**, 1284 (1980).
48. Wong. K., Kasperovich, V., Tikhonov, G., and Kresin, V. V., *Appl. Phys. B,* **73**, 407 (2001).
49. Pearson, R. G., *Hard and Soft Acids and Bases*, Dowden, Hutchinson and Ross, Stronsberg, (1973).
50. Parr, R. G., and Pearson, R. G., *J. Amer. Chem. Soc.*, **195**, 7512 (1983).
51. Parr, R. G., Donelly, R. A., Levy, M., and Palke, E. W., *J. Chem. Phys.*, **68**, 3801 (1978).
52. Alonso, J. A., and Balbás, L. C., *Structure and Bonding*, **80**, 229 (1993).
53. Almbladh, C. O., and von Barth, U., *Phys. Rev. B*, **31**, 3231 (1985).
54. Leuchner, R. E., Harms, A. C., and Castleman, A. W., *J. Chem Phys.*, **91**, 2753 (1989); *ibid* **94**, 1093 (1991).
55. Pearson, R. G., *Chemical Hardness: Applications from Molecules to Solids*, Wiley-VCH, Weinheim (1997).
56. Mineva, T., Russo, N., and Toscano, M., *Int. J. Quantum Chem.*, **80**, 105 (2000).
57. Jaque, P., and Toro-Labbé, A., *J. Chem. Phys.*, **117**, 3208 (2002).
58. Martin, T. P., Bergmann, T., Göhlich, H., and Lange, T., *Chem. Phys. Lett.*, **172**, 209 (1990).
59. Martin, T. P., *Phys. Reports,* **273**, 199 (1996).
60. Besoke, K., and Wagner, H., *Phys. Rev. B*, **8**, 4597 (1973).
61. Montejano, J. M., Iñiguez, M. P., and Alonso, J. A., *Solid State Commun.*, **71**, 591 (1995).
62. Iñiguez, M. P., López, M. J., Alonso, J. A., and Soler, J. M., *Z. Phys. D*, **11**, 163 (1989).
63. Knight, W. D., Clemenger, K., de Heer, W. A., and Saunders, W., *Phys. Rev. B*, **31**, 2539 (1985).

64. Selby, K. Vollmer, M., Masui, J., Kresin, V., de Heer, W. A., and Knight, W. D., *Phys. Rev. B*, **40**, 5417 (1989).
65. De Heer, W. A., Milani, P., and Chatelain, A., *Phys. Rev. Lett.*, **63**, 2834 (1989).
66. Schäfer, R., Schlecht, S., Woenckhaus, J., and Becker, J. A., *Phys. Rev. Lett.*, **76**, 471 (1996).
67. Mie, G., *Ann. Phys.* (Leipzig), **25**, 377 (1908).
68. Beck, D. E., *Phys. Rev. B*, **30**, 6935 (1989).
69. Kronik, L., Vasiliev, V., and Chelikowsky, J. R., *Phys. Rev. B*, **62**, 9992 (2000).
70. Stampfli, P., and Bennemann, K. H., *Phys. Rev. A*, **39**, 1007 (1989).
71. Rubio, A., Balbás, L. C., and Alonso, J. A., *Z. Phys. D*, **19**, 93 (1991).
72. Pacheco, J. M., and Ekardt, W., *Ann. Physik*, **1**, 255 (1992); *Phys. Rev. B*, **47**, 6667 (1993).
73. Alonso, J. A., and Girifalco, L. A., *Phys. Rev. B*, **17**, 3735 (1978).
74. Rubio, A., Balbás, L. C., Serra, Ll, and Barranco, M., *Phys. Rev. B*, **40**, 10950 (1990).
75. Solliard, C., and Flueli, M., *Surf. Sci.*, **156**, 487 (1985).
76. Rubio, A., Balbás, L. C., and Alonso, J. A., *Solid State Commun.*, **75**, 139 (1990).
77. Rayane, D., Allouche, A. R., Bennichou, E., Antoine, R., Aubert-Frecon, M., Dugourd, Ph., Broyer, M., Ristori, C., Chandezon. F., Huber, B. A., and Guet, C., *Eur. Phys. J. D*, **9**, 243 (1999).
78. Solovyov, I. A., Solovyov, A. V., and Greiner, W., *Phys. Rev. A*, **65**, 53203 (2002).
79. Kümmel, S., Berkus, T., Reinhard, P. G., and Brack, M., *Eur. Phys. J. D*, **11**, 239 (2000).
80. Moullet, I., Martins, J. L., Reuse, F., and Buttet, J., *Phys. Rev. B*, **42**, 11598 (1990).
81. Calaminici, P., Jug, A., and Koster, A. M., *J. Chem. Phys.*, **111**, 4613 (1999).
82. Kummel, S., Akola, J., and Manninen, *Phys. Rev. Lett.*, **84**, 3287 (2000).
83. Stott, M. J., and Zaremba, E., *Phys. Rev. A*, **21**, 12 (1980).
84. Zangwil, A., and Soven, P., *Phys. Rev. A*, **21**, 1561 (1980).
85. Gross, E. K. U., Dobson, J. F., and Petersilka, M., *Density Functional Theory II*, Ed. R. F. Nalewajski, *Topics in Current Chemistry*, **18**, 81. Springer–Verlag, Berlin (1986),
86. De Heer, W. A. , Selby, K., Kresin, V., Masui, J., Vollmer, M., Chatelain, A., and Knight, W. D., *Phys. Rev. Lett.*, **59**, 1805 (1987).
87. Bertsch, G. F., and Broglia, R. A., *Oscillations in Finite Quantum Systems*, Cambridge University Press, Cambridge (1994).
88. Goldhaber, M., and Teller, E., *Phys. Rev.*, **74**, 1046 (1948).
89. Brack., M., *Rev. Mod. Phys.*, **65**, 677 (1993).
90. Bohigas, O., Lane, A. M., and Martorell, J., *Phys. Reports*, **51**, 267 (1979).

91. Bohm, D., and Pines, D., *Phys. Rev.*, **92**, 609 (1953).
92. Thouless, D. J., *Nucl. Phys.*, **22**, 78 (1961).
93. Brack, M., *Phys. Rev. B*, **39**, 3533 (1989).
94. Parks, J. H., and McDonald, S. A., *Phys. Rev. Lett.*, **62**, 2301 (1989).
95. Serra, Ll., Garcías, F., Barranco, M., Navarro, J., Balbás, L. C., Rubio, A., and Mañanes, A., *J. Phys.: Cond. Matter*, **1**, 10391 (1989).
96. Serra, Ll., Garcías, F., Barberán, N., Barranco, M., Navarro, J., and Rubio, A., *Z. Phys. D*, **19**, 89 (1991).
97. Rubio, A., Balbás, L. C., and Alonso, J. A., *Phys. Rev. B*, **46**, 4891 (1992).
98. Rubio, A., Alonso, J. A., Blase, X., and Louie, S. G., *Int. J. Mod. Phys.*, *B*,**11**, 2727 (1997).
99. Penzar, Z., Ekardt, W., and Rubio, A., *Phys. Rev. B*, **46**, 4891 (1992).
100. Selby, K., Kresin, V., Masui, J., Vollmer, M., de Heer, W. A., Scheideman, A., and Knight, W., *Phys. Rev. B*, **43**, 4565 (1991).
101. Bonacic-Koutecky, V., Fantucci, P., Fuchs, C., Gatti, C., Pittner, J., and Polezzo, S., *Chem. Phys. Lett.*, **213**, 522 (1993).
102. Saito, S., Betsch, G. F., and Tomanek, D., *Phys. Rev. B*, **43**, 6804 (1991).
103. Pacheco, J. M., and Ekardt, W., *Ann. Physik*,**1**, 255 (1992); *Phys. Rev. B*, **47**, 6667 (1993).
104. Alonso, J. A., Rubio, A., and Balbás, L. C., *Philos. Mag. B*, **69**, 1037 (1994).
105. Reiners, T., and Haberland, H., *Phys. Rev. Lett.*, **77**, 2440 (1996).
106. Brechignac, C. Cahuzac, P., Charlier, F., de Frutos, M., and Leignier, J. *Chem. Phys. Lett.*, **189**, 28 (1992).
107. Borggreen, J., Choudhury, P., Kebaili, N., Lundsberg-Nielsen, L., Lützenkirchen, K., Nielsen, M. B., Pedersen, J., and Rasmusen, H. D., *Phys. Rev. B*, **48**, 17507 (1993).
108. Tiggesbäumker, J., Köller, L., Lutz, H. O., and Meiwes-Broer, K. H., *Chem. Phys. Lett.*, **190**, 42 (1992).
109. Ekardt, W., and Penzar, Z, *Phys. Rev. B*, **43**, 1322 (1991).
110. Lauritsch, G., Reinhard, P. G., Meyer, J., and Brack, M., *Phys. Lett. A*, **160**, 179 (1991).
111. Kasperl, S., Kohl, C., and Reinhard, P. G., *Phys. Lett. A*, **206**, 81 (1995).
112. Koskinen, M., Lipas, O. P., and Manninen, M., *Z. Phys. D*, **35**, 285 (1995).
113. Yannouleas, C., and Landman, U., *Phys. Rev. B*, **51**, 1902 (1995).
114. Bonacic-Koutecky, V., Fantucci, P., and Koutechy, J., *Chem. Rev.*, **91**, 1935 (1991).
115. Röthlisberger, U., and Andreoni, W., *J. Chem. Phys.*, **94**, 8129 (1991).
116. Kohl, C., Montag, B., and Reihnard, P. G., *Z. Phys. D*, **35**, 57 (1995).
117. Montag, B., and Reihnard, P. G., *Phys. Rev. B*, **51**, 14686 (1995).
118. Montag, B., Reihnard, P. G., and Meyer, J., *Z. Phys. D*, **32**, 125 (1994).
119. Reiners, T., Orlik, W., Ellert, Ch., Schmidt, M., and Haberland, H., *Chem. Phys. Lett.*, **215**, 357 (1993).
120. Rubio, A., Balbás, L. C., and Alonso, J. A., *Z. Phys. D*, **26**, 284 (1993).

121. Alonso, J. A., Balbás, L. C., and Rubio, A., *Int. J. Quantum Chem.*, **56**, 499 (1995).
122. Schöne, W. D., Ekardt, W., and Pacheco, J. M., *Phys. Rev. B*, **50**, 11079 (1994).
123. Rojas, H. N., Godby, R. W., and Needs, R. J., *Phys. Rev. Lett.*, **74**, 1827 (1995).
124. Blase, X., Rubio, A., Cohen, M. L., and Louie, S. G., *Phys. Rev. B*, **52**, 2225 (1995).
125. Rubio, A., Alonso, J. A., Blase, X., Balbás, L. C, and Louie, S. G., *Phys. Rev. Lett.*, **77**, 247 (1996).
126. The calculated value of the static polarizability of Li_8 given in ref. [126] is not correct. The corrected calculated value is 97 A^3. See also Benichou, E., Antoine, R., Rayane, D., Vezin, B., Dalby, F. W., Dugourd, Ph., Broyer, M., Ristori, C., Chandezon, F., Huber, B. A., Rocco, J. C., Blundell, S. A., and Guet, C., *Phys. Rev. A*, **59**, 1 (1999).
127. Blanc, J., Bonacic-Koutecky, V., Broyer, M., Chevaleyre, J., Dugourd, Ph., Koutecky, J., Scheuch, C., Wolf, J. P., and Wöste, L., *J. Chem. Phys.*, **96**, 1793 (1992).
128. Vasiliev, I. , Ogut, S., and Chelikowsky, J. R., *Phys. Rev. Lett.*, **82**, 1919 (1999).
129. Wang, C. R. C., Pollak, S., Cameron, D., and Kappes, M. M., *J. Chem. Phys.*, **93**, 3787 (1990).
130. Bonacic-Koutecky, V., Fantucci, P., and J. Koutecky, J., *J. Chem. Phys.*, **93**, 3802 (1990); *Chem. Phys. Lett.*, **166**, 32 (1990).
131. Pacheco, J., and Martins, J. L., *J. Chem. Phys.*, **106**, 6039 (1997).
132. Flocard, H., Koonin, S. E., and Weiss, M. S., *Phys. Rev. C*, **17**, 1682 (1978).
133. Yabana, K., and Bertsch, G. F., *Phys. Rev. B*, **54**, 4484 (1996).
134. Marques, M. A. L., Castro, A., and Rubio, A., *J. Chem. Phys.*, **115**, 3006 (2001).
135. Marques, M. A. L., Castro, A., Bertsch, G. F., and Rubio, A., *Computer Phys. Commun.*, **151**, 60 (2003).
136. Bonacic-Koutecky, V., Pittner, J., Fuchs C., Fantucci, P., Guest, M. F., and Koutecky, J., *J. Chem. Phys.*, **104**, 1427 (1996).
137. Ellert, C., Schmidt, M., Haberland, H., Veyret, V., and Bonacic-Koutecky, V., *J. Chem. Phys.*, **117**, 3731 (2002).
138. Moseler, M., Häkkinen, H., and Landman, U., *Phys. Rev. Lett.*, **87**, 053401 (2001).
139. Schmidt, M., Ellert, C., Kronmüller, W., and Haberland, H., *Phys. Rev. B*, **59**, 10970 (1999).

6. Melting and Fragmentation of Metal Clusters

6.1 Melting Transition

The melting transition of clusters of inert gas atoms has been discussed in Section 3.3.2. Apart from its scientific interest, the melting of small particles may have some technological implications. In sintering processes, fine powders are compressed and heated until the particles coalesce. A linear reduction of the melting temperature as a function of the inverse particle radius $1/R$ has been observed. This is mainly due to the substantial fraction of atoms on the surface [1, 2]. Consequently, lower sintering temperatures are required for particles with very small radii. In addition, given the present trend to nanoscale technologies, the extremely small size of the components will affect their electrical and mechanical stabilities at elevated temperatures. The case of metallic clusters presents specially interesting features. Since the melting temperatures are higher, compared to those of the inert gas clusters, the experimental problem of observing the melting transition is, in principle, more tractable. The vanishing of the electron diffraction pattern of the crystalline solid phase has been used to study the melting of small gold and tin particles supported on surfaces [1, 2]. On the other hand, theoretical simulations become substantially more difficult because the interatomic potentials are more complex in metals. The alkali metal clusters represent a particularly intriguing case.

6.1.1 Experiments for large alkali clusters

The observed magic numbers of alkali clusters with sizes between 1500 and 22000 atoms indicate (see Section 4.6) that these clusters grow as a

solid polyhedron with the atoms arranged in an icosahedral or a cuboctahedral (*fcc*) structure (the set of atomic shell closing numbers do not distinguish between the two structures). The experiments show that the melting point of alkali metal clusters depends strongly on the cluster size.
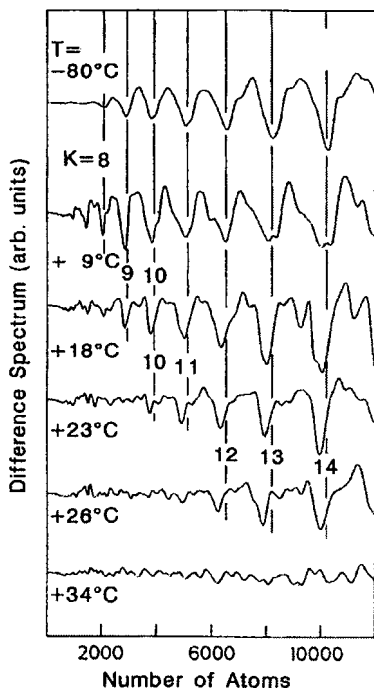

Figure 6.1. Difference mass spectra of sodium clusters using near-threshold photoionization. Abundance minima are compared with geometric shell closings (vertical lines). Reproduced from T. P. Martin *et al.*, *J. Chem. Phys.***100**, 2322 (1994) with permission of the American Institute of Physics.

A method introduced by Martin and coworkers [3] and applied to sodium clusters is based on monitoring the disappearance of the geometric shell structure in the abundance mass spectra as the clusters are progressively heated. Sodium vapor was quenched in cold (100 K)

He gas having a pressure of 1 mbar, and the clusters formed were transported by the He gas stream through a nozzle. The nozzle, made of copper metal, was heated resistively. Carefully chosen dimensions of the length and inner diameter of the nozzle ensures that the clusters come into thermal equilibrium with the nozzle walls, and in this way the temperature of the clusters can be controlled. After leaving the nozzle, the heated clusters were ionized with a 415 nm laser pulse. These photons have energy close to the ionization threshold of the clusters. A known feature, not yet fully explained (see however, the discussion in Section 5.5) is that the ionization potential is a local maximum for large clusters with full geometrical shells (sizes $N = N_K$), and that *IP* drops to a lower value for $N = N_K + 1$. From this size and up to the next shell closing *IP* grows smoothly. Consequently, for photon energies near to the ionization threshold, the ionization cross section favors open shells and the intensity in the mass spectrum shows an oscillatory structure with minima at the geometrical shell closing numbers [4, 5].

Table 6.1. Melting temperatures T_m of Na$_N$ clusters, and ratio between T_m and bulk melting temperature T_{mb}. R is the cluster radius.

Shell	N	$R(\text{Å})$	T_m	T_m/T_{mb}
6	923	16.0	288 ± 4	0.776
7	1415	18.4	288 ± 4	0.776
8	2057	20.9	288 ± 4	0.776
9	2869	23.3	294 ± 2	0.792
10	3871	25.8	298 ± 2	0.803
11	5083	28.2	298 ± 2	0.803
12	6525	30.7	303 ± 3	0.817
13	8217	33.1	303 ± 3	0.817
14	10179	35.6	303 ± 3	0.817

Some of these spectra are shown in Fig. 6.1, where a smooth average function has been subtracted from the spectra in such a way that the spectrum oscillates around zero. Each spectrum has been marked by the corresponding nozzle temperature, that is, the temperature of the clusters. The spectrum at $T = -80°$ C shows seven oscillations for sizes between

2000 and 10000 atoms, and the minima correlate with the number of atoms required to fill icosahedral or cuboctahedral shells (indicated by the vertical lines) [6]. The minima only occur for a low intensity of the ionizing radiation (< 0.05 mJ/cm^2). At $18°$ C the features for the smallest shells begin to disappear, and at the same time the minima for the larger shells shift to lower N. The first effect indicates that the smallest clusters in the spectrum have melted and this erases the peculiar size differences in the ionization efficiency noticed for the lowest temperatures. The second effect indicates that the increasing temperature also affects the structure of the larger clusters. At $23°$ C, shells corresponding to shell numbers $K = 6, 7, 8$ and 9 have disappeared. Two more shells, $K = 10$ and 11, disappear at $26°$ C. Finally, all the shells have disappeared at $34°$ C. The measured melting temperatures T_m are collected in Table 6.1, as well as the ratio between T_m and the measured bulk value $T_{mb} = 371$ K.

A thermodynamic argument [7, 8] gives the following expression for the melting temperature of spherical particles as a function of its radius R

$$\frac{T_m}{T_{mb}} = 1 + c \cdot \frac{1}{R} \ , \tag{6.1}$$

where c is a constant. If the clusters are assigned the radius of a sphere into which N sodium atoms can be packed, assuming the filling factor of an icosahedron (that radius is given also in Table 6.1), and the ratio T_m/T_{mb} is plotted versus $1/R$, then the measured ratio does not extrapolate well to the value of 1. Two main factors might account for the discrepancy. Bulk sodium has the *bcc* structure while the structure of clusters with 1500–20000 atoms is most likely icosahedral. A transition to the *bcc* structure has to occcur for still larger sizes, and this indicates that the clusters studied in Fig. 6.1 perhaps are not yet in the asymptotic region, with respect to Eq. (6.1). A second possibility is that surface melting may occur before volume melting, with the surface disordering affecting the ionization cross sections.

6.1.2 Calorimetric measurements of melting of medium size clusters

A different way of measuring the melting temperatures has been employed for smaller clusters. The method introduced by Haberland and

coworkers [9–13] determines directly the caloric curve $E = E(T)$, and melting is associated to a change in the slope of that curve. The basic process underlying this experiment is the temperature dependence of the photofragmentation pattern of a size-selected cluster

$$Na_N^+(T) + n\hbar\omega \rightarrow Na_{N-x}^+ + x\,Na. \tag{6.2}$$
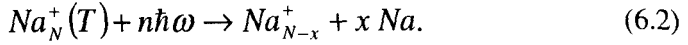
That is, the cluster sequentially absorbs n photons of energy $\hbar\omega$ and emits on the average x neutral atoms.
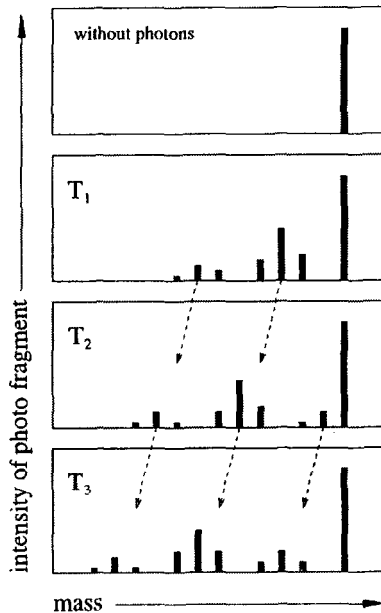

Figure 6.2. Schematic photofragmentation mass spectra as a function of the temperature of the heat bath. The uppermost panel is the spectrum of the selected cluster without excitation. Reproduced from M. Schmidt *et al.*, *Phys. Rev. Lett.* **79**, 99 (1997) with permission of the American Physical Society.

The first step in the experiment is to produce a beam of cluster ions of known temperature. This is achieved by passing the beam through a thermalization chamber containing He gas. After 10^5–10^6 collisions with

the buffer gas the clusters acquire a canonical distribution of internal energy. Next, a time-of-flight mass spectrometer is used to select a given size, for instance Na_{139}^+ in the specific experiment now described [9]. The beam of clusters of selected size and fixed temperature is irradiated with a laser of fixed photon energy $\hbar\omega$. The absorbed photons heat the clusters an these begin evaporating Na atoms, as in Eq. (6.2), when the cluster reaches its evaporation temperature. The photofragmentation spectrum is characteristic of the initial temperature of the clusters and the photon energy $\hbar\omega$. An example is shown in the second panel of Fig. 6.2. The photon energy in that experiment was chosen shuch that an average of four neutral atoms are ejected per absorbed photon. At the temperatute T_1 the first three peaks to the left of the initially selected cluster result from absorption of n photons by the cluster. Those three masses correspond to Na_{137}^+, Na_{136}^+ and Na_{135}^+, that is, to the emission of two, three and four Na atoms, respectively. The next group of three masses, Na_{133}^+, Na_{132}^+ and Na_{131}^+, result from the absorption of $n+1$ photons, *etc*. That is, different numbers of absorbed photons lead to separate groups of fragments with the distance between two groups corresponding to exactly one photon. The experiment can be repeated, but now thermalizing the initial cluster ion beam at a temperature different from T_1. The third and fourth panels of the figure show the measured photofragmentation spectra for temperatures T_2 and T_3 higher that T_1. The mass distributions shift to smaller cluster sizes. Temperature T_2 is an intermediate case; however, for T_3 the intensity maxima occur for the same masses as for T_1. In other words, the first three peaks at T_3, similar to the first three peaks at T_1, result from the absorption of n-1 photons.

Consequently, the effect of the temperature increment $\delta T = T_3 - T_1$ is the same as that of an energy increase $\delta E = \hbar\omega$ due to the absorption of an additional photon. Figure 6.3 shows the measured intensity of the particular fragment Na_{136}^+, corresponding to a loss of three atoms, as a function of the initial temperature of the parent Na_{139}^+. A maximum of intensity means that one of the maxima seen in Fig. 6.2 has reached this photofragment, while a minimum in Fig. 6.3 indicates that the chosen photofragment is in between two such distributions in Fig. 6.2. The energy difference between maximum and minimum is therefore

$\delta E = \hbar \omega / 2$, so the mean heat capacity in the temperature range between maximum and minimum is

$$C(T) \approx \frac{\delta E}{\delta T} = \frac{\hbar \omega / 2}{T_2 - T_1} \qquad (6.3)$$
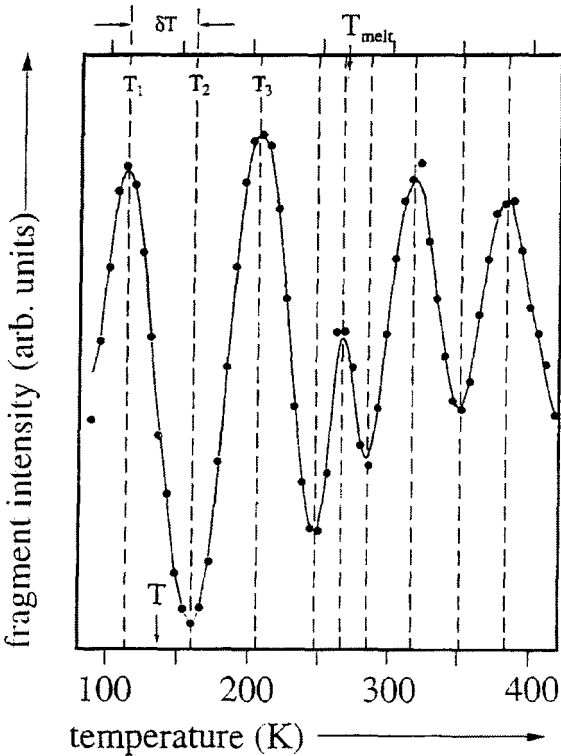
with $T = (T_1 - T_2)/2$.

Figure 6.3. Intensity of fragment Na_{136}^+ as a function of the temperature of the selected parent Na_{139}^+. Extrema are indicated by the vertical lines. Reproduced from M. Schmidt *et al.*, *Phys. Rev. Lett.* **79**, 99 (1997) with permission of the American Physical Society.

Repeating the procedure for all maxima and minima of the observed cluster fragments allows to generate the heat capacity curve $C(T)$, plotted in Fig. 6.4. A peak is observed in that curve, and fitting the data to a Gaussian function in the neighborhood of the melting point

$$C(T) = \frac{q}{\Delta\sqrt{2}} e^{-(T-T_m)^2/2\Delta^2} \qquad (6.4)$$

gives $q = 1.98$ eV, $\Delta = 12.6$ K, and $T_m = 267$ K. For comparison, $q = 3.69$ eV and $T_{ms} = 371$ K for melting of the solid metal. The reduction in both quantities for clusters is understandable since a cluster has a substantial fraction of atoms on its surface.
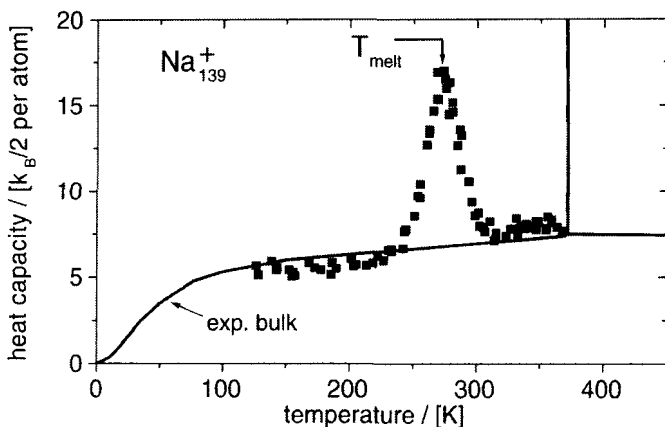
Figure 6.4. Measured heat capacity of Na_{139}^+. The continuous line corresponds to solid sodium. Reproduced from R. Kusche *et al.*, *Eur. Phys. J. D* **9**, 1 (2000) with permission of Springer–Verlag.

Returning to Fig. 6.3, one can notice that the distance δT between maximum and minimum decreases in the vicinity of the melting point. From Eq. (6.3) a smaller δT gives a larger $C(T)$. An improved method has been developed by the same authors that allows to obtain directly the caloric curve [10].

The measured melting temperatures of clusters Na_{55} to Na_{350} are given in Fig. 6.5 as a function of size [14]. T_m lies in a band between 200

and 300 K and shows substantial oscillations. Most properties of clusters show a trend of quickly converging to their bulk values as the cluster size increases. However, that trend is absent in T_m. This is not too surprising since the trend is not clear even for the very large clusters of Table 6.1. More surprising is the absence of a correlation between the maxima of T_m and the magic numbers for the filling of electronic or geometrical shells. The electronic magic numbers control the size dependence of a number of properties of sodium clusters, and for the range of sizes in Fig. 6.5, the electronic magic numbers are $N = 59$, 93, 139, 199, ... (notice that the clusters are singly ionized, so the number of valence electrons is N-1). On the other hand, the geometric magic numbers for icosahedral structures are $N = 55$, 147 and 309.
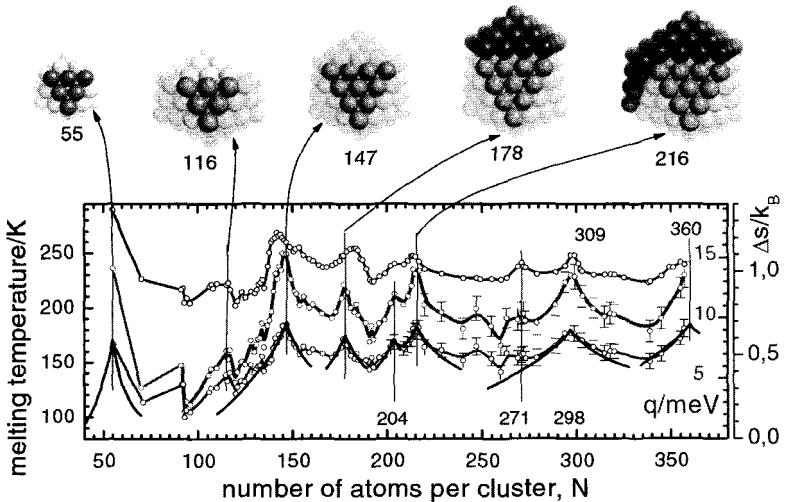
Figure 6.5. Size dependence of the melting temperature (upper curve), latent heat of fusion per atom (middle curve) and the entropy change upon melting (lower curve) of Na_N^+. Error bars are given only for N above 200. The error bars for T_{melt} have about the size of the symbol used. The solid lines overlapping partially with the entropy data result from a calculation using a hard sphere model. The upper panel indicates icosahedral growth pattern. Reproduced from H. Haberland *et al.*, *Phys. Rev. Lett.* **94**, 035701 (2005) with permission of the American Physical Society.

The explanation for the behavior of T_m has been provided by Haberland *et al.* [14]. In the heat bath used to thermalize the clusters the ensemble acquires a canonical energy distribution [15], and this ensemble undergoes melting when the free energies ($E - TS$) of the solid (*s*) and the liquid (*l*) are equal. This gives $E_s - T_m S_s = E_l - T_m S_l$, that is,

$$T_m = \frac{E_l - E_s}{S_l - S_s} = \frac{q}{\Delta S / N} .$$ (6.5)

One can notice in Fig. 6.5 that the latent heat of fusion q and the entropy of melting per atom $\Delta S/N$ have almost the same size dependence: both display oscillations with the cluster size N and their maxima are clearly correlated with the filling of geometric shells, mainly icosahedral. Filling of complete icosahedral shells shows up at $N = 55$, 147, and icosahedra with "caps" added or subtracted are recognized at $N = 116$, 178, 216. However, due to the similar size dependence of q and $\Delta S/N$, their ratio T_m becomes a smoothed function of N where the effects of shell closing are hidden.

The caloric curves of sodium clusters have some universal features independent of the cluster size: apart from the transition region, the values of the specific heat correspond well to bulk Na, as one can see in Fig. 6.4. Averaged over many cluster sizes $C = 3.3 \pm 0.05$ k_B per atom for the solid phase and $C = 4.08 \pm 0.05$ k_B for the liquid. Another interesting result is that backbending, that is, a negative heat capacity, has been discovered in the experimental caloric curve of Na_{147} [13], consistent with earlier predictions of the possibility of a negative microcanonical heat capacity for small systems (see also Section 3.3.4).

6.2 Computer Simulation of Melting

6.2.1 Computer simulations using approximate methods

The computer simulations reveal a complex picture of the melting of alkali metal clusters. An essential difference with respect to the case of inert gases studied in Chapter 3 is that the potential energy giving the interaction between alkali atoms in the cluster cannot be expressed as a

sum of two-body terms, and the computer simulations become substantially more difficult. Calvo and Spiegelman [16] performed Monte Carlo (MC) simulations for Na clusters with 8 to 147 atoms using an empirical many-atom potential of the Embedded Atom Model (EAM) family [17], with an analytical form derived in the context of the tight-binding (TB) formalism [18]. The same authors also performed simulations using a TB Hamiltonian [19]. The unification of DFT and molecular dynamics (MD) formulated by Car and Parrinello [20] allows for an explicit treatment of the electronic degrees of freedom, and Rytkönen *et al.* [21] have presented results for the melting of Na_{40}. However, the relatively large number of atoms required a fast heating rate in the simulations. The reason can be appreciated by writing the equations of motion for the ions

$$M_i \frac{d^2 \mathbf{R}_i}{dt^2} = \mathbf{F}_i = -\frac{\partial E[n;\{\mathbf{R}_j\}]}{\partial \mathbf{R}_i}, \qquad (6.6)$$

where $\mathbf{R}_i$ indicates the ionic positions and $\mathbf{F}_i$ the forces on the ions. The electron density $n(\mathbf{r})$ and the energy $E[n;\{\mathbf{R}_j\}]$ of the cluster have to be calculated at each step, that is, for each geometrical configuration of the atoms in a MD trajectory, and this becomes tedious when those quantities are obtained by solving the Kohn–Sham equations of the DFT [22], that is Eqs. (4.7). Large computational savings can be obtained by using an *orbital free* (OF) energy functional in the Car–Parrinello MD simulations, that is, an energy functional in which the kinetic energy of the electrons is formulated as a functional of the valence electron cloud $n(\mathbf{r})$. The expression

$$T[n] = \frac{3}{10}\left(3\pi^2\right)^{2/3} \int n(\mathbf{r})^{5/3} d^3r + \lambda \frac{1}{72} \int \frac{|\nabla n(\mathbf{r})|^2}{n(\mathbf{r})} d^3r \qquad (6.7)$$

is characteristic of such a family of energy functionals. The first term on the r.h.s. is the kinetic energy in the Thomas–Fermi model, obtained by using locally the expresion for a free electron gas [22], and the second

one is a correction accounting for the inhomogeneities of the electron density. The value of the constant λ depends on the type of density variations in the system (notice that the orbital free functionals have been briefly introduced in Section 5.1). In this case the electron density $n(\mathbf{r})$ corresponding to a given configuration of the atoms is obtained directly by integrating the Euler equation

$$\frac{\delta E[n]}{\delta n(\mathbf{r})} = \mu \ , \tag{6.8}$$

where μ is the chemical potential, and the expression on the left hand side of this equation is the functional derivative of the total energy functional. $E[n]$ is the sum of several terms. One of these is the electronic kinetic energy of Eq. (6.7) and the remaining terms are well known (see Chapter 4): electron–ion interaction, classical electron–electron interaction and electronic exchange and correlation.

Using this functional for the kinetic energy of the valence electrons, with $\lambda = 1$, which is adequate for a slowly varying density [22, 23], and replacing the ion cores by local pseudopotentials, the melting of Na clusters has been studied [24, 25] by constant energy MD simulations. The melting transition was identified in the simulations by an analysis of the usual indexes, namely the specific heat (Eq. (3.8)) and the bond length fluctuations δ (Eq. (3.11)). For small clusters a melting transition in stages is predicted [24]. For Na_8 and Na_{20} the melting transition is spread over a broad temperature interval of ≈ 100 K. The heat capacity of Na_8 presents a sharp peak at $T = 110$ K, coincident with an stepwise increase of δ. This is followed by a steady increase of $\delta(T)$, until a leveling off occurs at $T \approx 220$ K. The temperature $T = 110$ K marks the onset of isomerization transitions among the permutational isomers of the low temperature structure (a dodecahedron). With increasing temperature, those isomerizations become more frequent and carry progressively stronger distortions of the structure, until at $T = 220$ K all the atoms diffuse across the cluster volume and its shape changes continuously, indicating that the liquid phase is fully established. Since this effect is progressive, it does not result in a peak in the specific heat. The specific heat of Na_{20} presents two peaks at 110 and 170 K, correlating with abrupt increases of δ at 110 and 160 K respectively.

Then δ levels off at $\approx$ 220 K. The peak at $T \approx$ 110 K marks the onset of isomerization transitions between permutational isomers almost preserving the low temperature structure (a capped double icosahedron). The peak at $T \approx$ 160 K arises from the transformation of the double icosahedron to a new structure with a single central atom. The exchanges of this atom with one of the 19 surface atoms occur at a slower rate than the interchanges between surface atoms. The 19 surface atoms are very mobile and the cluster shape fluctuates a great deal. Finally, at $T \approx$ 220 K the structure has become very fluid.

Constant temperature MD simulations by Bulgac [26, 27] using a phenomenological interatomic potential found for Na_8 a transition at $T \approx$ 100 K, from the solid-like phase to a phase characterized by occasional atom interchanges while the atoms stay for relatively long periods close to their equilibrium positions. Monte Carlo (MC) simulations by Calvo and Spiegelmann [16] using an empirical potential predicted melting at $T \approx$ 80–100 K, while tight-binding MC simulations [28] predict $T_m \approx$ 200 K. In view of the complex behavior revealed by the orbital free simulations those early results are not surprising. For Na_{20} the tight-binding [28] and empirical potential simulations [16, 26, 27] predict melting in two steps, the first one involving the surface atoms only. The occurrence of melting in steps has been associated to a soft repulsive short-range (core–core) interatomic interaction [29]. This is, indeed, the case for sodium [24].

Direct calorimetric measurements of the melting temperature of such small clusters have not been performed , but the temperature dependence of the photoabsorption cross section has been reported [30, 31] for Na_N^+, $N = 4$–16. Although the spectra do not show evidence for a sharp melting transition, encouraging comparison between theory and experiment can be established. The spectrum of Na_8 does not change appreciably until $T = 105$ K, where it begins to evolve in a continuous way. One can notice that this temperature is close to the temperature ($T = 110$ K) predicted by the OF simulations for the beginning of a broad melting transition.

The complex behavior of small Na clusters could be expected, because in those clusters most of the atoms lie on the surface. Only for larger clusters inner atoms begin to experience a bulk-like environment. The melting of Na_{55}, Na_{92} and Na_{142} has been studied by MD simulations using the OF energy functional [25]. The precise low temperature structure of those clusters is not known. DFT calculations within the

CAPS model (see Section 4.7.2) for Na_{55} predict a structure close to icosahedral [32]. Calvo and Spiegelmann [16] also predicted icosahedral structures for Na_{55}, Na_{93}, Na_{139} and Na_{147}. Consequently, icosahedral structures (complete or incomplete) were taken as plausible candidates to start the OF simulations of the heating process for Na_{55}, Na_{92} and Na_{142} [25]. The specific heat of Na_{142} displays a main peak at $T \approx 270$ K and a smaller one at $T \approx 240$ K. Those two peaks are so close that only one slope change is distinguished in the caloric curve. After an analysis of the atomic motions the peak at $T \approx 240$K can be associated with surface melting. The diffusion coefficient

$$D(T) = \frac{1}{6}\frac{d}{dt}\left\langle r^2(t)\right\rangle_T \qquad (6.9)$$

which is obtained from the long time behavior of the mean square atomic displacement

$$\left\langle r^2(t)\right\rangle = \frac{1}{Nn_t}\sum_{j=1}^{n_t}\sum_{i=1}^{N}\left[\mathbf{r}_i\left(t_{0j}+t\right)-\mathbf{r}_i\left(t_{0j}\right)\right]^2 , \qquad (6.10)$$

shows a sharp increase of slope at this temperature. In the last equation n_t is the number of time origins t_{0j} considered along a trajectory, and the average is taken over the whole trajectory. The peak at $T \approx 270$ K represents complete melting. At low temperatures the radial atomic density distribution (with respect to the cluster centre) displays the atomic shells characteristic of the icosahedron. Those shells broaden as T increases. Above the surface melting temperature, the shells disappear gradually, and further changes in the slope of $D(T)$ are not detected. At $T \approx 270$ K the atomic density distribution is nearly uniform across the cluster. The experimental melting temperature of Na_{142} is near 270 K (see Fig. 6.5)), in excellent agreement with the theoretical prediction. Also the latent heats of fusion, q_m(experimental) = 14 meV/atom, and q_m(theoretical) = 15 meV/atom, are in good agreement.

Two-step melting is also predicted for Na_{92}, with a small peak in the specific heat at $T \approx 130$ K, and a large peak corresponding to homogeneous melting at $T \approx 240$ K. In this case the two features are well separated. The position of the high peak and the latent heat, $q_m = 8$

meV/atom, are in excellent agreement with experiment, $T \approx 220$ K and $q_m = 6$ meV/atom. $D(T)$ is again very sensitive to surface melting, when appreciable diffusive motion begins. The results of the MC simulations [16] for clusters with sizes in the range on 100 atoms are consistent with the OF simulations: two-step melting is predicted for Na_{139} and Na_{93}, the two features being close in Na_{139} and well separated in Na_{93}.
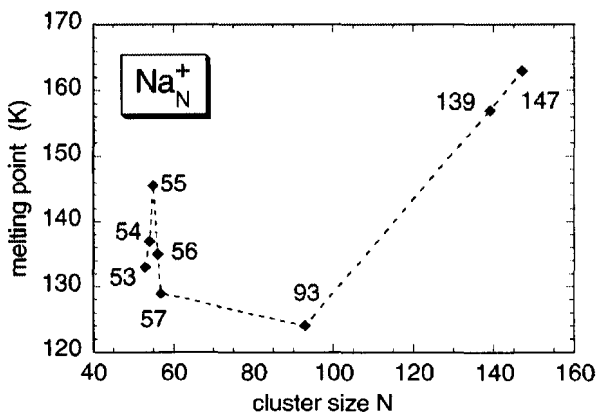

Figure 6.6. Melting points found in the Orbital Free method for singly charged clusters. Reproduced from P. Blaise and S. A. Blundell, *Phys. Rev. B* **63**, 235409 (2001) with permission of the American Physical Society.

The orbital free simulations predict that Na_{55} melts in a single step at $T \approx 190$ K. The single step melting is also predicted by the MC simulations [16]. The experiments indicate a substantial enhancement of the size dependent melting temperature at $N = 55$ (see Fig. 6.5). The melting temperature of this cluster is even higher than that of Na_{142}^+, which is a local maximum. Neither the OF simulations discussed above or the MC simulations reproduce this feature. Blaise and Blundell [33] performed OF calculations for a value $\lambda = 1.44$ in the functional of Eq. (6.7). The calculated melting points, shown in Fig. 6.6, show that T_m of Na_{55}^+ is a local maximum compared to clusters with similar sizes, but again this melting temperature is clearly smaller than those of clusters in the size range of about 140 atoms. Another observation from Fig. 6.6 is that the calculated melting temperatures are substantially smaller than the experimental ones. They are also smaller than the melting

temperatures obtained by Aguado *et al.* [24, 25], and the main reasons may be the different pseudopotential used and the different value of λ in the kinetic energy functional; differences in the statistical mechanics technique used to obtain T_m may also contribute.

Improved results have been recently obtained [34] with a kinetic energy functional $T[n] = T_W + T_\beta$, where T_W is the second term in the r.h.s. of Eq. (6.7), with $\lambda = 9$, and

$$T_\beta = \frac{3}{10} \int n(\mathbf{r})^{\frac{5}{3}-2\beta} \tilde{k}(\mathbf{r})^2 d^3r \,, \tag{6.11}$$

$$\tilde{k}(\mathbf{r}) = (2k_F^0)^3 \int k(\mathbf{s})w_\beta(2k_F^0|\mathbf{r}-\mathbf{s}|)d^3s \tag{6.12}$$

where $k(\mathbf{r}) = (3\pi)^{1/3} n(\mathbf{r})^\beta$, k_F^0 is the Fermi wave vector corresponding to the mean electron density n_0 in the cluster and $w_\beta(x)$ is a weight function. With this new functional, and $\beta = 0.51$, the predicted melting temperatures of Na_N clusters with $N = 55, 92, 147, 181, 249, 271, 281,$ and 299 differ from the experimental values by about 10 K only. Although very small clusters have not been studied, this OF functional leads to more compact heat capacity curves with a single maximum, in better agreement with experiment. A shoulder replaces the pre-peak obtained using the functional of Eq. (6.7) and this shoulder reflects the fact that melting begins at the surface

6.2.2 Ab initio simulations

The Kohn–Sham formulation of DFT has been combined with the MD methodology by Car and Parrinello [20], providing a powerful formalism to perform first principles dynamical simulations. The melting of small clusters of simple metals has been studied using this formalism. Blundell and coworkers [35] studied Na_8 and Na_{20} with the double objective of testing ionic pseudopotentials and of comparing the results with those of the OF simulations. The results of all models are qualitatively similar, but the precise positions of the peaks in the specific heat are sensitive to the pseudopotential. Na_8, Na_{10}, Na_{14}, Na_{20}, Na_{40} and Na_{55}^+ were studied by Rytkönen *et al.* [21]. The simulations for each cluster started from a

low temperature structure known from other works, or expected. In the case of Na_{40} a rather spherical structure, cut from the icosahedron, was assumed. At about 175 K this cluster transforms to an energetically more favorable structure characterized by an octupole deformation. This structure, evidently more stable than the starting one at low *T*, preserves the main features of the electronic structure, that is, the electronic shells well known from the jellium model, and has a wider HOMO–LUMO gap. The melting transition was explored with two traditional indicators, the caloric curve and the diffusion coefficient. Na_{20} was observed to melt in the region 235–275 K. Na_{40} melts around 300–350 K. Melting broadens the density of electronic states of this cluster, but the HOMO–LUMO gap remains open, approximalety 0.4 eV wide. The gap only closes at higher temperatures. Na_{55}^+ melts around 310–360K. For clusters smaller than Na_{20} the melting region could not be identified. Liquid Na_{40} also exhibits enhanced octupole deformation, and liquid Na_{20} and Na_{55}^+ are prolate. The predicted melting temperatures appear too large compared to the experimental ones of Fig. 6.5, and this may be due to the fast heating rate in the simulations, which prevents achieving true thermal equilibrium at a given temperature.

The thermal behavior of Al_{13}^- and Al_{14} shows some differences [36]. A distinct transition does not show up in the heating simulations, and isomerizations between the starting icosahedral structures and other structures, mainly decahedral, are seen frequently. Those isomerizations, which are reflected as peaks in the potential energy as a function of temperature, occur by a mechanism where the atoms collectively twist between the different isomers and no diffusion is involved. For instance, in the case of Al_{14} the outermost atom does not float around. Instead, this atom often inserts itself into the cluster, causing a "new" outer atom to pop out on the opposite side. Some of the isomerizations in Al_{13}^- involve more drastic structural changes, causing the cluster to depart from its low temperature quasi-spherical shape, and, in fact, the behavior at the highest temperatures studied ($\approx$ 1500 K) is consistent with a molten phase. The vibrational density of states of Al_{13}^-, obtained as the Fourier Transform (power spectrum) from the velocity–velocity autocorrelation function, shows a shift towards lower frequencies as *T* increases, and a gradual smearing out, supporting the interpretation of gradual melting above 1000 K. The melting of bulk aluminum metal

occurs at 933 K, and it is likely that the difficulties for performing long simulations may account for the overestimation.

6.3 Clusters with Abnormally High Melting Temperature

The fact that the melting point of finite particles is lower than the melting point of the bulk material is well established, but the evolution of T_m with the cluster size can be very intricate, as for the sodium clusters considered in Section 6.1.2. Small Sn clusters present even more surprising features, since melting temperatures higher than the bulk value have been reported [37]. Ion mobility experiments were performed to search for the melting transition. In an ion mobility experiment [38] mass selected cluster ions are pulled through a buffer gas by a weak electric field and the average collision cross section of the ion with the gas atoms is measured. The cross sections depend very sensitively of the cluster shape; that is, compact spherical clusters have lower collision cross sections than prolate or oblate clusters, so the mobility measurements in conjunction with theoretical simulations are able to provide information on cluster shapes. This approach has been used [39] to examine the room temperature structures of Sn_N^+ clusters with N up to 68. Clusters with N between 25 and 35 adopt prolate geometries, and DFT calculations show that the structural growth pattern has similarities with the structures found for Si and Ge clusters [37, 39]. A change to a roughly spherical shape is expected on melting, so this transition should be easily detected by the mobility experiments.

Measurements were performed, using He as the buffer gas, for several temperatures up to 555 K, which is 50 K above the melting temperature of bulk Sn (505 K). Figure 6.7 shows the measured mobilities at 300, 378 and 555 K. The plot gives relative mobilities, obtained by dividing the measured mobility by the mobility calculated for a sphere of volume NV_a , where V_a is the volume per atom in the bulk solid. Values significantly less than 1.0 indicate that the geometries deviate substantially from sphericity The results for the three temperatures are nearly identical, indicating that the Sn clusters retain their prolate shapes up to at least $T = 555$ K, so the conclusion is that the clusters remain solid. It is intriguing if Si and Ge, belonging to the same column of the Periodic Table, would present similar features. However

the much higher melting temperatures of those two elements in the bulk, 1687 K and 1201 K, respectively, makes experiments difficult. The high melting points of some clusters may have technological implications. Nanodevices built from those materials may retain their structural integrity and functionality at much higher temperatures than anticipated, and this may result particularly interesting in the case of Si and Ge.
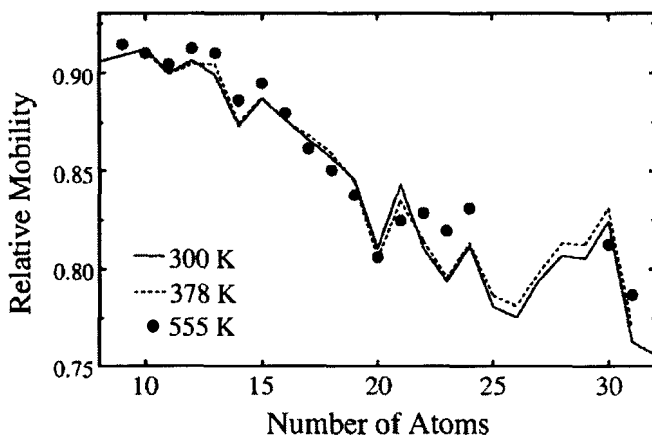

Figure 6.7. Mobilities of tin cluster cations at several temperatures. Values significantly less than 1.0 indicate geometries substantially deviating from spherical. Reproduced from A. A. Shvartsburg and M. F. Jarrold, *Phys. Rev. Lett.* **85**, 2530 (2000) with permission of the American Physical Society.

Theoretical calculations have attempted to explain the peculiar behavior of the Sn clusters. DFT calculations for $N < 20$ have confirmed the prolate structures [40]. The calculated binding energies are exceptionally large. For instance, the binding energy of Sn_{10} (2.77 eV/atom) is only 11% lower than the calculated cohesive energy of bulk Sn (3.08 eV/atom). Taking into account that in small clusters most atoms are on the surface, the implication of the large binding energies is that the bonds between the Sn atoms in the clusters are stronger than in the bulk, and this was proposed as the main reason for the high melting points. It is useful to notice that the theoretical prediction for the bulk cohesive energy is rather good; the experimental value is 3.14 eV/atom.

However, the measured binding energies [41] of Sn_N with $N < 8$ are about 15–20% lower than the calculated values (these grow from 1.208 eV/atom for Sn_2 to 2.628 eV/atom for Sn_8). So, if one assumes similar errors for clusters in the size range 9–20 atoms, the true binding energies may not be so high.

Joshi *et al.* [42] have performed *ab initio* MD simulations of the heating of Sn_{10}. The ground state structure at low temperature is a tetra-capped trigonal prism. This structure can be seen as the tricapped trigonal prism (TTP), that is a trigonal prism with atoms capping the three lateral faces, plus one additional atom capping one of the basal faces of the prism. The TTP unit is often found in the Sn clusters [40]. A first isomer of Sn_{10} lies 0.06 eV above the ground state and retains the TTP unit. Other isomers lie about 1 eV or more above the ground state, and in those the TTP unit is absent or highly distorted. The localization of the electron density in the ground state indicates that the bonding is significantly covalent. It may be useful to notice that the most common solid allotropic form of Sn below 286 K (α-Sn) is a semiconductor with covalent bonding, while the stable form above that temperature, β-Sn, is metallic. The DFT simulations of the heating produce an specific heat curve with a shoulder around 500 K and a main broad peak at a much higher temperature (2300 K). The position of the shoulder correlates with the temperature at which the root mean square bond length fluctuations significantly increase. Inspection of the atomic motions reveals that the shoulder is due to structural isomerizations between the ground state and the first isomer. Those isomerizations preserve the TTP, and the only effect is that the atom capping the triangular face moves towards one side of the triangle. The system can subsequently return to the lowest energy structure by a different route involving some interchange of atoms. Only at much higher temperature are other isomers visited.

The same authors studied Sn_{20} [43]. Its ground state structure is prolate, formed by two TTP units stacked end to end. Several low lying isomers were found, corresponding to different relative orientations of the two TTP units. Those isomers have excitation energies of order 0.01 eV per atom. Other higher lying isomers are nonprolate, and have energies ≈ 0.1 eV per atom above the ground state. The DFT molecular dynamics simulations of the heating of Sn_{20} predict a specific heat curve characterized by a small peak around 500 K and a broad main peak

centered at $\approx$ 1200 K with a shoulder on its left side, at $\approx$ 800 K. The small peak at 500 K is due to internal rearrangements within each TTP unit which do not distort their shape. The distortion of at least one TTP unit begins around 800 K, together with the interchange of atoms between the two units. Finally, the collapse of the prolate structure towards a more compact one occurs at $\approx$ 1200 K. This collapse will cause a change in cluster mobility in the experiments. The analysis of the rms bond length fluctuations δ (Eq. (3.11)) shows that the value $\delta = 0.1$, that according to the Lindemann rule indicates melting in the bulk, is reached quite early, around 650 K. This arises from the atomic interchanges within the individual TTP units, but a full diffusive behavior of the atoms over the whole cluster only occurs at $\approx$ 1200 K and above, so the main transition at this temperature was identified as the melting of Sn_{20}. A drastic reduction of the HOMO–LUMO gap also occurs at $T \approx$ 1200 K. This is due to the disordering introduced in the system and not to a change in the nature of the bonding from covalent to metallic. In fact, the average number of nearest neighbors does not change after the collapse of the prolate structure. In conclusion, the fact that practically all the atoms in small Sn clusters are surface atoms, so that the atomic coordination remains necessarily low, helps to preserve the covalent bonding, and the persistence of the covalent bonding seems to be the reason for the high melting temperatures.

Tin and lead nanocrystals offer similar surprises. Onion-like graphitic carbon cages containing Sn and Pb nanocrystals inside have been produced by Banhart and coworkers [44]. Figure 6.8 shows an electron microscopy image of a Sn nanocrystal with a diameter of 14 nm, with a spherical graphitic particle formed by several carbon shells firmly wrapped around the nanocrystal. Irradiation under the electron beam is required to produce a perfect encapsulation. The lattice fringes of the core of the particle show the presence of Sn in the solid crystalline phase. The spacing of the fringes is 0.29 nm, corresponding to the (200) lattice planes of β-Sn. The specimen temperatures were varied between room temperature and 1100 K, and, in fact, the image of the figure was taken at 770 K.

A striking observation is that the nanocrystal is solid at a temperature well above the usual melting temperature of solid β-Sn (T_m = 505 K). Further observations at higher temperatures of 920 and 1020 K indicated that the encapsulated nanocrystals are molten at those temperatures. As

for Sn, superheating has also been observed for Pb nanocrystals [44]. Although the melting temperature of Pb is 600 K, encapsulated Pb nanocrystals were observed to be solid at 740 K. On the other hand, the encapsulated Pb nanoparticles are molten at 870 K, indicating that the melting occurred between those two temperatures.
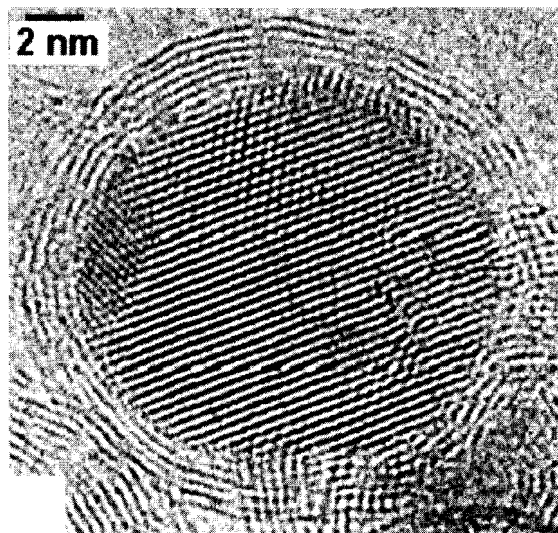
Figure 6.8. Sn nanocrystal with a diameter of 24 nm encapsulated by a graphitic particle with onion-like structure. The nanocrystal shows the lattice fringes of the crystalline structure of solid β-Sn, although the specimen is superheated to 770 K. Reproduced from. F. Banhart, E. Hernández and M. Terrones, *Phys. Rev. Lett.* **90**, 185502 (2003) with permission of the American Physical Society.

The mechanism proposed by Banhart *et al.* for the observed superheating is an increase of pressure inside the carbon onions. The observed self-compression of carbon onions and the nucleation of diamond crystals in their nucleus under irradiation [45] indicate that irradiation leads to a buildup of high pressure at the cluster core. This occurs because the electron irradiation causes the sputtering of carbon atoms from the outer graphitic shells. In parallel with this case, the superheating of the encapsulated nanocrystals could be due to the high pressures exerted by the graphitic shells. This proposal is supported by

the results of molecular dynamics simulations of the heating of Pb crystals under pressure [45]. No explicit encapsulating cage was modeled in those simulations, but the use of a large cell, with 256 atoms, and periodic boundary conditions, emulates the effect of encapsulation. The application of a small pressure (0.5 GPa) only raises the melting temperature by some 20 K. But at 2.5 GPa the crystal does not melt up to 860 K. This is close to the temperature at which all the encapsulated Pb nanocrystals were observed to be liquid. Then, a pressure of 2–3 GPa was estimated for the effect of the graphitic onions of the nanoclusters. Evidently, this mechanism for raising the melting temperature is different from that operating in the small free Sn clusters, but it is intriguing that those effects have only been detected for Sn (and Pb).

6.4 Optical Properties and Melting

A comprehensive study of the temperature dependence of the optical spectrum of Na_N^+ clusters with $N \leq 16$ has been published by Haberland [30, 31]. The optical spectra of all these clusters shows sharp features at low temperatures, and those features broaden as the temperature is increased, although the broadening is not accompanied by an overall shift. Between 35 and 105 K the number of peaks in each spectrum remains constant. At low temperatures the clusters have a definite geometrical structure and the atoms just oscillate around the equilibrium positions. The measured spectra agree well with those calculated by theoretical methods taking into account the structure of the clusters [46], although some small details are still not reproduced. For temperatures higher than 105 K the changes in the optical spectrum are significant. The peaks broaden, although for some clusters the number of peaks does not change. This is the case, for instance, for Na_4^+ and Na_5^+. The line width for these two clusters increases linearly with $T^{1/2}$. For other clusters, some peaks merge into a broader one. For instance, the low temperature double peak of Na_9^+ becomes one broad peak at higher temperature; for Na_{11}^+, six well resolved lines transform into two broad peaks. All those changes occur gradually as the temperature is increased and no special feature can be detected indicating melting. This is not surprising, since the melting transition in small Na clusters occurs over an extended temperature region, as discussed in Section 6.1.3. The

optical spectra measured at high temperatures, when the clusters are certainly molten, are consistent with the predictions of the jellium model.

6.5 Fragmentation of Multiply Charged Clusters

6.5.1 Surface and Coulomb forces

Multiply charged clusters X_N^{q+} have been observed only above a critical size N_c known as the effective appearance size [47], which depends on the metal X and on the charge state $q+$. In the case of alkali metals, the effective appearance sizes for the observation of doubly charged clusters are around 24 for $Li_N{}^{2+}$ and $Na_N{}^{2+}$ [48–51], 19 for $K_N{}^{2+}$ [48, 51] and 19 for $Cs_N{}^{2+}$ [52]. Critical sizes of clusters as highly ionized as $Na_N{}^{7+}$ and $Cs_N{}^{7+}$ have also been determined [53, 54]. Those critical sizes are found by studying charged clusters produced by multi-step ionization of hot larger clusters that lose a sizable part of their excitation energy by evaporating neutral atoms. This causes the ionized clusters X_N^{q+} to shrink up to sizes $N \approx N_c$. For sizes around N_c atom evaporation competes with another dissociation channel that we can call fission, in which two charged fragments, usually of different size, are emitted. However, multiply charged clusters have also been detected below N_c. This occurs when those species are created in a multi-step ionization process starting from cold neutral clusters [49, 50], and indicates the existence of a stabilizing fission barrier. These experimental facts show that cluster fission is a barrier-controlled process.

The process of cluster fission has close analogies to the fission of nuclei [47]. In both cases a charged droplet becomes unstable towards the division into two or more fagments. In simple terms, the multiply charged cluster can be viewed as a droplet, which due to the unbalanced excess positive charge tends to deform through elongated shapes keeping the total volume constant. But the shape deformation increases the surface and then the surface energy of the cluster. This decreases the cohesion and builds an energy barrier that prevents the spontaneous fission of the cluster for large cluster sizes, even when the sum of the energies of the fission products is lower than the energy of the multiply charged parent. For small clusters, on the other hand, the Coulomb

repulsion may be so strong that there is no barrier and fission becomes spontaneous. From the classic work of Rayleigh [55] for a charge droplet, it is known that the relative weight between the repulsive and cohesive forces can be expressed by the fissibility parameter

$$x = \frac{E_{coulomb}^{sphere}}{2E_{surface}^{sphere}} , \qquad (6.13)$$

and the physical picture is shown in Fig. 6.9. When the repulsive Coulomb energy equals twice the surface energy of the droplet, that is, when $x = 1$, the barrier is zero. So, for $x \geq 1$ the cluster is intrinsically unstable. For x smaller than 1 there is a barrier, and fission from internally excited clusters can be observed as long as the barrier remains smaller or comparable to the activation energy of other decay modes, such as the evaporation of neutral atoms.
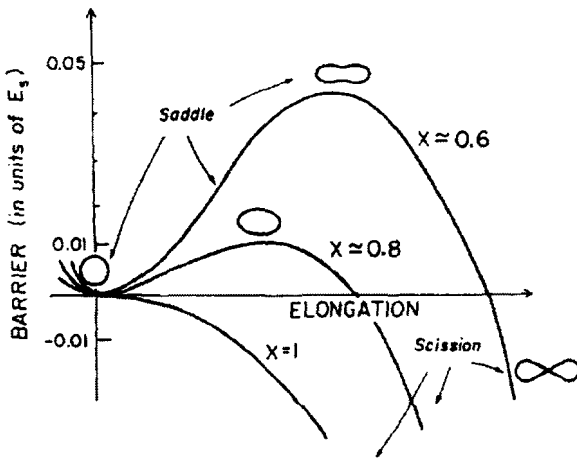
Figure 6.9. Fission of multiply charged clusters. The energy is given in units of the surface energy. The equilibrium shape is at a local energy minimum, but the interplay between the short-range cohesive forces and Coulomb repulsion allows the system to separate after passing a deformation barrier. Fission occurs spontaneously for a fissibility parameter higher than or equal to 1.

Most experiments performed for metal clusters correspond to sizes close to N_c. Electronic shell effects are manifested in the fission experiments. An early experiment of silver clusters produced by sputtering [56] analyzed the fission from parents containing 12 to 22 atoms, finding evidence for a preference of products with an even number of electrons, and between these, those corresponding to electron numbers 2 or 8 were prominent. More recent investigations [57] performed with an ion trap indicate a strong preference for the emission of the charged trimer Ag_3^{2+}. In a study of doubly charged gold clusters produced by a liquid metal ion source [58, 59] the tendency of even-electron clusters to fission rather than to evaporate neutral atoms becomes clear, while the opposite occurs for odd-electron clusters. Superimposed to this odd–even alternation is a sizable increase of the fission to evaporation rate as the size decreases from Au_{18}^{2+} to Au_{12}^{2+}. Also, Au_3^+ was observed to be the dominant fission channel, although not the only one. Preferential emission of singly charged fragments with 2 and 8 electrons has also been observed for Li, Na and K [48, 60, 61].

Early theoretical studies of the fragmentation of doubly charged Sodium and Magnesium clusters [62] through the process

$$X_N^{2+} \rightarrow X_{N-p}^+ + X_p^+ \qquad (6.14)$$

based on a comparison of the energies of the parent (initial state) and the products (final state), calculated within the Spherical Jellium Model, correctly indicated that emission of closed shell fragments is likely to occur. However, consideration of the fission barrier is necessary in order to understand the nature of N_c and to calculate its value.

The preferred decay channel of hot large clusters is the evaporation of neutral atoms

$$X_N^{2+} \rightarrow X_{N-1}^{2+} + X \qquad (6.15)$$

because the heat of evaporation ΔH_e is lower than the barrier against fission. On the other hand, small hot clusters undergo fission, as in (6.14), because the fission barrier is, in that case, smaller than ΔH_e. A schematic view of the two cases appears in Fig. 6.10. ΔH_e is given by the energy difference

$$\Delta H_e = E\left(X_{N-1}^{2+}\right) + E(X) - E\left(X_N^{2+}\right) \qquad (6.16)$$

and the fission barrier height F_m is the difference between the energies of the fissioning cluster at the saddle point and the parent cluster

$$F_m = E(saddle) - E\left(X_N^{2+}\right). \qquad (6.17)$$
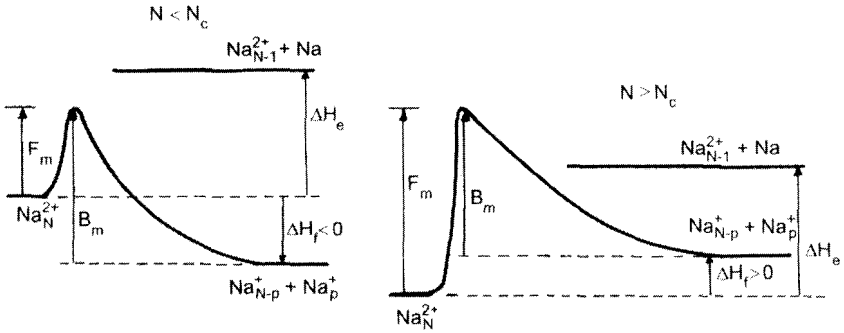
Figure 6.10. Competition between fission and evaporation from doubly charged clusters. ΔH_e and ΔH_f are the heats of evaporation and fission, respectively. F_m and B_m are the fission and fusion barriers. The left and right panels correspond to situations below and above the effective appearance size N_c.

Methods for determining the fission barrier have been proposed [48], employing the branching ratio for fission to evaporation corresponding to the same doubly charged cluster, and the dissociation energy of that cluster singly ionized. Other attempts rely on theoretical calculations.

6.5.2 Models and calculations of cluster fission

Several theoretical approaches have been developed to understand the facts observed in the cluster fission experiments. One of the simplest methods to calculate the barrier heights is provided by the Liquid Drop Model (LDM), in which the metallic character of the fissioning system is taken into account by explicitly concentrating the charge on the surface [59, 63]. The model has been applied to interpret the experimental results for the observation of multiply charged Na clusters Na_N^{q+} ($q \leq 10$) produced in collisions between neutral clusters and multiply charged

inert gas ions [64]. Those experiments observed the spontaneous barrierless fission predicted for $x \geq 1$, that for doubly charged alkali clusters corresponds to sizes smaller than $N \approx 10$. Electronic shell effects have been included in this model by applying Strutinsky's shell correction method [65] to study the symmetric [66] and asymmetric [67] fission of doubly charged silver clusters and highly charged alkali metal clusters [54, 68]. The basic expression for the total energy of a cluster in this model is given by

$$E(N, q, shape) = E_{LD}(N, q, shape) + E_{shell}(N, q, shape) \quad (6.18)$$

which has to be compared to Eq. (4.20). The fact that the cluster has a positive charge q is explicitly indicated in Eq. (6.18), so a new term depending on the net charge (see Section 5.1) has to be added to the usual bulk and surface terms of Eq. (4.21). The variation of the shape of the cluster along the fragmentation path (see Fig. 6.9) is needed to calculate the fission barrier. Since the LDM does not consider the spillout of the electronic density at the cluster surface, Yannouleas and Landman have corrected the LDM to include spillout effects [69].

An accurate study of fission, employing molecular dynamics and the DFT formalism, has been performed for small doubly charged sodium and potassium clusters [70–72]. These calculations, which use the Local Spin Density Approximation for exchange and correlation, confirm the influence of electronic shell effects on the fission energetics and barrier heights, and also indicate the predominance of an asymmetric fission channel and the appearance of double hump fission barrier shapes. Such microscopic calculations become difficult for large clusters, and the fission of large alkali metal clusters has been studied by the simpler Jellium Models.

Jellium calculations based on an Extended Thomas–Fermi (ETF) functional (see Eq. (6.7)) have been performed for the symmetric and asymmetric fission of doubly charged sodium clusters [73, 74]. Although the semiclassical ETF model does not account for electronic shell effects, it has the merit of incorporating the electronic spillout in a selfconsistent way. Fission barriers were first obtained using a Two-Jellium-Spheres Model (TJSM) [73, 75]. This model is based on the reasonable assumption that, since the Coulomb force is long ranged, in many cases of interest the fissioning fragments are already preformed in

the cluster before overcoming the fission barrier. This situation is different from the nuclear physics case, where the short-range nuclear forces lead to compact fissioning configurations, and the fission products are rarely preformed even at the saddle point [76]. The cluster fragmentation path is then obtained by increasing the distance between the two jellium spheres. The simplifying approximations of the TJSM also allowed to calculate fission barriers using the Kohn–Sham formalism of DFT [75].

To go one step beyond the TJSM, an axially symmetric Deformed Jellium Model (DJM) has been used [74, 77]. In that case, the path is described by a series of deformed jellium shapes connecting a spherical configuration associated to the parent cluster with the final configuration corresponding to the two separated fragments. More precisely, the positive background was modeled by axially symmetric shapes [78, 79] corresponding to two spheres smoothly joined by a portion of a third quadratic surface of revolution. This family of shapes is characterized by the values of three parameters: the asymmetry Δ, the distance s between the centers of the emerging fragments, and a parameter λ which takes into account the neck deformation. Evidently, asymmetric shapes are necessary to describe asymmetric fission.

For a configuration characterized by a set of values of the parameters Δ, s and λ, the electron density is calculated within the chosen scheme (Kohn–Sham or Orbital-Free). The density of the jellium background is constant, so its total volume is conserved during the scission process. Other parameterizations of the background have also been employed [80, 81]. To calculate the barrier for a selected fission channel within the DJM, for instance the emission of a singly-charged trimer, the results obtained following different fragmentation pathways, defined by relations between the parameters λ and s (the asymmetry Δ is fixed by the size of the final fragments) have to be compared. A simple choice is a parameterization based on two jellium spheres, firts intersecting, next touching and finally separated [82, 83], as in the example at the bottom in Fig. 6.11. This is just the TJSM. Other possibility is to start with a jellium sphere and then follow the path corresponding to a cone capped with spheres up to an arbitrary value of s where a concave neck starts to form; after that point one assumes the fastest variation of the neck and continues with two separated jellium spheres.
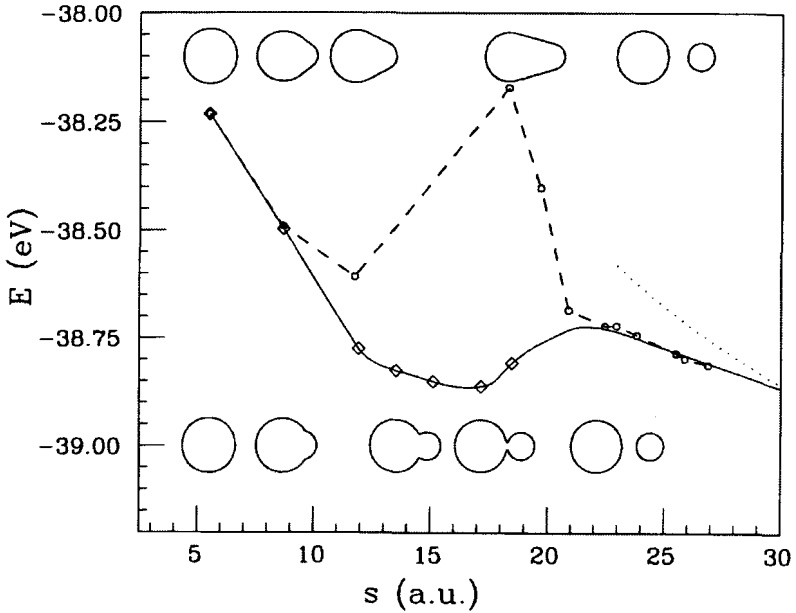
Figure 6.11. Total energy of Na_{24}^{2+} in the emission of Na_3^+ for two different parameterizations of the background: the dashed line corresponds to the jellium shapes shown at the top and the solid line to those at the bottom. The dotted line is the classical Coulomb barrier. Reproduced from J. A. Alonso *et al.*, *Fission Dynamics of Atomic Clusters and Nuclei*, Eds. J. da Providencia *et al.*, World Scientific, Singapore (2001), p. 163, with permission of World Scientific.

As a first example of the calculation of the fission barrier in the DJM [77, 84], Fig. 6.11 shows the emission of Na_3^+ from Na_{24}^{2+}

$$Na_{24}^{2+} \rightarrow Na_{21}^{+} + Na_3^{+}, \qquad (6.19)$$

using the Kohn–Sham formalism. The emission of the charged trimer is the most common fission channel observed for alkali metal clusters, and one could draw a loose parallel with the emission of an alpha particle in nuclear physics. In this particular example the other fragment, Na_{21}^{+}, is also a closed shell cluster, which favors even more this fission channel

[50]. Two different parameterizations of the background are compared. The jellium shapes corresponding to the first one appear on the upper part of the figure. In this path the parent cluster is forced to elongate up to $s = 18.3$ a.u. and scission, that is, the formation of two disconnected jellium pieces, occurs at $s = 23.0$ a.u. After scission, the energy (dashed line) tends slowly towards the classical Coulomb barrier (the dotted curve). This parameterization leads to a barrier height of 0.44 eV, which originates from the deformation energy needed to elongate the parent cluster. This value is obtained as the difference between the energy at the maximum of the barrier, which occurs at $s = 18.3$ a.u., and the energy of the local minimum at $s = 11.8$ a.u. This minimum is, in fact, the ground state of the parent cluster for this particular jellium parameterization. That is, the ground state of Na_{24}^{2+} is nonspherical because this cluster has the outermost electronic shell only partially filled.

In a second parameterization of the background, with shapes given as interpenetrating spheres on the lower part of the figure, the neck starts forming at $s = 6.1$ a.u. Again the ground state of the parent cluster is deformed and occurs for $s \approx 17$ a.u. The configuration of two touching jellium spheres ($s = 16.8$ a.u.) is very close to the jellium scission point ($s = 17.2$ a.u.). The fissioning tendency of Na_{24}^{2+} is apparent, since the Na_{21}^+ and Na_3^+ fragments are preformed in the parent ground state. It was noticed in Section 4.4 that some neutral clusters can be viewed as supermolecules formed by smaller, particularly stable clusters. This is again the case for Na_{24}^{2+}. In fact, since this cluster is doubly charged, the electrostatic repulsion between the two components enhances this effect.

The evolution of the electronic single-particle energies along the fission path of interpenetrating spheres is given in Fig. 6.12. Starting with a fictitious spherical parent Na_{24}^{2+}, the deformation first splits the highly degenerate levels and lowers the total energy. For the configuration corresponding to the ground state, $s \approx 17$ a.u., the electronic levels have reassembled in a configuration consistent with the interpretation of the cluster as a supermolecule $Na_{21}^+-Na_3^+$. A similar fragment preformation is found, for instance, for Na_{12}^{2+} in the Cylindrically Averaged Pseudopotential Scheme (CAPS) [85], and for K_{12}^{2+} in DFT molecular dynamics calculations [70].
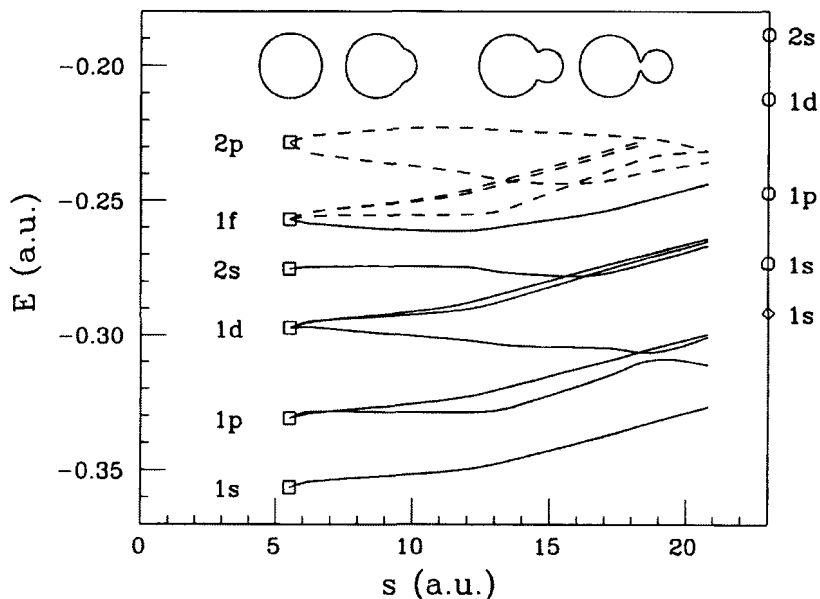
Figure 6.12. Evolution of the electron energies with fragment separation for the fission of Na_{24}^{2+}. Jellium background shapes are given at the top. Solid and dashed curves correspond to filled and empty levels, respectively. The squares on the left give the energy levels of the spherical parent, and the symbols on the right give those of the separate fragments Na_{21}^{+} and Na_3^{+}. Reproduced from A. Rigo, *et al.*, *Surf. Rev. Lett.* **3**, 617 (1996) with permission of World Scientific.

Other background parametrizations have been studied for the reaction (6.19) and it has been found that the path described in terms of jellium spheres leads to the minimum energy barrier. This is because the two fragments are magic. The energy difference between the maximum of the barrier at $s \approx 22$ a.u. and the ground state at $s \approx 17$ a.u. gives a fission barrier height $F_m = 0.14$ eV. This value can also be obtained from the relation

$$F_m = B_m + \Delta H_f \qquad (6.20)$$

where B_m is the fusion barrier height, that is, the barrier seen by approaching the fragments from large separation, and the heat of fission

ΔH_f is the difference between the energy of the fragments at infinite separation and the energy of the parent cluster in its ground state configuration (see Fig. 6.10). In this case (it is convenient to stress that the fragments are spherical but the parent is deformed), $\Delta H_f = -0.90$ eV. The fusion barrier height B_m has nearly the same value in the Orbital Free and Kohn–Sham approaches. From Eq. (6.20), this means that the influence of shell structure on the fission barrier height is essentially due to its effect on the heat of fission.

At very large separations, the interaction between the fragments is just the pure Coulomb repulsion between point charges. The deviation from the simple Coulomb repulsion for small separations can be considered as a chemical effect of the electronic charge gluing the fragments [86]: the interacting clusters mutually polarize their electronic clouds, giving rise to a bonding contribution which is effective even if the two positive jellium pieces do not overlap. The fusion barrier can then be written [87]

$$B(s) = \frac{(q-1)e^2}{s} + V(s) \qquad (6.21)$$

for the general case of a parent with charge $+q$ and fragments with charges $+(q\text{-}1)$ and $+1$. For the emission of a singly charged trimer, good agreement with the calculated fusion barriers of alkali metal clusters has been obtained with the form

$$V(s) = -V_0 R_0 e^{-\alpha(s-R_0)} \qquad (6.22)$$

of the bonding potential $V(s)$, where $V_0 = 0.008/r_s$ and $R_0 = R_1 + R_2$ is the sum of the radii of the two fragments. A qualitative justification of the form of $V(s)$ has been given by Garcias *et al.* [87]. Crucial for that justification is the exponential decay of the electron densities of the separated fragments. A single value $\alpha = 0.2$ describes the entire alkali group. Garcias *et al.* [87] combined the fusion barriers calculated in this way (assuming singly charged trimer emission) with the heats of fission calculated by a classical liquid drop model, to obtain fission barrier heights of alkali clusters with charges $+q = 1\text{-}7$. Evaluating the heat of evaporation of neutral monomers also using the liquid drop model, a

comparison of ΔH_e and F_m leads to the effective appearance sizes given in Table 6.2. The predictions are in good agreement with the experimental appearance sizes, except for Na clusters with very high charge ($+q = 6$ or 7).

Table 6.2. Calculated [87] and experimental (in parentheses) [53, 54] effective appearance sizes for the observation of multiply charged alkali metal clusters as a function of the charge $+q$.

$+q$	Li	Na	K	Rb	Cs
+2	24	26	24	24	23
	(25 ± 1)	(27 ± 1)	(20 ± 1)	(19 ± 1)	(19 ± 1)
+3	56	63	59	59	57
		(63 ± 1)	(55 ± 1)	(54 ± 1)	(49 ± 1)
+4	103	117	110	109	105
		(123 ± 2)	(110 ± 5)	(108 ± 1)	(94 ± 1)
+5	164	185	173	172	165
		(206 ± 4)			(155 ± 2)
+6	240	268	249	247	236
		(310 ± 10)			(230 ± 5)
+7	330	366	337	335	319
		(445 ± 10)			(325 ± 10)

As a second example of the application of the Deformed Jellium Model, let us consider the symmetric fission reaction

$$Na_{42}^{2+} \rightarrow Na_{21}^{+} + Na_{21}^{+}. \tag{6.23}$$

The parent and the fragments are closed shell clusters, with 40 and 20 valence electrons respectively, and consequently these adopt spherical configurations in the jellium model. In a Kohn–Sham calculation [75], the fission path was described by configurations corresponding to two

interpenetrating spheres up to the scission point and to two separated spheres afterwards. The resulting fission barrier height was $F_m = 0.37$ eV and the heat of fission is $\Delta H_f = -0.58$ eV, that is, the reaction is exothermic.

The electron density corresponding to the saddle configuration is given in Fig. 6.13 and shows the fragments almost separated. The dramatic influence of shell effects is appreciated when the barriers obtained by KS and ETF methods are compared using the same jellium parameterization (spheres). The fusion barriers are similar, $B_m(\text{KS}) = 0.95$ eV and $B_m(\text{ETF}) = 0.84$ eV, but the heats of fission are very different, ΔH_f (KS) $= -0.58$ eV and ΔH_f (ETF) $= 2.33$ eV. In other words, the reaction is exothermic in the KS case and endothermic in the semiclassical case. The large value of ΔH_f (ETF) is essentially a surface effect. Breaking the spherical parent into two fragments of equal size leads to a substantial increase in the surface area. This increases so much the energy that symmetric fission is very unfavorable. On the other hand, in the KS case the high stability provided by the closed shell configuration of the fragments is enough to compensate for the increase in the surface area. Adding B_m and ΔH_f leads to very different values for the fission barrier: F_m (KS) $= 0.37$ eV and F_m (ETF) $= 3.17$ eV. Taking into account that the energy necessary to evaporate a neutral Na atom from clusters or from the metal is approximately 1 eV, the KS calculation predicts the symmetric fission of a hot Na_{42}^{2+} cluster as more favorable than the evaporation of a neutral atom. The difference between the KS and ETF fission barriers compared here is so large because the shell effects are strong, since both fragments have closed shell electronic configurations. In other cases, smaller differences between KS and ETF results are expected.

In a parametrization of the DJM developed by Lyalin and coworkers [88, 89], the parent, with the form of an ellipsoid of revolution, splits into two independently deformed spheroids of smaller sizes. Before scission, the two small spheroids intersect each other as in the overlapping spheres model shown at the bottom part of Fig. 6.11. The parametrization by spheroids gives improved results when one of the fragments has an open shell configuration, for example in the reaction $Na_{10}^{2+} \rightarrow Na_7^+ + Na_3^+$. In this case Na_7^+ is oblate. The calculated fission barrier is 0.16 eV for the ellipsoidal parametrization, and much higher for a parametrization with intersecting spheres. The study of the

dissociation of Na_{18}^{2+} allows to compare the symmetric and asymmetric channels, $Na_{18}^{2+} \rightarrow Na_{15}^{+} + Na_{3}^{+}$ and $Na_{18}^{2+} \rightarrow Na_{9}^{+} + Na_{9}^{+}$, in a case when they are expected to be competitive because both involve magic fragments, Na_{3}^{+} and Na_{9}^{+} respectively. Unsurprisingly, the fission barriers are nearly identical, $F_m = 0.50$ eV for the asymmetric channel and $F_m = 0.48$ eV for the symmetric one; the difference is not significant considering the accuracy of the model.
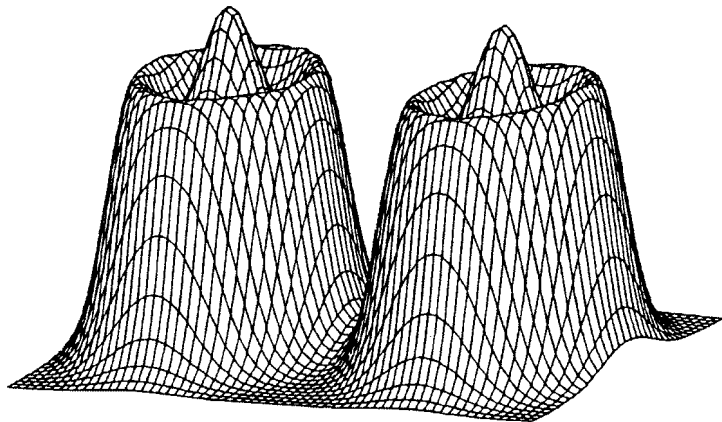
Figure 6.13. Valence electron density at the saddle point (maximum of the fission barrier) for the symmetric fission of Na_{42}^{2+}.

Table 6.3 presents the fission barriers obtained for the asymmetric fission of Na_{10}^{2+} and for the symmetric and symmetric fission of Na_{18}^{2+}, compared to the results of molecular dynamics (MD) simulations also based on the DFT formalism. In addition, results of the two-center ellipsoidal parametrization of the DJM using the Hartree–Fock (HF) method are included. The MD calculation of Montag and Reinhard [90] employed the same exchange–correlation functional as in the DJM [89], so the difference of 0.51 eV between the respective barriers for Na_{10}^{2+} can be attributed to the effects of the ionic structure; the ionic structure in the MD calculation of Montag and Reinhard was described by the CAPS model (see Section 4.7.2). The influence of the ionic effects is expected to decrease for larger clusters, and already for Na_{18}^{2+} the two descriptions of the ionic background, DJM and CAPS, produce barriers

in close agreement. One should also notice that different schemes in the MD simulations lead to some differences in the barriers. The HF method treats electronic exchange, that is the Fermi correlations arising from the antisymmetry of the total wave function, exactly, but neglects Coulombic correlations. This leads to discrepancies in the barriers. In particular Na_{10}^{2+} is unstable in HF.

Table 6.3. Comparison of calculated fission barriers heights (in eV).

Parent (Channel)	HF[89]	LDA[89]	MD [90]	MD [72]	MD [70]
Na_{10}^{2+} (asym.)	0	0.16	0.67	0.50	0.71
Na_{18}^{2+} (asym.)	0.36	0.50	0.50		
Na_{18}^{2+} (sym.)	0.63	0.48	0.52		

The early prediction that fission paths involving closed shell fragments are preferred was based on a comparison of the total energies of initial and final products [62]. Its success can be understood from the form of Eq. (6.20). For a given size N of the parent, the value of the fusion barrier B_m varies smoothly with the sizes $(p, N-p)$ of the singly charged fragments. In contrast ΔH_f is very sensitive to p, having the smallest values for those fission channels involving one or two magic fragments. Consequently, fission channels leading to magic fragments actually have lower fission barriers compared to other channels.

Experiments pertaining to the low fissibility regime $x << 1$ have addressed the competition between the fission channel corresponding to the magic product X_3^+ and more symmetric channels involving the higher magic clusters X_9^+ and X_{21}^+. The results for the fission channels of doubly charged Li, Na and K clusters with sizes $N = 24-27$ are shown in Fig. 6.14 [61]. The clusters were ionized and warmed by a Nd-YAG laser, and after rapid sequential evaporation the doubly charged clusters reached evaporative ensemble (*EE*) temperatures [91] of 700 ± 100 K,

400 ± 100 K and 300 ± 100 K for the Li, Na and K clusters, respectively. Only one fission channel is present for the smallest parent, $N = 24$. This is the double magic channel $Na_3^+ + Na_{21}^+$ (notice that only the large fragments are shown in the figure, due to details of the experimental setup). An increase in the parent size opens new channels and leads to differences between the three elements. The charged trimer is still the dominant fission product for Li, while Na_{21}^+ is the dominant one for K, and Na shows an intermediate behavior. That is, the asymmetry of the fission process is reduced for K, as compared to Li and Na.
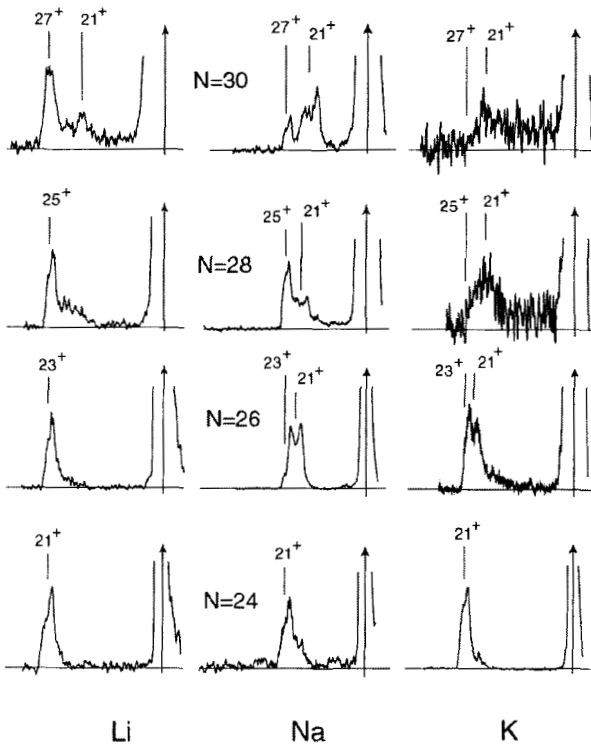
Figure 6.14. Fission channels in time-of-flight experiments for Li_N^{2+}, Na_N^{2+} and K_N^{2+} with $N = 24, 26, 28, 30$. The peak marked by an arrow corresponds to the parent and those on the left to the larger fragments. Reproduced from C. Yannouleas *et al.*, *Phys. Rev. Lett.* **17**, 173403 (2002) with permission of the American Physical Society.

A trend is observed in this figure towards opening the channels involving heavier magic fragments ($p = 9$ and $p = 21$) both when going up vertically by increasing the size of the parent and going horizontally from left to right. These tendencies are explained by calculating the free energy differences

$$Q_p^T = F_p^+ + F_{N-p}^+ - F_N^{2+} \tag{6.24}$$

at the *EE* temperatures for all the possible (p, N-p) fission channels, using the Liquid Drop Model with shell corrections [91]. The argument for using this equation is that for each species the Coulomb repulsion at the top of the barrier, measured by the kinetic energy release, is approximately constant for all the fission channels in the size range considered in these experiments. Consequently one can see from Eq. (6.21) that the preferred fission channels are controlled by Q_p^T. In fact, the effect of the finite temperature is very important. If ΔH_f is used instead of the finite-temperature Q_p^T, then the trends observed at the *EE* temperature are not explained well, since a tendency for high magic fragments, $p = 9$ or $p = 21$, is obtained in many cases. By increasing the temperature the electronic entropy has the effect of quenching the shell effects and this affects the higher shells more, so the channels involving heavy magic fragments become disfavored with respect to the trimer. This is the reason why heavy magic fragments are observed in the case of K, which has a low *EE* temperature, while X_3^+ is mainly seen for Li, with a higher *EE* temperature.

6.6 Optical Response Along the Fission Path

We consider the symmetric fission of Na_{18}^{2+}, that is,

$$Na_{18}^{2+} \rightarrow Na_9^+ + Na_9^+ . \tag{6.25}$$

TDLDA calculations of the optical spectrum were performed [84] by employing the Cylindrically Averaged Pseudopotential model (see Section 4.7.2), and the results are given in Fig. 6.15.
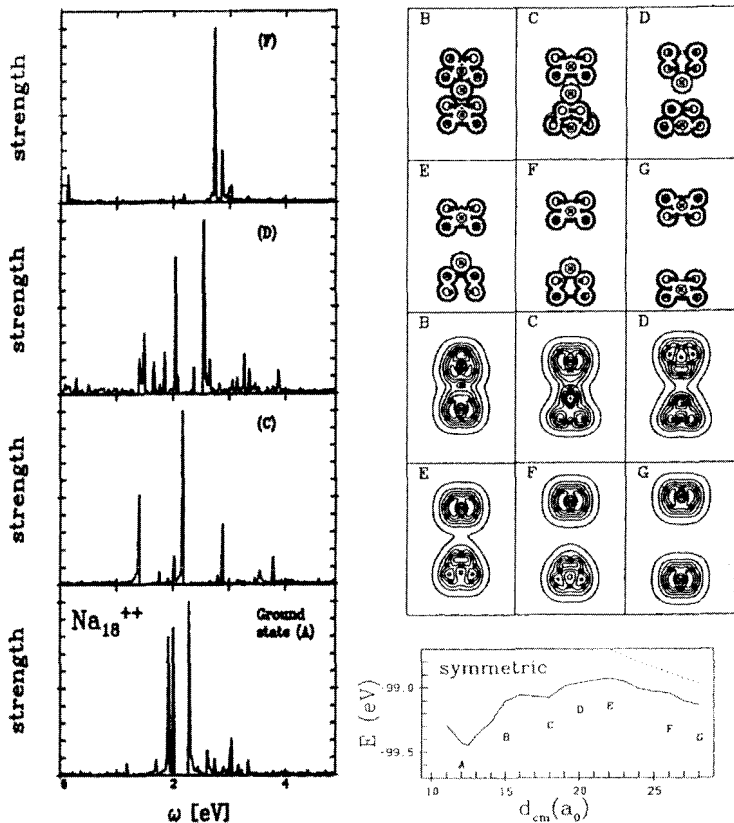
Figure 6.15. Symmetric fission of Na_{18}^{+2}. Ionic and electronic distributions at various stages (B, C, D, E, F, G) of the fission process are shown in the right panels and the optical response is given in the left panel. The fission barrier is shown on the lower right panel. Reproduced from J. A. Alonso *et al.*, *Fission Dynamics of Atomic Clusters and Nuclei*, Eds. J. da Providencia *et al.*, World Scientific, Singapore (2001), p. 163, with permission of World Scientific.

The ground state configuration [89] hints at preformed subunits Na_{15}^{+} and Na_3^{+}. Its energy corresponds to the point in the energy curve labeled A. Nevertheless, the barriers for the asymmetric and symmetric fission channels are practically equal (see Table 6.3). Other configurations of the cluster along the symmetric fission channel are shown in the figure, together with the corresponding electronic

distributions. The structure changes between configurations A and B, where symmetry is established. This rearrangement corresponds to a large difference in energy between the two configurations. Ionic scission takes place at stage D only shortly before reaching the saddle point E, while the electron cloud breaks up rather late after the saddle point, around configuration F.

The linear optical response, shown on the left of Fig. 6.15, gives an enlightening picture of the various stages along the fission path. The ground state configuration (A) exhibits a pronounced resonance between 2 and 2.2 eV. With increasing deformation along the fission path we first observe, basically up to stage D, a gradual increase in the fragmentation of the spectrum, but still centered around 2 eV. The connectivity of the electron cloud still existing in stages C and D suffices to center the dipole spectrum around 2 eV, while the ions are already fully separated at stage D. A marked change occurs when the electron densities separate at stage F and beyond. The fragmentation disappears and is replaced by the clean plasmon resonance of free Na_9^+ around 2.7–2.8 eV.

The optical response thus provides an enlightening tool of analysis of the various configurations along the fission path. It might be experimentally feasible to follow such a fission path by time-resolved recording of the electronic response following short laser pulses. One might even hope to have access to fission time scales and thus be able to estimate viscosity effects, in a way somewhat similar to the nuclear case.

6.7 From Fission to Fragmentation to Coulomb Explosion

In Sections 6.5 and 6.6 the fission process has been described adiabatically. This provides information on structural and dynamical properties of metal clusters. It can even address the competition between fission and evaporation, as discussed by Fröbrich [92] to explain the observed effective appearance sizes, calculating the time scale of cluster decay by an evaporation theory similar to that used to describe the statistical deexcitation of compound nuclei [93]. However the dynamical situations accessible to metal clusters are not exhausted.

Recent progress in laser technology has opened new avenues of research in the domain of nonlinear cluster dynamics. Lasers actually offer an ideal tool for spanning various dynamical regimes, ranging from

the linear regime with plasmon-dominated dynamics (Section 6.5), to the semi linear regime of multi photon processes [94, 95] and the strongly nonlinear regime of Coulomb explosion [96, 97]. From the theoretical side, only effective mean field theories based on DFT have up to now been able to deal with such different situations and dynamical regimes for clusters. These calculations [98] have exploited the experience acquired in Nuclear Physics.

Let us first sketch the various steps in the response of highly excited metal clusters. Experimentally, one can consider two classes of rapid, intense, excitations: collisions with energetic highly charged ions [99] and irradiation by intense femtosecond laser pulses [95, 100]. In both cases the excitation takes place between tens of fs down to below 1 fs. This time is directly comparable to characteristic time scales of the valence electron cloud. And not surprisingly, the cluster response is primarily of electronic nature. The first stage of the reaction is thus a direct emission of electrons and a collective oscillation of the Mie plasmon. This stage is characterized by time scales of the order 1–10 fs. In a second stage, still of purely electronic nature, damping of the collective electronic motion takes place, both by means of Landau-like damping (excitation of resonances in the continuum) and by electron–electron collisions. The time scales associated to these effects are variable depending on the cluster size (Landau-like damping) and the deposited excitation energy (electron–electron collisions). Landau-like damping takes 10–20 fs and collisional effects around 10–100 fs. After that, the electronic degrees of freedom slowly couple to the ionic motion, and may lead to the explosion of the charged cluster on long times (several hundreds of fs). Two mechanisms are at work here: i) the net charge of the cluster following ionization; ii) energy exchanges between the hot electron cloud and the still cold ions. The two effects interfere constructively to activate ionic motion and lead to evaporation, fission or fragmentation. Thermal evaporation of electrons proceeds on a very long time scale, usually slower than ionic processes (monomer evaporation, fragmentation). It can become competitive in the 100 fs range only for very hot clusters.

In order to illustrate the various stages of the excitation and response of metal clusters in the nonlinear regime, two examples are considered, focusing first on the electronic response. Figure 6.16 represents the first stage (*i.e.*, electronic) in the response of Na_{93}^+ irradiated by an intense

laser pulse [84]. The cluster is treated in the jellium approximation and the laser pulse is modeled by a ramp pulse (trapezium form) with a total duration 100 fs. The intensity is $I = 10^{10}$ W/cm^2, and the photon frequency, $\hbar\omega \approx 3.1$ eV, is slightly above the Mie resonance for this cluster.
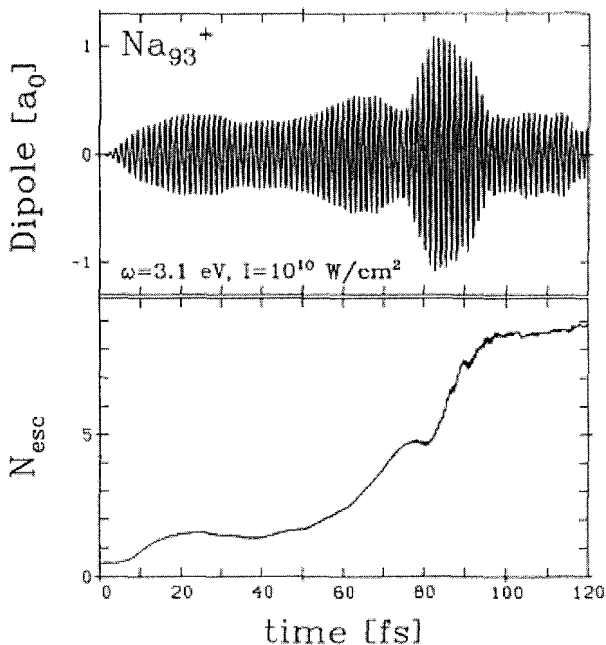
Figure 6.16. Electronic response of Na$_{93}^+$ to a 100 fs laser pulse of peak intensity 10^{10} W/cm^2. The upper panel gives the dipole moment along the axis of laser polarization, and the lower panel the number of emitted electrons. Reproduced from J. A. Alonso *et al.*, *Fission Dynamics of Atomic Clusters and Nuclei*, Eds. J. da Providencia *et al.*, World Scientific, Singapore (2001), p. 163, with permission of World Scientific.

The response depends crucially on the actual laser frequency [98, 101]. For laser frequencies sufficiently far away from the plasmon resonance, the dipole response follows closely the pulse profile and disappears when the laser pulse profile vanishes. On the contrary, for laser frequencies close to the Mie resonance, the laser may attach the resonance; this results in a sizeable electron emission and the dipole

response survives the laser pulse as it generated a true eigenfrequency of the system. The example considered in the figure corresponds to a situation in which the plasmon actually comes into play during the process. For the first 50 fs, the laser pulse remains above resonance and the electronic dipole moment $D(t)$ (upper panel) follows the profile of the pulse. Still, the intensity is enough to induce the ionization of the cluster. The electronic cloud of the ionized cluster is more compressed (the ionic background does not change in the model) and this shifts the plasmon resonance towards higher frequencies, and thus closer to the laser frequency. From about 50 fs on, the Mie plasmon couples resonantly with the laser, which leads to a jump in ionization. The process reaches a peak until the violent electron emission produces a further blueshift of the plasmon that detunes the plasmon from the laser. Still, even after the pulse has been switched off and electron emission has leveled off, the electron cloud continues performing collective oscillations at the actual plasmon frequency of the system (namely, for the net charge of the cluster). This example illustrates the role of the plasmon resonance in triggering ionization. For the short pulse considered, the ions remain fixed and do not interfere with the ionization process. However, this is not the case when longer pulses are considered. Indeed, experiments [97] for platinum clusters suggest that the highly charged cluster rapidly undergoes a Coulomb expansion, with a time scale around 100–500 fs. Interference can thus occur between the laser pulse and the ionic motion, which may produce an enhanced ionization.

A second example shows how the ionic motion can interfere with the excitation process provided the latter is long enough. For this purpose, the excitation of Na_{41}^+ subjected to a long laser pulse (240 fs) of frequency $\omega_{laser} = 2.86$ eV has been simulated using the TDLDA [102]. The results are given in Fig. 6.17. An explicit account of the ions is required and pseudopotentials were used to model the ion–electron interaction The third panel, giving the number of electrons emitted, N_{esc}, shows that ionization proceeds in several steps. Again, in a first stage lasting for about 80 fs, the response is fully electronic, and is characterized by a low ionization. But the net charge of the cluster shifts the plasmon upwards until it comes into resonance with the laser. This results in a sudden increase in ionization around 100 fs, leaving the cluster in a state with a net charge 5+. Up to that stage, the situation is similar to the previous case of Na_{93}^+. From then on, ionization proceeds

at a slower pace until another burst of electrons occurs around 250 fs stripping about 5 electrons. The lowest panel gives the electric dipole signal $D(t)$. It is clear that large slopes in ionization (N_{esc}) are correlated with large dipole amplitudes, which again reflects resonant conditions.
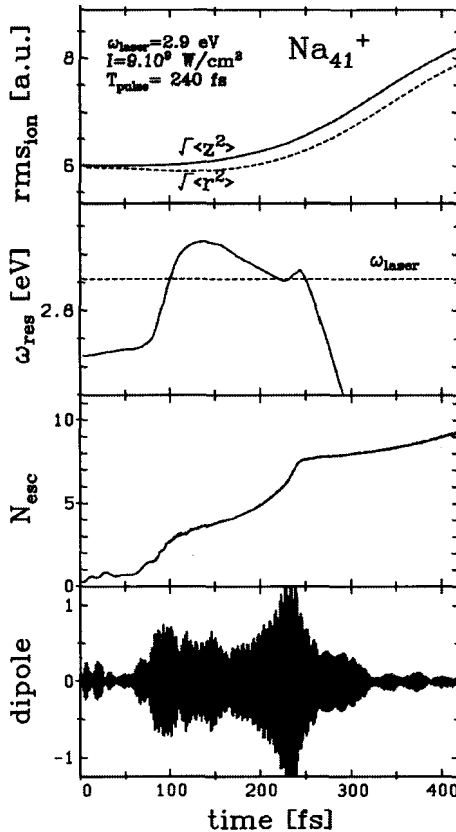
Figure 6.17. Simulation of the excitation of $Na_{41}{}^+$ with a laser of frequency $\omega_{laser} = 2.86$ eV, intensity $I = 9 \times 10^{9}$ W/cm^2 and pulse length 240 fs. From top to bottom: global extension of the ionic distribution in z- (along laser polarization) and axial r-direction (transverse to laser polarization); average resonance frequency $\omega_{res}(t)$ for the actual structure and charge state; number of emitted electrons N_{esc} and dipole signal. Reproduced from E. Suraud and P. G. Reinhard, *Phys. Rev. Lett.* **85**, 2296 (2000) with permission of the American Physical Society.

An unambiguous link between the two observables is established by plotting in the second panel the instantaneous plasmon frequency $\omega_{res}(t)$, calculated for the instantaneous structure and charge of the cluster. The laser frequency is the dashed horizontal line in the same panel. The correlation between large slopes in N_{esc} and resonant conditions is striking. The first coincidence at time 100 fs reflects the blueshift due to the first stage of ionization and thus corresponds to an electronic effect. It also triggers the time at which a sizeable Coulomb expansion of the ionic distribution begins (see also uppermost panel). And it is noteworthy that this occurs rather soon (about 50 fs) after the violent initial charging. But the Coulomb expansion in turn leads to a redshift of the resonance (see Eq. (5.34)), which is responsible for the second coincidence at around 230 fs. The system thus acquires a much higher charge state and ends up in a violent Coulomb explosion.

6.8 Caloric Curves of Fragmenting Clusters

The multifragmentation of hydrogen cluster ions colliding with helium atoms produces a caloric curve with a shape in agreement with a bound cluster to gas transition generated by Coulombic forces (see Section 3.3.4). Brechignac and coworkers have detected a bound cluster to vapor phase transition in Sr clusters using a different approach [103]. The neutral clusters are first produced in a gas aggregation source. Ionization (and excitation) with a first laser pulse produces an evaporative ensemble of Sr_N^+ cluster ions at a temperature $T_0 = 700$ K $\pm$ 50 K. The charged clusters are then accelerated before entering a time-of-flight mass spectrometer. There, a second laser with photons of energy $h\nu$ excites the cluster packet of interest (that is, clusters of a selected size) inducing fragmentation. A retarding potential allows for the time dispersion of the fragments, showing that ion fragments result from the evaporation of neutral atoms, whose number is proportional to $h\nu$. For well defined excitation, the velocity of the emitted atoms has a Maxwellian probability distribution.

The experiment measures the translational kinetic energy release of the ejected neutral atoms. For warm N-atom clusters ejecting a single neutral atom, the temperature of the evaporative clusters may be obtained from the kinetic energy release of the fragments. When the

photon energy is such that more atoms are emitted, the process can be considered as a series of sequential atom emissions. By increasing step by step the photon energy, the result of the experiment is a curve giving the cluster temperature (the translational temperature of the ejected neutral atoms) versus the energy deposited in the cluster by the laser prior to fragmentation.
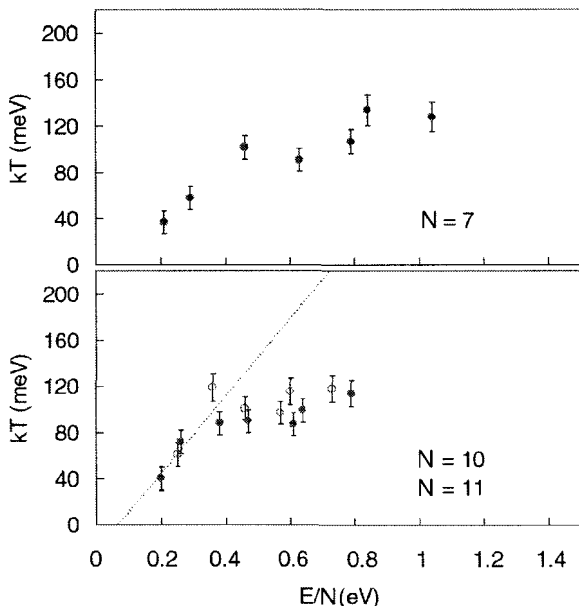
Figure 6.18. Caloric curves fo Sr_N^+ determined from the kinetic energy release of emitted neutral atoms versus excitation energy per atom. For $N = 10$ (solid dots) and $N = 11$ (open dots) the caloric curves rise first and saturate to a limiting temperature, in agreement with a bound cluster to gas transition. $N = 7$ has not fully developed that behavior. Reproduced from C. Bréchignac *et al.*, *Phys. Rev. Lett.* **89**, 203401 (2002) with permission of the American Physical Society.

The caloric curves for Sr_7^+, Sr_{10}^+ and Sr_{11}^+ are plotted in Fig. 6.18. For the two larger sizes, the caloric curves, after an initial rise with a slope 1/3, reach an almost constant value for kT about 85–110 meV. This indicates that a phase transition occurs at a temperature $T = 1000$–1300

K. This temperature is above the melting point (1050 K) and below the boiling point (1655 K) of bulk Sr, and has been interpreted as the temperature for a bound cluster to vapor phase transition. For the small clusters Sr_5^+ (not shown in the figure, but see ref. [103]) and Sr_7^+, evidence for the transition is not as clear.

References

1. Buffat, P., and Borel, J. P., *Phys. Rev. A*, **13**, 2287 (1976).
2. Lai, S. L., Guo, J. Y., Petrova, V., and Ramanath, G., and Allen, L. H., *Phys. Rev. Lett.*, **77**, 99 (1996).
3. Martin, T., Näher, U., Schaber, H., and Zimmermann, U., *J. Chem. Phys.*, **100**, 2322 (1994).
4. Martin, T. P., Bergmann, T., Göhlich, H., and Lange, T., *Chem. Phys. Lett.*, **172**, 209 (1990).
5. Martin, T. P., *Phys. Reports*, **273**, 199 (1996).
6. Martin, T. P., Bergmann, T., Göhlich, H., and Lange, T., *J. Phys. Chem.*, **95**, 6421 (1991).
7. Takagi, M., *J. Phys. Soc. Japan*, **9**, 361 (1954).
8. Hanszen, K. J., *Z. Phys. Chem.*, **157**, 523 (1960).
9. Schmidt, M., Kusche, R., Kronmüller, W., von Issendorf, B., and Haberland, H., *Phys. Rev. Lett.*, **79**, 99 (1997).
10. Schmidt, M., Kusche, R., von Issendorf, B., and Haberland, H., *Nature*, **393**, 238 (1998)
11. Kusche, R., Hippler, M., Schmidt, M., von Issendorf, B., and Haberland, H., *Eur. Phys. J. D*, **9**, 1 (2000).
12. Schmidt, M., Hippler, M., Donges, J., Kronmüller, W., von Issendorf, B., and Haberland, H., *The Physics and Chemistry of Clusters*, Ed. E. E. B. Campbell and M. Larsson, World Scientific, Singapore, p. 22 (2001),
13. Schmidt, M., Kusche, R., Hippler, M., Donges, J., Kronmüller, W., von Issendorf, B., and Haberland, H., *Phys. Rev. Lett.*, **86**, 1191 (2001).
14. Haberland, H., Hippler, M., Donges, J., Kostko, O., Schmidt, M., and von Issendorf, B., *Phys. Rev. Lett.*, **94**, 035701 (2005).
15. Schmidt, M., Donges, J., Hippler, M., and Haberland, H., *Phys. Rev. Lett.*, **90**, 103401 (2003).
16. Calvo, F., and Spiegelmann, *Phys. Rev. Lett.*, **82**, 2270 (1999); *J. Chem. Phys.*, **112**, 2888 (2000).
17. Daw, M. S., Baskes, M. I., *Phys. Rev. B*, **29**, 6443 (1984).
18. Gupta, R. P., *Phys. Rev. B*, **23**, 6265 (1981).
19. Poteau, R., and Spiegelmann, F., *Phys. Rev. B*, **45**, 1878 (1993).
20. Car, R., and Parrinello, M., *Phys. Rev. Lett.*, **55**, 2471 (1985).

21. Rytkönen, A., Häkkinen, H., and Manninen, M., *Phys. Rev. Lett.*, **80**, 3940 (1998); *Eur. Phys. J. D*, **9**, 451 (1999).
22. Lundqvist, S., and March, N. H., Eds., *Theory of the Inhomogeneous Electron Gas*, Plenum, New York (1983).
23. Hohenberg, P. , and Kohn, W. *Phys. Rev.* **136**, 864B (1964).
24. Aguado, A., López, J. M., Alonso, J. A., and Stott, M. J., *J. Chem. Phys.*, **111**, 6026 (1999).
25. Aguado, A., López, J. M., Alonso, J. A., and Stott, M. J., *J. Phys. Chem.*, **105**, 2386 (2001).
26. Bulgac, A., and Kusnezov, D., *Phys. Rev. B*, **45**, 1988 (1992).
27. Ju, N., and Bulgac, A., *Phys. Rev. B*, **48**, 2721 (1993).
28. Poteau, R., Spiegelmann, F., and Labastie, P., *Z. Phys. D.*, **30**, 57 (1994).
29. Rey, C., García Rodeja, J., Gallego, L. J., and Grimson, M., *Phys. Rev. E*, **57**, 4420 (1998).
30. Schmidt, M., Ellert, C., Kronmüller, W., and Haberland, H., *Phys. Rev. B*, **59**, 10970 (1999).
31. Haberland, H., *Metal Clusters*, Ed. W. Ekardt, John Wiley & Sons, New York (1999), p. 181.
32. Kümmel, S., Brack, M., and Reinhard, P. G, *Phys. Rev. B*, **62**, 7602 (2000).
33. Blaise, P., and Blundell, S. A., *Phys. Rev. B*, **63**, 235409 (2001).
34. Aguado, A., and López, J. M., *Phys. Rev. Lett.*, **94**, 233401 (2005).
35. Vichare, A., Kanhere, D. G., and Blundell, S. A., *Phys. Rev. B*, **64**, 45408 (2001).
36. Akola, J., and Manninen, M., *Phys. Rev. B*, **63**, 193410 (2001).
37. Shvartsburg, A. A., and Jarrold, M. F, *Phys. Rev. Lett.*, **85**, 2530 (2000).
38. Von Helden, G., Hsu, M. T., Kemper, P. R., and Bowers, M. T., *J. Chem. Phys.*, **95**, 3835 (1991).
39. Shvartsburg, A. A., and Jarrold, M. F, *Phys. Rev. A*, **60**, 1235 (1999).
40. Majumder, C., Kumar, V., Mizuseki, H. , and Kawazore, Y., *Phys. Rev. B* , **64**, 233405 (2001).
41. Desideri, A., and Cocke, D. L., *J. Chem. Phys.*, **62**, 731 (1975).
42. Joshi, K., Kanhere, D. G., and Blundell, S. A., *Phys. Rev. B*, **66**, 155329 (2002).
43. Joshi, K., Kanhere, D. G., and Blundell, S. A., *Phys. Rev. B*, **67**, 235413 (2003).
44. Banhart, F., Hernández, E., and Terrones, M., *Phys. Rev. Lett.*, **90**, 185502 (2003).
45. Banhart, F., and Ajayan, P. M., *Nature* , **382**, 433 (1996).
46 Bonacic-Koutecky, V., Pittner, J., Fuchs C., Fantucci, P., Guest, M. F., and Koutecky, J., *J. Chem. Phys.*, **104**, 1427 (1996).
47. Näher, U., Bjornholm, S., Frauendorf, S., Garcias, F., and Guet, C., *Phys. Reports*, **285**, 245 (1997).
48. Bréchignac, C., Cahuzac, Ph., Carlier, F., and de Frutos, M., *Phys. Rev. B*, **49**, 2825 (1994).

49. Bréchignac, C., Cahuzac, Ph., Carlier, F., and Leygnier, J., *Phys. Rev. Lett.*, **63**, 1368 (1989).

50. Bréchignac, C., Cahuzac, Ph., Carlier, F., and de Frutos, M., *Phys. Rev. Lett.*, **64**, 2893 (1990).

51. Bréchignac, C., *The Physics and Chemistry of Clusters*, Eds. E. E. B. Campbell and M. Larsson, *Proceedings of the Nobel Symposium* **117**, 42. World Scientific, Singapore (2001).

52. Martin, T. P., *J. Chem Phys.*, **81**, 4426 (1984).

53. Martin, T. P., Näher, U., Göhlich, H., and Lange, T., *Chem. Phys. Lett.*, **196**, 113 (1992).

54. Näher, U., Frank, S., Malinowski, L., Zimmermann, U., and Martin, T. P., *Z. Phys. D.*, **31**, 191 (1994).

55. Rayleigh, L., *Phil. Mag.*, **14**, 185 (1882).

56. Katakuse, I., Ito, H., and Ichihara, A., *Int. J. Mass Spectrom. Ion Proc.*, **97**, 47 (1990).

57. Sweikhard, L., Beiersdorfer, P., Bell, W., Dietrich. G., Krückeberg, S., Lützenkirchen, K, Obst, B., and Ziegler, J., *Hyperf. Interact.*, **99**, 97 (1996).

58. Saunders, W. A., *Phys. Rev. Lett.*, **64**, 3046 (1990).

59. Saunders, W. A., *Phys. Rev. A*, **46**, 7028 (1992).

60. Bréchignac, C., Cahuzac, Ph., Carlier, F., and Leygnier, J., and Sarfati, A., *Phys. Rev. B* , **44**, 11386 (1991).

61. Yannouleas, C., Landman, U., Bréchignac, C., Cahuzac, Ph., Concina, B., and Leygnier, J., *Phys. Rev. Lett.*, **89**, 173403 (2002).

62. Iñiguez, M. P., Alonso, J. A., Aller, A., and Balbás, L. C., *Phys. Rev. B*, **34**, 2152 (1986).

63. Lipparini, E., and Vitturi, A., *Z. Phys. D*, **17**, 57 (1990).

64. Chandezon, F., Tomita, S., Cormier, D., Grübling, P., Guet, C., Lebius, H., Pesnelle, A., and Huber, B. A., *Phys. Rev. Lett.*, **87**, 153402 (2001).

65. Brack, M., Damgaard, J., Jensen, A. S., Pauli, H. C., Strutinsky, V. M., and Wong, C. Y., *Rev. Mod. Phys.* **44**, 320 (1972).

66. Nakamura, M., Ishii, Y., Tamura, A., and Sugano, S., *Phys. Rev. A*, **42**, 2267 (1990).

67. Koizumi, H., Sugano, S., and Ishii, Y., *Z. Phys. D*, **26**, 264 (1993); **28**, 223 (1993).

68. Yannouleas, C., Landman, U., and Barnett, R. N., *Metal Clusters*, editor W. Ekardt (Wiley, New York, 1999), p. 145.

69. Yannouleas, C., and Landman, U., *Phys. Rev. B*, **51**, 1902 (1995).

70. Barnett, R. N., Landman, U., and Rajagopal, G., *Phys. Rev. Lett.*, **67**, 3058 (1991).

71. Bréchignac, C., Cahuzac, Ph., Carlier, F., de Frutos, M., Barnett, R. N., and Landman, U., *Phys. Rev. Lett.*, **72**, 1636 (1994).

72. Blaise, P., Blundell, S. A., Guet, C., and Zopa, R. R., *Phys. Rev. Lett.*, **87**, 063401 (2001).

73. Garcias, F., Alonso, J. A., López, J. M., and Barranco, M., *Phys. Rev. B,* **43**, 9459 (1991).
74. Garcias, F., Mañanes, A., López, J. M., Alonso, J. A., and Barranco,M., *Phys. Rev. B* **51**, 1897 (1995).
75. Garcias, F., Alonso, J. A., Barranco, M., López, J. M., Mañanes, A., and Nemeth. J., *Z. Phys. D*, **31**, 275 (1994).
76. Ring, P., and Schuck, *The Nuclear Many-Body Problem*, Springer–Verlag, Berlin (1980).
77. Rigo, A., Garcias, F., Alonso, J. A., López, J. M., Barranco, M., Mañanes, A., and Nemeth. J., *Surf. Rev. Lett.*, **3**, 617 (1996).
78. Hasse, H., and Myers, *Geometrical Relationships of Macroscopic Nuclear Physics*, Springer–Verlag, Berlin (1988).
79. Blocki, J., Planeta, R., Brzychczyk, J., and Grotowski, K., *Z. Phys. A*, **341**, 307 (1992).
80. Yannouleas, C., and Landman, U., *J. Phys. Chem.*, **99**, 14577 (1995).
81. Vieira, A., and Fiolhais, C., *Phys. Rev. B*, **57**, 7352 (1998).
82. Saito, S., and Cohen, M. L., *Phys, Rev. B*, **38**, 1123 (1988).
83. Engel, E., Schmitt, U. R., Lüdde, H. J., Toepfer, A., Wüst, E., Dreizler, R. N., Knospe, O., Schmidt, R., and Chattopadhyay, *Phys, Rev. B*, **48**, 1862 (1993).
84. Alonso, J. A., Barranco, M., Garcias, F., Reinhard, P. G., and Suraud, E., *Fission Dynamics of Atomic Clusters and Nuclei*, Eds. J. da Providencia, D. M. Brink, F. Karpechine and F. B. Malik, World Scientific, Singapore (2001), p. 163.
85. Montag, B., and Reinhand, P. G., *Phys. Lett. A*, **193**, 380 (1994); *Z. Phys. D*, **33**, 265 (1995).
86. López, J. M., Alonso, J. A., March, N. H., Garcias, F., and Barranco, M., *Phys. Rev. B* **49**, 5565 (1994).
87. Garcias, F., Lombard, R. J., Barranco, M., Alonso, and J. A., López, *Z. Phys. D*, **33**, 301 (1995).
88. Lyalin, A., Solovyov, A., Greiner, W., and Semenov, S. K., *Phys. Rev. A*, **63**, 3653 (2000).
89. Lyalin, A., Solovyov, A., and Greiner, W., *Phys. Rev. A*, **65**, 043202 (2002).
90. Montag, B., and Reinhard, P. G., *Phys. Rev. B*, **52**, 16365 (1995).
91. Bréchignac, C., Busch, H., Cahuzac, Ph., and Leygnier, J., *J. Chem. Phys.* , **101**, 6992 (1994).
92. Fröbich, P., *Phys. Lett. A*, **202**, 99 (1995).
93. Weiskopf, V., *Phys. Rev.* **52**, 295 (1937).
94. Hohmann, H., Callegari, C., Furrer, S., Grosenick, D., Campbell, E. E. B., and Hertel, I. V., *Phys. Rev. Lett.*, **73**, 1919 (1994).
95. Schlipper, R., Kusche, R., von Issendorff, B., and Haberland, H., *Phys. Rev. Lett.*, **80**, 1194 (1998).
96. Lezius, M., Dobosz, S., Normand, D., and Schmidt, M., *Phys. Rev. Lett.*, **80**, 261 (1998).

97. Köller, L., Schumacher, M., Köhn, J., Teuber, S., Tiggesbäumker, J., and Meiwes-Broer, K. H., *Phys. Rev. Lett.*, **82**, 3783 (1999).
98. Calvayrac, F., Reinhard, P. G., Suraud, E., and Ullrich, C., *Phys. Rep.* **337**, 493 (2000).
99. Chandezon, F., Guet, C., Huber, B. A., Jalabert, D., Maurel, M., Monnand, E., Ristori, C., and Rocco, J. C., *Phys. Rev. Lett.*, **74**, 3784 (1995).
100. Baumert, T., and Gerber, G., *Adv. At. Mol. Opt. Phys.*, **35**, 163 (1995).
101. Ullrich, C. A., Reinhard, P. G., and Suraud, E., *J. Phys. B.*, **30**, 5043 (1997).
102. Suraud, E., and Reinhard, P. G., *Phys. Rev. Lett.*, **85**, 2296 (2000).
103. Bréchignac, C., Cahuzac, Ph., Concina, B., and Leygnier, J., *Phys. Rev. Lett.*, **89**, 203401 (2002).

7.   Bimetallic Clusters

7.1 Introduction

Mixing two vapors and expanding the mixture [1] produces new clusters that, in the case of metals, are the microscopic analogue of the bulk alloys. In the case of bulk alloys, different stable phases appear for a given pair of metals, characterized by specific crystal structures and usually by fixed concentrations. Transitions to another phase can occur when a critical temperature is reached. Also, some of those phases can be stable over an extended range of atomic concentrations, specially for alloys very rich in one of the components. All this makes the simple book-keeping of the alloy phases of binary systems a whole subject, and compilations of phase diagrams exist. An additional variable enters the picture in the case of finite clusters; this is the number of atoms in the cluster. The field of heteroclusters is then very rich and broad. An example has been presented in Section 3.3.3, where the melting of mixed inert gas clusters was studied using computer simulations as a tool. In this chapter the interest is shifted to mixed clusters of metallic elements, and some representative topics have been selected from the abundant literature.

7.2 Alloying Effects in Alkali Metal Clusters

Supersonic beam expansions of a mixture of lithium and sodium vapors have produced mixed clusters [1]. This is remarkable because Li and Na do not form solid alloys and also present a miscibility gap in the liquid phase. Other salient features are: (a) the magic numbers, corresponding to the most abundant cluster sizes, are the same as for pure Li and Na clusters; (b) Li enrichment, compared to the composition in the vapors, is

205

observed in the clusters. The fact that the magic numbers do not change is easily understood. The ions in the alkali metals are relatively small compared to the atomic volumes and the effective ionic pseudopotentials are weak. Then, a jellium with the concentration-averaged background density is a good description of the mixed clusters. But, evidently this simple model cannot account for the distribution of the atoms in the clusters. The SAPS model allows to get some qualitative trends about the ionic distribution [2]. Although only relatively small clusters have been studied, a general feature obtained is that the Na atoms are at higher distances from the cluster center than the Li atoms. This can be viewed as a manifestation of the tendency to phase separation existent in solid and liquid Li–Na alloys. This phase separation tendency is less pronounced in small clusters, and this is corroborated by the calculated negative value of the heat of solution of a Li impurity in Na clusters (the negative value means that the process is energetically favorable). The negative value explains, in addition, why the mixed clusters form in the supersonic expansion experiments. The observed Li enrichment was explained by calculating the heat for the exchange reaction

$$\mathrm{Li}_m \mathrm{Na}_n + \mathrm{Li} \rightarrow \mathrm{Li}_{m+1} \mathrm{Na}_{n-1} + \mathrm{Na} \,. \qquad (7.1)$$
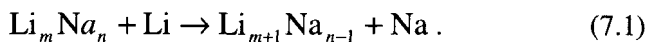
The calculated reaction energies are negative, indicating that the replacement of a Na atom by a Li atom in an exchange collision in the beam is favorable.

The tendency for the Na atoms to be on the surface in mixed Li–Na clusters has been confirmed by calculations [3, 4] for $\mathrm{Li}_m \mathrm{Na}$ and $\mathrm{Na}_m \mathrm{Li}$ with m up to 12, and for $\mathrm{Na}_{8-n} \mathrm{Li}_n$. The ground state structures of the $\mathrm{Li}_m \mathrm{Na}$ clusters are similar to those for the corresponding Li_{m+1} pure clusters, and the Na atom occupies, in all cases, positions on the surface. In contrast, the Li impurity in the Na-rich $\mathrm{Na}_m \mathrm{Li}$ clusters, is located in internal positions for sizes $\mathrm{Na}_6 \mathrm{Li}$ and higher. The different behavior was ascribed to the weaker binding between Na and Li atoms, as compared to Li–Li, and to the smaller ionic radius of Li compared to Na. The structures of the clusters with 8 atoms are given in Fig. 7.1. As the Na fraction increases, there is a transition from the C_{3v} symmetry of Li_8 (also $\mathrm{Li}_7 \mathrm{Na}$ and $\mathrm{Li}_6 \mathrm{Na}_2$) to the D_{2d} symmetry of Na_8 (also LiNa_7 and $\mathrm{Li}_2 \mathrm{Na}_6$), going through an intermediate T_d structure for intermediate compositions ($\mathrm{Li}_5 \mathrm{Na}_3$, $\mathrm{Li}_4 \mathrm{Na}_4$ and $\mathrm{Li}_3 \mathrm{Na}_5$). Also in this case the tendency of Na atoms

for surface sites is evident. Na-rich clusters exhibit internal Li atoms, but there are no internal Na atoms in Li-rich clusters. The segregation is specially clear in the middle of the series, where the Na atoms are capping faces of an internal core formed by the Li atoms.
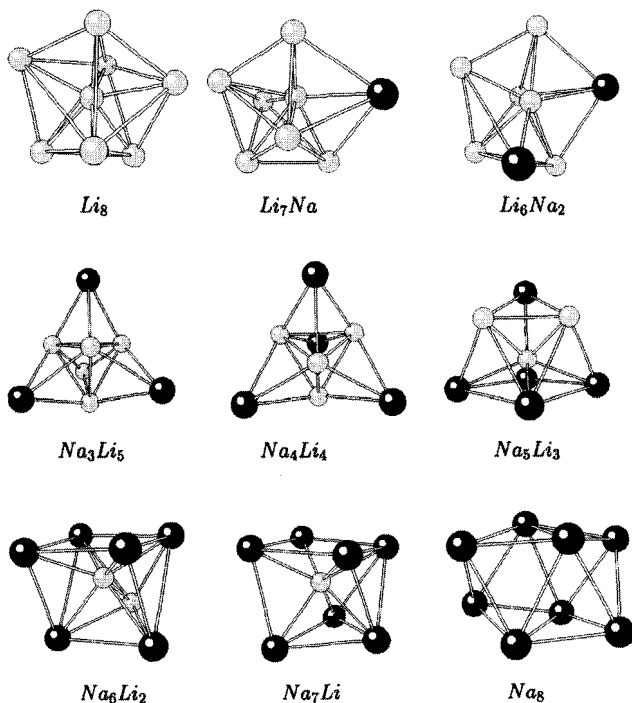
Figure 7.1. Geometries of mixed Li–Na clusters with 8 atoms. Dark and light spheres represent Na and Li atoms, respectively. Reproduced from M. D. Deshpande *et al.*, *Phys. Rev. A* **65**, 53204 (2002) with permission of the American Physical Society.

The difference between the Wigner–Seitz radii of bulk Na and Li is 0.72 a.u., and this difference increases to 0.87 and 1.81 a.u. for the K–Na and Cs–Na pairs, respectively. One might expect that the weak segregation tendency found in Li–Na clusters will be enhanced for Na–K and Na–Cs. Indeed, the atomic distribution in Na–K clusters [5] obtained by the SAPS model differs drastically from the Li–Na case. For instance,

the Na and K atoms in $Na_{10}K_{10}$ form well separated layers, with K on the surface. Although the SAPS model cannot be used confidently to reproduce the fine details of the atomic distributions, the main features of the radial distribution can be trusted. In fact, the tendency for K to segregate at the surface of Na–K clusters, which is driven by the lower surface energy of the heavier element, is also predicted by molecular dynamics simulations using the Car–Parrinello DFT method [6]. A difference between the bulk Li–Na and Na–K alloys is that an ordered compound, of composition Na_2K, forms in the second case. The calculated atomic distribution of large clusters like $Na_{34}K_{34}$ shows that not all K atoms segregate to the surface [5]; there is an alternation of Na and K atomic layers, which could be interpreted as a precursor of the ordering tendency in the solid at the equiatomic composition. Calculations for Na–Cs clusters also predict layer alternation, with Cs on the surface [7]. The first feature is consistent with the existence of a bulk ordered Na_2Cs compound. The second agrees with the results of Monte Carlo simulations of the liquid–vapor interface of Na–Cs alloys; those simulations yield segregation of Cs atoms to the surface [8]. In spite of the layering effects, the electronic structure of the mixed clusters remains simple and the calculated magic numbers (also the measured ones in the case of Li–Na) coincide with the well kown shell closing numbers of the unmixed clusters.

7.3 Collective Electronic Excitations

Surface segregation of one atomic species affects the collective electronic response. The ground state structure of $Na_{20}K_{20}$ obtained with the SAPS model is composed of three layers surrounding a central Na atom. All the Potassium atoms are on the surface and the two inner layers have Na atoms only. The photoabsorption spectrum [5] calculated by TDLDA shows a resonance peak at 2.1 eV representing the collective oscillation of the electrons against the ionic background. The tail of the resonance extends up to 3 eV and concentrates a sizeable amount of oscillator strength. The position of the collective resonance is closer to the corresponding resonance of pure K clusters calculated with the same method, compared to pure Na clusters; this is a manifestation of the fact that the cluster surface, whose electron density contributes most to the

collective excitation, is formed by K atoms in $Na_{20}K_{20}$. A calculation of the photoabsorption spectrum for other isomers allows to analyze the sensitivity of the spectrum to the structural features [5]. When the positions of some Na and K atoms are interchanged, preserving other features of the cluster geometry, a shift of the resonance peak to higher energy occurs as Na replaces K on the surface. More drastic variations of the structure produce pronounced changes in the spectrum, like the broadening and fragmentation of the plasmon peak. The optical response of mixed Li–Na clusters has also been studied [9]. In summary, the shape of the photoabsorption spectrum is sensitive to the cluster geometry and to the degree of segregation of one component to the surface; so, a comparison between measured and calculated spectra may be useful to elucidate the structure of mixed clusters.

Very small mixed clusters have been studied by *ab initio* methods. Motivated by the measurements of the optical absorption spectra of $LiNa_3$ and Li_2Na_2 [10], Configuration Interaction (CI) calculations have been performed for those two clusters [11], as well as Hartree–Fock calculations for the whole family Li_nNa_{4-n} [12]. The optical response was obtained in both cases from CI calculations for excited electronic states. The two studies give planar rhombic forms as the most stable structures: slightly distorted for $LiNa_3$ and Li_3Na, and undistorted for Li_4, Na_4 and Li_2Na_2. The photoabsorption spectrum is sensitive to n. The spectrum of Na_4 resembles that obtained from the Mie–Drude theory for an ellipsoidal droplet with three different axes. But, as Li atoms replace Na atoms, the deviations from the Mie theory become increasingly large. The measured spectra of $LiNa_3$ and Li_2Na_2 are explained by the *ab initio* calculations. The calculations discovered low lying isomers in each Li_nNa_{4-n} case, corresponding to different ways of arranging the Li and Na atoms in the four vertices of the rhombus. The comparison between the experimental absorption spectrum of Li_2Na_2 and the spectra calculated for the three isomers detected confirmed that the best agreement is obtained for the lowest energy isomer. On the other hand, the calculated spectra for the two singlet isomers of $LiNa_3$ are so similar that it was not possible to distinguish which isomer or whether a combination of both singlet isomers contributes to the measured spectrum.

TDLDA calculations for the whole $Na_{8-n}Li_n$ family [4] obtained single plasmon peaks at both ends of the series, Li_8 and Na_8, consistent with a spherically symmetric electron density of both clusters. The

replacement of one or two atoms in the homogeneous clusters produces an spheroidal deformation of the density and introduces extra shoulders in the spectrum. In the middle of the series, for Li_5Na_3 and Li_4Na_4, the resonance is fragmented in two close peaks. These two clusters have tetrahedral symmetry and, as a rule, the oscillator strength in the absorption spectra of clusters with nonspherical shape is spread over a wide energy range, thus leading to broader spectra.

7.4 Divalent and Monovalent Impurities in Alkali Metal Clusters

Supersonic expansion experiments with mixed metal vapors [13, 14] have shown that some changes occur in the magic numbers of Na and K clusters when these are doped with divalent impurities: Ba, Sr, Eu, Ca, Yb, Mg and Zn dopants in Na clusters, and Mg, Hg and Zn dopants in K clusters. The results for clusters containing a single impurity are given in Table 7.1, which also includes some monovalent impurities. For some impurities a new magic number corresponding to ten valence electrons is found (clusters in the lower part of the table). Also, the magic number corresponding to 18 valence electrons vanishes *in most cases* (except for those systems at the top of the table). The single coordinate

$$\Delta n_+ = n_+^0(\text{impurity}) - n_+^0(\text{host}),\qquad(7.2)$$

that is, the difference between the average valence densities in the pure host and impurity solids, allows to separate the doped clusters of the table into two subsets [15]. Values of Δn_+ roughly higher than 0.008 a.u. induce changes in the magic numbers. This is the case for Mg and Zn impurities in Na, and for Mg, Hg and Zn impurities in K. In contrast there are no changes for $\Delta n_+ < 0.008$ a.u.

The success of this coordinate immediately suggests an extension of the Spherical Jellium Model, in which the impurity, located at the center of the host cluster, is modeled by a positive background with density $n_+^0(\text{impurity})$ and radius R_{imp}, embedded in a background with density equal to $n_+^0(\text{host})$, representing the host [15]. The radius of the doped cluster is determined by R_{imp} and the number of host atoms. Calculations

for this jellium-on-jellium model show that the binding energy of the s-type electrons ($l = 0$) increases in comparison to the undoped cluster because the presence of the impurity induces a more attractive potential in the central region of the cluster, whereas the binding energies of electrons with $l > 1$ change little. Consequently, the magnitude of the gap between the 2s and 1d shells (see Fig. 4.3 for the case of the pure Na_{20}) decreases with increasing Δn_+. When Δn_+ becomes close to 0.008 a.u. or higher, reordering of these two subshells occurs, and the filling order changes to 1s 1p 2s 1d. Clusters with 10 valence electrons then adopt the closed shell electronic configuration 1s^2 1p^6 2s^2, which accounts for the experimental observation of the new magic number. The magic number corresponding to 20 electrons, associated to the configuration 1s^2 1p^6 2s^2 1d^{10}, is still present for clusters with $n_+ \geq 0.008$ a.u., but evidently there is no shell closing for 18 electrons.

Table 7.1. Abundance maxima observed in $A_N B$ clusters. Maxima are characterized by the number of valence electrons. Also given is the difference between the jellium background densities of A and B. Data collected from [15].

A/B	$n^0_+(B)-n^0_+(A)$ (a.u)	Maxima
Na/Ba	0.0008	8, 18
Na/Sr	0.0014	8, 18-20
K/Na	0.0018	8, 20
Na/Eu	0.0023	8, 18
Na/Li	0.0029	8, 20
Na/Ca	0.0029	8, 20
Na/Yb	0.0033	8, 20
K/Li	0.0047	8, 20
Na/Mg	0.0088	8-10
K/Mg	0.0106	10, 20
K/Hg	0.0106	10, 21
Na/Zn	0.0155	10, 20
K/Zn	0.0173	10, 20

These conclusions are confirmed by calculations [14] using a Wood–Saxon potential modified to account for the presence of the impurity. Zhang *et al.* [16] also noticed the 2s–1d inversion in their pseudopotential calculations. For larger clusters and strongly attractive

impurities Yeretzian [14] predited an inversion between the $2p$ and $1f$ shells, which would give rise to magic clusters with 26 electrons and would cause the magic number 40 to vanish. Experiments for the relevant host–impurity combinations in this size range have not been performed.

Small anomalies have been observed [14] with respect to the general trends discussed, and these have been ascribed to structural effects beyond the jellium-type models [14, 17]. Also, better agreement with experiment is achieved by relaxing one of the constraints of the jellium-on-jellium model: Yannouleas *et al.* [18] varied the impurity background density n^0_+(impurity), and then R_{imp}, while maintaining n^0_+(host) equal to its bulk value. An appropriate selection of the effective value of n^0_+(impurity) leads to a better matching of the calculated magic numbers with experiment.

The optical response has been studied using the jellium-on-jellium model. The calculated optical spectrum of Na_8Zn is characterized by two closely spaced lines at 2.87 eV, carrying 26 % of the total strength, and a stronger line at 2.57 eV which carries 42 % of the strength. This is in good agreement with the experimental double peak, formed by a higher energy component at 2.97 eV, which carries a smaller amount of strength than the lower energy component at 2.63 eV [18]. The fragmentation is due to the near degeneracy between the plasmon peak and the $2s \rightarrow 2p$ and $1p \rightarrow 3s$ particle–hole transitions. This was obtained for an impurity background density corresponding to $r_s(Zn) = 1.15$ a.u., a value substantially smaller than the standard value of $r_s = 2.31$ a.u. for bulk Zn (see the definition of the electron density parameter r_s in Section 5.7.2). The small value of r_s indicates a strong attractive potential at the impurity site, which produces the downwards shift of those transitions required for the degeneracy with the plasmon to develop. The spectrum of Na_8 contains a single line at 2.53 eV, so the effect of the Zn atom on the optical response is evident. The need for such a small value of r_s may be related to the application of the jellium model to an element like Zn, at the end of the transition metal group. As another example of the influence of impurities on the optical response one can consider the three related clusters $K_{19}Rb$, K_{20} and $K_{19}Na$, all of them having 20 valence electrons [18]. The calculated optical spectrum of K_{20} shows a split plasmon due to a degeneracy between the collective excitation and a $2s \rightarrow 3p$ particle–hole transition. In the case of $K_{19}Na$, the impurity shifts

the $2s$ level downwards, so the energy of the $2s \rightarrow 3p$ transition increases. At the same time the energy of the plasmon remains unchanged, and the consequence is that a single line dominates the spectrum. The opposite effect occurs for a Rb impurity. The energy of the $2s \rightarrow 3p$ transition is lowered and the plasmon splitting is more pronounced.

Table 7.2. Binding energy $\mathcal{E}$ and character of the molecular orbitals in Na_8Zn. Jellium model orbitals are given for comparison. Data collected from [18].

	Molecular orbitals		Jellium	
	$\mathcal{E}$ (eV)	c_l		$\mathcal{E}$ (eV)
$1d_t$	-1.88	0.980 ($l=2$)	$1d$	-2.02
$2a_{1g}$	-2.81	0.985 ($l=0$)	$2s$	-2.71
$1t_{1u}$	-3.89	0.985 ($l=1$)	$1p$	-3.68
$1a_{1g}$	-7.41	0.995 ($l=0$)	$1s$	-6.05

In order to test of the reliability of the model, Yannouleas *et al.* [18] have performed parallel jellium-on-jellium and molecular orbital calculations for K_8Mg, Na_8Zn and K_6Mg, comparing the electronic structures resulting from the two methods. In the molecular orbital calculations, the geometry was assumed to be a body centered cube for K_8Mg and Na_8Zn, and a centered octahedron for K_6Mg. For the jellium-on-jellium calculations the densities $n^0_+(\text{impurity})$ and $n^0_+(\text{host})$ were assumed equal to the corresponding bulk values. For those two geometries the molecular orbital electronic configurations are of the type $(1a_{1g})^2 (1t_{1u})^6 (2a_{1g})^6$, and $(1a_{1g})^2 (1t_{1u})^6$, respectively. Comparison with the jellium calculations is based on the correspondence $1s \rightarrow 1a_{1g}$, $1p \rightarrow 1t_{1u}$, $2s \rightarrow 2a_{1g}$ and $1d \rightarrow (1d_t + 1d_e)$. To illustrate the validity of this correspondence, the molecular wave-functions were decomposed into

spherical harmonics with respect to the cluster center. The coefficient c_l of the spherical harmonics with the maximum weight is given in Table 7.2 for Na_8Zn, and the correspondence is very good. The table also gives the binding energies. Both calculations reproduce the downward shift of the $2s$ level below the $1d$ level. The agreement between the electronic configurations extends also to K_8Mg and K_6Mg. *Ab initio* calculations by for Li_mBe, Li_mMg and Na_mMg are consistent with this conclusion [19–22]. The ground state electronic configurations are $(1a_{1g})^2$ $(1t_{1u})^6$ for the A_6X centered octahedron, $(1a'_1)^2$ $(1e'_1)^4$ $(1a''_2)^2$ $(2a'_1)^1$ for the A_7X regular pentagonal bypiramid and $(1a_{1g})^2$ $(1t_{1u})^6(2a_{1g})^2$ for the A_8X centered cubic form, respectively.

In spite of the explanation of the new magic number corresponding to 10 electrons, both calculations (two-step jellium and molecular) have difficulties in accounting for the absence of a peak at $N_e = 8$, that is, for 8 electrons, when the peak at $N_e = 10$ is present (the only case when both peaks are present in the experimental spectrum is Na_mMg). This is because both calculations exhibit comparable gaps between the $1p$ and $2s$ subshells. The discrepancy suggests that the actual $2s$ level is probably closer to the $1p$ subshell, that is more bound. In the two-step jellium model it suffices to increase the value of n^0_+(impurity) to produce the necessary downward shift of the $2s$ level, and this is the effect produced by the modification of r_s(impurity) introduced by Yannouleas *et al.* [18]. The same effect can be obtained in the framework of the molecular calculations by relaxing the geometrical constraints.

Ab initio molecular dynamics calculations for Na_mMg ($m = 6$–9, 18) have found that, in general, the Mg impurity is not located at the cluster center, although it becomes increasingly surrounded by Na atoms as m increases [17]. This produces electronic configurations that do not adapt as well to the two-jellium picture as if Mg is at the center: $1d$–$2s$ mixing is present, reflecting the lowering of the symmetry. However, Na_mMg is probably one the most unfavorable cases to apply the two-step jellium model. Δn_+ is small for systems in the upper part of Table 4.1 and the location of the impurity is unimportant because the perturbation that it produces is weak. On the other hand, when Δn_+ is large, for systems at the bottom of the Table, the impurity defines the effective center of the cluster potential (see Section 7.5 for the case of a higher difference in valence between impurity and host), and again the location of the impurity becomes unimportant.

The location of the impurity is an interesting question in itself, that has been studied by comparative calculations for Li_mBe and Li_mMg with $m \leq 12$ [23]. The ground state geometries are rather similar up to $m = 5$, but the growth patterns differ significantly for $m \geq 6$. The structure of Li_6Be is an octahedron with the Be atom at the center, and the Be impurity is trapped in the interior of the cluster for $m \geq 6$. In contrast, the Mg atom avoids internal positions and this affects strongly the structure of the clusters. Even for $m = 12$ the Mg atom resides on the surface of the cluster. The different behavior can be explained on the basis of the atomic size of the constituent atoms and the relative strength of the bonds between them. The ionic radius of Mg (1.36 Å) is larger than the ionic radius of Li (1.25 Å), while that of Be (0.89 Å) is substantially smaller. In addition, the Li–Be bond (0.391 eV) is stronger that the Li–Mg bond (0.263 eV), and both are weaker than the Li–Li bond. This makes difficult for Mg to go inside. That is, the cluster minimizes the energy by maximizing the number of Li–Li bonds.

7.5 Higher Valence Impurities

Impurities with a valence higher than two produce a stronger perturbation of the host cluster. The calculated equilibrium structures of Li_mAl clusters [24] are three-dimensional for $m \geq 3$. This is in contrast with pure Li clusters, for which two-dimensional structures prevail up to Li_6 [25]. For $m \leq 5$, the Al atom does not occupy an internal position; however for larger clusters the Al atom is internally located, surrounded by the Li atoms. The binding energy of the cluster, the evaporation energy of a Li atom $\Delta E_{vap}(m) = E(Li_{m-1}Al)+E(Li)-E(Li_mAl)$, and the ionization potential *IP* display a monotonic increase for $1 \leq m \leq 5$ and then a drop at $m = 6$. This indicates the high stability of Li_5Al, which has eight electrons. The structure of this cluster is roughly the same as that of Na_5Pb shown in Fig. 7.2, with the Al atom a little more distant from the plane of four Li atoms. The analysis of the orbital energy eigenvalues shows a doubly occupied orbital at ≈ -7.5 eV with *s* character about the Al site, and a manifold of three closely spaced and doubly occupied states with predominant *p* character at ≈ -3.5 eV, that is, separated 4 eV from the *s*-like level. The charge density indicates that the bonding is covalent, with charge accumulation in the regions connecting Al and Li

ions. The electronic structure of Li$_m$Al clusters with $m \leq 5$ reflects the localized, atomic-like nature of the orbitals, and the properties of Li$_5$Al are related to the closing of the Al $3p$ shell, albeit perturbed by the lithium environment by hybridization, bonding and crystal field effects. Further addition of Li atoms to Li$_5$Al leads to a picture consistent with the delocalized shell model, with the ordering of the $1d$ and $2s$ levels reversed from that corresponding to the homogeneous jellium model, just as in the case of the divalent impurities at the botton of Table 7.1.

The tetravalent impurities of group 14, C, Si, Ge, Sn and Pb, form another interesting case. Supersonic expansion of lead–sodium vapor from a hot oven source led to the observation of an exceptionally abundant Na$_6$Pb cluster [26]. Several DFT calculations have investigated the nature of this species [27–29]. A related cluster, Li$_6$C, had earlier been studied computationally [30] and later observed as a product formed from the vaporization of solid C$_2$Li$_2$. The calculated ground state geometries of Na$_m$Pb for m up to 7, are given in Fig. 7.2. Up to $m = 7$ each new added Na atom binds directly to the Pb atom and the coordination of the Pb atom increases. Up to Na$_5$Pb, the Pb atom is on the cluster surface, allowing the Na atoms to come in closer contact with one another and bind, albeit weakly. The lowest energy structure of Na$_6$Pb is an octahedron, which for the first time has the Pb atom in the interior of the cluster. A seventh Na atom also binds to Pb, but at this stage the Pb atom appears to be fully coordinated and an additional atom, in Na$_8$Pb, is not directly bound to Pb, but begins forming a second Na shell [27].

The electronic configuration of the free Pb atom is $6s^2 6p^2$ and the electronic structure of the occupied valence orbitals of Na$_6$Pb is $(1a_{1g})^2$ $(1t_{1u})^6 (2a_{1g})^2$. The $1a_{1g}$ cluster level, which is localized on the Pb atom and has dominant s character, is substantially more bound than the other levels due to the very attractive s-part of the Pb pseudopotential (the difference in binding energy between the $1a_{1g}$ level and the $1t_{1u}$ manifold is 7 eV). This $1a_{1g}$ level can be identified with the $6s$ level of the Pb atom. The HOMO level $2a_{1g}$ is doubly occupied and there is a gap of 1 eV between this level and the LUMO (of e_g symmetry). The electron density is spherically symmetric, consistent with the closed shell character of Na$_6$Pb [28]. The bonding charge, defined as the difference between the cluster density and the superposition of the atomic densities, also has a spherically symmetric shape, and is maximal in the region

between the Pb atom and the shell of Na atoms. The filling of the $1t_{1u}$ levels in the series Na_mPb ending with Na_6Pb can be viewed as the filling of the atomic $6p$ shell of Pb, perturbed evidently by the effect of the surrounding Na atoms. In summary, the electronic structure of small Na_mPb clusters is dominated by the presence of the Pb atom.
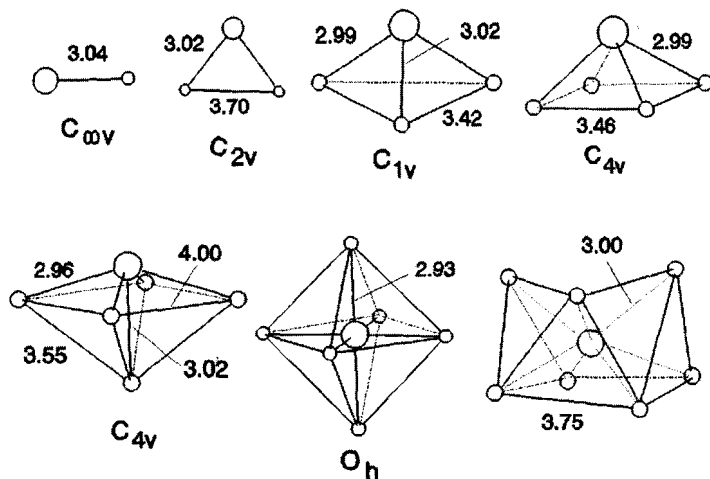
Figure 7.2. Lowest energy structures of Na_mPb, $m = 1-7$. Small spheres represent Na atoms and the large one the Pb atom. Symmetries are indicated, and bond lengths are given in Å. Reproduced from L. C. Balbás and J. L. Martins, *Phys. Rev. B* **54**, 2937 (1996) with permission of the American Physical Society.

The closed shells structure of Na_6Pb is, of course, responsible for the observed high abundance of this cluster [26] but a full explanation requires considering other Na_mPb clusters. The energy to remove a Na atom from those clusters (or evaporation energy) is plotted in Fig. 7.3 [31]. There is a pronounced odd–even oscillation of the evaporation energy as a function of m and the smallest value occurs for Na_7Pb. The explanation proposed for the high abundance of Na_6Pb is based on a two-step mechanism [32]. Under the experimental conditions of a Pb concentration of the order of 10% in the mixed Pb–Na vapor, growth of mixed clusters containing a single Pb atom is favorable compared to other possibilities. Formation of pure Pb clusters is unlikely because of

the small concentration of Pb in the Na–Pb vapor mixture. The gain in binding energy in the step

$$Na_{m-1}Pb + Na \rightarrow Na_m Pb \qquad (7.3)$$
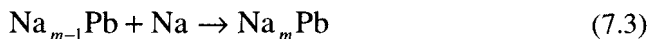
that can be called the capture energy, can be read from Fig. 7.2; this is equal to the evaporation energy of Na_mPb. It is positive, that is, the process is exothermic, so the clusters tend to grow. This capture energy is higher than the capture energy for the growth of small pure Na clusters, and consequently mainly Na_mPb clusters will form if there is a supply of Pb atoms. The competition between different Pb atoms to form Na_mPb clusters and the fact that the capture energy of Fig. 7.2 quickly decreases as m increases suggest that most clusters will not grow larger than Na_7Pb or Na_8Pb and this completes the first part of the argument.
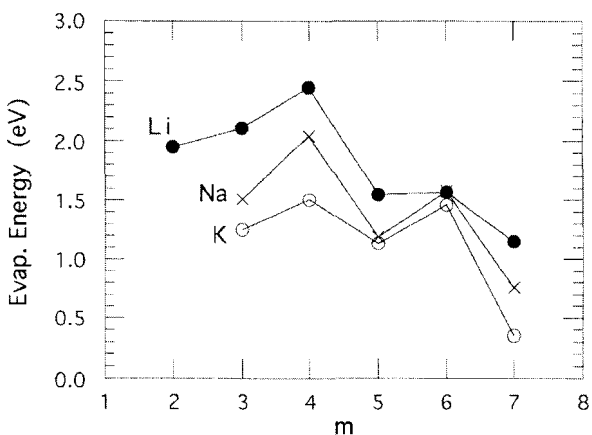
Figure 7.3. Energy required to remove an alkali atom from Li_mPb, Na_mPb and K_mPb. Reproduced from J. A. Alonso *et al.*, *Chem. Phys. Lett.* **289**, 451 (1988) with permission of Elsevier.

On the other hand, during the growth process the clusters become hot, and they can cool down by evaporating Na atoms. The evaporation energy increases by a factor of more than 2 between the two consecutive evaporation events $Na_7Pb \rightarrow Na_6Pb + Na$ and $Na_6Pb \rightarrow Na_5Pb + Na$, so it is reasonable to expect that the evaporation cascade stops after the first of those two reactions because of the high evaporation energy of the

second one, and in this way the population of Na_6Pb becomes highly enriched. Evidence for enormous differences in the abundance arising from relatively small differences in the evaporation energies is well documented in experiments for $(C_{60})_N$ [33]. The spectrum of cold $(C_{60})_N$ clusters is smooth. For laser heated clusters, the abundance of $(C_{60})_{13}$, a compact cluster with the form of an icosahedron, is eight times larger than the abundance of $(C_{60})_{14}$, even if the evaporation energy of $(C_{60})_{14}$, that is, the energy to remove a C_{60} molecule, is only 20% smaller than the evaporation energy of $(C_{60})_{13}$.

Li_6C and Na_6Pb are just two clusters in a broad class M_6X, where X = C, Si, Ge, Sn, Pb and M = Li, Na, K, Rb, Cs. This family has been studied by Marsden [34] and Schleyer [29]. Their structure is the centered octahedron of Fig. 7.1. The single exception is Li_6Sn; in this case the Sn atom is on the surface, but coordinated to the six Li atoms [35]. The special location may be due to the similar atomic radii of Sn and Li. The bonding in the entire family is similar, having substantial ionic character. Most of the clusters are quite floppy, and the most rigid one is Li_6C, which is exceptionally stable (1108 KJ/mole, relative to separated atoms [34]). The binding energy increases as the alkali atom changes from Cs to Li, and this reflects the residual alkali–alkali bonding. On the other hand, by changing the tetravalent atom, the binding energies decrease in the order $M_6C > M_6Si \approx M_6Ge > M_6Sn \approx M_6Pb$, and this order follows the variation of the Allred–Rochow electronegativity scale [36] down group 14. This means that the stability of Na_6Pb is relatively low compared with other M_6X clusters. Hence, a large number of clusters in this family await experimental synthesis.

The charge transfer to the impurity induces a weakening of the bonds between the alkali atoms compared to the corresponding pure alkali clusters, and this affects their thermal properties. Comparative simulations of the thermal behavior of Li_6Sn and Li_7 indicate that Li_7 exhibits solid-like behavior at 100 K (showing only small atomic oscillations) whereas liquid-like behavior is observed for Li_6Sn at that temperature [35]. The values of the r.m.s bond length fluctuation δ (see Eq. (3.11)) for Li_6Sn are 0.07 at 100 K and 0.17 at 300 K, which are much higher than the values 0.036 and 0.063 for Li_7 at the same temperatures, respectively.

The ionization potentials of Cs clusters containing oxygen impurities display pronounced drops at some particular sizes [37] that reveal the

occurrence of closed electronic shells. The electronic configuration of the oxygen atom is $1s^2\, 2s^2\, 2p^4$. In the clusters, the $2p$ shell of the oxygen atom becomes filled by electrons donated by the Cs atoms forming O^{2-} anions, and the remaining valence electrons of the cluster behave according to the shell model [38]. That is, Cs_nO_x clusters have $m-2x$ nearly free electrons. The drops in the ionization potential are reproduced by the calculations [38].

Halogen impurities represent the extreme case of a large difference of electronegativity with respect to the alkali host. At the same time, only one extra electron is required to fill the external p shell of the halogen atoms, and experiments and calculations confirm this picture. Optical absorption measurements for Na_9X (X = F, Cl, Br and I) [39] and for $Na_{10}Br_2$ indicate that each halogen atom ties up one of the metallic electrons, leaving eight delocalized electrons in the cluster. The collective plasmon is red-shifted and broadened with respect to Na_8. Quantum chemical calculations for Li_9F have revealed where the F atom resides [40]. The ground state has low symmetry (C_s), and the F atom resides in an external position and has three close neighbors. The low lying isomers have low or not symmetry, with the atom again in external positions. This contrasts with the high symmetry of Li_8 and Li_9^+. For the ground state and the two lowest lying isomers of Li_9F, the three highest occupied Molecular Orbitals and the LUMO are composed mainly of Li atomic orbitals, and the HOMO–LUMO gaps have a magnitude similar to the gap in Li_8 and Li_9^+. The optical spectrum of the doped cluster, calculated by the Configuration Interaction method taking into account single excitations only, shows a red shift with respect to that of Li_8 and a large spreading of the allowed transitions due to the substantially lower symmetry.

7.6 Impurities in Aluminum Clusters

Carbon exhibits different bonding behavior in Al clusters depending on their size and charge [41]. Neutral Al_3C has a C_{2v} structure. Addition of an electron leads to a D_{3h} symmetry for Al_3C^- with an Al–C bond length of 3.61 a.u. Al_4C has a Jahn–Teller distorted planar structure with the carbon atom four-fold coordinated but somehow displaced from the center of a deformed square (one of the Al–Al bonds is broken). A nearly

degenerate tetrahedral isomer also exists. Addition of an electron lifts the degeneracy favoring the planar structure and reducing the distortion in Al_4C^-. The structures of neutral and anionic Al_5C are planar, with the C atom four-fold coordinated to Al atoms like in Al_4C. The fifth Al atom is attached to the pair of Al atoms forming one edge of the distorted square. Al–C bond lengths in all these small clusters are between 3.50 and 4.04 a.u., similar to the bond lengths in the AlC dimer (3.78 a.u.). The energy to remove the C atom is larger for Al_4C (7.32 eV) compared to the other two clusters (6.78 and 6.88 eV for Al_3C and Al_5C, respectively). In addition, the adiabatic electron affinity of Al_4C (2.18 eV) is lower. These two features can be justified if Al acts as a monovalent atom, like in the pure small Al_N clusters, and the electrons, one per Al atom, go to fill the $2p$ shell of C in Al_4C. The bonding between C and Al in these small Al_mC clusters is covalent [41].

Al_{13} has a very symmetrical (icosahedral) structure and 39 valence electrons, short of just one to become a magic cluster with 40 electrons. As expected the measured electron affinity of Al_{13} is large, 3.6 eV [42], a value similar to that for Cl (3.61 eV), which has the highest affinity among the elements of the Periodic Table. Al_{13}^- is then a very stable anion. The same number of electrons, 40, is obtained by replacing one Al atom by a tetravalent atom, C, Si, Ge, Sn or Pb, and it has been conjectured that icosahedral $Al_{12}X$ clusters with X = C, Si, Ge, Sn or Pb, could become candidates for cluster assembled materials. Calculations for $Al_{12}C$ have predicted an icosahedral structure with the C atom in the center of the icosahedron [41, 43, 44]. Also, the electron affinity of $Al_{12}C$ is smaller than for the clusters of neighbor sizes $Al_{11}C$ and $Al_{13}C$, and the energy to remove an Al atom is larger. A prediction of icosahedral structure was also made for $Al_{12}Si$ and $Al_{12}Ge$, but for $Al_{12}Sn$ the Sn atom was predicted to substitute an Al atom on the surface of the icosahedron [44–46].

The electronic structure of this family has been probed by photoelectron spectroscopy (PES) [47]. The PES spectra of $Al_{12}X^-$ with X = C, Ge, Sn, Pb, measured at two photon energies, 193 nm and 266 nm, are shown in Fig. 7.4, where the spectrum of Al_{13}^- is also given. The spectrum of Al_{13}^- is well understood. Starting with the shell model and reducing the symmetry by taking into account the icosahedral

structure   leads   to   the   electronic   configuration
$1a_g^2 1t_{1u}^6 1h_g^{10} 2a_g^2 1t_{2u}^6 1g_u^8 2t_{1u}^6$. Theoretical calculations suggest that the
features labeled A and B in panels (a) and (b) of this figure correspond to
electron detachments from the $1t_{2u}$, $1g_u$ and $2t_{1u}$ orbitals, which are
closely spaced in energy [48].
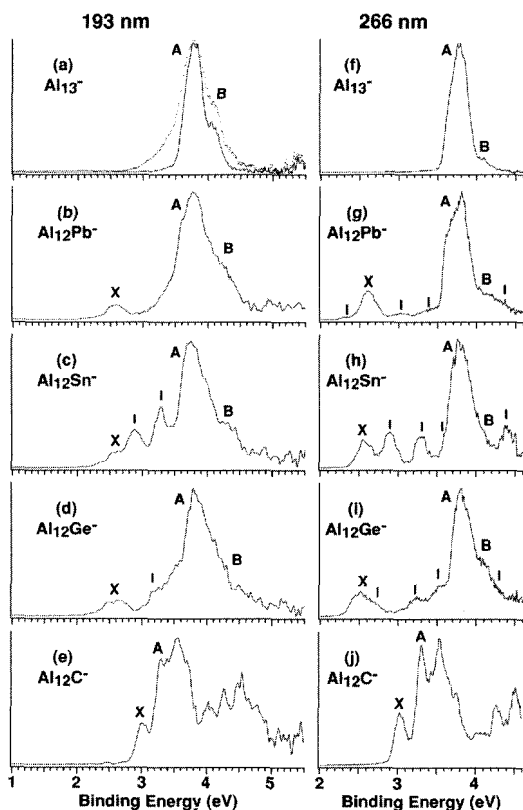
Figure 7.4. Photoelectron spectra of pure and doped Al cluster anions taken at
193 and 166 nm. The continuous and dotted spectra in panel (a) correspond to
vibrational temperatures of about 260 K and 570 K, respectively. The bar
symbols represent nonicosahedral features. Reproduced from X. Li and L. S.
Wang, *Phys. Rev. B*, **65**, 153404 (2002), with permission of the American
Physical Society.

The extra electron of $Al_{12}X^-$ is expected to occupy the next level, $1h_u$, and a large gap should be observed in the spectrum. The gap is observed in the spectrum of $Al_{12}Pb^-$, with a weak feature (X) at lower energies followed by broad features, A and B, at higher energies. The close similarity with the A and B features of Al_{13}^- indicates a rigid filling of the electronic shells for the icosahedral structure. Confirming this idea, features X, A and B are also evident in the spectra of $Al_{12}Sn^-$ and $Al_{12}Ge^-$. The weaker features observed in the spectrum of $Al_{12}Pb^-$ taken at 266 nm, and marked as solid bars, are interpreted as corresponding to a minor isomer, which is more prominent in the spectra of $Al_{12}Sn^-$ and $Al_{12}Ge^-$. The relative intensities of the extra features in $Al_{12}Sn^-$ and $Al_{12}Ge^-$ strongly depend on the source conditions [47]. Calculations for $Al_{12}Sn$ had predicted a structure in which the Sn atom substitutes an Al atom on the surface of the icosahedron. The shape of the PES spectrum indicates, probably, that both this isomer and the isomer with the Sn atom on the center of the cluster are present in the experiments. The PES of $Al_{12}C^-$ is completely different. It shows much higher adiabatic and vertical electron detachment energies and a smaller gap. The spectral features are not dependent on the source conditions, indicating that a single isomer is responsible for the spectrum. Calculations have consistently predicted the icosahedral structure for neutral $Al_{12}C$ [41, 43–45], but the anionic species appears to have a lower symmetry, C_{2v} [41], accounting for the complexity of the spectrum.

Another way of doping Al_{13} in order to have 40 electrons is by attaching a hydrogen atom. $Al_{13}H$ clusters have been produced and exhibit a HOMO–LUMO gap of 1.4 ± 0.2 eV, measured by photoelectron spectroscopy (PES) of the negatively charged species $Al_{13}H^-$ [49]. The calculated ground state structure of $Al_{13}H$ [50] preserves the icosahedral structure of Al_{13}. This icosahedron has a small oblate distortion with two triangular faces slightly closer to the central atom than the other faces, and the H atom sits in a hollow position above the center of one of those two special faces. The distance from the H atom to the cluster center is 5.68 a.u. and the distances between the

central and the surface Al atoms range between 5.00 and 5.08 a.u. The density of electronic states [50] for the predicted structure is consistent with the measured photoelectron spectrum [49]. The binding energy of H to Al_{13} is 3.4 eV [50, 51] and the barrier for diffusion to another hollow position in a neighbor face is 0.08 eV. The state of the H atom can be described as a negatively charged impurity screened by the surrounding electron gas [52], similarly to a H impurity embedded in a vacancy in the Al metal.

Replacing an Al atom in an Al_N cluster by an element of the same group, like B or In, does not change the number of valence electrons. In a mass spectrometric study [53], the intensity distribution of $Al_{N-1}B^-$ was found to be very similar to that of Al_N^-, and magic numbers appear at $N = 13$ and $N = 23$. On the other hand, $Al_{11}B_2^-$ is not magic in the spectrum of clusters with two substituted atoms, that is, $Al_{N-2}B_2^-$. DFT calculations for $Al_{N-1}B^-$ and $Al_{N-1}B$ show that the structures for $N = 12–14$ are based on the icosahedron, and that the B atom occupies the central site of the cluster [54]. $Al_{12}B$ is the most stable cluster of the series, both in the neutral and charged states, and this explains the observed high abundance of $Al_{12}B^-$. Two effects contribute to this high stability: the number of electrons in $Al_{12}B^-$ is 40, a shell closing number; on the other hand the structure is complact and nearly spherical. Also the structures of neutral and charged $Al_{N-2}B_2$ ($N = 12–14$) are based on the icosahedron: the structures are only slightly distorted and again one of the B atoms occupies the central position. In addition $Al_{11}B_2^-$ is more stable than neighbor clusters: the gain in binding energy in the step $Al_{10}B_2^- + Al \rightarrow Al_{11}B_2^-$ is larger than the gains in the steps $Al_9B_2^- + Al \rightarrow A_{10}B_2^-$ and $Al_{11}B_2^- + Al \rightarrow Al_{12}B_2^-$. Wan and Fournier [54] have proposed that the reason for the absence of a high abundance peak of $Al_{11}B_2^-$ resides on the relative stability of the neutrals $Al_{N-2}B_2$: the most stable of these is $Al_{12}B_2$, so the lower abundance of the neutral precursor ($Al_{12}B_2$) accounts for the absence of of a high abundance of the charged species $Al_{11}B_2^-$.

References

1. Kappes, M. M., Schär, M., and Schumacher, E. J., *J. Phys. Chem.*, **91**, 658 (1987).
2. López, M. J., Iñiguez, M. P., and Alonso, J. A., *Phys, Rev. B*, **41**, 5636 (1990).
3. Deshpande, M. D., Kanhere, D. G., Vasiliev, I., and Martin, R. M., *Phys. Rev. A*, **65**, 33202 (2002).
4. Deshpande, M. D., Kanhere, D. G., P. V. Panat, Vasiliev, I., and Martin, R. M., *Phys. Rev. A*, **65**, 53204 (2002).
5. Bol, A., Martín, G., López, J. L., and Alonso, J. A., *Z. Phys. D*, **28**, 311 (1993).
6. Ballone, P., Andreoni, W., Car, R., and Parrinello, M. *Europhys. Lett.*, **8**, 73 (1989).
7. Mañanes, A., Iñiguez, M. P., López, M. J., and Alonso, J. A., *Phys. Rev. B*, **42**, 5000 (1990).
8. Rice, S. A., *Z. Phys. Chem.* **156**, S53 (1988).
9. Balbás, L. C., Rubio, A., and Torres, B., *Z. Phys. D*, **31**, 269 (1994).
10. Pollack, S., Wang, C. R. C., Dahlsheid, T. A., and Kappes, M. M., *J. Chem. Phys.* **96**, 4918 (1992).
11. Bonacic-Koutecky, V., Gaus, J., Guest, M., and Koutecky, J., *J. Chem. Phys.* **96**, 4934 (1992).
12. Dahlseid, T. A., Kappes, M. M., Pople, J. A., and Ratner, *J. Chem. Phys.* **96**, 4924 (1992).
13. Kappes, M., Schär, M., Yeretzian, C., Heiz, U., Vayloyan, A., and Schumacher, E., *Physics and Chemistry of Small Clusters*, NATO ASI Series B, Vol. 158. Eds. Jena, P., Rao, B. K., and Khanna, S. N., Plenum Press, New York (1987), p. 263.
14. Yeretzian, C., *J. Phys. Chem.*, **99**, 123 (1995).
15. Baladrón, C., and Alonso, J. A., *Physica B*, **154**, 73 (1988).
16. Zhang, S. B., Cohen. M. L., and Chou, M. Y., *Phys. Rev. B*, **36**, 3455 (1987).
17. Röthlisberger, U., and Andreoni, W., *Chem. Phys. Lett.*, **198**, 478 (1992).
18. Yannouleas, C., Jena, P., and Khanna, S. N., *Phys. Rev. B*, **46**, 9751 (1992).
19. Pewestorf, W., Bonacic-Koutecky, V., and Koutecky, J., *J. Chem. Phys.*, **89**, 5794 (1988).
20. Fantucci, P., Bonacic-Koutecky, V., Pewestorf, W., and Koutecky, J., *J. Chem. Phys.*, **91**, 4229 (1989).
21. Bonacic-Koutecky, V., Fantucci, P., Fuchs, C., Koutecky, J., and Pittner, J., *Z. Phys. D*, **26**, 17 (1993).
22. Bonacic-Koutecky, V., Cespiva, L., Fantucci, P., Fuchs, C., Koutecky, J., and Pittner, J., *J. Chem. Phys.*, **186**, 275 (1994).
23. Deshpande, M., Dhavale, A., Zope, R. R., Chacko, S., and Kanhere, D., *Phys. Rev. A*, **62**, 063202 (2000).

24. Cheng, H. P., Barnett, R. N., and Landman, U., *Phys. Rev. B* **48**, 1820 (1993).
25. Bonacic-Koutecky, V., Fantucci, P., and Koutecky, J., *Chem. Rev.*, **91**, 1035 (1991).
26. Yeretzian, C., Röthlisberger, U., and Schumacher, E., *Chem. Phys. Lett.*, **237**, 334 (1995).
27. Chang, J., Stott, M. J., and Alonso, J. A., *J. Chem. Phys.*, **104**, 8043 (1996).
28. Balbás, L. C., and Martins, J. L., *Phys. Rev. B*, **54**, 2937 (1996).
29. Von R. Schleyer, P., and Kapp, J., *Chem. Phys. Lett.* **255**, 363 (1996).
30. Würthwein, E. U., Sen, K. D., Pople, J. A., and Von R. Schleyer, P., *Inorg. Chem.*, **22**, 496 (1983).
31. Alonso, J. A., Molina, L. M., López, M. J., Rubio, A., and Stott, M. J., *Chem. Phys. Lett.*, **289**, 451 (1988).
32. Molina, L. M., López, M. J., Rubio, A. Alonso, J. A., and Stott, M. J., *Int. J. Quantum Chem.* **69**, 341 (1998).
33. Hansen, K., Hohmann, H., Müller, R., and Campbell, E. E. B., *J. Chem. Phys.*, **105**, 6088 (1996).
34. Marsden, C. J., *Chem.Phys. Lett.*, **245**, 475 (1995).
35. Joshi, K., and Kanhere, D. G., *Phys. Rev. A*, **65**, 043203 (2002).
36. Allred, A. L., and Rochow, E. J., *J. Inorg. Nucl. Chem.*, **5**, 264 (1958).
37. Bergman, T., Limberger, H., and Martin, T. P., *Phys. Rev. Lett.*, **60**, 1767 (1988).
38. Lammers, U., Borstel, G., Mañanes, A., and Alonso, J. A., *Z. Phys.D*, **17**, 203 (1990).
39. Koretsky, G., Dahlseid, T., Pollack, S., Wang, C., Hunter, J., Alameddin, G., Cameron, D., Liu, S., and Kappes, M., *Ber. Bunsen-Ges. Phys. Chem.*, **96**, 1270 (1992).
40. Dahlseid, T. A., Pople, J. A., Ratner, M. A., and Kappes, M. M., *J. Phys. Chem*, **98**, 8851 (1994).
41. Rao, B. K., and Jena, P., *J. Chem. Phys.*, **115**, 778 (2001).
42. Li, X., Wu, H., Wang, X. B., and Wang, L. S., *Phys. Rev. Lett.*, **81**, 1909 (1998).
43. Seitsonen, A. P., Laaksonen, K., Nieminen, R. M., and Klein, M. L., *J. Chem. Phys.*, **103**, 8075 (1995).
44. Gong, X. G., *Phys. Rev. B*, **56**, 1091 (1997).
45. Gong, X. G., and Kumar, V., *Phys. Rev. Lett.*, **70**, 2078 (1993).
46. Kumar, V., Bhattacharjee, S., and Kawazoe, Y., *Phys. Rev. B*, **61**, 8541 (2000).
47. Li, X., and Wang, L. S., *Phys. Rev. B*, **65**, 153404 (2002).
48. Akola, J., Manninen, M., Hakkinen H., Landman, U., Li, X., and Wang, L. S., *Phys. Rev. B*, **60**, R11297 (1999).
49. Burkart, S., Blessing, N., Klipp, B., Müller, J., Ganteför, G., and Seifert, G., *Chem. Phys. Lett.*, **301**, 546 (1999).

50. Duque, F., Mañanes, A., Molina, L. M., López, M. J., and Alonso, J. A., *Int. J. Quantum Chem.*, **86**, 226 (2002).
51. Khanna, S. N., and Jena, P., *Chem. Phys. Lett.*, **218**, 383 (1994).
52. Mañanes, A., Duque, F., Méndez, F., López, M. J., and Alonso, J. A., *J. Chem. Phys.*, **119**, 5128 (2003).
53. Nakajima, A., Sugioka, T., Kishi, T., and Kaya, K., *Physics and Chemistry of Finite Systems: From Clusters to Crystals*, Eds P. Jena, S. N. Khanna and B. K. Rao, Kluwer, Dordrecht, Vol. I, p. 99 (1992).
54. Wan, J., and Fournier, R., *J. Chem. Phys.*, **119**, 5949 (2003).

This page intentionally left blank

8.   Clusters of the Transition Metals

8.1 Noble Metal Clusters

8.1.1 Electronic shell effects

The free atoms of the transition metals series have an incomplete d shell in the ground state or in low lying excited states. The d electrons are responsible for many properties of these elements as free atoms or in the bulk phase. In the same way, most properties of clusters of the transition elements reflect the rather localized behavior of the d electrons.

Cu, Ag and Au occupy a special place at the end of the $3d$, $4d$ and $5d$ periods respectively. The d shell is filled with 10 electrons and the valence shell contains a single s electron. The d band is well buried below the Fermi level in the bulk metal and this leads one to expect some similarities between the electronic structure of noble metal clusters and the alkali metal clusters. Experiments for noble metal clusters [1, 2] indicate the existence of shell effects similar to those observed in alkali clusters. For instance, the mass spectrum of cationic clusters obtained by bombarding the metal with inert gas ions shows two types of anomalies. The first one, observed for small clusters, is an odd–even alternation of the abundance, such that the population of odd-N clusters is higher than the population of even-N clusters. The other anomaly is that a steep drop of the cluster intensities occurs after the sizes $N = 3, 9, 21, 35, 41, 59, \ldots$ By focusing on the external s electrons, the experimental observations are explained by a model similar to that for alkali clusters, that is, assuming that the s electrons are confined in a smooth spherically symmetric potential well. In the bombardment experiments the clusters are born ionized, so the mass spectrum reflects the relative stabilities of charged clusters in which the number of electrons is N-1. From the list

given above, N-1 = 2, 8, 20, 34, 40, 58, ... which reproduce the shell closing numbers of alkali clusters. Negatively charged clusters can be produced by the same technique and their magic numbers again correspond to $N + 1$ = 8, 18, 34, 40, ... electrons. The ionization potential shows the expected drops at the electronic shell closings [3].

Photoelectron spectroscopy (PES) studies of cluster *anions* X_N^- give direct information on the structure of the spectrum of electronic energy levels (see Fig. 5.2). The structure of the spectrum is very rich and every cluster species has its own fingerprint. The photoelectron threshold can be taken as an estimate of the electron affinity. When the corresponding neutral cluster X_N has closed shells, the electron is extracted from the lowest unoccupied molecular orbital (LUMO) of X_N. Consequently the photoelectron threshold reflects the shell effects. Indeed, measured detachment energies of Ag_N^- [4] and Cu_N^- [5, 6] show drops between N = 7 and N = 8, and between N = 19 and N = 20, which again indicate major shell closings. Cha *et al.* [7] have analyzed the PES of Cu_N^- clusters with N = 1–18, focusing on the region of the spectrum of that is predominantly of *s*-like character (that is, derived from the atomic 4*s* orbitals). The observed peaks can be qualitatively assigned to the electronic shells of the ellipsoidal jellium model if one takes into account additional effects like shake-up processes (the simultaneous excitation of bound electrons accompanying the photoemission process), multiplet splittings (caused by the spin–spin interaction of the electrons) and *s–d* hybridization (for orbitals located close to the 3*d* band).

Chemical probes also point to electronic structure that can be undestood in terms of the spherical jellium model. Winter *et al.* [8] have recorded the mass spectrum of Cu clusters, generated by laser vaporization of copper metal, after the clusters have passed through a flow tube reactor with O_2 added to the gas flow. The observed result is that Cu_{20}, Cu_{34}, Cu_{40}, Cu_{58} and Cu_{92} are unreactive towards O_2 and the lack of reactivity is ascribed to the closed shell electronic structure of these clusters.

In spite of the successful description of some properties of noble metal clusters by a shell model that neglects the d electrons, these are required to explain a number of properties. The d electrons contribute to the bonding in a crucial way. The contribution of the d band to the cohesive energy of noble metals is also well documented [9, 10].

8.1.2 Interplay between d and s electrons

The analysis in Section 8.1.1 provides information on the electronic structure in the energy region near the top of the occupied molecular states of the cluster. But one can probe deeper down into the structure of electronic levels. Ultraviolet Electron Spectroscopy (UPS) has been used [6, 11] to probe the $3d$ electrons of Cu_N^- anions with N up to about 400. A large peak is found, roughly 2 eV deeper than the weak initial threshold, and this large peak moves smoothly with cluster size. For small clusters its position merges with the position of the d levels of the atom and for large clusters the peak matches well with the onset of the $3d$ band of bulk Cu. This feature is attributed to the photodetachment of $3d$ electrons. Unlike the large size-dependent variations of the UPS threshold, which is associated to the $4s$ electrons, the $3d$ feature shifts monotonously with the cluster size.

In the band picture of the noble metals, with localized d electrons and extended s electrons, the s–d mixing is substantial [10]. The picture is far from that of the free electrons in the alkali metals. It is, therefore, intriguing how well the shell model works in noble metals. Fujima and Yamaguchi [12] have performed DFT calculations for Cu_N clusters with sizes up to $N = 19$ and a variety of model structures. The analysis of the molecular orbitals (MO) shows that these are of two types. The first type is formed by MOs built from atomic $3d$ orbitals. These span a narrow energy range of a width comparable to that of the d band of the solid, and do not mix much with the second type of MOs, which are derived from atomic $4s$ and $4p$ orbitals. The $3d$ charge is localized around atoms, whereas the sp charge is extended over the whole cluster. Fujima and Yamaguchi related their results to the shell model. Disregarding the MOs with d-character on the atoms, the sequence of the remaining MOs can be reproduced rather well by considering a spherical model potential with a small anharmonic term. This is essentially the form of the effective potential in the spherical jellium model. However, when the cluster lacks a central atom, as is the case of the icosahedral structure of Cu_{12}, a three-dimensional Gaussian potential barrier had to be added to simulate the missing atom. The good one-to-one correspondence between the energy levels of the full calculation and those of the model potential leads to the explanation of why the shell model is applicable to Cu clusters. For $3 \leq N < 8$, the d band is located in the energy gap between the molecular levels with overall symmetries comparable to

those of the $1S$ and $1P$ jellium levels (here, the angular momentum quantum number of the delocalized jellium levels are labeled with capital letters, to avoid confusion with the atomic s, p and d orbitals), between the $1P$ and $1D$ levels for $9 \leq N < 18$, between the $1D$ and $2S$ levels for $19 \leq N < 20$, and so on. The atomic d levels are always filled.

8.1.3 Structure

Massobrio *et al.* [13] have performed DFT calculations optimizing the structures of Cu clusters with $N \leq 10$. In general, the ground state and local minimum structures are similar to those of Na_N, although the Cu clusters tend to prefer more compact arrangements. The angular decomposition of the molecular orbitals shows that these bear some relation to the shell model, although this character is significantly less pronounced than in Na clusters. The degree of s–d hybridization appears to be larger compared to the results of Fujima and Yamaguchi [12], and a likely reason is the fact that the later authors assumed more symmetric geometries. Massobrio *et al.* extended their calculations to cluster anions [14] and used the results to interpret the measured photoelectron spectra [7]. A linear chain was obtained for Cu_3^-, a planar trapezoidal configuration (C_{2v} symmetry) for Cu_5^-, two nearly degenerate isomers with C_{3v} (capped octahedron) and D_{5h} (pentagonal bipyramid) symmetries, respectively, for Cu_7^-, and a bicapped pentagonal bipyramid (C_2 symmetry) for Cu_9^-. One-electron vertical detachment energies were calculated as a difference of selfconsistent total energies

$$\Delta E(k) = E_{final}(k) - E_{initial} \tag{8.1}$$

where $E_{initial}$ is the total energy of the initial state of Cu_N^-, characterized by occupations $(n_1, \ldots n_k, \ldots n_M)$ of the M electronic eigenstates, and $E_{final}(k)$ is the total energy when an electron has been removed from a given state k. This energy is obtained in a constrained calculation for the electronic configuration $(n_1, \ldots n_k-1, \ldots n_M)$ in which the wave function of the k-th eigenstate is kept frozen whereas the other wave functions are allowed to relax. In this way screening is included, although the relaxation of the hole is not. With this procedure a consistent

interpretation of the photoelectron spectra of Cu_3^-, Cu_5^-, Cu_7^- and Cu_9^- was achieved. The early interpretation [7] in terms of the ellipsoidal jellium model remains valid to a large extent. The comparison with experiment supports the C_{3v} structure for Cu_7^-. Massobrio *et al.* were also able to account for finite temperature effects by running molecular dynamics simulations for Cu_7^- at $T = 300$ K and 400 K and taking temporal averages of the density of states and of the excitation energies. Thermal broadening led to a splitting of the first peak in the calculated photoelectron spectrum of this cluster, whose magnitude agrees well with the experimental splitting of 0.12 eV.

Small Ag_N clusters and their positive and negative ions have been studied by Bonacic-Koutecky and coworkers [15, 16]. Cluster geometries were optimized at the Hartree–Fock level, replacing the cores by an effective core potential. For the different isomers obtained in this way, a Configuration Interaction treatment of the $5s$ electrons was carried out to recalculate the energies. Concerning trimers, only the anionic one Ag_3^- is linear, whereas the neutral and cationic trimers are planar. All cationic clusters larger than tetramers assume three-dimensional geometries, starting with Ag_5^+, which is a trigonal bipyramid. But the competition between two and three-dimensional structures is more pronounced for neutral and anionic clusters. Ag_5 and Ag_5^- are still planar and Ag_6, that marks the transition to three-dimensional structures in the neutral case, is a rather flat pentagonal pyramid. Three-dimensional structures of anion clusters also begin with Ag_6^-, which is a bicapped deformed tetrahedron. The net charge also influences the precise three-dimensional geometries adopted for $N \geq 7$. Binding energies per atom increase with cluster size and indicate a sligthly higher stability of systems with eight valence electrons. This becomes confirmed by a large drop of *IP* between Ag_8 and Ag_9 and also by the pronounced minimum of the electron affinity at Ag_8. The comparison of the measured photodetachment spectra [4, 17] of the anions with the calculated vertical detachment energies and with the energies of the excited states of the neutral species at the linear geometries of the anions allowed an assignment of the anionic cluster geometries that confirmed the results of the total energy optimizations.

8.1.4 Special properties of gold clusters

Interest in gold clusters derives from their unusual catalytic properties for selective oxidation of CO [18, 19], their resistance to oxidation [20] and for enabling selective binding of DNA [21]. Also gold clusters have potential applications in nanoelectronics [22, 23]. Gold clusters present peculiar differences with respect to the copper and silver clusters.
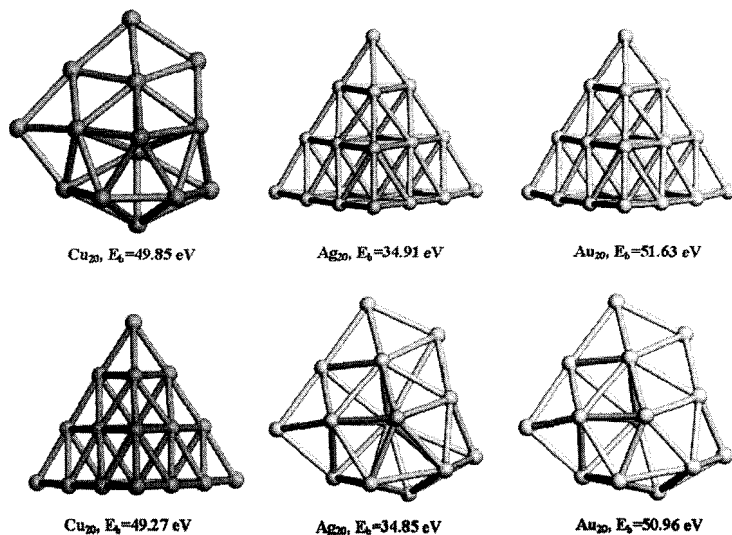
Figure 8.1. Lowest energy and metastable structures of Cu_{20}, Ag_{20} and Au_{20}, and their binding energies. Reproduced from J. Wang, G. Wang and J. Zhao, *Chem. Phys. Lett.* **380**, 716 (2003) with permission of Elsevier.

Au_{20} has a HOMO–LUMO energy gap of 1.77 eV, measured by photoelectron spectroscopy of the anion [24]. This gap is even larger than the gap in C_{60} (1.57 eV), suggesting that Au_{20} should have an inert chemical character and a symmetrical geometry. DFT calculations have predicted for the neutral and the anionic clusters a tetrahedral (T_d) structure [24, 25], surprisingly similar to that shown for Na_{20} in Fig. 4.9. This is a small piece of bulk gold with a small relaxation. Each of the four surfaces represents a (111) surface of *fcc* gold. Each planar surface of the cluster contains ten atoms, and all except one of those ten atoms

are shared by two or three facets. The binding energy of the neutral cluster is 51.63 eV (or 2.58 eV per atom). The comparison with Cu and Ag clusters of the same size reveals interesting differences [25]. The ground state structure of Cu_{20} has a compact C_s structure given in Fig. 8.1. Its total binding energy with respect to the separated atoms, is 49.85 eV. The tetrahedral isomer of Cu_{20} has a binding energy of 49.72 eV, which is very close, only 0.13 eV lower. In the Au case the stability is reversed and the binding energy of the T_d structure (51.63 eV) is 0.67 eV higher than the binding energy of the C_s structure. As an intermediate case, the T_d and C_s structures of Ag_{20} are nearly degenerate.

Table 8.1. Minimum size for the onset of three-dimensional geometries in neutral and charged noble metal clusters. Data collected from [27].

	Cation	Neutral	Anion
Cu	5	7	6
Ag	6	7	6
Au	8	12	13

The ground state structure of neutral and anionic Au_{20} formed from planar facets is perhaps not too surprising in view of the fact that small Au clusters also tend to be planar up to larger sizes than the corresponding Cu or Ag clusters. Gas phase mobility experiments have provided evidence for two-dimensional structures of Au_N^- extending up to Au_{12}^- at least [26]. DFT calculations corroborate this conclusion, predicting that anionic Au clusters are planar up to $N = 13$ or 14 [26–28]. Au is then the metallic element having the largest two-dimensional clusters. In contrast Cu_N^- and Ag_N^- become three-dimensional earlier [26, 27]. Table 8.1 gives the predictions for the onset of three-dimensional geometries for cationic, neutral and anionic clusters of the three noble metals, from DFT calculations using scalar relativistic pseudopotentials and a basis of numerical pseudoatomic orbitals [27]. The early occurrence of three-dimensional structures for silver is also demonstrated by ion mobility experiments for Ag_N^+ [28].

The tendency of Au to favor planar structures is due to relativistic effects. The main factors are the stabilization of the atomic $6s$ orbital and

the destabilization of the $5d$ orbitals, bringing them closer in energy [29]. This enhances the s–d hybridization. The relativistic contraction of the $6s$ orbital also contributes to a shortening of the interatomic bond distances, resulting in an increase of the d–d overlap between orbitals of neighbor atoms. Consequently the d electrons are more delocalized over the cluster volume and the d band is wider compared to Cu_N^- and Ag_N^-. These features have the effect of favoring planar structures [29].

The situation concerning the structure of medium size and large gold clusters is controversial. X-ray powder diffraction studies of clusters with sizes $N = 38$, 75, 101, 146, 200, 225 and 459 passivated with organic molecules have been interpreted as revealing ordered structures with an underlying *fcc* lattice: truncated octahedra for $N = 38$, 225 and 459, and truncated decahedra for the rest [30]. But Garzon and coworkers [31] have performed calculations using semiempirical many-atom potentials whose results, corroborated by DFT calculations [32], suggest instead that the structures for many sizes between $N = 38$ and $N = 75$ are disordered. For two cases studied in detail, Au_{38} and Au_{75}, calculated structure factors for those disordered geometries agree equally well with experiment as the structure factors from the *fcc* ordered structures.

8.1.5 Optical properties

The core affects the valence electrons of atoms through the exclusion principle, its mean Coulomb potential, many-body core–valence correlations and core relaxation following atom aggregation. In contrast to alkali clusters, where the core electrons do not strongly affect the optical properties, a different situation is found for the noble metal clusters due to the s–d hybridization. The measured surface plasmon frequencies of negatively charged silver clusters are redshifted with respect to the free electron value, and the redshift increases with decreasing cluster size [33, 34]; in contrast these are blueshifted for positive and neutral clusters, and the shift is larger for positive clusters. This behavior is connected with the $4d$ electrons. For example, the s–d polarization screens the electron–electron interaction and reduces the bulk plasma frequency of silver from the free electron value of 9 eV to the experimental value of 3.8 eV.
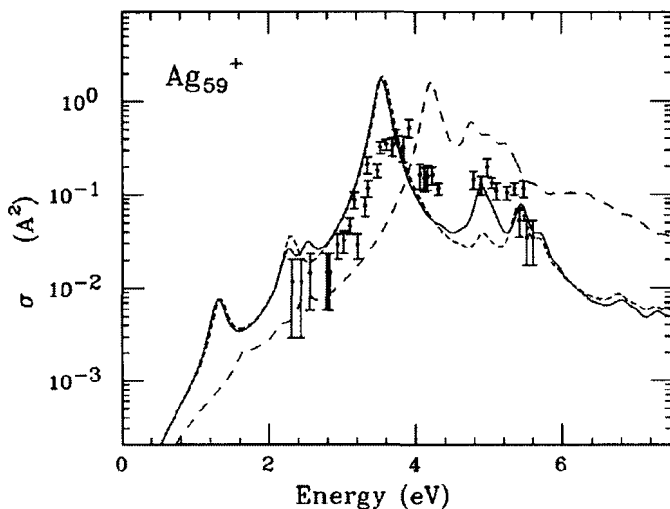
Figure 8.2. Experimental (points with error bars) and calculated (lines) photoabsorption cross section per electron of Ag_{59}^+. Continuous and short dashed curves are for *bcc* and *fcc* geometries, respectively, including core polarization. The long dashed curve is for an *fcc* cluster without core polarization. Reproduced from L. Serra and A. Rubio, *Phys. Rev. Lett.* **78**, 1428 (1997) with permission of the American Physical Society.

Liebsch [35] has proposed a model in which the 5*s* electrons of Ag are described by a uniform jellium model and the effects associated with the polarization of the 4*d* electrons are included by means of a background with the experimental dielectric function $\varepsilon_d(\omega)$ of the bulk metal and a radius R_d slightly smaller than the radius R of the jellium background. The role of the nonpolarizable surface layer is important, since it accounts for the different screening in the interior of the cluster and at its surface. The TDLDA (see Chapter 5) for this model reproduces qualitatively the characteristic features of the static and dynamical optical response of Ag clusters [36]. The role of the nonpolarizable surface layer is reflected in the opposite behavior of the surface plasmon with increasing cluster size in positive and negatively charged systems: the induced density is located inside the polarizable background in the first case and outside in the second, and there is a reduction of the thickness $R-R_d$ as the size of the cluster increases due to the progressive formation of an inner region of atoms with bulk-like coordination. The

model is supported by calculations of the dynamical polarizabilities of a Ag^+ core in different environments [36, 37]. Ions in the interior of the cluster respond like ions in the metal, and ions at the surface respond much like free ions. The difference is a consequence of the more efficient electronic screening in the bulk.

A generalized TDLDA for the optical response of metal clusters has been presented where both valence and core polarization responses are treated microscopically [38]. As in the dielectric model, the decrease of the plasmon frequency with increasing cluster size can be assigned to the evolution of the core polarizability from the free ion regime in small clusters to the fully embedded core in large ones (namely, to the building up of the polarizable background with increasing cluster size). The cross section of Ag_{59}^+ obtained within that formalism is compared in Fig. 8.2 with experiment [33] and with the normal TDLDA without core effects. Good agreement with experiment is only achieved for the full calculation. The specific structure assumed for the cluster (*fcc* or *bcc*) introduces only minor changes in the optical spectrum indicating that core polarization effects are more important than the particular structure of the cluster, and this supports the success of the dielectric continuum model. The theory reproduces the observed cluster size dependence of the surface plasmon frequency.

8.2 General Bonding Properties in Clusters of Transition Metals

One of the recurrent themes in the physics and chemistry of clusters is the analysis of the similarities and differences between the properties of clusters and those of the corresponding bulk material. The beauty of clusters stands from the fact that their properties are size-dependent and this size specificity has potential interest for technological applications. On the other hand one should also recognize that some trends along groups or across periods of the Periodic Table are already imprinted in clusters with few atoms. This is the case for the cohesive properties of $3d$ and $4d$ metals. Painter [39] has performed DFT calculations for model clusters of $3d$ elements, constraining the clusters to be formed by six atoms in an octahedral structure (this defines a lattice fragment of the *fcc*, *bcc* and *hcp* lattices), and allowing for interatomic bond length

relaxation. The $3d$ metals exhibit a broad spectrum of mechanical properties [10]. The experimental cohesive energy E_c of Sc is 3.90 eV/atom. This quantity increases for Ti and has a maximum for V. After this maximum it decreases, showing a minimum of 2.92 eV/atom for Mn. E_c increases again to the right of Mn, having a broad maximum for Fe, Co and Ni, and finally it decreases for Cu. The trend of the Wigner–Seitz radius R_{WS} (the radius of an atomic cell in the metal) is simpler. R_{WS} has a roughly parabolic behavior (lower values in the middle of the series) with Mn deviating although rather weakly, having a value of R_{WS} slightly larger than the interpolated value. This small deviation reflects the minimum of E_c. These trends have been reproduced by band calculations for the bulk metals [40], except for some weak deviations. Painter [39] demonstrated that the trends in the binding energy and interatomic distance of the octahedral clusters reproduce well the experimental trends for the solid metals, with small deviations that are, precisely, the same found for the bulk calculations. Of course, although the trend is well reproduced, the binding strength is lower for clusters and the interatomic distances are also smaller. The conclusion is that the trend in the cohesive energy originates largely from the localized near-neighbor interactions present within the primitive cluster itself.

Table 8.2. Binding energy per atom, distance from atoms to the cluster center, and average magnetic moment per atom for octahedral six-atom clusters. Data collected from [41].

Cluster	E_b (eV)	D (a.u.)	$\overline{\mu}(\mu_B)$
Y	3.53	4.40	0.00
Zr	5.23	3.96	0.33
Nb	5.07	3.64	0.67
Mo	4.05	3.40	0.33
Tc	4.91	3.36	0.33
Ru	4.70	3.40	1.00
Rh	4.03	3.48	0.99
Pd	3.14	3.50	0.00
Ag	1.56	3.76	0.33
Cd	0.39	4.48	0.00

A similar study was done for clusters of 4d elements [41]. A model of a regular octahedral cluster with six atoms was again employed, and the structure was allowed to relax radially. The calculated binding energies per atom and the distance D from the atoms to the cluster centre are given in Table 8.2 (the magnetism will be discussed in Chapter 9). The binding energy E_b shows maxima at Zr and Tc, separated by a minimum at Mo. It also drops to small values near the end of the period for Ag and Cd. This is also the general behavior of the experimental cohesive energy of the bulk metals [10]. The only small differences with respect to the bulk trend are that the first maximum for the bulk metals occurs for Nb (instead of Zr) and the second maximum for Ru. But it is useful to notice that Tc and Ru have very similar cohesive energies and Tc_6 and Ru_6 have also very similar binding energies, so the discrepancies are minor and one can conclude that a good qualitative correspondence exists between clusters and bulk metals concerning the variation of the binding energy across the 4d period.

The Wigner–Seitz radius also shows a simple parabolic variation with a minimum around the middle of the period, and the calculated interatomic distances of the clusters (as well as D of Table 8.2) roughly agree to this behavior. The nearly parabolic behavior of E_b is a consequence of the change from bonding to antibonding character of the d orbitals as the d band filling increases. In the same way as for the 3d-clusters, binding energies and interatomic distances are smaller than in the bulk. There is also a striking correlation between the width of the occupied valence band in clusters and bulk metals. Although the bandwidth of the clusters is smaller, a parabolic variation between Y and Pd is found in both cases; Ag and Cd deviate from that trend because the 4d band is filled in those two cases and the 5s-derived band of nearly free electrons is very broad.

8.3 Electronic and Atomic Structure

Diffraction techniques are not useful to elucidate the structure of very small clusters, but theoretical DFT calculations can be performed with some confidence. Some representative cases will now be discussed.

8.3.1 Nickel clusters

Reuse and Khanna [42] have performed calculations for nickel clusters, Ni_N (N = 2–6, 8, 13). The local spin-density approximation (LSDA) was employed for exchange and correlation, and the inner cores were replaced by nonlocal pseudopotentials. Their main results are that the binding energy varies with size N in a non-monotonous way and that all the clusters have nonzero spin in their ground state (magnetic properties of the transition metals clusters will be discussed in Chapter 9). They found a bond length of 3.78 a.u. and a binding energy E_b of 3.32 eV (or 1.61 eV/atom) for the ground state of Ni_2 . The total spin is S = 1, and this value is consistent with early measurements on matrix isolated clusters [43]. The experimental bond length is between 4.07 and 4.16 a.u. and the estimated binding energy is 2.1 eV [44, 45]. The errors are typical of the LDA: an overestimation of the binding energy and a contraction of the bond length. The geometry of Ni_3 in a solid argon matrix is triangular with C_{2v} symmetry. The apex angle is estimated between 90° and 120° [46]. The symmetry of the ground state found by Reuse and Khanna is also C_{2v} (but near equilateral) with a binding energy of 1.96 eV/atom. The calculated spin was S = 1, the same as in the experiment. They also found C_{2v} (S = 2) and linear (S = 2) low lying isomers. Two degenerate structures with a binding energy of 2.34 eV/atom coexist in the calculated ground state of Ni_4: one is a deformed tetrahedron with D_{2d} symmetry and the other is a square, and both have S = 3. The ground state of Ni_5, is a triangular bipyramid with S = 4 and E_b = 2.83 eV/atom. This structure is 0.2 eV/atom more stable than a square pyramid. For larger clusters the structural study was restricted. An octahedron was initially assumed for Ni_6, although it was allowed to distort. The octahedron showed only minor distortions and the ground state has E_b = 3.27 eV/atom and S = 3. The geometries up to Ni_6 have been later confirmed by other DFT calculations [47, 48].

These results reveal the complexity of clusters of the transition metals: there are normally several low lying states with close energies. One of the reasons is the competition between (i) compact structures maximizing the number of bonds, and (ii) directional bonding compatible with the orientation and filling of the d orbitals. For example, the triangular configuration of Ni_3 optimizes the number of bonds but forces d orbitals into a symmetry which is not optimal for their bonding (the d orbitals in an atom have a square symmetry). In contrast, the linear

geometry of Ni_3 permits to form undistorted d orbital combinations, but it has fewer bonds. The DFT calculations indicate that the linear isomer is only marginally less stable.

Using the binding energies, Reuse and Khanna have calculated fragmentation channels, that is, the energy required to break the Ni_N cluster into two fragments of sizes M and N-M. The channel requiring less energy is the loss of a single atom ($M = 1$) except for Ni_4, that prefers to dissociate into two Ni_2 fragments. The fragmentation energies amount to 3.21, 2.68, 2.92, 4.81 and 5.47 eV for Ni_2, Ni_3, Ni_4, Ni_5 and Ni_6 respectively, so Ni_3 has the lowest fragmentation energy. These results agree with collission induced fragmentation experiments [49].

Ni_7 has been studied in detail. Experiments analyzing its reactivity with nitrogen (N_2) were interpreted as suggesting that the structure is an octahedron with an atom capping one of the faces [50], while early calculations had predicted a pentagonal bipyramid [51]. Nayak *et al.* [52] first noticed that the pentagonal bipyramid is also consistent with a part of the reactivity data, and then optimized both structures using DFT, finding that these are nearly degenerate. The total binding energies are 3.70 eV/atom for the capped octahedron and 3.65 eV/atom for the bipyramid. The magnetic moment is the same for both isomers, 1.14 μ_B /atom (μ_B indicates the Bohr magneton), in fair agreement with the experimental result of 1.53 μ_B [53]. Molecular dynamics simulations using a many body interatomic potential [54] allowed to obtain further insight into the stability of the two structures. The simulations showed that the catchment area for the capped octahedron is much wider than that for the pentagonal bipyramid. In summary, neither the chemical reactivity, nor the magnetic experiments, are inconsistent with the presence of the two isomers in a molecular beam. The results were confirmed by a more complete study of Ni_7 (and Ni_8 also) [55]. The ground state of Ni_7 was the capped octahedron, and a pentagonal bipyramid (Jahn–Teller distorted) was found as the first low lying isomer, only 0.07 eV/atom above the capped octahedron. The ground state of Ni_8 was a distorted bisdisphenoid structure with D_2 symmetry (it can be seen as a rectangular Ni_4 cluster with a dimer above the first diagonal of the rectangle and another dimer below the second diagonal), and several isomers (capped pentagonal bipyramid, bicapped trigonal prism, star, cube and square antiprism) lie close to each other within a narrow range of 0.07 eV/atom above the ground state.

Ni$_{13}$ was also studied in detail [56]. The radial sizes of clusters with perfect icosahedral and cuboctahedral shapes were first optimized for several spin configurations and the lowest energy was obtained for the icosahedral geometry and $S = 4$ ($E_b = 4.23$ eV/atom). The HOMO has a degeneracy of 5 and is occupied by only 3 electrons; the cluster then prefers to undergo Jahn–Teller distortion. By allowing all the interatomic distances to vary independently the cluster distorts to a D_{3d} symmetry, producing a gain in binding energy of 0.16 eV. The distortion is nevertheless, very small, and the total spin does not change. $S = 4$ corresponds to a magnetic moment of 0.61 μ_B per atom.

The isomerism that occurs in small Ni clusters may have a role on the interpretation of the photodetachment spectra of cluster anions. In the photodetachment process a transition occurs from the cluster anion in its ground electronic state to a state of the neutral cluster with the same geometry of the anion. According to the DFT calculations [57] Ni$_2^{2-}$ has two isomers with only slightly different bond lengths ($d = 2.19$ Å and 2.21 Å, respectively). Their binding energies are very similar (2.38 eV and 2.35 eV, respectively) but the spin multiplicities are different (2 and 4, respectively). The study of neutral Ni$_2$ with the same bond lengths as the anions gave triplet and singlet states for $d = 2.19$ Å and triplet and quintet states for $d = 2.21$ Å. Four groups of electronic transitions are identified in the photodetachment spectrum of Ni$_2^{2-}$ [45]: band X (0.9 eV), band I (1.7–2.1 eV), band II (2.1–2.9 eV) and band III (≥ 2.9 eV). This spectrum was interpreted [57] as having contributions from the two nearly degenerate anionic states. Band I was assigned to transitions from Ni$_2^{2-}$ (doublet) to neutral Ni$_2$ (triplet) and from Ni$_2^{2-}$ (quartet) to neutral Ni$_2$ (triplet). Band II was assigned to transitions from Ni$_2^{2-}$ (quartet) to Ni$_2$ (quintet) and band III was assigned to transitions from Ni$_2^{2-}$ (doublet) to Ni$_2$ (singlet). Band I was left unassigned. Ni$_3^{2-}$ also has two structures, linear and triangular, nearly degenerate (atomization energies of 5.04 and 5.01 eV respectively) and with the same spin multiplicity (both are quartets), although an energy barrier of 0.8 eV separates those two structures. Consideration of these two isomers and of different spin states of the corresponding neutrals helps to interpret the photodetachment experiments [58].

The photoabsorption spectrum of Ni_N clusters has been calculated [59] for $N = 2$–6 and $N = 13$ using first order perturbation theory. The positions of the most intense transition and secondary peaks in the spectrum change with cluster size and the spectrum becomes richer as N increases. Two isomers were considered for Ni_4: the square isomer has a main absorption peak at 3.09 eV and the D_{2d} isomer at 3.36 eV. This indicates that the photoabsorption spectrum can provide a fingerprint for the geometry.

8.3.2 Iron clusters

It is interesting to compare the structures of small iron clusters calculated by Ballone and Jones [60] with those of nickel clusters presented in Section 8.3.1. The ground state of Fe_3 is an equilateral triangle (C_{3v} symmetry) with $S = 4$, bond length $d = 4.04$ a.u. and binding energy $E_b = 3.04$ eV/atom. For comparison we recall that the total spin of Ni_3 is $S = 1$. Low lying isomers with the same geometrical structure and spins $S = 3$ and $S = 5$ were also found, as well as a high lying C_{3v} isomer with $S = 0$, and a linear, asymmetric form (the two bond lengths are different). So, similarly to the case of Ni_3, a variety of isomers is found. The ground state of Fe_4, with $S = 6$ and $E_b = 3.55$ eV/atom, can be viewed as a distorted tetrahedron opened up into a butterfly (C_{2v} symmetry). Two low lying isomers were found with $S = 7$ (more open) and $S = 5$ (more compact), and also a square isomer lying 3.0 eV above the most stable C_{2v} structure. The C_{2v} structure of Fe_4 is rather similar to the D_{2d} structure of Ni_4, but the planar isomer is less stable for Fe. The lowest energy structure of Fe_5 is a trigonal bipyramid, with $E_b = 3.90$ eV/atom and $S = 7$. There are several low lying isomers with the same structure, although with different spin and interatomic distances. Isomers with the form of a square pyramid and a planar pentagon have smaller cohesive energies. Notice that the ground state of Ni_5 is also a trigonal bipyramid. The ground state of Fe_6, with $E_b = 4.01$ eV/atom and $S = 10$, results from capping the trigonal bipyramid. An octahedron compressed towards the mid plane, also with $S = 10$, is only 0.02 eV/atom higher in energy. Another isomer is a pentagonal pyramid with $E_b = 3.90$ eV/atom. The lowest energy structure of Fe_7 is a pentagonal bipyramid with $S = 11$ and $E_b = 4.37$ eV/atom. Two isomers with $S = 11$ and large binding energies also exist: one is a tetrahedron capped on three of its four faces (incomplete stellated tetrahedron), with $E_b = 4.26$ eV/atom, and the other

is a bicapped trigonal bipyramid (E_b = 4.23 eV/atom). A capped octahedron lies 0.25 eV/atom above the ground state. The multitude of isomers with energies close to that of the ground state could be present together with the ground state in experiments probing the reactivity or the magnetism of those clusters.

Another DFT calculation [61] using linear combinations of numerical atomic orbitals as basis sets gives ground state structures in agreement to those of Ballone and Jones [60]. The only difference is that the stability of the two lowest energy structures of Fe_6 is inverted, but the binding energies are again similar. This calculation also predicted the structures of larger clusters. Fe_8 is a bidisphenoid, Fe_9 a tricapped trigonal prism and Fe_{10} a bicapped square antiprism. The structures of Fe_{11}, Fe_{12} and Fe_{13} are based on icosahedral packing, but Fe_{14} and Fe_{15} have nonicosahedral symmetries (C_{2v} and D_{6h} respectively). Finally Fe_{16} and Fe_{17} follow a growth pattern based on the structure of Fe_{15}. A conclusion from the calculations for small Ni and Fe clusters is that compact structures are more stable than open structures, and that the ground state structures of small Ni_N and Fe_N clusters of the same size are remarkable similar. Spin plays a role in determining the most stable structures. The large spin energies that result from unpaired spins in transition elements often compensate for the lowered occupancy of bonding orbitals that this requires.

8.3.3 Niobium clusters

Nb is a nonmagnetic metal and Nb clusters are expected to be simpler than Ni or Fe clusters. Spin polarized DFT calculations with LDA and nonlocal GGA (Generalized Gradient Approximation) exchange–correlation functionals have been performed [62]. The dimer has a triplet ground state. The bond dissociation energies are 5.8 eV (LDA) and 5.4 eV (GGA), and the last one is in good agreement with experiment (5.2 eV). Bond lengths are very similar: 2.08 Å (LDA) and 2.10 Å (GGA). At the LDA level Nb_3 is an isosceles triangle. The symmetry increases with ionization, and Nb_3^+ becomes an equilateral triangle. Nb_4 is a perfect tetrahedron whose bond length expands upon ionization. Nb_5 is a trigonal bipyramid, like Ni_5 and Fe_5. Ionization again expands the cluster and breaks the symmetry. Nb_6 has the form of a planar rhombus with two atoms above the basal plane, aligned along the long diagonal, and Nb_7 is a distorted pentagonal bipyramid. Some similarities with the structures

of Fe and Ni clusters then exist. Reoptimization of the structures of Nb_3, Nb_4 and Nb_5 by performing GGA calculations led to small changes on the bond lengths and lowered the cluster symmetries. The ground state spin multiplicities were not affected, and the binding energies were reduced by some tenths of an eV, improving the comparison with experiment. A break in the slope of the binding energies versus N indicates that Nb_4 is particularly stable, and the same conclusion is obtained from the energy to remove one atom, which has a maximum for Nb_4.

The similar energies of structural isomers, discussed in some detail for the Ni and Fe clusters above, introduces some uncertainties in the theoretical prediction of the ground state geometry of small clusters. A reliable determination of cluster structures can be made by comparing the measured photoelectron spectrum with theoretical predictions for different isomers. The photoelectron spectra of Nb_N^- with $N = 3–8$ have been compared [63] to spectra calculated using the LSDA. The binding energies of the electrons of the anionic cluster were calculated in two steps. These were first approximated by a generalized transition state (GTS) formula [64]

$$E_i^{GTS} = -[\varepsilon_i(1) + 3\varepsilon_i(1/3)]/4 \qquad (8.2)$$

where $\varepsilon_i(\nu)$ is the energy eigenvalue of orbital ϕ_i obtained in a selfconsistent calculation with the occupation number n_i fixed equal to ν. This formula can be viewed as an approximation to the Δ selfconsistent field method (ΔSCF), that evaluates the energy difference between the anionic ground state and an excited electronic configuration of the neutral. For the particular case of the lowest bound (*lb*) electron, the binding energy, which is equal to the electron affinity *EA* of the neutral, can be obtained rigorously by subtracting the ground state energy of the neutral cluster at the anion equilibrium geometry from that of the anion. In the second step all the binding energies from Eq. (8.2) were shifted by the quantity

$$\Delta = EA - E_{lb}^{GTS} \qquad (8.3)$$

with typical values of this shift being $\Delta = 1.25$ eV. A number of isomers were obtained for Nb_N^- and the ground state had a structure almost identical to that of the neutrals for $N = 3$–7. In general, the calculated spectrum corresponding to the lowest energy structure leads to better agreement with experiment, although the agreement is far from perfect due to the approximate treatment of the binding energies. Only in two cases the measured spectrum was asigned to a low lying isomer: to an isosceles triangle (instead of the equilateral triangle) for Nb_3, and to a distorted trigonal bipyramid (instead of an ideal one) for Nb_5. In both cases the energy difference between those isomers and the ground state is small. Evidence was also found for the coexistence of two isomers of Nb_8 under some experimental conditions.

The ionization potentials of neutral Nb_N [65] and the measured photoelectron spectra of Nb_N^- allow to establish a correlation between electronic structure and reactivity [66]. The reactivities of the neutral clusters with H_2 follow a simple pattern: Nb_8, Nb_{10} and Nb_{16} are relatively unreactive while the other clusters readily chemisorb hydrogen. The measured vertical detachment energies (VDE) of Nb_N^- display an even–odd alternation in the region $N = 6$–17, with high VDEs for odd N, low ones for even N, and specially pronounced minima for $N = 8$ and 10. For $N > 16$ the VDEs increase steeply, with no even–odd alternation [66]. Even–odd alternation in the behavior of different properties is usually observed in clusters of simple metals with an odd number of valence electrons per atom (see Section 5.2). The free Nb atom has five valence electrons in the electronic configuration $4d^4 5s^1$. The observed even–odd alternation indicates that the even-numbered neutral clusters Nb_8, Nb_{10}, Nb_{12}, Nb_{14} and Nb_{16} have a closed HOMO level and that the aditional electron occupies the LUMO, giving rise to a small peak at low binding energy in the experimental PES spectrum. Instead, when the HOMO is half-occupied (odd N), the extra electron fills the HOMO and this results in a high VDE for the corresponding anionic clusters.

If the neutral cluster has closed electronic levels, the HOMO–LUMO gap can be measured directly in the photoelectron spectrum of the anionic species. Large HOMO–LUMO gaps were found for $N = 8$, 10 and 16, consistent with the pronounced local minima in the VDEs (approximately equal to the electron affinities). All the features discussed

above correlate precisely with the measured reactivities: the clusters with the largest gaps (N = 8, 10, 16) have the lowest reactivities with H_2. The reactivity of Nb_{10} with CO is also abnormally small [67]. In fact, large gaps are related to low reactivities through the chemical index *hardness* of Section 5.4: a chemically hard cluster is unreactive. Nb_{15} has a photoelectron spectrum very different from those of neighbor sizes. This, plus the fact that the VDE increases steadily and without odd–even oscillations for $N > 16$, has been interpreted [66] as a possible indication of a geometrical shell closing at $N = 15$.

8.3.4 Titanium and Vanadium clusters

The outer electrons of the Ti atom are in the configuration $3d^2\, 4s^2$. With only two d electrons, the electronic structure of the clusters is expected to be simpler than that for elements in the middle or in the second half of the $3d$ series. Discrete features are observed in the photoelectron spectrum of Ti_N^- only for $N \leq 8$ [68]. In this range the photoelectron spectrum changes from N to N+1, reflecting their molecular nature. Starting with Ti_8^- the spectrum becomes simple: a prominent feature appears near the detachment threshold whose width increases with N. The width is about 1 eV in the range Ti_{20}^- to Ti_{50}^-. This broad feature is similar to the single broad feature in the valence photoemission spectrum of the bulk metal, which has a width of 2 eV and is due to the $3d$ band [69]. The detachment threshold (or electron affinity of the neutral cluster) displays an even–odd oscillation below $N = 8$ and a monotonous increase for N larger than 8. For N larger than ≈ 30 the affinities are fitted well by a relation like (5.7) with $c = 0.125$, that is

$$EA = W - \frac{5}{8}\frac{e^2}{R}\ . \qquad (8.4)$$

That relation shows that the convergence of EA towards the bulk is not fast; for instance $EA(Ti_{64}) = 2.6$ eV, whereas the bulk work function is $W = 4.33$ eV. The evolution of the shape of the photoelectron espectrum was interpreted as an early metallization of the clusters [68], perhaps due to close packed structures. A pronounced narrowing of the PES feature

occurs for Ti_{55}^-. This feature and the behavior of the dissociation energies of small Ti_N^+ clusters [70] suggest that the structures of some of them could be icosahedral.

The electronic configuration of the vanadium atom is $3d^3 \, 4s^2$. The characteristics of the PES spectra of V_N^- with $N \leq 65$ allow to separate those clusters in four size regions [71]. The spectrum is molecular-like up to V_{12}^-. Then, V_{13}^- to V_{16}^- form a transition region from discrete spectra to a two-band spectra. For V_{17}^- the first of those two features is narrow and peaks at 2 eV (near threshold) and the second band is broad and centered at a binding energy of ≈ 3.2 eV. Between V_{17}^- and V_{60}^- the two features converge to a single broad feature, and finally, for $N > 60$ the PES changes very little with N. PES spectra recorded at a higher photon energy reveal a new peak at 5.2 eV for V_{17}^- and larger clusters. This feature and the broad feature near 3.2 eV have been correlated [71] with similar broad features in the PES spectra of bulk vanadium. Wu *et al.* [71] proposed that these bulk-like effects have their origin in the inner region of the clusters. Consequently they interpret the sharper peak that emerges from V_{13}^- and gradually merges with the broad peak as due to the cluster surface. This interpretation suggests that starting from V_{13}^- the cluster already has surface and internal regions, and starting from V_{17}^- the internal region has some similarity to the bulk. The sharp peak is most likely due to states derived from the *s* atomic orbitals and the broad feature due to the *d* states. As the cluster size grows the *d* band widens and the two features merge: the density of states of bulk vanadium near the Fermi level is mostly of *d* character [40]. In contrast to titanium, the electron affinity does not show odd–even effects. The electron affinity has local minima for V_5 and V_{12} and maxima for V_4 and V_{10}. The affinities then become smooth for $N \geq 17$ and are fitted extremely well by the metallic drop model of Eq. (8.4).

The electronic structure of V_4^+ has been studied by optical absorption spectroscopy [72]. The experiment measured the intensity depletion of the complex V_4^+Ar against the wavelength of the irradiation laser and the spectrum obtained was treated as the optical absorption spectrum of the underlying cluster V_4^+ because the inert Ar atom is weakly attached and

does not significantly affect the geometry or the electronic structure of V_4^+. The measured spectrum was compared to approximate calculations based on DFT. Several plausible geometrical structures were examined: a distorted tetrahedral structure with C_{2v} symmetry, a tetrahedron (T_d), a rhombus and a parallelogram, and only the first one was able to reproduce the experimental spectrum, although not perfectly. An extensive search for the lowest energy structure of V_4^+ confirmed that the C_{2v} structure is the ground state isomer. The relatively broad widths (0.2 eV) of the measured absorption peaks were assigned to vibrations related to a specific deformation coordinate that connects the C_{2v} and T_d structures.

8.3.5 Chromium clusters

Small chromium clusters show peculiarities that make them special compared to other $3d$ clusters. The electronic structure of the free atom, $3d^5 \, 4s^1$, has six unpaired electrons. This half-filled electronic configuration leads to strong d–d bonding in Cr_2 with an unusually short bond length of 1.68 Å, compared to 2.50 Å for the bcc solid metal. DFT calculations [73] show that the dimer is a closed shell molecule with a strong sextuple bond. The strong bonding arises from the filling of the $3d$-bonding molecular orbitals: $\sigma_{3d}^2 \, \pi_{3d}^4 \, \delta_{3d}^4 \, \sigma_{4s}^2 \left({}^1\Sigma_g^+ \right)$. This electronic structure is very robust and controls the growth of small clusters [73]. The optimized geometries of Cr_3 to Cr_{11} are given in Fig. 8.3. Cr_3 is composed of a dimer plus an atom: the electronic structure of the dimer is virtually unchanged and the third atom remains in its atomic electronic state, leaving six unpaired electrons in the cluster. An additional atom pairs up with the third one and Cr_4 is formed by two dimers with strong internal bonds and weak inter-dimer bonding. The dimerization effect controls the growth up to $N = 11$: all those clusters are formed by dimers with short bond lengths and one (in Cr_5, Cr_7, Cr_9) or two (in Cr_{10}) isolated atoms bonded to adjacent dimers. The strong dimer bonds are represented by the heavy lines in the figure. Cr_{11} has a structure similar to that of Cr_{10} with a third isolated atom at the cluster center.

The dimer route stops at Cr_{12}: the Cr–Cr distances in the dimers suddenly become large and dimer-like bonds cannot be identified anymore for $N > 11$. Cr_{12} reminds a small fragment of a bcc solid and for this reason the structures studied for $N \geq 13$ were bcc fragments [74]. In

summary, the structures are controlled by the interplay between intra-dimer and inter-dimer interactions. For the smaller clusters the intra-dimer interaction dominates. The inter-dimer interaction becomes stronger as the cluster size increases leading to the transition from dimer growth to *bcc*-like structures.
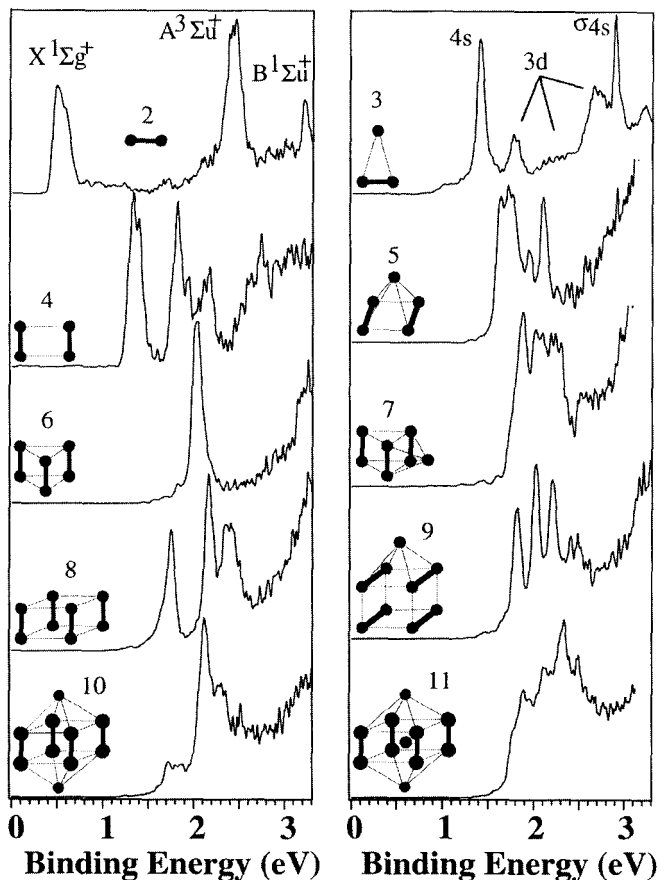
Figure 8.3. Photoelectron spectra of Cr_N^-, $N = 2$–11, taken at a photon energy of 3.49 eV. The structure of each cluster is shown. Strong dimer bonds are represented by thick lines. Reproduced from L. S. Wang *et al.*, *Phys. Rev. B* **55**, 12884 (1997) with permission of the American Physical Society.

The dimer growth route implies an odd–even effect that has been observed as an alternation in the magnitude of the dissociation energies for $N < 10$ [75]. Odd–even effects are observed in the photoelectron spectra of Cr_N^- [74]. The measured PES for $N = 3$–11 are shown in Fig. 8.3. Those spectra are characterized for having several discrete features: clusters with even N have fewer features near the threshold and a distinct gap, while clusters with odd N show more complex spectra with congested features near threshold, in particular for $N = 5, 7, 11$. The even–odd alternation disappears above Cr_{12}^- [74]. The electron affinity also shows the odd–even alternation [75]. The closed shell electronic structure of Cr_2 produces a large gap between the HOMO - σ_{4s} and the LUMO - σ_{4s}^* , as seen in the PES of Cr_2^- : the two prominent peaks, labelled X and A in the figure, correspond to the removal of one electron from the σ_{4s}^* and σ_{4s} levels, respectively.

As indicated above the electronic structure of Cr_3 can be described as $(\sigma_{3d}^2 \pi_{3d}^4 \delta_{3d}^4 \sigma_{4s}^2)$ $3d^5$ $4s^1$, that is, with the third atom in its atomic configuration having all its six electrons unpaired. The orbital degeneracy is lifted under the C_{2v} symmetry of Cr_3, so the $3d$ orbitals of the odd atom are split into five nondegenerate orbitals. The 4s orbital of the odd atom (weakly mixed with the σ_{4s} orbital of the dimer) becomes the HOMO of Cr_3 and the extra electron in Cr_3^- fills this level. The first feature in the PES spectrum of Cr_3^- at 1.4 eV corresponds to the removal of an electron from the atomic 4s orbital. The prominent peak at 2.9 eV arises from the removal of an electron from the σ_{4s} orbital of the dimer. This orbital has a larger binding energy than the corresponding σ_{4s} orbital in Cr_2 because of its interaction with the 4s orbital of the odd atom. All the features between the 4s and σ_{4s} peaks are due to the $3d$ electrons of the odd atom. It should be noticed that all the features ascribed to the odd atom in Cr_3 fall inside the region of the HOMO–LUMO gap of Cr_2. The spectra of Cr_4^- and Cr_8^- show gaps of 0.48 and 0.41 eV, respectively, suggesting that the neutrals have closed shells. The spectrum of Cr_6^- is unusual, with an intense threshold peak and a

high electron affinity. All these features are explained by the DFT calculations, confirming that Cr_4 and Cr_8 are closed shell clusters. On the other hand Cr_6 has an open shell configuration, and the extra electron of the anion goes to the partially filled HOMO, in constrast to Cr_4^- and Cr_8^-, where the extra electron goes to the LUMO of the neutrals. This results in the large electron affinity of Cr_6 compared to Cr_4 and Cr_8.

The electronic structure of the odd clusters from Cr_5 to Cr_9 can be described, as for Cr_3, as arising from the interaction between the levels of the even cluster of size (N-1) and the odd atom: the energy levels of the odd atom are bunched near the HOMO and in the region of the HOMO–LUMO gap of the luster of size (N-1). The larger electron affinities of the odd clusters compared to the even ones occur again because the extra electron goes to the open shell HOMO in the odd clusters. Cr_{10} and Cr_{11} deviate slightly from the dimer growth route since they have four dimers instead of five. Still their PES spectra resemble those of the even and odd clusters respectively. Finally the PES spectra of Cr_{12} to Cr_{15} indicate that the even–odd alternation effects vanish. All the PES of large clusters have similarities, with a sharp feature near threshold that smoothly merges with other features as N increases. Beyond Cr_{24} a single broad band is observed near threshold (in experiments with photon energies of 3.49 and 4.66 eV). In this size range the spectrum already resembles the first bulk feature [76] and further similarities appear for experiments at higher photon energies. It is convenient to stress that the odd–even alternation effects observed for Cr clusters have a different origin compared to those observed for alkali and noble metal clusters.

8.4 Thermionic Emission from Refractory Metal Clusters

The physical process underlying the PES spectra is the following

$$M_N^- + \hbar\omega \rightarrow M_N + e^-$$
$$\rightarrow M_N^* + e^- \qquad (8.5)$$
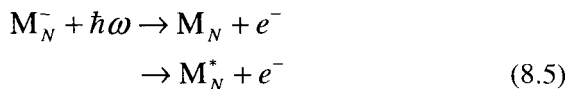
that is, the absorption by a cluster anion of a photon of energy larger than the electron affinity of the neutral leads to the prompt emission of an

electron on a time scale of femtoseconds, leaving the cluster in its ground state M_N or in an excited state M_N^*. But this is not the only possible process. The absorbed energy can be rapidly thermalized by the internal vibrational degrees of freedom of the cluster anion, that then reaches a superheated state $(M_N^-)_{E_1}$ with internal energy E_1, and subsequently the hot cluster anion can emit an electron, leaving the neutral cluster in a state with lower internal energy E_2. That is

$$M_N^- + \hbar\omega \rightarrow \left(M_N^-\right)_{E_1} \rightarrow \left(M_N^-\right)_{E_2} + e^- . \qquad (8.6)$$
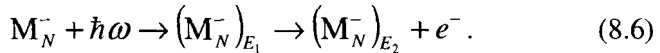
It takes time to focus the energy back into the electron emission channel, so the emission of the electron by this process is delayed in time compared to the direct photoemission. Another difference between the two processes is that direct photoemission leads to a discrete spectrum while in delayed photoemission, that is related to the thermionic emission of electrons from hot metal surfaces [77], the energy of the emitted electrons exhibits a quasicontinuous distribution. The spectrum of kinetic energies is a smooth exponential function corresponding to a "temperature" $T = \left(E_1 / k_B\right)\left(3N - 6\right)$, where E_1 is the excitation energy (energy of the photon), and $3N$-6 is the number of vibrational degrees of freedom.

Delayed ionization (lifetimes greater than 10^{-7} s) was first observed in neutral clusters of the refractory metals (W, Nb, Ta) [78–80]. A detailed study has been performed for W to analyze the contributions from prompt and delayed ionization [81]. Starting from W_2^- the PES spectrum shows sharp peaks at low binding energies (between 1.5 and 2.5 eV) assigned to direct photoemission, and a smooth thermionic signal that increases monotonically with increasing binding energy. The overlap region between the two components of the spectrum goes from 2.5 to 3 eV. The two components are also observed for larger clusters. The sharp peaks arise from direct photoemission from occupied $5d$- and $6s$-derived molecular orbitals. The smooth signal is fitted well by a Boltzmann distribution for the intensity

$$I = Ae^{-E_{kin} / k_B T} \qquad (8.7)$$

where the temperature corresponds to a photon energy $\hbar\omega$ = 4.025 eV used in the experiments. Evidently, when the time constant of the thermionic emission (TE) is much longer than the time scale of the experiment (usually around 0.1 μs) only direct photoemission would be observed. This is the reason why the integrated TE intensity decreases with increasing N: as the number of degrees of freedom increases, the photon energy is distributed over a larger number of vibrational modes and it takes longer to focus the energy back into the electron emission channel.

Before the observation of thermionic emission from hot tungsten clusters, the standard cooling mechanism detected for different types of superheated clusters had been the evaporation of neutral fragments, mostly monomers. The faster of the two cooling mechanisms, delayed ionization or fragmentation, is going to dominate, and the time constants depend on the respective energy thresholds: these are the electron affinity in the case of TE and the binding energy of the atom for the evaporative cooling. For the refractory metal clusters the threshold for evaporation is larger than the electron affinity (3–4 times larger in W_N) and TE dominates. This can already be predicted from the properties of the bulk metals: a small ratio between the work function W and the cohesive energy per atom E_c and a small value of W are the conditions for good thermionic emitters, and these conditions are best satisfied by the refractory metals; in particular the ratio is 0.5 for tungsten. In contrast, when the magnitudes of the electron affinity and the evaporation energy are similar, the two cooling mechanisms are competitive. This is the case for alkali cluster anions: Reiners and Haberland [82] have observed atom and electron emission from Na_{91}^-. For neutral or positively charged clusters of most metals the cooling mechanism is atom evaporation since in this case the ionization potential is usually larger than the binding energy of an atom, even for the simple sp metal clusters. By storing the W_N^- anions in a Penning trap, delayed electron emission on the millisecond time scale has been observed [83].

Delayed ionization attributed to a thermionic emission process is not specific of pure refractory metal clusters and has been also observed for metal carbide clusters, metal oxide clusters (Nb_nO_m) and metalcarbohedrenes Ti_8C_{12} and V_8C_{12} .

8.5 Nonmetal to Metal Transition

The characterization of metallic behavior is clear for bulk systems, where band theory concepts apply. This concept is more subtle for small clusters. Very small clusters can be considered nonmetallic, having a discrete distribution of electronic states, and a critical size N_c is required before this distribution turns into a quasicontinuous one in the region around the Fermi level ε_F Scanning tunneling spectroscopy experiments of deposited clusters measure their conductance. Those experiments have been performed for transition and noble metal clusters [84–86] and probe the density of states at the Fermi level. The tunneling conductance decreases markedly with a decrease of the cluster size when the cluster diameter is smaller than 1 nm and shows the emergence of an energy gap, suggesting that small clusters are indeed nonmetallic.

Kubo [87] has proposed that a cluster presents metallic character when the average level spacing becomes smaller than the thermal energy $k_B T$, that is, when

$$D(\varepsilon_F) \ge \frac{1}{k_B T} \tag{8.8}$$

where $D(\varepsilon)$ is the density of states. A square d band model introduced by Friedel [88] within a tight-binding (TB) framework can be extended to clusters, and the density of states can be expressed (the model neglects sp electrons)

$$D(\varepsilon) = \frac{10N}{W(N)} \quad , \quad \text{for} \quad -\frac{W(N)}{2} \le \varepsilon - \varepsilon_d \le \frac{W(N)}{2}, \tag{8.9}$$

and $D(\varepsilon) = 0$, otherwise. Here the factor 10 is the total number of electrons in a full d shell and ε_d is the atomic d level. The band width $W(N)$ can be related to the average atomic coordination $Z(N)$ using a second-moment approximation [89]

$$W(N) = W_b [Z(N)/Z_b]^{1/2} \tag{8.10}$$

where W_b and Z_b are the band width and the coordination number in the bulk, respectively. Using the last two equations, the condition given by Eq. (8.8) can be written in the form

$$\frac{10N}{W_b}\left(\frac{Z_b}{Z(N)}\right)^{1/2} \geq \frac{1}{k_B T}. \qquad (8.11)$$

This relation shows that the critical size N_c is determined by the variation of $Z(N)$. *Zhao et al.* [90] have used for $Z(N)$ a simple approximation

$$Z(N) = \frac{Z_b(N-1)}{Z_b + (N-1)} \qquad (8.12)$$

that leads to the expression for the critical size

$$N_c = [12G(T) + 171]^{1/2} - 6 \qquad (8.13)$$

with $G(T) = [(1/k_B T)(W_b/10Z_b)]^2$. Taking $Z_b = 12$, the value for an *fcc* crystal, and using known metal band widths [91], the following critical sizes are obtained for a temperature of 120 K: $N_c(\text{Fe}) = 50$, $N_c(\text{Co}) = 39$, $N_c(\text{Ni}) = 34$, $N_c(\text{Pd}) = 50$.

The approximation for the coordination number in Eq. (8.12) depends only on N and takes no account of the cluster geometry. $Z(N)$ has been evaluated exactly for Co, Ni and Pd clusters of two structural types: a) particles with an underlying *fcc* lattice and cuboctahedral (CO) shape, and b) icosahedral particles [92]. In both cases the critical sizes for $T = 110$ K are $N_c(\text{Co}) = 31$, $N_c(\text{Ni}) = 27$, and $N_c(\text{Pd}) = 43$, a little smaller than the values obtained using Eq. (8.12). For *bcc* Fe clusters with spherical or cube shapes, the critical sizes for $T = 110$ K are $N_c(\text{Fe}) = 33$ and $N_c(\text{Fe}) = 35$ respectively, again smaller than the value from Eq. (8.12). Tunneling experiments probing the density of states at the Fermi level have been performed for Fe clusters supported on a substrate at room temperature [84]. Those experiments indicate that the nonmetal to metal transition occurs for $N_c \approx 35$. The theoretical prediction [92] given above is consistent with this experimental value.
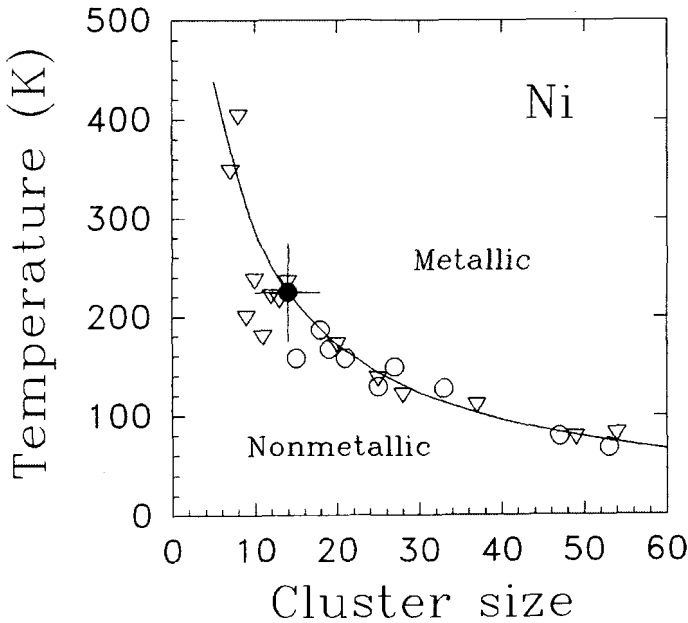
Figure 8.4. Calculated nonmetal–metal phase diagram of Ni clusters. The
continuous line gives the result for a rectangular *d* band model. Squares and
triangles give the boundary obtained from tight-binding calculations. The filled
square is an experimental point obtained from the ionization potential.
Reproduced from F. Aguilera-Granja *et al.*, *Solid State Commun.* **104**, 635
(1997) with permission of Elsevier.

X-ray spectroscopy indicates that the nonmetal to metal transition of
Pd occurs for cluster radii in the range 7–10 Å [93], while the theoretical
model predicts a size range 5–8 Å (40–120 atoms) depending on the
temperature. N_c can also be estimated from an analysis of the ionization
potential. For a metallic droplet *IP* follows the relation (5.6), or in terms
of N,

$$IP(N) = W + \alpha N^{-1/3} \qquad (8.14)$$

where α is a material-dependent constant. In practice, *IP* follows this
relation rather well except for small sizes, and N_c can be identified with

the size when the measurements begin to deviate from (8.14). Employing measured ionization potentials [94] one obtains $N_c(\text{Fe}) \cong 28$, $N_c(\text{Ni}) \cong 20$, and $N_c(\text{Co}) \cong 17$. The estimated temperatures in those measurements are 225 ± 50 K, and for those temperatures N_c (Fe) $\cong$ 18–21, N_c (Ni) $\cong 14$ and N_c (Co) $\cong$ 15 are obtained from Eq. (8.11). The comparison is satisfactory considering the approximations in the square band model and the errors in determining N_c from the ionization potentials.

The theoretical model can be improved in a calculation without any assumptions about the shape of the density of states. Aguilera-Granja *et al.* [95] have solved selfconsistently a TB hamiltonian for the 3*d* and 4*sp* electrons of Ni clusters in a mean field approximation. The geometries for $N \leq 14$ were obtained using an interatomic many-body potential and for larger clusters the geometries correspond to a model of icosahedral growth (see Section 8.6). Using the Kubo criterion of Eq. (8.8) leads to the phase diagram of Fig. 8.4. The triangles delineate a boundary separating regions of nonmetallic and metallic character. The boundary is smooth for $N \geq 14$ and it becomes steep and irregular for lower sizes. The figure also contains a number of squares, representing results for other plausible cluster geometries, and the phase boundary is not very sensitive to the geometries. The filled square (with error bars) is an experimental point estimated from the ionization potentials. This point fits well on the predicted boundary.

Au_{55} clusters covered by a $(PPh_3)_{12}Cl_6$ ligand shell consisting of 12 triphenil-phosphine molecules and six Cl atoms have been prepared. The ligand shell helps to stabilize the gold cluster and to prevent the coagulation with other clusters. The ligand shell also has a strong influence on the electronic properties, giving the cluster a nonmetallic character. X-ray irradiation of the clusters induces damage of the ligands and reduces their influence on the gold clusters. As a result the cluster becomes metallic [96], as put in evidence by the finite density of states at the Fermi level measured by ultraviolet photoelectron spectroscopy (UPS).

8.6 Atomic Shell Effects

As discussed in previous chapters the mass spectrum of clusters formed in a supersaturated vapor arises as a consequence of a complex process

involving growth and evaporation that results in an abundance population I_N which is a non-smooth function of the cluster size. Features like pronounced maxima of I_N or pronounced steps are interpreted as revealing the existence of specially stable cluster sizes. The origin of this stability in the case of clusters of the alkaline elements is the filling of electronic shells (see Chapter 4), and for clusters of inert gases, the features in the mass spectrum are due to the formation of atomic shells (see Chapter 3). Magic number effects have been traditionally difficult to observe in the mass spectrum of transition metal clusters, although recent work [97] presents evidence of magic numbers in Fe, Ti, Zr, Nb and Ta clusters. Since the magic numbers appear in the mass spectrum mainly from the evaporative cooling step, the difficulty for observing magic clusters of transition elements may be due, at least in part, to their large binding energies, that would require stringent high temperature conditions to induce fragmentation in the cluster source. But a variety of alternative experiments on chemical reactivity, ionization potentials, photoelectron spectroscopy, fragmentation and magnetism have revealed the existence of specially stable clusters of transition metals [98]. The experiments have helped in many cases to infer the geometrical structure of those clusters. A large part of the experimental information on transition metal clusters is consistent with a pattern of icosahedral growth.

8.6.1 Reactivity of Ni clusters

Pellarin *et al.* [99] have analyzed the mass spectrum of Ni and Co clusters containing between 100 and 800 atoms. Those spectra were obtained using time-of-flight mass spectrometry and near-threshold photoionization. A highly stable cluster of size N_m has a higher ionization potential compared to neighbor clusters of sizes $N_m + 1$, $N_m + 2$,... Then, when the photon energy is lowered just below the ionization potential of the cluster of size N_m, only the clusters of sizes $N_m + 1$, $N_m + 2$,... present in the molecular beam will be detected in the mass spectrum, but not the size N_m. This provides an efficient method for analyzing the variations in stability of clusters as a function of size. For nickel clusters, a sharp increase in the abundance was observed at some particular cluster sizes. The strongest effects occur after $N_m = 55$, 147, 309 and 561. On intuitive grounds, the structure of these highly stable clusters could correspond to complete icosahedra or cuboctahedra. Additional evidence

for icosahedra instead of cuboctahedra comes from the fact that, above N = 200, enhanced stability was observed every time that a face of an icosahedron was covered in the process of building the next icosahedron. Chemical probe experiments [50, 100–104] point to icosahedral symmetry of Ni clusters in some size regions (the results are discussed below). This conclusion is derived from the measured saturation coverages and adsorption free energies of H_2O, NH_3 and especially N_2 molecules.

The experimental inferences have motivated a detailed study of a growth model based on the formation of icosahedral structures with an increasing number of shells [105] and this model has been confronted in detail with the reactivity experiments. The icosahedral structure of Ni_{13} is supported by DFT calculations [56]. The competition between the FC and MIC coverings of the Ni_{13} icosahedron (see Section 3.1 for a description of the FC and MIC coverings) has been studied [105] by using the embedded atom method (EAM) [106, 107] to model the interatomic interactions. The binding energy of the cluster is given in the EAM as

$$E_b = \sum_i F_i\left(\rho_i^h\right) + \frac{1}{2}\sum_{i \neq j} \phi_{ij}\left(r_{ij}\right). \tag{8.15}$$

Each contribution $F_i\left(\rho_i^h\right)$ represents the embedding energy of atom i in an effective uniform medium whose density ρ_i^h is approximated by the superposition of the atomic density tails of the atoms around site i. On the other hand $\phi_{ij}(r_{ij})$ is a residual core–core repulsion between atoms i and j separated by a distance r_{ij} that can be parameterized in terms of adjustable parameters. The function $F_i\left(\rho\right)$ and the parameters in $\phi_{ij}(r_{ij})$ are obtained empirically from the properties of the bulk metal.

The first six atoms added to Ni_{13} form an FC umbrella (see Fig. 3.3), leading to a double icosahedron structure for Ni_{19}. This structure has also been found using the effective medium theory [108] or other other many-atom potentials. Addition of more atoms completes the next two FC umbrellas at Ni_{23} and Ni_{26}. Completion of the FC umbrellas leads to special stability for the Ni clusters with N = 19, 23 and 26. Then, a transition to MIC structures occurs after Ni_{26}. Before achieving full

coverage, MIC umbrellas fill up successively at $N = 28, 32, 36, 39, 43,$ 46 and 49, and the icosahedron is completed at $N = 55$. The cluster becomes very stable with the filling of each new umbrella. This is appreciated in Fig. 8.5 where the energy E_{vap} required to remove one atom from Ni_N (see Eq. 2.9) is plotted versus N. Peaks appear when FC umbrellas are completed for $N < 28$ and when MIC umbrellas are completed for $N \geq 28$. The figure also shows the increase ΔN_b in the number of bonds between Ni_{N-1} and Ni_N. The magnitude of ΔN_b shows a perfect correlation with E_{vap}.
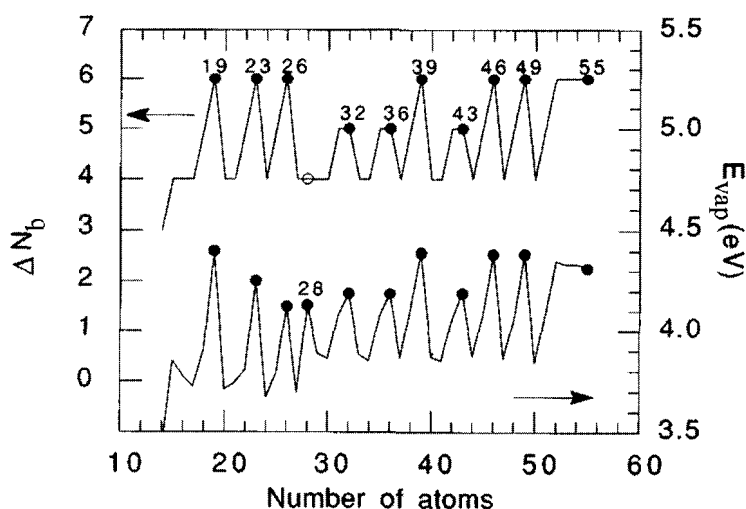
Figure 8.5. Difference in binding energy ΔE_{vap} and change ΔN_b in the number of bonds between Ni_{N-1} and Ni_N versus N. The black circles indicate filled umbrellas. Reproduced from J. M. Montejano-Carrizales *et al.*, *Phys. Rev. B* **54**, 5961 (1996) with permission of the American Physical Society.

A similar pattern develops for $N > 55$. FC coverage is first preferred (see Fig. 3.3) and the first umbrella is filled for Ni_{71}. It is relevant to notice that the five faces of the umbrella are filled in order, and one, two, three, four and five faces are completed for $N = 58, 61, 64, 67$ and 71, respectively. An FC to MIC transition occurs at Ni_{74} and MIC decoration leads to the filling of umbrellas for $N = 83, 92, 101, 110, 116, 125, 131$

and 137, and to a complete icosahedral shell for Ni_{147}. Enhanced stability is predicted by filling those MIC umbrellas (and the different faces of the FC umbrella), and also for other particular sizes, $N = 77$, 86, 95, 104 and 119. The stability of the last ones has been explained by analyzing in detail the increase in the number of bonds as the cluster grows [105].

The interpretation of the chemical probe experiments of Parks and coworkers [50, 100–104] is based on some rules for estimating the number of binding sites for nitrogen molecules: (1) N_2 binds directly to individual nickel atoms in a standing-up configuration; (2) a Ni atom with a coordination number of four or less binds two N_2 molecules; (3) Ni atoms with coordination five to eight bind one N_2 molecule; (4) Ni atoms with coordination nine bind N_2 molecules only weakly or not at all, and (5) Ni atoms with coordination ten or more do not bind N_2 molecules [102]. The analysis of the adsorption results points to icosahedral symmetry for $N < 29$ and $N > 48$. Those measurements indicate that Ni_{13} and Ni_{55} are perfect icosahedra, and that the growth is of the FC-type up to $N = 26$, whereas Ni_{28} is a fragment of Ni_{55} with three MIC umbrellas. So, the coincidence with the theoretical calculations is good since these predict the FC to MIC transition at Ni_{27}–Ni_{28}. The region $28 < N < 48$ has not been studied in detail, although some results of N_2 uptake shows some evidence for *fcc* packing for some clusters in this size region [50, 104]. On the other hand one can correlate a minimum in the experimental adsorption free energy of H_2O on Ni_{32} with the peak of E_{vap} corresponding to the filling of four umbrellas.

The adsorption of nitrogen has been analyzed in detail for Ni_{38} and Ni_{39}. The saturation coverages of different molecules (N_2, H_2O, CO) in Ni_{38} suggest have that the structure of this cluster is a truncated *fcc* octahedron, and this is supported by calculations based on many-body potentials (see Chapter 9). Two saturation levels are evident in the uptake data of nitrogen on Ni_{39} at very low temperatures [109], one at $Ni_{39}(N_2)_{27}$ and another at $Ni_{39}(N_2)_{32}$ and these have been interpreted to represent the saturation of two separate isomers. With a long time for relaxation of the bare clusters before reaction the second isomer (isomer A) becomes favored over the first one (isomer B), and for this reason isomer A was considered to be the ground state of Ni_{39}. This cluster has 32 surface atoms with coordination between five and eight, according to the binding rules for adsorption. Then, the structure of Ni_{39} is not related to that of Ni_{38}, which is an *fcc* octahedron that binds 24 nitrogen

molecules at saturation. A candidate is the fragment of Ni_{55} obtained by removing a 16-atom cap. The surface of this cluster has 32 binding sites available for adsorption: 22 of those atoms have coordination six and the remaining 10 atoms have coordination eight. Another candidate is the most stable isomer calculated by Wetzel and De Pristo [110] using an Effective Medium method: this isomer is composed of two 16-atom caps joined together along their symmetry axis, one staggered relative to the other, surrounding a 7-atom pentagonal bipyramid. The caps are formed by one apex atom surrounded by five atoms (like an apex of an icosahedron) and ten additional atoms forming the belt of the cap. This structure also binds 32 molecules: 12 surface atoms have coordination six and 20 surface atoms have coordination eight. A small rotation of one cap with respect to the axis of the internal pentagonal bipyramid leads to the next most stable isomer of Wetzel and De Pristo: this presents 27 sites for N_2 adsorption, 12 of those atoms have coordination six, 10 have coordination seven and 5 atoms have coordination eight. Parks *et al.* [109] have proposed these two lowest energy isomers calculated by Wetzel and De Pristo to correspond to isomers A and B, respectively, in the reactivity experiments. This interpretation is further supported by the fact that the experiments show conversion of isomer A to isomer B with increasing nitrogen pressure in the reactor and retroconversion back to isomer A for even higher pressure. This reveals that the relative stability of isomers A and B changes with the number of adsorbed molecules. These changes can be explained by looking at the number of atoms with coordination six, seven and eight and noticing that the binding of N_2 to atoms of coordination six is the strongest, so those atoms will be the first ones to be covered, then atoms of coordination seven (favoring isomer B), and finally atoms of coordination eight (favoring conversion back to isomer A). This dependence of isomer stability on the degree of adsorption introduces a warning concerning the interpretation of the cluster geometries inferred from reactivity experiments.

After Ni_{55}, the experiments are consistent with FC covering up to the formation of a 16-atom umbrella for Ni_{71}, although the structures of Ni_{66} and Ni_{67} remain yet unidentified. The binding of water molecules [111] shows minima at $N = 58$, 61 and 64, that correspond to the filling of faces of the umbrella. But the icosahedral growth model does not explain the lack of a minimum in the binding energy for $N = 67$ and the existence of a minimum for $N = 69$. Results for the ammonia uptake and

measurements of the binding of water molecules [111] reveal size oscillations correlating with the formation of MIC umbrellas for $N > 71$ [98]. Other features, like the maxima in the water binding at $N = 66$ and 81 are not explained by the model. Other group has studied the reactivity of small Ni_N^+ clusters with CO [112]. The saturation limits can be explained by the icosahedral growth model, starting with a pentagonal bipyramid for Ni_7^+ and capping this structure to build up an icosahedron at Ni_{13}^+ and a double icosahedron at Ni_{19}^+.

Other calculations have been performed for Ni clusters using many-body potentials [113, 114], an effective medium theory [108, 115] and the embedded atom method [113, 116–122]. The EAM calculations give support to the icosahedral structures, at least for sizes not far from shell closing. A semiempirical tight-binding method has been applied [123, 124] to compare the relative stabilities of Ni clusters with icosahedral and *fcc*-like structures for $N = 13$, $N = 55$ and a few sizes in between. The picture arising from the tight-binding calculations is that the icosahedral structures are preferred near the closed shell sizes and that a strong competition develops for open shell clusters in between. It is fair to conclude that uncertainties exists about the structure of Ni clusters for sizes in the region midway between closed shells. On the other hand, since the icosahedral clusters Ni_{13} and Ni_{55} turn out to be so much stable, a metastable growth of icosahedral clusters in some experiments may be conceivable.

Knicklebein [125] measured the electric dipole polaribility of Ni clusters in the size range $N = 12–58$. The relatively low polarizabilities observed for $N = 19, 23, 26, 29, 32, 43$ and 55 can be correlated with the compact structure of clusters with filled umbrellas. On the other hand, clusters with $N = 21, 22, 25$ and 49–53 display anomalously high polarizabilities; in the icosahedral model, their structures are derived from closed shell icosahedra or poly-icosahedra by removing one or more atoms.

8.6.2 Shell effects in other clusters

The formation of clusters of Ti, Fe, Zr, Nb and Ta has been studied by time-of-flight mass spectrometry and for the first time magic numbers have been detected in the mass spectra of clusters of transition metals [126]. The reason for the difficulty in observing those effects could be the stringent high temperature conditions required for the evaporation of

atoms from clusters with a large binding energy. All the elements listed above have in common the observation of the magic numbers $N = 7$, 13 and 15. In addition, $N = 19$ and 23 are seen for Fe, and $N = 19$ and 25 for Ti. The spectra of Nb and Ta shows $N = 22$ and 29. Ti_7, Ti_{13} and Ti_{15} show substantially higher binding energy than the neighbor clusters in collision-induced dissociation experiments [49]. The magic numbers $N = 7$, 13, 19 and 23 were interpreted as revealing icosahedral structure [126]. Although the calculations reported in Section 8.6.1 above pertain to Ni clusters, the binding is due mainly to the d electrons, like in other transition metals, so one can expect some similarities in the magic numbers of these elements. $N = 7$ also fits into the icosahedral picture [5,34]. It forms a pentagonal bipyramid, which is a fragment of an icosahedron. DFT calculations support the pentagonal bypiramid and icosahedral shell structure for Ti_7 and Ti_{13} respectively [127]. The calculations of Dieguez *et al.* [61] predict a local maximum in stability for Fe_{15} (with D_{6h} symmetry) compared to clusters of adjacent sizes. Also one may notice in Fig. 8.5 a local stability maximum at $N = 15$. The magic number $N = 29$ cannot be explained by Fig. 8.5, but we recall that, after $N = 26$, the next FC umbrella would become completed for $N = 29$. So it is conceivable that the FC to MIC transition might occur later in Nb and Ta clusters compared to Ni.

8.7 Gold Clusters with Impurities

The existence of electronic shells in noble metal clusters, derived from the outermost s electrons has been discussed in Section 8.1.1. Doping the clusters with impurities of the $3d$ period (Sc, Ti, V, Cr, Mn, Fe, Co and Ni) produces some changes in the magic numbers [128]. Table 8.3 gives the features observed in photofragmentation experiments. In those experiments the cluster beam was irradiated with a high fluence laser and the photo-fragments recorded showed a size distribution with an enhanced abundance of the clusters given in the table in the column labelled N. The data corresponds to the case of a single impurity, that is $Au_N Sc$, $Au_N Ti$,... The same table shows that the experimental results can be explained by a simple shell model in which the impurity contributes with n_v delocalized electrons to the cluster, with n_v also given in the table. For instance, for scandium-doped clusters the intensity drops occur

after Au_6Sc^+, $Au_{16}Sc^+$ and $Au_{32}Sc^+$. If one assumes that the Sc atom contributes three electrons (two s electrons and one d electron) to the delocalized cloud, then those three clusters contain 8, 18 and 34 delocalized electrons, respectively. Titanium doping produces abundance discontinuities at Au_5Ti^+ and $Au_{15}Ti^+$, which match the magic numbers 8 and 18 if the Ti atom contributes four electrons. The electronic configurations of the free Sc and Ti atoms are $3d^1 4s^2$ and $3d^2 4s^2$, respectively, so the experimental results indicate that all those $3d$ and $4s$ electrons become part of the delocalized cloud.

Table 8.3. Observed shell features. Drops in the abundance pattern occur after $Au_N X^+$. n_v is the number of delocalized electrons contributed by the impurity, and n_e denotes the total number of delocalized electrons, corresponding with the observed steps. Data collected from [128].

X	Valence	N	n_v	n_e
Au	$4f^{14}5d^{10}6s^1$	3, 9, 19, 21, 35	1	2, 8, 18, 20, 34
Sc	$3d^1 4s^2$	6, 16, 32	3	8, 18, 34
Ti	$3d^2 4s^2$	5, (15), 27	4	8, 18, (30)
V	$3d^3 4s^2$	5, 7	2 ?	6, 8
Cr	$3d^5 4s^1$	1, 5, 7, 17, (19), 33	2	2, 6, 8, 18, (20), 34
Mn	$3d^5 4s^2$	1, 5, 7, 17, (19), 33	2	2, 6, 8, 18, (20), 34
Fe	$3d^6 4s^2$	1, 5, 7, 17, (19), 33	2	2, 6, 8, 18, (20), 34
Co	$3d^7 4s^2$	1, 5, 7, 17, (19), 33	2	2, 6, 8, 18, (20), 34
Ni	$3d^8 4s^2$	2,8,18	1	2, 8, 18

The fragmentation pattern of gold clusters with Cr, Mn, Fe and Co impurities shows abundance steps at $N = 1, 5, 7, 17, (19)$, and 33. Assuming that the dopant atom contributes two electrons, the observed drops correspond to 2, 6, 8, 18, (20), and 34 electrons. The features for a Ni impurity can be explained by assuming that just one electron is delivered. All the magic numbers seen above are well known from the electronic shell model (six electrons correspond to an oblate subshell closure in the deformed jellium model; see also Fig. 5.3).

The values of n_v can be justified by the difference in the spatial localization of the $3d$ orbitals. The large size of the d wave functions at the begining of the $3d$ series (Sc, Ti) facilitates the hybridization with the Au orbitals. In contrast, the d electrons are more localized for Cr, Mn, Fe, Co and Ni, and only the $4s$ electrons contribute to the delocalized cloud.

8.8 Doubly Charged Clusters

Very small doubly charged clusters of the sp metals are unstable against dissociation into singly charged species. However, the bonding between the atoms in transition metals is stronger and doubly charged dimers like Mo_2^{2+} have been detected in mass spectrometric studies [129]. Early theoretical calculations for the $3d$ series [130] have been followed by more accurate DFT calculations for Ni_2^{2+} [131], Mn_2^{2+} and Co_2^{2+} [132]. Calculations at the GGA level predict for the ground state of neutral Ni_2 a triplet with a valence configuration $1\sigma^2 1\pi^4 2\pi^2 (\uparrow) 2\sigma^2 1\delta^4 3\sigma^2 2\delta^4$.

This configuration can be referred to as $(\pi\pi)$ to indicate where the unpaired electrons defining the triplet state are. Several quintet states of Ni_2^{2+} were found to be metastable against dissociation, that is, stabilized by a fission barrier. The binding energies (or, in other words, the height of the fission barriers) and the harmonic vibrational energies are given in Table 8.4. Those metastable states having at least one σ unpaired electron (the first four states in the table) dissociate into $Ni^+ (d^9)$ + Ni^+ (d^8s^1, quartet). On the other hand the configurations showing exclusively π and δ unpaired electrons (the last four in the Table) dissociate into $Ni^+ (d^8s^1$, doublet) + $Ni^+ (d^8s^1$, quartet). The binding energies in the second group range between 0.5 and 1.0 eV, and are smaller in the first group. The bond distance is, in all cases, larger than the bond distance of

neutral Ni_2 (the calculated bond length of Ni_2 using the same method is 4.06 a.u., and the experimental value is 4.16 a.u. [131]). This fact suggests that the full occupancy of the 3σ molecular orbital (MO) gives an additional stability that is not attained when this bonding MO is only partially occupied. Lifetimes can be calculated as

$$\tau = \frac{1}{\nu T} \qquad (8.16)$$

where ν is the vibrational frequency (in seconds) and T is the transmission coefficient through the barrier. Using the semiclassical WKB approximation to calculate T predicts extremely large lifetimes.

Table 8.4. Equilibrium bond distance r_e (in a. u.), binding energy BE (in eV), vibrational frequency ω (in cm^{-1}) and valence electronic configuration of metastable quintet states of Ni_2^{2+}.

Config.	r_e	BE	ω_e	Valence Configuration
$\sigma\sigma\pi\pi$	4.57	0.29	173	$1\sigma^2 1\pi^4 2\sigma^2 2\pi^2 1\delta^4 2\delta^3 3\sigma^1$
$\sigma\sigma\pi\delta$	4.93	0.14	131	$1\sigma^2 1\pi^4 2\sigma^2 2\pi^3 1\delta^3 2\delta^3 3\sigma^1$
$\sigma\sigma\delta\delta$	5.46	0.05	112	$1\delta^2 2\delta^4 1\sigma^2 2\sigma^1 1\pi^4 2\pi^4 3\sigma^1$
$\sigma\pi\pi\delta$	5.12	0.06	102	$1\pi^4 1\sigma^2 2\pi^3 1\delta^2 2\delta^2 2\sigma^3 3\sigma^1$
$\pi\pi\pi\pi$	5.27	0.57	176	$1\pi^2 1\pi^1 1\sigma^2 2\sigma^2 1\delta^4 2\delta^4 3\sigma^2$
$\pi\pi\pi\delta$	4.99	0.73	181	$1\pi^3 2\pi^1 1\sigma^2 1\delta^2 2\delta^4 2\sigma^2 3\sigma^2$
$\pi\pi\delta\delta$	4.71	0.96	203	$1\delta^2 2\delta^4 1\pi^4 1\pi^2 1\sigma^2 2\sigma^2 3\sigma^2$
$\pi\delta\delta\delta$	4.74	0.82	194	$1\delta^2 2\delta^3 1\pi^4 1\sigma^2 2\pi^3 2\sigma^2 3\sigma^2$
$\delta\delta\delta\delta$	4.91	0.69	184	$1\delta^2 2\delta^3 1\pi^4 1\sigma^2 2\pi^4 2\sigma^2 3\sigma^2$

Mn_2^{2+} is characterized by a relatively low density of low energy metastable states, about 2 states/eV. The lowest energy metastable state is a singlet in which the two Mn ions are antiferromagnetically coupled. The electronic configuration of this state is $1\sigma^2 2\sigma^2 1\pi^4 1\delta^4$, its bond length is 5.56 a.u. and the barrier height is 0.16 eV [132]. Other metastable states present higher spin multiplicities. Co_2^{2+} presents a density of low energy metastable states of about 7 states/eV, substantially denser than in Mn_2^{2+}. The lowest energy state is a septet of electronic configuration $1\sigma^2 2\sigma^1(\uparrow)3\sigma^{*1}(\uparrow)1\pi^4 2\pi^{*2}(\uparrow)1\delta^4 2\delta^{*2}(\uparrow)$ and a fission barrier of 0.95 eV. Lifetimes for low vibrational quantum states of both Mn_2^{2+} and Co_2^{2+} are very large, suggesting that the corresponding metastable states could be detected by experimental measurements.

References

1. Katakuse, I., Ichihara, T., Fujita, Y., Matsuo, T., Sakurai, T., and Matsuda, H., *Int. J. Mass Spectrom. Ion Proc.*, **67**, 229 (1985).
2. Katakuse, I., Ichihara, T., Fujita, Y., Matsuo, T., Sakurai, T., and Matsuda, H., *Int. J. Mass Spectrom. Ion Proc.*, **74**, 33 (1986).
3. Knickelbein, M. B., *Chem. Phys. Lett.*, **192**, 129 (1992).
4. Ganteför, G., Gausa, M., Meiwes Broer, K. H., and Lutz, H. O., *J. Chem. Soc. Faraday Trans.*, **86**, 2483 (1990).
5. Leopold, D. G., Ho, J., and Lineberger, W. C., *J. Chem. Phys.*, **86**, 1715 (1987).
6. Pettiete, C. L., Yang, S. H., Craycraft, M. J., Conceicao, J., Laaksonen, R. T., Chesnovsky, O., and Smalley, R. E., *J. Chem. Phys.*, **88**, 5377 (1988).
7. Cha, C. Y., Ganteför, G., and Eberhardt, W., *J. Chem. Phys.*, **99**, 6308 (1993).
8. Winter, B. J., Parks, E. K., and Riley, S. J., *J. Chem. Phys.*, **94**, 8618 (1991).
9. Williams, A. R., Gelatt, D., and Janak. J. F., *Theory of Alloy Phase Formation*, Ed. L. H. Bennet, The Metallurgical Soc. of AIME, Warrendale (1980), p. 40.
10. Alonso, J.A., and March, N.H., *Electrons in Metals and Alloys*, Academic, London (1989).
11. Chesnovsky, O., Taylor, K.J., Conceicao, J., and Smalley, R.E., *Phys. Rev. Lett.*, **64**, 1786 (1990).
12. Fujima, N., and Yamaguchi, T., *J. Phys. Soc. Japan* , **58**, 1334 (1989).

13. Massobrio, C., Pasquarello, A., and Car, R., *Chem. Phys. Lett.*, **238**, 215 (1995).
14. Massobrio, C., Pasquarello, A., and Car, R., *Phys. Rev. Lett.*, **75**, 2104 (1995); *Phys. Rev. B*, **54**, 8913 (1996).
15. Bonacic-Koutecky, V., Cespiva, L., Fantucci, P., and Koutecky, J., *J. Chem. Phys.* , **98**, 7981 (1993).
16. Bonacic-Koutecky, V., Cespiva, L., Fantucci, P., Pittner, J., and Koutecky, J., *J. Chem. Phys.*, **100**, 490 (1994).
17. Ho, J., Ervin, K.M., and Lineberger, W.C., *J. Chem. Phys.*, **93**, 6986 (1990).
18. Heiz, U., and Schneider, W. D., *J. Phys. D: Appl. Phys.*, **33**, R85 (2000).
19. López, N., and Norskov, J. K., *J. Am. Chem. Soc.*, **124**, 11262 (2002).
20. Boyen, H. G., Kästle, G., Weigl, F., Koslowski, B., Dietrich, C., Ziemann, P., Spatz, J. P., Riethmüller, S., Hartmann, C., Möller, M., Schmid, G., Garnier, M. G., and Oelhafen, P., *Science*, **297**, 1533 (2002).
21. Elghanian, R., Storhoff, J. J., Mucic, R. C., Letsinger, R. L., and Mirkin, C. A., *Science*, **277**, 1078 (1988).
22. Chen, S., Ingram, R. S., Hostetler, M. J., Pietron, J. J., Murray, R. W., Schaaff, T. G., Khoury, J. T., Alvarez, M. M., and Whetten, R. L., *Science*, **280**, 2098 (1998).
23. Templeton, A. C., Wuelfing, W. P., and Murray, R. W., *Acc. Chem. Res.*, **33**, 27 (2000).
24. Li, J., Li, X., Zhai, H. J., and Wang, L. S., *Science*, **299**, 864 (2003).
25. Wang, J., Wang, G., and Zhao, J., *Chem. Phys. Lett.*, **380**, 716 (2003).
26. Furche, F., Ahlrichs, R., Weis, P., Jacob, C., Gilb, S., Bielweiler, T., and Kappes, M. M., *J. Chem. Phys.*, **117**, 3120 (2002).
27. Fernández, E. M., Soler, J. M. Garzón, I. L., and Balbás, L. C., *Phys. Rev. B*, **70**, 165403 (2004).
28. Weis, P., Bierweiler, Th., Gilb, S., and Kappes, M. M., *Chem. Phys. Lett.* , **355**, 355 (2002).
29. Häkkinen, H., Moseler, M., and Landman, U., *Phys. Rev. Lett.*, **89**, 33401 (2002).
30. Cleveland, C. L., Landman, U., Schaaff, T. G., Shafigullin, M. N., Stephens, P. W., and Whetten, R. L., *Phys. Rev. Lett.*, **79**, 1873 (1997).
31. Michaelian, K., Rendon, N., and Garzón, I. L., *Phys. Rev. B* , **60**, 2000 (1999).
32. Garzón, I. L., Michaelian, K., Beltrán, M. R., Posada-Amarillas, A., Ordejón, P., Artacho, E., Sanchez-Portal, D., and Soler, J. M., *Phys. Rev. Lett.*, **81**, 1600 (1998).
33. Tiggesbäumker, J., L. Köller, L., Meiwes-Broer, K. H., and Liebsch, A., *Phys. Rev. A* , **48**, R1749 (1993).
34. Tiggesbäumker, J., L. Köller, L., Meiwes-Broer, K. H., and Liebsch, A., *Chem. Phys. Lett.* , **268**, 428 (1996).
35. Liebsch, A., *Phys. Rev. Lett.*, **71**, 145 (1993); *Phys. Rev. B*, **48**, 11317 (1993).

36. Serra, L., and Rubio, A., *Z. Phys. D*, **40**, 262 (2997).
37. Rubio, A., Alonso, J. A., Blase, X., and Louie, S. G., *Int. J. Mod. Phys. B*, **11**, 2727 (1997).
38. Serra, L., and Rubio, A., *Phys. Rev. Lett.*, **78**, 1428 (1997).
39. Painter, G. S., *Phys. Rev. Lett.*, **70**, 3959 (1993).
40. Moruzzi, V. L., Janak, J. F., and Williams, A. R., *Calculated Elctronic Properties of Metals*, Pergamon, New York (1978).
41. Zhang, G. W., Feng, Y. P., and Ong, C. K., *Phys. Rev. B*, **54**, 17208 (1996).
42. Reuse, F.A. and Khanna, S.N., *Chem. Phys. Lett.*, **234**, 77 (1995).
43. Moskovits, M. and Hulse J.E., *J. Chem. Phys.*, **66**, 3988 (1977).
44. Morse, M.O., Hansen, G.P., Langridge-Smith, P.R.R., Zheng, L.S., Geusic, M.E., Michalopoulos, D.L., and Smalley, R.E., *J. Chem. Phys.*, **80**, 5400 (1984).
45. Ho, J., Polak, M.L., Ervin, K.M., and Lineberger, W.C., *J. Chem. Phys.*, **99**, 8542 (1986).
46. Moskovits, M., and Dilella, D.P., *J. Chem. Phys.* , **72**, 2267 (1980).
47. Castro, M., Jamorski, C., and Salahub, D.R., *Chem. Phys. Lett.*, **271**, 133 (1997).
48. Reddy, B.V., Nayak, S.K., Khanna, S.N., Rao, B.K., and Jena, P., *J. Phys. Chem. A*, **102**, 1748 (1998).
49. Lian, L., Su C.X., and Armentrout, P.B., *J. Chem. Phys.*, **97**, 4084 (1992).
50. Parks, E.K., Zhu, L., Ho, J. , and Riley, S.J., *J. Chem. Phys.*, **102**, 7377 (1995).
51. Nygren, M.A., Siegbahn, P.E.M., Wahlgren, U., and Akeby, H., *J. Chem. Phys.*, 3633 (1992).
52. Nayak, S.K., Reddy, B., Rao, B.K., Khanna, S.N., and Jena, P., *Chem. Phys. Lett.*, **253**, 390 (1996).
53. Apsel, S.E., Emmert, J.W., Deng, J., and Bloomfield, L.A., *Phys. Rev. Lett.*, **76**, 1441 (1996).
54. Finnis, M.W., and Sinclair, J.E., *Phil. Mag.* , **50**, 45 (1984).
55. Desmarais, N., Jamorski, C., Reuse, F.A., and Khanna, S.N., *Chem. Phys. Lett.*, **294**, 480 (1998).
56. Reuse, F.A., Khanna, S.N., and Bernel, S., *Phys. Rev. B*, **52**, R11650 (1995).
57. Weber, S. E., and Jena, P., *Chem. Phys. Lett.*, **281**, 401 (1997).
58. Ervin, K.M., Ho, J., and Lineberger, W.C., *J. Chem. Phys.*, **99**, 8542 (1993).
59. Reuse, F.A., and Khanna, S.N., *Eur. Phys. J. D*, **6**, 77 (1999).
60. Ballone, P., and Jones, R.O., *Chem. Phys. Lett.*, **233**, 632 (1995).
61. Diéguez, O., Alemany, M. M. G., Rey, C., Ordejón, P., and Gallego, L. J., *Phys. Rev. B*, **63**, 205407 (2001).
62. Goodwin, L., and Salahub, D.R., *Phys. Rev. A*, **47**, R774 (1993).
63. Kietzmann, H., Morenzin, J., Bechtold, P.S., Ganteför, G., Eberhardt, W., Yang, D.S., Hackett, P.A., Fournier, R., Pang, T. and Chen, C., *Phys. Rev. Lett.*, **77**, 4528 (1996).

64. Williams, A.R., de Groot, R.A. and Sommers, C.B., *J. Chem. Phys.*, **63**, 628 (1975).
65. Zhao, J., Chen, and Wang, G., *Phys. Lett. A*, **214**, 211 (1996).
66. Kietzmann, H., Morenzin, J., Bechthold, P.S, Ganteför, G. and Eberhardt, W., *J. Chem. Phys.*, **109**, 2275 (1998).
67. Holmgren, L., Andersson, M. and Rosen, A., *Surf. Sci.*, **331-333**, 231 (1995).
68. Wu, H., Desai, S.R., Wang, L.S., *Phys. Rev. Lett.*, **76**, 212 (1996).
69. Feibelmann, P.J. and Himpsel, F.J., *Phys. Rev. B.*, **21**, 1394 (1980).
70. Lian, L., Su, C.X. and Armentront, P.B., *J. Chem. Phys.*, **97**, 4084 (1992).
71. Wu, H., Desai, S.R., Wang, L.S., *Phys. Rev. Lett.*, **77**, 2436 (1996).
72. Minemoto, S., Terasaki, A., Imoto, H. and Kondow, T., *J. Chem. Phys.*, **109**, 9737 (1998).
73. Cheng, H. and Wang, L.S., *Phys. Rev. Lett.*, **77**, 51 (1996).
74. Wang, L.S., Wu, H. and Cheng, H., *Phys. Rev. B*, **55**, 12884 (1997).
75. Su, C.X., and Armentrout, P.B., *J. Chem. Phys.*, **99**, 6506 (1993).
76. Klebanoff, L. E., Victora, R. H., Falicov, L. M., and Shirley, D. A., *Phys. Rev. B*, **32**, 1997 (1985).
77. Herring, C., and Nichols, M. H., *Rev. Mod. Phys.*, **21**, 185 (1949).
78. Leisner, T., Athanassenas, K., Echt, O., Kandler, D., Kreisle, D., and Recknagel, E., *Z Physik D*, **20**, 127 (1991).
79. Amrein, A., Simpson, R. and Hackett, P., *J. Chem. Phys.*, **94**, 4663 (1991).
80. Leisner, T., Athanassenas, K., Kreisle, D., Recknagel, E. and Echt, O., *J. Chem. Phys.*, **99**, 9670 (1993).
81. Weidele, H., Kreisle, D., Recknagel, E., Schulze Icking-Konert, G., Hanschuh, H., and Eberhardt, W., *Chem. Phys. Lett.*, **237**, 425 (1995).
82. Reiners, T., and Haberland, H., *Phys. Rev. Lett.*, **77**, 2440 (1996).
83. Weidele, H., Kreisle, D., Recknagel, E., Kluge, M. J., Lindiger, M., Schweihard, L., Walther, C., and Ziegler, J., *J. Chem. Phys.*, **110**, 8754 (1999).
84. First, P.N., Stroscio, J.A., Dragoset, R.A., Pierce, D.T. , and Celotta, R.J., *Phys. Rev. Lett.*, **63**, 1416 (1989).
85. Wawro, A., Kasuya, A., Czajka, R., and Nishina, Y., *Surf. Rev. Lett.*, **3**, 97 (1996).
86. Vinod, C.P., Kulkarni, G.U., and Rao, C.N.R., *Chem. Phys. Lett.*, **289**, 329 (1998).
87. Kubo, R., Kawabata, A., and Kobayashi, S., *Ann. Rev. Mater. Sci.*, **14**, 49 (1984).
88. Friedel, J., *The Physics of Metals.* Ed. J.M. Ziman, Cambridge University Press (1969), p. 340.
89. Pastor, G., Dorantes-Dávila, J., and Bennemann, K.H., *Chem. Phys. Lett.*, **148**, 459 (1988).
90. Zhao, J., Chen, X. and Wang, G., *Phys. Rev. B* , **50**, 15424 (1994).

91. Harrison, W.A., *Electronic Structure and the Properties of Solids*, Freeman, San Francisco (1980).

92. Aguilera-Granja, F., Alonso, J.A. and Montejano-Carrizales, J.M., *Current Problems in Condensed Matter*. Ed. J.L. Morán-López, Plenum, New York (1998) p. 109.

93. Wertheim, G.K., *Z. Phys. D*, **12**, 319 (1983).

94. Parks, E.K., Klots, T.D., and Riley, S.J., *J. Chem. Phys.*, **92**, 3813 (1990).

95. Aguilera-Granja, F., Bouarab, S., Vega, A., Alonso, J.A. and Montejano-Carrizales, J.M., *Solid State Commun.*, **104**, 635 (1997).

96. Boyen, H. G., Kästle, G., Weigl, F., Ziemann, P., Schmidt, G., Garnier, M. G., and Oelhafen, P., *Phys. Rev. Lett.*, **87**, 276401 (2001).

97. Sakurai, M., Watanabe, K., Sumiyama, K., and Suzuki, K., *J. Chem. Phys.*, **111**, 235 (1999).

98. Alonso, J. A., *Chem. Rev.* , **100**, 637 (2000).

99. Pellarin, M., Baguenard, B., Vialle, J.L., Lermé, J., Broyer, M., Miller, J. and Perez, A., *Chem. Phys. Lett.*, **217**, 349 (1994).

100. Klots, T.D., Winter, B.J., Parks, E.K., and Riley, S.J., *J. Chem. Phys.*, **92**, 2110 (1990).

101. Klots, T.D., Winter, B.J., Parks, E.K. and Riley, S.J., *J. Chem. Phys.*, **95**, 8919 (1991).

102. Parks, E.K., and Riley, S.J., *Z Phys. D*, **33**, 55 (1995).

103. Parks, E.K., Winter, B.J., Klots, T.D., and Riley S.J., *J. Chem. Phys.*, **96**, 8267 (1992).

104. Parks, E.K., Zhu, L., Ho, J., and Riley, S.J., *J. Chem. Phys.*, **100**, 7206 (1994).

105. Montejano-Carrizales, J. M., Iñiguez, M. P., Alonso, J. A., and López, M. J., *Phys. Rev. B*, **54**, 5961 (1996).

106. Foiles, S.M., Baskes, M.I. , and Daw, M.S., *Phys. Rev. B*, **53**, 7983 (1986).

107. Daw, M.S., and Baskes, M.I., *Phys. Rev. B*, **29**, 6443 (1984).

108. Stave, M.S., and De Pristo, A.E., *J. Chem. Phys.*, **97**, 3386 (1992).

109. Parks, E. K., Kerns, K. P., and Riley, S. J., *J. Chem. Phys.*, **109**, 10207 (1998).

110. Wetzel, T. L., and De Pristo, E. A., *J. Chem. Phys.*, **105**, 573 (1996).

111. Parks, E. K., Winter, B. J., Klots, T. D., and Riley, S. J., *J. Chem. Phys.*, **94**, 1882 (1991).

112. Vajda, S., Woolf, S., Leisner, T., Busolt, U., Wöste, L. H., and Wales, D. J., *J. Chem. Phys.*, **107**, 3492 (1997).

113. Rey, C., Gallego, L.J., García-Rodeja, J., Alonso, J.A. and Iñiguez, M.P., *Phys. Rev. B*, **48**, 8253 (1993).

114. Garzón, I.L. and Jellinek, J., *Physics and Chemistry of Finite Systems: From Clusters to Crystals*. Ed. P. Jena, S.N. Khanna and B.K. Rao, Kluwer, Dordrecht (1992), Vol. I, p. 405.

115. Stave, M.S., Sanders, D. E., Raeker, T. J., and De Pristo, A.E., *J. Chem. Phys.*, **93**, 4413 (1990).

116. García-Rodeja, J., Rey , C., Gallego, L.J., and Alonso, J.A., *Phys. Rev. B*, **49**, 8495 (1994).
117. Güvenc, Z.B., Jellinek, J., and Voter, A.F., *Physics and Chemistry of Finite Systems: From Clusters to Crystals*. Ed. P. Jena, S.N. Khanna and B.K. Rao. Kluwer, Dordrecht (1992), Vol. I, p. 411.
118. Jellinek, J., and Güvenc, Z.B., *The Synergy between Dynamics and Reactivity at Clusters and Surfaces*. Ed. L.J. Farrugia, Kluwer, Dordrecht (1995) p. 217.
119. Rey, C., García-Rodeja, J., and Gallego, L.J., *Phys. Rev. B*, **54**, 2942 (1996).
120. Vlachos, D.G., Schmidt, L.D., and Aris, R., *Z. Phys. D* , 26, S156 (1993).
121. Cleveland, C.L., and Landman, U., *J. Chem. Phys.* 94, 7376 (1991).
122. Montejano-Carrizales, J.M., Iñiguez, M. P. , and Alonso, J.A., *J. Cluster Sci.*, **5**, 287 (1994).
123. Lathiotakis, N. N., Andriotis, A. N., Menon, M., and Connolly, J., *Europhys. Lett.*, **29**, 135 (1995).
124. Lathiotakis, N. N., Andriotis, A. N., Menon, M., and Connolly, J., *J. Chem. Phys.*, **104**, 992 (1996).
125. Knickelbein, M., *J. Chem. Phys.*, **115**, 5957 (2001).
126. Sakurai, M., Watanabe, K., Sumiyama, K., and Suzuki, K., *J. Chem. Phys.*, **111**, 235. (1999).
127. Zhao, J., Qiu, Q., Wang, B., Wang, J., and Wang, G., *Solid State Commun.* **118**, 157 (2001).
128. Neukermans, S., Janssens, E., Tanaka, H., Silverans, R. E., and Lievens, P., *Phys. Rev. Lett.*, **90**, 33401 (2003).
129. Tsong, T. T., *Surf. Sci.*, **177**, 593 (1986).
130. Liu, F., Press, M. R., Khanna, S. N., and Jena, P., *Phys. Rev. Lett.*, **59**, 2562 (1987).
131. Pis Diez, R., and Alonso, J. A., *Chem. Phys. Lett.*, **332**, 481 (2000).
132. Pis Diez, R., Alonso, J. A., Matxain, J. M., and Ugalde, J. M. *Chem. Phys. Lett.*, 372, 82 (2003).

This page intentionally left blank

9. Magnetism

9.1 Some Basic Concepts

Since the clusters in a molecular beam are free from any interation with a matrix, it becomes possible to determine their intrinsic magnetic properties. The dependence of the magnetic properties on the cluster size can be determined in a Stern–Gerlach experiment, in which the clusters interact with an applied inhomogeneous magnetic field and are deflected from the original trajectory. The deflection of a cluster traveling with a velocity v transversally to the field gradient direction (defined as the z direction) is given by [1, 2]

$$d = K \frac{M(B)}{mv^2} \frac{\partial B}{\partial z}$$

(9.1)

where m is the cluster mass, $\partial B / \partial z$ is the magnetic field gradient and K is a constant which depends on the geometry of the apparatus. This equation indicates that the deflection is proportional to the cluster magnetization $M(B)$. The experiments [1–8] are normally analyzed assuming that the ferromagnetic clusters are single-domain particles following the super paramagnetic behavior [9], which is true under conditions such that the thermal relaxation time is much lower than the time required by the clusters to pass through the poles of the Stern–Gerlach magnet [10]. In that case the atomic moments of a particle with N atoms are coupled by the exchange interaction, giving rise to a total magnetic moment μ_N that is free of the cluster lattice. This orientational freedom allows the magnetic moment to align with an external magnetic field. For an ensemble of particles in thermodynamic equilibrium in an external field B the magnetization (that is, the average projection of the

magnetic moment along the field direction) reduces, in the low field limit ($\mu_N \ll k_B T$) and for large particles, to

$$M(B) = \frac{\mu_N^2 B}{3k_B T} . \tag{9.2}$$

Equations (9.1) and (9.2) can be used to determine μ_N. The average magnetic moment $\overline{\mu} = \mu_N / N$ of the monodomain particle is analogous to the saturation magnetization of the bulk, but in zero field a monodomain particle has a magnetic moment different from zero.

The magnetism is sensitive to the symmetry, atomic coordination and interatomic distances in the cluster. These three characteristics are inter-related. Let us consider the free atoms as an extreme case. Fe, Co and Ni have eight, nine and ten outer electrons, respectively, to be distributed in the $3d$ and $4s$ shells. Hund rules require the spin to be a maximum and this leads to electronic configurations $3d\uparrow^5 \, 3d\downarrow^1 \, 4s^2$ for Fe, $3d\uparrow^5 \, 3d\downarrow^2 \, 4s^2$ for Co, and $3d\uparrow^5 \, 3d\downarrow^3 \, 4s^2$ for Ni. The $3d\uparrow$ and $3d\downarrow$ subshells are separated by the exchange interaction. These atoms have nonzero spins, and since the spin magnetic moment of an electron is 1 Bohr magneton (μ_B), the atoms have substantial moments. When the atoms come together in a cluster or a metal, the overlap between the atomic orbitals of neighbor atoms gives rise to energy bands. The levels corresponding to $4s$ electrons produce a free electron-like band with a width in the solid of $W = 20$–30 eV, while the d electrons stay localized on the atomic sites, and the d band width is much smaller, typically 5–10 eV in the bulk. The crystal potential stabilizes the d and s states by different amounts. This, plus *spd* hybridization, leads to charge transfer from s to d states, and the number of s electrons for systems other than the atom is close to 1. Assuming that the $3d$ orbitals are atomic-like, the Hund rule requires the majority $3d\uparrow$ sub-band to be fully occupied with five electrons per atom while the minority $3d\downarrow$ sub-band has two, three and four electrons per atom in Fe, Co and Ni respectively. The difference in the number of spin $\uparrow$ and spin $\downarrow$ $3d$ electrons per atom is $n_d(\uparrow)$ - $n_d(\downarrow)$ = 3, 2, 1 for Fe, Co and Ni respectively, and the magnetic moments per atom are $\overline{\mu}$ (Fe) = 3 μ_B, $\overline{\mu}$ (Co) = 2 μ_B, $\overline{\mu}$ (Ni) = 1μ_B.

These values are quite close to the magnetic moments of very small clusters. The bulk moments, $\overline{\mu}$ (Fe) = 2.2 μ_B, $\overline{\mu}$ (Co) = 1.7 μ_B, $\overline{\mu}$ (Ni) = 0.64μ_B, are smaller, and their noninteger values originate in the partial delocalization of the $3d$ electrons, which also contributes to the mutual alignment of the moments. This is known as itinerant exchange.

The onset of delocalization of the d electrons has been studied by comparing the photoelectron spectra of Ni_N^- and Pd_N^- to those of Cu_N^- [11, 12]. In small Cu clusters the orbitals of the $3d^{10}$ shell are well localized and bonding is due to the $4s$ electrons mainly. The photoelectron spectra of Ni_N^- with $N \leq 6$ is similar to the spectra for Cu_N^-. The reason is that the $3d$ orbitals of Ni clusters ($N < 7$) are well localized and the interaction between the $3d^9$ cores is negligible. The spectra of larger clusters reflects the delocalization of the $3d$ electrons. Data for small Pd_N^- clusters presents some similarities to Ni_N^-.

The variation of the average magnetic moment as a function of the cluster size is not smooth in general. The overal decay is due to the increasing number of nearest neighbors, an effect that enhances the itinerant character of the d electrons. On the surface of the clusters the number of neighbors is still low compared to the bulk, so only when the number of surface atoms becomes small compared to the total number of atoms in the cluster, $\overline{\mu}_N$ converges to $\overline{\mu}_{bulk}$. Furthermore, small clusters have structures that are not simple fragments of the crystal. All these ingredients affect the detailed broadening of the electronic levels to form the d bands. So the exchange splitting between $\uparrow$ and $\downarrow$ d sub-bands, the charge transfer from the s to the d band and the sd hybridization depend on the cluster size N, and control the evolution of $\overline{\mu}_N$.

9.2 Size Dependence of the Magnetic Moments

The magnetic moments of Fe, Co and Ni clusters with sizes up to 700 atoms have been measured [1, 2, 7, 8] under conditions where the clusters follow superparamagnetic behavior, for low cluster temperatures (vibrational temperature T_{vib} = 78 K for Ni and Co clusters, and 120 K for Fe clusters). The results are shown in Fig. 9.1. The magnetic moment

per atom decreases for increasing cluster size and converges to the bulk value for a few hundred atoms; this convergence is faster for the Ni clusters. However, in the three cases weak oscillations are superimposed to the global decrease of $\overline{\mu}$.
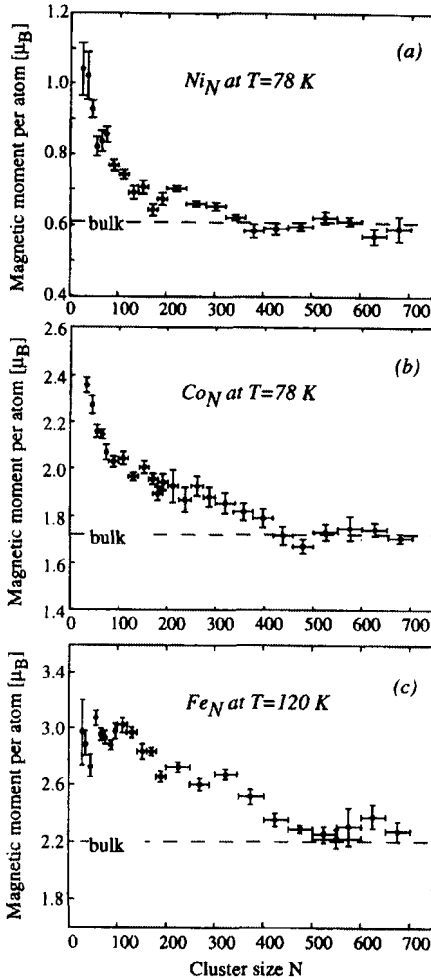
Figure 9.1. Magnetic moments per atom of Ni, Co and Fe clusters. Reproduced from I. M. L. Billas, A. Chatelain W. D. de Heer, *J. Mag. Mag. Mater.* **168**, 64 (1997) with permission of Elsevier.

Experiments have also been performed for clusters of $4d$ and $5d$ metals, that are nonmagnetic in the bulk [13]. Rhodium is an intriguing case. Rh clusters with less than 60 atoms show magnetic moments, but larger clusters are nonmagnetic. Clusters with about ten atoms have magnetic moments $\overline{\mu} \approx 0.8\mu_B$, and $\overline{\mu}$ decays quickly between $N = 10$ and $N = 20$ ($\overline{\mu}(\text{Rh}_{20}) = 0.2\ \mu_B$), showing, however, oscillations that produce large moments for Rh_{15}, Rh_{16} and Rh_{19}. Rhodium was the first case in which magnetism was observed in clusters of a nonmagnetic metal. This behavior is different from that shown by clusters of the $3d$ elements Fe, Co and Ni, where the variation of $\overline{\mu}$ extends over a much wider range of cluster sizes. In contrast to Rh, Ruthenium and Palladium clusters with 12 to more than 100 atoms are reported nonmagnetic [13].

The decay of $\overline{\mu}$ with cluster size can be explained using simple models [14]. Neglecting the contribution of the sp electrons and using the Friedel model of a rectangular d band [15], the local density of electronic states (LDOS) with spin σ at site i can be expressed [16]

$$D_i^{\sigma}(\varepsilon) = \frac{5}{W_i} \quad \text{for} \quad -\frac{W_i}{2} < \varepsilon - \varepsilon_d^{\sigma} < \frac{W_i}{2} \qquad (9.3)$$

Here ε_d^{σ} is the energy of the center of the σ spin sub-band, and W_i is the local band width (assumed equal for $\uparrow$ and $\downarrow$ spins). The second moment approximation in tight-binding theory [16] gives W_i proportional to the square root of the local coordination number Z_i

$$W_i = W_b (Z_i / Z_b)^{1/2} \qquad (9.4)$$

where W_b and Z_b refer to the solid. If the d band splitting $\Delta = \left| \varepsilon_d^{\uparrow} - \varepsilon_d^{\downarrow} \right|$ is assumed equal to the bulk value, the local magnetic moment

$$\mu = \int_{-\infty}^{\varepsilon_F} \left[D_i^{\uparrow}(\varepsilon) - D_i^{\downarrow}(\varepsilon) \right] d\varepsilon \qquad (9.5)$$

becomes

$$\mu_i = \left(\frac{Z_b}{Z_i}\right)^{1/2} \mu_b \quad \text{if} \ \ Z_i \geq Z_c$$

$$= \mu_{\text{dimer}} \qquad \text{otherwise} \qquad (9.6)$$

where Z_c is the limiting coordination below which the magnetic moment of that atom adopts the value for the dimer. For instance, for Ni one can choose $Z_c = 5$ [17]. The average magnetic moment $\overline{\mu}_N = (1/N)\sum\limits_{i=1}^{N}\mu_i$ strongly depends on the ratio of the number of surface atoms and bulk-like atoms in the cluster. The surface atoms have small Z_i and large μ_i, while the internal atoms have $Z_i = Z_b$ and $\mu_i = \mu_b$. For small clusters, most atoms are on the surface and $\overline{\mu}$ is large. But as N increases, the fraction of surface atoms decreases and with it $\overline{\mu}$. The simple expression

$$\overline{\mu} = \mu_b + \left(\mu_s - \mu_b\right)N^{-1/3} \qquad (9.7)$$

where μ_s is the magnetic moment of surface atoms, was proposed by Jensen and Bennemann [18]. The formula displays the decrease of $\overline{\mu}$ towards μ_b with increasing N. However, the experiments indicate that $\overline{\mu}$ varies with N in an oscillatory way and its explanation requires detailed consideration of the geometry and the electronic structure.

9.3 Magnetic Shell Models

Since the transition metal clusters do not show the magic numbers associated to the closing of electronic shells characteristic of *sp* elements, it appears reasonable to expect the oscillations of $\overline{\mu}$ to be associated to the development of atomic shells, and several magnetic shell models have been developed. In a first model [1, 2, 7] the clusters were assumed to be formed by several concentric atomic shells and the magnetic moment of an atom was taken to depend only on how deep the atom is located below the surface. Values μ_1, μ_2, μ_3, ... are assigned to atoms in layers 1, 2, 3, ... where layer 1 indicates the most external, or

surface layer, and so on. The moments μ_i were assumed independent of the cluster size. Then the observed trend of a decrease of $\bar{\mu}$ with increasing N is reproduced by assigning the following empirical values for μ_1, μ_2, μ_3, μ_4, ...: (1.2, -0.4, 0.6, 0.8, 0.67, 0.65, 0.62, 0.6) for Ni, (2.7, 0.4, 1.6, 1.45, 1.9, 1.9, 1.9, 1.7) for Co, and (3, 3.2, 0, 0, 3.2, 3, 2.8, 2.5) for Fe, in units of μ_B. These values indicate that the moments of atoms in the surface layer are enhanced with respect to those on inner layers. This model, however, does not reproduce the intriguing oscillations of $\bar{\mu}$.

Another shell model, proposed by Jensen and Bennemann [18] assumes that the clusters grow shell-by-shell and the atoms occupy the sites of an underlying *bcc* or *fcc* lattice. The global shapes assumed are the cube, octahedron and cuboctahedron. In addition to those regular shapes, another model of growth was considered assuming the successive occupation of coordination shells around the cluster center: each coordination shell is formed by those atoms at a common distance from the center, and this yields clusters with spherical shape. In order to assign magnetic moments to the atoms the general rule holds that the moments are different for different atomic shells, and even more, the moments may vary within the most external shells. The average coordination number Z is largest for almost filled atomic shells. Then maxima of Z should correspond to minima of $\bar{\mu}$, and oscillations of $\bar{\mu}(N)$ as a function of N are expected as a consequence of the formation of successive atomic shells. This oscillatory behavior modulates the decay of $\bar{\mu}$ given by Eq. (9.7). Using these models, the number of atoms corresponding to clusters with closed atomic shells can be calculated and these numbers are given in Table 9.1 for *fcc* clusters with cube, octahedron and cuboctahedron shapes, and for *bcc* clusters with cube and octahedron shapes. For cubes and octahedrons the table also includes results for clusters with rounded edges, obtained by removing all edge atoms from the closed shell clusters.

The numbers obtained are compared in the table with the meassured sizes [1, 2, 7] for which minima of $\bar{\mu}$ are obtained for Fe, Co and Ni clusters in the size range $30 < N < 700$. The comparison is suggestive: the experimental minima $\bar{\mu}_{min}$ roughly correspond to the growth of *bcc* cubes for Fe clusters, *fcc* cubes for Ni clusters and *fcc* octahedrons for Co clusters. Although the correlation is not quantitative enough to allow for a definite conclusion about the cluster structure, it provides some

support for the idea that the oscillations of $\bar{\mu}$ are related to the formation of atomic shells.

Table 9.1. Cluster size N for various cluster structures with closed atomic shells. The structures are *fcc* and *bcc* and the cluster shape is that of a cube, an octahedron (oct) or a cuboctahedron (cuboc). Asterisks refer to rounded clusters with edge atoms removed. Calculated N are compared to experimental sizes showing minima of the average magnetic moment. Data collected from [18].

	Closed shell cluster size					$N(\bar{\mu}_{min})$		
shell								
n	fcc cube	fcc oct	fcc cuboc	bcc cube	bcc oct	Fe	Co	Ni
2*	43	43	-	15	27		50	
2	63	85	55	35	57	45	85	72
							129	
3*	140	165		59	89		173	131
3	172	231	147	91	143	85	232	175
4*	321	399		145	203	150	355	260
4	365	489	309	189	289	191	483	381
5*	610	777	-	285	385	273		625
5	666	891	561	341	511			
6*	1031	1331		491	651			
6	1099	1469	923	559	825	551		

The comparison can be made more quantitative by making proposals for the local moments that take into account the atomic environment. A statistical model has been proposed [18] in which the average magnetic moment per atom of the outermost shell (shell 1) is assumed to be

$$\bar{\mu}_1 = (1 - X_1)\mu_{at} + X_1\mu_s \qquad (9.8)$$

where X_1 is the concentration of statistically occupied sites in that shell. μ_{at} is the magnetic moment of an atom without nearest neighbors in the topmost shell, and μ_s is that for a surface atom surrounded by other atoms in the topmost shell, taken to be similar to μ for a surface atom in

the solid. Next, the average magnetic moment of shell 2 below shell 1 was taken to depend on the concentration X_1 of occupied sites on shell 1:

$$\overline{\mu}_2 = (1 - X_1)\mu_s + X_1\mu_b \qquad (9.9)$$

This means that the magnetic moment of an atom in shell 2 is equal to μ_s if this atom has no nearest neighbors in shell 1, and is equal to the bulk value μ_b if it is covered by atoms of shell 1. For shell 3, *etc.*, magnetic moments are taken equal to μ_b. From the last two equations, the magnetic moment per atom becomes

$$\overline{\mu}_N = \frac{X_1 N_1 \overline{\mu}_1 + N_2 \overline{\mu}_2 + \overline{N}_b \overline{\mu}_b}{X_1 N_1 + N_2 + N_b} \qquad (9.10)$$

where N_1 and N_2 are the number of sites in shells 1 and 2, respectively, N_b is the total number of atoms in the inner shells, and $N = X_1 N_1 + N_2 + N_b$. The magnetic moment from (9.10) yields oscillations with minima near closed shells and maxima for half-filled shells. The results are given by the solid curves of Fig. 9.2, with the following parameters: for Fe, $\mu_{at} = 4.0\ \mu_B$, $\mu_s = 3.0\ \mu_B$, $\mu_b = 2.21\ \mu_B$; for Co, $\mu_{at} = 3.0\ \mu_B$, $\mu_s = 1.9\ \mu_B$, $\mu_b = 1.72\ \mu_B$; for Ni, $\mu_{at} = 1.2\ \mu_B$, $\mu_s = 0.7\ \mu_B$, $\mu_b = 0.62\ \mu_B$. Consistently with Table 9.1, *bcc* cubes are assumed for Fe, *fcc* octahedrons for Co and *fcc* cubes for Ni.

Another model [18] assumes that the magnetic moment at site *i* is determined by the local number of nearest neighbors, that is

$$\mu_i = \mu_i(Z_i). \qquad (9.11)$$

A smooth dependence on Z_i can be obtained from the magnetic moments for surfaces and thin films. For a *bcc* lattice the local atomic properties are affected by the second neighbors, so μ_i has to depended also on $Z_i^{(2)}$. These can be taken into account by defining an effective coordination number $Z_i = Z_i^{(1)} + \beta Z_i^{(2)}$, where the coefficient β describes the effective contribution of second neighbors. A reasonable value for *fcc* clusters is $\beta = 0.25$ [14]. The results from the models of Eqs. (9.10) and

(9.11), with parameters $\mu = \mu(Z)$ given by Jensen [18], are compared to experiment in Fig. 9.2. The statistical model of Eq. (9.10) yields the minima and the more realistic model of Eq. (9.11) improves the magnitude of $\bar{\mu}$. The comparison with experiment is encouraging, but a clear evidence for a distinct cluster structure cannot be claimed.
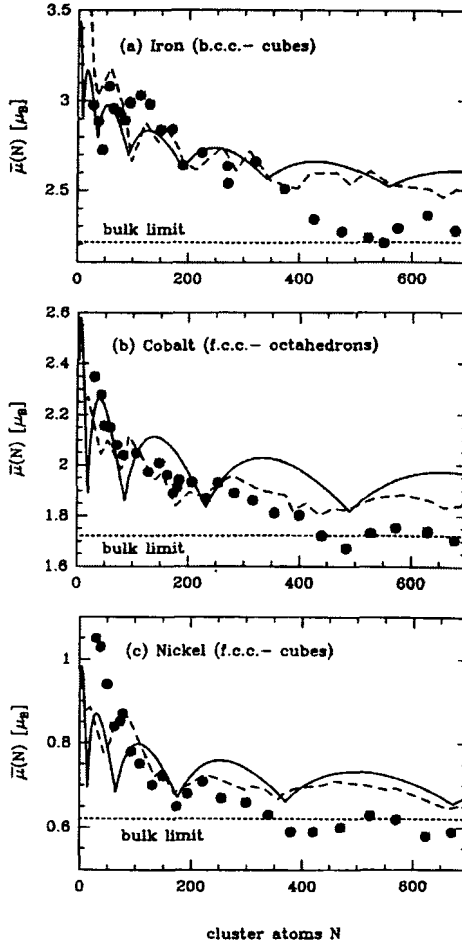
Figure 9.2. Average magnetic moments of Fe, Co and Ni clusters. Solid curves are from the model of Eq. (9.10), dashed curves from Eq. (9.11) and dots are experimental results. Adapted from P. Jensen and K. H. Bennemann, *Z. Phys. D* **35**, 273 (1995) with permission of Springer–Verlag.

Jensen and Bennemann [18] have also studied Rh clusters with N up to 40, because these clusters order ferromagnetically [13] although the bulk is nonmagnetic. They found that growing an *fcc* cuboctahedron by caps yields better agreement with experiment than a symmetrical occupation of sites in the topmost shell. The growth by caps is expected to give larger cohesive energies because it enhances the number of nearest neighbor contacts in the topmost shell.

9.4 Temperature Dependence of the Magnetic Moments

In the ferromagnetic ground state of a transition metal the spins are mutually aligned. Rising the temperature T introduces disorder and the net magnetic moment decreases. For the bulk, it vanishes at the Curie temperature T_c. The behavior of $\bar{\mu}$ with T provides information on the strength and stability of the ferromagnetic order. Billas *et al.* [1, 2, 7] have analyzed the variation of $\bar{\mu}$ for Ni, Co and Fe clusters. Ni and Co behave in the expected way. For a given size, $\bar{\mu}$ decreases with increasing T, except for an initial plateau in Ni clusters or an initial rise of a magnitude no larger than 5% in Co clusters. As the cluster size grows up $\bar{\mu}(T)$ approaches the saturation magnetization curve of the bulk metal. However, this convergence has to be qualified. Phase transitions are sharp only for very large systems, and in a finite system the transition becomes smeared out in temperature. The $\bar{\mu}(T)$ curve for Ni clusters of sizes $N = 500$–600 already follows closely the bulk curve at low T, but at higher temperature the behavior of $\bar{\mu}(T)$ is less sharp and it appears to approach zero much more slowly due to the finite size effects. This smearing out (that, of course, occurs also for smaller clusters) agrees with predictions using a finite Heisenberg model [19]. At temperatures around the Curie temperature of the bulk, the measured magnetic moments of the clusters are still substantial, suggesting that magnetic ordering is still present at these elevated temperatures. In fact, neutron scattering experiments for bulk ferromagnets indicate that ferromagnetic correlations persist at temperatures higher than T_c, leading to a short-range magnetic order with a correlation radius of the order of 19 a.u. [20], which is a size similar to that of the free clusters in the experiments of Billas *et al.*

For the Fe clusters $\overline{\mu}(T)$ behaves in a different way. First, the temperatures for the occurrence of the magnetic phase transition are below T_c (bulk), although again $\overline{\mu}$ does not go to zero. More important, the thermal behavior of $\overline{\mu}(T)$ differs a lot for different cluster sizes and there is not obvious convergence towards bulk behavior. Billas *et al.* have suggested this to be a consequence of a structural transition interfering with the purely magnetic transition, as in bulk Fe. The influence of short-range magnetic order (SRMO) on $\overline{\mu}$ at high temperature has been analyzed by Pastor *et al.* [21]. They first noticed that $\overline{\mu}_N(T)$ decreases with increasing temperature in the experiments of Billas, reaching an approximately constant value above a temperature $T_c(N)$. This is expected for a magnetically disordered state [19]. However, the magnetization was significantly larger than the value $\overline{\mu}_N(T=0)/\sqrt{N}$ corresponding to N randomly oriented atomic magnetic moments. If one assumes some SRMO in the cluster, characterized by the average number v of atoms in a SRMO domain, then the magnetization per atom of a cluster of N atoms at $T > T_c(N)$ is given by

$$\overline{\mu}_N(T > T_c) \cong \overline{\mu}_N(T = 0)\sqrt{\frac{v}{N}} \quad , \qquad (9.12)$$

which represents the average $\sqrt{\langle \mu^2 \rangle}$ of N/v randomly oriented SRMO domains, each carrying a magnetic moment $v\overline{\mu}_N(T = 0)$. The disordered local moment picture, without SRMO, corresponds to $v=1$. The actual value of v for $3d$ transition metal clusters can be estimated from known surface and bulk results. A value $v = 15$ (which includes up to next-nearest neighbors in a *bcc* lattice) seems a reasonable estimate for Fe clusters, whereas for Ni the SRMO is expected to be stronger, and values of v between 19 and 43 are reasonable. Using these values of v and Eq. (9.12), good agreement is obtained with experiment, providing evidence for the existence of SRMO in these clusters above $T_c(N)$.

Heat capacities have been measured for the clusters in a beam [22]. For the Ni clusters the heat capacity C_V attains a maximum at 350 K and

then decreases to the classical value. This feature is associated with the decrease in magnetic moment and indicates that the effect is due to the phase transition from the ferromagnetic to the paramagnetic state of the clusters. The heat associated to the transition is 0.022 eV per atom, that is comparable to the bulk counterpart, 0.018 eV per atom. The shape of the peak corresponds to what may be expected for a magnetic transition in a mean field model. In the same way, the mean field approximation accounts well for the peak of C_V observed in Co clusters. The results for Fe are again more difficult to interpret. Both for low and high temperature the heat capacity falls below the bulk value. And, although the position of the peak coincides with a strong decrease of $\bar{\mu}$, the shape of the mean field peak does not reproduce the experiment.

9.5 Magnetic Moments of Nickel Clusters and their Interpretation

Apsel *et al.* have performed accurate measurements of the magnetic moments of size-selected Nickel clusters [8] and the results are plotted in Fig. 9.3. The experimental moments show an overall decrease with increasing cluster size, but oscillations are superimposed to this behavior. $\bar{\mu}$ shows a deep minimum at Ni_{13}, a small one at Ni_{19} and another minimum at Ni_{55}–Ni_{56}, so one would guess that the clusters grow following an icosahedral pattern. Another minimun is observed near Ni_{34}. Between Ni_{13} and Ni_{34}, as well as between Ni_{34} and Ni_{56}, $\bar{\mu}$ goes through broad maxima displaying also fine oscillations. Finally, for $N < 10$, where $\bar{\mu}$ decreases rapidly with increasing N, there is a local minimum at Ni_6 and a local maximum at Ni_8.

9.5.1 Tight-binding studies

Most studies attempting to understand these results have used the tight-binding (TB) method. For this reason we present here a brief account of this formalism. For a given geometrical arrangement of the atoms in the Ni cluster the spin-polarised electronic structure can be determined by solving selfconsistenly a TB Hamiltonian for the $3d$, $4s$ and $4p$ valence

electrons in a mean field approximation [24]. In the unrestricted Hartree–Fock approximation this Hamiltonian has the expression

$$H = \sum_{i\alpha\sigma} \varepsilon_{i\alpha\sigma} \hat{n}_{i\alpha\sigma} + \sum_{ij} \sum_{\alpha\beta\sigma} t_{ij}^{\alpha\beta} c_{i\alpha\sigma}^{+} c_{j\beta\sigma} \tag{9.13}$$

where $c_{i\alpha\sigma}^{+}$ is the operator for the creation of an electron with spin σ and orbital state α ($\alpha = s, p_x, p_y, p_z, d_{xy}, d_{yz}, d_{xz}, d_{x^2-y^2}, d_{3z^2-r^2}$) at the atomic site i, $c_{j\alpha\sigma}$ is the annihilation operator, and $\hat{n}_{i\alpha\sigma} = c_{i\alpha\sigma}^{+} c_{i\alpha\sigma}$. The hopping integrals $t_{ij}^{\alpha\beta}$ between orbitals α and β at neighbor atomic sites i and j are assumed to be spin-independent, and are usually fitted to reproduce the first principles band structure of the metal at the observed lattice constant. The variation of the hopping integrals with the interatomic distance r_{ij} is often assumed to follow a power law $(r_0/r_{ij})^{l+l'+1}$, where r_0 is the bulk equilibrium distance and l and l' are the angular momenta of the two orbitals involved in the hopping [25].
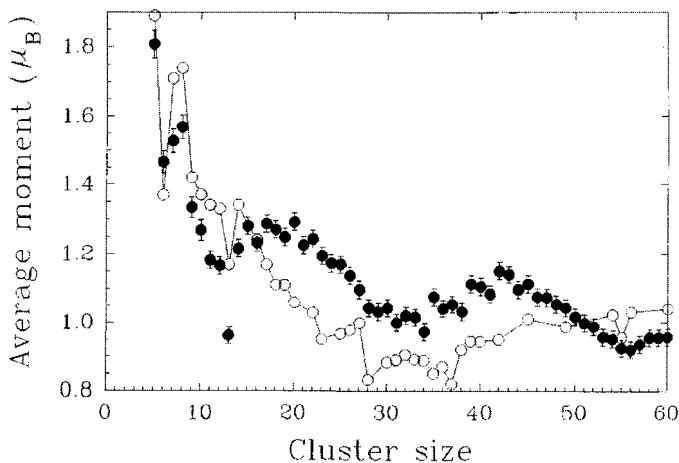
Figure 9.3. Calculated magnetic moments of Nickel clusters (empty circles) compared to the experimental results. Reproduced from J. A. Alonso, *Chem. Rev.* **100**, 637 (2000) with permission of the American Chemical Society.

The spin-dependent diagonal terms contain all the many-body contributions, and can be written in a mean-field approximation as

$$\varepsilon_{i\alpha\sigma} = \varepsilon_{i\alpha}^0 + \sum_{\beta\sigma'} U_{\alpha\beta}^{\sigma\sigma'} \Delta v_{i\beta\sigma'} + \sum_{j\neq i} \frac{e^2}{r_{ij}} \Delta v_j + Z_i \Omega_\alpha \ . \qquad (9.14)$$

Here, $\varepsilon_{i\alpha}^0$ are the bare orbital energies of the paramagnetic bulk metal. The second term gives the shifts of the energies due to screened intra-atomic Coulomb interactions, and $\Delta v_{i\beta\sigma} = v_{i\beta\sigma} - v_{i\beta\sigma}^0$, where $v_{i\beta\sigma} = <\hat{n}_{i\beta\sigma}>$ is the average occupation of the spin-orbital $i\beta\sigma$, and $v_{i\beta\sigma}^0$ is the corresponding occupation in the paramagnetic solution of the bulk. The intra-atomic Coulomb integrals $U_{\alpha\beta}^{\sigma\sigma'}$ can be equivalently expressed in terms of two more convenient quantities, the exchange and direct integrals, $J_{\alpha\beta} = U_{\alpha\beta}^{\uparrow\downarrow} - U_{\alpha\beta}^{\uparrow\uparrow}$ and $U_{\alpha\beta} = (U_{\alpha\beta}^{\uparrow\downarrow} + U_{\alpha\beta}^{\uparrow\uparrow})/2$, respectively, and then the intra-atomic term of Eq. (9.14) becomes split in two contributions

$$\sum_{\beta\sigma'} U_{\alpha\beta}^{\sigma\sigma'} \Delta v_{i\beta\sigma'} = \sum_\beta U_{\alpha\beta} \Delta v_{i\beta} + z_\sigma \sum_\beta \frac{J_{\alpha\beta}}{2} \mu_{i\beta} \qquad (9.15)$$

where $\Delta v_{i\beta} = \Delta v_{i\beta\uparrow} + \Delta v_{i\beta\downarrow}$, $\mu_{i\beta} = \Delta v_{i\beta\uparrow} - \Delta v_{i\beta\downarrow}$, and z_σ is the sign function ($z_\uparrow = -1, z_\downarrow = +1$). The first contribution in Eq. (9.15) arises from the change in electronic occupation of the orbital $i\beta$ and the second from the change of the magnetization (spin polarization). $U_{\alpha\beta}$ and $J_{\alpha\beta}$ are usually parametrized. The difference between s and p direct Coulomb integrals is often neglected by writing $U_{ss} = U_{sp} = U_{pp}$, and it is also assumed that $U_{sd} = U_{pd}$. The ratio between the magnitudes of U_{ss}, U_{sd} and U_{dd} can be taken from atomic Hartree–Fock calculations, and the absolute value of one of them, for instance U_{dd}, estimated by some means [26]. Typical values for these ratios are 0.32 : 0.42 : 1 for Fe and U_{dd} = 5.40 eV [24]. All the exchange integrals involving s and p electrons are usually neglected and J_{dd} is determined in order to

reproduce the bulk magnetic moment. Typical values for Ni, Co and Fe do not differ much from $J_{dd} = 1 eV$.

The third term in the Eq. (9.14) represents the Coulomb shifts resulting from charge transfer between the atoms $\Delta V_j = V_j - V_j^0$, where $V_j = \sum_{\beta\sigma} \langle \hat{n}_{j\beta\sigma} \rangle = \sum_{\beta} \langle \hat{n}_{j\beta\uparrow} \rangle + \langle \hat{n}_{j\beta\downarrow} \rangle$ is the total electronic charge at atom j, and V_j^0 is the corresponding reference bulk value. In Eq. (9.14) the interatomic Coulomb interaction integrals V_{ij} have been approximated as $V_{ij} \approx e^2/r_{ij}$. Finally, the last term in that equation takes into account the energy-level corrections due to nonorthogonality effects and to the crystal field potential of the neighboring atoms, which are approximately proportional to the local coordination number Z_i. The spin-dependent local electronic occupations and the local magnetic moments $\mu_i = \sum_{\alpha} \left(\langle \hat{n}_{i\alpha\uparrow} \rangle - \langle \hat{n}_{i\alpha\downarrow} \rangle \right)$ are selfconsistently determined from the local densities of states $\rho_{i\alpha\sigma}(\varepsilon)$

$$\langle \hat{n}_{i\alpha\sigma} \rangle = \int_{-\infty}^{\varepsilon_F} \rho_{i\alpha\sigma}(\varepsilon) d\varepsilon \qquad (9.16)$$

which can be calculated at each iteration by using a recursion method [27]. The Fermi energy ε_F is determined from the condition of global charge neutrality. In this way, the local magnetic moments $\mu_i = \sum_{\alpha} \mu_{i\alpha}$ and the average magnetic moment $\overline{\mu} = \left(\sum \mu_i \right)/N$ are obtained at the end of the selfconsistent cycle. The theoretical framework presented here is general, although some of the calculations to be discussed below may incorporate slight changes with respect to the basic method.

The results of TB calculations for the average magnetic moments of Ni clusters [28, 29] are compared in Fig. 9.3 with the experimental values of Apsel *et al.* [8]. Two main ideas can used to interpret the results. The first one is that the local magnetic moments decrease when the local coordination around an atom increases. The second idea is that the average magnetic moment decreases when the interatomic distances

decrease (the electronic d band becomes wider). In metallic clusters, the average coordination generally increases with increasing cluster size N, and also the average nearest neighbor distance d_n increases with N, from the value for the molecule to the value for the bulk. In a growing cluster the two effects oppose each other and the resulting behavior of $\bar{\mu}(N)$ can be very rich. For $N \leq 20$ the geometrical structures employed to perform the electronic structure calculations were obtained from molecular dynamics (MD) simulations using a semi-empirical interatomic potential [30, 31] based on TB theory, with parameters fitted to properties of Ni_2 and bulk Ni. This potential, often called the Gupta potential [31], contains many-atom terms. The qualitative agreement between calculated magnetic moments and experiment is very good in the small cluster size range. The theory predicts pronounced local minima of $\bar{\mu}$ at $N = 6$ and $N = 13$, and a local maximum at $N = 8$. The atomic structures for $N = 5$–16 are plotted in Fig. 9.4.
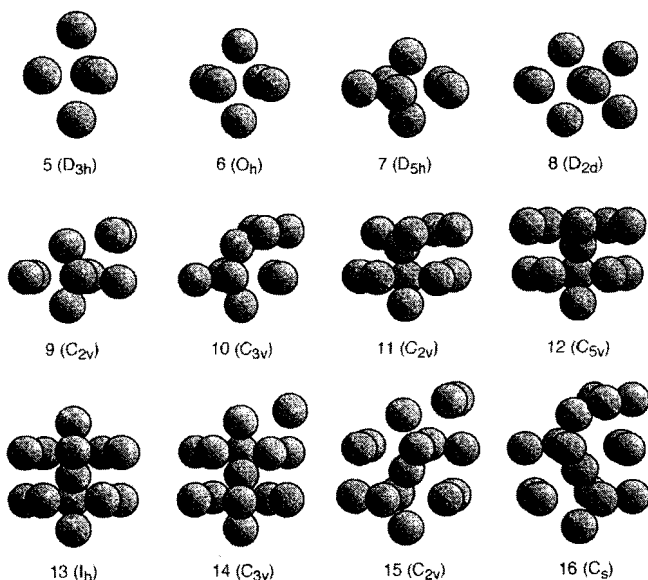
Figure 9.4. Ground state geometries of Ni clusters with 5 to 16 atoms, obtained using the Gupta potential. Reproduced from S. Bouarab *et al.*, *Phys. Rev. B* **55**, 13279 (1997) with permission of the American Physical Society.

The structure of Ni_{13} is an icosahedron (in agreement with the more accurate calculations reviewed in Chapter 8). The coordination of the surface atoms is $Z = 6$. Either by removing or by adding one atom, the resulting clusters, Ni_{12} and Ni_{14}, contain some atoms with coordination smaller than six. This leads to an increase of the local magnetic moment of those atoms. Consequently, the minimum of $\overline{\mu}$ at Ni_{13} is explained by its compact structure. Ni_6 is an octahedron with atoms of coordination $Z = 4$. In Ni_7, which has the structure of a pentagonal bipyramid, the coordination of two atoms increases to $Z = 6$, remaining equal to four for the rest. Ni_8 has four atoms with coordination $Z = 5$ and four atoms with coordination $Z = 4$, which leads to a mean coordination slightly lower than in Ni_7 ; then the coordination increases again for Ni_9 . This would lead us to expect a maximum of $\overline{\mu}$ for Ni_8 , which is indeed observed in the experiment, and a minimum for Ni_7 . Instead, the observed and calculated minimun occurs at Ni_6, and the reason is that the average first neighbor distance d_n has a local maximum at Ni_7. The larger value of d_n works against the increase of the coordination number from Ni_6 to Ni_7, and produces the minimum of $\overline{\mu}$ at Ni_6. In summary, the oscillations of $\overline{\mu}$ for small N can be explained by two purely geometrical effects: compact clusters have small values of $\overline{\mu}$, and clusters with large interatomic distances have large $\overline{\mu}$.

In Fig. 9.5 the orbital-projected densities of states of Ni_5, Ni_6 and Ni_7 are compared [28]. The occupied states of the majority-spin sub-band have mainly d character with the exception of the peak at the Fermi energy, which has sp character; d holes are present in the minority-spin sub-band. Integration of the density of states gives d magnetic moments with values of 1.6 μ_B, 1.52 μ_B and 1.50 μ_B for Ni_5, Ni_6 and Ni_7 respectively. A comparison with the moments of Fig. 9.3 indicates that the sp electrons make an important contribution. The sp moments in Ni_5 (0.29 μ_B) and Ni_7 (0.21μ_B) reinforce the d moment, while for Ni_6 the sp moment (-0.15μ_B) points in the opposite direction. The sp contribution to $\overline{\mu}$ decays rather quickly with cluster size.

A conclusion from the geometries plotted in Fig. 9.4 is the pattern of icosahedral growth. Since icosahedral growth appears to be consistent with the reactivity experiments, as discussed in Chapter 8, Aguilera-Granja *et al.* [29] assumed icosahedral clusters also for $N > 20$. The structures obtained previously with the Embedded Atom method [32]

(see Chapter 8) were reoptimized, using the Gupta potential [31], to have consistency with the study for $N \leq 20$. In addition, extensive MD simulations were done for a few selected sizes. In all cases the icosahedral structures were recovered as the ground state, except for Ni_{38}, which is an exceptional case to be discussed later.
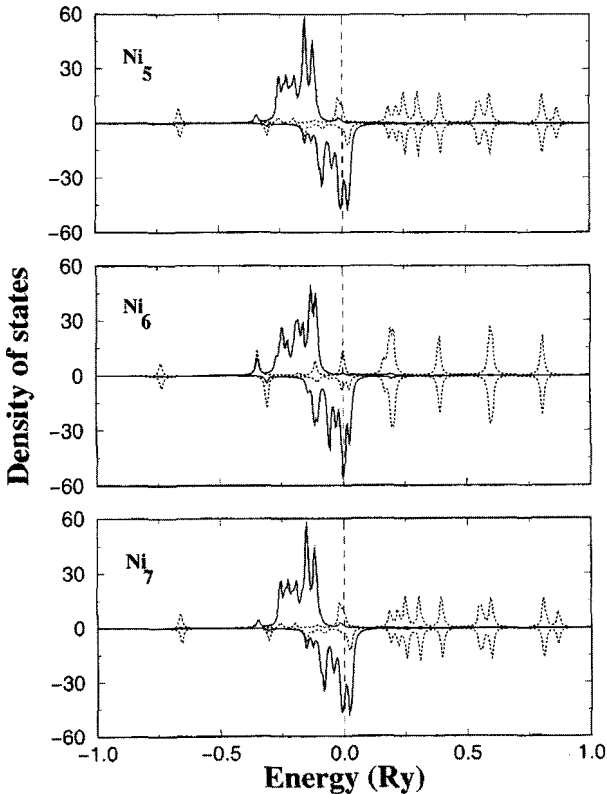
Figure 9.5. Density of states: *sp* (dashed lines) and *d* (continuous lines). Positive and negative values correspond to up and down spins, respectively. The Fermi level is at the energy zero. Adapted from S. Bouarab *et al.*, *Phys. Rev. B* **55**, 13279 (1997) with permission of the American Physical Society.

Returning to Fig. 9.3, the calculated magnetic moments reveal for $N > 20$ a broad trend of a decrease of $\overline{\mu}$ for sizes up to $N \approx 28$, followed

by a weak increase between N $\approx$ 28 and $N = 60$. This behavior is mainly related to the variation of the average coordination number $\overline{Z}$, which grows smoothly with N up to $N = 27$ and then shows up a break. This explains the overall decrease of $\overline{\mu}$ in that region. By extrapolating $\overline{Z}(N)$ to sizes larger than $N = 27$, it was found [29] that the actual values of $\overline{Z}(N)$ fall below that extrapolated curve for sizes N between 27 and 54, and the same argument explains the behavior of $\overline{\mu}$ in that size region: the break in $\overline{Z}$ at $N = 27$ suggests a flattening of $\overline{\mu}$, which is confirmed by the calculations. The break in the behavior of the coordination number is due to the FC to MIC transition, occurring precisely at $N = 28$ (see Chapter 8).

The calculated minimum of $\overline{\mu}$ at $N = 55$ has a clear correspondence with a minimum in the measured magnetic moment. Also the calculated minimum in the region Ni_{27}–Ni_{37}, associated to the FC to MIC transition, seems to correspond to the broad experimental minimum of $\overline{\mu}$ in that region. The experiments show also a weak minimum at Ni_{19}, that can be tentatively associated to the double icosahedron structure of this cluster, although this local minimum does not show up in the calculations. Another weak feature, a drop of $\overline{\mu}$ between Ni_{22} and Ni_{23} has a counterpart in the calculation (Ni_{23} is a triple icosahedron). One may conclude with some confidence that the minima displayed by the measured magnetic moments give additional support to a pattern of icosahedral growth.

It was stated above that Ni_{38} is an exceptional case. The results of experiments [33] measuring the saturation coverage of Ni_{38} with different molecules (N_2, H_2, CO) indicate that the structure of this cluster is a truncated octahedron cut from an *fcc* lattice. Motivated by this result, a detailed comparison between the energies of *fcc* and icosahedral structures for a number of clusters was performed by Aguilera-Granja *et al.* [29]. $N = 36$, 37, 38 and 39 were selected to cover sizes in the neighborhood of Ni_{38}. For $N = 13$, 19, 43 and 55, one can construct *fcc* clusters with filled coordination shells around a central atom, and for $N = 14$, 38 and 68, clusters with filled coordination shells around an empty octahedral site of the *fcc* lattice. Finally $N = 23$, 24 and 44 are of interest for comparison with other works. In all the cases the icosahedral structure was predicted more stable, except precisely for Ni_{38}. The

difference in binding energy between the two structures is, however, small: lower than 0.2 eV between Ni_{24} and Ni_{39}, and it increases as N departs from this region. The geometry of Ni_{38} is a compact structure formed by three complete coordination shells around an empty octahedral site. The six atoms of the internal octahedron are fully coordinated ($Z = 12$). For this structure $\overline{\mu} = 0.99\,\mu_B$, that cuts the difference between the experimental and theoretical results to one-third of the value reported in Fig. 9.3 for the icosahedral structure. The moderate increase of $\overline{\mu}$ with respect to that for the icosahedral structure is due to the lower average coordination in the *fcc* structure ($\overline{Z}$ *(fcc)* = 7.58, and $\overline{Z}$ (ico) = 7.74). $\overline{\mu}$ is very similar for the icosahedral and *fcc* structures of Ni_{36} (0.87 and 0.86 μ_B respectively). Since energy differences between isomers in the region $N = 24$–40 are small (within 0.4 eV), the possibility of different isomers contributing to the measured values of the magnetic moment should not be excluded.

Explaining the observed maxima of $\overline{\mu}$ is a more difficult task. Those maxima are not seen in the TB results. One possibility, suggested by some calculations [34, 35], is that the structures are *fcc* instead of icosahedral in the regions corresponding to those maxima. Guevara *et al.* [34] then predict sharp maxima of $\overline{\mu}$ at Ni_{19} and Ni_{43} and minima at Ni_{28} and Ni_{55}. But the study of the reactivity experiments in Chapter 8 suggest that Ni_{19} is a double icosahedron. So the only clear prediction in favor of the *fcc* structure may be the maximum of $\overline{\mu}$ at Ni_{43}.

In order to further investigate the effect of the geometrical structure Rodríguez-López *et al.* [36] have performed additional TB calculations for cluster structures proposed by other authors. The results were compared to experiment and to the icosahedral growth model. The main conclusion was that the differences in $\overline{\mu}$ produced by the different cluster structures are not large. For all sets of structures $\overline{\mu}$ shows an overal decrease with increasing N, and the oscillations at small N are reproduced reasonably well. But all the calculations predict a faster approach to $\overline{\mu}$. These results do not resolve the discrepancies between tight-binding calculations and experiment, indicating that a possible misrepresentation of the exact geometry is not the only missing ingredient. Another possibility that has been suggested is that the

treatment of the *sp* electrons in the TB model may not be accurate enough, and this idea is expanded in the next section.

9.5.2 Influence of the s electrons

An alternative for explaining the behavior of the magnetic moment of Ni clusters has been proposed by Fujima and Yamaguchi [37]. Although, in our opinion , the model is not adequate to explain the minima of $\overline{\mu}$, it may well contain the additional ingredients required to explain the maxima. It is intriguing that the observed maxima of $\overline{\mu}$ are located at N = 8 and N = 71 and near N = 20 and N = 40 [8]. These numbers remind us of some of the electronic shell closing numbers of the alkali and noble metal clusters (N = 8, 20, 40, 72). The model of Fujima and Yamaguchi in fact distinguishes between localized 3*d*-derived levels and delocalized molecular orbitals derived from the atomic 4*s* electrons, and neglects any hybridization between *d* and delocalized electrons. The delocalized electrons are treated as moving in an effective harmonic potential. The corresponding energy levels lie above the Fermi energy in very small Ni clusters. But, as N grows, the binding energy of these delocalized electronic states increases and the levels become successively buried below the 3*d* band. The model assumes that this occurs abruptly when the number of delocalized electrons is just enough to fill a shell in that harmonic potential. Associated to this step-wise effect there is a sudden increase of the number of holes at the top of the minority spin *d* band, since the total number of valence electrons per Ni atom is 10: the number of holes is equal to the number of unpaired electrons in the cluster, so an abrupt increase of $\overline{\mu}$ occurs. The step-wise mechanism of transfer of 4*s*-derived levels from above the Fermi energy to below the *d* band is supported by density functional calculations [38]. Then the maxima of $\overline{\mu}$ observed in the experiments for $N \leq 100$ could be related to this effect. However in the model the maxima and the minima of $\overline{\mu}$ are too close due to the drastic assumption of the transfer of a whole shell at once when the conditions of electronic shell closing are met. This is in contrast to the experimental observation, where the maxima and minima are well separated and, furthermore, the minima appear to be due to structural effects.

9.6 Density Functional Studies for Ni, Fe and Cr Clusters

9.6.1 Nickel clusters

DFT calculations of the magnetic moments become difficult for large clusters, especially if one wishes to determine the lowest energy geometrical structure. For this reason only small clusters have been studied. Reuse and Khanna [39] have calculated $\bar{\mu}$ for Ni_N with $N = 2$–6, 8 and 13. In agreement with experiment, the calculations predict $\bar{\mu}$ (Ni_6) < $\bar{\mu}$ (Ni_5) and $\bar{\mu}$ (Ni_{13}) < $\bar{\mu}$ (Ni_8), but the magnetic moments of Ni_6 and Ni_8 were nearly equal, while the experiment gives a larger moment for Ni_8 (see Fig. 9.3). The geometries employed were similar to those employed in the TB calculations of Bouarab *et al.* [28], except for Ni_8. Bouarab *et al.* have performed additional TB calculations with the same structures and interatomic distances of Reuse and Khanna, and the magnetic moments differed by no more than $0.06\,\mu_B$ from the TB values of Fig. 9.3, so the differences between the TB and the DFT results have to be ascribed to the different treatment of the electronic interactions and not to differences in geometry or interatomic distances [29]. Desmarais *et al.* [40] have studied Ni_7 and Ni_8. The same value of $\bar{\mu} = 1.14\ \mu_B$ was obtained for the ground state (capped octahedron) of Ni_7 and all its low lying isomers (pentagonal bipyramid, tri-capped tetrahedron and capped trigonal prism). Similarly, a moment $\bar{\mu} = 1.0\,\mu_B$ was obtained for the ground state and the low lying isomers of Ni_8. The insensitivity of the magnetic moments to atomic structure in Ni_7 and Ni_8, also found for Ni_4 [39], is striking. Reddy *et al.* [41] have calculated the magnetic moments of Ni_N up to $N = 21$. For $N \leq 6$ they employed *ab initio* geometries (discussed in Section 8.3.1), and for $N > 6$ the geometries were optimized with the Finnis–Sinclair potential [42]. Compared to experiment, the calculations predict substantially lower moments, and important discrepancies occur in the detailed variation of $\bar{\mu}$ with cluster size. Those discrepancies are surprising.

Fujima and Yamaguchi [43] have calculated the local magnetic moments of Ni clusters, that is, the magnetic moments at different atomic sites. *Fcc* structures and bulk interatomic distances were assumed, with an octahedron and a cuboctahedron for the shapes of Ni_{19}

and Ni$_{55}$, respectively. No significant differences were found between the magnetic moments of atoms at different surface sites, but the moments of atoms in the layer immediately below the surface are smaller by $\approx$ $0.2\,\mu_B$. The average magnetic moments $\overline{\mu}$ (Ni$_{19}$) = $0.58\,\mu_B$ and $\overline{\mu}$ (Ni$_{55}$) = $0.73\,\mu_B$ are significantly smaller than the measured ones. Pacchioni *et al.* [44] calculated the electronic structure of Ni$_6$, Ni$_{13}$, Ni$_{19}$, Ni$_{38}$, Ni$_{44}$, Ni$_{55}$, Ni$_{79}$ and Ni$_{147}$. The structures assumed were icosahedral (for Ni$_{13}$, Ni$_{55}$, Ni$_{147}$) or with O_h symmetry (for Ni$_6$, Ni$_{13}$, Ni$_{19}$, Ni$_{38}$, Ni$_{44}$, Ni$_{55}$, Ni$_{79}$; in most cases fragments of an *fcc* crystal). The nearest neighbor distances were fixed equal to the nearest neighbors distance in the bulk (4.70 a.u.). Convergence of the binding energy and average magnetic moment to the bulk limit was not observed even for the largest cluster, Ni$_{147}$. On the other hand the width of the 3*d* band is almost converged for $N = 40$–50. In summary, the explanation of the detailed variation of the magnetic moment of Ni clusters as a function of cluster size is still an open problem.

9.6.2 Iron and and Chromium clusters

Fujima and Yamaguchi [43] also studied Fe and Cr clusters with $N = 15$ and 35, assuming a *bcc* structure: a rhombic dodecahedron. A low value of μ for atoms on layer-2 is obtained for Fe (the notation used is that of Section 9.3; layer-1 is the surface layer and layer-2 is the first layer below the surface). For Cr, an alternation of the signs of the local moments as a function of the distance to the cluster center is found; the absolute values of the local moments decrease with increasing local coordination, and also decrease for decreasing interatomic distance. For Fe clusters, in contrast, the local moments are less sensitive to the local atomic coordination. The calculations of Cheng and Wang [45] show also that the Cr clusters are antiferromagnetic, and the dimer growth route discovered by these authors (see Section 8.3.5) leads to the prediction of an odd–even alternation of the average magnetic moments: small magnetic moments for clusters with even N and large moments for odd N. The large moments arise from the quasiatomic character of the capping atoms; the dimer-paired even-N clusters have low $\overline{\mu}$ because of the strong intra dimer 3*d*–3*d* interaction. In most cases the calculated moments are within the upper limit of $0.77\,\mu_B$ imposed by the

experiments [46]. But for Cr_{12} and Cr_{13} the predicted $\bar{\mu}$ is larger than this limit.

9.7 Experiments and Calculations for Mn Clusters

The properties of Mn are peculiar. This metal has the smallest bulk modulus and cohesive energy of all the $3d$ metals, and the most complex lattice structure, with several allotropic forms. Some of its bulk phases are antiferromagnetic, while monolayers [47] and supported clusters [48] exhibit nearly degenerate ferromagnetic and antiferromagnetic states. The bond length of the dimer, 6.43 a.u., is larger than the nearest neighbor distance in the bulk, in contrast to all other transition metals. Mn_2 is considered close to a Van der Waals molecule, with an estimated binding energy between 0.1 and 0.6 eV [49]. This special character arises from the electronic configuration of the atom, $3d^5 4s^2$. The electrons of the half-filled $3d$ shell are more localized compared to other $3d$ atoms and do not interact with those of the other atom in the dimer, and consequently the binding arises from the weak interaction between the filled $4s^2$ shells. A nonmetal to metal transition is expected to occur for clusters of a certain critical size. From an analysis of the reactivity of the clusters with hydrogen, Parks *et al.* [50] have suggested that this transition occurs at Mn_{16}, although the ionization potential does not display any special feature at that size.

9.7.1 Clusters with less than ten atoms

Interesting possibilities arise from the large magnetic moment of the free atom ($5\mu_B$) and the weak interaction between the atoms in Mn_2. One could expect that the magnetic moments retain their atomic character in small Mn clusters. If these moments couple ferromagnetically, a Mn_N cluster would carry a remarkably large moment of $5N\mu_B$. The only experiments measuring the magnetic moments of Mn clusters with less that ten atoms are for clusters embedded in matrices (experiments for clusters with more than ten atoms are discussed later in this section). Electron spin paramagnetic resonance (ESR) experiments of Mn_2 in inert gas matrices yield an antiferromagnetic configuration, but Mn_2^+ is

ferromagnetic with a total magnetic moment of $11\,\mu_B$ [51]. Mn_4 in a silicon matrix appears to have a moment of $20\,\mu_B$ [52]. Mn_5^+ embedded in inert gas matrices has a moment of $25\,\mu_B$ although the cluster actually studied could be larger [53]. It is worth noting that neutral Mn_2 is antiferromagnetic while the other clusters are ferromagnetic.

The results of calculations are controversial. An early Hartree–Fock calculation [54] predicted a $^1\Sigma_g^+$ ground state for Mn_2 resulting from the antiferromagnetic coupling of the localized spins. Fujima and Yamaguchi used DFT and a LCAO (linear combination of atomic orbitals) description of the wave functions to study Mn_2 to Mn_7 [55]. The interatomic distances were optimized for constrained geometries, and all the clusters in that group were predicted to show antiparallel spin ordering. Nayak and Jena [56] have optimized the equilibrium geometries for $N \leq 5$ at two levels of approximation: the local spin-density approximation (LSDA) and the generalized gradient approximation (GGA). The bond length and the binding energy of Mn_2 are sensitive to the treatment of exchange and correlation and only the GGA calculations explain some of the experimental results (the calculated bond length is 6.67 a.u. and the binding energy 0.06 eV). The use of diffuse functions in the basis set was found to be crucial to yield a weakly bonded molecule. Mn_2 is predicted ferromagnetic with a magnetic moment of $10\,\mu_B$ The binding energy increases in Mn_2^+ and the bond length decreases, since the electron is removed from an antibonding orbital. The total magnetic moment of Mn_2^+ is $11\,\mu_B$, in agreement with the estimation from experiments for clusters in rare gas matrices. The predicted geometries of Mn_3, Mn_4 and Mn_5 are compact: an equilateral triangle, a Jahn–Teller distorted tetrahedron and a trigonal bipyramid, respectively. The strength of the bonding increases significantly with respect to the dimer due to s–d hybridization, although it still remains small compared to other transition metal clusters. The predicted ground state geometries are consistent with those deduced from experiments in matrices. A hyperfine pattern of 21 lines was observed for Mn_4 embedded in a silicon matrix [52], indicating that the four Mn atoms are equivalent (the four atoms are equivalent in a tetrahedron). The triangular bipyramid is one of the possible structures of Mn_5 consistent with the ESR measurements [53]. The calculated

interatomic distances decrease substantially from Mn_2 to Mn_3, reflecting the onset of delocalization and hybridization between atomic orbitals at various sites. But, the most striking property of these clusters is their ability to retain their atomic moments. Mn_3, Mn_4 and Mn_5 in their ground state are predicted to be ferromagnetic, with moments of $\overline{\mu} = 5 \ \mu_B$ per atom in the three cases (low lying isomers are also ferromagnetic, with high magnetic moments). These large magnetic moments put small Mn clusters in a special place within the transition metal series and give expectations for using those molecular magnets in future high density information storage technology. Calculations for monolayers and supported clusters lead to the same conclusion, and recent experiments bear out the possibility of large moments [57, 58]. Experiments on free Mn_2 may clarify the discrepancy between experiment (on matrices) and theory concerning the magnetic character of this cluster.

Table 9.2. Calculated average bond distance d, number of bonds per atom, N_B, magnetic moment per atom, $\overline{\mu}$, and binding energy per atom, E_b, for Mn clusters. Also spin gaps Δ_1 and Δ_2. Data collected from [59].

N	d(a.u.)	N_B	$\overline{\mu}(\mu_B)$	E_b (eV/at)	$\Delta_1(eV)$	$\Delta_2(eV)$
2	4.927	0.5	5.0	0.50	0.65	1.30
3	5.093	1.0	5.0	0.81	0.46	1.38
4	5.162	1.5	5.0	1.19	0.62	2.31
5	5.053	1.8	4.6	1.39	0.50	0.79
6	5.002	2.0	4.3	1.56	0.90	1.13
7	4.970	2.1	4.2	1.57	0.70	0.47
8	4.957	2.2	4.0	1.67	0.93	0.37

Calculations by Pederson *et al.* [59] provide further insight on this discrepancy. They performed a detailed study of Mn$_2$ using LDA and GGA functionals. Their conclusion is that this dimer is ferromagnetic with a total moment of $10\mu_B$, an equilibrium bond length of 4.93 a.u. and a binding energy of 0.99 eV. An antiferromagnetic state was also found with larger bond length (5.13 a.u.) and smaller binding energy (0.54 eV). The characteristics of this isomer are closer to those of Mn$_2$ in matrices. A plausible resolution of the discrepancies for the dimer is that the ferromagnetic state is the true ground state of free Mn$_2$ but Van der Waals interactions between the dimer and the matrix may stretch the bond, leading to the appearance of an antiferromagnetic state in the embedded cluster.

Larger clusters were also studied. Mn$_3$ also has different magnetic states close in energy. The ground state is an isosceles triangle in a ferromagnetic configuration (total moment of $15\mu_B$). A frustrated antiferromagnetic state also exits with the atomic *d* spins of the shorter side of the triangle ferromagnetically coupled, while the third atom is antiferromagnetically coupled to the other two (the triangle is very close to equilateral). This state, with a net magnetic moment of $5\mu_B$, is only 0.014 eV above the ground state. Mn$_4$ is a tetrahedron with a total moment of $20\mu_B$. For the intriguing case of Mn$_5$ the calculations predict a trigonal bipyramid with a net spin of $23\mu_B$, lower than the measured moment of $25\mu_B$. Trigonal bipyramid and square pyramid states with a moment of $25\mu_B$ are 0.62 eV and 1.20 eV above the ground state, respectively. Pederson and coworkers then concluded that either the matrix influences the ground state multiplicity of Mn$_5$ or the cluster formed in the experiment is other than Mn$_5$; this later possibility had also been admitted in the original experimental work [53]. A square bipyramid and a pentagonal pyramid were investigated for Mn$_6$. The total moments are $26\mu_B$ and $28\mu_B$, respectively, and Mn$_6$ was proposed [59] as a possible candidate for the cluster with $\mu = 25\mu_B$ observed in the ESR experiments [53]. The structure of Mn$_7$ is formed by two eclipsed triangles with a single atom cap (C_{3v} symmetry). Its ionization energy ($IP = 5.51$ eV) is in good agreement with experiment ($IP = 5.44$ eV) [60].

To summarise the results, Table 9.2 gives the average bond distance, the number of bonds per atom, the average magnetic moment per atom and the binding energy for Mn_2 to Mn_8. Also given are the two spin gaps $\Delta_1 = \varepsilon_{HOMO}^{majority} - \varepsilon_{LUMO}^{minority}$ and $\Delta_2 = \varepsilon_{HOMO}^{minority} - \varepsilon_{LUMO}^{majority}$. These represent the energy required to move charge from the HOMO of one spin sub-band to the LUMO of the other. The two spin gaps have to be positive for the system to be magnetically stable.

9.7.2 Clusters with more than ten atoms

Using Stern–Gerlach deflection (see Section 9.1) Knickelbein [61] has measured the magnetic moments of Mn_N clusters for sizes between $N = 11$ and $N = 99$. The results, given in Fig. 9.6, were obtained from Eq. (9.2) assuming the superparamagnetic behavior.
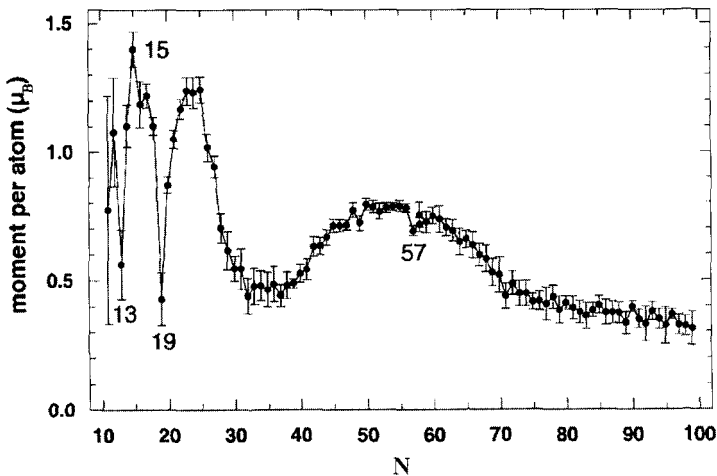
Figure 9.6. Measured magnetic moments per atom of Mn_N clusters as a function of cluster size. Reproduced from M. B. Knickelbein, *Phys. Rev. Lett.* **86**, 5255 (2001) with permission of the American Physical Society.

Distinct local minima of $\overline{\mu}$ are obtained for Mn_{13} and Mn_{19}, which suggest icosahedral growth in that size range. The minima are then a consequence of the higher atomic coordination in those species. Beyond Mn_{19} the magnetic moments oscillate with increasing size, showing a

minimum around Mn_{32}–Mn_{37} and a broad maximum at Mn_{47}–Mn_{56} followed by a weak local minimum at Mn_{57}. The maximum value of the magnetic moment found in that experiment was $\bar{\mu}$ = $1.4\,\mu_B$, substantially below the calculated moments for small clusters given in Table 9.2, and this result is puzzling.

The interpretation of the experimental results has been challenged by Guevara *et al.* [62]. They have performed TB calculations for clusters up to Mn_{62} using several model structures: icosahedral, *bcc* and *fcc*. For each cluster size and structure they find several magnetic solutions. In general the magnetic moments are not ferromagnetically aligned. From the comparison of the experimental and calculated moments they suggest that the structures are mainly icosahedral for $N < 30$, while for larger clusters *bcc* structures begin to compete with the icosahedral growth. Jena and coworkers [63, 64] arrived at a similar conclusion concerning the magnetic ordering. They propose that nonferromagnetic ordering is responsible for the small moments measured for the Mn clusters. In that case the ordering has to be ferrimagnetic, that is, the magnitude of the moments at the different atomic sites is different, or the number of atoms with spins ↑ and ↓ are unequal, or both. This proposal is supported by DFT calculations for Mn_{13} [63] and, more convincingly, by a combined experimental and theoretical analysis of Mn_7 [64]. The measured magnetic moment of Mn_7 is $0.72 \pm 0.42\,\mu_B$ per atom, a reduction of a factor of 7 from the free atom. The calculations predict a distorted pentagonal bipyramid for the structure. The magnitude of the local moments, calculated by integrating the spin densities on spheres around the atoms, is about $5\,\mu_B$, but the coupling is ferrimagnetic and the net magnetic moment is only $0.71\,\mu_B$ per atom, in good agreement with the measured value. Two isomers nearly degenerate with the ground state were also discovered. Their structure is again a distorted pentagonal bipyramid and the coupling is also ferrimagnetic.

9.8 Magnetism in Clusters of the 4d Metals

All the 4d metals are nonmagnetic in the bulk phase. But, since the free atoms are magnetic due to the Hund rules, it should not be surprising that small clusters of some of these elements are magnetic. Experiments [13]

show that Rh clusters with less than 60 atoms are magnetic and that Ru and Pd clusters with less than 12 atoms are magnetic also. Several calculations have investigated the magnetic properties of those clusters assuming model structures. Trends across the $4d$ period have been studied by performing LCAO calculations within the frame of the DFT formalism for clusters formed by six atoms in octahedral arrangement. The binding trends have been discussed in Section 8.2 and the calculated magnetic moments per atom are given in Table 8.2. Each cluster, except Y_6, Pd_6 and Cd_6, has a finite magnetic moment and the largest moments occur for Ru_6 and Rh_6 ($1.00\,\mu_B$ and $0.99\,\mu_B$, respectively). The large moments of Ru_6 and Rh_6 can be understood from the shape of the total density of states (DOS), which is characterized for having a large peak in the energy region of the Fermi level [65]. The high DOS contributes strongly to the large moments because a small exchange splitting (that is, the shift between up and down spin sub-bands) results in a sizable difference between the population of up and down spin electrons. In fact Ru_6, Rh_6 and Nb_6 have the largest exchange splittings accross the $4d$ period. In contrast, the Fermi levels of the bulk metals lie in a dip of the DOS. The main contribution to the DOS of the occupied valence band of the clusters is from the d electrons and this gives support to some models in which the sp electrons are altogether neglected. Two factors contribute to the large DOS near ε_F: first, the band width is narrower in the cluster than in the solid, due to the reduced atomic coordination, and second, the high symmetry (octahedral) assumed in the calculation. The last effect suggests that some of the magnetic moments of Table 8.2 may be overestimated.

9.8.1 Rhodium clusters

The experiments for Rh clusters [13] reveal an oscillatory pattern of $\overline{\mu}(N)$ with large values for $N = 15$, 16 and 19, and drops for $N = 13$–14, 17–18, and 20. A number of DFT calculations have been performed for a few selected clusters in that size range, assuming symmetric structures except for the smallest ones [66–71]. The conclusion is that the clusters are magnetic, in qualitative agreement with experiment. However, the results for $\overline{\mu}$ for the same N show a lot of dispersion.

The selfconsistent TB method has been employed to study several clusters in the range $9 \leq N \leq 55$ [72]. Only the $4d$ electrons were

included in the calculations, and mainly model structures (*fcc, bcc* or icosahedral) were considered, although atomic relaxation preserving the cluster symmetry was allowed (a Born–Mayer pair potential was used to account for core–core repulsion). Sizable contractions with respect to the bulk bond length were obtained (from 2 to 9 %), and these affect the magnetic moments. The calculated magnetic moments oscillate and tend to decrease with increasing N. A twisted double-square pyramid yields the largest cohesive energy for Rh_9 (2.38 eV/atom), and its magnetic moment, $\bar{\mu} = 0.66\,\mu_B$, is in good agreement with experiment ($\bar{\mu} = 0.8 \pm 0.2\,\mu_B$). For Rh_{11} the icosahedral and the *fcc* structures are degenerate, although only the magnetic moment of the former isomer ($\bar{\mu} = 0.73\,\mu_B$) is consistent with experiment ($\bar{\mu} = 0.8 \pm 0.2\,\mu_B$). The most stable structure for Rh_{13} is *bcc* with $\bar{\mu} = 0.62\,\mu_B$, in better agreement with experiment ($\bar{\mu} = 0.48 \pm 0.13\,\mu_B$) than the other structures considered. In the range $15 \le N \le 43$, *fcc* structures are predicted, and although the magnetic moments are larger than the measured ones, the trends of the size dependence are correctly reproduced: local minima at $N = 13$ and 17 and maxima at $N = 15$ and 19. This suggests that the underlying structure in the range $15 \le N \le 20$ may be *fcc*, especially since the other structures fail to reproduce those oscillations. Finally the icosahedral structure is more stable for $N = 55$ and its nonmagnetic character is also in agreement with experiment. In summary, the structures predicted as most stable by the TB calculation give a consistent agreement with the measured magnetic moments.

Considering the distribution of local magnetic moments in those calculations, the *bcc* isomers order ferromagnetically and the local atomic moments tend to increase from the cluster center to the surface. Compact structures (*fcc* and icosahedral) are more complex and the magnetic order is sometimes antiferromagnetic-like, with μ changing sign between adjacent shells. A similar behavior has been predicted for Rh surfaces (*fcc*) and thin films [73]. The effect of the *sp* electrons was analyzed for Rh_{13}. Those electrons contribute to the binding energy but the bond lengths, the relative stabilities between isomers and the total magnetic moments are not altered; although the local moments are more sensitive to *sp–d* hybridization.

In another TB calculation for Rh_N (N = 13, 19, 43, 55 and 79) with *fcc* structures, ferromagnetic order was found for Rh_{13}, Rh_{19} and Rh_{43}, and antiferromagnetic configurations for Rh_{55} and Rh_{79} [74]. The magnetic moments of the two largest clusters are very close to experiment, and this was interpreted as supporting *fcc* structures for $N >$ 40. The magnetic to nonmagnetic transition was estimated at $N \approx 80$.

The relationship between the magnetism, topology and reactivity has been studied for Rh_4 using DFT at the GGA level [75]. This cluster has two isomers: the ground state is a tetrahedron with a binding energy of 2.41 eV/atom. The second isomer, a square, is 0.60 eV/atom less stable. The tetrahedron is nonmagnetic and the square is magnetic with a moment of $1\,\mu_B$ /atom; the difference can be due to the different atomic coordination, three in the tetrahedron and two in the square. More insight is obtained from the analysis of the distribution of orbital energy levels. The square isomer has a larger number of states near the HOMO, and it is known from extended systems that a large density of states near the Fermi energy usually leads to magnetic structures. By simulating the reaction of the two Rh_4 isomers with H_2 the following conclusions were noted: (1) H_2 dissociates and binds atomically to both isomers; (2) the binding energy of H_2 to the nonmagnetic isomer is larger by a factor of 2; (3) the spin multiplicity of both isomers changes. This indicates that the reactivity of transition metal clusters may depend sensitively on their magnetic structure and topology and, in fact, the existence of isomers has been detected in reactivity experiments. Only the magnetic isomer of Rh_4 can be deflected in a Stern–Gerlach magnet. On the other hand, the two reacted forms of Rh_4H_2 are magnetic and have different spin multiplicities. Consequently the two reacted clusters will be deflected differently in a Stern–Gerlach field. This provides a possible way to test the theoretical predictions.

9.8.2 Ruthenium and Palladium clusters

Tight-binding [72, 76] and DFT calculations [67, 77] have been performed for Ru clusters. The TB method predicts lower average magnetic moments, in better agreement with the experimental upper limits [13], but one has to bear in mind that the *sp* electrons were not included in the calculations. The magnetic to nonmagnetic transition is estimated to occur at $N \approx 19$, a value in satisfactory agreement with the

experimental bound $N \geq 13$ [13]. Antiferromagnetic alignment of the local moments is preferred for most of the structures studied.

The magnetism of small Palladium clusters is controversial. It has not been confirmed in the experiments of Cox *et al.* [13], but these authors did not exclude the possibility of magnetism and set upper limits of 0.40 μ_B/atom for Pd_{13} and 0.13 μ_B/atom for Pd_{105}. DFT calculations for Pd clusters support the existence of small magnetic moments [78–80]. Calculations of Moseler *et al.* [80] for neutral clusters with $N \leq 7$ and $N = 13$ predict a monotonic decrease of $\overline{\mu}$ between Pd_2 ($\overline{\mu} = 1\,\mu_B$) and Pd_7 ($\overline{\mu} = 0.3\,\mu_B$), and an unexpected high value of 0.62 μ_B for Pd_{13}. Negatively charged clusters show more complex behavior. The average magnetic moment oscillates and has large values for $N = 5, 7$ and 13 ($\overline{\mu} = 0.6, 0.7$ and 0.54 μ_B, respectively). The total magnetic moment arises from sizable local atomic moments of magnitude 0.3–0.6 μ_B. These couple antiferromagnetically in some cases (singlet states, $S = 0$) and align ferromagnetically in other cases.

9.9 Effect of Adsorbed Molecules

Ligand molecules induce perturbations on the electronic structure of the atoms forming the surface of the cluster. A striking effect is the quenching of the magnetic moments in Ni clusters caused by the adsorption of CO [81]. Nickel cluster carbonyl complexes like $[Ni_9(CO)_{18}]^{2-}$ display vanishing magnetic susceptibilities, indicating Ni moments of $0\mu_B$. Electronic structure calculations for $[Ni_6(CO)_{12}]^{2-}$, $[Ni_{32}(CO)_{32}]^{n-}$, $[Ni_{44}(CO)_{48}]^{n-}$ and other complexes predict low spin structures, consistent with the very low magnetic susceptibilities measured for macroscopic samples of these compounds [81, 82]. The explanation is that ligands with σ lone pairs, like CO, interact repulsively with the diffuse $4sp$ electrons of the Ni atoms, inducing a transition $3d^9 4s^1 \rightarrow 3d^{10}$ that fills the $3d$ shell. The calculations show that this repulsive destabilization is produced even by a shell of He atoms [44]. Stern–Gerlach magnetic deflection experiments for $Ni_N CO$ clusters with $N = 8–18$ reveal that the presence of a single CO molecule reduces the magnetic moment of most of those clusters [83]. The quenching

effect is particularly large for Ni_8, Ni_9, Ni_{15} and Ni_{18}. For instance, the total magnetic moment of Ni_8 is reduced by $\approx 5\,\mu_B$, that is, $0.63\,\mu_B$ per atom.

DFT studies of the adsorption of NH_3 by small Ni clusters ($N = 1-4$) also indicate a significant effect on the magnetism [84]. Adsorption of NH_3 leads to a decrease of the Ni moments, which are completely quenched when the number of NH_3 molecules equals the number of Ni atoms. The nitrogen atom binds directly to a Ni atom and the quenching of the magnetic moment of Ni occurs because the Ni–N bond distance is short. When the number of NH_3 molecules is larger than the number of Ni atoms, the Ni–N bonds are stretched due to steric hindrance, the Ni–N distances exceed the critical distance of 3.59 a.u. and magnetism reappears.
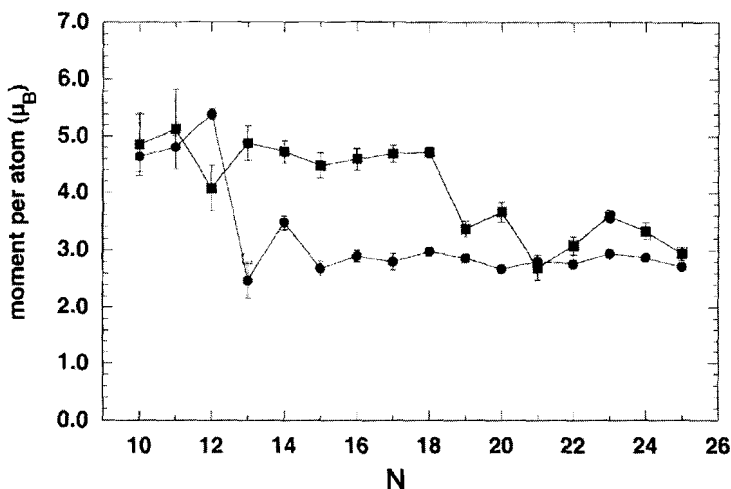
Figure 9.7. Measured magnetic moments of Fe_N (circles) and Fe_NH_m (squares). Adapted from M. B. Knickelbein, *Chem. Phys. Lett.* **353**, 221 (2002) with permission of Elsevier.

However, adsorbates can also increase the magnetic moments of ferromagnetic clusters. Figure 9.7 shows the measured magnetic moments of free and hydrogenated Fe clusters [85]. Under the conditions of the experiment the Fe clusters become saturated with a layer of

dissociatively chemisorbed hydrogen. For most of the sizes reported, the clusters $Fe_N H_m$ have larger magnetic moments than the corresponding pure Fe_N species. The enhancement is particularly large for $N = 13$–18. This finding contrasts with analogous studies for Ni clusters, in which hydrogenation quenches the magnetic moments [85].

9.10 Determination of Magnetic Moments by Combining Theory and Photodetachment Spectroscopy

For very small clusters the total magnetic moment is also small and the deflection in the Stern–Gerlach magnetic field may be within the error of the experiment. For those cases a method has been proposed to determine magnetic moments that is based on combining theoretical calculations for the neutral and anionic species with electron photodetachment experiments [86]. The idea goes as follows. Let us imagine that a ferromagnetic anionic cluster has n unpaired spins, and then a magnetic moment $n\mu_B$ and multiplicity $M = n+1$. When an electron is detached from the anion, the neutral cluster will have a multiplicity of $M+1$ if the electron was removed from the minority band, or $M-1$ if the electron was removed from the majority band. The measured photoelectron energy peaks can be compared to theoretical calculations where one first determines the ground state of the anion, including its spin multiplicity M, and the energy for the transition to the neutral species with multiplicities $M+1$ and $M-1$ at the anion geometry. If there is quantitative agreement between the calculated energies and the observed peaks, one can conclude that the calculated multiplicity must be correct.

The method has been tested for Ni_5 [86]. The experimental photodetachment spectrum shows a prominent and broad peak at 10.80 eV and a minor peak at 2.11 eV [87]. A detailed search was undertaken of the equilibrium structures of Ni_5^- corresponding to spin multiplicities $M = 2, 4, 6, 8$ and 10, and of neutral Ni_5 with spin multiplicities $M = 1, 3, 5, 7$ and 9, using DFT with the GGA for exchange and correlation. In the case of the neutral cluster the ground state is a nearly perfect square pyramid with multiplicity $M = 7$ (total magnetic moment of $6\mu_B$). This state is nearly degenerate with a distorted trigonal bipyramid with $M = 5$

($\mu = 4\mu_B$). In the case of Ni_5^- the structure, for all the spin muliplicities studied, is a slightly distorted square pyramid. The ground state structure corresponds to $M = 8$, and this structure can only arise by adding an electron to the majority spin band of neutral Ni_5 with $M = 7$ (which is the ground state of Ni_5). The structure of Ni_5^- with $M = 6$ is only 0.05 eV above the ground state, so both isomers with $M = 6$ and 8 are expected to exist in the beam. The calculated vertical transition energies from the anionic to the neutral cluster are plotted in Fig. 9.8.
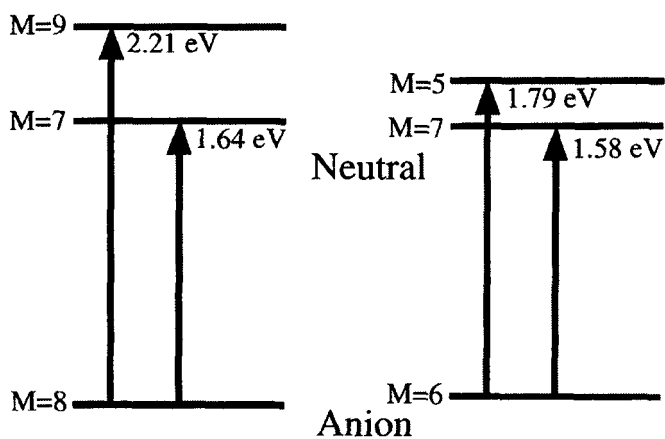
Figure 9.8. Transitions from the Ni_5^- isomers with spin multiplicity M to the corresponding neutrals with multiplicities differing by ± 1 from the anion. Adapted from S. Khanna and P. Jena, *Chem. Phys. Lett.* **336**, 476 (2001) with permission of Elsevier.

The left side shows the transitions from the ground state of the anion (with $M = 8$) to the states of the neutral cluster with the anion geometry and $M = 7$ and 9 (the transition energies are obtained as a difference of the total energies of the corresponding clusters). These transitions yield energies of 1.64 eV and 2.21 eV; on the other hand, the transitions from the $M = 6$ state of Ni_5^- yield energies of 1.58 eV and 1.79 eV. It is plausible that the broad peak reported in the experiments arises from

transitions from both isomers of Ni_5^-, while the peak at 2.11 eV can only originate from the state of Ni_5^- with $M = 8$.

9.11 Noncollinear Magnetism

The γ phase of solid iron exhibits a spin-spiral structure. Noncollinear magnetic configurations occur easily in systems with low symmetry or disordered ones. Consequently one could expect noncollinear spin configurations in clusters of the transition metals. The usual DFT calculations described in previous sections assume spin alignment through the system. However some generalized LSDA calculations allowing for noncollinear magnetic structures have been performed for solids and this idea has been extended to clusters [88, 89]. In this method, an LSDA scheme in which the local direction of the magnetization is fully unconstrained as a function of position is combined with *ab initio* molecular dynamics. In the LSDA [90] the one-electron states are described by spinors $\Psi(\mathbf{r}) = (\phi_1(\mathbf{r}), \phi_2(\mathbf{r}))$ with two components. The electronic density matrix is defined

$$\Gamma_{\alpha\beta}(\mathbf{r}) = \sum_i f_i \ \phi_{\alpha i}(\mathbf{r}) \phi_{\beta i}(\mathbf{r}) \tag{9.17}$$

where α and β are spin indices and f_i is the occupation number of the ith-single-particle state. This density matrix can be written

$$\Gamma(\mathbf{r}) = \frac{1}{2}\rho(\mathbf{r})\,\sigma_0 + \frac{1}{2}\sum_k m_k(\mathbf{r})\,\sigma_k \tag{9.18}$$

where $\rho(\mathbf{r})$ is the electronic charge density, σ_0 is the unit matrix, σ_k ($k = x, y, z$) are the Pauli spin matrices, and $m_k(\mathbf{r})$ are the cartesian components of the spin-density vector $m(\mathbf{r})$. In this scheme the spin quantization axis of each state can vary with position. Following the *ab initio* MD scheme the electronic wave functions Ψ_i and the atomic positions $\mathbf{R}_i$ are simultaneously optimized by minimizing the total energy

for noncollinear spin structures [90, 91]. The magnetic moment of each atom in the clusters is then calculated by integrating the spin density within spheres of appropriate radius centered on the atoms.

d/d_{bulk}	Cr	Mn	Fe
1.00	2.23	3.98	2.86
0.95	1.60	3.65	2.86
0.90	0.29		1.71
0.85	0.29		
0.80	0.29	0.81	0.29

$|\mu_B|/$atom

☐ collinear(P)   ⬚ collinear(AP)   ▨ coplanar   ■ non
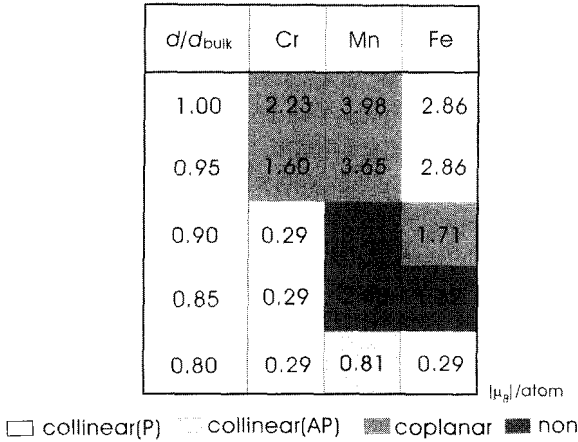
Figure 9.9. Character of the arrangement of the spin magnetic moments in pentagonal bipyramidal clusters with interatomic distances ranging from d_{bulk} to 80% d_{bulk}. Reproduced from N. Fujima, *Eur. Phys. J. D* **16**, 185 (2001) with permission of EDP Sciences.

Calculations for Fe$_5$ [88] give a trigonal bipyramid (D_{3h} symmetry) with a noncollinear spin arrangement for the ground state. The three atoms of the basal plane have magnetic moments of 2.72 μ_B pointing in the same direction and the two apical atoms have moments of magnitude 2.71 μ_B tilted in opposite directions by approximately 30° with respect to the moments of the basal atoms. The binding energy of the cluster is $E_b = 3.46$ eV/atom and its total moment is 14.6 μ_B. An isomer with D_{3h} structure was also found having a collinear spin arrangement with atomic moments of 2.58 μ_B and 2.55 μ_B for the basal and apical atoms, respectively. Its energy is only 0.01 eV/atom above the ground state. The ground state of Fe$_3$ is an equilateral triangle with collinear spin arrangement. Its total moment is 8.00 μ_B and the binding energy $E_b = 2.64$ eV/atom. A linear isomer with noncollinear arrangement was also

found: the central atom has a moment of $1.27\,\mu_B$ oriented perpendicular to the linear axis and the two edge atoms have moments of magnitude $2.89\,\mu_B$, tilted by $\pm 10°$ with respect to the cluster axis. The total moment of the cluster is $2.04\,\mu_B$ and its binding energy is $E_b = 2.17$ eV/atom. Linear isomers were also found with collinear ferromagnetic and antiferromagnetic spin configurations. The total moments of those two isomers are $6.00\,\mu_B$ and $0.00\,\mu_B$ and their binding energies 1.80 and 2.15 eV/atom, respectively. Calculations for Fe_2 and Fe_4 gave also collinear ground states.

The nature of the spin arrangement depends sensitively on the interatomic distances. A comparative study for Cr_7, Mn_7 and Fe_7 with the pentagonal bipyramid structure, including the variation of the interatomic distance d from the bulk value d_{bulk} to a value 20 % lower, appears summarized in Fig. 9.9 [89]. For Cr_7 with d_{bulk} the magnetic moments are arranged in a coplanar noncollinear configuration. When d decreases the magnetic moments change to parallel order. The situation is similar for Mn_7 with d close to d_{bulk}, that is, the cluster shows a coplanar configuration of the spins. However, for decreasing d, a non coplanar configuration first appears, and this changes to a collinear antiparallel one with further decrease of d. Finally the spin arrangement in Fe_7 is parallel for $d \approx d_{bulk}$ and $d \approx 0.8\,d_{bulk}$, and it is noncollinear for d in between the above two limits.

References

1. Billas, I. M. L., Chatelain, A., and De Heer, W. D., *Science*, **265**, 1682 (1994).
2. Billas, I. M. L., Chatelain, A., and De Heer, W. D., *J. Mag. Mag. Mater.*, **168**, 64 (1997).
3. Cox, D. M., Trevor,D. J., Whetten, R. L., Rohlfing, E. A., and Kaldor, A., *Phys. Rev. B*, **32**, 7290 (1985).
4. de Heer, W. A., Milani, P., and Chatelain, A., *Phys. Rev. Lett.*, **65**, 488 (1990).
5. Bucher, J. P., Douglass, D. C., and Bloomfield, L. A., *Phys. Rev. Lett.*, **66**, 3052 (1991).
6. Douglass, D. C., Cox, A., Bucher, J. P., and Bloomfield, L. A., *Phys. Rev. B*, **47**, 12874 (1993).

7. Billas, I. M. L., Becker, J. A., Chatelain, A., and De Heer, W. A., *Phys. Rev. Lett.*, **71**, 4067 (1993).
8. Apsel S.E., Emmert J.W., Deng J., and Bloomfield L.A., *Phys. Rev. Lett.*, **76**, 1441 (1996).
9. Khanna, S. N., and Linderoth, S., *Phys. Rev. Lett.*, **67**, 742 (1991).
10. Dattagupta, S., and Mahanti, S. D., *Phys. Rev. B*, **57**, 10244 (1998).
11. Gantefor, G., and Eberhardt, W., *Phys. Rev. Lett.*, **76**, 975 (1996).
12. Ho, J., Polak, M.L., Ervin, K.M., and Lineberger, W.C., *J. Chem. Phys.*, **99**, 8542 (1986).
13. Cox, A. J., Lourderback, J. G., and Bloomfield, L. A., *Phys. Rev. Lett.*,**71**, 923 (1993); Cox, A. J., Lourderback, J. G., Apsel, S. E., and Bloomfield, L. A., *Phys. Rev. B*, **49**, 12295 (1994).
14. Zhao, J., Chen, X., Sun, Q., Liu F., and Wang, G., *Phys. Lett. A* , **205**, 308 (1995).
15. Friedel, J., *The Physics of Metals*. Ed. J.M. Ziman, Cambridge University Press (1969), p. 340.
16. Pastor, G., Dorantes-Dávila, J., and Bennemann K.H., *Chem. Phys. Lett.*, **148**, 459 (1988).
17. Aguilera-Granja, J.M. Montejano-Carrizales and J.L. Morán-López, *Solid State Commun.*, **107**, 25 (1998).
18. Jensen, P., and Bennemann, K. H., *Z. Phys. D*, **35**, 273 (1995).
19. Binder, K., Rauch, H., and Wildpaner, V., *J. Phys. Chem. Solids*, **31**, 391 (1970).
20. Mook, H. A., *J. Magn. Magn. Mater.*, **31-34**, 305 (1983).
21. G.M. Pastor, G. M., and Dorantes-Dávila, J., *Phys. Rev. B*, **52**, 13799 (1995).
22. Hirt, A., Gerion, D., Billas, I. M. L., Chatelain, A., and De Heer, W. A., *Z. Phys. D*, **40**, 160 (1997).
23. Alonso, J. A., *Chem. Rev.*, **100**, 637 (2000).
24. Vega, A., Dorantes-Dávila, J., Balbás, L. C., and Pastor, G. M., *Phys. Rev. B*, **47**, 4742 (1993).
25. Heine, V., *Phys. Rev.*, **153**, 673 (1967).
26. Pastor, G. M., Dorantes-Dávila, J., and Bennemann, K. H., *Physica B* , **149**, (1988); *Phys. Rev. B*, **40**, 7642 (1989).
27. Haydock, R., *Solid State Phys.*, **35**, 215 (1980).
28. Bouarab, S., Vega, A., López, M. J., Iñiguez, M.P., and Alonso, J. A., *Phys. Rev. B*, **55**, 13279 (1997).
29. Aguilera-Granja, F., Bouarab, S., López, M. J., Vega, A., Montejano-Carrizales, J. M., Iñiguez , M. P., and Alonso, J. A., *Phys. Rev. B*, **57**, 12469 (1998).
30. Ducastelle, F., *J. Physique (Paris)* , **31**, 1055 (1970).
31. Gupta R.P., *Phys. Rev. B*, **23**, 6265 (1981).
32. Montejano-Carrizales, J. M., Iñiguez, M. P., Alonso, J. A., and López, M. J., *Phys. Rev. B*, **54**, 5961 (1996).

33. Parks, E. K., Nieman, G. C., Kerns, K. P., and Riley, S. J., *J. Chem. Phys.*, **107**, 1861 (1997).
34. Guevara, J., Parisi, F., Llois, A. M., and Weissmann, M., *Phys. Rev. B*, **55**, 13283 (1997).
35. Lathiotakis, N. N., Andriotis, A. N., Menon, M., and Connolly, J., *J. Chem. Phys.*, **104**, 992 (1996).
36. Rodríguez-López, J. L., Aguilera-Granja, F., Vega, A., and Alonso, J. A., *Eur. Phys. J. D*, **6**, 235 (1999).
37. Fujima N., and Yamaguchi, T., *Phys. Rev. B*, **54**, 26 (1996).
38. Fujima N., and Yamaguchi, T., *J. Phys. Soc. Japan*, **58**, 3290 (1989).
39. Reuse F.A., and Khanna, S.N., *Chem. Phys. Lett.*, **234** , 77 (1995).
40. Desmarais N., Jamorski C., Reuse F.A., and Khanna S.N., *Chem. Phys. Lett.*, **294**, 480 (1998).
41. Reddy B.V., Nayak S.K., Khanna S.N., Rao B.K., and Jena P., *J. Phys. Chem. A*, **102**, 1748 (1998).
42. Finnis M.W., and Sinclair J.E., *Phil. Mag.*, **50**, 45 (1984).
43. Fujima, N., and Yamaguchi, T., *Mater. Sci. Eng. A*, **217**, 295 (1996).
44. Pacchioni, G., Chung, S. C., Krüger, S., and Rösch, N., *Chem. Phys.*, **184**, 125 (1994).
45. Cheng, H., and Wang, L.S., *Phys. Rev. Lett.*, **77**, 51 (1996).
46. Douglass, D. C., Bucher, J. P., and Bloomfield, L. A., *Phys. Rev. B*, **45**, 6341 (1992).
47. Blügel, S., Drittler, B., Zeller, R., and Dederichs, P. H., *Appl. Phys. A*, **49**, 547 (1989).
48. Stepanyuk, V. S., Hergert, W., Wildberger, K., Nayak, S. K., and Jena, P., *Surf. Sci. Lett.*, **384**, L892 (1997).
49. Morse, M. D., *Chem. Rev.*, **86**, 1049 (1986).
50. Parks, E. K., Nieman G. C., and Riley, S. J., *J. Chem. Phys.*, **104**, 3531 (1996).
51. Van Zee, R. J., and Weltner, W., *J. Chem. Phys.*, **89**, 4444 (1988).
52. Ludwig, G. W., Woodbury, H. H., and Carlson, R. O., *J. Phys. Chem. Solids*, **8**, 490 (1959).
53. Baumann, C. A., Van Zee, R. J., Bhat, S., and Weltner, W. *J. Chem. Phys.*, **78**, 190 (1983).
54. Nesbet R.K., *Phys. Rev.*, **135**, A460 (1964).
55. Fujima N., and Yamaguchi, T., *J. Phys. Soc. Japan*, **64**, 1251 (1995).
56. Nayak, S. K., and Jena, P., *Chem. Phys. Lett.*, **289**, 473 (1998).
57. Schieffer, P., Krembel, C., Hanf, M. C., Bolmont D., and Gewinner, G., *J. Magn. Magn. Mater.*, **165**, 180 (1997).
58. Rader, O., and Gudat, W., *Phys. Rev. B*, **56**, 5053 (1997).
59. Pederson, M. R., Reuse, F., and Khanna, S. N., *Phys. Rev. B*, **58**, 5632 (1998).
60. Koretsky, G. M., and Knickelbein, M. B., *J. Chem. Phys.*, **106**, 9810 (1997).
61. Knickelbein, M. B., *Phys. Rev. Lett.*, **86**, 5255 (2001).

62. Guevara, J., Llois, A. M., Aguilera-Granja, F., and Montejano-Carrizales, J. M., *Phys. Stat. Sol. B*, **239**, 457 (2003).
63. Nayak, S. K., Nooijen, M. and Jena, P., *J. Phys. Chem. A*, **103**, 9853 (1999).
64. Khanna, S. N., Rao, B. K., Jena. P., and Knickelbein, M., *Chem. Phys. Lett.*, **378**, 374 (2003).
65. Zhang G.W., Feng Y.P. and Ong C.K., *Phys. Rev. B*, **54**, 17208 (1996).
66. Galicia, R., *Rev. Mex. Fís.*, **32**, 51 (1985).
67. Reddy, B. V., Khanna, S. N., and Dunlap, B., *Phys. Rev. Lett.*, **70**, 3323 (1993).
68. Piveteau, B., Desjonquéres, M. C., Olés, A. M., and Spanjard, D., *Phys. Rev. B*, **53**, 9251 (1996).
69. Jinlong, Y., Toigo, F., Kelin, W., and Manhong, Z., *Phys. Rev. B*, **50**, 7173 (1994).
70. Jinlong, Y., Toigo, F., and Kelin, W., *Phys. Rev. B*, **50**, 7915 (1994).
71. Li, Z. Q., Yu, J. Z., Ohno, K., and Kawazoe, Y., *J. Phys: Condens. Matter*, **7** , 47 (1995).
72. Villaseñor-González, P., Dorantes-Dávila, J., Dreyssé, H., and Pastor, G., *Phys. Rev. B*, **55**, 15084 (1997).
73. Chouairi, A., Dreyssé, H., Nait-Laziz, H., and Demangeat, C., *Phys. Rev. B*, **48**, 7735 (1993); Mokrani, A., and Dreyssé, H., *Solid State Commun.*, **90**, 31 (1994).
74. Guirado-López, R., Spanjaard, D., and Desjonquéres, M. C., *Phys. Rev. B*, **57**, 6305 (1998).
75. Nayak, S. K., Weber, S. E., Jena, P., Wildberger, K., Zeller, R., Dederichs, P. H., Stepanyuk, S. V., and Hergert, W., *Phys. Rev. B*, **56**, 8849 (1997).
76. Guirado-López, R., Spanjaard, D., and Desjonquéres, M. C., and Aguilera-Granja, F., *J. Magn. Mag. Mater.*, **186**, 214 (1998).
77. Kaiming, D., Jinlong, Y., Chuamyun, X., and Kelin, W., *Phys. Rev. B*, **54**, 2191 (1996).
78. Lee, K., *Phys. Rev. B*, **58**, 2391 (1998).
79. Lee, K., *Z. Phys. D*, **40**, 164, (1997).
80. Moseler, M., Häkkinen, H., Barnett, R. N., and Landman, U., *Phys. Rev. Lett.*, **86**, 2545 (2001).
81. Van Leeuwen, D. A., Van Ruitenbeek, J. M., de Jongh, L. J., Ceriotti, A., Pacchioni, G., Häberlen, O. D., and Rösch, N., *Phys. Rev. Lett.*, **73**, 1432 (1994).
82. Pacchioni, G., and Rösch, N., *Acc. Chem. Res.*, **28**, 390 (1995).
83. Knickelbein, M. B., *J. Chem. Phys.*, **115**, 1983 (2001).
84. Chen, B., Castleman, A. W., and Khanna, S. N., *Chem. Phys. Lett.*, **304**, 423 (1999).
85. Knickelbein, M. B., *Chem. Phys. Lett.*, **353**, 221 (2002).
86. Khanna, S., and Jena, P., *Chem. Phys. Lett.*, **336**, 476 (2001).
87. Wang, L. S., and Wu, H., *Z. Phys. Chem.*, **203**, 45 (1998).
88. Oda, T., Pasquarello, A., and Car, R., *Phys. Rev. Lett.*, **80**, 3622 (1998).

89. Fujima, N., *Eur. Phys. J. D*, **16**, 185 (2001).
90. Von Barth, U., and Hedin, L., *J. Phys. C.*, **5**, 1629 (1972).
91. Kübler, J., Höck, K., Sticht, J., and Williams, A. R., *J. Phys. F*, **18**, 469 (1988).

10.   Clusters of Ionic Materials

10.1 Nearly Stoichiometric Metal Halide Clusters

A salt like NaCl is composed of closed shell ions, Na^+ and Cl^-, with electronic configurations similar to those of the rare gas atoms Ne ($1s^2$ $2s^2$ $2p^6$) and Ar ($1s^2$ $2s^2$ $2p^6$ $3s^2$ $3p^6$), respectively. The cohesion in the crystal is explained as a balance between attractive and repulsive forces between the ions. The attractive interaction comes from the Coulombic attraction between anions and cations, which tend to be nearest neighbors. In contrast, cation–cation and anion–anion repulsion prevents these from being nearest neighbors. Although the electrostatic interaction between anions and cations is attractive, the overlap between the closed electronic shells leads to a strong short-range repulsion arising from the Pauli exclusion principle, and sets a minimal distance of approach between nearest neighbors. These effects can be taken into account by an interionic potential of the form

$$V_{ij}\left(r_{ij}\right) = \frac{Z_i Z_j e^2}{r_{ij}} + A e^{-r_{ij}/\varphi} \qquad (10.1)$$

where r_{ij} indicates the separation between two ions i and j. The second term represents the short-range repulsion between ions with closed electronic shells, and the first one is the long range Coulombic interaction (attraction or repulsion) between point charges of magnitudes $Z_i e$ and $Z_j e$ (Z_i and Z_j can be positive or negative). The parameters A and φ are usually determined by a fit to the experimental cohesive properties of the solid [1].

When an intense beam of ions with high kinetic energy (for instance, 5 kV Xe⁻ ions) is directed against the surface of an alkali halide crystal, secondary ions are ejected from the surface and these can be detected by the usual mass spectrometric techniques. Those secondary ions include not only molecules, but also small and large clusters. The method of gas aggregation from material evaporated in an oven can also be used to produce the clusters. A mass spectrum of $(CsI)_nCs^+$ clusters shows that the intensity peak corresponding to $(CsI)_{13}Cs^+$, that is $[Cs_{14}I_{13}]^+$, is very strong [2], and analogous studies of NaCl and CuBr clusters show that $[Na_{14}Cl_{13}]^+$ and $[Cu_{14}Br_{13}]^+$ also have enhanced abundances [3, 4].
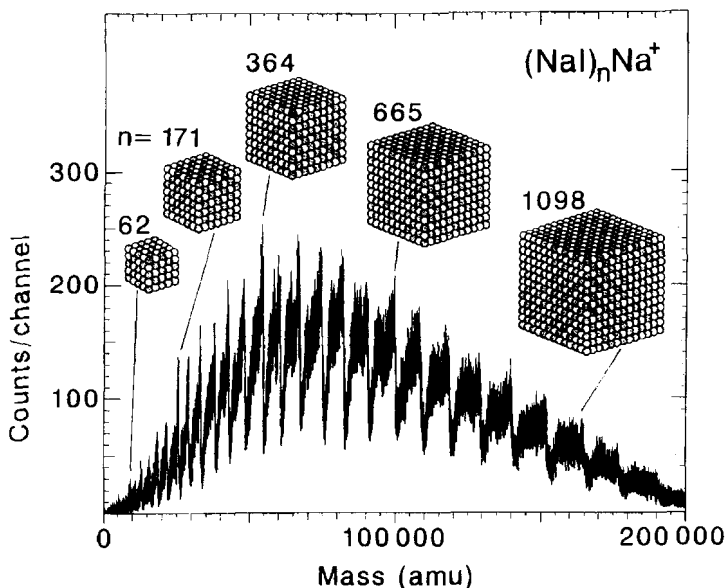
Figure 10.1. Mass spectrum of $(NaI)_nNa^+$ clusters. Each oscillation corresponds to the completion of a face of a rectangular box. Some peaks corresponding to clusters with the structure of perfect cubes are identified. Reproduced from T. P. Martin, *Phys. Rep.* **273**, 199 (1996) with permission of Elsevier.

Total energy calculations using the interatomic potential of Eq. (9.1) indicate the higher stability of these clusters compared to neighbor sizes, which arises from a very symmetrical structure. That structure is a small

fragment of the rock salt (or NaCl) lattice with the shape of a perfect cube, and it can be denoted as $(3\times3\times3)$, indicating that the number of ions along each of the three perpendicular edges of the cube is three, and consequently the total number of ions forming that tiny cube is 27. Other significant features in the mass spectrum are a sharp decrease of the intensity just after $n = 22$, 37 and 62. A similar analysis suggests that these additional features can also be explained by the enhanced stability of very symmetrical clusters with the shape of rectangular boxes, which are again perfect fragments of a rock salt crystal. With a similar notation, those rectangular boxes (often called cuboids) can be denoted as $(3\times3\times5)$, $(3\times5\times5)$ and $(5\times5\times5)$, respectively, the last one being again a perfect cube. Figure 10.1 shows a mass spectrum of $(NaI)_nNa^+$ clusters [5]. The spectrum emphasizes the features for large cluster sizes. The interpretation of the oscillations in the intensity is that these clusters tend to grow as tiny nanocubes. The cluster intensity is a maximum for the perfect cubes $(m\times m\times m)$, and then drops sharply after those clusters. The peaks corresponding to perfect cubes with $m = 5$ (125 atoms), 7 (343 atoms), 9 (729 atoms), 11 (1331 atoms) and 13 (2197 atoms) are explicitly indicated in the figure. There are more oscillations and peaks in between those of perfect cubes, and the interval between those oscillations corresponds to the number of atoms required to cover one face of cuboids formed in the growth from the cube $(m\times m\times m)$ to the next cube $(m+1 \times m+1 \times m+1)$. What makes these results nontrivial is the fact that while many alkali halide crystals have the six-fold coordinated rock salt structure, others show a different crystal structure: for example, the CsCl, CsBr and CsI crystals show the eight-fold coordinated CsCl structure, which is related to a *bcc* lattice (the cations occupy the center of a cube formed by eight anions, and vice versa), and CuBr has a crystal structure of the Zinc Blende type. So a transition to the structure of the bulk is expected for still larger cluster sizes.

The structure of cuboids cutted from the NaCl lattice has been assigned indirectly. Electron diffraction has allowed a more direct investigation of the structure of $(CsI)_nCs^+$ clusters with $n = 30$–39 [6]. With this technique, size-selected cluster ions are injected in a radio-frequency (rf) trap, where the clusters are thermalized by exposure to He gas at the desired temperature (300 K in the experiment of Parks *et al.* [6]). After evacuating the He gas, an electron beam passes through the the rf trap chamber and the diffraction image is recorded. In the range of

sizes studied, $n = 30$–39, the similarity of the diffraction patterns is striking with the only exception of $n = 32$. The main difference is a shift in the diffraction peak at an electron momentum transfer $s = 3.5$ Å^{-1}.
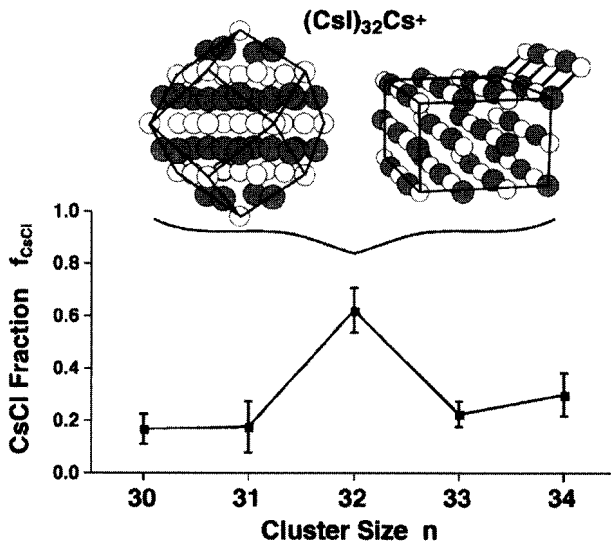
Figure 10.2. Fraction of CsCl structure present in the molecular diffraction studies of $(CsI)_n Cs^+$. The CsCl and NaCl isomers are shown for $n = 32$. Reproduced from S. Krückeberg *et al.*, *Phys. Rev. Lett.* **85**, 4494 (2000) with permission of the American Physical Society.

The mass spectrum indicates that $(CsI)_{31}Cs^+$ is a particularly stable cluster for which a ($3 \times 3 \times 7$) NaCl-type structure is expected, and the similarity of the diffraction patterns indicates that the other clusters, except $n = 32$, also have the NaCl structure. On the other hand a perfect rhombic dodecahedral fragment of the CsCl lattice, shown in Fig. 10.2, can be constructed for $(CsI)_{32}Cs^+$. The measured diffraction data were fitted by a theoretical model in which the diffraction patterns are calculated for an ensemble of clusters with a fraction f_{CsCl} of them having the CsCl structure and the rest having the NaCl structure. The best fits are obtained for the fractions shown in Fig. 10.2. The results can be interpreted as indicating the coexistence of the two structures, although the population is dominated by the NaCl structure, except for $n = 32$.

10.2 Nonstoichiometric Metal Halide Clusters

Now let us turn to the question of why in the previous section the attention has been focussed on clusters of composition $(MX)_nM^+$, where M indicates the metal and X the halide element. The relative intensity of cesium subchloride clusters formed by quenching Cs vapor in a mixture of He and Cl_2 is given in Fig. 10.3 [3]. The different spectra plotted are such that the number of Cl atoms is fixed in each particular spectrum and the variable is the number of Cs atoms.
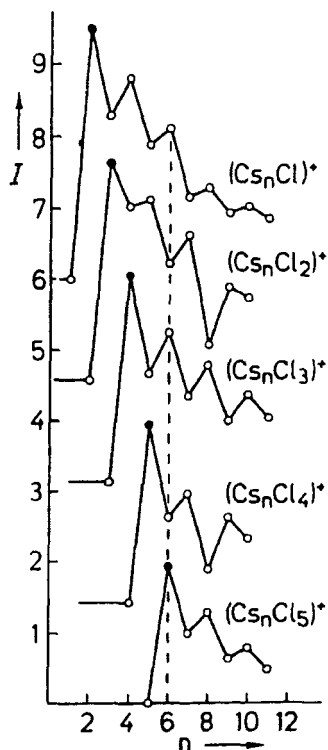
Figure 10.3. Intensity of cesium subchloride clusters formed by quenching Cs vapor in a mixture of He and Cl_2. Each spectrum contains a fixed number of Cl atoms. Filled circles correspond to clusters containing ions with rare gas electronic configurations. Reproduced from T. P. Martin, *Angew. Chem. Int. Ed. Ingl.* **25**, 197 (1986) with permission of Wiley.

The top spectrum indicates that only one Cl atom is incorporated into the cluster. The mass peaks corresponding to $[Cs_2Cl]^+$, $[Cs_4Cl]^+$, $[Cs_6Cl]^+$, $[Cs_8Cl]^+$, ... that is, with an even number of Cs atoms, are stronger than the peaks for odd number of Cs atoms. On the other hand, when two Cl atoms are incorporated into the cluster, an odd number of Cs atoms is preferred, that is, the peaks $[Cs_3Cl_2]^+$, $[Cs_5Cl_2]^+$, $[Cs_7Cl_2]^+$ ... are stronger. A look at the whole group of spectra reveals that, if the number of Cs atoms plus the number of Cl atoms is odd, the peak in the mass spectrum is strong.

Considering first the top spectrum, corresponding to $[Cs_NCl]^+$ clusters, the single Cl atom forms a Cl^- anion, and this leaves N-2 nearly free electrons in the cluster. This subsystem displays the usual odd–even features associated to pure alkali clusters discussed in Chapter 5. That is, clusters with N-2 even are more stable, and consequently more abundant than clusters with N-2 odd. The same argument explains the oscillations in the other spectra. For instance, for clusters of composition $[Cs_NCl_2]^+$, the number of nearly free electrons is N-3; then clusters with N-3 even are more stable than those with N-3 odd.

One can also observe that the most abundant cluster in each spectrum, namely $[Cs_2Cl]^+$, $[Cs_3Cl_2]^+$, $[Cs_4Cl_3]^+$, $[Cs_5Cl_4]^+$, $[Cs_6Cl_5]^+$, contains exclusively cations and anions with rare gas electronic configurations. For instance, $[Cs_2Cl]^+$ contains two Cs^+ cations and one Cl^- anion, and so on. Those precisely the clusters of nearly stoichiometric composition discussed in Section 10.1. As the partial pressure of Cl increases the mass spectrum simplifies considerably, becoming dominated by the nearly stoichiometric clusters $(CsCl)_nCs^+$.

10.3 Small Neutral Clusters

Quantum chemical calculations for small neutral alkali halide clusters [7–9] show that there is a competition between cuboid structures resembling fragments of a rock salt lattice and prismatic structures formed by a stacking of hexagonal rings.

The results obtained from the calculations for $(MX)_n$ clusters present well defined structural trends that can be parametrized in a map using the cation and anion radii as coordinates [9]. Figure 10.4 shows an example for clusters of the specific composition $(MX)_6$: each cluster is

represented in the plot by a point of coordinates (r_C, r_A), that is, the cation (M^+) and anion (X^-) radii. The two competitive structures are a hexagonal prism and a structure formed by two cubes sharing one face, that is a ($3 \times 2 \times 2$) cluster in the notation of Section 10.1. The two structures are characterized by different symbols: clusters whose ground state is the hexagonal structure are indicated by circles, and the cubic clusters are represented by squares. An empirical straight line can be drawn separating the two families. The same line separates the hexagonal prism and the rock salt fragments for $(MX)_9$ clusters. In this case the hexagonal prism is composed of three stacked hexagonal rings, and the rock salt fragment can be labeled as ($3 \times 2 \times 3$). The boundary line actually depends a little on n.
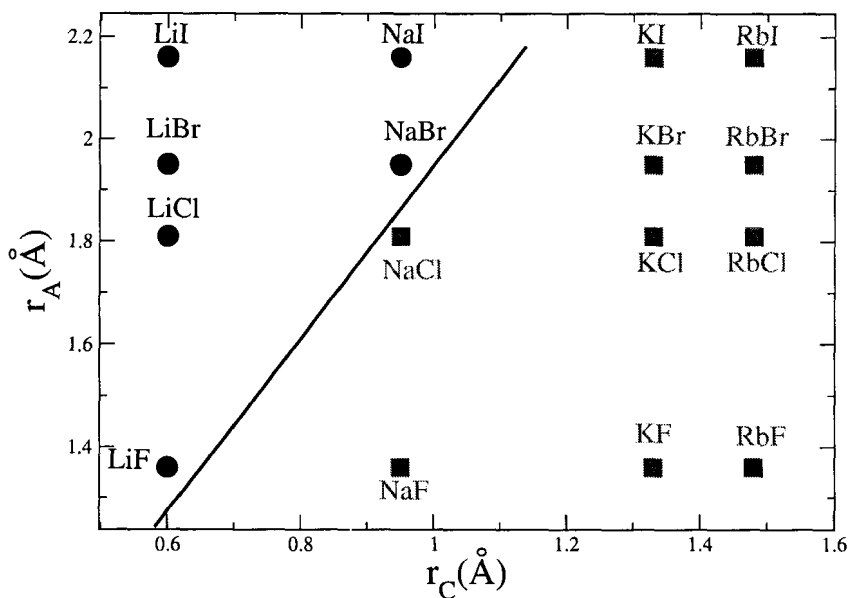
Figure 10.4. Structural stability map for $(MX)_6$ clusters. Using as coordinates the cation and anion radii, a boundary has been drawn separating clusters with hexagonal structure (circles) from those with cubic structure (squares). Redrawn from data in [9].
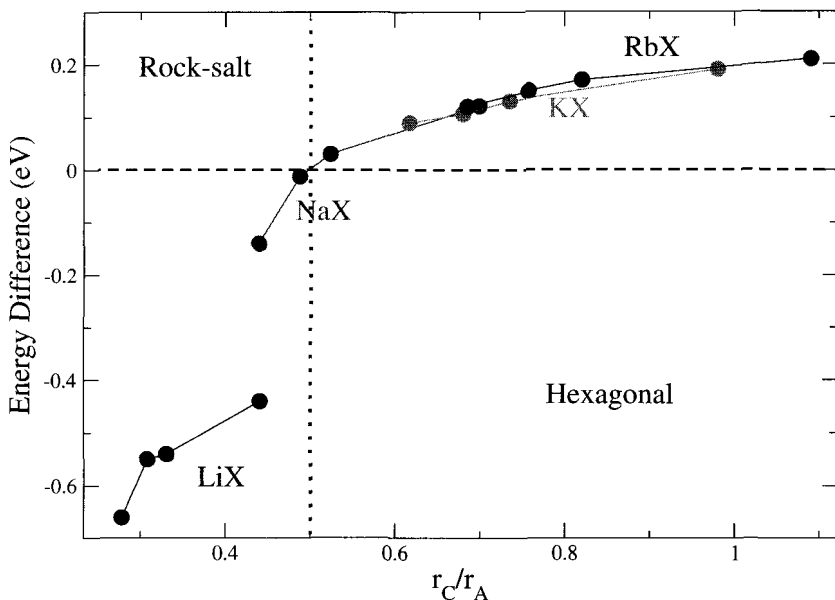
Figure 10.5. Energy difference between hexagonal and rock salt isomers of $(LiX)_6$, $(NaX)_6$, $(KX)_6$ and $(RbX)_6$ clusters versus the ratio of the cation and anion radii. A ratio of 0.5 separates these structures. Redrawn from data in [9].

The competition between hexagonal and cubic structures can be further simplified to a one-parameter plot. In Fig. 10.5 the difference in energy between the two isomers has been plotted as a function of the ratio of the cation and anion radii, r_C / r_A, again for $n = 6$. A correlation exists between these two magnitudes, and a critical ratio of 0.5 separates clusters whose ground state is a hexagonal prism from those with a rock salt structure. The hexagonal prism is the stable structure when a large disparity exists between the cation and anion radii, for $r_C / r_A < 0.5$; on the other hand, the rock salt structure becomes more stable when the ionic radii are not so different ($r_C / r_A > 0.5$). The binding energy of the clusters can be written as a sum of the electrostatic Madelung energy of interaction between point-like ions and quantum mechanical contributions [9]. The Madelung interaction alone already produces the separation between structures shown in Fig. 10.5, provided that the calculation of the Madelung energy is performed for each isomeric structure with the interatomic distances predicted by the full quantum chemical calculation.

10.4 Structural Transitions

Isomerization transitions between alkali halide clusters have been probed by techniques like photoelectron spectroscopy [10]; however, the most striking results have been obtained from ion mobility experiments. Those experiments have shown that the $(\text{NaCl})_n \text{Cl}^-$ clusters with more than 30 molecules experience structural transitions between different $(j \times k \times l)$ rectangular box-like structures [11]. To illustrate this point Fig. 10.6 shows drift time distributions for $(\text{NaCl})_{35} \text{Cl}^-$ measured at three different temperatures, taken with a fixed drift voltage of 7 kV.
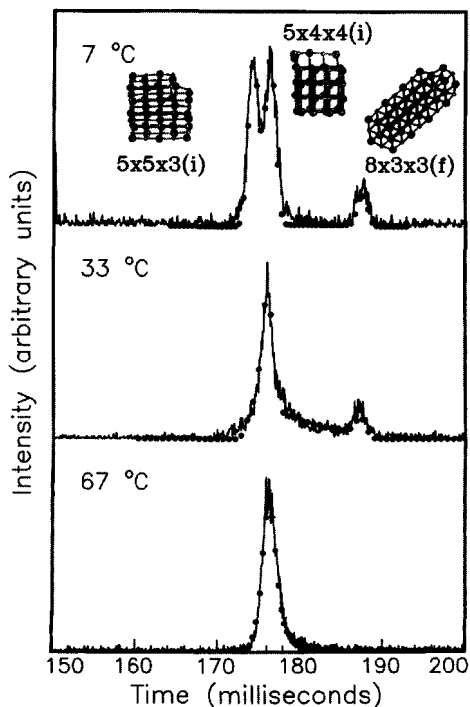
Figure 10.6. Drift time distributions for (NaCl)₃₅Cl⁻ at 7, 33 and 67°C with a drift voltage of 7 kV. Labels *f* and *i* indicate a cuboid with a vacancy and with an incomplete face, respectively. Reproduced from R. R. Hudjins *et al.*, *Phys. Rev. Lett.* **78**, 4213 (1997) with permission of the American Physical Society.

In the experiment the size-selected charged clusters enter a drift tube and are accelerated by an applied electric field, travelling through the tube that contains a helium buffer gas. Some ions then exit through a small hole and are focused into a mass spectrometer. The three peaks in the distribution in the upper panel of the figure correspond to three structural isomers that have been separated because their very different shapes lead to different mobilities through the buffer gas. These have been assigned to an incomplete (5×5×3) structure, that is, a cuboid with an incomplete face, an incomplete (5×4×4) structure, and a (8×3×3) structure with a single defect (a vacancy, or F center). These structures have been assigned by comparing the measured mobilities with the mobilities calculated for different structures optimized using an ionic interaction potential including polarization effects [12]. At the lowest temperature (300 K) the three isomers are present, but as the temperature is increased in the drift tube the (8×3×3) and (5×5×3) structures convert into the (5×4×4). These transitions involve the relocation of many atoms in the cluster.

Table 10.1. Activation energies for transitions between isomeric structures of NaCl clusters. The geometries are identified by their (j× k× l) dimensions. Letters c, f and i indicate a cuboid, a cuboid with a vacancy (or F center) and a cuboid with an incomplete face, respectively. Data collected from [10].

Cluster	Converting isomer geometry	Product isomer geometry	Activation Energy (eV)
$(NaCl)_{30} Cl^-$	(7× 3× 3) i	(4× 4× 4) i	0.57 ± 0.05
$(NaCl)_{35} Cl^-$	(8× 3× 3) f	(5× 4× 4) i	0.57 ± 0.05
$(NaCl)_{35} Cl^-$	(5× 5× 3) i	(5× 4× 4) i	0.53 ± 0.05
$(NaCl)_{36} Cl^-$	(6× 5× 3) i	(5× 5× 3) c	0.44 ± 0.05
$(NaCl)_{37} Cl^-$	(6× 5× 3) i	(7× 3× 3) i	0.36 ± 0.05

Activation energies E_a for these transitions, obtained from the Arrhenius equation

$$k = Ae^{-E_a / k_B T} \tag{10.2}$$

are given in Table 10.1. In this equation A is the frequency factor and k is the rate constant for the thermally activated structural transformation. Rate constants are obtained from the measured drift time distributions [11]. Activations energies for $(NaCl)_{30} Cl^-$, $(NaCl)_{36} Cl^-$ and $(NaCl)_{37} Cl^-$ are also reported in Table 10.1. The activation energies for the whole group range between 0.3 and 0.6 eV. These values are smaller than the activation energy for the migration of an ion vacancy in solid NaCl [13], so it is likely that the mechanism for the structural transformations observed involves a sequence of surface diffusion steps.
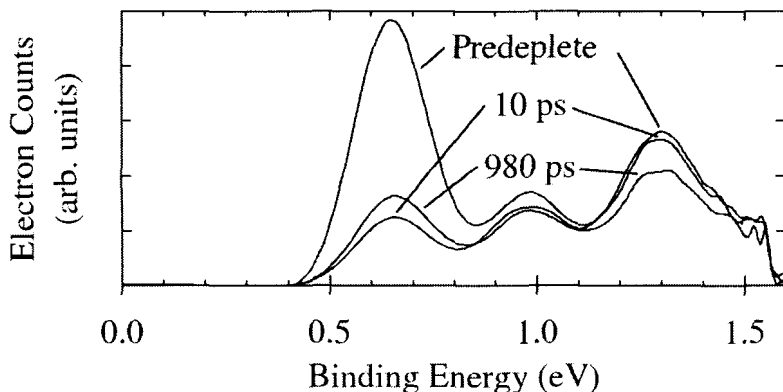
Figure 10.7. Photoelectron spectra of $Cs_4 I_4^-$ taken with 1.55 eV photons and a nozzle temperature of 300 K. The spectrum with the "predeplete" label is the reference spectrum. The other two are taken with delays of 10 and 980 ps after a 0.60 eV depleting pulse. The lowest isomer (left peak) was substantially depleted, but becomes replenished at the expense of the other two. Reproduced from A. J. Dally and L. A. Bloomfield, *Phys. Rev. Lett.* **90**, 063401 (2003) with permission of the American Physical Society.

Time resolved studies of the thermal isomerization have also been performed [14]. Figure 10.7 shows some photoelectron spectra of $Cs_4 I_3^-$ taken with photons of 1.55 eV. The three peaks correspond to three

different isomers present in the beam, and the spectrum provides a measure of the relative abundances of those isomers. The spectrum with the "predeplete" label is the reference spectrum for a temperature of 300 K. The other two correspond to the cases when, before the spectroscopic "probe" pulse a depleting pulse has been applied to selectively remove one of the isomers (the isomer corresponding to the left peak). The delays between the depleting pulse and the probe pulse are 10 ps and 980 ps respectively, and those two spectra show that the initially depleted isomer progressively regains its population at the expense of the other two isomers. This is due to the isomerization of the two non depleted isomers into the depleted one as the cluster ensemble evolves to re-establish the steady state.

References

1. Kittel, Ch., *Introduction to Solid State Physics*, 7th Edition, Wiley, New York (1996).
2. Campana, J. E., Barlak, T. M., Colton, R. J., De Corpo, J. J., Wyat, J. R., and Dunlap, B. I., *Phys. Rev. Lett.*, **47**, 1046 (1981).
3. Martin, T. P., *Angew. Chem. Int. Ed. Ingl.*, **25**, 197 (1986).
4. Martin, T. P., *Phys. Rep.*, **95**, 167 (1983).
5. Martin, T. P., *Phys. Rep.*, **273**, 199 (1996).
6. Krückeberg, S., Schooss, D., Maier-Borst, M., and Parks, J. H., *Phys. Rev. Lett.*, **85**, 4494 (2000).
7. Ochsenfeld, C., and Ahlrichs, R., *Ber. Bunsenges. Phys. Chem.*, **98**, 34 (1994).
8. Aguado, A., Ayuela, A., López, J. M., and Alonso, J. A., *J. Phys. Chem. B*, **101**, 5944 (1997).
9. Aguado, A., Ayuela, A., López, J. M., and Alonso, J. A., *Phys. Rev. B*, **56**, 15353 (1997).
10. Fatemi, D. J., Fatemi, F. K., and Bloomfield, L. A., *Phys. Rev. B*, **47**, 7480 (1993).
11. Hudjins, R. R., Dugord, P., Tenenbaum, J. M., and Jarrold, M. F., *Phys. Rev. Lett.*, **78**, 4213 (1997).
12. Dugord, P., Hudjins, R. R., and Jarrold, M. F., *Chem. Phys. Lett.*, **267**, 186 (1997).
13. Etzel, H. W., and Maurer, R. J., *J. Chem. Phys.*, **18**, 1003 (1950).
14. Dally, A. J., and Bloomfield, L. A., *Phys. Rev. Lett.*, **90**, 063401 (2003).

11. Carbon Clusters

11.1 Carbon Fullerenes

Carbon, with atomic number 6 and a ground state electronic configuration $1s^2\,2s^2\,2p^6$, is the most versatile element of the Periodic Table. It gives origin to Organic Chemistry. The most stable solid form of pure carbon is graphite, formed by planar carbon layers bound to the neighbor layers by weak Van der Waals forces. So the layers can be exfoliated easily. On the other hand the binding of the carbon atoms within a layer is very strong. The atoms form a honeycomb-like two-dimensional lattice. In this lattice the electrons of the carbon atoms form sp^2 hybrid orbitals that interact strongly with the three neighbor atoms leading to the formation of localized strong σ bonds at angles of $120°$ and delocalized weak π bonds. Another form of carbon, of interest in solid state physics, is diamond. In this case the formation of sp^3 hybrid orbitals leads to tetrahedral coordination around each atom. In spite of the weak interlayer binding energy of graphite, this is the most stable form of carbon, that is, the phase with the highest binding energy.

11.1.1 Discovery of the fullerenes

In laser vaporization experiments Rohlfing et al. [1] observed carbon clusters in the range from 40 to 300 atoms. A remarkable feature was that only clusters with an even number of atoms appeared in the mass spectrum. The interest in carbon clusters had been enhanced by the detection in the interstellar medium of carbon molecules with a chain structure, HC_5N, HC_7N, HC_9N, and $HC_{11}N$ [2]. Those molecules were expected to form in the carbon-rich red giant stars [2, 3].
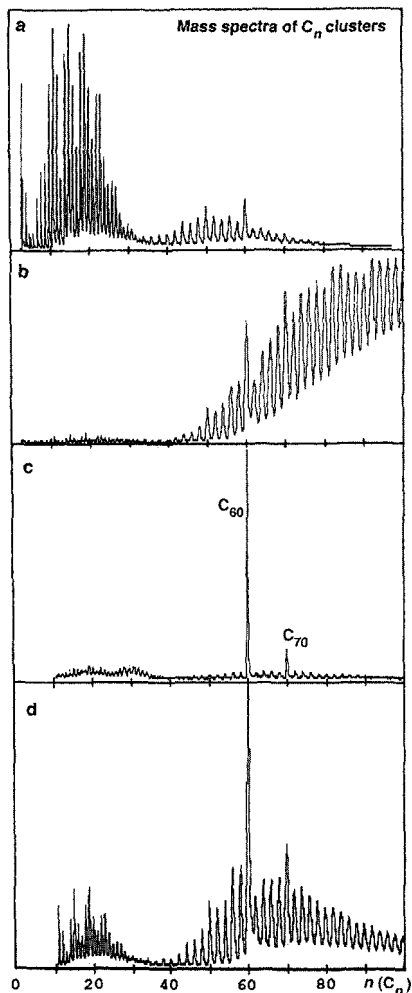
Figure 11.1. Mass spectra of carbon clusters. The degree of clustering increases from (a) to (c). Reproduced from H. Kroto, *Science* **242**, 1139 (1988) with permission of the American Association for the Advancement of Science.

Kroto and coworkers [4] used laser vaporization of graphite to synthesize carbon clusters with the objective of simulating interstellar carbon chemistry in the laboratory. In the course of those experiments they noticed that some clusters were extremely abundant, in particular

C_{60}, and to a lesser extent C_{70}. This is evident from the mass spectra shown in Fig. 11.1. They proposed for C_{60} a very symmetrical structure with the 60 atoms occupying the vertices of a truncated regular icosahedron. That structure is shown in Fig. 12.2. Each atom is bonded to three others along the edges of the truncated icosahedron. The molecule is then a skeletal version of the Archimedean polyhedron, much like the network in one of the geodesic domes built by the architect Buckminster Fuller. This result confirmed the early theoretical predictions that had given hints for the existence of molecules with icosahedral structure [5], the highest symmetry in a molecular point group. In fact, Osawa [6] had proposed the C_{60} molecule as a chemically stable molecule and a Hückel-type electronic calculation had estimated its HOMO–LUMO energy gap [7].
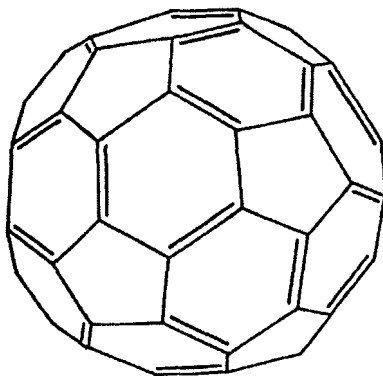
Figure 11.2. Structure of C_{60} showing the double and single bonds.

The advance in the study of C_{60} was initially slow due to the difficulty in obtaining samples. The original technique of laser vaporization of graphite films in a helium atmosphere gave a poor output of C_{60} and C_{70} in gas phase. A breakthrough was the discovery by Krätschmer and coworkers [8] that an electric arc discharge between two graphite electrodes immersed in a helium gas at pressure of 200 torr could generate large quantities of C_{60} and C_{70}. The clusters were part of the soot produced in the discharge. The separation of the fullerenes from

the rest of the soot is possible using solvents (toluene) or sublimation techniques. The discovery of this efficient method to obtain fullerenes was followed by an avalanche of experiments studying dissociation channels, the optical and ultraviolet spectrum and the chemical reactivity with different atoms and molecules. In fact, the experimental confirmation of the geometrical structure proposed for C_{60} was achieved when ultraviolet and Raman spectroscopy studies became possible due to the availability of samples in the amounts required for those experiments.

The general name of fullerenes is used for the family of carbon clusters with the structure of a closed cage formed by an even number of atoms that form hexagonal and pentagonal rings. According to the Euler theorem, that relates the number of faces, edges and vertices of a polyhedron, this is possible only if the cage has 12 pentagonal rings and a variable number ($f_6 \neq 1$) of hexagonal rings. It is then the number of hexagonal rings, f_6, which distinguishes the different members of the fullerene family. The fullerenes with $60n^2$ atoms ($n = 1, 2, 3 ...$), that is, C_{60}, C_{240}, C_{540}, ... are the most spherical ones and present an electronic structure of closed shells.

11.1.2 Electronic structure of C_{60}

The 60 atoms of C_{60} are placed on the vertices of a truncated icosahedron. The average distance between first neighbor carbon atoms is close to the bond distance in graphite (2.68 a.u.), and the radius of the spherical cavity is 6.71 a.u. The atoms are bonded forming 12 pentagonal rings and 20 hexagonal rings and each pentagon is fully surrounded by hexagons. Similarly to the case of graphite, three electrons of each atom in C_{60} form sp^2 hybrids which give rise to strong σ bonds with the three neighbors. But the curvature induced by the pentagons distorts a little those σ bonds and introduces some sp^3 character. The fourth electron fills an orbital perpendicular to the surface and forms a π bond with a neighbor atom. Each atom forms single bonds with two of its first neighbors and a double bond with the third one. Then, although all 60 carbon atoms are equivalent, the bonds are not. The 60 single bonds are localized along the edges connecting pentagons and hexagons, and the 30 double bonds along the edges joining hexagons. In this way a structure of alternated single and double bonds is formed that stabilizes

the structure. Nuclear Magnetic Resonance experiments [9] have estimated lengths of 2.75 a.u. and 2.63 a.u. for the single and double bonds, respectively.
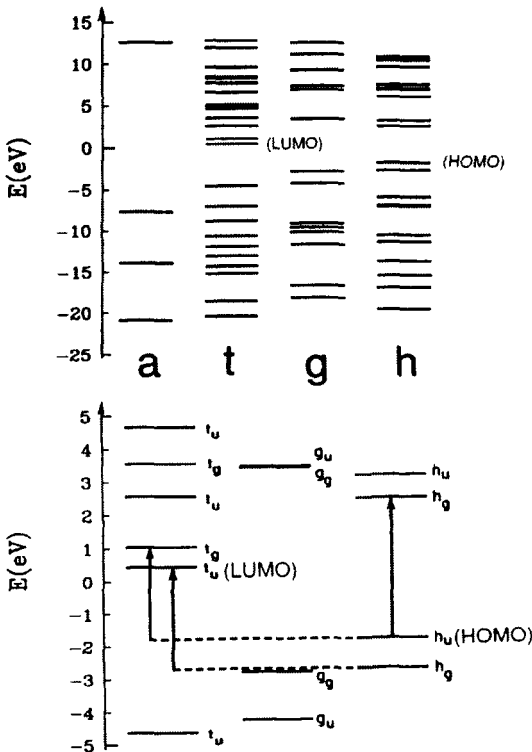
Figure 11.3. Single-particle energy level spectrum of C_{60} obtained from a tight-binding calculation. The lower panel is an expansion of the region around the Fermi level. Allowed transitions between states with even (g) and odd (u) parity are indicated by the arrows. Reproduced from G. F. Bertsch *et al.*, *Phys. Rev. Lett.* **67**, 1690 (1991) with permission of the Americal Physical Society.

The structure of the electronic energy levels obtained from a tight-binding calculation is shown in Fig. 11.3 [10]. The energy levels are grouped according to the different irreducible representations of the I_h symmetry group. The calculations considered four electrons per atom. The total width of the occupied band is 19.1 eV, very close to the values

obtained in DFT calculations [11]. The calculated HOMO–LUMO energy gap is 2.2 eV, close to the experimental value of 1.9 eV [12].

The σ states are far from the Fermi level. The bonding σ states are more than 7 eV below the HOMO, and the antibonding states are more than 6 eV above the LUMO. The transport and electronic properties are then determined by the π electrons, which are closer to the Fermi level. Since the π electrons are moving in an effective potential with a symmetry which is roughly spherical, the occupied π states can be approximately classified in terms of the angular momentum quantum number l. The lowest π state, with A_g symmetry, corresponds to $l = 0$ (s state). The next two groups of states belong to the irreducible representations T_u and H_g and have the character of $l = 1$ (p states) and $l = 2$ (d states), respectively. The next group, with $l = 3$ (f states), experiences a small splitting in states with T_u and G_u symmetries, respectively. In the same way, the group with $l = 4$ splits into states with G_g and H_g symmetries. The highest occupied state (HOMO), with H_u symmetry, belongs to a group with $l = 5$. This subshell is occupied with ten electrons. The LUMO, with symmetry T_u, is also part of a subshell with $l = 5$. The transition between the HOMO and LUMO states is optically forbidden because the two states have the same parity (u-states). The three lowest allowed transitions are $h_u \rightarrow t_g$, $h_g \rightarrow t_u$ and $h_u \rightarrow h_g$, with approximate excitation energies 2.9, 3.1 and 4.1 eV, respectively [10]. An interesting feature of C_{60} is the high ionization potential, 7.6 eV; its electron affinity, 2.65 eV, is similar to that of typical electron-acceptor organic molecules (like TCNQ, whose electron affinity is 2.82 eV).

11.1.3 Other fullerenes

The smallest fullerene, C_{20}, is a dodecahedron formed by twelve five-membered rings and no hexagonal rings. Any other larger even-atom fullerene can be formed, with the only exception of C_{22}. As the number of atoms grows, the number of hexagonal rings also increases, reaching the value $f_6 = 12$ for C_{60}, which is the first fullerene in which the pentagonal rings do not share any edges. The carbon atoms in the fullerenes are then not equivalent, with the exceptions of C_{20} and C_{60}. In general the strain generated by closing the cage concentrates on the vertices of the pentagons, and only for C_{20} and C_{60} this strain is

uniformly distributed between all the atoms. The fullerene form is not necessarily the most stable isomeric form for some of the clusters. In the case of C_{20} different theoretical calculations favor other geometries [13–15]. Monocyclic and bicyclic rings, chains and tadpole (a ring with a small chain attached) structures have been detected in species produced by laser vaporization of graphite. This result appears reasonable in view of the large strain in the fullerene form of C_{20}. Actually, calculations of the free energy of competing isomers [15] give the monocyclic ring as the most stable isomer at 2500 K (the temperatures in laser vaporization experiments are around 2000 K). Nevertheless, the hydrogenated $C_{20}H_{20}$ species is known to exist because the presence of the H atoms allows for a substantial sp^3 component in the bonding of each carbon atom with its environment (formed by three C atoms and one H atom), and by using $C_{20}H_{20}$ as a precursor the fullerene form of C_{20} has been produced and detected by photoelectron spectroscopy [16]. The bowl form of $C_{20,}$ which is a fragment of C_{60} formed by a central pentagon surrounded by five hexagons has been produced starting with the same precursor.

The observation that the cluster distributions originally produced only contained even numbers of carbon atoms may arise from the fact that only even-numbered clusters can close to form fullerenes. Odd number clusters can begin to curl so as to tie up all dangling bonds, but at least one atom will remain with an untied dangling bond. This makes the odd-numbered clusters too reactive to survive in a condensing carbon vapor. Reactivity experiments have confirmed this: all carbon clusters with odd N are highly reactive.

The fragmentation behavior of fullerenes upon laser excitation has provided information about their structure [17]. When C_N^+ cations with $N < 31$ are irradiated with ultraviolet light the clusters dissociate by losing a C_3 fragment [18]. But the dissociation channel changes drastically for larger clusters. The even-numbered clusters, that is, the fullerenes, are difficult to photodissociate and when irradiated with sufficient laser intensity they lose a C_2 dimer. C_{60}^+ is by far the most difficult to dissociate. In contrast, the odd-numbered clusters lose a single carbon atom. These results are consistent with the fullerene model: the loss of a dimer transforms the C_N fullerene into the C_{N-2} fullerene. Upon further loss of C_2 fragments the cage becomes increasingly strained, until the strain is so large that the cage opens up when C_{32}^+ is irradiated.
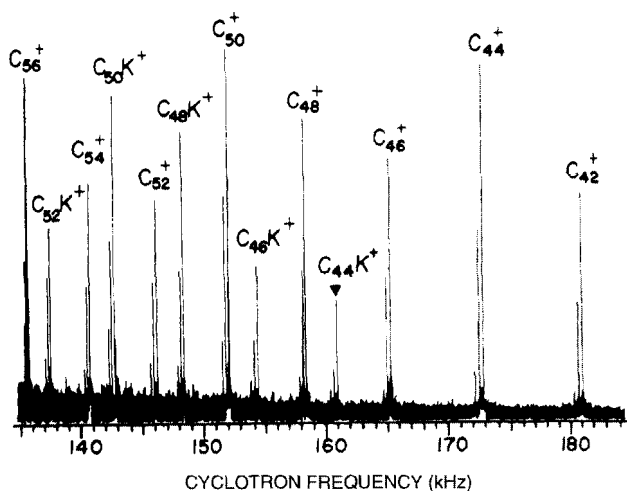
Figure 11.4. Low mass portion of the daughter ion fragments produced by intense laser excitation of $C_{60}K^+$. Reproduced from F. D. Weiss *et al.*, *J. Amer. Chem. Soc.* **110**, 4464 (1988) with permission of the American Chemical Society.

The critical size when the cage opens changes if a large atom is encapsulated inside. Evidence for this effect is provided in Fig. 11.4, which shows the results of irradiating $C_{60}K^+$ and a similar amount of the bare C_{64}^+ fullerene with an ArF excimer laser [19]. The distribution of bare fullerene fragments originates from C_{64}^+ and extends down to C_{32}^+. Similar to C_{60}, $C_{60}K^+$ is highly photoresistant and dissociates by losing a carbon dimer, producing $C_{58}K^+$, then $C_{56}K^+$ and so on. The C_NK^+ products terminate at $C_{44}K^+$. In a similar experiment for $C_{60}Cs^+$, the C_NCs^+ products terminate earlier, at $C_{48}Cs^+$, due to the larger size of the Cs atom [19].

11.2 Fullerene Collisions

The relatively easy production of fullerene beams has allowed the use of neutral and charged fullerenes, with positive and negative charges typically between $-2e$ and $+5e$, either as targets or as projectiles in

collision experiments. An essential property in those studies is the capacity to store a substantial amount of energy in a high number of vibrational degrees of freedom.

11.2.1 Collisions at medium to high energies

Many experiments have been performed studying collisions in the range of energies between a few tens of eV and a few keV. The main purpose has been to shed light on the mechanisms of insertion of different species in the fullerenes and also on the mechanisms of the fragmentation induced by the collisions. The most frequent experiment is to send a beam of neutral or ionized fullerenes (C_{56}^+, C_{58}^+, C_{60}^+, C_{70}^+) against a gaseous target (He, Ne, Ar, Li^+, Na^+, K^+, O_2, CO_2, $(CH_2)_3$, C_3H_6, SF_6). Endohedral complexes, that is, with the atom or molecule inside the fullerene cage, can only be produced when the collision energy is above a certain threshold which depends on the nature of the colliding species. Even under the best conditions, endohedral complexes occur only in a small fraction of the total number of collisions. The insertion mechanism is also sensitive to the nature of the colliding species. A small and light atom, like He and Li^+, penetrates inside the fullerene when the incidence trajectory goes precisely through the center of a hexagonal carbon ring [20–22]. In contrast, heavier atoms or ions like Ne, Na^+ or K^+ do not enter directly [22, 23]. In this case the impact breaks some of the bonds and opens up a window on the fullerene surface that allows the passing of the atom. The endohedral complex forms only if the fullerene is able to reconstruct its structure trapping the atom inside. Often the endohedral complexes formed are unstable due to the high energy absorbed in the collision, and fragment in a short time. The fragmentation of the complex may release the trapped atom or can lead to a smaller endohedral fullerene by loss of a few carbon atoms.

The nature of the products formed in the collision-induced fragmentation of fullerenes depends mostly on the nature of the colliding species. The analysis of the mass spectra of the collision products reveals the presence of fullerenes C_N^+ with $N \geq 32$ and rings or linear chains with $N < 32$. These results are consistent with the photofragmentation behavior discussed in Section 11.1.3. A drastic case of fragmentation occurs when C_{60} is irradiated with heavy ions. In this case the cluster disintegrates into individual carbon atoms [24].

11.2.2 Collisions at low to medium energies

When the collision energies are low, say lower than 150 eV, other processes become important instead of fragmentation: charge transfer between the colliding species, formation of substitutional complexes and formations of adducts (species adsorbed on the fullerene surface). However these collisions can also produce endohedral complexes. In the collisions with atomic cations the fullerene transfers one electron to the cation (except in collisions with the alkaline species Li^+, Na^+, K^+). The electron transfer actually occurs before the collision, when the two objects are approaching. One can say that the collision occurs between the neutral atom and the charged fullerene. Experiments studying low energy collisions (2–80 eV) between neutral fullerenes and different atomic cations have indicated that the tendency towards chemical reaction varies drastically from one species to another [25]. There is no activation barrier for the formation of some adducts XC_{60}^+, $X = B$, C, C_2, and these complexes survive for at least a few milliseconds. Other species like N^+ react to produce substitutional complexes. The collisions with some special cations like F^+ only lead to charge transfer between the flying objects, but not to other effects.

11.2.3 Collisions with surfaces

The collisions of C_{60} with semiconducting surfaces are particularly interesting. Covalent bonds form in some cases between the surface atoms and the fullerene and as a consequence the fullerene may remain adsorbed on the surface or may leave the substrate with some defects on the cage. In other cases the fullerene breaks up, and the fragments may remain bonded to the substrate surface giving rise to the localized growth of carbon layers. Experiments [26, 27] and simulations [28] studying collisions of C_{60}^+ with graphite and diamond surfaces have revealed that these are highly inelastic processes in which the incident fullerene loses a substantial fraction of its kinetic energy, that is employed in heating the surface. For impact energies up to about 200 eV fragmentation of the fullerenes is not observed. These rebound with a center of mass kinetic energy of about 15 eV, independent of the incident energy. The fullerene becomes highly deformed during the impact but is able to recover its structure. But for energies higher than 200 eV the fullerene fragments with the successive loss of C_2 units. Collisions with the (100) surface of

Si show a behavior similar to that just described for graphite and diamond surfaces. When the substrate surface terminates as free radicals, such as H, CH_3 or CF_3, the exchange of energy is smaller and the fragmentation threshold is displaced to higher energies.

11.3 Coating of Fullerenes

11.3.1 Alkali metal coverage

Early experiments [29] analyzed the photodetachment spectra of mass selected $(C_{60}K_x)^-$ anions with $x = 1$, 2 and 3, produced by laser desorption from a $C_{60}K_6$ crystal (see Section 12.4.3 on alkali-doped fullerene solids). Those studies suggested that the K atoms are dispersed, and not clustered, on the cage surface. The linear decrease of the electron affinities with increasing x indicates that the external s electron of each K atom is transferred to the three-fold degenerate t_u LUMO level of C_{60}. Further studies achieved a more complete coating by Li, Na and K [30] by using two ovens to produce the fullerene and the metal vapors and mixing the two vapors in a low pressure inert gas condensation cell. For small coverage, the character of the mass spectra of $(C_{60}K_x)^+$ and $(C_{60}Li_x)^+$ changes at $x = 7$. There is a pronounced abundance peak at this size and an even–odd alternation develops for $x > 7$: cluster ions with an odd number of alkali atoms are more abundant (more stable) than those with an even number. For the Na case the alternation was observed up to $x = 35$; this cluster and also $x = 21$ appear to be special, being followed by abrupt abundance drops.

Figure 11.3 gives the positions of the electronic levels of C_{60} in the energy region near the HOMO. The first few metal atoms transfer their single valence electron to the t_u LUMO level of C_{60}. This level becomes filled with six electrons, and this corresponds to the case $x = 7$. Consequently, the bonding of the alkali atoms to the fullerene appears to be ionic for $x \leq 7$, with the adsorbed atoms surrounding the cage while repelling each other. The filling of the t_u level is corroborated by experiments for doubly-charged clusters $(C_{60}K_x)^{++}$ and $(C_{60}Li_x)^{++}$: in this case $x = 8$ dominates the spectrum.

Turning to higher coverage, the even–odd oscillations in the abundance for $x > 7$ suggest that the nature of the bonding changes after the t_u level is filled: the charge transfer ceases and the alkali atoms are bonded not only to C_{60} but also to other alkali atoms. An explanation of the odd–even alternation in $(C_{60}Na_x)^+$ has been proposed based on the following growth model [30]. The first seven Na atoms arrange on the surface of the fullerene in a configuration such that they stay as far apart as possible in order to lower their mutual repulsion. The eight atom pairs with one of these ions to form a charged dimer Na_2^+. The ninth atom then joins the dimer to form a rather stable trimer cation Na_3^+. Following this type of growth all seven ions are successively converted into Na_3^+ trimers and the odd–even alternation in the stability develops. At the end of this process the fullerene is covered by seven Na_3^+ units and this stable configurarion correlates with the abrupt change in the mass spectrum for $(C_{60}Na_{21})^+$. However, the odd–even alternation continues, although somehow attenuated, until $(C_{60}Na_{35})^+$. It is now useful to recall the the odd–even oscillations observed in the ionization potential of pure alkali metal clusters (see Section 5.2) arise from two effects: the presence of delocalized electrons in the cluster, and the softness of the ionic background against shape deformations. These effects lead to a lifting of all the electronic degeneracies, except the two-fold degeneracy of each electronic level due to spin. The explanation based on the model of trimer ions, on the other hand, is based on the sequential filling of rather localized orbitals. The drops in the abundance after $(C_{60}Na_{21})^+$ and $(C_{60}Na_{35})^+$ are suggestive of closed shell effects (notice that 20 and 34 are magic numbers of pure alkali clusters) and may support the delocalized picture.

The mass spectrum of Li-coated fullerenes shows the usual characteristics of other alkali-coated fullerenes, but with a main difference: a strong peak appears for $(C_{60}Li_{12})^+$. The peak also appears for the doubly charge clusters $(C_{60}Li_{12})^{++}$ and this fact may indicate that the stability has a geometric origin. In fact, DFT calculations show that the lowest energy structure of $C_{60}Li_{12}$ preserves the icosahedral symmetry of the pure fullerene, with the Li atoms above the center of the twelve pentagonal rings, at a distance of 2.91 a.u. Due to the presence of the Li atom, the C_{60} cage relaxes a little, reducing the difference between the lengths of the double and single bonds [31]. The lengthening of the double bonds arises from the transfer of electrons to the antibonding t_u

and t_g orbitals (see Fig. 11.3). The cluster has closed electronic shells and the binding energy of the Li atoms to the fullerene amounts to 2.6 eV per Li atom. An analysis of the spatial location of the t_u and t_g orbitals indicated that the charge transfer to C_{60} is significant, with the highly charged fullerene stabilized by the surrounding cations.

The configurations for lower coverage, calculated from a semi-empirical quantum chemical method are also interesting [32]. The Li atoms in $C_{60}Li_x$ adopt positions above hexagonal rings for $x = 1$–8. For coverages $x = 1$–4 the Li atoms stay as far as possible. In $C_{60}Li_8$ the Li atoms above hexagons form a cube, and the structures for $x = 7$, 6 and 5 are obtained by removing one, two and three Li atoms, respectively, from the vertices of the cube. The transition from hexagonal to pentagonal positions occurs for $x = 9$. Evidently the number of pentagonal rings available exhausts at $x = 12$, and the additional atom in $C_{60}Li_{13}$ sits on a hexagon. The intensity anomalies observed in the mass spectra correlate with the cluster stability, and more in particular with the calculated energy ΔE_{vap} to remove a Li atom from the $C_{60}Li_x$ cluster. This evaporation energy shows that it is much easier to evaporate one Li atom from $C_{60}Li_{13}$ than from $C_{60}Li_{12}$. So, the population of $C_{60}Li_{12}$ should be large when the clusters detected form after one or several evaporative steps from warm larger clusters. Substantial drops of ΔE_{vap} are also predicted after $C_{60}Li_6$, $(C_{60}Li_7)^+$ and $(C_{60}Li_8)^{++}$, that also correlate with peaks in the mass spectra of singly and doubly charged clusters, but these features are, instead, driven by electronic effects: the filling of the t_u level. It is somehow surprising that a very stable $C_{60}M_{12}$ cluster only forms for Li but not for Na or K. The reason is probably the size difference between Li and the other alkali atoms.

11.3.2 Coverage by other metals

As discussed in the previous section, the stability of fullerene clusters coated by alkali atoms appears to be mostly determined by its electronic configuration with the main exception of $C_{60}Li_{12}$. On the other hand the coating by alkaline earth atoms like Ca, Sr, and Ba appears to be governed by geometrical rules, and more precisely by the completion of successive layers around a central core [33]. The main feature in the mass spectrum of Ca-coated C_{60} is a sharp drop in the intensity after $C_{60}Ca_{32}$. This is observed for singly and doubly ionized species, implying

that the origin of the high stability of $C_{60}Ca_{32}$ is geometrical. The obvious structure that can be proposed for this cluster has Ca atoms placed on top of each of the 12 pentagonal rings and the 20 hexagonal rings of the fullerene. This structure can be considered as the first metallic layer ($K = 1$) covering C_{60}. To verify the validity of this model the experiment was repeated with C_{70}, which has 12 pentagonal and 25 hexagonal rings. Indeed the mass spectrum was found to have a strong peak at $(C_{70}Ca_{37})^+$.

K = 1
$C_{60}M_{32}$

K = 2
$C_{60}M_{104}$

K = 3
$C_{60}M_{236}$

K = 4
$C_{60}M_{448}$
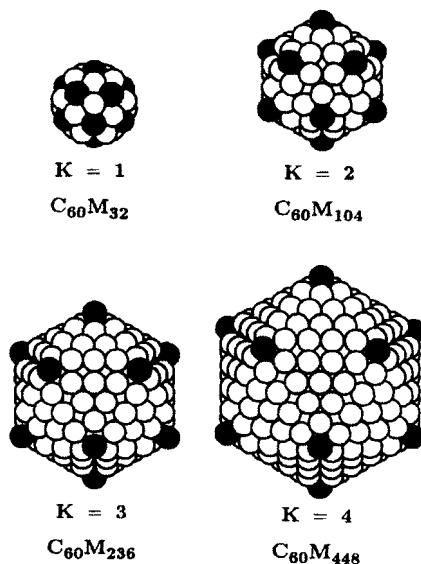
Figure 11.5. Arrangement of Ca atoms covering the C_{60} fullerene with one, two, three and four layers. The Ca atoms represented as black spheres highlight the icosahedral shape. Reproduced from U. Zimmermann *et al., J. Chem. Phys.* **101**, 2244 (1994) with permission of the American Physical Society.

Other prominent features are observed at $x = 104$ for C_{60} and at $x = 114$ for C_{70}. These appear to indicate the completion of the second metal layer ($K = 2$). Evidence for the formation of a third layer at $x = 236$ and a fourth layer at $x = 448$ has been found by the observation of edges in the spectrum of $(C_{60}Ca_x)^+$.

The structures proposed for these clusters [33] are shown in Fig. 11.5. The first metal layer, formed by 32 atoms, has icosahedral symmetry, and the dark spheres correspond to the 12 atoms forming the vertices of the icosahedron. The second layer can be constructed by first placing one atom above each of the 12 vertices and then filling each of the 20 triangular faces formed with one inner triangle of three atoms. These inner triangles have length two, that is, there are two atoms along the edge. The number of atoms forming this second shell is 72. The structure that results can be viewed as an edge-truncated icosahedron. To form the third and fourth layers one atom is again placed above each of the 12 vertices, and the triangular faces are then covered with atoms forming equilateral triangles of lengths 3 and 4, respectively. By this construction, clusters $C_{60}Ca_{32}$, $C_{60}Ca_{104}$, $C_{60}Ca_{236}$ and $C_{60}Ca_{448}$ are obtained, in agreement with the sizes corresponding to peaks or edges observed in the mass spectrum.
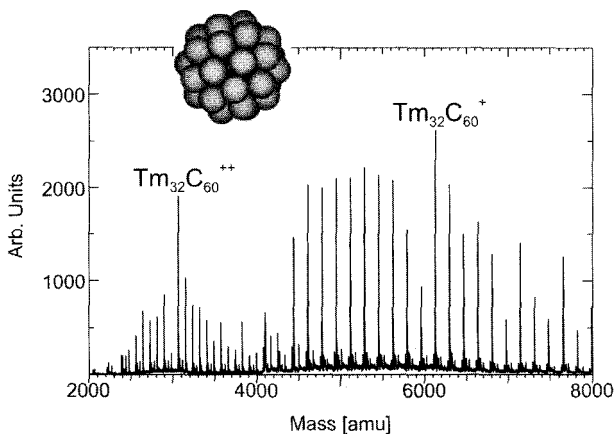
Figure 11.6. Mass spectrum of photoionized $C_{60} Tm_x$ clusters containing singly and doubly ionized species. A strong peak is observed for $x = 32$. Reproduced from N. Malinowski *et al.*, *Eur. Phys. J. D.* **9**, 41 (1999) with permission of EDP Sciences.

C_{60} has also been coated by thulium (Tm), a lanthanide metal [34]. A mass spectrum of $(C_{60}Tm_x)^+$ and $(C_{60}Tm_x)^{++}$ with x between 20 and 42,

given in Fig. 11.6, shows that the peak at $x = 32$ stands out strongly both for singly charged and doubly charged clusters. This unambiguously indicates a geometric origin of the stability, similar to the case of alkaline earth coating: namely, the covering of the twelve pentagonal and the twenty hexagonal faces of the fullerene. This is further confirmed by measurements of the spectrum of coated C_{70} clusters, $(C_{70}Tm_x)^+$ and $(C_{70}Tm_x)^{++}$, where a strong peak is detected for $x = 37$, corresponding to the covering of the 12 pentagonal faces and 25 hexagonal faces of C_{70}. Adding an atom to a cluster with closed geometric shells leads to a decrease of stability of the cluster with only one atom in the new shell. This feature is not observed in Fig. 11.6, but it was observed in the coating by Ba [33]. The different behavior is due to the different atomic size. The 32 barium atoms form a symmetric layer that is also close-packed. Thulium atoms, on the other hand, are substantially smaller than the Ba atoms, and additional Tm atoms can still find places on the first coating layer without a great loss in stability.

11.4 Optical Properties of Carbon Clusters

11.4.1 Fullerenes

A variety of experiments (photoabsorption, photoionization, X-rays and electron energy loss spectroscopies) [35–39] have detected two collective excitations in C_{60}: a broad excitation at an energy above 20 eV, with a linewidth of near 10 eV, that can be ascribed to the collective motion of electrons in σ bonds linking neighbor carbon atoms in the C_{60} cage, and another excitation at ≈ 6 eV, arising from the collective motion of the electrons in π orbitals extending in and out of the cage. Two similar resonances have been observed for graphite, and are explained in the same way [40], but not for diamond or amorphous carbon, where only the higher one is observed. The photoabsorption spectrum calculated by the direct solution of the time dependent Kohn–Sham equations within the DFT framework (see Section 5.7.6) is shown on the bottom panel of Fig. 11.7 [41].

Larger fullerenes are no longer spherical and their optical properties become more complex. For example, C_{76} is chiro-optical [42, 43]. The

upper panel of Fig. 11.7 illustrates for the fullerenes a fact well known for metallic clusters: the form of the collective resonance in a system with delocalized electrons is dictated by the shape of the cluster. Therefore the spheroidal shape of C_{70} leads to a splitting of the low frequency π plasmon in two resonances, with the lower one occuring for the external field applied along the long axis direction (called z axis in the figure). The σ plasmon is much less sensitive to the specific cluster shape and its energy is similar for C_{60} and C_{70}. Furthermore, it does not depend on the direction of the applied field with respect to the symmetry axis of the cluster.
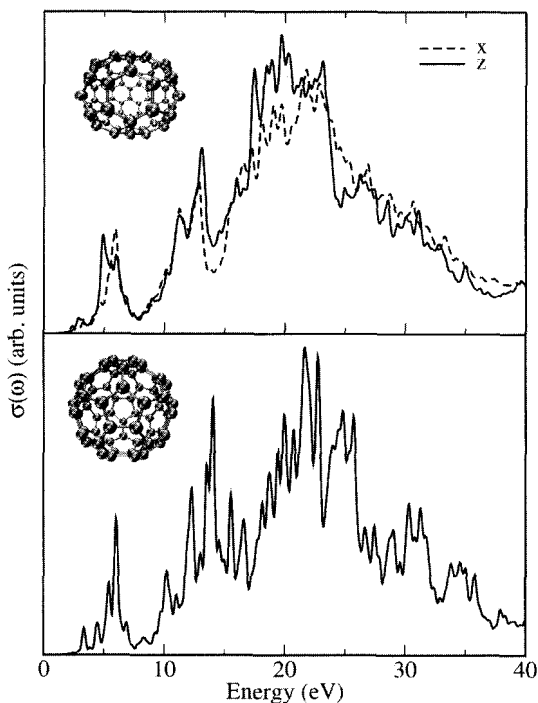
Figure 11.7. Calculated photoabsorption cross section $\sigma(\omega)$ (in arbitrary units) of C_{60} (bottom panel) and C_{70} (top panel). $\sigma(\omega)$ for C_{70} is given along the two principal symmetry axes. Reproduced from A. Castro *et al.*, *J. Comput. Theoret. Nanoscience* **1**, 230 (2005) with permission of American Scientific Publishers.

11.4.2 Medium size clusters

Medium size carbon clusters are predicted to have a wide variety of isomers with the form of cages, bowls, planar graphitic structures, rings and linear chains. The study of the different isomers may help to understand the way fullerenes form [44], a question still under study. The uncertainties about the most stable geometrical structure of C_{20} were pointed out in Section 11.1.3. Thus it is important to look for experimental methods to determine the structure that are sensitive enough to be usable with the available cluster beam intensities; optical spectroscopy appears to fulfill the requirements.

The geometrical structures of six members of the C_{20} family are given in Fig. 11.8: the smallest fullerene (cage), which is a Jahn–Teller distorted dodecahedron, the ring, the bowl, and three other cage structures, labeled as (d), (e) and (f) in the figure. Structures (d) and (f), related by a Stone–Wales transformation [45], are composed of four hexagons, four pentagons, and four four-membered rings. Those structures are the six isomers with lower energy as calculated by Jones using DFT within the LDA approximation [13]. Other structures, such as bicyclic rings, chains and tadpoles may be favored by entropy at high temperature and have been observed experimentally. However, neither of them seem to be a possible low temperature ground state.

The results of TDDFT calculations [46] of the optical absorption spectrum are also shown in Fig. 11.8. The dipole strength functions shown have been averaged over all orientations of the system. In the case of the ring, the response in the direction perpendicular to the ring plane is almost negligible below 8 eV compared with the response within the plane. Also for the quasi-planar bowl isomer the perpendicular response is extremely weak in that energy range. While present molecular beam experiments are not able to discriminate between the different spatial directions, the averaged spectra are still sufficiently different to discriminate between the structures without ambiguity.

Two regions can be distinguished in all the spectra: (a) the peaks in the near ultraviolet, and (b) a broad absorption that starts at around 7.5 eV. Focusing attention on the lower energy peaks, the ring exhibits the largest optical gap and also the strongest collective transition. The bowl also shows a high optical threshold, larger than 5 eV, but the intensity of the first significant transition is an order of magnitude weaker than in the ring. The relative intensities of the peaks, the fact that the first excitation

is separated in two for the bowl, and the relative strength of the excitations in the 6–7 eV region, can all be used to distinguish the bowl from the ring.
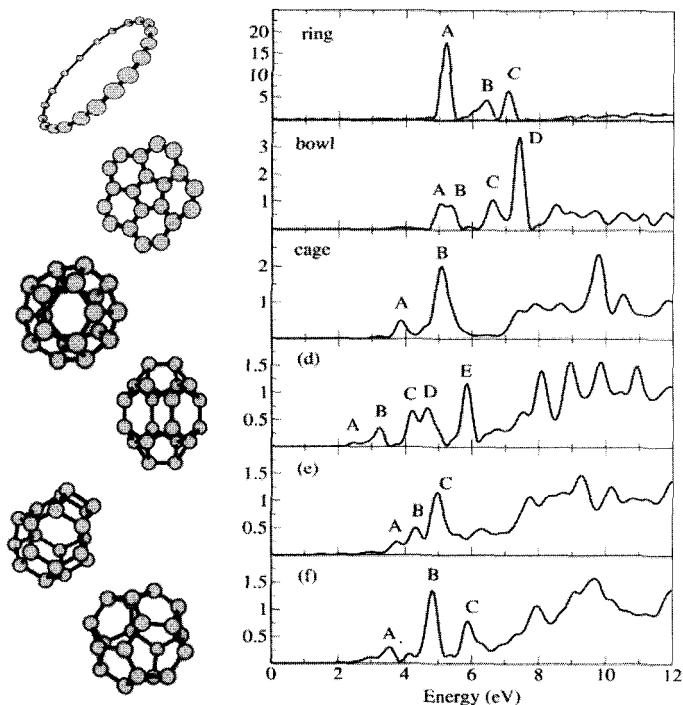
Figure 11.8. Calculated dipole strength function, in eV^{-1}, for several isomers of C_{20}. The absorption spectrum clearly discriminates between the different isomers. Adapted from A. Castro *et al., J. Chem. Phys.* **116**, 1930 (2002) with permission of the American Institute of Physics.

The spectra of the four three-dimensional isomers start at much lower energy and are more similar to each other, which is expected from their similar geometries. The fullerene isomer exhibits two peaks at 3.9 and 5.1 eV. Most of the strength concentrates above the ionization threshold and has a broad plateau starting at around 7 eV. This is different from planar-like isomers, where an important fraction of the strength appears below 7 eV. Isomer (d) can be distinguished by the

presence of a transition at quite low energy, 2.5 eV, as well as by the fragmentation into many states going up to 6 eV. Isomer (e) differs from the fullerene by the presence of a transition (labelled B in the figure) between the transitions that would be seen in the cage. The spectrum of isomer (f) is similar to that of the fullerene up to the second peak, but it is shifted down by about 0.3 eV. However, isomer (f) also has a third peak near 6 eV, in a region where there is a gap in the spectrum of the fullerene cage, and that difference would be definitive.

11.4.3 Coated fullerenes

The photoabsorption cross section of C_{60} coated by a layer of Na atoms has been calculated by using the TDLDA and a simple structural model [47]. The positive ionic background was modeled as two concentric thin spherical layers, one on top of the other, the inner one representing the fullerene cage and the outer one modeling the alkali metal coating. Since the collective plasmon excitation in pure sidium clusters lies at energies $\approx$ 2–3 eV, only the π electrons of the fullerene were taken into account. The positive background charge density of the Na layer was fixed equal to its value for the bulk metal, and its thickness depends on the number of Na atoms forming the coating layer. The outer surface of the cluster resembles a lot the surface of pure Na clusters. The development of the metallic coating layer becomes reflected in the photoabsorption spectrum.

For small Na coverage, the interaction between the valence electrons of the Na atoms and the unoccupied levels of the fullerene is strong and the calculation predicts the fragmentation and spreading of the π plasmon of C_{60} down to lower energies, and a reduction of its amplitude. This is mainly due to the fragmentation of the collective resonance caused by the interaction with particle–hole excitations. Then the characteristic features of the π plasmon progressively vanish as the size of the coating layer grows up. At the same time, a new feature develops at lower energies that can be related to the surface plasmon of pure Na clusters. For $(C_{60}Na_{93})^+$ the Na surface plasmon is well developed and the cluster responds much like a pure ionized Na cluster; however, the collective resonance has a broad tail extending at high energies.

The fragmentation of the collective resonance may have relevance for the interpretation of experiments by Martin and coworkers [48].

These authors have produced C_{60} clusters coated with Cs. For large coverage, say $(C_{60}Cs_x)^+$ with $x \approx 300$, the photoabsorption spectrum is very similar to that of large pure Cs clusters, except for a more intense tail. As x decreases a fragmentation of the plasmon occurs that resembles that obtained in the TDLDA calculations for $(C_{60}Na_x)^+$. Thus, the simple model of two spherical jellium slabs appears to afford a plausible explanation for the optical absorption spectrum of alkali-coated C_{60} clusters.

11.4.4 Multilayered fullerenes

The study of carbon dust formation by stars led to the discovery of the fullerenes in the laboratory [4]. It was soon speculated that these clusters could form part of the carbon component in the interstellar dust. The ultraviolet (UV) absorption spectrum of interstellar dust contains a peak at 5.7 eV (4.6 μm^{-1}), and since fullerenes also show strong absorption features around 6 eV, the stellar absorption band has been interpreted as due to the excitation of the π plasmon in fullerene-like particles. The possible contribution of multishell carbon particles was proposed [49] following the discovery of carbon particles with shell-like structures in the laboratory [50]. Hyperfullerenes formed by multiple concentric shells, sometimes called carbon onions, can be obtained by electron irradiation of carbon soot [51], and also by heat treatment and electron beam irradiation of nanodiamond [52]. The particles can have spherical or polyhedral forms and sometimes have an inner cavity at the particle center [53]. Recent measurements of the ultraviolet–visible (UV–VIS) absorption spectrum of well dispersed carbon onions closely match the interstellar feature [54]. The carbon onions were prepared by striking an arc discharge between two carbon electrodes submerged in water or in liquid nitrogen. Thin films dried in air were then prepared and measurements of the UV–VIS spectra were performed for the as-prepared samples and also for samples annealed at 600 °C.

The results are presented in Fig. 11.9: spectrum (d) corresponds to the samples before annealing, and spectra (e) and (f) correspond to the annealed samples. Also shown are the spectra of polyhedral graphite (a), amorphous carbon (b) and the interstellar absorption feature (c). All spectra measured before annealing are similar to those reported by de Heer and Ugarte for carbon onions dispersed in water, having a

maximum centered around 4.0 μm^{-1} and large widths of 2.0–3.5 μm^{-1}. The large widths are attributed to the contamination of the carbon onion film by polyhedral graphite particles and amorphous carbon. Annealing eliminates all contaminants and then the spectrum changes dramatically, showing the peak around 4.55 ± 0.1 μm^{-1} (5.7 eV) with reduced width, in substantial agreement with the interstellar UV absorption spectrum. Carbon onions are then strong candidates for the origin of the UV interstellar absorption peak at 4.6 μm^{-1}.
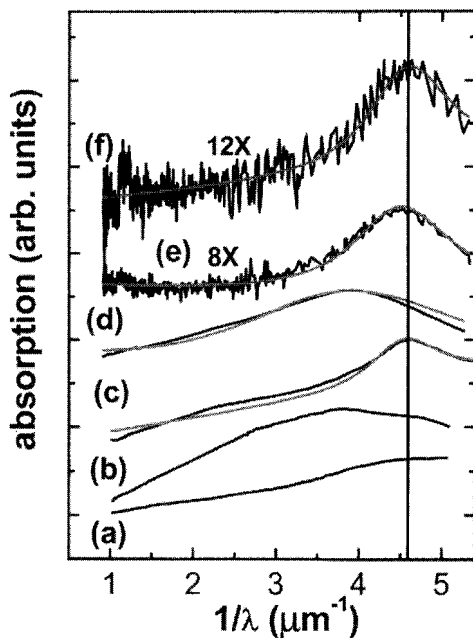
Figure 11.9. Absorption spectra of different carbon materials and the interstellar absorption feature. (a) corresponds to polyhedral graphite powder and (b) to carbon soot. (c) is the interstellar absorption feature [55], (d) is a spectrum obtained from carbon onion films prior to annealing, and spectra (e) and (f) are taken after annealing. The light curves in (c), (d), (e) and (f) represent the Drude function used to obtain the peak position and width from the measured data. Adapted from M. Chhowalla, *et al.*, *Phys. Rev. Lett.* **90**, 155504 (2004) with permission of the American Physical Society.

11.5 Metalcarbohedrenes

A class of very stable clusters with formula M_8C_{12}, where M is an early transition metal (M = Ti, V, Zr, Nb, Hf), was discovered by Castleman and coworkers in 1992 [56–58]. The clusters of this family are called metalcarbohedrenes (or metcars for short). The first metalcarbohedrene, Ti_8C_{12} appeared as a totally dominant peak in the mass spectrum of titanium carbide cluster cations $Ti_nC_m^+$. Immediately, interest in those clusters grew from the initial expectation that the geometrical structure could possibly be a pentagonal dodecahedron similar to that of a 20-atom fullerene. Production of macroscopic quantities of Ti_8C_{12} in the soots generated in arc discharges between two composite Ti–C electrodes has been reported [59, 60]. The quantity of metcars in the soot is about 1% but attemps of purification, either in solution or as a solid material have failed so far.

11.5.1 Structure and infrared vibrational spectroscopy

The ground state structure of the metcars has generated a lot of debate [61]. Early studies [56–58] proposed the pentagonal dodecahedral structure of T_h symmetry for them. This structure, shown in Fig. 11.10, can be viewed as a fullerene cage formed by twelve pentagons and no hexagons. Each pentagon is formed by two metal atoms and three carbon atoms. This assignment was motivated by the reaction behavior of Ti_8C_{12} and V_8C_{12} with NH_3 molecules, and by ligand titration experiments which suggested that the eight metal atoms had similar coordination.

Based on DFT calculations, different authors have later proposed alternative configurations more stable than the T_h structure. One of these is a tetracapped tetrahedron whose optimized structure is a small distortion of the ideal T_d structure shown in the middle panel of Fig. 11.10: four metal atoms form an inner tetrahedron with short metal–metal bond distances, and the other four atoms cap the faces of the inner tetrahedron, defining an outer tetrahedron [62–64]. This structure can be obtained from the T_h structure by a concerted displacement of four metal atoms to give the inner tetrahedron, while the other four metal atoms move outward to give the outer tetrahedron and the six C_2 units perform 45° rotations (clockwise or anticlockwise). The calculations indicate that the T_d structure is more stable in Ti_8C_{12} by about 15 eV and that this transformation occurs essentially with no barrier, suggesting that the

pentagonal dodecahedron is not a true metastable isomer. A low lying
isomer with D_{2d} symmetry [64–66], is shown in the lower panel of Fig.
11.10. This is a true isomer and its energy lies closely above that of the
distorted tetracapped tetrahedron for Ti_8C_{12}. These results for the T_h, T_d
and D_{2d} structures were confirmed by Configuration Interaction
calculations [67]. More recent DFT calculations have proposed a ground
state with C_{3v} symmetry [68], which appears to be essentially the same as
the distorted tetracapped tetrahedron. The calculated ionization potential
and electron affinity are in good agreement with the experiment, $I = 4.4$
$\pm$ 0.02 eV [69] and $EA = 1.05$ eV [70]. Work for other metcars, Zr_8C_{12},
V_8C_{12} and Nb_8C_{12}, arrived at similar conclusions: the distorted T_d
structure is the ground state, with the D_{2d} isomer lying 2 eV above [71].
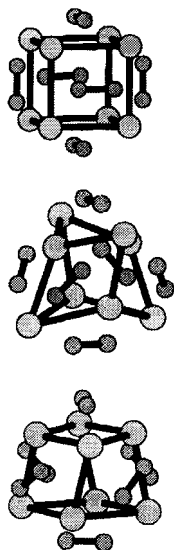
Figure 11.10. Symmetric structures of Ti_8C_{12} exhibiting T_h (upper panel), T_d
(middle panel) and D_{2d} (lower panel) symmetries. Reproduced from G. K.
Gueorguiev and J. M. Pacheco, *Phys. Rev. Lett.* **88**, 115504 (2002) with
permission of the American Physical Society.

The infrared (IR) vibrational spectrum of the metcars in the gas
phase has been measured [70]. Since the IR spectrum carries information

on the cluster structure, comparisons of the experimental spectra with those calculated for competitive structures have been performed [64, 68, 71]. The main feature in the spectrum of Ti_8C_{12} is a broad high energy peak centered around 1395 cm^{-1}, which reflects the vibrations of the dicarbon system. The position and width of this peak is best reproduced by assuming a high temperature mixture of the C_{3v} and D_{2d} isomers [68].
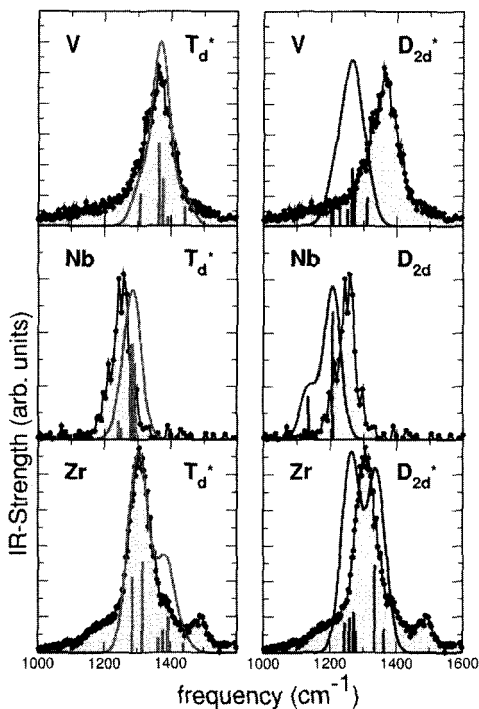
Figure 11.11. Comparison between experimental vibrational infrared spectra of V_8C_{12}, Zr_8C_{12} and Nb_8C_{12} metcars (dark lines through the experimental points) and spectra calculated for the (distorted) T_d and D_{2d} isomeric structures (vertical spikes). The solid light lines arise from a folding of the calculated peaks with Gaussians. Reproduced from G. K. Gueorguiev and J. M. Pacheco, *Phys. Rev. A*. **68**, 241401 (2003) with permission of the American Physical Society.

The analysis for the Zr_8C_{12}, V_8C_{12} and Nb_8C_{12} metcars is shown in Fig. 11.11. The experimental IR spectra are represented by the dark lines joining the experimental points. The area under those lines is shaded. On

the other hand the vertical spikes correspond to the calculated spectra and the light continuous lines are obtained by folding the calculated absorption peaks with normalized Gaussian functions of width 50 cm⁻¹. The left and right panels correspond to calculations for the (distorted) T_d^* and D_{2d}^* structures (the experimental spectra are plotted in both panels). For the three metcars the calculated IR spectrum corresponding to the T_d^* structure provides a better comparison with the experimental spectrum, but a detailed comparison suggests the possibility that more than one isomer may be present in the molecular beam.

B.E./atom M8C12
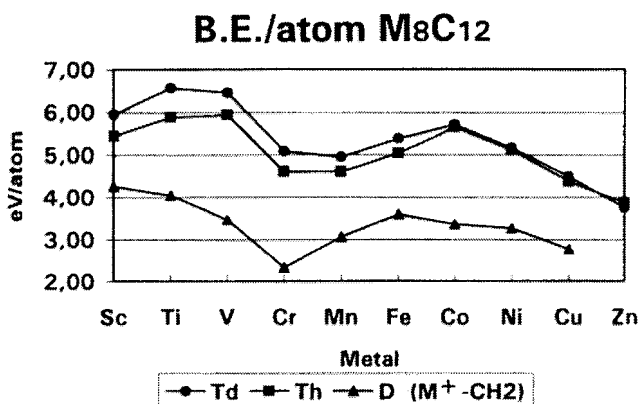
Figure 11.12. Calculated binding energies for the tetrahedral (T_d symmetry) and dodecahedral (T_h symmetry) structures of the M_8C_{12} metcars of the first transition metal series. Those values are compared with the experimental M–C bond energies for M^+–CH_2 molecules. Reproduced from M. M. Rohmer, M. Bénard and J. M. Poblet, *Chem. Rev.* **100**, 495 (2000) with permission of the American Chemical Society.

Most investigations of metcar clusters deal with the metcars of the early transition elements. However, magic peaks corresponding to the M_8C_{12} stoichiometry have also been observed for Cr and Mo [73]. In the case of Fe, that stoichiometry is followed by a truncation in the mass spectrum [73]. The results of a calculation of the bonding energies for the whole series of metcars across the $3d$ metal row are shown in Fig. 11.12 [61]. The two structures T_d and T_h were considered. The highest stability occurs for the Ti and V metcars, in agreement with

photofragmentation experiments [73]. The behavior of the binding energies when the element M evolves across the $3d$ row is quite similar to the corresponding variation of the measured $M^+–C$ bond energies for the $M^+–CH_2$ molecules [74]; therefore the variation seen for the metcars arises from the general trend of the metal–ligand bond energies.

One observation from this figure is that the binding energy of the metcar is not necessarily correlated with its observability: Sc_8C_{12} has a higher binding energy than Cr_8C_{12} but only the second metcar has been detected. The observability of the M_8C_{12} then depends on the relative stabilities of this and other M_xC_y clusters. Another unexpected result concerns the competition between the tetrahedral and dodecahedral structures. While the much higher stability of the tetrahedral conformation is well documented for metcars of the early transition elements, the situation is less clear for late transition metals.

11.5.2 Other physical properties of metcars

The laser vaporization of mixtures of metal and carbide powders easily produces binary-metal metcars [75, 76]. In particular, this technique was used to produce a series of clusters $Ti_{8-x}Zr_xC_{12}$. The mass spectra showed a series of peaks with a regular evolution of the intensities as a function of x, that has been interpreted as arising from the purely statistical substitution of Ti by Zr. This is made possible by two facts [77]: (a) the substitution of Ti by Zr either in the inner metal tetrahedron of the T_d structure or in the outer tetrahedon produces only minimal changes of the binding energy, and (b) the binding energy varies smoothly with x. The ionization potentials of these binary-metal metcars have been determined from the photoionization efficiency curves near threshold [69]. The values obtained for the two pure metcars are 4.40 ± 0.02 and 3.95 ± 0.02 eV for Ti_8C_{12} and Zr_8C_{12} respectively. Those values are in excellent agreement with computed ionization potentials for the T_d structure [61].

Delayed ionization and delayed emission of Ti^+ and V^+ ions has been observed following multiphoton absorption by the Ti and V metcars [78]. For delayed ionization to occur, with characteristic times in the microseconds range (in contrast to the femtosecond time scale of prompt ionization), the ionization potential has to be smaller than the dissociation energy of the cluster. In such a case, competition between prompt ionization and dissociation may lead to delayed ionization. This

condition is met by the metcars. In addition to this requirement, the cluster must provide its own "heat bath" allowing to store the excitation energy. The experiment also indicates delayed emission of Ti^+ and V^+ ions and that the ionization behavior is similar for the two different photon wavelengths used for the multiphoton excitation. This suggests that the "heat bath" has a broad region of closely spaced excited states at an energy close to the sum of the dissociation energy of the cluster and the ionization potential of the atom (Ti or V). This places that region at around 13 eV for the Ti metcar. Time dependent DFT calculations of the excitation spectrum of M_8C_{12} predicted a broad collective excitation centered around 12 eV [79, 80], a result which supports the interpretation of the experiment [78].

11.5.3 Chemical reactivity

$Ti_8C_{12}^+$ reacts easily with polar molecules like H_2O, NH_3 and CH_3OH (methanol) forming association products $Ti_8C_{12}^+(P)_n$ with n from 1 up to 8. The reaction proceeds through succesive attachment of the reactant molecules to each metal center [81]. Stepwise association of π-bonded molecules without permanent dipole moment, such as benzene (C_6H_6) and ethylene (C_2H_4), has also been observed but in this case no more than four molecules can be attached [81, 82]. The termination of the association sequence at $n = 4$ has been interpreted as giving support to the tetrahedral structure of the metcar with two types of metal sites. Association reactions with pyridine also terminate at $Ti_8C_{12}^+(piridine)_4$, but with acetone (($CH_3)_2CO$) up to five adducts $Ti_8C_{12}^+(acetone)_{1-5}$ have been observed [83]. Reactions of neutral Ti_8C_{12} with methane (CH_4) reveal binding of up to five molecules, with the most intense peak corresponding to $n = 4$ [84].

Replacement of Ti by Nb changes the reactivity of the metcar. $Ti_7NbC_{12}^+$ and $Nb_8C_{12}^+$ react with acetone, giving adducts with one or two oxygen atoms ($Ti_7NbC_{12}^+O$, $Ti_7NbC_{12}^+O_2$, $Nb_8C_{12}^+O$, $Nb_8C_{12}^+O_2$). This indicates that the niobium-containing metcars can induce carbon–oxygen bond breaking [82]. The chemical stability of $Ti_8C_{12}^+$ is also evident by comparing its reaction pattern with acetone to the reaction pattern of the neighbor titanium carbide cluster $Ti_8C_{11}^+$ [83]. The last cluster is able to break the chemical bonds of acetone to give $Ti_8C_{11}^+(COCH_3)$, but not the first one.

$Ti_8C_{12}^+$ breaks the I–C bond when it reacts with CH_3I (methyl iodide) forming the single $Ti_8C_{12}^+I$ adduct [85]

$$Ti_8C_{12}^+ + CH_3I \rightarrow Ti_8C_{12}^+(I) + CH_3. \qquad (11.1)$$
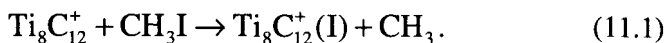
Again, substitution of Ti by Nb increases the reactivity. $Nb_8C_{12}^+$ is able to bind up to five I atoms, forming $Nb_8C_{12}^+(I)_{1-5}$, and reaction with other methyl halides produces $Nb_8C_{12}^+(Br)_{1-5}$ and $Nb_8C_{12}^+(Cl)_{1-4}$. The V metcar produces $V_8C_{12}^+(X)_{1-4}$ with $X = Cl$, Br and I. The distinct chemical behavior of the Ti metcar on one hand and the Nb and V metcars on the other, appears to be correlated to the number of weakly coupled metal electrons accommodated in the slightly antibonding set of metal orbitals. The calculations suggest that this number is two for neutral Ti_8C_{12}. One of these is then available in the cationic metcar to give a strong covalent bond with I. In the V or Nb metcars eight more metal electrons become available, and four of them, accommodated on molecular orbitals localized on the outer tetrahedron, should be weakly coupled [61]. This accounts for the increased reactivity. At variance with $Ti_8C_{12}^+$, $V_8C_{12}^+$ reacts with oxygen to give first $V_8C_{10}^+$. This cluster reacts again with oxygen to give other metal–carbon clusters and oxidation products [86]. The difference in reactivity between $Ti_8C_{12}^+$ and $V_8C_{12}^+$ is again ascribed to the larger number of metal electrons in the V metcar, which tend to populate nonbonding orbitals.

11.6 Other Metal–Carbon Clusters: from Small Clusters to Nanocrystals

Small M_xC_y clusters can be obtained from the fragmentation of metcar cations, and the nature of the fragments depends on the metallic element M. The photodissociation of $Ti_8C_{12}^+$ and $V_8C_{12}^+$ proceeds through the succesive loss of metal atoms, while ZrC_2 fragments are also observed in the dissociation of $Zr_8C_{12}^+$ [87]. This indicates that the Zr–C bonds are stronger. Clusters smaller than the metcars, like $V_7C_{12}^+$, $V_7C_{11}^+$ or $V_6C_{11}^+$, are also observed in the mass spectra of metal–carbon clusters obtained by arc-discharge techniques. In the region of large cluster sizes, strong peaks have been found for $Zr_{13}C_{22}$, $Zr_{14}C_{23}$, $Zr_{18}C_{29}$ and $Zr_{22}C_{35}$,

corresponding to an approximate metal to carbon ratio 2/3 [88]. Those peaks were originally interpreted as fused metcar structures: for instance, $Zr_{13}C_{22}$ would correspond to two fused dodecahedra sharing a pentagonal face, with one metal atom substituted by a carbon atom (an alternative interpretation [89] is discussed below). Similar clusters have been produced for Nb. In the case of Ta, the clusters correspond to a metal to carbon ratio near 1/1 [90], and have been assigned to nanocrystals with the rock salt (NaCl) structure, like those plotted in Fig. 10.1. Clusters $Ta_{14}C_{13}$ and $Ta_{18}C_{18}$ can be interpreted as $(3\times3\times3)$ and $(3\times3\times4)$ parallelepipedic cuboids. In fact, depending on the experimental conditions, the production of nanocrystals and clusters of stoichiometry 2:3 can be competitive. The competition also becomes manifested in the dissociation of nanocrystals [91]: the main products of the laser dissociation of the $Ti_{17}C_{19}^+$ $(3\times3\times4)$ nanocrystal are the $Ti_8C_{12}^+$ metcar and the $Ti_{14}C_{13}^+$ $(3\times3\times3)$ crystallite. On the other hand the main product of the dissociation of $Ti_{14}C_{13}^+$ is $Ti_8C_{13}^+$, which has been interpreted as an endohedral metcar, C inside $Ti_8C_{12}^+$. Other species have also been interpreted as endohedral metcars, like $V_8C_{13}^+$ and the more peculiar $Ti_8C_{14}^+$ (C_2 inside $Ti_8C_{12}^+$).

Cluster anions of stoichiometry 2:3 have also appeared as magic peaks in the experiments of Wang and coworkers [92]: $Ti_{13}C_{22}^-$ and $Ti_{14}C_{24}^-$. The first of these two clusters can be built starting with the $Ti_{13}C_{14}$ $(3\times3\times3)$ crystallite, which has carbon atoms on the eight corners of the cube, and replacing each of these C atoms with a carbon dimer, as shown in the panel (a) of Fig. 11.13. Wang *et al.* have proposed that this is the most stable structure of $Ti_{13}C_{22}^-$. To arrive at this conclusion they first optimized the structure of two fused dodecahedra using DFT, obtaining the structure shown in panel (b), that can be viewed as two fused tetracapped tetrahedra, differing only by 0.04 eV/atom from the optimized C_2-decorated cubic structure. Although the energy difference between the two structures is rather small, two pieces of experimental information are in favor of the decorated cubic structure: its calculated electron affinity and the simulated photoelectron spectrum agree closely with experiment. The theoretical density of states (DOS) spectrum was built by broadening the occupied single-particle energy levels with Gaussians of width 0.2 eV [89].
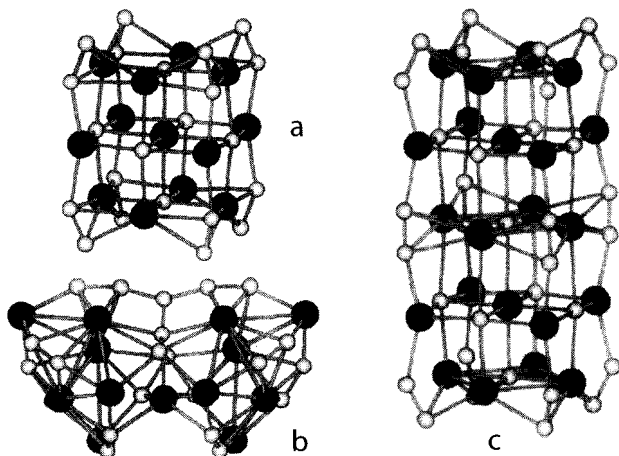
Figure 11.13. Cubic-like structures with three and five layers, representing $Ti_{13}C_{22}$ (a) and $Ti_{22}C_{35}$ (c), and an alternative structure for $Ti_{13}C_{22}$ in the form of two fused tetracapped tetrahedra (b). Adapted from L. S. Wang and H. Chen, *Phys. Rev. Lett.* **78**, 2983 (1997) with permission of the American Physical Society.

Then, a layer-by-layer growth based on the presence of C_2 dimers at the periphery of a cubic structural framework accounts for most of the magic peaks [89] earlier assigned to multicage structures. In the case of the $Ti_{13}C_{22}$ nanocrystal, the $3\times3\times3$ structure is composed of three layers in an ABA configuration: two Ti_4C_9 layers sandwiching a Ti_5C_4 layer. Stacking alternatively A and B layers in this way yields clusters of stoichiometries closely corresponding to the experimental magic sizes

$$AB \rightarrow M_9C_{13}\left(Ti_9C_{15}^-, V_9C_{15}^-\right)$$

$$ABA \rightarrow M_{13}C_{22}\left(Ti_{13}C_{22}^-, V_{13}C_{22}^-, Zr_{13}C_{22}^+, Zr_{14}C_{21}^+, Zr_{13}C_{22}^+\right)$$

$$ABAB \rightarrow M_{18}C_{26}\left(Zr_{18}C_{27}^+\right)$$

$$ABABA \rightarrow M_{22}C_{35}\left(Zr_{22}C_{35}^+\right)$$
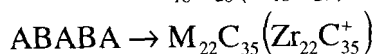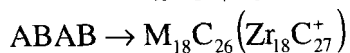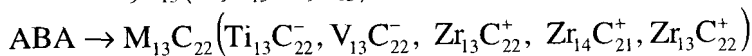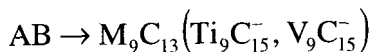
The optimized geometry of the five layer structure is shown in panel (c) of Fig. 11.13.

References

1. Rohlfing, E. A., Cox, E. A., and Kaldor, A., *J. Chem. Phys.*, **81**, 3322 (1984).
2. Kroto, H., *Int. Rev. Phys. Chem.*, **1**, 309 (1981).
3. Kroto, H., *Science*, **242**, 1139 (1988).
4. Kroto, H., Heath, J. R., O'Brien, S. C., Curl, R. F., and Smalley, R. E., *Nature*, **318**, 162 (1985).
5. Tisza, L., *Z. Physik*, **82**, 48 (1933).
6. Osawa, E., *Kagaku (Kyoto)* , **25**, 854 (1970).
7. Bochvar, D. A., and Gal'pern, E. G., *Proc. Acad. Sci. USSR*, **209**, 239 (1973).
8. Kratschmer, W., Lamb, L. D., Fostiropoulos, K., and Huffman, D. R., *Nature*, **347**, 354 (1990).
9. Johnson, R. D., Bethune, D. S., and Yannoni, C. S., *Acc. Chem. Res.*, **25**, 169 (1992).
10. Bertsch, G. F., Bulgac, A., Tománek, D., and Wang, Y., *Phys. Rev. Lett.*, **67**, 1690 (1991).
11. Saito, S., and Oshiyama, A., *Phys. Rev. Lett.*, **66**, 2637 (1991); Saito, S., Oshiyama, A., Miyamoto, Y., Hamada, N., and Sawada, S., *Nanotechnology*, **3**, 167 (1992).
12. Weaver, J. H., Martins, J. L., Komeda, T., Chen, Y., Ohno, T. R., Kroll, G. H., Troullier, N., Haufler, R. H., and Smalley, R. E., *Phys. Rev. Lett.*, **66**, 1741 (1991).
13. Jones, R. O., *J. Chem. Phys.*, **110** , 5189 (1999).
14. Bylaska, E. J., Taylor, P. R., Kawai, R., and Weare, J. H., *J. Phys. Chem.*, **100**, 6966 (1996).
15. Lu, J., Re, S., Choe, Y., Nahase, S., Zhou, Y., Han, R., Peng, L., Zhang, X., and Zhao, X., *Phys. Rev. B*, **67**, 125415 (2003).
16. Prinzbach, H., Weiler, A., Landenberger, P., Whal, F., Wörth, J., Scott, L. T., Gelmomt, M., Olevano, D., and Issendorff, B. V., *Nature*, **407**, 60 (2000).
17. Curl, R. F., and Smalley, R. S., *Science*, **242**, 1017 (1988).
18. Geusic, M. E., Jarrold, M. E., McIlrath, T. J., Freeman, R. R., and Bowers, M. T., *J. Chem. Phys.*, **86**, 3862 (1986).
19. Weiss, F. D., Elkind, J. L., O'Brien, S. C., Curl, R. F., and Smalley, R. E., *J. Amer. Chem. Soc.*, **110**, 4464 (1988).
20. Ross, M. M., and Callahan, J. H., *J. Phys. Chem.*, **95**, 5720 (1991).
21. Weiske, T., Böhme, D. K., Hrussak, J., Kratschmer, W., and Schwarz, H., *Angew. Chem. Int. Ed. Engl.*, **30**, 884 (1991).
22. Wan, Z., Christian, J. F., Basir, Y., and Anderson, S., *J. Chem. Phys.*, **108**, 9390 (1993).
23. Caldwell, K. A., Giblin, D. E., Hsu, C. H., Cox, D., and Gross, M. L., *J. Amer. Chem. Soc.*, **113**, 8519 (1991).

24. Kalish, R., Samoiloff, A., Hoffman, A., Uzan-Saguy, C., McCulloch, D., and Prawer, S., *Phys. Rev. B*, **48**, 18235 (1993).
25. Basir, Y., Wan, Z., Christian, J. F., and Anderson, S. L., *Int. J. Mass Spectrom. Ion Proc.* **138**, 173 (1994).
26. Beck, R., St John, P., Alvarez, M. M., Diederich, F., and Whetten, R. L., *J. Phys. Chem.*, **95**, 8402 (1991).
27. Busmann, H. G., Lill, Th., Reif, B., and Hertel, I. V., *Surf. Sci.*, **272**, 146 (1992).
28. Galli, G., and Mauri, F., *Phys. Rev. Lett.*, **73**, 3471 (1994).
29. Wang, L. S., Cheshnovsky, O., Smalley, R. E., Carpenter, J. P., and Hwu, S. J., *J. Chem. Phys.*, **96**, 4028 (1992).
30. Martin, T. P., Malinowski, N., Zimmermann, U., Näher, U., and Schaber, H., *J. Chem. Phys.*, **99**, 4210 (1993).
31. Kohanoff, J., Andreoni, W., and Parrinello, *Chem. Phys. Lett.*, **198**, 472 (1993).
32. Zimmermann, U., Burkhart, A., Malinowski, N., Näher, U., and Martin, T. P., *J. Chem. Phys.*, **101**, 2244 (1994).
33. Zimmermann, A., Malinowski, N., Näher, U., Frank, S., and Martin, T. P., *Phys. Rev. Lett.* , **72**, 3542 (1994).
34. Malinowski, N., Branz, W., Billas, I. M. L., Heinebrodt, M., Tast, F., and Martin, T. P., *Eur. Phys. J. D.,* **9**, 41 (1999).
35. Lichtenberger, D. L., Jatcko, M. E., Nebesny, K. W., Ray, C. D., Huffman, D. R., and Lamb, *Chem. Phys. Lett.*, **176**, 203 (1991).
36. Weaver, J. H., Martins, J. L., Komeda, T., Chen, Y., Ohno, T. R., Kroll, G. H., and Troullier, N., *Phys. Rev. Lett.* , **66**, 1741 (1991).
37. Keller, J. W., and Copland, M. A., *Chem. Phys. Lett.*, **193**, 89 (1992).
38. Ajie, H., Alvarez, M. M., Anz, S. J., Beck, R. D., Diederich, F., Fostiropoulos, K., Huffman, D. R., Krätschmer, W., Rubin, Y., Schriver, K. R., Sensharma, D., and Whetten. R. L., *J. Phys. Chem.*, **94**, 8630 (1990).
39. Hertel. I. V., Steger, H., de Vries, J., Weisser, B., Menzel. C., Kamke, B., and Kamke, W., *Phys. Rev. Lett.* , **68**, 784 (1992).
40. Marinopoulos, A, G., Reinig, L., Olevano, V., Rubio, A., Pichler, T., Liu, X., Knupfer, N., and Fink, J., *Phys. Rev. Lett.* , **89**, 076402 (2002).
41. Castro, A., Marques, M. A. L., Alonso, J. A., and Rubio, A., *J. Comput. Theoret. Nanoscience*, **1**, 230 (2004).
42. Hawkins, J. M., and Meyer, A., *Science*, **260**, 1918 (1993).
43. Yabana, K., and Bertsch, G. F., *Phys. Rev. A.*, **60**, 1273 (1999).
44. Goroff, N. S., *Acc. Chem. Res.*, **29**, 77 (1996).
45. Stone, A. J., and Wales, D. J., *Chem. Phys. Lett.*, **28**, 501 (1986).
46. Castro, A., Marques, M. A. L., Alonso, J. A., Bertsch, G. F., Yabana, K., and Rubio, A., *J. Chem. Phys.*, 116, 1930 (2002).
47. Rubio, A., Alonso, J. A., López, J. M., and Stott, M. J., *Phys. Rev. B*, **49**, 17397 (1994).

48. Frank, S., Malinowski, N., Tast, F., Heinebrodt, M., Billas, I. M. L., and Martin, T. P., *Z. Phys. D*, **40**, 250 (1997).
49. Kroto, H. W., and McKay, K., *Nature*, **331**, 328 (1988).
50. Iijima, *J. Phys. Chem.*, **91**, 3466 (1987).
51. Ugarte, D., *Nature*, **359**, 707 (1992).
52. Kuznetsov, V. L., Chuvilin, A. L., Butenko, Y. V., Mal'kov I. Y., and Titov, V. M., *Chem. Phys. Lett.*, **222**, 343 (1994).
53. De Heer, W. A., and Ugarte, D., *Chem. Phys. Lett.*, **207**, 480 (1993).
54. Chhowalla, M., Wang, H., Sano, N., Teo, K. B. K., Lee, S. B., and Amaratunga, G. A. J., *Phys. Rev. Lett.*, **90**, 155504 (2004).
55. Fitzpartick, E. L., and Massa, D., *Astrophys. J.*, **307**, 286 (1986).
56. Guo, B. C., Kerns, K. P., and Castleman, A. W., *Science*, **255**, 1411 (1992).
57. Guo, B. C., Wei, S. W., Purnell, J., Buzza, S., and Castleman, A. W., *J. Phys. Chem.*, **96**, 4166 (1992).
58. Guo, B. C., Wei, S. W., Purnell, J., Buzza, S., and Castleman, A. W., *Science*, **256**, 515 (1992).
59. Cartier, S. F., Chen, Z. Y., Walder, G. J., Saleppy, C. R., and Castleman, A. W., *Science*, **260**, 195 (1993).
60. Selvan, R., and Pradeep, T., *Chem. Phys. Lett.*, **309**, 149 (1999).
61. Rohmer, M. M., Bénard, M., and Poblet, J. M., *Chem. Rev.*, **100**, 495 (2000).
62. Dance, I., *J. Chem. Soc. Chem. Commun.*, **24**, 1779 (1992).
63. Dance, I., *J. Amer. Chem. Soc.*, **118**, 6309 (1996).
64. Gueorguiev, G. K., and Pacheco, J. M., *Phys. Rev. Lett.*, **88**, 115504 (2002).
65. Chen, H., Feyereisen, M., Long, X. P., and Fitzgerald, G., *Phys. Rev. Lett.*, **71**, 1732 (1993).
66. Lou, L., and Nordlander, P., *Chem. Phys. Lett.*, **224**, 439 (1994).
67. Rohmer, M. M., Bénard, M., Bo, C., and Poblet, J. M., *J. Amer. Chem. Soc.*, **117**, 508 (1995).
68. Baruath, T., Pederson, M. R., Lyn, M. L., and Castleman, A. W., *Phys. Rev. A*, **66**, 053201 (2002).
69. Sakurai, H., and Castleman, A. W., *J. Phys. Chem. A*, **102**, 10486 (1998).
70. Wang, L. S., Li, S., and Wu, H., *J. Phys. Chem.*, **100**, 19211 (1996); Li, S., Wu, H., and Wang, L. S., *J. Am. Chem. Soc.*, **119**, 7517 (1997).
71. Gueorguiev, G. K., and Pacheco, J. M., *Phys. Rev. A.*, **68**, 241401 (2003).
72. Van Heijnsbergen, D., Von Helden, G., Duncan, M. A., Van Roij, A. J. A., and Meijer, G., *Phys. Rev. Lett.*, **83**, 4983 (1999).
73. Pilgrim, J. S., and Duncan, M. A., *J. Am. Chem. Soc.*, **115**, 6958 (1993).
74. Armentrout, P. B., Sunderlin, L. S., and Fisher, E., *Inorg. Chem.*, **28**, 4436 (1989).
75. Cartier, S. F., May, B. D., and Castleman, A. W., *J. Chem. Phys.*, **100**, 5384 (1994).
76. Cartier, S. F., May, B. D., and Castleman, A. W., *J. Phys. Chem.*, **100**, 8175 (1996).

77. Muñoz, J., Pujol, C., Bo, C., Poblet, J. M., Rohmer, M. M., and Bénard, M. J. M., *J. Phys. Chem. A*, **101**, 8345 (1997).
78. May, B. D., Cartier, S. F., and Castleman, A. W., *Chem. Phys. Lett.*, **242**, 265 (1995).
79. Rubio, A., Alonso, J. A., and López, J. M., *An. Fís. (Spain)*, **89**, 174 (1993).
80. Martínez, J. I., Castro, A., Rubio, A., Poblet, J. M., and Alonso, J. A., *Chem. Phys. Lett.*, **398**, 292 (2004).
81. Guo, B. C., Kerns, K. P., and Castleman, A. W., *J. Amer. Chem. Soc.*, **115**, 7415 (1993).
82. Deng, H. T., Kerns, K. P., and Castleman, A. W., *J. Amer. Chem. Soc.*, **118**, 446 (1996).
83. Kerns, K. P., Guo, B. C., Deng, H. T., and Castleman, A. W., *J. Amer. Chem. Soc.*, **117**, 4026 (1995).
84. Sakurai, H., and Castleman, A. W., *J. Chem. Phys.*, **111**, 1426 (1999).
85. Deng. H. T., Guo, B. C., Kerns, K. P., and Castleman, A. W., *J. Phys. Chem.*, **98**, 13373 (1994).
86. Yeh, C. S., Afzaal, S., Lee, AS. A., Biun, Y. G., and Freiser, B. S., *J. Amer. Chem. Soc.*, **116**, 8806 (1994).
87. Pilgrim, J. S., and Duncan, M. A., *J. Amer. Chem. Soc.*, **115**, 4395 (1993).
88. Castleman, A. W., *Z. Phys. D*, **26**, 159 (1993).
89. Wang, L. S., and Chen, H., *Phys. Rev. Lett.*, **78**, 2983 (1997).
90. Lu, W., Huang, R., Ding, J., and Yang, S., *J. Chem. Phys.*, **104**, 6577 (1996).
91. Pilgrim, J. S., and Duncan, M. A., *J. Am. Chem. Soc.*, **115**, 9724 (1993).
92. Wang, L. S., Wang, X. B., Wu, H., and Cheng, H., *J. Amer. Chem. Soc.*, **120**, 6556 (1998).

This page intentionally left blank

12. Assembling of New Materials from Clusters

12.1 General Principles

The assembling of atomic clusters opens the possibility of building materials with novel properties. Two main difficulties are encountered in synthesizing those materials. First of all, there is the production of large quantities of clusters of a specific size. Second, for the assembling to be successful, the clusters have to retain their character. Typical clusters can interact with each other and coalesce to form larger clusters, destroying the original properties. Unlike clusters, molecules do not lose their identity when they form molecular solids. This is because molecules have a high intrinsic stability, that is, they are magic species with a fixed number of atoms and a special composition. One can then expect that the so called *magic clusters*, with their specially unreactive electronic structure may be good candidates to form the builing blocks of new assembled materials.

This condition of stability of neighbor clusters against coalescence has been analyzed [1] by studying a cluster dimer $(X_{13})_2$ built from two icosahedral clusters formed by atoms interacting through Lennard–Jones potentials

$$U_{ij}\left(r_{ij}\right) = 4\varepsilon_{ij}\left[\left(\frac{\sigma_{ij}}{r_{ij}}\right)^{12} - \left(\frac{\sigma_{ij}}{r_{ij}}\right)^{6}\right]. \tag{12.1}$$

All the hard-sphere diameters σ_{ij} were assumed to be equal, $\sigma_{ij} = \sigma$, but the depth ε_{ij} of the interaction potential between atoms in the same

cluster, $\varepsilon_{ij}^{11} = \varepsilon_{ij}^{22}$, was assumed to be different from the depth ε_{ij}^{12} between atoms in different clusters of the dimer. Molecular dynamics simulations of the thermal heating of the dimer indicated that the condition

$$\varepsilon_{ij}^{12} << \varepsilon_{ij}^{11} \qquad (12.2)$$

improves the stability of the dimer against coalescence. The propotypical example of a clustered material is the fullerite crystal, formed by the self-assembling of C_{60} clusters [2]. In this material the condition given by Eq. (12.2) is precisely fulfilled because there are two well differentiated types of bonding in the system: a strong covalent bonding between the neighbor C atoms in each cluster and a weak Van der Waals bonding between different C_{60} clusters.

The assembling of clusters of metallic elements has also been suggested in the early 1990s [3], although the requirement imposed by (12.2) is rather stringent in this case, because the interatomic interactions are more delocalized and these clusters are more reactive. The less reactive clusters are those which have an electronic structure of closed shells. The reactivity of the metallic clusters can be lowered by coating the clusters with organic molecules, and assemblies of passivated gold nanoclusters have been prepared [4], but much work remains to be done to discover the conditions required for a successful synthesis of cluster assembled materials. In general an assembled cluster-solid will be metastable (like the fullerite crystal, which is less stable than graphite), trapped in a deep minimum of the potential energy surface protected by sizeable energy barriers.

In the usual solids assembled from atoms, there is only one characteristic length scale, that can be measured by the lattice constant. The bonding between those atoms is well defined: it can be either ionic, covalent, metallic or of Van der Waals type. The energy bands are due to the overlap between the atomic orbitals, and the vibrations of the atoms lead to acoustic and optical phonon modes. On the other hand, materials assembled from clusters have two length scales, characterized by the intra-cluster and inter-cluster distances, respectively, and the bonding between the atoms in a cluster may be different fom the inter-cluster bonding. Energy bands are due, in this case, to the overlap between

cluster molecular orbitals. Two kinds of vibrational modes appear: intra-cluster and inter-cluster modes.

12.2 Crystalline Intermetallic Compounds Containing Clusters

The equiatomic crystalline alloys of Pb and the alkali metals M = Na, K, Rb, Cs (but not Li) contain tetrahedral Pb_4 clusters surrounded by the alkali atoms [5], and the unit cell of the alloy, known from X-ray studies, is shown in Fig. 12.1. The same clustering occurs for alloys of the alkali metals with Si, Ge or Sn, which are elements in the same column as Pb in the Periodic Table. The study of this family of alloys provides useful insight on the problem of assembling clusters to form new materials.
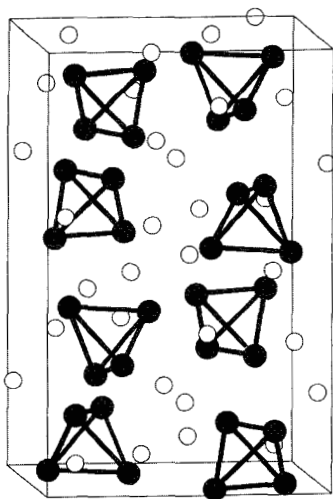
Figure 12.1. Unit cell of the crystalline ordered alloy NaPb. The tetrahedral Pb_4 clusters (dark structures) are surrounded by the alkali atoms (light spheres).

Each Pb_4 cluster in those alloys is surrounded by alkali atoms that cap the faces and the edges of the tetrahedron. The free clusters X_4Pb_4, having the stoichiometry 1:1 of the solid, are relevant to understand the

structure of those alloys and have been investigated by DFT calculations [6]. The lowest energy structure of all the free X_4Pb_4 clusters consists of a Pb_4 tetrahedron surrounded by another, oppositely oriented alkali tetrahedron. The atoms of the outer tetrahedron cap the faces on the inner one. The ground state of the free Pb_4 cluster has the structure of a planar rhombus, and the change from the planar to the tetrahedral structure by adding the four alkali atoms results from a charge transfer effect. The electronic configuration of the Pb atom is $6s^2\ 6p^2$, so Pb_4 has 16 valence electrons. Although neutral Pb_4 is planar, the cluster also has a low lying tetrahedral isomer with an interesting characteristic: the LUMO of that tetrahedral isomer is a four-fold degenerate level (including spin) and a large gap exists above this LUMO. In other words, 20 electrons would lead to a closed shell magic cluster for tetrahedral symmetry. The difference of electronegativity between the Pb and the alkali atoms leads to electron transfer from the alkali atoms to the Pb_4 unit, and the transferred electrons go to fill the LUMO of Pb_4. With four alkali atoms added to Pb_4, this becomes a Pb_4^{4-} poly-anion with closed electronic shells. The four cations sit on symmetrical positions above the four faces of the tetrahedron and play the role of stabilizing the negatively charged inner region of the cluster.

Large HOMO–LUMO gaps have been calculated for this family of clusters: 2.54 eV for Li_4Pb_4, 1.92 eV for Pb_4Na_4 and 1.36 eV for K_4Pb_4. However, the large HOMO–LUMO gap in the free clusters is not enough to explain the clustering observed in the alloys, since Pb_4 clusters form in the alloy when the alkali partner is Na, K, Rb or Cs, but not when the partner is Li. This exception occurs, surprisingly, in the case of the largest gap. A cluster with a large gap should be less reactive than others with small gaps. Passivity is, nevertheless, difficult to achieve in metallic clusters because the molecular orbitals are substantially delocalized and the overlap between orbitals of different clusters may lead to strong cluster–cluster interaction. In these alloys the interaction becomes reduced when the size of the cations is large enough. This idea is illustrated by the map in Fig. 12.2, where the clusters are represented in terms of two coordinates, the HOMO–LUMO gap and the diameter of the alkali cation [7]. In addition to the X_4Pb_4 clusters, other closed shell clusters of compositions X_4Pb and X_6Pb are included.

The clusters X_4Pb are also very stable [8]. The structure of X_4Pb clusters is a nearly perfect pyramid with the Pb atom in the apex and the

four alkali atoms forming the basal plane [6, 8], except for the case of Li_4Pb, where the pyramid is distorted and the structure looks like a trigonal bipyramid with the Pb atom forming part of the common basis of the two pyramids. In spite of the high stability of the X_4Pb clusters, crystalline alloys with compositions near 20 atomic % Pb do not present any clustering features. The cluster Na_6Pb was found extremely abundant in gas phase experiments [9]. Its structure is that of an octahedron enclosing the Pb atom (see Section 7.5), and this cluster has been suggested as a candidate to form cluster-solids [10].
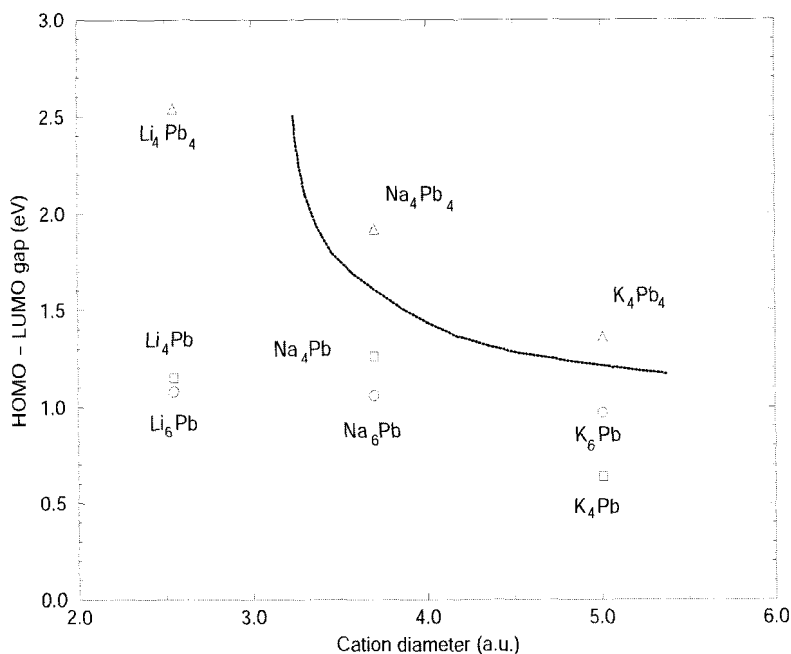
Figure 12.2. Structural map for clusters in terms of two coordinates: the HOMO–LUMO gap and the cation diameter. Only the clusters on the upper right hand corner are related to solid alloys showing clustering effects. Reproduced from F. Duque *et al.*, *Int. J. Quantum Chem.* **86**, 226 (2002) with permission of Wiley.

The empirical curve drawn in Fig. 12.2 separates the two clusters related to stable cluster-solids, Na_4Pb_4 and K_4Pb_4, from the rest. The conclusion is that a large HOMO–LUMO gap and a large cation size are both required for the occurrence of clustering in the solid. In the case of Li_4Pb_4, the reason preventing clustering in the solid is the small size of the Li^+ cation. Clusters of composition X_6Pb are, evidently, bad candidates, in spite of the early expectations. The emerging picture for the crystal compounds associated to the X_4Pb_4 clusters is that the alkali cations are not part of the cluster *in the crystal*. Strictly speaking, the closed shell Pb_4^{4-} poly-anions are the clustered units, and the cations play an important coating role that allows for the survival of the poly-anions in the solid (the cations also play the evident role of contributing to the global electrical neutrality of the solid). For the coating to be effective, the size of the cations has to be large enough. On the other hand, clusters with compositions X_4Pb and X_6Pb do not lead to clustering in solid alloys.

Those ideas have been confirmed by DFT computer simulations of the assembling of K_4Pb_4, Na_4Pb_4 and Li_4Pb_4 clusters [11]. In the XPb crystals with X = Na, K, Rb and Cs, the Pb_4 clusters form a body centered tetragonal *(bct)* lattice with axes ratio $c/a = 1.676$ (see Fig. 12.1), and the simulations start by placing the Na_4Pb_4 clusters in a *bct* lattice with the same c/a ratio but with dimensions c and a multiplied by a factor $f = 2$. The factor f was then reduced in steps maintaining $c/a = 1.676$. As f is reduced, the Na_4Pb_4 units cannot keep their independent identities and, in order to pack efficiently, two Na atoms of each cluster move from their original positions above faces of the Pb_4 tetrahedron to positions above edges. More precisely, each Pb_4 tetrahedron becomes fully covered by alkali cations capping the faces and the edges of the tetrahedron, and each cation is shared by two Pb_4 units. The structure obtained at the end of the simulation is precisely the observed structure of the crystalline compound. The density of electronic states shows a small gap at the Fermi level, so the crystal is a narrow gap semiconductor. The binding energy gained by assembling the clusters is $E_{assembling} = 4.09$ eV per cluster, to be compared with a value of $E_{clustering} = 11.19$ eV of the binding energy of the Na_4Pb_4 cluster with respect to the separated atoms. $E_{assembling}$ is nearly one third of $E_{clustering}$. The results are similar for the simulation of the assembling of K_4Pb_4 clusters, with the poly-anions even more efficiently isolated from each other because of

the larger diameter of K^+ compared to Na^+. In this case $E_{assembling}$ = 4.14 eV, and $E_{clustering}$ = 10.54 eV, so the ratio of the two quantities is again near one third. The cohesive energies of the two crystals with respect to the separated atoms, are given in Table 12.1.

Table 12.1. Cohesive energy (eV/atom) for MPb solid compounds (M = Li, Na, K) with the CsCl structure and with the structure arising from assembling of the M_4Pb_4 clusters. Data collected from [11].

Alloy	Cluster-assembled	CsCl
LiPb	2.325	2.415
NaPb	1.910	1.895
KPb	1.835	1.545

The simulation of the assembling of Pb_4Na_4 clusters gave completely different results. As the lattice constant of the supercrystal is reduced the clusters interact strongly. Each Pb_4 tetrahedron opens up taking a butterfly (bent rhombus) shape. Distances between Pb atoms in neighbor butterflies are similar to bond lengths inside the butterflies, and the strong interaction gives metallic character to the assembled solid. The assembled solid is metastable; its structure is based on an interconnected network of Pb_4 butterflies which cannot be characterized as a solid containing clusters. Furthermore, calculations for the LiPb alloy with the experimental CsCl structure give a cohesive energy of 2.415 eV/atom, that is larger than the cohesive energy of the assembled metastable PbLi solid (see Table 12.1). Also in agreement with experiment Table 12.1 shows that the body centered tetragonal NaPb and KPb clustered solids have higher cohesive energies than the CsCl phase.

The conclusion is that a closed shell structure and a large HOMO–LUMO gap are necessary conditions, but these are not enough to guarantee a successful cluster self-assembling. The reactivity of metallic clusters is large and one has learned from the family of alloys formed by alkali metals and elements of the Si group that an efficient way of passivating the clusters is by using an appropriate coating. In fact, experimentalists have already used this tool to produce assemblies of size-selected gold clusters coated by organic molecules [4].

12.3 Boron Clusters in Solids

Some boron-rich solids exist that can be considered as assembled from
clusters [12, 13]. In particular, Fig. 12.3 shows the α-rombohedral phase
of pure boron. Its basic unit is a 12-atom icosahedron where six of those
12 atoms are bonded to atoms in neighbor icosahedral units. The
formation of those icosahedral clusters is remarkable since gas phase B_{12}
clusters are not specially stable [14] and, furthermore, the most stable
structures of free B_{12} are quasi-planar [15, 16] (see also Section 4.8.2).
The stability of the icosahedral units in the crystal has been attributed to
the formation of three-center bonds, where the three atoms bind by piling
up charge in the center of the triangular faces.
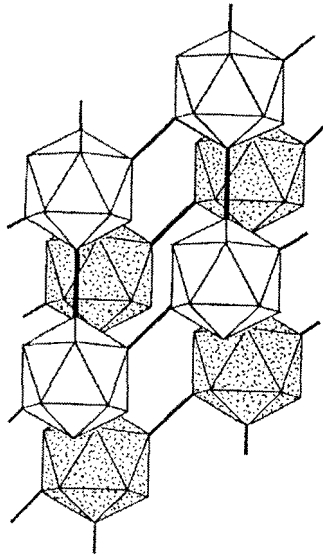
Figure 12.3. Structure of α-rombohedral boron. Notice the icosahedral B_{12} units.

A super-icosahedral structure that can be denoted as $B_{12}(B_{12})_{12}$ forms
in $B_{56}Y$ and $B_{66}Y$ crystals [17, 18]. In this structure each vertex and the
center of the super-icosahedron are ocuppied by icosahedral B_{12} clusters,
and the Y atoms occupy interstitial sites. Those discrete super-

icosahedral units have been directly observed by scanning tunneling microscopy [17] and high resolution electron microscopy (HREM) [18].
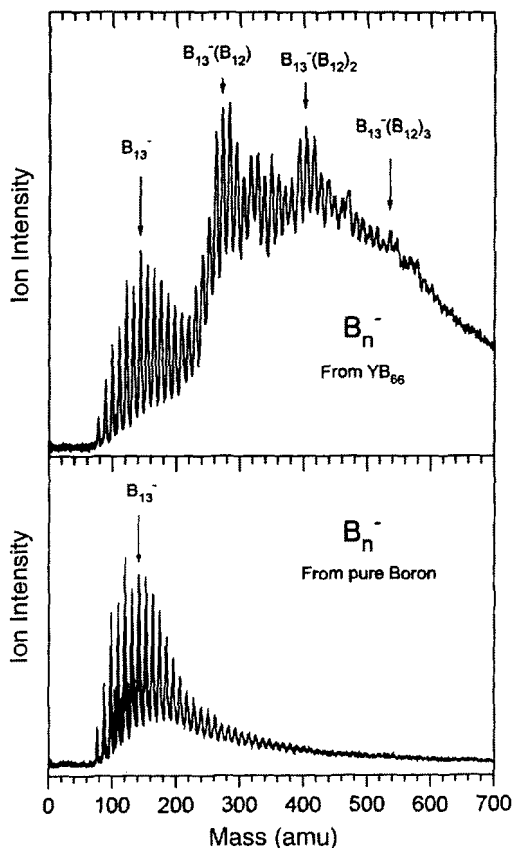
Figure 12.4. Mass spectrum of boron cluster anions obtained from laser vaporization of $B_{66}Y$ and pure boron solids. Reproduced from S. J. Xu *et al.*, *Chem. Phys. Lett.* **379**, 282 (2003) with permission of Elsevier.

Intriguing structures that appear to be related to the assembling of boron clusters have been produced by laser vaporization of the $B_{66}Y$ solid. A mass spectrum of cluster anions is shown in Fig. 12.4, and a spectrum obtained by the same method from a pure boron solid is shown

for comparison [19]. In the low mass range both spectra show local intensity maxima at B_{11}^- and B_{13}^-, but at higher masses the spectra are completely different. The spectrum from the ablated $B_{66}Y$ solid repeats the main features observed in the low mass range, that is, local maxima are seen for $B_{13}^-(B_{12})_2$ and $B_{13}^-(B_{12})_3$, and it is also likely that $B_{13}^-(B_{12})$ is a magic species. The periodic appearance of B_{12} units was interpreted as originating from the direct ablation of B_{12} icosahedral cages from the super-icosahedral $B_{66}Y$ crystal. Less clear is the nature of the B_{13}^- core in all those clusters and Xu *et al.* [19] speculated with a formation mechanism in which two B_{12} units react and dissociate after electron attachment to give $B_{13}^- + B_{11}$.

12.4 Assembling of C_{60} Fullerenes

12.4.1 $(C_{60})_N$ clusters

Apart from the geometrical shells of atoms seen in large metallic clusters (see Section 4.6) and inert gas clusters (see Chapter 3), another type of shells occurs in the clusters of C_{60} molecules, that is, shells of clusters. A previous example of shells of clusters has been discussed in Section 12.3; namely, the super-icosahedral $B_{12}(B_{12})_{12}$ structures. The fullerene molecule C_{60} has been studied in Chapter 11, and for our present purposes it is worth to notice that the interaction between different C_{60} molecules is weak compared to the C–C bonding in a molecule. In fact, the measured binding energy between the two C_{60} molecules in the dimer $(C_{60})_2$ is only 0.275 ± 0.08 eV [20]. This binding energy was determined by fitting an Arrhenius law to the measured temperature dependent decay rate for the dissociation reaction

$$\left(C_{60}\right)_2 \rightarrow C_{60} + C_{60}. \qquad (12.3)$$

In sharp contrast, the energy of the fragmentation reaction

$$C_{60} \rightarrow C_{58} + C_2 \qquad (12.4)$$

is about 10 eV [21]. This means that the structure of each fullerene molecule remains intact when these form $(C_{60})_N$ clusters. The method of production of these clusters is the usual one. A vapor of C_{60} molecules enters a low pressure inert gas condensation cell, the vapor is quenched by collisions with the cold He gas, and $(C_{60})_N$ clusters condense out of the vapor [22]. The clusters are then photoionized with an excimer laser without destroying them. Since the interest in the experiment was to investigate which clusters are particularly stable, it was necessary to heat the clusters up to a temperature at which these evaporate fullerene molecules (the heating is achieved with a second laser). The most stable clusters evaporate less, so the population of very stable clusters in the beam grows at the expense of the less stable ones.
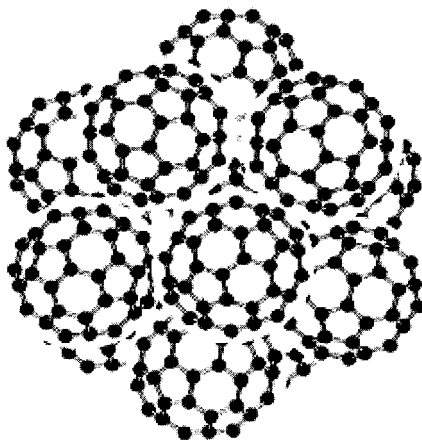
Figure 12.5. The icosahedral cluster $(C_{60})_{13}$.

Strong peaks appear in the mass spectrum of the $(C_{60})_N^+$ clusters for $N = 13, 19, 23, 27, 35, 39, 43, 46, 49$ and 55. Those peaks are consistent with an icosahedral structure (see Chapter 3). The high stability of $(C_{60})_{13}$ was also demonstrated by the experiments of Hansen *et al.* [23]. Figure

12.5 shows the icosahedral structure of $(C_{60})_{13}$. Furthermore, other mass peaks were observed after $N = 55$ which are also consistent with that structure: a high mass peak appears each time three C_{60} molecules are added to $(C_{60})_{55}$. In fact, one can appreciate in Fig. 3.3 that a particularly stable configuration is achieved every time three molecules cover one of the facets of the Ico55.

The experimental situation is then quite clear, but subsequent theoretical calculations led to a puzzling situation. All the calculations [24–27] predict close packed or decahedral structures above a critical cluster size N_c in the range $N_c = 13$–16. This occurs for a variety of different potentials describing the C_{60}–C_{60} interaction. The reason for the disappearance of the icosahedral structures is that the intermolecular potential between two C_{60} molecules is short-ranged, that is, its attractive minimum is too narrow. For a short-range potential, structures with high internal strain, like the icosahedron, become unfavorable because these involve nearest neighbor distances that deviate from the equilibrium pair separation of the potential [28]. It was first thought that the discrepancy could be due to the fact that the calculations were performed for neutral $(C_{60})_N$ clusters, while the experiments correspond to charged $(C_{60})_N^+$ species. In order to test that hypothesis new experiments were performed for both neutral and charged clusters [20, 29]. The new feature in those experiments is that the temperature of the clusters was carefully monitored. Instead of using a laser to warm up the clusters, heating was achieved by passing the cluster beam through a thermalization cell which is able to keep a constant temperature profile (± 5 K) over a long distance of about 9 cm. The residence time of the clusters and the carrier He gas in this thermalization region can be varied between 0.5 ms and 1 ms. For the purposes of studying neutral and charged clusters, the experimental set up allowed to ionize the $(C_{60})_N$ clusters either before entering the thermalization cell or after leaving the cell.

Experiments for a heating temperature $T_h = 490$ K and a residence time of 0.5 ms in the thermalization cell led to an important conclusion: the magic numbers, the same ones of the early experiment [22], are not sensitive to the charge state of the clusters (neutral, positive and negativel clusters were studied). In addition, by extending the size range to larger clusters, the icosahedral structure was confirmed by the observation of the formation of umbrellas in between the main two peaks $N = 55$ and $N = 147$. Then, when the annealing temperature in the cell is

increased to 585 K, the icosahedral magic numbers begin to disappear and are replaced by other strong peaks. The new peaks, $N = 38, 48, 58, 61, 64, 68, 71, 77, 84, 89, 91, 96$ and 98, shown in Fig. 12.6, mainly occur for $N \geq 35$. On the other hand, some peaks remained unchanged in the low mass region, $N = 13, 19, 26, 28, 31, 33$ and 35.
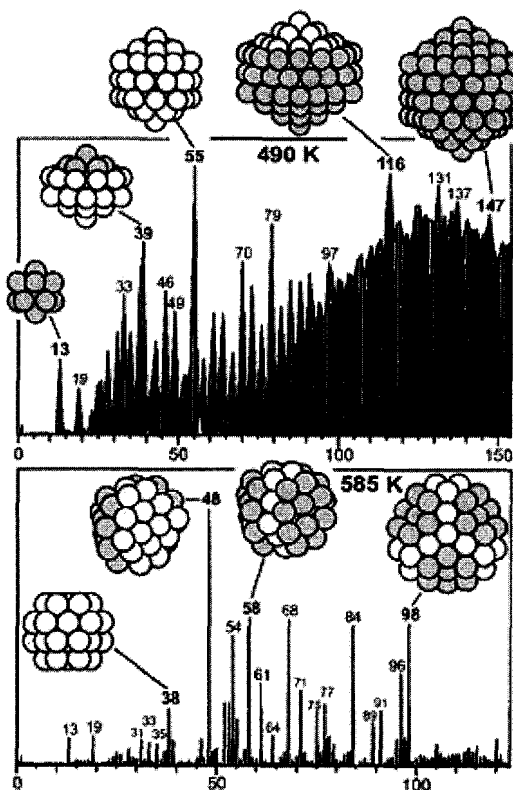
Figure 12.6. Mass spectra of $(C_{60})_N$ clusters recorded at cell temperatures of 490 K and 585 K, and heating times of 0.5 ms. Some representative structures are shown, where each C_{60} molecule is represented by a sphere. Structures obtained by heating at 490 K are icosahedral. Those at 585 K are close-packed, decahedral or octahedral. Reproduced from W. Branz *et al.*, *Phys. Rev. B* **66**, 94107 (2002) with permission of the American Physical Society.

The new set of high peaks is consistent with the results of structural optimizations [27] using a C_{60}–C_{60} potential derived by Pacheco and Prates-Ramalho (PPR) from *ab initio* calculations [30]. This potential, which consists of a pair potential plus a three-body term of the Axilrod–Teller form [31] predicts that the global energy minima are based on the icosahedral structure up to $N = 15$. Above this size the structures are decahedral or close-packed. Highly stable cuboctahedral and decahedral structures are predicted for $(C_{60})_{38}$ and $(C_{60})_{48}$, respectively (see those structures in Fig. 12.6). The peaks at $N = 64, 71$ and 75 are explained by structures based on the 75-Marks decahedron [32]. Also the peaks at $N = 31, 33, 35$ are compatible with small decahedra.

The series of observed peaks $N = 61, 68, 77, 84, 91, 96$ and 98, most likely correspond to a newly discovered structure, the 98-Leary tetrahedron [33]. This can be viewed as a stellated *fcc*-based tetrahedron of 56 molecules, whose six faces are covered by hexagonal arrangements of seven molecules (the hexagon and a molecule at its center). Then, by appropriate truncations and remotions of patches from the 98-Leary tetrahedron, the clusters with $N = 91, 84, 77, 68$ and 61 result. In addition, by restricting to structures based on the 98-Leary tetrahedron, the sizes $N = 61, 68, 77, 84, 91, 96$ and 98 have enhanced stability compared to other sizes. These Leary structures are not global minima for the PPR potential, but the energy difference compared to the optimal structures for those sizes is small: between 0.1 eV and 1 eV. $N = 54$ is observed as a peak at $T = 585$ K in Fig. 12.6, but it has not been included in the list given above because it is just a remnant of $N = 55$, and it disappears by a further moderate increase of temperature (at $T = 610$ K).

In summary, the icosahedral structures are not the most stable structures at $T = 0$ K for $N \geq 13$–16. At finite temperatures the vibrational entropy contribution to the free energy becomes relevant, but an analysis reveals that the icosahedral structures are again unfavorable with respect to competing structures at $T = 490$ K. So, the interpretation of the differences observed between the two panels of Fig. 12.6 is that the spectrum at 490 K corresponds to clusters kinetically trapped in metastable icosahedral configurations. Then, annealing at 585 K leads to a transition to the close-packed, decahedral and tetrahedral structures, lowest in free energy at that temperature (although the structures based on the Leary tetrahedron are not the global minima at $T = 0$ K, their vibrational entropy is larger than those for the alternative decahedral or

close-packed structures). Molecular dynamics simulations [20, 34] produce the following picture of the kinetic trapping. First of all, one has to keep in mind that the icosahedral structures represent the minimum energy structures of small $(C_{60})_N$ clusters. In particular the icosahedron $(C_{60})_{13}$ is very stable, so this cluster can act as an embryo for metastable growth following an icosahedral path. Something similar occurs for $N = 25$. Its lowest energy structure is decahedral, but it is a fragment of Ico55, and an icosahedral pathway is again possible. Icosahedral growth is facilitated by the fact that, in the range of sizes of interest here, the potential energy landscape is such that the funnel leading to icosahedral structures is broad, *i.e.*, easy to find. In contrast, the funnel leading to the global energy minimum is usually deep but narrow, and then difficult to find, and it is separated from the icosahedral funnel by high rearrangement energy barriers. This is a consequence of the sticky C_{60}–C_{60} potential [27]. For this reason, trapping in the metastable icosahedral funnel occurs during growth at low temperatures, or by annealing at $T = 490$ K. Once trapped, it takes long time, or high annealing temperatures, to escape from the metastable structure by overcoming the high potential energy barriers. The simulations confirm the metastable icosahedral growth at moderate temperatures [34], corresponding to the experimental features at 490 K, and the structural transition to the nonicosahedral structures at higher temperatures [20].

12.4.2 Fullerene solids

C_{60} is soluble in aromatic solvents like benzene or toluene. This property is used to separate C_{60} from other carbon particles produced by an arc discharge between graphite electrodes [2]. As the solvent evaporates a crystal formed by C_{60} molecules is obtained. In fact, the production of gram quantities of C_{60} by this technique initiated an intensive experimentation with this material which, first of all, allowed for the confirmation of the buckyball structure proposed by Kroto *et al.* five years earlier [35]. X-ray and neutron diffraction experiments have indicated that the molecules are assembled in a close-packed *fcc* lattice with one molecule per primitive *fcc* unit cell, or four molecules per simple cubic unit cell. The lattice constant of the *fcc* lattice is $a = 26.77$ a.u. [36]. The distance between the centers of neighbor molecules is 18.93 a.u. and so the distance between the carbon shells is 5.52 a.u., smaller than the distance between layers in graphite (6.33 a.u.) but longer

than typical C–C chemical bond lengths. The C_{60} solid, which has been called *fullerite*, is the prototypical example of a solid material assembled from clusters. The stability of the solid, similarly to the $(C_{60})_N$ clusters, arises from the weakly attractive Van der Waals forces between the C_{60} molecules. Due to this weak attraction and to the nearly spherical shape of the molecules, these are spinning rapidly with three rotational degrees of freedom about their positions in the *fcc* lattice for temperatures above $T_1 \approx 261$ K [37]. Due to the fast rotation, all the molecules are equivalent. When the solid is cooled below that temperature, an orientational ordering transition occurs [36, 38]. The molecules lose two of their three degrees of rotational freedom and the structure is simple cubic with a lattice constant $a = 26.78$ a.u. and four molecules per unit cell, because the four molecules become inequivalent below T_1. In the new phase the rotational motion occurs around four specific (111) directions, and is a hindered rotation in which adjacent molecules develop strongly correlated orientations. The reduction of the degrees of freedom affects many properties of the solid phase. Due to the molecular nature of the fullerite solid, its electronic structure is determined by that of the C_{60} molecules: a clear correspondence exists between the electronic levels of the molecule and the energy bands of the solid. The σ states of the molecule remain almost unmodified when the solid forms. On the other hand the π states, which are closer to the Fermi level, experience a substantial dispersion. A semiconductor with relatively narrow valence and conduction bands (widths of about 0.4 eV) and a direct gap of 1.5 eV forms.

The structure of solid C_{70} is more complex, and evolves through several different structures as a function of the temperature. At high temperatures, $T \gg T_1 = 340$ K, the structure is close-packed *fcc*. In this phase the C_{70} molecules rotate freely. Then, at lower temperature but still higher than T_1 some authors [39] have reported the existence of a hexagonal close-packed (*hcp*) structure with an ideal lattice ratio $c/a = 1.63$. However other authors [40] propose that the *fcc* phase is the only stable one above T_1. At intermediate temperatures between $T_2 \approx 280$ K and T_1 the long axis of the molecules begins to align, and anisotropy develops in the crystal. Many groups have found evidence for a structural transition near T_1 [38]. Below this temperature, anisotropy appears. Some authors propose that this phase derives from the high temperature *fcc* structure by the elongation of the structure along a

unique (111) direction and the freezing out of the molecular rotation about an axis perpendicular to the long axis of the molecule [41]. The proposed structure is rhombohedral. But other samples have displayed a transition to an *hcp* structure with $c/a = 1.82$ [39]. The larger ratio is associated to the orientation of the molecules along their long axis, as the molecular motion freezes into rotations about the five-fold axis of the molecule. As the temperature is lowered below T_2 the rotation about the long axis is also frozen. The structure below T_2 is monoclinic [39].

12.4.3 Alkali-doped fullerene solids

Several stable crystalline phases have been prepared by doping the fullerene solid with alkali metal atoms. In those compounds the alkali atoms intercalate in interstitial positions between the C_{60} molecules, forming solids of M_xC_{60} composition. The alkali atoms donate the valence electrons to the fullerene molecules, which become negatively charged molecular anions C_{60}^{x-}. The doped solids may retain the original *fcc* structure of the fullerite or may transform to a different structure. The pure C_{60} solid has no free carriers for electrical transport, but in the doped solid the electrons trasferred to the fullerene molecules gradually fill the three-fold degenerate t_{1u} levels of C_{60}. The electrical resistivity shows a minimum at $x = 3$ and this phase is observed to be metallic, corresponding to a half-filled t_{1u}-derived conduction band [37].

The structures of stable phases that form at the compositions M_1C_{60}, M_3C_{60}, M_4C_{60} and M_6C_{60} are shown in Fig. 12.7. In the M_1C_{60} phase, observed for M = Na, K, Rb and Cs, the alkali ions occupy octahedral sites, thereby forming a rock salt (NaCl) crystal structure [40]. This phase is stable only in a limited range of temperatures (410–460 K). The reported lattice constants for $K_{1.4}C_{60}$ (26.59 a.u.), $Rb_{0.9}C_{60}$ (26.61 a.u.), and Cs_1C_{60} (26.68 a.u.), are a little smaller than that for the pure C_{60} solid (26.78 a.u.). The rock salt structure becomes distorted to a pseudo body centered orthorhombic phase when it is cooled below $\approx$ 373 K. For Rb_1C_{60} the lattice constants are $a = 17.808$ a.u., $b = 19.099$ a.u. and $c = 26.896$ a.u. The distance between C_{60}^- anions in the a direction is substantially reduced and the formation of polymeric chains of C_{60}^- molecules along that direction has been proposed for K_1C_{60} and Rb_1C_{60} [42]. The importance of this polymerized phase derives from the fact that

it is stable in air at ambient pressure, unlike all other alkali-doped C_{60} phases, which are highly reactive.
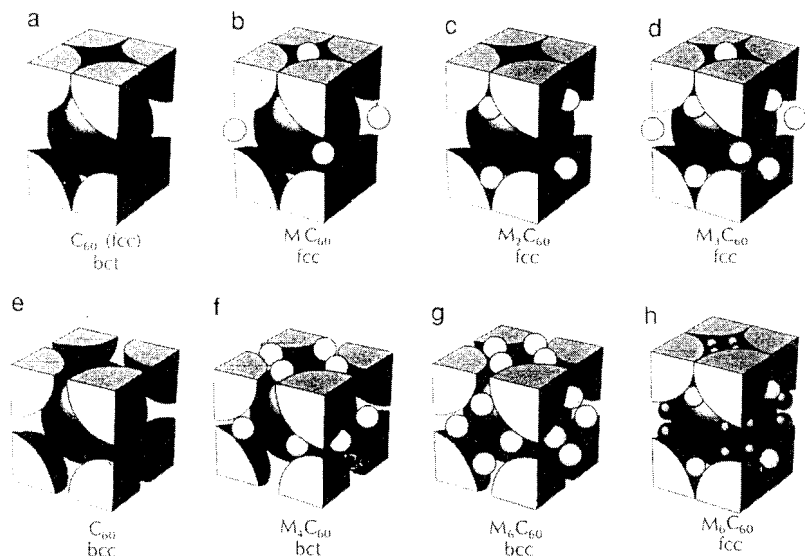
Figure 12.7. Crystal structure of pristine C_{60} and of alkali metal fullerites with compositions M_1C_{60}, M_2C_{60}, M_3C_{60}, M_4C_{60} and M_6C_{60}.

Superconductivity with a relatively high T_c has been discovered in the M_3C_{60} compounds (T_c (K_3C_{60}) = 19 K, and T_c (Rb_3C_{60}) = 30 K). The basic *fcc* structure of the M_3C_{60} phase is given in panel (d) of Fig. 12.7. The alkali ions occupy either tetrahedral or octahedral sites. The tetrahedral sites are twice as numerous as the octahedral ones. The phase M_2C_{60} results from the occupation of only the tetrahedral sites (see panel (c)), and the phase M_1C_{60} from the occupation of the octahedral sites only. In the BCS theory of superconductivity the transition temperature is given as

$$k_B T_c = 1.13 \ \omega_{ph} e^{-1/N(E_F)V} \tag{12.5}$$

where ω_{ph} is an average phonon frequency for mediating electron pairing, $N(E_F)$ is the density of electronic states at the Fermi level and V is the superconducting pairing interaction. This formula indicates that higher values of T_c can be achieved by increasing $N(E_F)$. The high density of states at the Fermi level for doped fullerenes occurs because of the predominantly molecular nature of this solid, which results in narrow electronic bands in K_3C_{60} in Rb_3C_{60} (widths of 0.5–0.6 eV). By introducing NH_3 molecules in the Na_2CsC_{60} compound to form the ternary compound $(NH_3)_4Na_2CsC_{60}$ the lattice constant changes from 26.705 a.u. to 27.350 a.u. As a result the density of states at the Fermi level increases and T_c increases from 10.5 to 29.6 K [43].

The phase M_4C_{60} is difficult to prepare and has a body centered tetragonal (*bct*) structure (see panel (f)). Theoretical calculations have predicted metallic character, but the experiments show semiconducting behavior. The maximum alkali content is achieved at M_6C_{60}. A *bcc* structure is found for M = K, Rb and Cs (see panel (g)). Six electrons are transferred to each C_{60} molecule, giving C_{60}^{6-} anions. This leads to a filled t_{1u}-derived band and a solid with semiconducting behavior, in agreement with experiment [44].

12.4.4 Melting in assemblies of C_{60} clusters

There are numerous computer simulations devoted to clarifying the existence, or otherwise, of a liquid phase of the fullerite [45]. Most of those works have used a model of rigid fullerenes with intermolecular interactions described by the potential of Girifalco [46]. This potential was derived by assuming a Lennard–Jones (LJ) pair interaction between atoms on different C_{60} molecules and averaging the carbon atom distributions so as to have a uniform density of carbon atoms over the fullerene surface. The intermolecular potential between two C_{60} units then takes the following analytical form

$$U(s) = -\alpha \left[\frac{1}{s(s-1)^3} + \frac{1}{s(s+1)^3} - \frac{2}{s^4} \right]$$
$$+ \beta \left[\frac{1}{s(s-1)^9} + \frac{1}{s(s+1)^9} - \frac{2}{s^{10}} \right] \tag{12.6}$$

where $s = r/2R$, r being the separation between the centers of the two interacting spheres and R their radius ($R = 6.71$ a.u.). The parameters $\alpha = 4.67735 \times 10^{-2}$ eV and and $\beta = 8.48526 \times 10^{-5}$ eV were determined by fitting the sublimation energy and the lattice constant of the bulk crystal. The critical point thermodynamic constants T_c (critical temperature), p_c (critical pressure) and molecular number density ρ_c obtained from Monte Carlo simulations using the Girifalco potential have the values $T_c = 1980$ K, $p_c = 38$ bar and $\rho_c = 0.44$ molecules/nm^3, and the triple point occurs at $T_t = 1880$ K, supporting the existence of a stable liquid phase over a narrow range of about 100 K. The critical compressibility ratio

$$Z_c = \frac{p_c}{\rho_c k_B T_c} \tag{12.7}$$

has a value of 0.32 [47], similar to the value 0.29 for the heavier condensed rare gases Ar, Kr and Xe. This is not surprising, for it is well known that a Lennard–Jones potential describes realistically the weak interaction between rare gas atoms. In contrast Z_c varies significantly through the five alkali metals [48], and for all of them the compressibility ratio is substantially lower than the above value of 0.29.

A further property of the liquid C_{60} phase is the shape of the coexistence curve. The high temperature phase diagram in the T–ρ plane is given in Fig. 12.8. Considering the difference $\rho_l - \rho_g$ between liquid and gas densities, scaled with the critical density ρ_c, along the coexistence curve, that is the variable

$$\eta = \frac{\rho_l - \rho_g}{\rho_c} \tag{12.8}$$

and also the average

$$\xi = \frac{\rho_l + \rho_g}{\rho_c}, \tag{12.9}$$

a good fit is obtained by the relation

$$\xi = 1 + 0.0164 \, \eta^3 \tag{12.10}$$

and one can notice a nearly perfect agreement of (12.10) with the empirical relation valid for insulating fluids like neon and ethylene [49].

C_{60} molecules have internal degrees of freedom, and some account of this fact is made in the study of Broughton, Lill and Johnson [50], who used a model of non-rigid C_{60} spheres in which a low frequency breathing mode was introduced. Then the total potential energy of the system was written as the sum of C_{60}–C_{60} interactions, described by a potential similar to the Girifalco potential (but with C_{60} spheres of variable radii), plus a term representing the breathing of non-rigid C_{60} molecules. No stable liquid phase was found in this model of non rigid spheres, but it proved possible to make predictions of some properties of a metastable liquid phase.
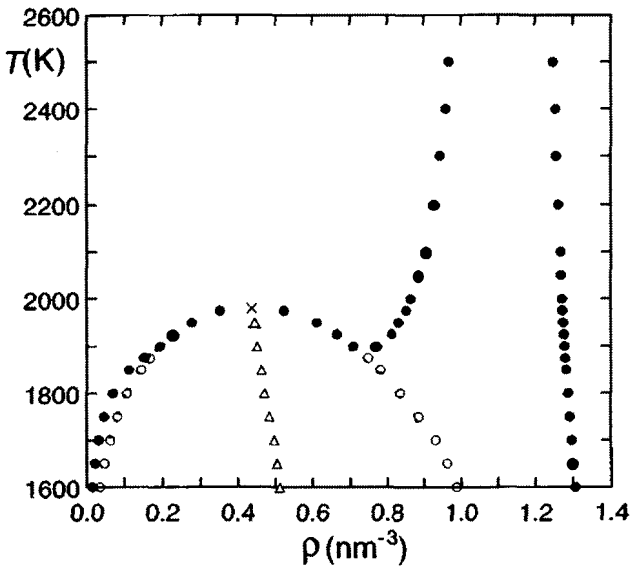
Figure 12.8. High temperature phase diagram of liquid C_{60}. Filled circles represent the stable phase boundary, open circles the metastable liquid–vapor binodal points and open triangles the mean density of the coexisting liquid and vapor. The cross in the middle is the liquid–vapor critical point. Adapted from M. Hasegawa and K. Ohno, *J. Chem. Phys.* **111**, 5955 (1999) with permission of the American Institute of Physics.

The very question of the thermal stability of the C_{60} molecules has a crucial influence on the practical observability of a stable or metastable C_{60} liquid. Experiments [51] indicate that in the gas phase under equilibrium conditions, the stability of C_{60} is limited to 1100–1200 K. The characteristic time scales for decomposition at temperatures $T =$ 1720–1970 K are in the millisecond range [52]. The heating of solid fullerite [53, 54] also leads to the decomposition of the material into amorphous carbon and graphite at temperatures $T =$ 1000–1300 K. In these solid state experiments the reaction took minutes to complete.

Two physical processes are responsible for the decomposition of the solid C_{60}. The first one is the reaction between neighbor molecules in solid fullerite, that becomes facilitated at high temperatures by the formation of local structural defects, like open windows, in the carbon cage [55]. The second physical process responsible for the thermal instability of fullerene materials in the gas or condensed phases concerns the isolated C_{60} molecules. The analysis of Matt *et al.* [21] has been able to reconcile the results of experiment and theory for the energy required to fragment the C_{60} molecule (into C_{58} and C_2). This fragmentation energy is about 10 eV. For a gas of C_{60} molecules in equilibrium with a vibrational temperature of 2000 K, the energy stored in the molecule is about 29 eV (or 14.5 eV for a vibrational temperature of 1000 K). Those excitation energies are high enough to allow, in principle, for the statistical fragmentation of the molecule in sufficiently large time scales. The two physical processes just discussed point towards the practical difficulties of heating solid fullerite to temperatures in the range where the hypothetical liquid C_{60} phase could be stable (roughly between 1900 K and 2000 K). If the fullerite solid could be fastly heated to those temperatures, the liquid phase will only be stable for a short time before the molecules begin to decompose. Those characteristics make that liquid certainly peculiar and difficult to observe.

The melting temperatures of low dimensional systems, *i.e.*, surfaces and clusters, are in general lower than those of the corresponding bulk materials. The open surfaces of the *fcc* fullerite, for instance the (1,1,0) surface, and also small clusters of C_{60} molecules are then good candidates for exhibiting melting temperatures lower than that of the bulk fullerite, and, eventually, lower than the decomposition temperature of C_{60} molecules. Therefore, liquid C_{60} could perhaps be observed in those low-dimensional systems. Indeed, it has been shown through

molecular dynamics simulations using the Girifalco potential that $(C_{60})_7$ clusters (where all the molecules are at the cluster surface) exhibit a solid-like to liquid-like phase transition with a melting temperature of about 600 K, well below the decomposition temperature of C_{60} molecules [56].

12.5 Simulations of the Assembling of Doped Aluminum Clusters to Form Clustered Materials

12.5.1 $Al_{12}X$ clusters with 40 valence electrons

It has been suggested that doped icosahedral clusters $Al_{12}X$ where X is an element of the carbon column in the Periodic Table, could be good candidates for forming cluster assembled materials [3]. As discussed in Section 7.6, the clusters of this family have 40 electrons in a closed shell configuration which is associated with high stability. Khanna and Jena [3] used DFT to construct the interaction potential curve between two tetrahedral Mg_4 clusters (the Mg_4 cluster is also a closed shell species with 8 electrons). Partial relaxation of the tetrahedral geometry was allowed as the two clusters approached each other, although the condition of individuality of the two clusters was imposed. With these constraints a weak attractive potential well (0.2 eV deep) was found and based on this result Khanna and Jena speculated that stable and symmetrical $Al_{12}Si$ and $Al_{12}C$ closed shell clusters might interact weakly when assembled into a solid.

This suggestion was investigated by Nieminen and coworkers [57]. As a first step, $Al_{12}Si$ rigid icosahedral clusters were assembled on a face centered cubic lattice and the equilibrium lattice constant was found by minimizing the total energy. A binding energy with respect to separated clusters of 6.1 eV per cluster was obtained for this minimum energy structure, but there was no energy gap in the density of states at the Fermi level and the system appeared to be metallic. In addition, the equilibrium lattice parameter was so small that the shortest intercluster Al–Al distance was less than the intracluster Al–Al bond length. Next, full relaxation of the atomic positions was allowed, and when equilibrium had been achieved the shortest Al–Al bonds had increased to

5.12 a.u. and open regions of the unrelaxed cluster lattice were more filled. The clusters had merged and the short-range atomic order indicated that the atoms had moved towards a close packed arrangement. Similar conclusions were reached for simulations with $Al_{12}C$: again it was found that although the isolated clusters were very stable, the *fcc* solid composed of $Al_{12}C$ clusters was unstable against melting when the atoms were allowed to rearrange individually [58].
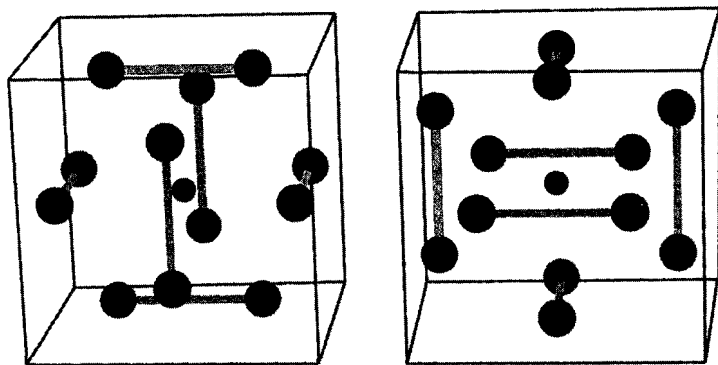
Figure 12.9. Relative orientation of neighbor clusters in the assembling of a solid of $Al_{12}C$ clusters. The C atom is the small sphere at the center of each cluster. Reproduced from X. C. Gong, *Phys. Rev. B* **56**,1091 (1997) with permission of the American Physical Society.

A simulation which successfully achieved cluster assembled $Al_{12}C$ and $Al_{12}Si$ solids was reported by Gong [59]. The electron density of $Al_{12}C$ is not spherical; there are protrusions and indentations. Taking account of these asymmetries in the electron densities of the isolated clusters, Gong designed a cubic-like structure with eight clusters per unit cell in which each cluster is oriented 90° with respect to all its near neighbors. The orientation of the clusters is illustrated in Fig. 12.9 . In this structure the overlap of the electron densities of neighboring clusters, shown in Fig. 12.10, is reduced compared to the overlap for a *fcc* structure. The equilibrium structure was found by minimizing the total energy, and the resulting solid had a small cohesive energy of ≈ 1.1

eV per cluster, implying that the $Al_{12}C$ and $Al_{12}Si$ clusters are condensed by a rather weak force.
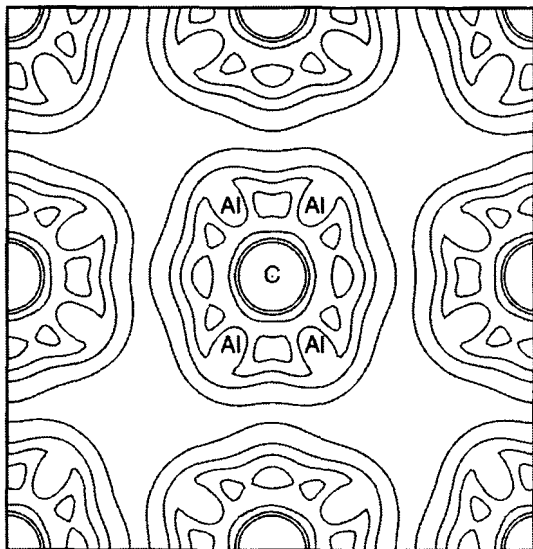
Figure 12.10. Contour map of the electron density in a (001) plane for the solid assembled from $Al_{12}C$ clusters. Reproduced from X. C. Gong, *Phys. Rev. B* **56**, 1091 (1997) with permission of the American Physical Society.

The clusters retained their identity in the solid, with the shortest intercluster Al–Al distance being much longer than the Al–Al intracluster bond length or the nearest neighbor distance in bulk aluminum. A molecular dynamics simulation of the solid at a temperature near 20 K provided a further check of the stability. Apart from vibrational motion of the atoms, the icosahedral structure of the $Al_{12}C$ clusters was unchanged during the 1.1 ps duration of the MD run.

12.5.2 Assembling of $Al_{13}H$ clusters

$Al_{13}H$, discussed in Section 7.6, is a very stable cluster having 40 valence electrons. The study of the $(Al_{13}H)_2$ dimer provides insight on the

assembling of these clusters [7, 60]. Figure 12.11 shows two isomers characterized by different relative orientations of the two Al_{13} units. On the left panel (isomer A) the clusters are oriented along a common C_{3v} symmetry axis of the icosahedron, but one of them is rotated 180 degrees with respect to the other around that axis. That is, the two clusters have parallel faces in contact, rotated 180 degrees one relative to the other.
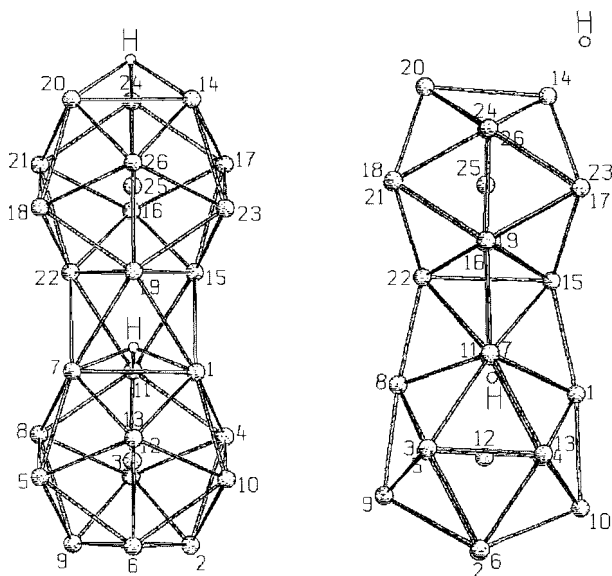
Figure 12.11. Two isomers of the $(Al_{13}H)_2$ dimer, characterized by different relative orientations of the two icosahedra. The binding energies with respect to the two separated $Al_{13}H$ clusters are 1.74 eV and 3.03 eV for the isomers on the left and right sides, respectively. Reproduced from F. Duque *et al.*, *Int. J. Quantum Chem.* **86**, 226 (2002) with permission of Wiley.

The potential energy of the dimer was calculated, for frozen cluster geometries, as a function of the cluster–cluster distance, and the energy minimum was obtained for a distance $R_m = 15.74$ a.u. between the centers of the clusters. For that minimum, the dimer was then subjected to a relaxation of all the atomic coordinates and the structure obtained, which is the one on the left panel in Fig. 12.11, shows that the identity of the clusters is preserved in the dimer. The binding energy of the dimer

with respect to the separated clusters is 1.74 eV. Similar calculations were performed for the clusters in the configuration given on the right panel of the same figure (isomer B). In that case the orientation of the clusters is such that the C_{2v} symmetry axis of each icosahedron coincides with the dimer axis and one of the clusters is rotated 90 degrees with respect to the other about that axis. In this configuration the clusters have edges in contact, perpendicular to each other. The equilibrium separation between the cluster centers is nearly the same for isomers A and B, but the interaction for isomer B is more attactive (the relaxed dimer structure has a binding energy of 3.03 eV) and at the same time the short-range repulsive wall rises more steeply. Thus, the relative orientation of the two clusters in isomer B appears to be more favorable for the purposes of cluster assembling. A similar structure with perpendicular contact edges was found to be the ground state of the pure $(Al_{13})_2$ dimer in the pair potential calculations of Sun and Gong [1]. The stability of the dimer suggests to investigate the possibility of forming linear nanowires from those clusters.

For the simulation of the self-assembling of a material from $Al_{13}H$ clusters [7, 60], the optimal relative cluster–cluster orientation found in $(Al_{13}H)_2$ suggests a favorable structure for the assembled solid similar to that in Fig. 12.9, such that neighbor clusters have edges in contact perpendicular to each other. This condition leads to a cubic lattice. The 12 surface atoms of the icosahedron, joined in pairs, have been arranged in Fig. 12.9 on the six faces of a cube. Each cluster has six nearest neighbor clusters with the optimal orientation. The energy of the assembled solid was first calculated as a function of the lattice constant, maintaining the structure of the clusters frozen. A curve with two minima was obtained. The outer minimum occurs with a large lattice constant of 32 a.u. and a small binding energy with respect to the isolated clusters of only 0.35 eV per cluster. A similar minimum was found by Gong in the simulations of the assembling of $Al_{12}C$ and $Al_{12}Si$ clusters. The lattice constant for the more relevant inner minimum is 24.2 a.u. and the assembled solid has metallic character, but the density of states is very different from that of bulk aluminum. In that arrangement the distances between Al atoms in neighboring clusters are comparable to the intracluster Al–Al distances. The gain in binding energy by the assembling is 15 eV per cluster, and this value is about one third of the internal binding energy of the free $Al_{13}H$ cluster. This

fraction is similar to that found earlier for the assembling of the Pb–alkali clusters. In contrast, that ratio is one order of magnitude smaller in the fullerite. The stability of the assembled solid was tested by performing molecular dynamics simulations at 150 K and duration of 3 ps and the results indicate that the assembled material is stable under those conditions, that is, the icosahedral units retain their structure with only moderate distortions. The main effect of the temperature is to allow for the migration of the H atoms to interstitial regions between the clusters. Similar dynamical simulations were performed for the assembling of the clusters in an *fcc*-type lattice, where each cluster is surrounded by twelve neighbor clusters and the optimal relative orientation is then lost. In this case the clusters do not retain their individual character and coalesce. These simulations support the idea that an optimized relative orientation of the clusters is a favorable condition for a successful assembling. This optimization can only be achieved for certain lattices.

12.5.3 Assembling of superionic cluster-solids

In the previous section it has been discussed how the attachment of a H atom to the Al_{13} cluster produces a very stable closed shells cluster with 40 electrons. Another way of achieving the same goal is by attaching an alkaline atom like K, Rb or Cs. The highly electronegative Al_{13} cluster behaves as a halogen atom and the $Al_{13}K$, $Al_{13}Rb$ or $Al_{13}Cs$ species can be viewed as ionic supermolecules $Al_{13}^-K^+$, $Al_{13}^-Rb^+$ and $Al_{13}^-Cs^+$, respectively. Since typical alkali halide molecules form ionic crystals with the NaCl (rock salt) or the CsCl structures, Khanna and Jena have proposed forming a new class of ionic crystals based on these supermolecules [61]. Total energy calculations have been performed for an $Al_{13}K$ solid assuming a CsCl-like superstructure, that is, two interpenetrating cubic lattices where each Al_{13}^- anion is surrounded by eight K^+ cations forming a cube, and vice versa [62]. For large lattice constants the internal structure preferred for the Al_{13} was the familiar icosahedron but it changed to a cuboctahedron as the lattice constant approached to the energy minimum. Connecting with the ideas exposed in Section 12.2, the alkali cations can also be considered as playing the role of keeping apart the large anions. However, the separation between the anions is not large enough and the Al_{13} units in different cages form

metallic bonds, indicating that the solid is less ionic than expected. In fact, due to the cuboctahedral structure of the Al_{13} units, the metastable assembled solid ressembles *fcc* Al.

An improved proposal started with the cluster $(BAl_{12})Cs$ [63]. In the ground state of the BAl_{12} cluster the B atom occupies the central position of the icosahedron. The choice of this cluster instead of Al_{13} was motivated by the fact that BAl_{12} is more stable (the binding energy per atom is 0.27 eV higher) because the smaller size of the B atom relaxes the surface strain in the icosahedron. In addition the ionic radius of Cs^+ is larger than the radius of K^+, so the anions are separated more efficiently. The calculated total energy of a solid with the CsCl structure built from $(BAl_{12})^-$ and Cs^+ units shows a minimum as the lattice constant is decreased. Further reduction of the lattice constant induces a change of the internal structure of $(BAl_{12})^-$ from icosahedral to cuboctahedral and a new minimum appears, only marginally more stable than the other. An interesting feature is that the two minima are separated by an energy barrier of about 0.3 eV, and Jena and coworkers suggested that it might be possible to assemble a $(BAl_{12})Cs$ solid with icosahedral subunits. In the related case of $(BAl_{12})Li$ the structure of the (BAl_{12}) unit is cuboctahedral (*fcc*) for all separation distances of interest [64]. At equilibrium, the assembled solid is metallic and can be considered as Al-like with B and Li impurities, and not as a solid of clusters. This could be expected from the small ionic radius of Li. On the other hand this result opens up a new possibility: the use of clusters to produce metastable crystalline or amorphous solids difficult to synthesize by standard methods. One may imagine extending the solid solubility of an impurity element on a host metal greatly over its equilibrium value, or even building new ordered intermetallic compounds.

References

1. Sun, D. Y., and Gong, X. G., *Phys. Rev. B*, **54**, 17051 (1996).
2. Kratschmer, W., Lamb, L. D., Fostiropoulos, K., and Huffman, D. R., *Nature*, **347**, 354 (1990).
3. Khanna, S. N., and Jena, P. *Phys. Rev. Lett.*, **69**, 1664 (1992).

4. Whetten, R. L., Koury, J. T., Alvarez, M., Murthy, S., Vezmar, I., Wang, L., Stephens, P. W., Cleveland, C. L., Luedtke, W. D., and Landman, U., *Adv. Materials.*, **8**, 428 (1996).
5. Van der Lugt, W., *J. Phys. : Condens. Matter*, **8**, 6115 (1996).
6. Alonso, J. A., Molina, L. M., López, M. J., Rubio, A., and Stott, M. J., *Chem. Phys. Lett.* **289**, 451 (1998).
7. Duque, E., Mañanes, A., Molina, L. M., López, M. J., and Alonso, J. A., *Int. J. Quantum Chem.*, **86**, 226 (2002).
8. Molina, L. M., López, M. J., Rubio, A., Alonso, J. A., and Stott, M. J., *Int. J. Quantum Chem.*, **69**, 341 (1998).
9. Yeretzian, C., Röthlisberger, U., and Schumacher, E., *Chem. Phys. Lett.*, **237**, 334 (1995).
10. Jinlong, Y., Kaiming, D., Chuanyun, X., and Kelin, W., *Phys. Rev. B*, **55**, 13293 (1997).
11. Molina, L. M., Alonso, J. A., and Stott, M. J., *J. Chem. Phys.*, **111**, 7053 (1999).
12. Housecroft, C. E., Ed, *Boranes and Metalloboranes*, John Wiley, New York (1990).
13. Emin, D., *Phys. Today*, Jan. 1997, p. 56.
14. La Placa, S. J., Roland, P. A., and Wynne, J. J., *Chem. Phys. Lett.*, **190**, 163 (1992).
15. Boustani, I., *Phys. Rev. B*, **55**, 16426 (1997).
16. Zhai, H. J., Kiran, B., Li, J, and Wang, L. S., *Nature Materials*, **2**, 827 (2003)
17. Perkins, C. L., Trenary, M., and Tanaka, T., *Phys. Rev. Lett.*, **77**, 4772 (1996)
18. Oku, T., *Solid State Commun.*, **127**, 689 (2003).
19. Xu, S. J., Nilles, J. M., Radisic, D., Zheng, W. J., Stokes, S., Bowen, K. H., Becker, R. C., and Boustani, I., *Chem. Phys. Lett.*, **379**, 282 (2003).
20. Branz, W., Malinowski, N., Enders, A., and Martin, T. P., *Phys. Rev. B*, **66**, 94107 (2002).
21. Matt, S., Echt, O., Scheier, P., and Märk, T. D., *Chem. Phys. Lett.*, **348**, 194 (2001).
22. Martin, T. P., Näher, U., Schaber, H., and Zimmermann, U., *Phys. Rev. Lett.*, **70**, 3079 (1993).
23. Hansen, K., Hohmann, H., Müller, R., and Campbell, E. E. B., *J. Chem. Phys,.* **105**, 6088 (1996); Hansen, K., Müller, R., Hohmann, H., and Campbell, Z. *Phys. D*, **40**, 361 (1997).
24. Doye, J. P. K., and Wales, D. J., *Chem. Phys, Lett.*, **262**, 167 (1996).
25. García-Rodeja, J., Rey, C., and Gallego, L. J., *Phys. Rev. B*, **56**, 6466 (1977).
26. Zhang, W., Liu, L., Zhuang, J., and Li, Y., *Phys. Rev. B*, **62**, 8276 (2000).
27. Doye, J. P. K., Wales, D. J., Branz, W., and Calvo, *Phys. Rev. B*, **64**, 235409 (2001).

28. Doye, J. P. K., Wales, D. E., and Berry, R. S., *J. Chem. Phys.* **103**, 4234 (1995).
29. Branz, W., Malinowski, N., Schaber. H., and Martin, T. P., *Chem. Phys. Lett.*, **328**, 245 (2000).
30. Pacheco J. M., and Prates-Ramalho, J. P., *Phys. Rev. Lett.,* **79**, 3873 (1997).
31. Axilrod, B. M., and Teller, E., *J. Chem. Phys.* **11**, 299 (1943).
32. Marks, L. D., *Philos. Mag. A*, **49**, 81 (1984).
33. Leary, R. H., and Doye, J. P. K., *Phys. Rev. E*, **60**, 6320 (1999).
34. Baletto, F., Doye, J. P. K., and Ferrando, R., *Phys. Rev. Lett.*, **88**, 75503 (2002).
35. Kroto, H., Heath, J. R., O'Brien, S. C., Curl, R. F., and Smalley, R. E., *Nature*, **318**, 162 (1985).
36. Dresselhaus, M. S., Dresselhaus, G., and Eklund, P. C., *Science of Fullerenes and Carbon Nanotubes*, Academic Press, San Diego (1996).
37. Johnson, R. D., Bethune, D. S., and Yannoni, C. S., *Acc. Chem. Res.*, **25**, 169 (1992).
38. Rao, A. M., and Eklund, P. C., *Cluster Assembled Materials*, Ed. K. Sattler, *Materials Science Forum*, Vol. 232, Trans Tech. Publ. Zurich (1996), p. 173.
39. Verheijen, M. A., Meekes, H., Meijer, G., Bennema, P., de Boer, J. L., van Smaalen, S., Tendeloo, G. V., Amelinckx, S., Muto, S., and van Landuyt, J., *Chem. Phys.*, **166**, 287 (1992).
40. Fischer, J. E., and Heiney, P. A., *J. Phys. Chem. Solids*, **54**, 1725 (1993).
41. Fischer, J. E., *Mater. Sci. Eng. B*, **19**, 90 (1993).
42. Stephens, P. W., Bortel, G., Falgel, G., Tegze, M., Jánossy, A., Pekker, S., Oszanyi, G., and Forró, L., *Nature*, **370**, 636 (1994).
43. Zhou, O., Fleming, R. M., Murphy, D. W., Rosseinsky, M. J., Ramirez, A. P., van Dover, R. V., and Haddon, R. C., *Nature*, **362**, 433 (1993).
44. Gu, C., Stepniak, F., Poirier, D. M., Jost, M. B., Benning, P. J., Chen, Y., Ohno, T. R., Martins, J. L., Weaver, J. H., Fure, J., and Smalley, R. E., *Phys. Rev. B*, **45**, 6348 (1992).
45. Hasegawa, M., and Ohno, K., *J. Chem. Phys.*, **111**, 5955 (1999).
46. Girifalco, L. A., *J. Phys. Chem.*, **96**, 858 (1992).
47. Alonso, J. A., López, M. J., March, N. H., and Lamoen, D., *Phys. Chem. Liq.*, **409**, 457 (2002).
48. Chapman, R. G., and March, N. H., *Phys. Chem. Liq.*, **16**, 77 (1986).
49. March, N. K., Tosi, M. P., and Chapman, R. G., *Phys. Chem. Liq.*, **18**, 195 (1988).
50. Broughton, J. Q., Lill, J. V., and Johnson, J. K., *Phys. Rev. B*, **55**, 2808 (1997).
51. Frum, C. L., Engleman, R., Hedderich, H. G., Bernath, P. F., Lamb, L. D., and Hoffman, D. R., *Chem. Phys. Lett.*, **176**, 504 (1991).
52. E. Kolodney, E., Tsipinyuk, B., and Budrevich, A., *J. Chem. Phys.* **100**, 8542 (1994).

53. Leifer, S. D., Goodwin, D. G., Anderson, M. S., and Anderson, J. R., *Phys. Rev. B*, **51**, 9973 (1995).
54. Stetzer, M. R., Heiney, P. A., Fischer, J. E., and McGhie, A. R., *Phys. Rev. B*, **55**, 127 (1997).
55. Marcos, P. A., Alonso, J. A, Rubio, A., and López, M. J., *Eur. Phys. J. D*, **6**, 221 (1999).
56. Gallego, L. J., García-Rodeja, J., Alemany, M. M. G., and Rey, C., *Phys. Rev. Lett.*, **83**, 5258 (1999).
57. Seitsonen, A. P., Puska, M. J., Alatalo, M., Nieminen, R. M., Milman, V., and Payne, M. C., *Phys. Rev. B* , **48** , 1981 (1993).
58. Seitsonen, A. P., Laaksonen, K., Nieminen, R. N., and Klein, M. L., *J. Chem. Phys.*, **103**, 8075 (1995).
59. Gong, X. G., *Phys. Rev. B*, **56** ,1091 (1997).
60. Duque, E., Molina, L. M., López, M. J., Mañanes, A., and Alonso, J. A., *Eur. Phys. J. D,* **16**, 285 (2001).
61. Khanna, S. N., and Jena, P., *Chem. Phys. Lett.*, **219**, 497 (1994).
62. Liu, F., Mostoller, M., Kaplan, T., Khanna, S. N., and Jena, P., *Chem. Phys. Lett.*, **248**, 213 (1996).
63. Ashman, C., Khanna, S. N., Liu, F., Jena, P., Kaplan, T., and Mostoller, M., *Phys. Rev. B*, **55**, 15868 (1997).
64. Zhu, Z. and Tian, B., *Solid State Commun.*, **108**, 891 (1998).

Index